

# nature

## SEEING RED

Submillimetre-scale gravitational redshift within an atomic clock



**Explosive power**  
The shocking science behind the Tongan volcanic eruption

**Coronavirus**  
Why has disability been left out of COVID discussions?

**Sound connections**  
Inner-ear anatomy affirms evolutionary tree of bats

# Nature.2022.02.19

[Sat, 19 Feb 2022]

- [This Week](#)
- [News in Focus](#)
- [Opinion](#)
- [Work](#)
- [Research](#)
- [Amendments & Corrections](#)

# This Week

- **[Eric Lander's resignation for bullying raises questions for the White House](#)** [ 15 February 2022]  
Editorial • The US science adviser had to go. The White House should assess how it deals with wrongdoing and consider a deeper examination of its scientific advisory system.
- **[Biden needs scientists with policy chops](#)** [ 11 February 2022]  
World View • Research eminence alone is not enough for top science posts.
- **[Retina-like sensors give machines better vision](#)** [ 08 February 2022]  
Research Highlight • Semiconductor-based devices that adapt to a wide range of light intensities could prove useful in self-driving vehicles and assembly lines.
- **[Puzzling spikes in ozone-eating chemical have a fiery cause](#)** [ 09 February 2022]  
Research Highlight • Scientists trace variation in methyl bromide levels to an increase in fires — which are linked to the climate pattern El Niño.
- **[Mini-DNA strands knock macroscale blocks into shape](#)** [ 10 February 2022]  
Research Highlight • Gel blocks up to 2 millimetres long are the biggest structures yet to be brought to order by microscopic lengths of DNA.
- **[Hundreds of strange filaments twist through the Galaxy's centre](#)** [ 07 February 2022]  
Research Highlight • Long structures that emit brilliant radio waves cannot be easily explained.
- **[A reindeer's yearning to travel can be read in its genes](#)** [ 10 February 2022]  
Research Highlight • The fingerprint of the last ice age can still be seen in the genomes of reindeer that make long migrations.
- **[Petrified puke shows that ancient winged reptiles purged](#)** [ 09 February 2022]  
Research Highlight • Pterosaurs, prehistoric beasts that lived alongside the dinosaurs, not only flew like birds, but also vomited like them.

- **Global survey finds scientists have more credibility than spiritual leaders** [ 07 February 2022]

Research Highlight • A lofty-sounding but vapid statement carried more weight with participants when they were told it came from a scientific source.

- EDITORIAL
- 15 February 2022

# Eric Lander's resignation for bullying raises questions for the White House

The US science adviser had to go. The White House should assess how it deals with wrongdoing and consider a deeper examination of its scientific advisory system.



Eric Lander soon after being nominated to be US science adviser in January 2021.Credit: Matt Slocum/AP/Shutterstock

When US President Joe Biden tapped the now-disgraced Eric Lander to be his science adviser, the grass-roots organization 500 Women Scientists wrote in *Scientific American* that “his nomination does not fill us with hope that he

will shepherd the kind of transformation in science we need if we are to ensure science delivers equity and justice for all”.

This and other warnings turned out to be prescient. Last week, Lander, whose position includes the role of director of the Office of Science and Technology Policy (OSTP), was forced out after it became public that an internal investigation had found that he had bullied and demeaned staff.

When a cabinet member heads for the exit because of wrongdoing, the person at the top will almost invariably utter the immortal words ‘lessons will be learnt’ before swiftly moving to appoint or announce a successor or, at the very least, an acting leader.

Alongside [considering successors to Lander](#), the Biden administration has some explaining to do. A number of major questions urgently need answering: why and how was bullying tolerated, especially considering the president’s assertion in early 2021 that he would fire anyone caught treating people with disrespect on the spot? Should this not have happened in Lander’s case, once the investigation into his behaviour was complete and the findings became known to the White House?

The administration also needs to explain why the existence of the investigation was not made public. Lander was allowed to stay on to try to resolve his behaviour — until the magazine *Politico* revealed that there had been an investigation and made its findings public. Does that mean we would never have known without the media’s reporting?

Another urgent question is whether whistle-blowers are being properly supported. It takes courage to come forwards and report misbehaviour at the top of an organization; when the person misbehaving is the head of an office in the White House, and reports to the president of the United States, it takes monumental courage.

Appointments to the government should require hefty due diligence. Was something remiss with that process? Lander was questioned about previous controversies during Senate confirmation hearings in April. For example, he had to apologize for understating the contributions of Jennifer Doudna and Emmanuelle Charpentier, who both helped to pioneer CRISPR gene-editing

technology, in an essay published in *Cell* called ‘The Heroes of CRISPR’ ([E. S. Lander \*Cell\* 164, 18–28; 2016](#)). Nevertheless, many in the scientific community — including *Nature* — still applauded Biden’s choice and [urged his team to pull together](#).

Finally, there is a question that needs to be asked about the role itself. Does a scientific advisory structure that is built around one individual’s leadership and their access to the president prevent the director from being held to the same standards expected of all other OSTP staff?

Researchers who study science and government are searching for answers to some of these questions. The White House should tap into their expertise.

## Channelling science

The United States, China, the European Union and Japan are among the world’s largest spenders on science and technology, and there are many similarities between their respective science systems. But there are notable differences, too. The United States, for example, has no government ministry or department for science — instead, responsibility for different science-focused agencies is shared between the government’s executive and legislative branches. The OSTP is also unusual; most nations do not have an equivalent office.

The OSTP exists, in part, to channel the scientific community’s opinions to the nation’s leadership. It also helps to identify future funding priorities; promotes a president’s own science agenda; and helps the government with the process of setting budgets for different science agencies.

Another unusual feature of the United States’s system is that the president’s science adviser and OSTP head leaves their post when the party in government changes. In many other countries that have a comparable office — such as India, New Zealand and the United Kingdom — the adviser does not immediately leave their job when there is a change of government. In New Zealand, the scientific adviser’s terms of reference include being able to brief the leader of the opposition party. Sometimes, a nation’s chief

science adviser is one of a larger group of scientific advisers attached to different government ministries, such as defence or foreign affairs.

There are pros and cons to each approach. A long-standing attraction of the US system is that the scientific community has an advocate for science and evidence reporting to the White House. But the system invests a considerable degree of influence and responsibility in one person.

All of this suggests that there are good reasons for researchers who study science systems to evaluate how the United States organizes its scientific advice to the president, and to ask whether other models should be considered. For example, should the OSTP continue to be led by one person, or is a shared leadership model more desirable? Would such a model even be possible? Would it be appropriate, or feasible, for the scientific adviser to stay in position when administrations change? Could that help to ensure at least some continuity in advisory structures, and in policies, when there is a change of government? And what are the benefits of having a scientific adviser who is able to continue in office when a new party takes over?

Conversely, what are the potential risks and downsides to changing a system that has long been envied around the world? Finding answers to these questions will not be straightforward, but asking the questions could open up different routes to positive change.

## The cabinet question

Researchers point out that the structure of the US president's scientific advisory system is unusual in one other respect. Last year, Biden placed Eric Lander in his cabinet. In the absence of a department for science, this enables the scientific adviser to be directly involved in government decisions that need scientific input or that affect science. The move was hailed by many as a welcome step. After the damage wreaked by the Trump administration, it would lead to closer connections between the White House, the scientific community and the executive branch of government. But it also presented a challenge.

Many science-policy researchers say that an adviser should advise, propose or comment on policy choices on the basis of a thorough evaluation of the available evidence by members of the scientific community. But, on the whole, they should leave implementing policy to others, such as science funding agencies or the departments headed by cabinet ministers (or secretaries, as they are usually called in the United States). This is why it is unusual for a science adviser to sit in the cabinet, the role of which is to oversee the implementation of the government's decisions.

In November, however, two former chiefs of the National Institutes of Health, Harold Varmus and Elias Zerhouni, proposed the creation of a cabinet-level Department of Technology and Science Policy ([H. Varmus and E. Zerhouni \*Nature\* 600, 30–32; 2021](#)). Among other things, this department would represent science in the cabinet and would take responsibility for some policy implementation that currently rests with OSTP, including the creation of an Advanced Research Projects Agency for Health or a plan to create a new pandemic-preparedness agency.

Researchers in the fields of economics and innovation, political science, sociology, and science and technology studies have analysed governance structures and systems extensively, and have given much thought to the benefits and risks of different ways of organizing how science advice gets to governments. These studies are intended to help to reduce conflicts of interest, to ensure that the machinery of government continues to function when there are problems, and, increasingly, to look for creative ways to support equity and inclusion. The separation of powers between the executive, legislature and judiciary is a core principle in democratic governance. Researchers need to ask whether this principle should apply to science policy, too.

## Awaiting answers

With the polarizing debates over subjects from climate change to COVID-19 vaccines and lockdowns, science in the United States is experiencing one of its most politicized periods. At the same time, the pandemic has raised the need for, and the public profile of, scientific advisers to new heights.

Lander's resignation is the Biden administration's first cabinet-level fall. The White House needs to take great care in what it does next. There is undoubtedly pressure to appoint Lander's successor swiftly — names are already being suggested to ensure continuity and steady the ship.

But important questions remain to be answered. The White House must address questions about Lander's behaviour and the nature of the OSTP environment, in which his bullying was allowed to happen, and must explain how it is supporting those who bravely came forwards. Meanwhile, researchers should investigate broader concerns, including questions about the structure of the system. Once the administration starts to address the questions that we and others are raising, it will discover that there could be much to gain from changing more than just the person at the top.

*Nature* **602**, 361-362 (2022)

*doi:* <https://doi.org/10.1038/d41586-022-00409-8>

---

This article was downloaded by **calibre** from <https://www.nature.com/articles/d41586-022-00409-8>

| [Section menu](#) | [Main menu](#) |

- WORLD VIEW
- 11 February 2022

# Biden needs scientists with policy chops



Research eminence alone is not enough for top science posts.

- [Kenneth Bernard](#) 0

It has been a rough few years for science-policy leadership in the United States. During the administration of former president Donald Trump, science was demeaned and undermined.

President Joe Biden promised the opposite. Scientists would ensure, he said, that “everything we do is grounded in science, facts and truth”. His hires made good on his promise to put science first — perhaps to a fault. Senior leaders in government science policy require a trifecta of skills: research expertise, proficiency in the art of interagency policy coordination, and a deep knowledge of the legislative budgeting process. These last two are not

intuitive for academic scientists, no matter how intelligent, and they are hard to learn in a high-profile leadership position.

This month, the first cabinet-level director of the White House Office of Science and Technology Policy (OSTP) resigned after acknowledging he had mistreated his staff. The vacancy his departure leaves comes on top of others — one at the head of the National Institutes of Health, another at the Food and Drug Administration. In my view, Biden should consider appointing only those with demonstrated policy chops and a history of working well with others.

Mid-career, I learnt the hard way how essential policy expertise is to these roles. As the health attaché at the US mission representing the United States to the World Health Organization (WHO) in Geneva, Switzerland, in 1994, I jumped in at the deep end of international health — a quagmire of biomedicine, politics, policy and budgets. At the WHO, consensus ruled; I learnt that negotiation was a bellicose artform cloaked in diplomatic courtesies.

During the administration of president Bill Clinton, I became the US National Security Council's first health-policy adviser. I had my name on my office door and expected policymakers to seek me out. They didn't. My first visitor was a marine with a sprained ankle. After that, I removed the details of my degrees from my door and business cards, and found that people took me more seriously. Being a competent policymaker carried more influence than being known as an accomplished scientist.

In the wake of the terrorist attacks of 11 September 2001, I was senior biodefence adviser to president George W. Bush. At policy meetings, ‘principals’ sat around the table; technical experts like me sat in the back row. In one such meeting, vice-president Dick Cheney proposed a national mass vaccination campaign to stymie potential terrorist attacks with smallpox virus. Unlike very safe modern vaccines, the older smallpox vaccine causes frequent and sometimes serious adverse reactions. Bush asked the scientists how many people would die. At least 300, we said. The president rejected the proposal on the spot. We'd done our job and he had done his; he had made a policy decision by weighing up the science-based risks versus the uncertain benefits.

Policy expertise is a skill acquired over time. Biden's chief of staff, Ron Klain, was the Ebola tsar during the administration of president Barack Obama. Although not an expert on disease, he surrounded himself with those who were and listened to them. His success came from how adeptly he could integrate research evidence with the demands of complicated public-health policy and legislative budgeting. (Policy without a budget is merely window dressing.)

Senior scientists need hands-on government-policy experience before they are placed in demanding leadership roles. Jane Lubchenco, the current deputy director for climate and the environment at the OSTP, has held several mid-level policy posts alongside her positions in academia. I'd like to see many more early- and mid-career scientists doing stints in policy jobs. (The science and technology policy fellowships offered by the American Association for the Advancement of Science and similar programmes perform a real national service.)

A policy decision is a complex political calculus of risks and benefits, and scientific evidence is just one input. The COVID-19 pandemic has forced the intersection of science and policy into a harsh spotlight for which it was ill-prepared. Scientists do science well, policymakers do policy well; few are fluent in both.

To be clear, senior scientists who make policy are not usually the same people who have scientific-advisory roles. Blurring the roles can undermine scientific credibility. That conflation underlies many problems of the US response to COVID-19, with scientists pulled out of their academic comfort zones and dropped into big policy jobs.

An example of a scientist who successfully informs policymakers is Anthony Fauci. Over the past forty years, he has advised every US president since Ronald Reagan. A big reason for his success is his deep scientific knowledge; a bigger reason is that he respects the distinction between scientific evidence and policymaking. The disgraceful personal attacks on Fauci in recent months were not the result of his superb explanations of the SARS-CoV-2 pandemic; they came after he was pressed to defend policy decisions that were beyond the scope of his advisory role.

Elite scientists can be profoundly naive about the value of expertise outside their field. In politics and policymaking, they are often outgunned. Science leaders involved in policy must remember first and foremost that considerations outside science always come into play, and policymakers should be the ones who take responsibility for making policy decisions. Explaining things is not the same as setting out the best course of action.

*Nature* **602**, 363 (2022)

*doi:* <https://doi.org/10.1038/d41586-022-00411-0>

---

This article was downloaded by **calibre** from <https://www.nature.com/articles/d41586-022-00411-0>

| [Section menu](#) | [Main menu](#) |

- RESEARCH HIGHLIGHT
- 08 February 2022

# Retina-like sensors give machines better vision

Semiconductor-based devices that adapt to a wide range of light intensities could prove useful in self-driving vehicles and assembly lines.

 Time courses of scotopic (top) and photopic (bottom) adaptation of MoS<sub>2</sub> phototransistor array, for the pattern of '8'.

The number '8' gradually becomes visible to a smart sensor as the device adjusts to dim (top) or bright (bottom) light. Credit: F. Liao *et al.*/*Nature Electron*.

Smart optical sensors inspired by the human retina could improve artificial-vision systems used in autonomous vehicles and industrial manufacturing<sup>1</sup>.

## Access options

Subscribe to Nature+

Get immediate online access to the entire Nature family of 50+ journals

\$29.99

monthly

[Subscribe](#)

Subscribe to Journal

Get full journal access for 1 year

\$199.00

only \$3.90 per issue

[Subscribe](#)

All prices are NET prices.

VAT will be added later in the checkout.

Tax calculation will be finalised during checkout.

Buy article

Get time limited or full article access on ReadCube.

\$32.00

[Buy](#)

All prices are NET prices.

### **Additional access options:**

- [Log in](#)
- [Learn about institutional subscriptions](#)

*Nature* **602**, 364 (2022)

*doi:* <https://doi.org/10.1038/d41586-022-00360-8>

## **References**

1. Liao, F. *et al.* *Nature Electron.* <https://doi.org/10.1038/s41928-022-00713-1> (2022).

---

This article was downloaded by **calibre** from <https://www.nature.com/articles/d41586-022-00360-8>

- RESEARCH HIGHLIGHT
- 09 February 2022

# Puzzling spikes in ozone-eating chemical have a fiery cause

Scientists trace variation in methyl bromide levels to an increase in fires — which are linked to the climate pattern El Niño.

The Amazon rainforest was burned in the Acre state of Brazil on the 17th November, 2014.

Flames charred the Brazilian rainforest in late 2014, during the onset of a climatic pattern called El Niño that is linked to high fire activity. Fires release the ozone-depleting gas methyl bromide. Credit: Ricardo Funari/Brazil Photos/LightRocket via Getty

The influence of the tropical Pacific Ocean extends all the way into the stratosphere: the ocean's waters affect the weather and thus the behaviour of fires in far-flung locales; these, in turn, drive emissions of a powerful ozone-depleting gas<sup>1</sup>.

## Access options

Subscribe to Nature+

Get immediate online access to the entire Nature family of 50+ journals

\$29.99

monthly

[Subscribe](#)

## Subscribe to Journal

Get full journal access for 1 year

\$199.00

only \$3.90 per issue

[Subscribe](#)

All prices are NET prices.

VAT will be added later in the checkout.

Tax calculation will be finalised during checkout.

## Buy article

Get time limited or full article access on ReadCube.

\$32.00

[Buy](#)

All prices are NET prices.

## Additional access options:

- [Log in](#)
- [Learn about institutional subscriptions](#)

*Nature* **602**, 364 (2022)

doi: <https://doi.org/10.1038/d41586-022-00356-4>

## References

1. Nicewonger, M. R., Saltzman, E. S. & Montzka, S. A. *Geophys. Res. Lett.* <https://doi.org/10.1029/2021GL094756> (2022).

This article was downloaded by **calibre** from <https://www.nature.com/articles/d41586-022-00356-4>

| [Section menu](#) | [Main menu](#) |

- RESEARCH HIGHLIGHT
- 10 February 2022

# Mini-DNA strands knock macroscale blocks into shape

Gel blocks up to 2 millimetres long are the biggest structures yet to be brought to order by microscopic lengths of DNA.

 Left, separated red and green hydrogel blocks. Right, self-assembled red and green hydrogel blocks.

Short DNA strands decorating the surfaces of gel blocks guide the cubes into a flower-like formation. Credit: OIST

DNA's organizing powers go big: strands of the genetic material can guide gel cubes large enough to be seen with the naked eye to assemble into groups<sup>1</sup>.

## Access options

Subscribe to Nature+

Get immediate online access to the entire Nature family of 50+ journals

\$29.99

monthly

[Subscribe](#)

Subscribe to Journal

Get full journal access for 1 year

\$199.00

only \$3.90 per issue

## Subscribe

All prices are NET prices.

VAT will be added later in the checkout.

Tax calculation will be finalised during checkout.

Buy article

Get time limited or full article access on ReadCube.

\$32.00

## Buy

All prices are NET prices.

## **Additional access options:**

- [Log in](#)
- [Learn about institutional subscriptions](#)

*Nature* **602**, 364 (2022)

*doi:* <https://doi.org/10.1038/d41586-022-00358-2>

## **References**

1. Sontakke, V. A. & Yokobayashi, Y. *J. Am. Chem. Soc.* **144**, 2149–2155 (2022).

---

This article was downloaded by **calibre** from <https://www.nature.com/articles/d41586-022-00358-2>

- RESEARCH HIGHLIGHT
- 07 February 2022

# Hundreds of strange filaments twist through the Galaxy's centre

Long structures that emit brilliant radio waves cannot be easily explained.

The MeerKAT image of the Galactic centre region is shown with the Galactic plane running horizontally across the image.

The central region of the Milky Way contains long filaments (extending from horizontal structure; artificially coloured) that might be a product of past activity by the supermassive black hole in the same region. Credit: I. Heywood, SARAQ

The Galaxy's population of mysterious filaments that emit bright radio waves is at least ten times larger than scientists realized<sup>[1,2](#)</sup>.

## Access options

Subscribe to Nature+

Get immediate online access to the entire Nature family of 50+ journals

\$29.99

monthly

[Subscribe](#)

Subscribe to Journal

Get full journal access for 1 year

\$199.00

only \$3.90 per issue

[Subscribe](#)

All prices are NET prices.

VAT will be added later in the checkout.

Tax calculation will be finalised during checkout.

Buy article

Get time limited or full article access on ReadCube.

\$32.00

[Buy](#)

All prices are NET prices.

### **Additional access options:**

- [Log in](#)
- [Learn about institutional subscriptions](#)

*Nature* **602**, 364 (2022)

*doi:* <https://doi.org/10.1038/d41586-022-00355-5>

## **References**

1. Yusef-Zadeh, F. *et al.* *Astrophys. J.* **925**, L18 (2022).
2. Heywood, I. *et al.* *Astrophys. J.* **925**, 165 (2022).
3. Yusef-Zadeh, F., Morris, M. & Chance, D. *Nature* **310**, 557 (1984).

This article was downloaded by **calibre** from <https://www.nature.com/articles/d41586-022-00355-5>

| [Section menu](#) | [Main menu](#) |

- RESEARCH HIGHLIGHT
- 10 February 2022

# A reindeer's yearning to travel can be read in its genes

The fingerprint of the last ice age can still be seen in the genomes of reindeer that make long migrations.



Should I stay or should I go? Some reindeer, also known as caribou, are homebodies; others migrate more than 1,000 kilometres a year. Credit: Mark Bradley, Parks Canada (CC-BY 4.0)

Some reindeer make epic migrations of more than 1,000 kilometres a year, whereas others stick close to home. Scientists have now linked a reindeer's tendency to migrate and its genetic heritage<sup>1</sup>.

## Access options

Subscribe to Nature+

Get immediate online access to the entire Nature family of 50+ journals

\$29.99

monthly

[Subscribe](#)

Subscribe to Journal

Get full journal access for 1 year

\$199.00

only \$3.90 per issue

## Subscribe

All prices are NET prices.

VAT will be added later in the checkout.

Tax calculation will be finalised during checkout.

Buy article

Get time limited or full article access on ReadCube.

\$32.00

## Buy

All prices are NET prices.

## **Additional access options:**

- [Log in](#)
- [Learn about institutional subscriptions](#)

*Nature* **602**, 365 (2022)

doi: <https://doi.org/10.1038/d41586-022-00357-3>

## **References**

1. Cavedon, M. *et al.* *PLoS Genet.* **18**, e1009974 (2022).

---

This article was downloaded by **calibre** from <https://www.nature.com/articles/d41586-022-00357-3>

- RESEARCH HIGHLIGHT
- 09 February 2022

# Petrified puke shows that ancient winged reptiles purged

Pterosaurs, prehistoric beasts that lived alongside the dinosaurs, not only flew like birds, but also vomited like them.

 A fossil of *Kunpengopterus sinensis* associated with a pellet, from the Late Jurassic Linglongta Locality of China.

A young pterosaur and the pellet (dark brown circle, left) of fish scales it regurgitated shortly before its death have been preserved in stone for more than 100 million years. Credit: J. Shunxing *et al.*/*Phil. Trans. R. Soc. B*

An analysis of fossilized puke has revealed that, just like people, extinct winged reptiles called pterosaurs could vomit — a habit that is providing clues to their diet and anatomy<sup>1</sup>.

## Access options

Subscribe to Nature+

Get immediate online access to the entire Nature family of 50+ journals

\$29.99

monthly

[Subscribe](#)

Subscribe to Journal

Get full journal access for 1 year

\$199.00

only \$3.90 per issue

[Subscribe](#)

All prices are NET prices.

VAT will be added later in the checkout.

Tax calculation will be finalised during checkout.

Buy article

Get time limited or full article access on ReadCube.

\$32.00

[Buy](#)

All prices are NET prices.

### **Additional access options:**

- [Log in](#)
- [Learn about institutional subscriptions](#)

*Nature* **602**, 365 (2022)

*doi:* <https://doi.org/10.1038/d41586-022-00361-7>

## **References**

1. Jiang, S. *et al.* *Phil. Trans. R. Soc. B* <https://doi.org/10.1098/rstb.2021.0043> (2022).

| [Section menu](#) | [Main menu](#) |

- RESEARCH HIGHLIGHT
- 07 February 2022

# Global survey finds scientists have more credibility than spiritual leaders

A lofty-sounding but vapid statement carried more weight with participants when they were told it came from a scientific source.



Atomic scientist and Nobel prize winner Professor Enrico Fermi writes on a chalkboard during a lecture in Milan, Italy.

A photograph of particle physicist Enrico Fermi was featured in a study of scientists' credibility — but few participants recognized him. Credit: Keystone/Getty

People are more likely to believe a cryptic claim if it comes from a scientist rather than a spiritual guru<sup>1</sup>.

## Access options

Subscribe to Nature+

Get immediate online access to the entire Nature family of 50+ journals

\$29.99

monthly

[Subscribe](#)

Subscribe to Journal

Get full journal access for 1 year

\$199.00

only \$3.90 per issue

[Subscribe](#)

All prices are NET prices.

VAT will be added later in the checkout.

Tax calculation will be finalised during checkout.

Buy article

Get time limited or full article access on ReadCube.

\$32.00

[Buy](#)

All prices are NET prices.

### **Additional access options:**

- [Log in](#)
- [Learn about institutional subscriptions](#)

*Nature* **602**, 365 (2022)

*doi:* <https://doi.org/10.1038/d41586-022-00359-1>

## **References**

1. Hoogeveen, S. *et al.* *Nature Hum. Behav.* <https://doi.org/10.1038/s41562-021-01273-8> (2022).

| [Section menu](#) | [Main menu](#) |

# News in Focus

- **Earliest humans, HIV variant and breakthrough COVID** [ 16 February 2022]  
News Round-Up • The latest science news, in brief.
- **Researchers frustrated as Biden's science adviser resigns amid scandal** [ 08 February 2022]  
News • Geneticist Eric Lander had a reputation for being a bully, scientists say, as they call for more inspiring leadership.
- **Nuclear-fusion reactor smashes energy record** [ 09 February 2022]  
News • The experimental Joint European Torus has doubled the record for the amount of energy made from fusing atoms — the process that powers the Sun.
- **South African scientists copy Moderna's COVID vaccine** [ 03 February 2022]  
News • Researchers at WHO technology-transfer hub complete first step in a project aimed at building capacity for vaccine manufacturing in low- and middle-income countries.
- **Omicron's molecular structure could help explain its global takeover** [ 03 February 2022]  
News • Multiple studies are revealing why the SARS-CoV-2 variant is so transmissible, but also seems to cause milder disease.
- **Brexit one year on: patience 'wearing thin' among UK scientists** [ 03 February 2022]  
News • Researchers brace for tense weeks ahead as Europe turns up the heat on research-programme negotiations.
- **Major African radio telescope will help to image black holes** [ 04 February 2022]  
News • US\$25-million facility in Namibia will be Africa's first millimetre-range radio telescope.
- **Why the Tongan eruption will go down in the history of volcanology** [ 09 February 2022]  
News Feature • The 15 January blast sent shock waves around the globe and defied scientific expectations. Researchers are now scrambling to work out why.

- **An ancient link between heart and head — as seen in the blobby, headless sea squirt** [ 14 February 2022]

News Feature • The vital connection between body parts provides insight into the evolution of vertebrates' closest kin.

---

| [Next section](#) | [Main menu](#) | [Previous section](#) |

- NEWS ROUND-UP
- 16 February 2022

# Earliest humans, HIV variant and breakthrough COVID

The latest science news, in brief.



Excavations at the Grotte Mandrin rock shelter uncovered stone tools, animal bones and hominin teeth. Credit: Ludovic Slimak

## Evidence of Europe's first *Homo sapiens* found in French cave

Archaeologists have found [evidence that Europe's first \*Homo sapiens\* lived briefly in a rock shelter in southern France](#) — before mysteriously vanishing.

A study published on 9 February argues that distinctive stone tools and a lone child's tooth were left by *H. sapiens* during a short stay, some 54,000 years ago — and not by Neanderthals, who lived in the rock shelter for thousands of years before and after that time ([L. Slimak et al. Sci. Adv. 8, eabj9496; 2022](#)).

The *H. sapiens* occupation, which researchers estimate lasted for just 40 years, pre-dates the previous earliest known evidence of the species in Europe by around 10,000 years.

Researchers excavating the Grotte Mandrin rock shelter in the Rhône Valley uncovered tens of thousands of stone tools, along with animal bones and hominin teeth. Most of the tools resemble artefacts found at Neanderthal sites across Eurasia. But one of the shelter's archaeological levels — dated to between 56,800 and 51,700 years ago — contains tools such as sharpened points and small blades that are more typical of early *H. sapiens* technology.

An analysis also found that the only hominin tooth in this layer is similar in shape to those of *H. sapiens* who lived in Eurasia during the last Ice Age. Other teeth found in Grotte Mandrin resemble those of Neanderthals.

"It is exciting to see that *Homo sapiens* was in western Europe several thousand years earlier than previously thought," says Marie Soressi, an archaeologist at Leiden University in the Netherlands. "It shows that the peopling of Europe by *Homo sapiens* was likely a long and hazardous process."

But some researchers are not so sure that the stone tools or tooth were left by our species. And the tooth's DNA has not yet been analysed to confirm its origins.

"I find the evidence less than convincing," says William Banks, a palaeolithic archaeologist at the French national research agency CNRS and the University of Bordeaux. He adds that there can be substantial overlap in the shapes of teeth from *H. sapiens* and Neanderthals.



The variant increases the number of HIV virus particles in infected people's blood. Credit: Cavallini James/BSIP/Science Photo Library

## Highly virulent HIV strain circulating in Europe

A [highly transmissible and damaging variant of HIV](#) has been circulating in the Netherlands for decades, researchers have found.

An analysis of more than 100 infected people suggests that the variant boosts the number of viral particles in a person's blood, making them more

likely to transmit the virus. The variant also seems to lead to a reduction in immune cells called CD4 T cells, so infected people are at risk of developing AIDS more rapidly than are those infected with other versions of HIV ([C. Wymant et al. Science 375, 540–545; 2022](#)).

The emergence of a more virulent form of HIV is “a reason to stay vigilant”, but not a public-health crisis. The mutations in the new variant don’t make it resistant to existing HIV drugs, says Joel Wertheim, an evolutionary biologist at the University of California, San Diego. “All of the tools in our arsenal should still work,” he says.

The study highlights the importance of HIV testing and treatment, says Salim Abdool Karim, director of the Durban-based Centre for the AIDS Programme of Research in South Africa. “It’s key to identify infected people quickly and start treatment early, because treatments work well, even against this variant,” he says.



A COVID-19 vaccination centre in Toyoake, Japan. Credit: Kyodo News/Getty

## Breakthrough COVID boosts immune protection

Two studies suggest that '[breakthrough' SARS-CoV-2 infections improve immune protection against several variants of the virus.](#)

People who catch SARS-CoV-2 and then are vaccinated tend to make lots of antibodies against the SARS-CoV-2 spike protein, and their antibody-containing blood serum excels at blocking a range of SARS-CoV-2 variants.

To test whether infection after vaccination confers similar benefits, scientists analysed serum from people who'd had such breakthrough infections; others infected before vaccination; and vaccinated people with no history of infection (pictured, a vaccination centre). Sera from both previously infected groups had more antibodies against the spike protein than did serum from those protected only by vaccines ([T. A. Bates et al. \*Sci. Immunol.\* <https://doi.org/gn9tgz>; 2022](#)).

A second study examined people who'd been infected and then given two doses of vaccine; who'd had two shots and then breakthrough infections; and who'd had a third vaccine dose but no infection. Serum levels of antibodies that blocked variants including Omicron were higher, and persisted for longer, in all three groups than in people who'd had two doses of vaccine and never been infected ([A. C. Walls et al. \*Cell\* <https://doi.org/gpdfp6>; 2022](#)).

*Nature* **602**, 367 (2022)

*doi:* <https://doi.org/10.1038/d41586-022-00412-z>

---

This article was downloaded by **calibre** from <https://www.nature.com/articles/d41586-022-00412-z>

- NEWS
- 08 February 2022

# Researchers frustrated as Biden's science adviser resigns amid scandal

Geneticist Eric Lander had a reputation for being a bully, scientists say, as they call for more inspiring leadership.

- [Jeff Tollefson](#),
- [Amy Maxmen](#),
- [Alexandra Witze](#) &
- [Lauren Wolf](#)



Eric Lander's resignation as science adviser will leave empty a position in US President Joe Biden's cabinet. Credit: Alex Wong/Getty

The US scientific community is reeling after President Joe Biden's top science adviser, Eric Lander, announced his resignation on 7 February. [Reporting by the news outlet \*Politico\*](#) reveals that a White House investigation has found that Lander violated the Biden administration's workplace policy by bullying and demeaning staff.

Researchers hope that leadership will soon be restored to the Office of Science and Technology Policy (OSTP), which Lander directed, so that it can continue with Biden's agenda — including creating a new biomedical-innovations agency and revamping the country's pandemic-preparedness plan. Some are already naming scientists who might be suited to replace Lander, who they say had a well-known reputation for abrasiveness and aggression towards his colleagues.

“Eric Lander is a successful researcher, but everyone knows that he is a bully,” says Kenneth Bernard, an epidemiologist and biodefence researcher who has worked for the US government under several presidential administrations. “He is widely known as arrogant and controlling.” Bernard, who testified before a White House advisory panel co-chaired by Lander under former president Barack Obama, notes that such behaviour can be particularly problematic at government agencies, where leaders must navigate varied viewpoints. “He was a bad fit from the beginning,” Bernard says.

But some did not expect his tenure to end in this way. “I expected his ambition to temper his natural inclination to be the smartest person in the room,” says Robert Cook-Deegan, who studies science and health policy at Arizona State University’s Washington DC campus. “I really am surprised that it blew up like this.”

## A disappointing situation

[The \*Politico\* story](#) revealed bombshell details of a toxic work environment at the OSTP. Rachel Wallace, who had served as the office’s general counsel

and has worked for the OSTP across several presidential administrations, filed a complaint in September alleging that Lander had engaged in abusive behaviour, including aggressive and demeaning interactions, particularly with women in the office. The investigation found “credible evidence of instances of multiple women having complained to other staff about negative interactions with Dr. Lander”, a White House official told *Politico*.

In a statement to *Nature*, an OSTP spokesperson said that the White House investigation, undertaken in late 2021, did not find “credible evidence of gender-based discrimination”. It did, however, identify credible violations of the White House’s Safe and Respectful Workplace Policy, the spokesperson said. The OSTP has not released the investigation report, and declined to do so to *Nature*, citing confidentiality surrounding personnel issues. Two congressional leaders [have requested copies](#) from Biden.

In his resignation letter to Biden, Lander said he is “devastated” at the harm his actions have caused, and that he takes full responsibility. “I have sought to push myself and my colleagues to reach our shared goals — including at times challenging and criticizing,” he wrote. “But it is clear that things I said, and the way I said them, crossed the line at times into being disrespectful and demeaning, to both men and women. That was never my intention.”

“This is obviously a deeply disappointing situation,” said Jennifer Doudna, a biochemist at the University of California, Berkeley, in an e-mail to *Nature*. But she adds that challenges create opportunities. “I hope we learn from this moment and support greater diversity and equity in science careers.”

The OSTP is now without a head, and Biden without a congressionally confirmed science adviser. The president must waste no time in appointing a replacement, says physicist Neal Lane at Rice University in Houston, Texas, who served as science adviser to former president Bill Clinton. “We just need, as quickly as possible, someone in the driver’s seat who’s respected inside and outside the White House,” Lane says.

## Past controversies

[When Biden nominated Lander](#) as his science adviser in early 2021, many scientists were thrilled that the president had for the first time elevated the role of OSTP director to his inner circle of advisers — the cabinet — giving science a seat at the table for high-level discussions. Lander had been a key figure in the race to sequence the human genome in the 1990s and early 2000s, and was the founding director of the Broad Institute of MIT and Harvard in Cambridge, Massachusetts, a biomedical research organization. He also co-led the President's Council of Advisors on Science and Technology (PCAST) under Obama.



Lander was the founding director of the Broad Institute of MIT and Harvard (shown here in a laboratory in 2005). Credit: Rick Friedman/Corbis via Getty

But at the time, critics [noted his reputation for being at the centre of controversies](#). These included an essay he wrote about the history of the gene-editing technique CRISPR that did not properly credit two prominent women, including Doudna, for their discoveries; associations with disgraced financier and convicted sex offender Jeffrey Epstein; and a toast he gave for James Watson, the co-discoverer of the structure of DNA, who has

frequently voiced racist, ableist and misogynistic views. During Lander's confirmation hearing last May, several senators expressed concern about his meetings with Epstein and about his downplaying of women in science.

On his first day in office last June, in response to questions about these issues, [Lander told \*Nature\*](#) that "for 35 years, I have been doing a tremendous amount around the values of lifting up people and building institutions that are broadly inclusive. Those are where my values are, and that is really where my work is."

The Broad Institute, from which Lander took an unpaid leave of absence when he became OSTP director, did not reply to *Nature*'s questions about whether his position would be restored.

## Turning things around

With the job of presidential science adviser open once again, researchers are recommending candidates who they think could turn things around. Bernard hopes that the next OSTP director will have had the experience of running a large, multisectoral science institute, such as a national laboratory, and will have navigated the intersection between policy, budget and science. He and others have suggested potential replacements, such as Jill Hruby, currently undersecretary for nuclear security at the US Department of Energy; Frances Arnold, a biochemical engineer and Nobel laureate who co-chairs Biden's PCAST; and Jo Handelsman, a microbiologist who was associate director for science at the OSTP under Obama.

Gigi Gronvall, a biosecurity researcher at Johns Hopkins University in Baltimore, Maryland, says that any replacement's management style will matter when it comes to being effective at the agency, but also because they serve as a model. One of the OSTP's core missions should be to ensure US scientific leadership for the next generation, and that means creating an environment that encourages women and people from under-represented communities to remain in science.

"I am hoping they push women, and especially women of colour, to the top of the list," says Emily Pinckney, the executive director of 500 Women

Scientists, an international advocacy group [that wrote about its opposition to Lander's appointment](#) in *Scientific American* in January 2021. She suggests that two researchers already at the OSTP are suited for the role: social scientist Alondra Nelson and ocean scientist Jane Lubchenco.

“Representation matters,” she says, explaining that challenges such as the pandemic and climate change disproportionately affect women and people of colour, and therefore scientists combating such issues must be able to connect with those communities.

## The road ahead

Most scientists expect the OSTP to continue its work under the leadership team assembled by Lander, but Cook-Deegan says the loss of the director comes at a crucial time.

Lander was in charge of Biden’s Cancer Moonshot initiative, a revival of the Obama administration’s effort to reduce rates of death from cancer, and he was leading efforts to create an Advanced Research Projects Agency for Health, a high-risk, high-reward funding agency to push for biomedical breakthroughs. He was also in charge of the search for a new director of the National Institutes of Health, following [the retirement of Francis Collins last year](#).

“There’s just a ton of work to get done, and OSTP is positioned to help on all these fronts,” Cook-Deegan says.

Other initiatives at the OSTP, such as a push to promote environmental justice and revamp scientific-integrity policies across the federal government, might actually move more quickly with Lander out of the way, says Andy Rosenberg, who heads the Center for Science and Democracy at the Union of Concerned Scientists, an advocacy group in Cambridge, Massachusetts. “I think Lander was slowing things down” by wanting to be directly involved in so many of the things the OSTP is trying to do, he says.

Roger Pielke Jr, a science-policy researcher at the University of Colorado Boulder, isn’t convinced that Lander was a major player in moving Biden’s agenda forward. But he does wonder whether the scandal might make future

presidents question whether they want to keep a science adviser in the cabinet. “Having a member of your cabinet resign in disgrace is a little bit different than having somebody in an obscure [White House] office do it,” he says.

The OSTP spokesperson says the office is well positioned to continue carrying out Biden’s science agenda. “The president has been very clear that science has a seat at the table and we will protect scientific integrity in this government — and that will continue through this transition,” they say.

Lander plans to depart the White House no later than 18 February.

*Nature* **602**, 369-370 (2022)

*doi:* <https://doi.org/10.1038/d41586-022-00375-1>

Additional reporting by Nidhi Subbaraman.

---

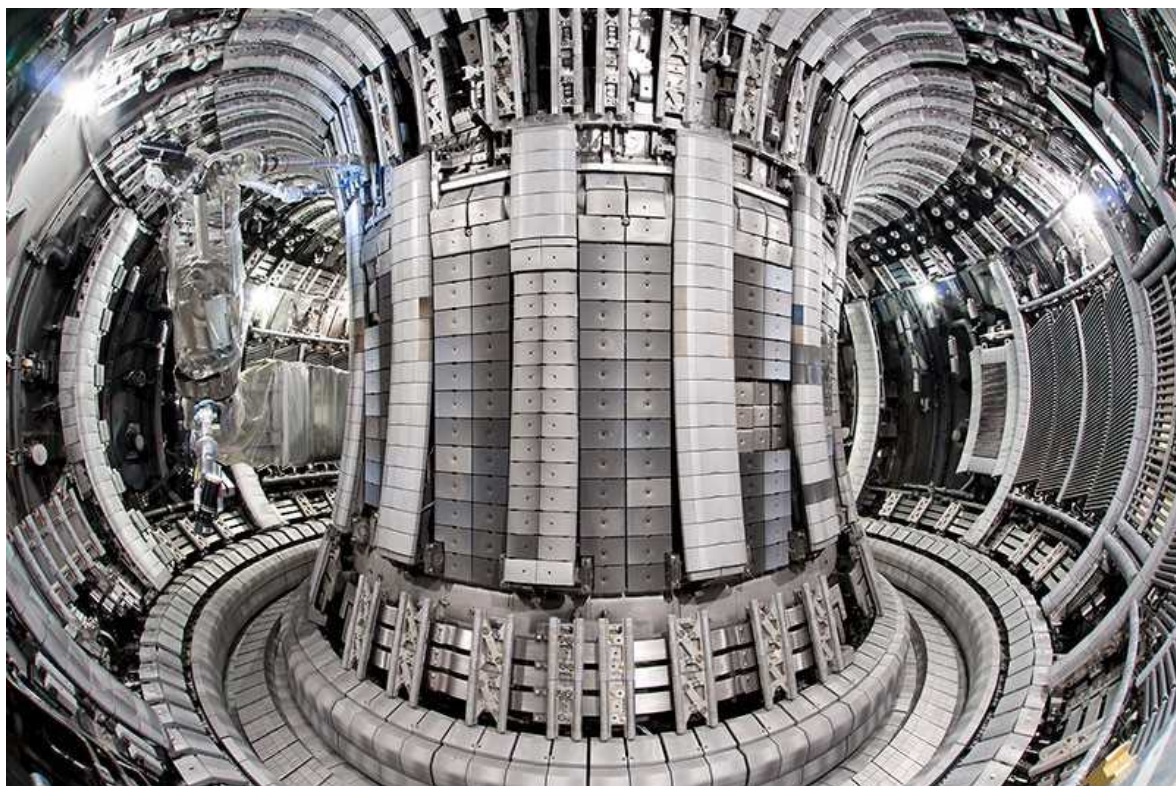
This article was downloaded by **calibre** from <https://www.nature.com/articles/d41586-022-00375-1>

- NEWS
- 09 February 2022

# Nuclear-fusion reactor smashes energy record

The experimental Joint European Torus has doubled the record for the amount of energy made from fusing atoms — the process that powers the Sun.

- [Elizabeth Gibney](#)



The Joint European Torus tokamak reactor near Oxford, UK, is a test bed for the world's largest fusion experiment — ITER in France. Credit: Christopher Roux (CEA-IRFM)/EUROfusion (CC BY 4.0)

A 24-year-old nuclear-fusion record has crumbled. Scientists at the Joint European Torus (JET) near Oxford, UK, announced on 9 February that they had generated the highest sustained energy pulse ever created by fusing together atoms, more than doubling their own record from experiments performed in 1997.

“These landmark results have taken us a huge step closer to conquering one of the biggest scientific and engineering challenges of them all,” said Ian Chapman, who leads the Culham Centre for Fusion Energy (CCFE), where JET is based, in a statement. The UK Atomic Energy Authority hosts JET, but its scientific programme is run by a European collaboration called EUROfusion.

If researchers can harness nuclear fusion — the process that powers the Sun — it promises to provide a near-limitless source of clean energy. But so far, no experiment has generated more energy than has been put in. JET’s results do not change that, but they suggest that a follow-up fusion-reactor project that uses the same technology and fuel mixture — the ambitious US\$22-billion ITER, scheduled to begin fusion experiments in 2025 — should eventually be able to reach this goal.

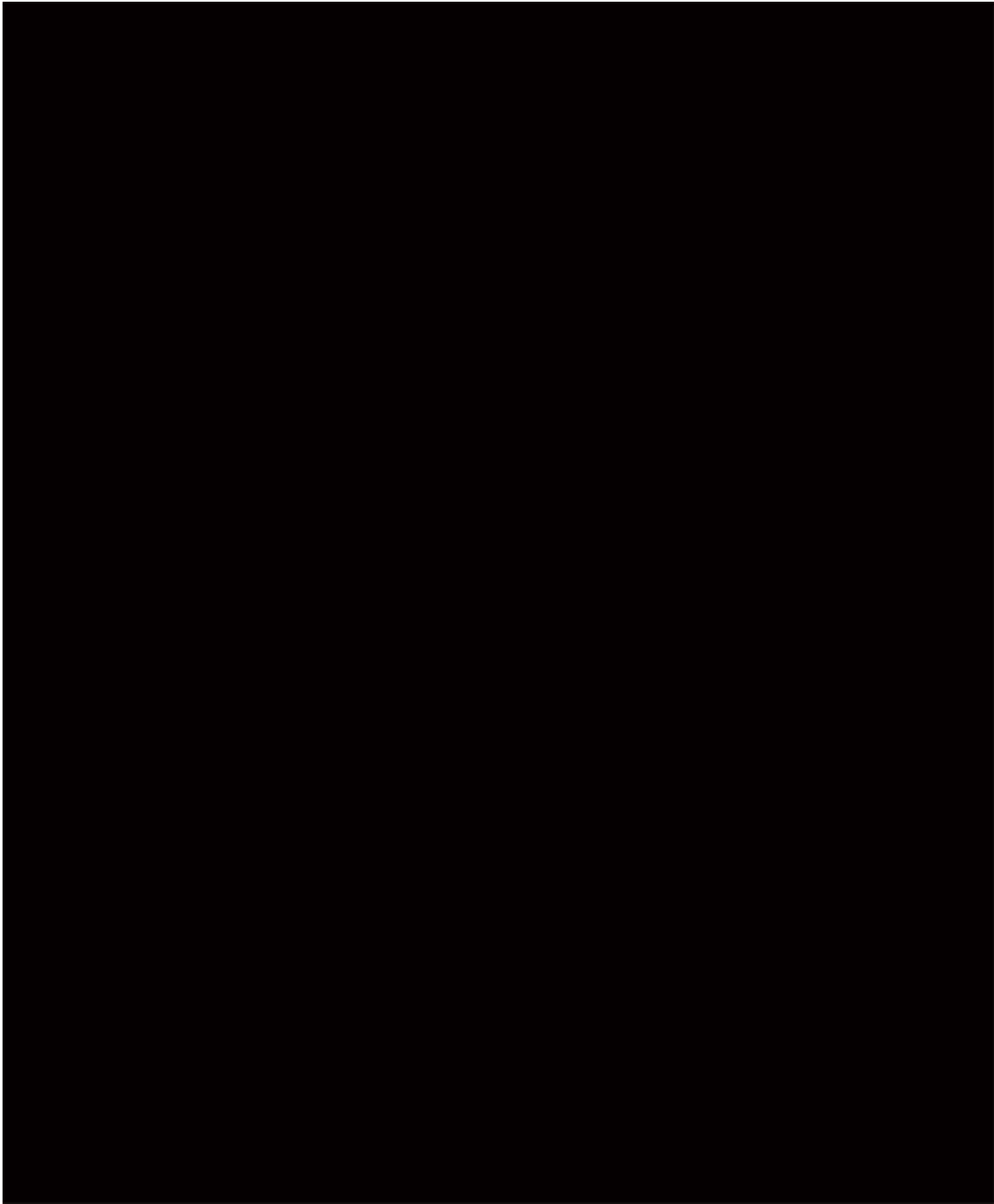
“JET really achieved what was predicted. The same modelling now says ITER will work,” says fusion physicist Josefina Proll at Eindhoven University of Technology in the Netherlands, who works on a different kind of reactor called a stellarator. “It’s a really, really good sign and I’m excited.”

## Two decades’ work

The experiments — the culmination of almost two decades of work — are important for helping scientists to predict how ITER will behave, and will guide its operating settings, says Anne White, a plasma physicist at the Massachusetts Institute of Technology in Cambridge who works on tokamaks, reactors that, like JET, have a doughnut shape. “I am sure I am not alone in the fusion community in wanting to extend very hearty congratulations to the JET team.”

JET and ITER use magnetic fields to confine plasma, a superheated gas of hydrogen isotopes, in the tokamak. Under heat and pressure, the isotopes fuse into helium, releasing energy as neutrons.

To break the energy record, JET used a [fuel made of equal parts tritium and deuterium](#) — the same mixture that will power ITER, which is being built in southern France. Tritium is a rare and radioactive isotope of hydrogen; when it fuses with the isotope deuterium, the reactions produce many more neutrons than do reactions between deuterium particles alone. That ramps up the energy output, but JET had to undergo more than two years of renovation to prepare the machine for the onslaught. Tritium was last used by a tokamak fusion experiment when JET set its previous record in 1997.



The record-breaking pulse in action inside JET's doughnut-shaped internal vessel. (It's [quite good with the sound on](#), too.) Credit: UKAEA

In an experiment on 21 December 2021, JET's tokamak produced 59 megajoules of energy over a fusion 'pulse' of 5 seconds — more than double

the 21.7 megajoules released in 1997 over around 4 seconds. Although the 1997 experiment still retains the record for ‘peak power’, that spike lasted for only a fraction of a second, and the experiment’s average power was less than half that of the latest test, says Fernanda Rimini, a plasma scientist at the CCFE who oversaw last year’s experimental campaign. The improvement took 20 years of experimental optimization, as well as hardware upgrades that included replacing the tokamak’s inner wall to waste less fuel, she says.

## Power ratio

Producing the energy over a number of seconds is essential for understanding the heating, cooling and movement happening inside the plasma that will be crucial to run ITER, says Rimini.

Five seconds “is a big deal”, adds Proll. “It is really, really impressive.”

Last year, the US Department of Energy’s National Ignition Facility set a different fusion record: it used laser technology to produce the highest recorded fusion power output relative to power in, a value called  $Q$ , where 1 would be generating as much power as is put in. The facility achieved a  $Q$  of 0.7 — a landmark for laser fusion that beat JET’s 1997 record. But the event was short-lived, producing just 1.3 megajoules over less than 4 billionths of a second.

JET’s latest experiment sustained a  $Q$  of 0.33 for 5 seconds, says Rimini. JET is a scaled-down version of ITER, at one-tenth of the volume — a bathtub compared to a swimming pool, says Proll. It loses heat more easily than ITER, so it was never expected to hit breakeven. If engineers applied the same conditions and physics approach to ITER as to JET, she says, it would probably reach its goal of a  $Q$  of 10, producing ten times the energy put in.

Fusion researchers are far from having all the answers. A remaining challenge, for example, is dealing with the heat created in the exhaust region of the ITER reactor. ITER’s exhaust will have a bigger area than JET’s, but the increase will not be in proportion to the surge in power it will have to

deal with. Research is under way to work out which design should best withstand the heat, but researchers are not there yet, says Proll.

JET's record-breaking run happened on the last day of a five-month campaign from which Rimini says scientists gleaned a wealth of information that they will analyse over the next few years. The final experiment pushed the device to its "absolute maximum", adds Rimini, who witnessed the landmark test in real time. "We didn't jump up and down and hug each other — we were at 2 metres distance — but it was very exciting."

The tritium experiments could be JET's swansong. Last year, EUROfusion decided to end JET's operations at the end of 2023, 40 years after they began. The UKAEA has said that it plans to decommission the experiment; JET hardware and operational expertise are to find homes in other projects at the site.

*Nature* **602**, 371 (2022)

*doi:* <https://doi.org/10.1038/d41586-022-00391-1>

---

This article was downloaded by **calibre** from <https://www.nature.com/articles/d41586-022-00391-1>

- NEWS
- 03 February 2022

# South African scientists copy Moderna's COVID vaccine

Researchers at WHO technology-transfer hub complete first step in a project aimed at building capacity for vaccine manufacturing in low- and middle-income countries.

- [Amy Maxmen](#)



Researchers at Afrigen Biologics and Vaccines are attempting to replicate Moderna's vaccine. Credit: Afrigen Biologics

Researchers at a South African biotechnology company say they have nearly completed the process of reproducing Moderna's mRNA vaccine against COVID-19, without Moderna's involvement.

The company, Afrigen Biologics and Vaccines in Cape Town, has made only microlitres of the vaccine, which is based on data that Moderna used to make its shot. But the achievement is a milestone for a major initiative launched by the World Health Organization (WHO) — a technology-transfer hub meant to build capacity for vaccine manufacturing in low- and middle-income countries.

During the COVID-19 pandemic, developers of mRNA vaccines — Moderna, based in Cambridge, Massachusetts, Pfizer, in New York City, and BioNTech, in Mainz, Germany — have sent more than 70% of their doses to wealthy nations, according to vaccine-distribution analyses. Meanwhile, millions of doses purchased by or promised to low- and middle-income countries have been delayed. “Moderna and Pfizer–BioNTech’s vaccines are mainly still going to just the richest countries,” says Martin Friede, the WHO official coordinating the hub. “Our objective is to empower other countries to make their own.”

Many steps remain before Afrigen’s mRNA vaccine candidate can be distributed to people in Africa and beyond, and it definitely won’t help to curb the pandemic this year. But the WHO hopes that the process of creating it will lay the foundation for a more globally distributed mRNA-vaccine industry.

Gerhardt Boukes, chief scientist at Afrigen — the firm at the core of the WHO’s hub — is proud to have helped with the first phase of the plan, which included creating messenger RNA that encodes a modified portion of the coronavirus SARS-CoV-2 and encapsulating it in a lipid nanoparticle that delivers the vaccine to cells. “We didn’t have help from the major COVID-vaccine producers,” he says, “so we did it ourselves to show the world that it can be done, and be done here, on the African continent.”

## Going it alone

When the WHO launched its [mRNA tech-transfer hub in South Africa](#) last June, it asked Moderna, Pfizer and BioNTech to help teach researchers in low- and middle-income countries how to make their COVID-19 vaccines. But the companies did not respond, and the WHO decided to go ahead without their help. Friede says the WHO chose to replicate Moderna's shot because more information on its development is available publicly, compared with Pfizer–BioNTech's vaccine, and because [Moderna has vowed not to enforce its patents](#) during the pandemic. Moderna did not respond to requests from *Nature* to comment on the WHO's decision to copy its vaccine.

With funds from countries including France, Germany and Belgium, South African researchers began chipping away at the project in late September. A team at the University of the Witwatersrand in Johannesburg took the lead on the first step: making a DNA molecule that would serve as a template to synthesize the mRNA. Although [Moderna has controversially patented](#) this sequence, researchers at Stanford University in California deposited it in the online database Virological.org in March last year.

Patrick Arbuthnot, director of gene-therapy research at the University of the Witwatersrand, says, “We were not intimidated, because mRNA synthesis is a fairly generic procedure.” Despite delays in the shipment of raw materials, the team completed this process in ten weeks and sent vials of mRNA to Afrigen in early December.

During this period, having heard about plans to mimic Moderna's shot, scientists from around the world e-mailed Afrigen researchers to offer assistance. Some of them were at the US National Institutes of Health, and had conducted foundational work on mRNA vaccines. “It was extraordinary,” says Petro Terblanche, Afrigen's managing director. “I think a lot of scientists were disillusioned with what had happened with vaccine distribution, and they wanted to help get the world out of this dilemma.”

On 5 January, Afrigen's researchers accomplished another tricky part of the process: they encapsulated the mRNA in a fatty nanoparticle made of a mixture of lipids. Boukes says they haven't yet used Moderna's specific lipid mixture, but rather one that was immediately available from the manufacturer of the machine that the laboratory uses to create lipid

nanoparticles. The researchers plan to use Moderna's lipid mixture as soon as one last analytical instrument arrives. After that, the team will analyse the formulation to ensure that it is truly a near copy of Moderna's vaccine.

## An empowerment process

The next set of challenges will be to make a lot more of the vaccine. Jason McLellan, a structural biologist at the University of Texas at Austin whose work was foundational to the development of several COVID-19 vaccines, says he is not surprised that South African researchers seem to have copied Moderna's vaccine, but he adds that scaling up production of that original shot required a lot of extra innovation by manufacturers.

For the next phase of the project, several companies in the global south will learn from Afrigen and attempt to create batches of vaccine themselves, in preparation for testing the shots in rodents. The WHO expects a Moderna mimic to be ready for phase I trials in people by the end of November.

What will happen next year remains uncertain. Charles Gore, director of the Medicines Patent Pool in Geneva, Switzerland — an organization working with the hub that is devoted to expanding drug and vaccine access around the world — says that the initiative has no intention of infringing Moderna's patents. Laboratory research is generally not subject to patent rules, Gore explains.

And he hopes that once the vaccine is ready for use, Moderna might then license its patents — or that by then, there might be alternatives that companies could produce without fear of a lawsuit. Scientists at several universities are currently developing next-generation mRNA vaccines that might be cheaper to make or not require the ultracold storage needed for Moderna and Pfizer–BioNTech's vaccines.

Although the pace of this effort will not meet the urgent need for vaccines across Africa, many researchers from the continent are enthusiastic. A reliance on vaccines from wealthy countries and companies has proved dangerous during the pandemic — only about 10% of people in Africa have been fully vaccinated — and this initiative aims to help nations to protect

themselves. “Global health’s dysfunction derives from power imbalances,” explains Olusoji Adeyi, president of the organization Resilient Health Systems in Washington DC. “Addressing that will come from countries in the global south developing their own capabilities and taking responsibility for their own health.”

*Nature* **602**, 372-373 (2022)

*doi:* <https://doi.org/10.1038/d41586-022-00293-2>

---

This article was downloaded by **calibre** from <https://www.nature.com/articles/d41586-022-00293-2>

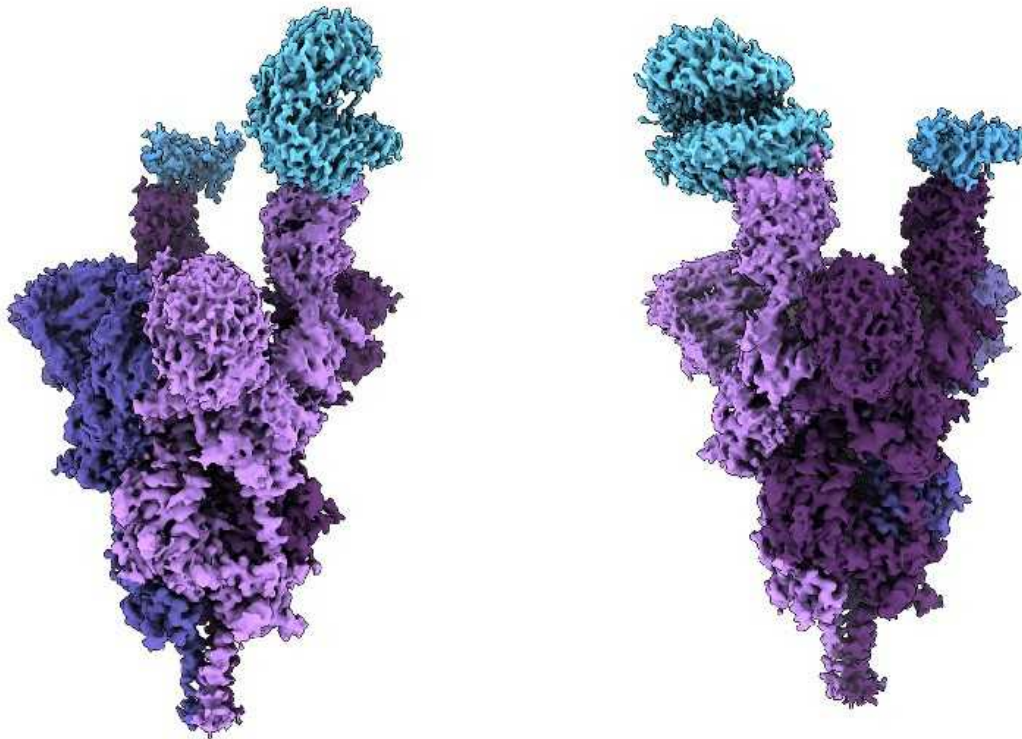
| [Section menu](#) | [Main menu](#) |

- NEWS
- 03 February 2022

# Omicron's molecular structure could help explain its global takeover

Multiple studies are revealing why the SARS-CoV-2 variant is so transmissible, but also seems to cause milder disease.

- [Diana Kwon](#)



Researchers have determined that despite its myriad mutations, Omicron's spike protein (purple, two views shown) binds tightly to the ACE2 receptor

(blue) on a person's cells.Credit: Dr Sriram Subramaniam, University of British Columbia

After it was [first detected in South Africa](#) last November, Omicron spread around the globe faster than any previous variant of the coronavirus SARS-CoV-2, readily infecting even those who had been vaccinated or previously had COVID-19. To learn how it was able to do this, scientists have turned to techniques such as cryo-electron microscopy, to visualize Omicron's molecular structure at near-atomic resolution.

By comparing Omicron's structure with that of the original version of SARS-CoV-2 and its other variants, they have begun to shed light<sup>1</sup> on which features of the highly mutated virus have enabled it to evade the body's immune defences, while also maintaining its ability to attack a person's cells. And they've begun to unpick why Omicron seems to cause milder disease than previous variants.

"Omicron is very different structurally than all the other variants we have known so far," says Priyamvada Acharya, a structural biologist at the Duke Human Vaccine Institute in Durham, North Carolina.

## Evading immune defences

Omicron has dozens of mutations not seen in the original SARS-CoV-2 strain that researchers first detected in Wuhan, China. More than 30 of those mutations are in the spike protein on the coronavirus's surface, which helps the virus to latch on to and infect host cells. No previous SARS-CoV-2 variant seems to have accumulated so many genetic changes. By comparison, the Delta and Alpha variants, dominant earlier in the pandemic, each have approximately ten mutations on their spike proteins.

Fifteen of Omicron's spike mutations are found in the protein's receptor binding domain (RBD), a region that binds to a receptor called ACE2 on a person's cells to gain entry. A research team including David Veesler, a structural biologist at the University of Washington in Seattle, has shown<sup>2</sup> that these changes, along with 11 mutations in a region of the spike called the N-terminal domain, have completely remodelled the areas of the protein

that are recognized by ‘neutralizing’ antibodies. These antibodies are generated after a person receives a vaccine against SARS-CoV-2 or is infected; they later recognize the pathogen and prevent it from entering cells. The remodelling severely hinders the ability of most neutralizing antibodies to recognize the virus.

With such a big shift in shape, there’s a huge question over how Omicron can still bind strongly to ACE2. “Normally, when you have so many mutations all over, you expect that you will also have compromised the ability to bind the receptor,” says Sriram Subramaniam, a structural biologist at the University of British Columbia in Vancouver, Canada.

Subramaniam and his colleagues answered the question by demonstrating that although some of the mutations in Omicron’s RBD hinder its ability to bind to ACE2, others strengthen it<sup>3</sup>. For example, the K417N mutation disrupts a key salt bridge — a bond between oppositely charged bits of protein — that helps to link the spike protein to ACE2. A combination of other mutations, however, helps to form new salt bridges and hydrogen bonds that strengthen the link to ACE2. The net effect is that Omicron bonds to ACE2 more strongly than does the original version of SARS-CoV-2, and as strongly as the Delta variant.

Veesler and his colleagues have also found<sup>2</sup> enhanced interactions between Omicron’s RBD and ACE2. Omicron has adopted a “very elegant molecular solution, where the mutations are mediating immune evasion while enhancing receptor binding”, Veesler says.

Martin Hällberg, a structural biologist at the Karolinska Institute in Stockholm, applauds the work by these groups, but points out that it’s an open question how some neutralizing antibodies can still detect Omicron. If researchers can understand the structural basis for that recognition, he adds, it might help to counter variants that emerge in future.

## Lingering mysteries

Some structural studies have also provided possible explanations for another of Omicron’s properties: that it seems to have more difficulty infecting the

lungs than the nose and throat. Some scientists say [this might explain](#) why Omicron seems to cause milder disease than other variants.

Many studies focus on two [possible mechanisms](#) by which SARS-CoV-2 and its variants might enter a person's cells after binding to ACE2. The first involves an enzyme on host cells called TMPRSS2, which cleaves off a piece of the spike, exposing a region that embeds into the cells' membranes; eventually, the virus fuses with the cells and injects its genetic material directly into them. The other, slower pathway involves the virus entering host cells through bubbles known as endosomes before releasing its contents.

Several groups have found evidence that Omicron prefers the slower route<sup>4</sup>. For example, Veesler and his colleagues found<sup>5</sup> that cleavage of the spike protein, required for the TMPRSS2 pathway, was less efficient for Omicron than for Delta. The researchers also noted that there are higher levels of TMPRSS2 in the lungs than in the upper airways — possibly explaining Omicron's preference for infecting the nose and throat.

But not everyone agrees that Omicron prefers this entry route. Bing Chen, a structural biologist at Harvard Medical School in Boston, Massachusetts, notes that some groups have reported evidence<sup>6</sup> for a slightly different mechanism than either of the other two. He suggests instead that Omicron's mildness is related to ACE2.

To bind to ACE2, the virus's RBD needs to flip from a 'down' to an 'up' position. In a preprint<sup>7</sup>, Chen and his colleagues have reported evidence that Omicron's RBD has difficulty moving into the 'up' conformation because of a structural change induced by one of its many mutations. As a result, Omicron requires higher levels of ACE2 to fuse with host cells than do other variants. "This could explain why Omicron doesn't really infect the lung cells, because lung cells generally have much lower ACE2 levels compared to the cells in the upper respiratory tract," Chen says. But further investigation is needed, he adds.

Open questions remain, but researchers are hoping to use structural knowledge about Omicron to help develop more effective treatments and

vaccines against it — and against future variants of concern. “Omicron really redefines what we thought variants look like,” Veesler says.

*Nature* **602**, 373-374 (2022)

*doi:* <https://doi.org/10.1038/d41586-022-00292-3>

## References

1. Gobeil, S. M-C. *et al.* Preprint at bioRxiv  
<https://doi.org/10.1101/2022.01.25.477784> (2022).
2. McCallum, M. *et al.* *Science* <https://doi.org/10.1126/science.abn8652> (2022).
3. Mannar, D. *et al.* *Science* <https://doi.org/10.1126/science.abn7760> (2022).
4. Peacock, T. P. *et al.* Preprint at bioRxiv  
<https://doi.org/10.1101/2021.12.31.474653> (2022).
5. Meng, B. *et al.* Preprint at bioRxiv  
<https://doi.org/10.1101/2021.12.17.473248> (2022).
6. Lamers, M. M. *et al.* Preprint at bioRxiv  
<https://doi.org/10.1101/2022.01.19.476898> (2022).
7. Zhang, J. *et al.* Preprint at bioRxiv  
<https://doi.org/10.1101/2022.01.11.475922> (2022).

---

This article was downloaded by **calibre** from <https://www.nature.com/articles/d41586-022-00292-3>

- NEWS
- 03 February 2022

# Brexit one year on: patience ‘wearing thin’ among UK scientists

Researchers brace for tense weeks ahead as Europe turns up the heat on research-programme negotiations.

- [Holly Else](#)



Prolonged Brexit negotiations mean some UK researchers have not yet been able to access EU grant funding. Credit: Belinda Jiao/SOPA Images/LightRocket via Getty

It has been just over a year since UK scientists celebrated a [long-awaited trade deal](#) between their government and the European Commission that defines their relationship after Brexit. After years of uncertainty, researchers welcomed the pact, which had wide ranging effects on science, including on data regulation, nuclear and space research and clinical trials.

It also promised to pave the way for a formal partnership between the United Kingdom and the Commission that would allow British researchers to bid for funding from the Commission's flagship €95-billion (US\$107-billion) research programme, [Horizon Europe](#), which started doling out money last month.

But the two sides have yet to ratify the final agreement because of a row over a customs border between Great Britain and the island of Ireland. As a result, the UK government has deployed its safety-net funding guarantee to underwrite successful bids by UK scientists for Horizon Europe funding in the programme's early stages.

"We're starting to become very concerned about the situation," says Jo Burton, a policy manager at the Russell Group, a consortium of top UK research universities, with headquarters in Cambridge.

Research-policy scholars say that the Commission is holding science "hostage" to achieve its wider political aims, and urge for progress in talks before patience in the United Kingdom wears out and the government abandons plans to associate, instead creating its own equivalent funder.

## Deal delayed

UK research was thrown into turmoil in the wake of the country's vote to leave the European Union in 2016. The uncertainty over the future UK-EU relationship [left many UK-based scientists in limbo](#), unsure whether workers and research funding would continue to flow freely between the two entities. Much of the confusion around immigration has been resolved: EU researchers working in the United Kingdom have opted to either leave the country or apply for permission to stay. The UK government also established new visa routes for scientists.

The eleventh-hour trade deal struck between Britain and the EU in January 2021 paved the way for Britain to ‘associate’ with Horizon Europe as a non-member state. It came as a huge relief to scientists, who finally had clarity that they would, in principle, be able to apply for funding from the bloc’s multibillion pot for research and development.

But the process has been held up by political negotiations. Late last year, the Commission’s research head, Mariya Gabriel, said that an association deal would not be inked until the EU’s disputes with Britain are resolved.

Those tensions centre on the Northern Ireland Protocol, a Brexit agreement between the two parties designed to prevent any checks on goods crossing the border between the Republic of Ireland, which remains in the EU, and Northern Ireland, part of the United Kingdom. The aim of the arrangement is to protect a historic treaty that ended years of political and religious violence on the island.



Britain's participation in joint science initiatives such as Earth-observation programme Copernicus are tied to whether it associates with Horizon Europe. Credit: Science History Images/Alamy

Without an association deal, scientists based in the United Kingdom will be locked out of Horizon Europe. Historically, UK scientists have had huge

success securing funding from the European Commission, consistently ranking among the top beneficiaries.

Already, the Commission's flagship blue-skies research agency, the European Research Council (ERC), has announced the winners of the first raft grants as part of Horizon Europe. The 46 successful scientists at UK institutions face an anxious wait to see whether they will be part of the programme — one of the most prestigious early-career schemes in the world — or if they will continue to rely on funds provided by the UK government.

“Association is being held hostage to the bigger political impasse of the Northern Ireland protocol,” says Martin Smith, head of the policy lab at Wellcome, the London-based biomedical funder. Despite both sides’ desire to reach an agreement, the impasse will be resolved only when they come to an agreement on Northern Ireland or if the Commission decides to separate the issue from the Horizon Europe deal, he says. “Patience is wearing thin.”

Other countries’ experiences of negotiating association deals suggest that the latter scenario is unlikely. Talks between the Commission and Switzerland, a non-EU country that has previously been an associate member of EU research programmes, have not yet begun because the two are divided over political issues — so scientists there can only bid for EU funding in certain schemes, which exclude ERC grants. And in 2014, a row over a Swiss referendum on immigration hampered the agreement that allowed researchers in the country access to the previous EU research programme, Horizon 2020. Swiss scientists were effectively locked out for the first six months and were allowed to participate in the full programme only when the Swiss government changed their immigration policy.

## Back-up funding

The stalling negotiations mean that the UK government has made contingency plans so that researchers will still be able to access funding in the event of a deadlock. As early as 2019, the government began [drawing up plans](#) to create its own version of the European funding scheme in the event of a no-deal Brexit. And last year’s research budget earmarked £2 billion per

year to either cover the costs of associating with Horizon Europe or to create domestic alternatives.

“We have been getting increasingly nervous and that has reached a critical point,” says Vivienne Stern, who leads Universities UK International in London, which represents institutions in the UK. The risk is that, despite their best intentions, British politicians might run out of patience with the EU and shun association in favour of domestic funding programmes.

It is not only the availability of EU research funding that hangs in the balance while talks are in deadlock. Britain’s ability to take part in other joint science programmes, such as the European Atomic Energy Committee and Earth-observation programme Copernicus are tied to whether it associates with Horizon Europe.

Currently, temporary workarounds are in place to ensure that the United Kingdom continues to participate in most of these programmes, including using domestic funding and participating in different ways. But researchers do not have any power to make decisions about the projects, including EUROfusion, a large EU consortium researching fusion energy.

In June last year, the EU ruled that the United Kingdom’s data-protection regulations were adequate. This means that data, including those from clinical trials, are able to flow between research collaborators as they did before Brexit. The EU will review the regulations on a regular basis, and UK data policies might change in the future. “This is one of those things that is never going to go away,” Smith says.

*Nature* **602**, 374-375 (2022)

*doi:* <https://doi.org/10.1038/d41586-022-00318-w>

---

This article was downloaded by **calibre** from <https://www.nature.com/articles/d41586-022-00318-w>

- NEWS
- 04 February 2022

# Major African radio telescope will help to image black holes

US\$25-million facility in Namibia will be Africa's first millimetre-range radio telescope.

- [Sarah Wild](#)



The Africa Millimetre Telescope in Namibia will be a repurposed version of the Swedish–ESO Submillimetre Telescope, which is currently located in La Silla, Chile. Credit: Y. Beletsky (LCO)/ESO

Astronomers across Africa and Europe have reacted with delight to news that Africa's first millimetre-range radio telescope is to be built.

The Africa Millimetre Telescope will fill a gap in the coverage of the [Event Horizon Telescope \(EHT\)](#), a global network of telescopes that can receive and analyse radio waves of around 1 millimetre in length — [in 2019 they published the first-ever image of a black hole's edge](#), known as its event horizon.

The telescope will be located on or near Table Mountain in the Gamsberg Nature Reserve in Namibia. It will be a repurposed 15-metre telescope, currently located at La Silla in Chile, which is being donated by the Onsala Space Observatory in Sweden and the European Southern Observatory, headquartered near Munich, Germany.

The project, confirmed at the end of last year, is “another step toward solidifying Africa’s position as a globally competitive and capable player in the field of astronomy”, says Charles Takalana, head of the secretariat at the African Astronomical Society in Cape Town, South Africa. The telescope will “fill a missing observing window on the continent” and will be crucial for Africa’s astrophysics communities, adds Roger Deane, who directs the Wits Centre for Astrophysics at the University of Witwatersrand in Johannesburg, South Africa.

The Africa Millimetre Telescope is a collaboration between Radboud University Nijmegen in the Netherlands and the University of Namibia in Windhoek. It will be about five years before the telescope gets to see first light. The project will cost around US\$25 million, including construction, operations and outreach projects in the southern African country. Half of its funding has come from Radboud University. Other funders include the University of Namibia, the European Southern Observatory and the Netherlands Research School for Astronomy based in Leiden.

The telescope team is working to complete what is called a critical design review, which will help to determine the observatory’s exact location on the mountain, whether it needs to be adjacent to the mountain, or located at another site; and whether extra funding will be needed.

Telescopes in the millimetre-wavelength range can image the event horizon of a black hole, says project manager Marc Klein Wolt, who is also managing director of the Radboud Radio Lab at Radboud University. At longer wavelengths, “you only saw a blob, but at the millimetre wavelengths, you start to see the edge”.

In 2019, the EHT team published a celebrated image of the supermassive black hole at the centre of the galaxy M87. It was the first picture to show the contour of a black hole’s event horizon. “That image was the start of a new science, like the first observation of gravitational waves was the start of a new science,” Klein Wolt says. Radboud University astrophysicist Heino Falcke, who announced the first black hole image, will be the Africa Millimetre Telescope’s scientific leader.

“You have to have a telescope in the Southern Hemisphere, in southern Africa, to make all those connections [to other telescopes in the network],” Klein Wolt says. “That would allow you to observe [the sky] as the Earth rotates,” he adds.



The Africa Millimetre Telescope will be built on or close to the 2,347-metre plateau of Mount Gamsberg (pictured), in the Gamsberg Nature Reserve of Namibia. Credit: Manfred Gottschalk/Alamy

However, the EHT will only require about one-fifth of the Africa Millimetre Telescope's total observation time, says astronomer Michael Backes, co-principal investigator of the project, who is based at the University of Namibia. "The lion's share of the time will be available for Namibian astronomers to develop their programmes," he says.

Possible projects in Namibia include monitoring the variations in the brightness of small and large black holes in collaboration with optical telescopes and  $\gamma$ -ray telescopes such as the High Energy Stereoscopic System (HESS), which is also located in Namibia, and the planned Cherenkov Telescope Array in Chile, says Backes.

In the past two decades, telescopes have been set up across southern Africa. Countries with relatively clear skies and low population densities are ideal for astronomy. Telescopes there cover a wide range of wavelengths — from the optical Southern African Large Telescope and radio telescope MeerKAT in South Africa to the HESS telescope in Namibia. Late last year, [the Square Kilometre Array \(SKA\) Observatory](#) began awarding contracts to build its giant radio telescope, which will have thousands of dishes in South Africa and one million antennas in Australia, when the project is complete.

However, finding trained scientists and engineers in the continent has historically been a challenge, says Carla Sharpe, head of the Africa programme at the Cape Town-based South African Radio Astronomy Observatory, which is not yet involved in the Africa Millimetre Telescope. Since 2005, when it threw its hat in the ring to host the SKA, South Africa has awarded more than 1,000 scholarships in astronomy and engineering to fill this talent chasm locally and in SKA Africa partner countries, including Namibia.

Backes says he hopes that the Africa Millimetre Telescope will help to expand Namibia's astronomy community. Klein Wolt adds that the team is still looking for more funding so that it can finalize the telescope location and continue to train astronomers in Namibia.

Projects such as the Africa Millimetre Telescope will help to achieve a larger programme in Africa in astronomy, radio astronomy and engineering, which are needed to help develop the continent, says Sharpe.

*Nature* **602**, 375 (2022)

*doi:* <https://doi.org/10.1038/d41586-022-00205-4>

---

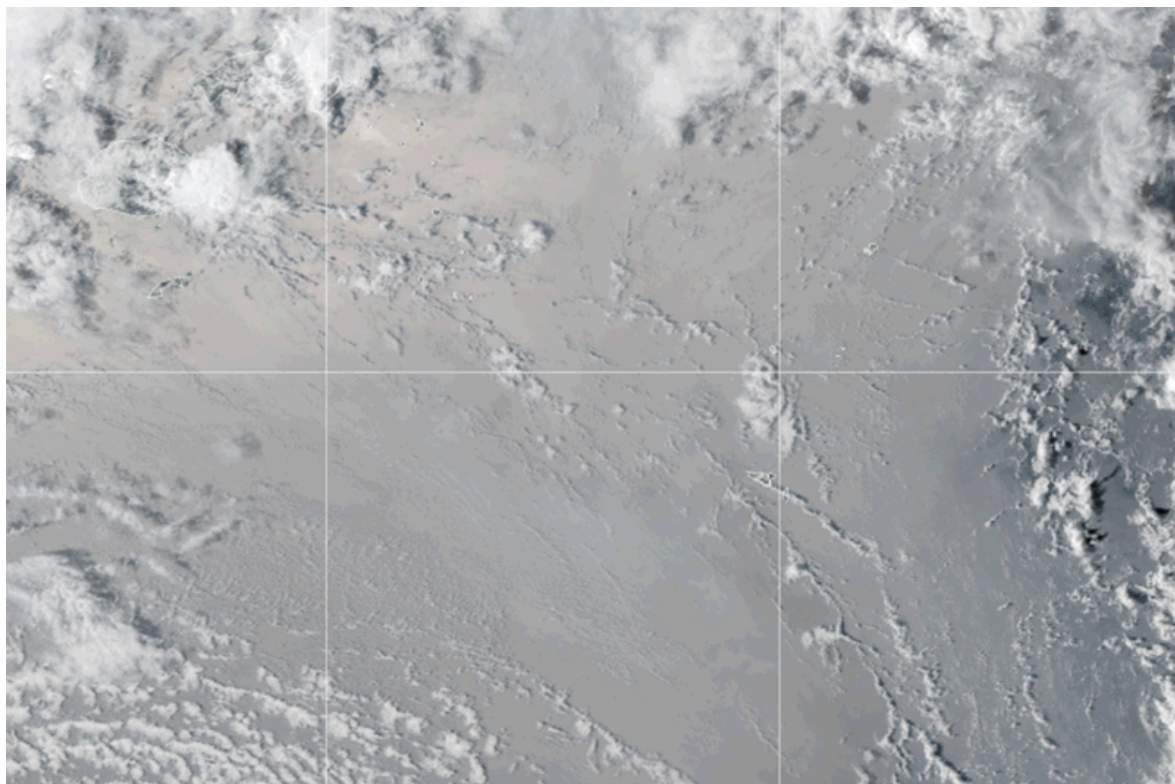
This article was downloaded by **calibre** from <https://www.nature.com/articles/d41586-022-00205-4>

- NEWS FEATURE
- 09 February 2022

# Why the Tongan eruption will go down in the history of volcanology

The 15 January blast sent shock waves around the globe and defied scientific expectations. Researchers are now scrambling to work out why.

- [Alexandra Witze](#)



The Hunga Tonga–Hunga Ha‘apai explosion was captured by several Earth-observing satellites.Credit: Visible Earth/NASA

The eruption that devastated Tonga on 15 January lasted just 11 hours, but it will take years for scientists to work out exactly what happened during the cataclysmic explosion — and what it means for future volcanic risks.

The volcano, named Hunga Tonga–Hunga Ha‘apai, sent a plume of ash soaring into the upper atmosphere and triggered a tsunami that destroyed homes on Tonga’s nearby islands. Reverberations from the eruption circled the globe multiple times.

The extraordinary power of the blast, captured by a range of sophisticated Earth-observing satellites, is challenging ideas about the physics of eruptions. Researchers are finding it hard to explain why the volcano sent a cloud to such heights, yet emitted less ash than would be expected for an eruption of such magnitude. And the shock waves that rippled through the atmosphere and oceans are unlike anything seen in the modern scientific era.

The eruption of Hunga Tonga–Hunga Ha‘apai is forcing scientists to rethink their ideas on the hazards posed by the many submarine volcanoes that lurk beneath the waves of the Pacific Ocean.

“It just basically rips the Band-Aid on our lack of understanding of what’s happening under water,” says Nico Fournier, a volcanologist at GNS Science in Taupo, New Zealand.



Tongan scientists observed an eruption of the volcano a day before the main blast. Credit: Tonga Geological Services/ZUMA Press

## Fresh danger

The eruption, which happened just 65 kilometres from the Tongan capital of Nuku‘alofa, has been a disaster for the more than 100,000 people living in Tonga. They are working to clear away the thick layer of ash that blanketed everything, to establish clean drinking-water supplies and to recover from the crop damage, estimated to equate to nearly 39 million Tongan pa‘anga (US\$17 million). At least three people have died in Tonga as a result of the eruption. The crisis is being compounded by COVID-19, with Tongans facing their first wave of cases, which started after relief ships arrived from other countries.

But earthquakes continue to shake the region, and the volcanic danger might not be over. Preliminary studies of ash from the 15 January eruption suggest that it was fed by a fresh batch of magma rising from inside Earth. Hunga Tonga–Hunga Ha‘apai could remain active for some time, with uncertain effects on the people of Tonga.

Geoscientists have limited ability to provide people in the region with a good sense of the future risks. “It’s a really difficult situation of wishing volcanology could give more to the local people,” says Janine Krippner, a volcanologist with the Smithsonian Institution’s Global Volcanism Program in Washington DC, who is based in New Zealand. “But right now, that’s not the case.”

Most of Hunga Tonga–Hunga Ha‘apai lies under water. It rises more than 2,000 metres from the sea floor and is part of the Tonga–Kermadec volcanic arc. This string of mostly underwater volcanoes sits above a massive geological collision zone, where the western edge of the Pacific plate of Earth’s crust dives beneath the Indo–Australian plate. The edge of the Pacific plate heats up as it sinks into the planet’s depths, and molten rock rises to feed the volcanoes of the Tonga–Kermadec arc.

Geological evidence shows that large eruptions have convulsed Hunga Tonga–Hunga Ha‘apai about once every millennium, with huge blasts that occurred in around ad 200 and ad 1100. The past century has brought smaller ones, in 1937 and 1988. By that point, the top of the volcano was

peeking out above the waves in the form of two small islands, named Hunga Tonga and Hunga Ha‘apai.

Then, in 2009, the volcano began spitting ash and steam in an eruption at Hunga Ha‘apai. In December 2014 and January 2015, another eruption formed new land that connected the two islands, forming a single landmass<sup>1,2</sup>.

Several research teams visited the new island soon after it formed and gathered samples of volcanic ash and rock. Geochemical analysis of that material, described in a paper in *Lithos*<sup>3</sup>, found that the 2009 and 2014–15 eruptions involved molten rock that had not risen recently from the great depths of Earth’s mantle.

Instead, it had spent some time at a geological way station, a magma chamber located 5–8 kilometres deep in Earth’s crust. While sitting there, the magma had gone through some tell-tale chemical changes, almost like wine ageing in a barrel, before ultimately erupting onto the surface.

The magma that erupted this January was different. Shane Cronin, a volcanologist at the University of Auckland in New Zealand, and his colleagues have analysed ash from the eruption that military relief workers scooped up near the airport on Tonga’s largest island. Chemical analysis shows that it differs from that of the 2014–15 eruptions. Cronin says that the fresh magma rose quickly, without spending much time undergoing chemical changes in the buried magma chamber.



Tongatapu island in Tonga before Tonga–Hunga Ha‘apai exploded, and after, covered in ash. Credit: Maxar via Getty

Geologist Taaniela Kula and his colleagues at the Tonga Geological Services in Nuku‘alofa have been collecting ash samples from islands across Tonga that Cronin and others are analysing. By studying ash from different islands, including noting how thickly and how widely it is distributed, researchers will be able to build up a better picture of how the eruption unfolded.

Surprisingly, there seems to have been relatively little ash emitted, given the size of the blast. That might be a result of the environment in which Hunga Tonga–Hunga Ha‘apai erupted: under water, but at a relatively shallow depth.

## The water factor

Volcanoes in deep water rarely erupt through the ocean surface in big blasts, because the pressure of the overlying water prevents gas bubbles from forming and growing with explosive force. But the volcanic vent that

erupted at Hunga Tonga–Hunga Ha‘apai on 15 January was just tens to 250 metres deep. That’s shallow enough that the water didn’t suppress the power of the blast, but deep enough for the erupting magma to encounter a lot of water.

Water can fuel explosive eruptions by flash-heating to form steam, which expands quickly. In this way, it efficiently transforms thermal energy from magma into the kinetic energy of an eruption, says Michael Manga, a geoscientist at the University of California, Berkeley. “Some of the most powerful eruptions have been through water,” he says.

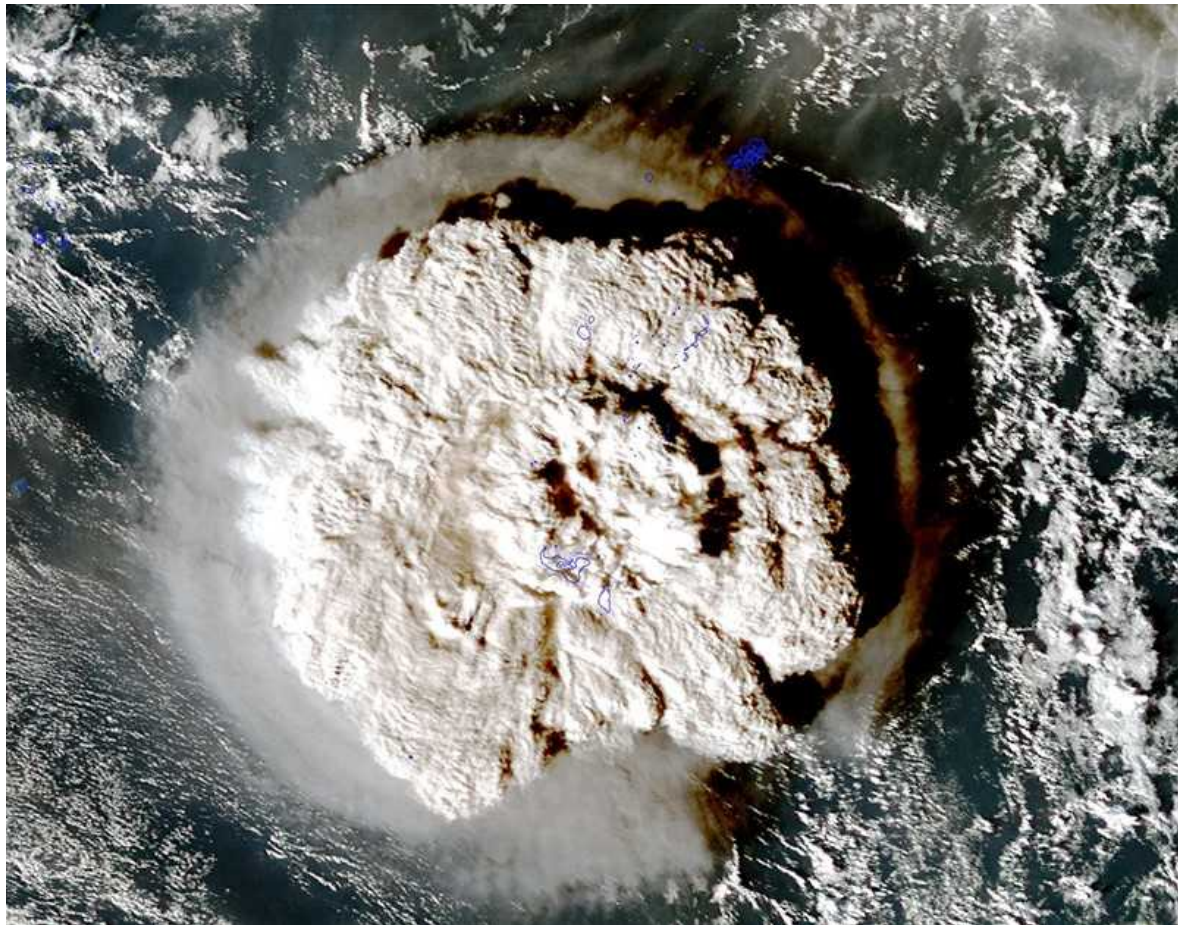
Another important factor is how much volcanic gas is mixed into the magma before it erupts. A gas-rich upwelling of magma might have fed the 15 January eruption by providing a large number of bubbles to fuel the explosion, says Raymond Cas, a volcanologist and emeritus professor at Monash University in Melbourne, Australia.

The eruption of Hunga Tonga–Hunga Ha‘apai is unusual in that it combined features not usually seen together, says Cas. Volcanologists know of other examples of eruptions that occurred under water, or under snow and ice, and thus incorporated water. Scientists have also seen extremely high eruption plumes that towered into the atmosphere. But Hunga Tonga–Hunga Ha‘apai is a unique example of both things happening together. It might ultimately come to serve as the prototype of a newly recognized type of eruption style, he says.

Most submarine eruptions don’t produce particularly high plumes. For instance, in 2012 the massive deep-sea eruption of Havre volcano, north of New Zealand, produced mainly a huge floating collection of lightweight pumice stones<sup>4</sup>. That eruption occurred at a depth of more than 900 metres. “We have relatively few cases where we see large plumes that breach the ocean surface,” says Kristen Fauria, a volcano scientist at Vanderbilt University in Nashville, Tennessee.

Yet the Hunga Tonga–Hunga Ha‘apai eruption plume soared to a height of at least 30 kilometres, well into the upper atmosphere, or stratosphere. That’s so high that researchers have been scrambling to understand what long-term impact it might have. High-resolution satellite imagery is allowing them to

track how ash, gas and certain chemical species are drifting through the atmosphere — in much more detail than they could in 1991, when Mount Pinatubo in the Philippines erupted even more powerfully than Hunga Tonga–Hunga Ha‘apai. “We have never seen anything like this,” says Anja Schmidt, a volcanologist at the German Aerospace Center in Oberpfaffenhofen.



The giant ash cloud that erupted from Hunga Tonga–Hunga Ha‘apai, taken by the Japanese satellite Himawari-8.Credit: EyePress News/Shutterstock

The Tonga volcano didn’t emit enough sulfur dioxide to change global climate, as eruptions from some other volcanoes have. It expelled an estimated 400,000 tonnes of SO<sub>2</sub>, whereas the 1991 eruption of Pinatubo ejected nearly 20 million tonnes. That blast temporarily cooled the planet by nearly 0.5 °C, as the sulfur formed sulfate particles that reflected some of the Sun’s radiation back into space.

One possible explanation for the discrepancy is that much of the SO<sub>2</sub> from Hunga Tonga–Hunga Ha‘apai might have ‘fallen out’ of the plume at low altitudes, before the plume got too high. But Hunga Tonga–Hunga Ha‘apai did throw ash high into the stratosphere, and researchers will be looking for signs of any impact on climate, Schmidt says. They will also be watching to see whether the volcanic material causes any destruction of stratospheric ozone, and whether the atmospheric waves the eruption unleashed affect atmospheric circulation patterns in the coming months.

Early findings could come from balloon experiments lofted into the Tongan eruption plume. Several research teams have already launched balloons carrying instruments from the island of La Réunion in the Indian Ocean. One such effort, led by the US National Oceanic and Atmospheric Administration, was able to measure volcanic particles up to a height of 28 kilometres as the plume drifted over La Réunion, says team member Elizabeth Asher, an atmospheric scientist at the Cooperative Institute for Research in Environmental Sciences in Boulder, Colorado. That’s so high that she expects to see the eruption’s atmospheric effects to linger for longer than they would after less-powerful eruptions.

## Ripple effects

Another aspect that could reshape volcanology is the way in which Hunga Tonga–Hunga Ha‘apai unleashed a rich variety of waves that rippled through the oceans and the atmosphere. The reverberations it sent around the world are reminiscent of those seen after the 1883 eruption of Krakatau in Indonesia, says Alan Robock, a climate scientist at Rutgers University in New Brunswick, New Jersey. [The eruption last month triggered pressure waves and gravity waves](#) in the atmosphere and tsunami waves all around the Pacific Ocean — even in distant ocean basins. GPS satellites also detected disturbances in the ionosphere, the layer of the atmosphere that lies above the stratosphere, starting at a height of 80–90 kilometres.

“There are huge pieces of this puzzle that we haven’t quite managed to pull together,” says Fournier.

The challenge now is to gather enough data to complete the puzzle. Volcanologists would normally monitor an active volcano using seismometers to study earthquakes in the surrounding area. There are currently no active seismometers in Tonga, so the large quakes that have been happening around Hunga Tonga–Hunga Ha‘apai since the 15 January eruption have not been tracked in much detail. The data that exist, however, suggest that the quakes are generated by fresh magma rising into the crust to refill the reservoir that was emptied by the large eruption, says Cronin.

Another priority is to survey the sea floor around the volcano to see which parts of its underwater structure have blown up or otherwise changed since previous surveys. Satellite radar imagery suggests that the top part of the volcano has subsided by at least 10 metres, Cronin says. But it is too dangerous to approach the volcano to do a scientific survey just yet.

Some early data might come from relief ships that have been travelling to and around Tonga, such as the one tasked with repairing the submarine cable that connects Tonga to Fiji. This was severed during the eruption, cutting off international communications. The cable might have been buried by a landslide coming off the side of the volcano, or cut in several places.

Foremost in everyone’s minds is what Hunga Tonga–Hunga Ha‘apai might do next. A group of international experts is providing information to the Tonga Geological Services to help the Tongan government to assess the risk and decide what to do. The researchers are weighing up three possible scenarios: the eruption could end, it could continue at a low level or there could be another massive blast. “All these scenarios are still live,” says Cronin.

Regardless of what the immediate future holds for this particular volcano, the eruption has volcanologists rethinking the hazards of submarine volcanoes more broadly, says Schmidt. “It’s a stark reminder that these kinds of volcanoes exist, that they pose a hazard, and that they are understudied.”

*Nature* **602**, 376-378 (2022)

*doi:* <https://doi.org/10.1038/d41586-022-00394-y>

# References

1. Cronin, S. J. *et al.* *Eos* <https://doi.org/10.1029/2017EO076589> (2017).
2. Garvin, J. B. *et al.* *Geophys. Res. Lett.* **45**, 3445–3452 (2018).
3. Brenna, M. *et al.* *Lithos* **412–413**, 106614 (2022).
4. Carey, R. *et al.* *Sci. Adv.* **4**, e1701121 (2018).

---

This article was downloaded by **calibre** from <https://www.nature.com/articles/d41586-022-00394-y>.

| [Section menu](#) | [Main menu](#) |

- NEWS FEATURE
- 14 February 2022

# An ancient link between heart and head — as seen in the blobby, headless sea squirt

The vital connection between body parts provides insight into the evolution of vertebrates' closest kin.

- [Amy Maxmen](#)

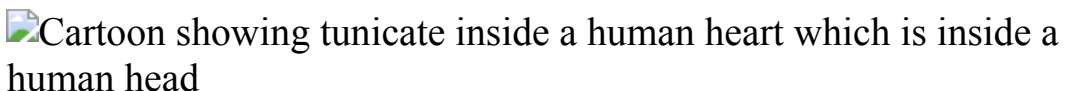


Illustration by Fabio Buonocore

*The head is stately, calm, and wise,*

*And bears a princely part;*

*And down below in secret lies*

***The warm, impulsive heart. — John Godfrey Saxe, 1898***

For centuries, writers have mused on the heart as the core of humanity's passion, its morals, its valour. The head, by contrast, was the seat of cold, hard rationality. In 1898, US poet John Godfrey Saxe wrote of such differences, but concluded his verses arguing that the heart and head are interdependent. "Each is best when both unite," he wrote. "What were the heat without the light?" At that time, however, Saxe could not have known that the head and the heart share a deep biological connection.

In the past 15 years, scientists have uncovered a developmental link between the two. In 2010, for example, researchers revealed that the same small pool of cells that divides and differentiates to form the heart in mouse embryos also gives way to muscles in their throats and lower heads<sup>1</sup>. Key components of the two are cut from the same cloth.

Even more surprising is that the embryonic head–heart connection pre-dates the evolutionary origin of vertebrates, and perhaps even of the head itself. Researchers stumbled on the link while studying sea squirts, blobby, sedentary marine creatures, found affixed to the sea floor, that have two openings — one for sucking water in and the other for squirting it out — hence the name.

Sea squirts belong to a group of spineless animals, called tunicates, that are vertebrates' closest living relatives, despite their many differences. And even though tunicates lack a true head, the evolutionary link between the head and heart is strong in them. “When I first heard about this, I was like, what are you talking about?” says Billie Swalla, an evolutionary developmental biologist at the University of Washington in Seattle, with a laugh.

Researchers have identified a group of cells in sea-squirt embryos that divide and differentiate to form both their hearts and the muscles in a structure similar to part of the vertebrate throat. This suggests that a head–heart connection arose before those two lineages diverged from one another hundreds of millions of years ago. Now, Swalla and other researchers are trying to determine how far back the link goes, and whether it arose in an immobile, headless animal, similar to the sea squirt, or one that faced forward as it swam, with a head evolving along with its heart. “That’s the question that keeps me up at night — that and COVID,” Swalla says.

## Looking for links

Most animals have a heart, in the vaguest sense of the word, meaning any vessel that pumps fluid around a body. But in vertebrates, the heart is a distinct, layered organ with parts for inflow and outflow that keep a rhythm. Until about a decade ago, the evolutionary origin of the chambered heart was mysterious, because similar forms of the organ weren’t apparent in

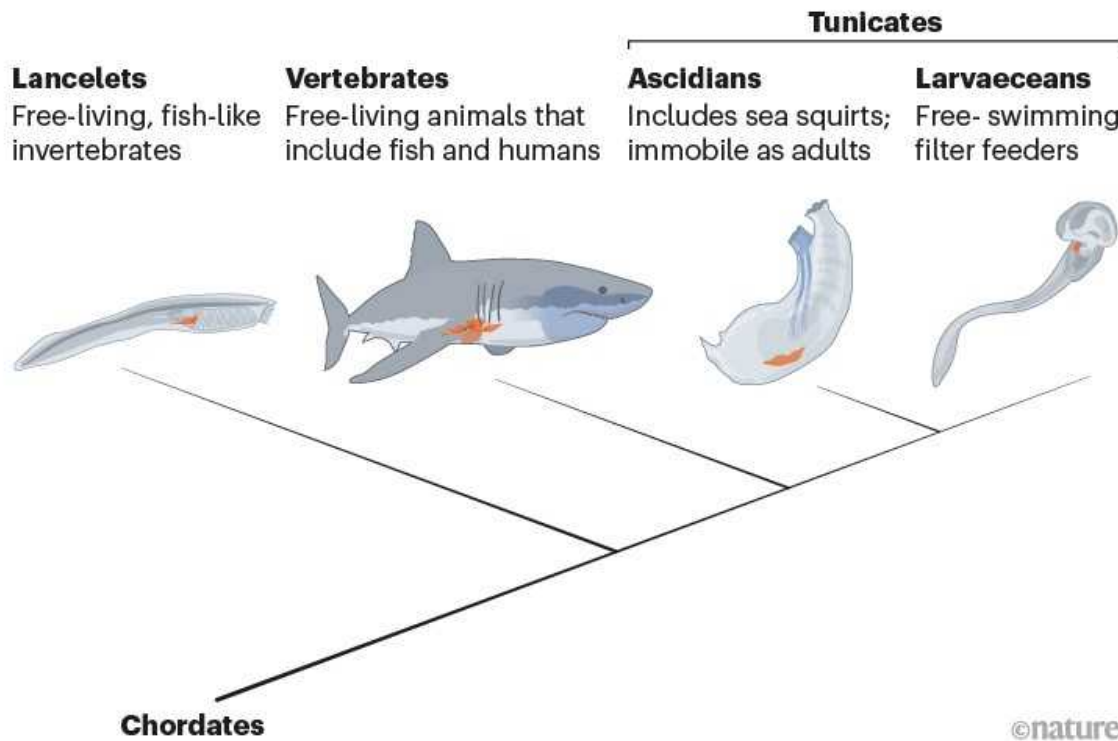
animals previously thought to be vertebrates' closest kin: the slim, mobile lancelet. These translucent, arrow-like animals have such a rudimentary circulatory system — a simple pumping tube — that purists consider them heartless. A link seemed to have been lost to time.

Curiosity was reignited in 2006, when a study suggested that lancelets were not, in fact, the closest living relative to vertebrates<sup>2</sup>. This analysis, based on genetic analyses of dozens of chordates, the phylum that includes vertebrates, lancelets and tunicates, found that the closest relations are actually the tunicates (see 'An evolving tree'). The rearrangement initially shocked many researchers because, whereas lancelets vaguely resemble fish, sea squirts look more like a large wad of gum — from the outside, at least. "Tunicates should therefore no longer be considered as 'primitive,'" the authors concluded.

## AN EVOLVING TREE

A rearrangement of the chordate family tree in 2006 made the mainly immobile tunicates, rather than the free-living lancelets, the closest kin to vertebrates.

The change made sense as researchers compared the development of muscles in the heart (orange) and pharynx (blue) across different species. But questions about the evolution of free-living and sedentary lifestyles remain.



Source: Ref. 6

Marine biologists who had examined the anatomy of tunicates were somewhat relieved by this result, however. Linda Holland, an evolutionary developmental biologist at the Scripps Institution of Oceanography at the University of California, San Diego, says that hypothetical scenarios about how the chordate body had evolved over evolutionary time “just didn’t make sense” with the earlier family tree. For example, the lancelet heart looks nothing like those of vertebrates, whereas the sea squirt’s bears certain similarities, and is sophisticated.

Beneath the tunicate’s unassuming exterior lies a layered, V-shaped heart surrounded by a spiral of muscle fibres that contract the organ in a gradual, wringing motion that keeps fluid flowing in one direction. The heart can also reverse the direction of flow.

## Heart cells on the move

To explore the evolution of the tunicate heart, Bradley Davidson, a postdoctoral researcher at the University of California, Berkeley, in the early 2000s, set his sights on the sea-squirt species *Ciona intestinalis*. He followed in a tradition of developmental biologists who, for more a century, had painstakingly tracked the division and migration of individual cells in embryos. Davidson genetically manipulated sea-squirt embryos so that cells that express a gene involved in vertebrate heart formation, *Mesp*, would glow green under fluorescent light. When he looked at the embryos under a powerful microscope, a clump of around 16 cells that would form the heart at later stages of development dutifully lit up.

In 2005, another postdoctoral researcher, Lionel Christiaen, joined the Berkeley lab, and decided to repeat Davidson’s experiment with *Mesp*. He photographed the embryos with the glowing clump of cells one morning, and then left campus. For no particular reason, he decided to return later that evening and check on them again. “It was a day when I was hungry for science,” recalls Christiaen, now an evolutionary biologist at the Sars International Center for Marine Molecular Biology at the University of Bergen in Norway.

To his surprise, some of the glowing green cells had migrated to the opposite side of the embryos, where they formed a ring near the animal's developing pharynx. In adult sea squirts, the pharynx fills with water, filters out plankton to the digestive system and releases the rest for the animal to squirt back out. In vertebrates, the pharynx is part of the throat. Fish use theirs to process gulps of water from their open mouths. Christaen was aware of work suggesting that muscles in the mouse heart derived from the same pool of embryonic cells as some in the lower head<sup>3</sup>. He wondered if he might be observing the same thing in tunicate embryos.

Shared heart-head precursors were not known back in 1983, when biologists studying vertebrate origins put forward the ‘new head’ theory<sup>4</sup> to describe the evolution of a distinct head with a thumping heart positioned just below. These authors depicted a scenario in which natural selection drove a cascade of features that improved the ability of vertebrates to eat and hunt. One such adaptation was the evolution of jaws from the neural-crest cells that give rise to the vertebrate skeleton. Other key adaptations would have included refined sense organs in the hunter’s new head, and a complex brain to integrate the signals.

The authors of this theory focused mostly on the cells that created jaws and other bones. They left open the evolution of muscles around the pharynx and lower head that would make jaws operable. The evolution of those muscles remained elusive for decades, until Christiaen found a clue in that ring of cells in the tunicate embryos with activated Mesp.



*Ciona intestinalis*, or sea squirts, are close relatives of vertebrates. Credit: Sue Daly/Nature Picture Library

Together with his colleagues, Christiaen ran a second experiment. This time, they made cells that express genes related to the formation of the lower vertebrate jaw — Islet and Tbx1/10 — glow green in tunicate embryos. Sure enough, these cells derived from the same pool of cells that created the heart. In a 2010 report<sup>5</sup>, the team coined the term ‘cardiopharyngeal’ to describe embryonic cells that form the heart and pharynx in tunicates, and they suggested that these cells were probably present in a shared ancestor of tunicates and vertebrates. Furthermore, they said these special cells would have been instrumental in the coevolution of the circulatory, respiratory and feeding system of vertebrates. “The cardiopharyngeal cells preceded the emergence of the jaw,” Christiaen says. “They were there ready to welcome head bones with muscles.”

## Have heart, won’t travel

Another evolutionary biologist studying the origin of vertebrates and their kin, Cristian Cañestro, at the University of Barcelona in Spain, says that Christiaen's study suggested that "the machinery that made a 'new head' was present in the last common ancestor" of vertebrates and tunicates. But did those ancestors actually have a head?

It is possible that they did, and that tunicates lost theirs. Two facts support this idea. Before they affix themselves to a rock or a bit of the sea floor, tunicate larvae are mobile, free-swimming creatures, with a definable front and tail. And one type of tunicate, a small group named larvaceans — because they superficially look like swimming larvae — remain mobile their entire lives. Less than few centimetres long, larvaceans fumble through the ocean wiggling their tails. That motion generates a water current that flows through a bubble-like 'house' they generate around their bodies, allowing them filter out plankton.

For some researchers, larvaceans' existence seemed to point in favour of a travelling tunicate ancestor. Cañestro decided it was time to learn more about the creatures, so he started a colony of them in the basement of his lab in Barcelona. Kept in a glass tank of circulating salt water, hundreds of larvaceans hover like dust for the duration of their fleeting lifespan. "On day five," Cañestro explains, "they explode, releasing hundreds of sperm or eggs that float at the surface of the water."

When his graduate student, Alfonso Ferrández, was searching for a doctoral project, Cañestro took him into the basement to see the larvaceans, and suggested he study the development of their hearts. Ferrández began by fishing for *Mesp* and other genes known to control heart development in tunicates and vertebrates. But couldn't find them. He played with protocols. He repeated experiments. He deployed a variety of computer programs to sift through genomic sequences. All to no avail. Finally, he and Cañestro concluded that most of the heart genes simply were not there. Missing genes wouldn't have been very surprising in the larvaceans — they have one of the smallest genomes in the animal kingdom — but it was curious, because they still have a beating heart and plenty of other body parts that the genes encode in other animals. "That's when I started to be very into this project," says Ferrández. "I wasn't in love with the heart story when I started, but this was interesting."

That enthusiasm kept Ferrández going as COVID-19 swept around the globe. Even during Spain’s strict lockdown, he got permission to go to the lab to keep the larvaceans alive, as he plugged away at his project. Although Mesp and other known genes were missing, he managed to recover a few genes that contributed to the formation of the organism’s simple heart, which comprises just eight muscle cells that rhythmically contract to pump fluid around the body. Over evolutionary time, larvaceans managed to survive gene loss, finding other ways to build body parts that allowed them to move, eat and procreate, says Cañestro. “Gene losses can be adaptive,” he says.

Rather than representing an ancestral condition, the larvaceans seem to be strange offshoots of the tunicate family, the Barcelona team concluded in a paper<sup>6</sup> published last November. With that being the case, the researchers suggested that the ancestor of tunicates was probably immobile like sea squirts rather than free-living like the highly modified larvaceans. “I love this paper,” says Davidson, now at Swarthmore College in Pennsylvania. To him, the work showcases how diversity arises in evolution from the same starting blocks.

But in all that diversity, a trail that traces back animals’ ancestry is hard to spot. Despite the latest larvacean study, Holland is unconvinced that tunicates were originally immobile. To support her argument, she lists reasons why sea squirts could be outliers, and names features that larvaceans share with lancelets, suggesting that they retain ties to an earlier state of being.

In the coming years, she and other researchers will continue to uncover details on how vertebrates and their closest kin develop, cell by cell, gene by gene, and they will learn what genomic tweaks occurred over hundreds of millions of years to make it all possible. The only seemingly sure thing at the moment is that these changes took place to the thump of a beating heart.

“The vertebrate heart probably evolved from something akin to a tunicate heart, but remember — tunicates are evolving rapidly,” Holland muses. “We’ll never know for sure what their common ancestor was like, except that it had a heart.”

*doi: <https://doi.org/10.1038/d41586-022-00413-y>*

## References

1. Lescroart, F. *et al.* *Development* **137**, 3269–3279 (2010).
2. Delsuc, F., Brinkmann, H., Chourrout, D. & Philippe, H. *Nature* **439**, 965–968 (2006).
3. Nathan, E. *et al.* *Development* **135**, 647–657 (2008).
4. Gans, C. & Northcutt, R. G. *Science* **220**, 268–273 (1983).
5. Stolfi, A. *et al.* *Science* **329**, 565–568 (2010).
6. Ferrández-Roldán, A. *et al.* *Nature* **599**, 431–435 (2021).

---

This article was downloaded by **calibre** from <https://www.nature.com/articles/d41586-022-00413-y>.

| [Section menu](#) | [Main menu](#) |

# Opinion

- **[Pandemics disable people — the history lesson that policymakers ignore](#)** [ 16 February 2022]  
Comment • Influenza, polio and more have shown that infections can change lives even decades later. Why the complacency over possible long-term effects of COVID-19?
- **[China: reform research-evaluation criteria](#)** [ 15 February 2022]  
Correspondence •
- **[Brazil opens highly protected caves to mining, risking fauna](#)** [ 15 February 2022]  
Correspondence •
- **[Catapult network busts biomedical bottlenecks](#)** [ 15 February 2022]  
Correspondence •
- **[Pollution — bring the field into the lab](#)** [ 15 February 2022]  
Correspondence •

- COMMENT
- 16 February 2022

# Pandemics disable people — the history lesson that policymakers ignore

Influenza, polio and more have shown that infections can change lives even decades later. Why the complacency over possible long-term effects of COVID-19?

- [Laura Spinney](#) 0



Virginia Lewis Hall's post-polio syndrome makes breathing difficult; the newspaper clipping shows her in an 'iron lung' respirator as a child.Credit: Tom Smart/New York Times/Redux/eyevine

When Ashley Shew turned up for an appointment at a medical centre in spring 2020, a member of staff told her she could remove her mask because only people with pre-existing conditions were vulnerable to COVID-19. Shew was surprised. "A hard-of-hearing amputee battered by chemotherapy and more", as she describes herself, she is a regular at the centre — the appointment that day concerned her prosthetic leg. Who, she wondered, did the staff member think counted as a person with pre-existing conditions?

The invisibility of disability is not new, says Shew, a 38-year-old philosopher who explores the intersection of technology and disability at Virginia Polytechnic Institute and State University in Blacksburg. "But it is particularly deadly that we don't frame COVID-19 as a disability issue," she says. "Even linguistically we're pointed away from it. 'Pre-existing conditions' is a way of not saying 'disability'."

From the beginning of this pandemic, people with disabilities understood that the disease would target them and would swell their ranks. Disability historians knew that there was a penumbra of ill health to previous mass-death events. Health economists warned that, as with tuberculosis, HIV and other diseases, morbidity would stalk mortality. Too many others have clung stubbornly to a belief that COVID-19 is something from which a minority of people die, and that most bounce back quickly and intact, with only their immune system updated. The longer the pandemic drags on, the harder it is to maintain that fiction.

Two years in, the debilitating tail of the pandemic has revealed itself in the form of tens of millions of people living with long COVID<sup>1</sup>. It is high time to ask whether attitudes to disability will change as a result. Will society grasp that the body can be altered for a long period — even permanently — by infectious disease, just as it seems to have accepted that the body politic will never be the same again? And will it make the necessary accommodations?

These questions have been asked before.

## Long influenza

Consider the ‘mother of all pandemics’ — the 1918 Spanish influenza outbreak. Even in the 1920s, scientists understood that this flu had neurological and other effects. The most notorious and debated of those — still — is the overlapping pandemic of encephalitis lethargica (EL) or ‘sleepy sickness’. Eighty per cent of EL survivors went on to develop a Parkinson’s-like disease<sup>2</sup>. According to cell biologist Richard Smeayne at the Jefferson Hospital for Neuroscience in Philadelphia, Pennsylvania, it has never been proved biologically that flu caused both EL and this post-encephalitic parkinsonism — at least not in the sense of catching the virus in flagrante in the brain tissue of people who had died. Yet the statistical case for it seems strong<sup>2</sup>.

The neurological tails of two subsequent flu pandemics, in 1957 and 1968, were less pronounced, but both were followed by rises in cases of encephalitis (brain inflammation), among other conditions<sup>2</sup>. Once again, researchers failed to demonstrate a clear causal link with an earlier flu infection, but it has since been established that the flu virus can infect the brain and trigger inflammation there and elsewhere in the body. Clinicians see this after every flu season, in a wave of strokes and heart attacks predominantly among older people<sup>3</sup>. And flu can cause encephalitis in children. It’s rare, but it can kill, and those who survive can be left with long-term brain damage<sup>2</sup>.

Flu is by no means the only infectious disease with long-term effects. For old foes such as measles and hepatitis, complications are well documented — such as the progressive neurological disorder subacute sclerosing panencephalitis and chronic liver disease, respectively. And researchers might even have good insight into the mechanisms that cause them.

With new diseases, or new variations on old diseases, long-range effects take time to be characterized. It took decades for researchers to prove a hunch that infection with the Epstein–Barr virus is a trigger for multiple sclerosis<sup>4</sup>, for example. There are reasons it’s not always easy to connect late-developing symptoms to the acute form of the disease, and identify a common cause.



Children attend a long-COVID clinic in Israel.Credit: Corinna Kern/Reuters

Take Ebola. Ever since the outbreak in West Africa in 2014, researchers have recognized a post-Ebola syndrome that affects the heart, brain, eyes and joints<sup>5</sup>. How the Ebola virus causes symptoms across so many organs is not yet clear. Studying the problem is complicated by the fact that, because Ebola is so deadly — killing around half those it infects — survivors experience significant social stigma.

Stigma can draw a veil of silence around a disease's chronic effects, with the result that they don't filter into the public consciousness. Jeanne Billioux, an infectious-diseases clinician at the US National Institute of Neurological Disorders and Stroke in Rockville, Maryland, has been following survivors of Ebola in Liberia since 2015. Many of them were expelled from their villages, she says: "They're getting better over time, but a significant proportion are still symptomatic."

## Post-polio syndrome

Before virologist Jonas Salk's polio vaccine was approved in 1955, the terrifying polio epidemics that swept North America and Europe each summer scarred the collective imagination. That mobilized support for the US non-profit organization March of Dimes, which helped to fund the vaccine. After 1955, there was a sense that the problem had been solved.

When, decades later, a proportion of the survivors of those epidemics relapsed — estimates vary between 20% and 85%<sup>6</sup> — their condition failed to elicit the same level of concern.

As encroaching respiratory and motor difficulties forced people back into dependence on aids for breathing and mobility, their priorities were reordered as radically as it's possible to imagine. Medical anthropologist and historian Joseph Kaufert at the University of Manitoba in Winnipeg, Canada, interviewed people with post-polio syndrome in the 1980s and 1990s<sup>7</sup>. “When I was up in the wheelchair it was just a matter of trying to breathe,” one man told him. “That was a day’s work.”

For Kaufert, the invisibility of these individuals owes much to a failure of collective memory. As their hard-won autonomy seeped away, they often reached out to the respiratory physicians who had treated them initially. But many had retired, and younger clinicians showed less interest. “It was really hard to build a career on an illness from the past,” Kaufert says.

In the 1980s, medical researcher Albert Sabin, who developed the polio vaccine that replaced Salk's, drew attention to post-polio syndrome, and March of Dimes took up the cause. It quickly became clear that there would be no silver bullet, no equivalent of the vaccine. The solution would involve mixing and matching therapies to suit each individual. That was a harder sell to the money-giving public.

Looking back over the twentieth century, it's impossible to ignore the scarring effects of infectious disease. Yet when a new virus emerged in late 2019, even the best-resourced nations failed to anticipate its long-term impact.

## The long haul

Long COVID is the latest reminder that epidemics have long tails – biologically, as well as psychologically, economically and socially. Since the persistent effects of COVID-19 were recognized 6 months into the pandemic, up to 200 symptoms have been reported<sup>8</sup> in 10 organ systems<sup>9</sup>, including the skin, brain<sup>10</sup>, heart<sup>11</sup> and gut. The recurring core<sup>12</sup> of these comprises loss of mobility, lung abnormalities, fatigue and cognitive and mental-health problems. But it's clear that long COVID is a catch-all term for a panoply of post-viral syndromes. Consequently, there is no simple test for it. Diagnosis is based on clinical symptoms, past infection with COVID-19 and the lack of an obvious alternative cause.

There was a tendency among medics to play down long COVID to begin with. Now, thanks in large part to the voice that 'long-haulers' found as they came together in a global online community that includes health-care workers, long COVID is the subject of large grants, research projects and a few specialist clinics, including for children.

Yet it continues to be overlooked by decision makers, who still present the costs and benefits of COVID-19 containment in terms of data on cases, hospitalizations and deaths alone. This means that in many countries, a burden of future disability is being created that could have been prevented, or reduced.



A man who has recovered from Ebola receives medication to help treat his long-term symptoms.Credit: Tommy Trenchard/MSF

In May 2021, health economists at the London School of Hygiene & Tropical Medicine estimated that COVID-induced disability might account for roughly 30% of the pandemic's overall health burden<sup>[13](#)</sup>. Theirs was an early, necessarily limited attempt at quantification. It excluded mental illness, for example. More recent estimates, made in the light of accumulating but still partial knowledge about long COVID, indicate that disability is likely to account for the lion's share of COVID-19's burden, and might disproportionately affect women, especially those who were infected young<sup>[14](#)</sup>.

These estimates remain crude, not least because too little is known about COVID-19's long-term effects on children. And they do not capture the impact of the predicted wave of disability on carers. Numbers will be refined as time goes on, and as data come in from ongoing studies, such as COVID-CNS (led by the University of Liverpool, UK, and King's College London) and STIMULATE-ICP (led by University College London).

Meanwhile, work proceeds on trying to understand how the coronavirus SARS-CoV-2 triggers long-term effects. Just how it damages the central nervous system is a matter of heated debate, for example<sup>15–19</sup>. One theory is that SARS-CoV-2 prompts a fleeting immune response that primes the brain for a later insult — genetic or environmental. If such a model applies more broadly, it might explain why it has been so hard to demonstrate a direct biological link<sup>15</sup> between viral infection and neurological disease, says Smeyne. It could also make it fiendishly difficult to predict who will succumb later. “It’s like, spin the wheel,” he says.

It could even turn the idea of pre-existing conditions on its head. Does transient infection itself create a vulnerability which, sometime later, might or might not translate into an epidemic of disability?

## Disability rights

In the past, awareness of the disability that contagion brings in its wake has translated into meaningful change. In the United States, for example, polio survivors Judith Heumann and Ed Roberts emerged as leaders of the disability-rights movement. They were influential in pushing through legislation intended to improve life for all people with disabilities, including the Rehabilitation Act of 1973 and the Americans with Disabilities Act of 1990.

One of long-haulers’ clearest demands has yet to be reflected on national or international data dashboards. Namely that the tsunami of COVID-induced disability is acknowledged in pandemic policymaking, not just in scientific grants, papers and clinics. “There is a strange disconnect whereby health ministers are now talking about the gravity of long COVID, but it features nowhere in the considerations on which they base their pandemic policy,” says Nisreen Alwan, a public-health specialist at the University of Southampton, UK, who is herself recovering from long COVID.

And many long-haulers have found common cause with clinically vulnerable people in calling out the ableism and disablism (see [go.nature.com/336rjwc](https://go.nature.com/336rjwc)) of policies that fail to keep COVID-19 case numbers low. Rampant spread not only raises the risk of more troublesome

variants evolving, it also sets more people up for long-term health problems — especially those who are already marginalized — and it limits the lives of millions for whom vaccines are unavailable or ineffective.

Public health has always privileged the acute over the chronic, but this is about more than discounting the future. It's about duelling models of disability — the medical and the social. When will it be safe for the adult with severe asthma to return to in-person work? How is the thriving child with an organ transplant to get educated if there's no vaccine for her, no masks or tests for her classmates, no notifying her parents when there's a case in class, and public messaging that runaway infection among children is fine?

The extent to which such conditions are disabling is largely determined by society's willingness to adapt, notes historian Catherine Kudlick, who directs the Paul K. Longmore Institute on Disability at San Francisco State University in California. She says: "Like disability in general, the pandemic causes you to re-evaluate your priorities and say, 'OK, what really matters?'"

Shew points out that, during the lockdowns triggered by the present pandemic, accommodations that disabled people had long campaigned for — remote working, and flexibility in working hours, communication format and metrics of productivity — were universally adopted. She worries that they'll be dropped in some futile quest to return to a pre-pandemic 'normal'. Yet she also draws hope from Heumann and Roberts.

If polio survivors could drive social change in the past century, perhaps COVID-19 survivors will in this one — making all disability more visible. "If it weren't built on suffering and death," Shew says, "it would be an exciting time to be thinking about disability rights."

*Nature* **602**, 383-385 (2022)

doi: <https://doi.org/10.1038/d41586-022-00414-x>

## References

1. Chen, C. *et al.* Preprint at medRxiv  
<https://doi.org/10.1101/2021.11.15.21266377> (2021).
2. Henry, J., Smeyne, R. J., Jang, H., Miller, B. & Okun, M. S. *Parkinsonism Related Dis.* **16**, 566–571 (2010).
3. Elkind, M. S. V. *et al.* *Stroke* **42**, 1851–1856 (2011).
4. Bjornevik, K. *et al.* *Science* **375**, 296–301 (2022).
5. Etard, J.-F. *et al.* *Lancet Infect. Dis.* **17**, 545–552 (2017).
6. Li Hi Shing, S. *et al.* *Front. Neurol.* **10**, 773 (2019).
7. Locker, D. & Kaufert, J. *Sociol. Health Illness* **10**, 23–40 (1988).
8. Pagel, C. & Yates, C. A. *Science* **374**, 403–404 (2021).
9. Davis, H. E. *et al.* *eClinicalMedicine* **38**, 101019 (2021).
10. Taquet, M., Geddes, J. R., Husain, M., Luciano, S. & Harrison, P. J. *Lancet Psychiatry* **8**, 416–427 (2021).
11. Xie, Y., Xu, E., Bowe, B. & Al-Aly, Z. *Nature Med.*  
<https://doi.org/10.1038/s41591-022-01689-3> (2022).
12. Groff, D. *et al.* *JAMA Netw. Open* **4**, e2128568 (2021).
13. Briggs, A. & Vassall, A. *Nature* **593**, 502–505 (2021)
14. Smith, M. P. *J. Clin. Epidemiol.* **142**, 54–59 (2022).
15. Spudich, S. & Nath, A. *Science* **375**, 267–269 (2022).
16. Khan, M. *et al.* *Cell* **184**, 5932–5949 (2021).
17. Song, E. *et al.* *J. Exp. Med.* **218**, e20202135 (2021).
18. Shabani, Z. *Acta Neurol. Belg.* **121**, 859–866 (2021).

19. Smeyne, R. J., Noyce, A. J., Byrne, M., Savica, R. & Marras, C. *J. Parkinson's Dis.* **11**, 31–43 (2021).
- 

This article was downloaded by **calibre** from <https://www.nature.com/articles/d41586-022-00414-x>

| [Section menu](#) | [Main menu](#) |

- CORRESPONDENCE
- 15 February 2022

# China: reform research-evaluation criteria

- [Baichang Zhong](#)<sup>0</sup>,
- [Xiaofan Liu](#)<sup>1</sup> &
- [Zehui Zhan](#)<sup>2</sup>

As Chinese researchers, we strongly agree that a broader range of research-evaluation criteria could help a greater diversity of institutions to perform well ([Nature 601, 166; 2022](#)). In our view, China's research would benefit from the SCOPE initiative — the inclusive evaluation framework developed by the International Network of Research Management Societies (see [go.nature.com/34t5](#)).

## Access options

Subscribe to Nature+

Get immediate online access to the entire Nature family of 50+ journals

\$29.99

monthly

[Subscribe](#)

Subscribe to Journal

Get full journal access for 1 year

\$199.00

only \$3.90 per issue

[Subscribe](#)

All prices are NET prices.

VAT will be added later in the checkout.

Tax calculation will be finalised during checkout.

Buy article

Get time limited or full article access on ReadCube.

\$32.00

[Buy](#)

All prices are NET prices.

### **Additional access options:**

- [Log in](#)
- [Learn about institutional subscriptions](#)

*Nature* **602**, 386 (2022)

*doi:* <https://doi.org/10.1038/d41586-022-00408-9>

---

This article was downloaded by **calibre** from <https://www.nature.com/articles/d41586-022-00408-9>

- CORRESPONDENCE
- 15 February 2022

# Brazil opens highly protected caves to mining, risking fauna

- [Hernani Fernandes Magalhaes de Oliveira](#) ORCID: <http://orcid.org/0000-0001-7040-8317><sup>0</sup>,
- [Daiana Cardoso Silva](#) ORCID: <http://orcid.org/0000-0003-1612-6452><sup>1</sup>,
- [Priscilla Lora Zangrandi](#) ORCID: <http://orcid.org/0000-0003-1406-944X><sup>2</sup> &
- [Fabricius Maia Chaves Bicalho Domingos](#) ORCID: <http://orcid.org/0000-0003-2069-9317><sup>3</sup>

Brazil's government has changed the designation of caves that warrant top priority for conservation (see [go.nature.com/3gy5](http://go.nature.com/3gy5)). Constituting some 13–30% of the country's 22,000 protected caves, these will now be open to commercial exploitation, which could seriously affect their vulnerable fauna.

## Access options

Subscribe to Nature+

Get immediate online access to the entire Nature family of 50+ journals

\$29.99

monthly

[Subscribe](#)

## Subscribe to Journal

Get full journal access for 1 year

\$199.00

only \$3.90 per issue

[Subscribe](#)

All prices are NET prices.

VAT will be added later in the checkout.

Tax calculation will be finalised during checkout.

## Buy article

Get time limited or full article access on ReadCube.

\$32.00

[Buy](#)

All prices are NET prices.

## Additional access options:

- [Log in](#)
- [Learn about institutional subscriptions](#)

*Nature* **602**, 386 (2022)

doi: <https://doi.org/10.1038/d41586-022-00406-x>

---

This article was downloaded by **calibre** from <https://www.nature.com/articles/d41586-022-00406-x>

- CORRESPONDENCE
- 15 February 2022

# Catapult network busts biomedical bottlenecks

- [Graeme Wilkinson](#) [ORCID: http://orcid.org/0000-0001-5855-2025](http://orcid.org/0000-0001-5855-2025)<sup>0</sup>  
&
- [Peter Simpson](#) [ORCID: http://orcid.org/0000-0003-0364-2685](http://orcid.org/0000-0003-0364-2685)<sup>1</sup>

Medicines Discovery Catapult, where we work, is an example of a non-profit organization focusing on research that benefits the scientific community but falls outside the remit of academic or commercial institutions (see [A. Marblestone \*et al. Nature\* 601, 188–190; 2022](#)). It forms part of the UK Catapult network, which translates research into products and develops solutions to industrial problems.

## Access options

Subscribe to Nature+

Get immediate online access to the entire Nature family of 50+ journals

\$29.99

monthly

[Subscribe](#)

Subscribe to Journal

Get full journal access for 1 year

\$199.00

only \$3.90 per issue

[Subscribe](#)

All prices are NET prices.

VAT will be added later in the checkout.

Tax calculation will be finalised during checkout.

Buy article

Get time limited or full article access on ReadCube.

\$32.00

[Buy](#)

All prices are NET prices.

**Additional access options:**

- [Log in](#)
- [Learn about institutional subscriptions](#)

*Nature* **602**, 386 (2022)

doi: <https://doi.org/10.1038/d41586-022-00407-w>

---

This article was downloaded by **calibre** from <https://www.nature.com/articles/d41586-022-00407-w>

- CORRESPONDENCE
- 15 February 2022

# Pollution — bring the field into the lab

- [Anna von Mikecz](#) ORCID: <http://orcid.org/0000-0002-2276-2140><sup>0</sup>  
&
- [Andrea Scharf](#) ORCID: <http://orcid.org/0000-0001-7787-445X><sup>1</sup>

In a reversal of Edith Heard's call to take molecular biology into the field ([Nature 601, 9; 2022](#)), we bring the field into the laboratory. We test the biological effects of environmental pollution on the wild counterparts of the model nematode roundworm *Caenorhabditis elegans*.

## Access options

Subscribe to Nature+

Get immediate online access to the entire Nature family of 50+ journals

\$29.99

monthly

[Subscribe](#)

Subscribe to Journal

Get full journal access for 1 year

\$199.00

only \$3.90 per issue

## Subscribe

All prices are NET prices.

VAT will be added later in the checkout.

Tax calculation will be finalised during checkout.

Buy article

Get time limited or full article access on ReadCube.

\$32.00

## Buy

All prices are NET prices.

## **Additional access options:**

- [Log in](#)
- [Learn about institutional subscriptions](#)

*Nature* **602**, 386 (2022)

*doi:* <https://doi.org/10.1038/d41586-022-00444-5>

---

This article was downloaded by **calibre** from <https://www.nature.com/articles/d41586-022-00444-5>

# Work

- **[African scientists engage with the public to tackle local challenges](#)** [ 15 February 2022]

Career Feature • Science-engagement initiatives in Africa disseminate knowledge and bridge the gap between research and the continent's people.

- **[Going with the gut to understand diseases](#)** [ 14 February 2022]

Where I Work • Paula Littlejohn researches how nutrients in early life affect long-term health.

- CAREER FEATURE
- 15 February 2022

# African scientists engage with the public to tackle local challenges

Science-engagement initiatives in Africa disseminate knowledge and bridge the gap between research and the continent's people.

- [Abdullahi Tsanni](#)

[Find a new job](#)



African researchers are leaving the lab to work directly with communities to tackle local problems.Credit: Ed Young/Eh! woza

One focus of the Falling Walls Science Summit 2021, an annual science conference that was held in Berlin in November, was to draw attention to some of the work that scientists in Africa are doing to engage with their countries' people.

*Nature* sat down with five science communicators at the summit to talk about their work and how they're tackling local challenges to bridge the gap between science and society in Africa.

## **YISALEMUSH ASEFA: Using radio to boost childhood vaccination**

*Clinical nurse and public-health professional at Jimma University, Ethiopia.*

In March 2020, my team of five and I created a community radio project, owned by and broadcast from Jimma University, Ethiopia, to promote childhood vaccination among communities in the country's Oromia region.

In Ethiopia, coverage with pentavalent vaccine — a single vaccine that protects children against diphtheria, pertussis, tetanus, hepatitis B and *Haemophilus influenzae* — was 33% among infants in 2017. There are several key reasons why many children have not been vaccinated on time. For example, local communities lack adequate maternal-health facilities, so many babies are born at home and do not receive their shots. There's also a lack of access to both reliable information on vaccines and the vaccines themselves.

Radio is one of the country's most popular communication channels, but health workers hadn't previously used it to engage with the public. Our programme aims to reach more people through FM broadcasting to ultimately improve childhood vaccination rates. Compared with other forms of media, radio is widely available in rural Ethiopia. Just over half of the country's households have a television set, and only about 20% of the population has reliable Internet access.

The programme aired between October 2020 and January 2021. It comprised a series of 10-minute dramas performed in the local Afaan Oromo language,

followed by a 10-minute discussion in the studio about childhood vaccination and then a 30-minute session for listeners to phone in with questions. We called it the 10+10+30 Radio Project. It had 12 episodes, each of which aired twice per week, every Friday and Sunday at 2:00 p.m.. The sessions were moderated by professional health-care workers, including nurses and doctors, who we trained to go on the radio, and the topics of the episodes were developed during group discussions with health workers, radio actors, mothers and other community members.



Yiselamush Asefa speaks about science engagement in Africa.Credit: Falling Walls Foundation

We've reached more than one million people in Jimma and have observed significantly higher vaccination rates in communities where the programme aired. Vaccination coverage in the intervention district was 85%, whereas in the control district it was 62.2%. It has also improved the health workers' communication skills and boosted their confidence in public engagement.

But we faced challenges, too. One week after we trained health workers on how to serve as radio panellists for the programme, the World Health

Organization announced the COVID-19 pandemic. It led to a six-month delay before our programme aired, and it was difficult to collect baseline data for the study. It was also challenging for the radio actors to perform in the studio because of social-distancing measures and lockdowns. Despite these setbacks, we've trained 13 health workers so far in how to speak clearly, reduce jargon and interact with listeners on radio. We hope to get more funding from our previous sponsor, the Bill & Melinda Gates Foundation, a research funder based in Seattle, Washington, and funding agencies in Ethiopia to scale up the project. We want to produce more episodes and translate the previous episodes into other local languages in Ethiopia.

To have an effective science-engagement programme, think deeply about your target audience. In our case, we ensured that local communities were involved during the planning and development of the episodes. Alongside focus-group discussions, we also pilot-tested the first episodes to assess whether they were likely to have an impact. You might not fully understand communities' needs until you engage with them.

## **ANASTASIA KOCH: Teenage tales of infectious disease on film**

*Director and co-founder of Eh!woza in Cape Town, South Africa.*

In 2014, while I was studying tuberculosis (TB) as a PhD student at the University of Cape Town, I realized that I had never engaged with anyone actually affected by the disease — even though it killed 58,000 people in South Africa in 2019. I came to feel that, although my work was important, it was too slow to make an impact on society. I started looking for other avenues to share my biomedical knowledge with the public. I met contemporary visual artist Ed Young while I was preparing a workshop to engage South African secondary-school students with biomedical research. I asked Ed to film the workshop. When the film was produced, the scientists and students were so excited — which led me to look into science communication more seriously.

Ed and I applied for the International Engagement Awards, provided by London-based funder Wellcome, and got funding in 2014 to create Eh! woza, a non-profit organization centred on science communication. We recruit secondary-school students from areas with high rates of HIV and TB, such as the Makhaza suburb of Khayelitsha, the largest township in Western Cape, and Masiphumelele, Cape Town, to visit laboratories and learn about biomedical research, including drugs and vaccines for these diseases and the clinical trials that test them. We train the participants in science communication and equip them with the skills and equipment to produce films and documentaries on the social impact of the diseases; we now have a series of such films available on our website.

Storytelling is powerful: it helps you to simplify complex narratives and humanize science. Our programme gives young people the space to tell their own stories about science and health. This is our core principle, and we strongly adhere to it. In South Africa, local communities' challenges are different from the ones people in more developed countries face. So, science communication isn't about sharing scientific information alone — we have to address people's needs. There is a social-justice element in this context.

My advice for researchers who are thinking of moving into science communication and engagement is: don't be afraid or intimidated. It might feel difficult at first, but it becomes easier along the way. Listen to the people you engage with and learn from the public. Science engagement can be difficult, but it's deeply rewarding.

Most of the time, teenagers are a lot of fun to work with, and they have loads of energy. But they do come with some challenges: some aren't very punctual, and many are attached to distractions such as smartphones and selfies. We sometimes have to ban phones during work time. A lot of the teenagers come from less-privileged communities, and it's really amazing to see their growth during the programme, but sad to see them leave at the end.

## **JUDY BAARIU: Science engagement for mental-health awareness**

*Research officer and project coordinator for the Difu Simo mental-health awareness campaign at the Kenya Medical Research Institute–Wellcome Trust Research Programme, Kilifi, Kenya.*

In many Kenyan communities, people with mental-health problems face stigma and discrimination. Some are even accused of witchcraft. This is something I encounter often in my work as a research officer at the Kenya Medical Research Institute (KEMRI)–Wellcome Trust Research Programme in Kilifi. In October 2019, to try to combat this, my collaborators and I launched Difu Simo, a mental-health engagement project in Kilifi. Difu Simo is a collaboration between the Documentary Institute of Eastern Africa in Nairobi, the Malindi District Cultural Association and the KEMRI–Wellcome Trust programme. The term *difu simo* is a phrase used by the people of Kigiriama, which loosely translates to ‘breaking free’.

Our aim is to raise awareness about mental illness and to demystify myths and misconceptions about the causes and management of mental-health problems. We engage with local communities to foster dialogue about mental illnesses as well as to encourage people with these conditions to seek proper care. We work with scientists, filmmakers, medical practitioners (both modern and traditional) and community members. Our communications are in Kiswahili — the lingua franca in Kenya — and Kigiriama to reach as many people as possible. We use tools such as documentary films and outreach activities, including music and dance, to educate the public on mental illness.



Judy Baariu delivers a speech at the Falling Walls Science Summit.Credit: Falling Walls Foundation

For example, last year we produced a series of videos with community members who've dealt with mental-health problems, and we use the videos to engage the wider population in Kilifi. Through our efforts, we have directly reached more than 5,000 community members, and the impact of our work has led to an increase in the number of people seeking help in mental-health facilities, according to our collaborators.

It's not easy to get people to go on film and talk about their mental illness, given the stigma they often face — especially because the films are shown to other community members who can recognize our participants. But using a participatory approach helped us to create trust. The success of science-engagement programmes depends on how you interact with community members and the confidence you help them to build, as well as understanding and patience.

As a health practitioner, I struggled a lot when I started engaging with these local communities, and it's difficult to change people's long-held cultural

beliefs, despite their lack of any scientific basis. My advice for scientists who want to implement similar work that includes engaging with local stakeholders is to be willing to listen to the community members, learn from them and collaborate with them — especially in health-promotion interventions. When you know what the community will respond to, you then build sustainable programmes. Science engagement can change how researchers work in communities: it is an opportunity for shared learning.

## KYEREWAA A. BOATENG: A documentary on deafness dispels misconceptions

*Community- and public-engagement officer at the West African Centre for Cell Biology of Infectious Pathogens, University of Ghana, Accra.*

Deafness in many Ghanaian communities is a sensitive issue, with lots of superstitions around the condition. It can be difficult for scientists to get blood samples for testing from people with deafness, for example, and to engage with their families. Also, researchers can face significant challenges when engaging with deaf people for research into some of the genetic factors that contribute to hearing impairment.

In my role as community-engagement officer, I work with scientists at the West African Centre for Cell Biology of Infectious Pathogens at the University of Ghana in Accra. My job is to lead scientists from their labs into communities to engage the public with their research.

To help scientists engage with the community, we developed two versions of a 25-minute documentary drama on the genetics of deafness, titled *A Smile of Hope*, with the aim of aiding hearing-impaired research at the centre. One version, designed for deaf people, uses only sign language. The other includes audio for people who can hear. Using the documentary, researchers can teach the science and genetics of hearing impairment to deaf people and their family members. It helps scientists to explain why these people are deaf and to dispel long-held misconceptions regarding the condition.



Kyrewaa Boateng on stage at the summit.Credit: Falling Walls Foundation

We have engaged more than 1,000 deaf people across Ghana — at schools for the deaf as well as at visits to family homes and local communities. We've found that the video has had an impact: after people watch it, they tell us they're more willing to give their blood for genetics research. In a multicultural society such as Ghana, those doing science engagement need to consider different cultures and customs in developing and designing campaigns.

When creating our documentary drama, we engaged deaf students, their parents and siblings, and community members in five regions of Ghana with different ethnic backgrounds to help make our film culturally acceptable and community-friendly. We organized focus-group discussions and conducted in-depth interviews with these stakeholders before developing scripts to maximize community sharing, listening and learning. We also involved a multidisciplinary team including genetics researchers, deaf actors, actors who can hear, public-engagement scholars and drama-production experts in Ghana. Scientists should listen to communities and learn to co-create successful science-engagement solutions.

# **STANLEY ANIGBOGU: Getting young girls into science**

*Storyteller and creative technologist in Onitsha, Anambra, and promotes STEM education for young girls in southeastern Nigeria.*

More than ten million children in Nigeria are not in school. Those in school face challenges when pursuing science, technology, engineering and mathematics (STEM) subjects. In particular, girls are under-represented in STEM, and enrolment is an uphill battle for them. Barriers such as gender bias and social norms and expectations prevent young girls from receiving an education and influence the subjects that they study at school. To help reverse this trend in Nigeria, I launched the STEM4HER programme in February 2021, to train young girls in STEM fields and to inspire them to become innovators and solve problems in their local communities.

STEM4HER is a series of classes for girls. They learn to develop ideas, identify problems in their communities and build technological solutions. Some participants have created portable hydroelectric generators, air purifiers and water-purification devices using locally sourced materials. We hope the girls will go on to become innovators and entrepreneurs.



Stanley Anigbogu hopes to inspire young girls to become inventors.Credit: Stanley Anigbogu

In 2021, we trained 350 girls. Some have won awards at local and international science fairs, including a prize of 350,000 naira (US\$850) from the Mandela Washington Fellowship Alumni Association of Nigeria's Beyond School Community Challenge 2021, sponsored by the US Embassy and Consulate in Nigeria. The girls will use the money to develop their inventions.

It's hard changing the girls' mindsets, especially for those from rural communities with limited educational resources. I use stories of talented African women in STEM, such as Grace Alele-Williams, a mathematician and the first female vice-chancellor of a university in Nigeria, and Francisca Nneka Okeke, a physicist and winner of the L'Oreal-UNESCO Women in Science Award 2013, to show the girls that they, too, can make a positive impact on their communities and the globe. I feel that storytelling is a strong technique for instilling confidence and encouragement in my students.

I am studying multimedia development at the National School of Applied Sciences in Kenitra, Morocco, but my courses are flexible. I am currently in my final year and returned to Nigeria in January 2020 to work on STEM4HER. After completing my degree, I hope to expand my skills in filmmaking and to inspire more girls. We need more girls in science.

*Nature* **602**, 535-537 (2022)

*doi:* <https://doi.org/10.1038/d41586-022-00415-w>

These interviews have been edited for length and clarity.

---

This article was downloaded by **calibre** from <https://www.nature.com/articles/d41586-022-00415-w>

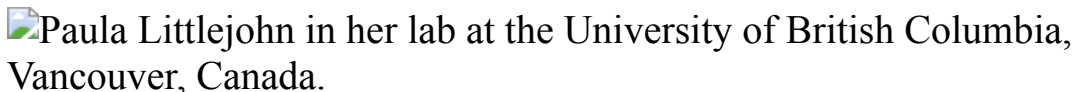
| [Section menu](#) | [Main menu](#) |

- WHERE I WORK
- 14 February 2022

# Going with the gut to understand diseases

Paula Littlejohn researches how nutrients in early life affect long-term health.

- [Virginia Gewin](#) <sup>0</sup>



Paula Littlejohn is a PhD researcher at the University of British Columbia, Vancouver, Canada. Credit: Leslie Kennah/Michael Smith Laboratories/UBC

Following my master's degree, I worked for around ten years for pharmaceutical companies, collecting data during clinical drug trials. As I tracked participants and the medicines they took, I realized that practising health care is essentially managing disease symptoms. That understanding motivated me to study how nutrition interacts with genetics to cause disease.

The microorganisms in our gut influence so much of our physical and mental health, from skin conditions to neurodegenerative disorders. I studied the gut microbiome in my own time, reading books and attending public lectures. For six months, I had in my drafts folder an introductory e-mail to Brett Finlay, who researches the gut microbiome at the University of British Columbia in Vancouver, Canada. After a colleague encouraged me to hit send, Brett replied within 10 minutes. I took on a PhD position in his

laboratory — studying how deficiencies in vitamins or minerals that are needed in only tiny quantities in early life can shape lifelong health.

In this photograph, I'm using an anaerobic chamber. It is kept at 37 °C and without oxygen — the perfect conditions in which to grow the gut's microbes. We investigate how entire gut microbial communities respond to, for example, micronutrient deficiencies.

Being an older graduate student has benefits: I have clear career goals and the focus to reach them, the ability to multi-task and a large support system outside the lab.

Ideally, my research could help to create more specialized nutritional guidelines. Right now, they are designed for 'healthy' individuals — but, as one study showed, only 2.7% of US people met modest criteria for a healthy lifestyle, such as doing 150 minutes of physical activity per week ([P. D. Loprinzi et al. Mayo Clin. Proc. 91, 432–442; 2016](#)). We need to create information on daily nutritional allowances that meets the needs of specific populations, rather than attempting to help everyone with the same guidance.

*Nature* **602**, 540 (2022)

*doi:* <https://doi.org/10.1038/d41586-022-00416-9>

---

This article was downloaded by **calibre** from <https://www.nature.com/articles/d41586-022-00416-9>

# Research

- **[Ear anatomy traces a family tree for bats](#)** [ 26 January 2022]

News & Views • How should the bat family tree be arranged? Analysis of bats' inner ear anatomy supports a previously proposed arrangement that was based on DNA analysis. The findings also shed light on the evolution of echolocation.

- **[Identification of human and mosquito receptors for alphaviruses](#)** [ 19 January 2022]

News & Views • Alphaviruses are transmitted by mosquitoes to many species, and can be fatal to humans. The identification of virus receptors that are evolutionarily conserved between mosquitoes and humans might explain the wide range of viral hosts.

- **[The glowing dusty heart of a hidden quasar](#)** [ 16 February 2022]

News & Views • The torus of dust surrounding a quasar — a very luminous supermassive black hole that accretes matter from its surroundings — has now been captured with high-resolution infrared imaging.

- **[Atomic clouds stabilized to measure dilation of time](#)** [ 16 February 2022]

News & Views • Tests of relativity once required accurate clocks separated by thousands of kilometres. Optical techniques have now made such tests possible in an atomic cluster measuring no more than one millimetre in size.

- **[Towards enduring autonomous robots via embodied energy](#)** [ 16 February 2022]

Perspective • The concept of 'Embodied Energy'—in which the components of a robot or device both store energy and provide a mechanical or structural function—is put forward, along with specific robot-design principles.

- **[Thermal imaging of dust hiding the black hole in NGC 1068](#)** [ 16 February 2022]

Article • Mid-infrared observations of the dusty structures of the galaxy NGC 1068 support the unified model of active galactic nuclei.

- **[Nuclear spin-wave quantum register for a solid-state qubit](#)** [ 16 February 2022]

Article • Via spin-exchange interactions with  $^{51}\text{V}^{5+}$  ions, an optically addressed  $^{171}\text{Yb}^{3+}$  qubit in a nuclear-spin-rich yttrium orthovanadate crystal is used to implement a reproducible nuclear-spin-based quantum memory, and entangled Yb–V Bell states are demonstrated.

- [\*\*Magnetic control of tokamak plasmas through deep reinforcement learning\*\*](#) [ 16 February 2022]  
Article • A newly designed control architecture uses deep reinforcement learning to learn to command the coils of a tokamak, and successfully stabilizes a wide variety of fusion plasma configurations.
- [\*\*Resolving the gravitational redshift across a millimetre-scale atomic sample\*\*](#) [ 16 February 2022]  
Article • Reducing the fractional uncertainty over the measurement of the frequency of an ensemble of trapped strontium atoms enables observation of the gravitational redshift at the submillimetre scale.
- [\*\*Differential clock comparisons with a multiplexed optical lattice clock\*\*](#) [ 16 February 2022]  
Article • Multiple ultracold ensembles of strontium atoms are trapped in the same optical lattice, realizing a multiplexed optical clock where precision measurements can benefit from having all atoms share the same trapping light and clock laser.
- [\*\*Scaling of the strange-metal scattering in unconventional superconductors\*\*](#) [ 16 February 2022]  
Article • Precise quantitative scaling laws are observed between the normalized T-linear coefficient and Tc among copper oxides, pnictides and a class of organic superconductors, suggesting a common underlying physics at work in these unconventional superconductors.
- [\*\*Hydrogen trapping and embrittlement in high-strength Al alloys\*\*](#) [ 16 February 2022]  
Article • Atom-scale analysis of hydrogen and other elements at the grain boundaries of a 7xxx aluminium alloy shows that co-segregation of elements favours grain boundary decohesion, and that hydrogen embrittlement is prevented by strong partitioning into the second-phase particles.
- [\*\*Warming weakens the night-time barrier to global fire\*\*](#) [ 16 February 2022]  
Article • An analysis of satellite observations and climate data shows that night-time fire intensity has increased over the past two decades owing to hotter and drier nights under anthropogenic climate change.
- [\*\*Evolution of inner ear neuroanatomy of bats and implications for echolocation\*\*](#) [ 26 January 2022]  
Article • The presence of a variety of highly derived spiral ganglion structures of the inner ear is associated with diverse echolocation strategies in yangochiropteran bats and distinguishes them from Yinpterochiroptera.

- **Genome-edited powdery mildew resistance in wheat without growth penalties** [ 09 February 2022]
 

Article • Tamlo-R32, an engineered wheat mutant allele of the Mildew resistance locus O (MLO) gene, confers resistance to powdery mildew, retains robust wheat growth, and can be transferred to other agriculturally important wheat varieties.
- **Moving bar of light evokes vectorial spatial selectivity in the immobile rat hippocampus** [ 09 February 2022]
 

Article • In response to visual stimuli, hippocampal neurons in a body-fixed rat can respond to and encode visual information without locomotion or task demand, similar to the visual cortex.
- **Sensory representation and detection mechanisms of gut osmolality change** [ 26 January 2022]
 

Article • Vagal afferents innervating the hepatic portal area respond to changes in gut osmolality and regulate thirst and drinking behaviour in mice.
- **VLDLR and ApoER2 are receptors for multiple alphaviruses** [ 20 December 2021]
 

Article • Studies using viral coat glycoproteins show that alphaviruses can enter cells via the very low-density lipoprotein receptor (VLDLR) and apolipoprotein E receptor 2 (ApoER2), members of an evolutionarily conserved family of lipoprotein receptors.
- **SARS-CoV-2 infection in free-ranging white-tailed deer** [ 23 December 2021]
 

Article • More than one-third of wild deer tested in northeast Ohio showed evidence of SARS-CoV-2 infection of human origin.
- **Evolution of enhanced innate immune evasion by SARS-CoV-2** [ 23 December 2021]
 

Article • The SARS-CoV-2 Alpha variant suppresses innate immune responses more effectively than isolates of first-wave SARS-CoV-2, and this is a result of mutations outside of the spike coding region that lead to upregulation of viral innate immune antagonists.
- **Streptococcal pyrogenic exotoxin B cleaves GSDMA and triggers pyroptosis** [ 02 February 2022]
 

Article • The Streptococcus pyogenes virulence factor SpeB triggers pyroptosis in keratinocytes by catalysing cleavage of host gasdermin A, a key event triggering the immune response to *S. pyogenes* infection.
- **Decade-long leukaemia remissions with persistence of CD4+ CAR T cells** [ 02 February 2022]
 

Article • Infusion of CD19-directed chimeric antigen receptor T cells into two patients with chronic lymphocytic leukaemia resulted in complete tumour remission and persistence of the infused cells more than ten years later.

- **Mapping clustered mutations in cancer reveals APOBEC3 mutagenesis of ecDNA** [ 09 February 2022]  
Article • An analysis of clustered substitutions and indels across 30 cancer types provides insight into the role of APOBEC3 in giving rise to clustered mutation events through its activity on extrachromosomal DNA.
- **Glioblastoma mutations alter EGFR dimer structure to prevent ligand bias** [ 09 February 2022]  
Article • Extracellular glioblastoma-associated mutations reduce the ability of the epidermal growth factor receptor to distinguish between its ligands.
- **A backbone-centred energy function of neural networks for protein design** [ 09 February 2022]  
Article • Modelling by SCUBA of the backbone-centred energy surface extends the diversity of designable proteins.
- **Mechanisms of inhibition and activation of extrasynaptic  $\alpha\beta$  GABA<sub>A</sub> receptors** [ 09 February 2022]  
Article • Cryo-electron microscopy structures are used to identify mechanisms underlying distinct features of extrasynaptic type A  $\gamma$ -aminobutyric acid receptors.

- NEWS AND VIEWS
- 26 January 2022

# Ear anatomy traces a family tree for bats

How should the bat family tree be arranged? Analysis of bats' inner ear anatomy supports a previously proposed arrangement that was based on DNA analysis. The findings also shed light on the evolution of echolocation.

- [M. Brock Fenton](#) 0

Echolocating animals, including most species of bat and echolocators such as dolphins, obtain information about their surroundings from the differences between outgoing signals that they emit and the echoes returning to them. Some blind people orient by echolocation using tongue clicks. Signals emitted by animals for echolocation can be used for orientation and communication, and the ability to echolocate allows animals to operate in the dark or under conditions of unpredictable lighting. Echolocation also provides evidence of bats' evolutionary history, as portrayed by their family tree. [Writing in Nature](#), Sulser *et al.*<sup>1</sup> present neuroanatomical evidence from an examination of canals in bats' inner ears. The data aid our understanding of bat evolution and the importance of echolocation.

## Access options

Subscribe to Nature+

Get immediate online access to the entire Nature family of 50+ journals

\$29.99

monthly

[Subscribe](#)

Subscribe to Journal

Get full journal access for 1 year

\$199.00

only \$3.90 per issue

[Subscribe](#)

All prices are NET prices.

VAT will be added later in the checkout.

Tax calculation will be finalised during checkout.

Buy article

Get time limited or full article access on ReadCube.

\$32.00

[Buy](#)

All prices are NET prices.

**Additional access options:**

- [Log in](#)
- [Learn about institutional subscriptions](#)

*Nature* **602**, 387-388 (2022)

*doi:* <https://doi.org/10.1038/d41586-022-00051-4>

**References**

1. Sulser, R. B., Patterson, B. D., Urban, D. J., Neander, A. I. & Lu, Z.-X. *Nature* **602**, 449–454 (2022).
2. Teeling, E. C. *et al.* *Nature* **403**, 188–192 (2000).
3. Fenton, M. B. & Simmons, N. B. *Bats: A World of Science and Mystery* (Univ. Chicago Press, 2015).
4. Simmons, N. B., Seymour, K. L., Habersetzer, J. & Gunnell, G. F. *Nature* **451**, 818–821 (2008).
5. Veselka, N. *et al.* *Nature* **463**, 939–942 (2010).
6. Wang, Z. *et al.* *Nature Ecol. Evol.* **1**, 0021 (2017).
7. Nojiri, T. *et al.* *Curr. Biol.* **31**, 1353–1365 (2021).

---

This article was downloaded by **calibre** from <https://www.nature.com/articles/d41586-022-00051-4>

| [Section menu](#) | [Main menu](#) |

- NEWS AND VIEWS
- 19 January 2022

# Identification of human and mosquito receptors for alphaviruses

Alphaviruses are transmitted by mosquitoes to many species, and can be fatal to humans. The identification of virus receptors that are evolutionarily conserved between mosquitoes and humans might explain the wide range of viral hosts.

- [Caroline K. Martin](#)    ORCID: <http://orcid.org/0000-0001-9448-9182><sup>0</sup>  
&
- [Margaret Kielian](#)    ORCID: <http://orcid.org/0000-0002-7395-4791><sup>1</sup>

The group of viruses called alphaviruses can cause severe disease, including inflammation of the brain (encephalitis) and of joints (arthritis). Despite the high disease potential of these viruses, which can cause fatal illness, there are currently no licensed vaccines or antiviral therapeutics available to tackle human alphavirus infections. [Writing in Nature](#), Clark *et al.*<sup>1</sup> now pinpoint key targets that enable several of these viruses to infect cells (Fig. 1).

## Access options

Subscribe to Nature+

Get immediate online access to the entire Nature family of 50+ journals

\$29.99

monthly

[Subscribe](#)

Subscribe to Journal

Get full journal access for 1 year

\$199.00

only \$3.90 per issue

[Subscribe](#)

All prices are NET prices.

VAT will be added later in the checkout.

Tax calculation will be finalised during checkout.

Buy article

Get time limited or full article access on ReadCube.

\$32.00

[Buy](#)

All prices are NET prices.

**Additional access options:**

- [Log in](#)
- [Learn about institutional subscriptions](#)

*Nature* **602**, 388-390 (2022)

*doi:* <https://doi.org/10.1038/d41586-022-00052-3>

**References**

1. Clark, L. E. *et al.* *Nature* **602**, 475–480 (2021).
2. Helenius, A., Kartenbeck, J., Simons, K. & Fries, E. *J. Cell Biol.* **84**, 404–420 (1980).
3. Holmes, A. C., Basore, K., Fremont, D. H. & Diamond, M. S. *PLoS Pathog.* **16**, e1008876 (2020).
4. Rose, P. P. *et al.* *Cell Host Microbe* **10**, 97–104 (2011).
5. Zhang, R. *et al.* *Nature* **557**, 570–574 (2018).
6. Ma, H. *et al.* *Nature* **588**, 308–314 (2020).
7. Nasar, F. *et al.* *Proc. Natl Acad. Sci. USA* **109**, 14622–14627 (2012).
8. Dieckmann, M., Dietrich, M. F. & Herz, J. *Biol. Chem.* **391**, 1341–1363 (2010).
9. Qiao, L. & Luo, G. G. *PLoS Pathog.* **15**, e1007874 (2019).
10. Ma, B., Huang, C., Ma, J., Xiang, Y. & Zhang, X. *Nature* **598**, 677–681 (2021).
11. Basore, K. *et al.* *Nature* **598**, 672–676 (2021).
12. Ganaie, S. S. *et al.* *Cell* **184**, 5163–5178 (2021).

---

This article was downloaded by **calibre** from <https://www.nature.com/articles/d41586-022-00052-3>

- NEWS AND VIEWS
- 16 February 2022

# The glowing dusty heart of a hidden quasar

The torus of dust surrounding a quasar — a very luminous supermassive black hole that accretes matter from its surroundings — has now been captured with high-resolution infrared imaging.

- [Robert Antonucci](#) 

An active galactic nucleus is a relatively tiny region at the centre of some galaxies that has abnormally high luminosity. Quasars are the most powerful active galactic nuclei. [Writing in \*Nature\*](#), Gámez Rosas *et al.*<sup>1</sup> report very sharp and sensitive imaging of a nearby active galactic nucleus, showing a glowing doughnut-shaped object surrounding the central black hole.

## Access options

Subscribe to Nature+

Get immediate online access to the entire Nature family of 50+ journals

\$29.99

monthly

[Subscribe](#)

Subscribe to Journal

Get full journal access for 1 year

\$199.00

only \$3.90 per issue

[Subscribe](#)

All prices are NET prices.

VAT will be added later in the checkout.

Tax calculation will be finalised during checkout.

Buy article

Get time limited or full article access on ReadCube.

\$32.00

[Buy](#)

All prices are NET prices.

### **Additional access options:**

- [Log in](#)
- [Learn about institutional subscriptions](#)

*Nature* **602**, 390-391 (2022)

*doi:* <https://doi.org/10.1038/d41586-022-00380-4>

## **References**

1. Gámez Rosas, V. *et al.* *Nature* **602**, 403–407 (2022).
2. Antonucci, R. *Nature* **495**, 165–167 (2013).
3. Tadhunter, C. & Tsvetanov, Z. *Nature* **341**, 422–424 (1989).

4. Ogle, P. M. *et al.* *Astrophys. J.* **482**, L37–L40 (1997).
5. Bock, J. J. *et al.* *Astron. J.* **120**, 2904–2919 (2000).
6. Lynden-Bell, D. *Nature* **223**, 690–694 (1969).
7. Krolik, J. H. & Begelman, M. C. *Astrophys. J.* **308**, L55–L58 (1986).
8. Krolik, J. H. & Begelman, M. C. *Astrophys. J.* **329**, 702 (1988).
9. Pfuhl, O. *et al.* *Astron. Astrophys.* **634**, A1 (2020).
10. Kishimoto, M. *Astrophys. J.* **518**, 676–692 (1999).
11. Krolik, J. H. *Astrophys. J.* **661**, 52–59 (2007).

---

This article was downloaded by **calibre** from <https://www.nature.com/articles/d41586-022-00380-4>

| [Section menu](#) | [Main menu](#) |

- NEWS AND VIEWS
- 16 February 2022

# Atomic clouds stabilized to measure dilation of time

Tests of relativity once required accurate clocks separated by thousands of kilometres. Optical techniques have now made such tests possible in an atomic cluster measuring no more than one millimetre in size.

- [Ksenia Khabarova](#) 0

As Albert Einstein predicted in his theory of general relativity, the gravitational field of a massive object distorts space-time, which causes time to move more slowly as one gets closer to the object. This phenomenon is known as gravitational time dilation, and it is measurable — particularly in the vicinity of a very massive object such as Earth. The measurement requires a sufficiently accurate clock, and, today, the most accurate timekeepers are atomic clocks, which keep time by detecting the transition energy between two electronic states in an atom. [Bothwell et al.](#)<sup>1</sup> and [Zheng et al.](#)<sup>2</sup> now report astounding progress in the stability of atomic clocks using ensembles of ultracold strontium atoms. Bothwell and colleagues even managed to measure the degree to which time is dilated by gravity — a quantity known as gravitational redshift — in a single atomic cloud.

## Access options

Subscribe to Nature+

Get immediate online access to the entire Nature family of 50+ journals

\$29.99

monthly

[Subscribe](#)

Subscribe to Journal

Get full journal access for 1 year

\$199.00

only \$3.90 per issue

[Subscribe](#)

All prices are NET prices.

VAT will be added later in the checkout.

Tax calculation will be finalised during checkout.

Buy article

Get time limited or full article access on ReadCube.

\$32.00

[Buy](#)

All prices are NET prices.

### **Additional access options:**

- [Log in](#)
- [Learn about institutional subscriptions](#)

*Nature* **602**, 391-392 (2022)

*doi:* <https://doi.org/10.1038/d41586-022-00379-x>

# References

1. Bothwell, T. *et al.* *Nature* **602**, 420–424 (2022).
2. Zheng, X. *et al.* *Nature* **602**, 425–430 (2022).
3. Vessot, R. F. C. *et al.* *Phys. Rev. Lett.* **45**, 2081–2084 (1980).
4. Brewer, S. M. *et al.* *Phys. Rev. Lett.* **123**, 033201 (2019).
5. Chou, C.-W., Hume, D. B., Rosenband, T. & Wineland, D. J. *Science* **329**, 1630–1633 (2010).
6. McGrew, W. F. *et al.* *Nature* **564**, 87–90 (2018).

---

This article was downloaded by **calibre** from <https://www.nature.com/articles/d41586-022-00379-x>

| [Section menu](#) | [Main menu](#) |

- Perspective
- [Published: 16 February 2022](#)

# Towards enduring autonomous robots via embodied energy

- [Cameron A. Aubin](#) ORCID: [orcid.org/0000-0002-2715-8137<sup>1</sup>](https://orcid.org/0000-0002-2715-8137)<sup>na1</sup>,
- [Benjamin Gorissen](#) ORCID: [orcid.org/0000-0001-8275-7610<sup>2,3</sup>](https://orcid.org/0000-0001-8275-7610),
- [Edoardo Milana](#) ORCID: [orcid.org/0000-0003-3389-3039<sup>3</sup>](https://orcid.org/0000-0003-3389-3039),
- [Philip R. Buskohl](#) ORCID: [orcid.org/0000-0001-5517-1956<sup>4</sup>](https://orcid.org/0000-0001-5517-1956),
- [Nathan Lazarus](#) ORCID: [orcid.org/0000-0002-2713-5314<sup>5</sup>](https://orcid.org/0000-0002-2713-5314),
- [Geoffrey A. Slipher](#) ORCID: [orcid.org/0000-0003-0532-0081<sup>6</sup>](https://orcid.org/0000-0003-0532-0081),
- [Christoph Keplinger](#) ORCID: [orcid.org/0000-0001-9151-4100<sup>7</sup>](https://orcid.org/0000-0001-9151-4100),
- [Josh Bongard](#) ORCID: [orcid.org/0000-0001-8515-0822<sup>8</sup>](https://orcid.org/0000-0001-8515-0822),
- [Fumiya Iida](#) ORCID: [orcid.org/0000-0001-9246-7190<sup>9</sup>](https://orcid.org/0000-0001-9246-7190),
- [Jennifer A. Lewis](#) ORCID: [orcid.org/0000-0002-0280-2774<sup>2</sup>](https://orcid.org/0000-0002-0280-2774)<sup>na1</sup> &
- [Robert F. Shepherd](#) ORCID: [orcid.org/0000-0002-0631-9587<sup>1</sup>](https://orcid.org/0000-0002-0631-9587)<sup>na1</sup>

[Nature](#) volume **602**, pages 393–402 (2022)

- 2118 Accesses
- 50 Altmetric
- [Metrics details](#)

## Subjects

- [Actuators](#)
- [Energy storage](#)
- [Materials for energy and catalysis](#)
- [Mechanical engineering](#)

- [Soft materials](#)

## Abstract

Autonomous robots comprise actuation, energy, sensory and control systems built from materials and structures that are not necessarily designed and integrated for multifunctionality. Yet, animals and other organisms that robots strive to emulate contain highly sophisticated and interconnected systems at all organizational levels, which allow multiple functions to be performed simultaneously. Herein, we examine how system integration and multifunctionality in nature inspires a new paradigm for autonomous robots that we call Embodied Energy. Whereas most untethered robots use batteries to store energy and power their operation, recent advancements in energy-storage techniques enable chemical or electrical energy sources to be embodied directly within the structures and materials used to create robots, rather than requiring separate battery packs. This perspective highlights emerging examples of Embodied Energy in the context of developing autonomous robots.

This is a preview of subscription content

## Access options

Subscribe to Nature+

Get immediate online access to the entire Nature family of 50+ journals

\$29.99

monthly

[Subscribe](#)

Subscribe to Journal

Get full journal access for 1 year

\$199.00

only \$3.90 per issue

[Subscribe](#)

All prices are NET prices.

VAT will be added later in the checkout.

Tax calculation will be finalised during checkout.

Buy article

Get time limited or full article access on ReadCube.

\$32.00

[Buy](#)

All prices are NET prices.

### **Additional access options:**

- [Log in](#)
- [Learn about institutional subscriptions](#)

**Fig. 1: Energy, control and actuating systems in modern robots.**

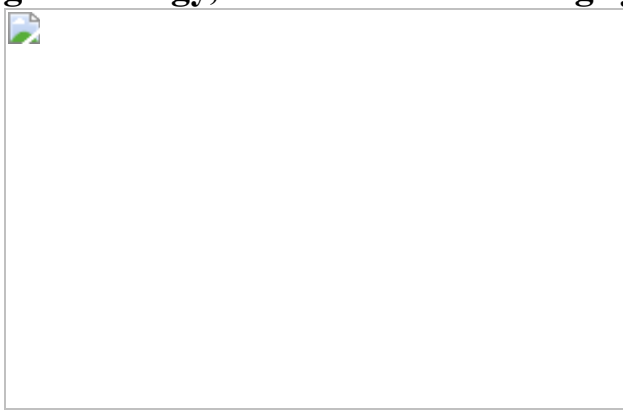


**Fig. 2: Energy storage and transduction form the framework of the Embodied Energy design process.**

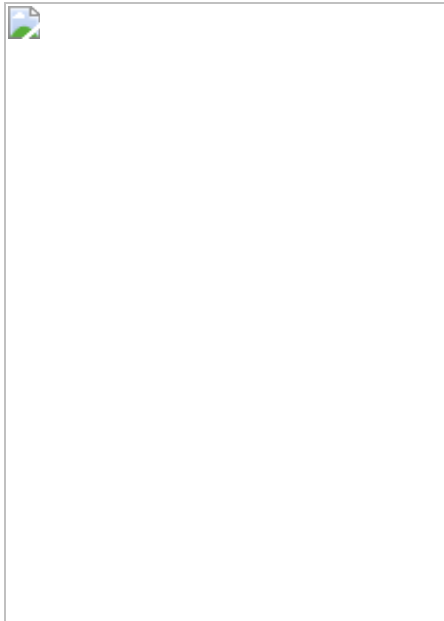
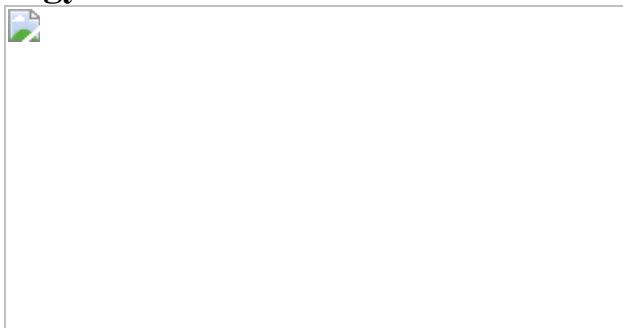


**Fig. 3: Multifunctional Ragone plot of Embodied Energy storage and energy transducer combinations.**



## References

1. Aubin, C. A. et al. Electrolytic vascular systems for energy-dense robots. *Nature* **571**, 51–57 (2019). **This paper details the development of a redox flow battery inspired multifunctional energy-storage system that uses a liquid electrolyte to simultaneously provide electrical energy and hydraulic actuation to an untethered soft robotic fish.**
2. Shepherd, R. F. et al. Using explosions to power a soft robot. *Angew. Chem. Int. Ed.* **52**, 2892–2896 (2013).

3. Wehner, M. et al. An integrated design and fabrication strategy for entirely soft, autonomous robots. *Nature* **536**, 451–455 (2016). **This work describes the creation of a fully autonomous soft robot that contains an embedded microfluidic logic circuit and is powered by the catalytic decomposition of an on-board monopropellant fuel.**
4. Ferreira, A. D. B. L., Nóvoa, P. R. O. & Marques, A. T. Multifunctional material systems: a state-of-the-art review. *Compos. Struct.* **151**, 3–35 (2016). **This review presents the state of the art in multifunctional material systems, including recent advancements in structural materials used in energy-storage systems.**
5. Christodoulou, L. & Venables, J. D. Multifunctional material systems: the first generation. *JOM* **55**, 39–45 (2003). **This review discusses early research into multifunctional material systems, placing some emphasis on materials used in energy-storage implementations.**
6. Sakagami, Y. et al. In *Proc. IEEE/RSJ International Conference on Intelligent Robots and Systems* **Vol. 3**, 2478–2483 (IEEE, 2002).
7. Shepherd, R. F. et al. Multigait soft robot. *Proc. Natl Acad. Sci. USA* **108**, 20400–20403. (2011).
8. Gorissen, B. et al. Hardware sequencing of inflatable nonlinear actuators for autonomous soft robots. *Adv. Mater.* **31**, e1804598 (2019). **This article describes an approach for embedding hardware intelligence into a robot with multiple, non-linear soft actuators, which are programmed via their structural sequence and passive flow restrictors.**
9. Thomas, J. P., Qidwai, M. A. & Kellogg, J. C. Energy scavenging for small-scale unmanned systems. *J. Power Sources* **159**, 1494–1509 (2006). **This paper reviews different energy scavenging technologies, such as solar, thermal and wind, and models their relative effectiveness in increasing the edurance of untethered, unmanned mechanical systems.**

10. Wei, C. & Jing, X. A comprehensive review on vibration energy harvesting: modelling and realization. *Renew. Sustain. Energy Rev.* **74**, 1–18 (2017).
11. Priya, S. & Inman, D. J. *Energy Harvesting Technologies* **21** (Springer, 2009).
12. Shi, B., Li, Z. & Fan, Y. Implantable energy-harvesting devices. *Adv. Mater.* **30**, 1801511 (2018).
13. Ryu, H., Yoon, H. & Kim, S. Hybrid energy harvesters: toward sustainable energy harvesting. *Adv. Mater.* **31**, 1802898 (2019).
14. Vallem, V., Sargolzaeiaval, Y., Ozturk, M., Lai, Y. C. & Dickey, M. D. Energy harvesting and storage with soft and stretchable materials. *Adv. Mater.* **33**, 2004832 (2021).
15. Treml, B. E. et al. Autonomous motility of polymer films. *Adv. Mater.* **30**, 1705616 (2018).
16. Thomas, J. P. & Qidwai, M. A. The design and application of multifunctional structure-battery materials systems. *JOM* **57**, 18–24 (2005).
17. Asp, L. E. & Greenhalgh, E. S. Structural power composites. *Compos. Sci. Technol.* **101**, 41–61 (2014). **This paper introduces the state-of-the-art in structural power composites and discusses material choices, applications and integration into existing technologies.**
18. Kim, T. H., Lee, S. J. & Choi, W. Design and control of the phase shift full bridge converter for the on-board battery charger of electric forklifts. *J. Power Electron.* **12**, 113–119 (2012).
19. Aglietti, G. S., Schwingshakl, C. W. & Roberts, S. C. Multifunctional structure technologies for satellite applications. *Shock Vib. Dig.* **39**, 381–391 (2007).

20. Roberts, S. C. & Aglietti, G. S. Structural performance of a multifunctional spacecraft structure based on plastic lithium-ion batteries. *Acta Astronaut.* **67**, 424–439 (2010).
21. Zhang, Y. et al. Multifunctional structural lithium-ion battery for electric vehicles. *J. Intell. Mater. Syst. Struct.* **28**, 1603–1613 (2017).
22. Wang, M. et al. Biomorphic structural batteries for robotics. *Sci. Robot.* **5**, eaba1912 (2020).
23. Holness, A. E., Perez-rosado, A., Bruck, H. A., Peckerar, M. & Gupta, S. K. In *Challenges in Mechanics of Time Dependent Materials Vol. 2* 155–162 (Springer, 2017).
24. Bar-Cohen, Y. *Electroactive Polymer (EAP) Actuators as Artificial Muscles: Reality, Potential, And Challenges* **136** (SPIE Press, 2004).
25. Kim, K. J. & Tadokoro, S. *Electroactive Polymers for Robotic Applications* (Springer, 2007).
26. Duduta, M., Hajiesmaili, E., Zhao, H., Wood, R. J. & Clarke, D. R. Realizing the potential of dielectric elastomer artificial muscles. *Proc. Natl Acad. Sci. USA* **116**, 2476–2481 (2019).
27. Wang, T. et al. Electroactive polymers for sensing. *Interface Focus* **6**, 20160026 (2016).
28. Biddiss, E. & Chau, T. Electroactive polymeric sensors in hand prostheses: bending response of an ionic polymer metal composite. *Med. Eng. Phys.* **28**, 568–578 (2006).
29. Pelrine, R., Kornbluh, R., Pei, Q. & Joseph, J. High-speed electrically actuated elastomers with strain greater than 100%. *Science* **287**, 836–839 (2000).
30. Anderson, I. A., Gisby, T. A., McKay, T. G., O'Brien, B. M. & Calius, E. P. Multi-functional dielectric elastomer artificial muscles for soft and smart machines. *J. Appl. Phys.* **112**, 041101 (2012).

31. Ji, X. et al. An autonomous untethered fast soft robotic insect driven by low-voltage dielectric elastomer actuators. *Sci. Robot.* **4**, eaaz6451 (2019).
32. Li, T. et al. Agile and resilient insect-scale robot. *Soft Robot.* **6**, 133–141 (2019).
33. Shintake, J., Rosset, S., Schubert, B., Floreano, D. & Shea, H. Versatile soft grippers with intrinsic electroadhesion based on multifunctional polymer actuators. *Adv. Mater.* **28**, 231–238 (2016).
34. Li, T. et al. Fast-moving soft electronic fish. *Sci. Adv.* **3**, 1602045 (2017).
35. Christianson, C., Goldberg, N. N., Deheyn, D. D., Cai, S. & Tolley, M. T. Translucent soft robots driven by frameless fluid electrode dielectric elastomer actuators. *Sci. Robot.* **3**, eaat1893 (2018).
36. Godaba, H., Li, J., Wang, Y. & Zhu, J. A soft jellyfish robot driven by a dielectric elastomer actuator. *IEEE Robot. Autom. Lett.* **1**, 624–631 (2016).
37. Chen, Y. et al. Controlled flight of a microrobot powered by soft artificial muscles. *Nature* **575**, 324–329 (2019).
38. Rothemund, P., Kellaris, N., Mitchell, S. K., Acome, E. & Keplinger, C. HASEL artificial muscles for a new generation of lifelike robots—recent progress and future opportunities. *Adv. Mater.* **33**, 2003375 (2021).
39. Acome, E. et al. Hydraulically amplified self-healing electrostatic actuators with muscle-like performance. *Science* **359**, 61–65 (2018).
40. Diteesawat, R. S., Helps, T., Taghavi, M. & Rossiter, J. Electro-pneumatic pumps for soft robotics. *Sci. Robot.* **6**, eabc3721 (2021).
41. Kellaris, N., Venkata, V. G., Smith, G. M., Mitchell, S. K. & Keplinger, C. Peano-HASEL actuators: muscle-mimetic,

electrohydraulic transducers that linearly contract on activation. *Sci. Robot.* **3**, eaar3276 (2018).

42. Keplinger, C., Li, T., Baumgartner, R., Suo, Z. & Bauer, S. Harnessing snap-through instability in soft dielectrics to achieve giant voltage-triggered deformation. *Soft Matter* **8**, 285–288 (2012).
43. Carrico, J. D., Kim, K. J. & Leang, K. K. In *Proc. IEEE International Conference on Robotics and Automation* 4313–4320 (IEEE, 2017).
44. Yeom, S. & Oh, I. A biomimetic jellyfish robot based on ionic polymer metal composite actuators. *Smart Mater. Struct.* **18**, 085002 (2009).
45. Chen, Z., Um, T. I. & Bart-smith, H. Bio-inspired robotic manta ray powered by ionic polymer–metal composite artificial muscles. *Int. J. Smart Nano Mater.* **3**, 296–308 (2012).
46. Fang, B., Ju, M. & Lin, C. K. A new approach to develop ionic polymer–metal composites (IPMC) actuator: Fabrication and control for active catheter systems. *Sens. Actuators A Phys.* **137**, 321–329 (2007).
47. Krishen, K. Space applications for ionic polymer-metal composite sensors, actuators, and artificial muscles. *Acta Astronaut.* **64**, 1160–1166 (2009).
48. Shahinpoor, M. & Kim, K. J. Ionic polymer–metal composites: IV. Industrial and medical applications. *Smart Mater. Struct.* **14**, 197–214 (2005).
49. Hebner, R. & Beno, J. Flywheel batteries come around again. *IEEE Spectr.* **39**, 46–51 (2002).
50. Mousavi, S. M. G., Faraji, F., Majazi, A. & Al-haddad, K. A comprehensive review of flywheel energy storage system technology. *Renew. Sustain. Energy Rev.* **67**, 477–490 (2017).

51. Fausz, J. L. & Richie, D. J. In *Proc. IEEE International Conference on Control Applications* 991–995 (IEEE, 2000).
52. Polygerinos, B. P. et al. Soft robotics: review of fluid-driven intrinsically soft devices; manufacturing, sensing, control, and applications in human-robot interaction. *Adv. Eng. Mater.* **19**, 1700016 (2017).
53. Rus, D. & Tolley, M. T. Design, fabrication and control of soft robots. *Nature* **521**, 467–475 (2015). **This review explores recent advancements in the field of soft robots, including how these robots can be fabricated, powered and controlled.**
54. Rich, S. I., Wood, R. J. & Majidi, C. Untethered soft robotics. *Nat. Electron.* **1**, 102–112 (2018). **This review focuses on technologies, approaches and challenges to developing untethered soft robots and actuators.**
55. Tang, Y. et al. Leveraging elastic instabilities for amplified performance: Spine-inspired high-speed and high-force soft robots. *Sci. Adv.* **6**, eaaz6912 (2020).
56. Gorissen, B., Melancon, D., Vasilos, N., Torbati, M. & Bertoldi, K. Inflatable soft jumper inspired by shell snapping. *Sci. Robot.* **5**, eabb1967 (2020).
57. Overvelde, J. T. B., Kloek, T., D’haen, J. J. A. & Bertoldi, K. Amplifying the response of soft actuators by harnessing snap-through instabilities. *Proc. Natl Acad. Sci. USA* **112**, 10863–10868 (2015).
58. Forterre, Y., Skotheim, J. M., Dumais, J. & Mahadevan, L. How the Venus flytrap snaps. *Nature* **433**, 421–425 (2005).
59. Pratt, G. A. & Williamson, M. M. In *Proc. 1995 IEEE/RSJ International Conference on Intelligent Robots and Systems* 399–406 (IEEE, 1995).

60. Seok, S. et al. In *Proc. IEEE International Conference on Robotics and Automation* 3307–3312 (IEEE, 2013).
61. Wehner, M. et al. Pneumatic energy sources for autonomous and wearable soft robotics. *Soft Robot.* **1**, 263–273 (2014).
62. Tolley, M. T. et al. In *Proc. IEEE/RSJ International Conference on Intelligent Robots and Systems* 561–566 (2014).
63. Truby, R. L. & Li, S. Integrating chemical fuels and artificial muscles for untethered microrobots. *Sci. Robot.* **5**, eabd7338 (2020). **This brief article highlights emerging robotic technologies that make use of combined, codesigned power-actuation systems containing chemical fuels to achieve high energy densities and untethered movement.**
64. Qidwai, M. A., Thomas, J. P., Kellogg, J. C. & Baucom, J. In *Proc. Smart Structures and Materials 2004: Active Materials: Behavior and Mechanics* 84–95 (2004).
65. Joshi, P. et al. In *Proc. SPIE's 9th Annual International Symposium on Smart Structures and Materials* 171–179 (SPIE, 2002).
66. Chen, Z. et al. Balancing volumetric and gravimetric uptake in highly porous materials for clean energy. *Science* **368**, 297–303 (2020).
67. Maeda, K., Shinoda, H. & Tsumori, F. Miniaturization of worm-type soft robot actuated by magnetic field. *Jpn. J. Appl. Phys.* **59**, SIIL04 (2020).
68. Do, T. N., Phan, H., Nguyen, T. & Visell, Y. Miniature soft electromagnetic actuators for robotic applications. *Adv. Funct. Mater.* **28**, 201800244 (2018).
69. Hines, L., Petersen, K., Lum, G. Z. & Sitti, M. Soft actuators for small-scale robotics. *Adv. Mater.* **29**, 1603483 (2017).

70. Mao, G. et al. Soft electromagnetic actuators. *Sci. Adv.* **6**, eabc0251 (2020).
71. Li, J. et al. Development of a magnetic microrobot for carrying and delivering targeted cells. *Sci. Robot.* **3**, eaat8829 (2018).
72. Peyer, K. E., Zhang, L. & Nelson, B. J. Bio-inspired magnetic swimming microrobots for biomedical applications. *Nanoscale* **5**, 1259–1272 (2013).
73. Hu, W., Lum, G. Z., Mastrangeli, M. & Sitti, M. Small-scale soft-bodied robot with multimodal locomotion. *Nature* **554**, 81–85 (2018).
74. Shen, W. & Zhu, S. Harvesting energy via electromagnetic damper: application to bridge stay cables. *J. Intell. Mater. Syst. Struct.* **26**, 3–19 (2015).
75. Asama, J., Burkhardt, M. R., Davoodi, F. & Burdick, J. W. In *Proc. IEEE International Conference on Robotics and Automation* 244–251 (IEEE, 2015).
76. Lazarus, N. & Meyer, C. D. Stretchable inductor with liquid magnetic core. *Mater. Res. Express* **3**, 036103 (2016).
77. Lazarus, N., Meyer, C. D., Bedair, S. S., Slipher, G. A. & Kierzewski, I. M. Magnetic elastomers for stretchable inductors. *ACS Appl. Mater. Interfaces* **7**, 10080–10084 (2015).
78. Jadhao, J. S. & Thombare, D. G. Review on exhaust gas heat recovery for I.C. engine. *Int. J. Eng. Innov. Technol.* **2**, 93–100 (2013).
79. Wang, E. H. et al. Study of working fluid selection of organic Rankine cycle (ORC) for engine waste heat recovery. *Energy* **36**, 3406–3418 (2011).
80. Li, N. et al. New twist on artificial muscles. *Proc. Natl Acad. Sci. USA* **115**, 11709–11716 (2018).

81. Kanik, M., Orguc, S., Varnavides, G. & Kim, J. Strain-programmable fiber-based artificial muscle. *Science* **365**, 145–150 (2019).
82. Gao, W., de Ávila, B. E. F., Zhang, L. & Wang, J. Targeting and isolation of cancer cells using micro/nanomotors. *Adv. Drug Deliv. Rev.* **125**, 94–101 (2018).
83. Li, D., Liu, C., Yang, Y., Wang, L. & Shen, Y. Micro-rocket robot with all-optic actuating and tracking in blood. *Light Sci. Appl.* **9**, 84 (2020).
84. Behl, B. M., Razzaq, M. Y. & Lendlein, A. Multifunctional shape-memory polymers. *Adv. Mater.* **22**, 3388–3410 (2010).
85. Liu, C., Qin, H. & Mather, P. T. Review of progress in shape-memory polymers. *J. Mater. Chem.* **17**, 1543–1558 (2007).
86. Lendlein, A., Behl, M., Hiebl, B. & Wischke, C. Shape-memory polymers as a technology platform for biomedical applications. *Expert Rev. Med. Devices* **7**, 357–379 (2010).
87. Small, W., Metzger, M. F., Wilson, T. S. & Maitland, D. J. Laser-activated shape memory polymer microactuator for thrombus removal following ischemic stroke: preliminary in vitro analysis. *IEEE J. Sel. Top. Quantum Electron.* **11**, 892–901 (2005).
88. Chenal, T. P., Case, J. C., Paik, J. & Kramer, R. K. In *Proc. IEEE/RSJ International Conference on Intelligent Robots and Systems (IROS 2014)* 2827–2831 (IEEE, 2014).
89. Liu, R. et al. Shape memory polymers for body motion energy harvesting and self-powered mechanosensing. *Adv. Mater.* **30**, 1705195 (2018).
90. Firouzeh, A., Salerno, M. & Paik, J. Stiffness control with shape memory polymer in underactuated robotic origamis. *IEEE Trans. Robot.* **33**, 765–777 (2017).

91. Jin, B. et al. Programming a crystalline shape memory polymer network with thermo- and photo-reversible bonds toward a single-component soft robot. *Sci. Adv.* **4**, aao3865 (2018).
92. Liu, Y., Du, H., Liu, L. & Leng, J. Shape memory polymers and their composites in aerospace applications: a review. *Smart Mater. Struct.* **23**, 023001 (2014).
93. Bellin, I., Kelch, S. & Lendlein, A. Dual-shape properties of triple-shape polymer networks with crystallizable network segments and grafted side chains. *J. Mater. Chem.* **17**, 2885–2891 (2007).
94. Ze, Q., Kuang, X., Wu, S., Wong, J. & Montgomery, S. M. Magnetic shape memory polymers with integrated multifunctional shape manipulations. *Adv. Mater.* **32**, 1906657 (2020).
95. Mohd Jani, J., Leary, M., Subic, A. & Gibson, M. A. A review of shape memory alloy research, applications and opportunities. *Mater. Des.* **56**, 1078–1113 (2014).
96. Laschi, C. et al. Soft robot arm inspired by the octopus. *Adv. Robot.* **26**, 709–727 (2012).
97. Rodrigue, H., Wang, W., Han, M. & Kim, T. J. Y. An overview of shape memory alloy-coupled actuators and robots. *Soft Robot.* **4**, 3–15 (2017).
98. Villanueva, A., Smith, C. & Priya, S. A biomimetic robotic jellyfish (Robojelly) actuated by shape memory alloy. *Bioinspir. Biomim.* **6**, 036004 (2011).
99. Kim, H., Song, S. & Ahn, S. A turtle-like swimming robot using a smart soft composite (SSC) structure. *Smart Mater. Struct.* **22**, 014007 (2013).
100. Koh, J. et al. Jumping on water: surface tension-dominated jumping of water striders and robotic insects. *Science* **349**, 517–522 (2015).

101. Jun, H. Y., Rediniotis, O. K. & Lagoudas, D. C. Development of a fuel-powered shape memory alloy actuator system: II. Fabrication and testing. *Smart Mater. Struct.* **16**, S95 (2007).
102. Odhner, L. U. & Asada, H. H. Sensorless temperature estimation and control of shape memory alloy actuators using thermoelectric devices. *IEEE/ASME Trans. Mechatronics* **11**, 139–144 (2006).
103. Yang, X., Chang, L. & Pérez-arancibia, N. O. An 88-milligram insect-scale autonomous crawling robot driven by a catalytic artificial muscle. *Sci. Robot.* **5**, eaba0015 (2020).
104. Kim, S. H. et al. Harvesting temperature fluctuations as electrical energy using torsional and tensile polymer muscles. *Energy Environ. Sci.* **8**, 3336–3344 (2015).
105. Goguel, O. & PAO. TRIZ 40 (Solid Creativity);  
[http://www.triz40.com/TRIZ\\_GB.php](http://www.triz40.com/TRIZ_GB.php)
106. Mitchenson, B. P. D. et al. Human and machine motion for wireless electronic devices. *Proc. IEEE* **96**, 1457–1486 (2008).
107. Johannisson, W. et al. A residual performance methodology to evaluate multifunctional systems. *Multifunct. Mater.* **3**, 025002 (2020). **This work discusses how the advantages of multifunctional systems over monofunctional systems can be determined mathematically and used to make design decisions.**
108. Ragone, D. V. *Review of Battery Systems for Electrically Powered Vehicles* Technical Paper 680453 (SAE, 1968). **This paper represents the first reported use of the ‘Ragone’ style plot, which allows for a comparison between the energy-density and power-density metrics of different energy-storage devices.**
109. Luo, X., Wang, J., Dooner, M. & Clarke, J. Overview of current development in electrical energy storage technologies and the application potential in power system operation. *Appl. Energy* **137**, 511–536 (2015).

110. Bossche, P. V. D. & Mierlo, J. V. SUBAT: an assessment of sustainable battery technology. *J. Power Sources* **162**, 913–919 (2006).
111. Madden, J. D. W. et al. Artificial muscle technology: physical principles and naval prospects. *IEEE J. Ocean. Eng.* **29**, 706–728 (2004).
112. Alici, G. Softer is harder: what differentiates soft robotics from hard robotics? *MRS Adv.* **3**, 1557–1568 (2018).
113. Power-to-weight ratio. *Wikipedia* [https://en.wikipedia.org/wiki/Power-to-weight\\_ratio](https://en.wikipedia.org/wiki/Power-to-weight_ratio) (2021).
114. Boretti, A. A. Energy recovery in passenger cars. *J. Energy Resour. Technol.* **134**, 022203 (2012).
115. Energy density. *Wikipedia* [https://en.wikipedia.org/wiki/Energy\\_density](https://en.wikipedia.org/wiki/Energy_density) (2021).
116. Water pumps & accessories. *Absolute Water Pumps* <https://www.absolutewaterpumps.com/> (2021).
117. Evans, J. Pump efficiency—what is efficiency? *Pumps & Systems* <https://www.pumpsandsystems.com/pump-efficiency-what-efficiency> (2012).
118. Oxidation of fatty acids. *Chemistry LibreTexts* <https://chem.libretexts.org/@go/page/234043> (2021).
119. Huber, J. E., Fleck, N. A. & Ashby, M. F. The selection of mechanical actuators based on performance indices. *Proc. R. Soc. A* **453**, 2185–2205 (1997). **This work reports on the mechanical characteristics of different types of actuator technologies.**
120. Evans, A., Strezov, V. & Evans, T. J. Assessment of utility energy storage options for increased renewable energy penetration. *Renew. Sustain. Energy Rev.* **16**, 4141–4147 (2012).

121. Love, L. J., Lanke, E. & Alles, P. Estimating the impact (energy, emissions and economics) of the U.S. fluid power industry. *Oak Ridge National Laboratory, Oak Ridge, TN* (2012).
122. Balki, M. K., Sayin, C. & Canakci, M. The effect of different alcohol fuels on the performance, emission and combustion characteristics of a gasoline engine. *Fuel* **115**, 901–906 (2014).
123. Peirs, J., Reynaerts, D. & Verplaetse, F. Development of an axial microturbine for a portable gas turbine generator. *J. Micromech. Microeng.* **13**, 5–11 (2003).
124. Lefebvre, A. H. Fuel effects on gas turbine combustion—ignition, stability, and combustion efficiency. *Trans. ASME* **107**, 24–37 (1985).
125. Liang, W., Liu, H., Wang, K. & Qian, Z. Comparative study of robotic artificial actuators and biological muscle. *Adv. Mech. Eng.* <https://doi.org/10.1177/1687814020933409> (2020).
126. Isermann, R. & Raab, U. Intelligent actuators—ways to autonomous actuating systems. *Automatica* **29**, 1315–1331 (1993).
127. Veale, A. J. & Xie, S. Q. Towards compliant and wearable robotic orthoses: a review of current and emerging actuator technologies. *Med. Eng. Phys.* **38**, 317–325 (2016).
128. Kedzierski, J., Holihan, E., Cabrera, R. & Weaver, I. Re-engineering artificial muscle with microhydraulics. *Microsyst. Nanoeng.* **3**, 17016 (2017).
129. Daerden, F. & Lefeber, D. Pneumatic artificial muscles: actuators for robotics and automation. *Eur. J. Mech. Environ. Eng.* **47**, 11–21 (2002).
130. Chen, H., Ngoc, T., Yang, W., Tan, C. & Li, Y. Progress in electrical energy storage system: A critical review. *Prog. Nat. Sci.* **19**, 291–312 (2009). **This review presents valuable numerical data for various electrical energy-storage technologies, including batteries, fuel**

**cells, flow batteries, superconducting magnetic energy storage and thermal energy storage.**

131. Sabihuddin, S., Kiprakis, A. E. & Mueller, M. A numerical and graphical review of energy storage technologies. *Energies* **8**, 172–216 (2015). **This paper displays performance and statistical data for a wide range of modern energy-storage technologies, and also discusses their advantages and deficiencies relative to each other.**
132. St. Pierre, R. & Bergbreiter, S. Toward autonomy in sub-gram terrestrial robots. *Annu. Rev. Control Robot. Auton. Syst.* **2**, 231–254 (2019).
133. Trimmer, W. S. N. Microrobots and micromechanical systems. *Sens. Actuators* **19**, 267–287 (1989).
134. Johannesson, W., Harnden, R., Zenkert, D. & Lindbergh, G. Shape-morphing carbon fiber composite using electrochemical actuation. *Proc. Natl Acad. Sci. USA* **117**, 7658–7664 (2020).
135. Kotikian, A. et al. Untethered soft robotic matter with passive control of shape morphing and propulsion. *Sci. Robot.* **4**, eaax7044 (2019).
136. Maccurdy, R., Katzschmann, R., Kim, Y. & Rus, D. In *Proc. IEEE International Conference on Robotics and Automation* 3878–3885 (IEEE, 2016).
137. Peele, B. N., Wallin, T. J., Zhao, H. & Shepherd, R. F. 3D printing antagonistic systems of artificial muscle using projection stereolithography. *Bioinspir. Biomim.* **10**, 055003 (2015).
138. Wallin, T. J. et al. Click chemistry stereolithography for soft robots that self-heal. *J. Mater. Chem. B* **5**, 6249–6255 (2017).
139. Treml, B., Gillman, A., Buskohl, P. & Vaia, R. Origami mechanologic. *Proc. Natl Acad. Sci. USA* **115**, 6916–6921 (2018).

140. Jiang, Y., Korpas, L. M. & Raney, J. R. Bifurcation-based embodied logic and autonomous actuation. *Nat. Commun.* **10**, 128 (2019).
141. Song, Y. et al. Additively manufacturable micro-mechanical logic gates. *Nat. Commun.* **10**, 882 (2019).
142. Preston, D. J. et al. Digital logic for soft devices. *Proc. Natl Acad. Sci. USA* **116**, 7750–7759 (2019).
143. Chau, N., Slipher, G. A., Brien, B. M. O., Mrozek, R. A. & Anderson, I. A. A solid-state dielectric elastomer switch for soft logic. *Appl. Phys. Lett.* **108**, 103506 (2016).
144. Wilson, K. E., Henke, E. M., Slipher, G. A. & Anderson, I. A. Rubbery logic gates. *Extreme Mech. Lett.* **9**, 188–194 (2016).
145. Henke, E.-F. M., Wilson, K. E., Slipher, G. A., Mrozek, R. A. & Anderson, I. A. In *Robotic Systems and Autonomous Platforms: Advances in Materials and Manufacturing* 29–40 (Woodhead Publishing, 2019).
146. McEvoy, M. A. & Correll, N. Materials that couple sensing, actuation, computation, and communication. *Science* **347**, 1261689 (2015).
147. Correll, N., Baughman, R., Voyles, R., Yao, L. & Inman, D. Robotic materials. Preprint at <https://arxiv.org/abs/1903.10480v1> (2019).
148. Van Meerbeek, I. M., De Sa, C. M. & Shepherd, R. F. Soft optoelectronic sensory foams with proprioception. *Sci. Robot.* **3**, eaau2489 (2018).
149. Nakajima, K., Hauser, H., Li, T. & Pfeifer, R. Information processing via physical soft body. *Sci. Rep.* **5**, 10487 (2015).
150. Honda unveils all-new ASIMO with significant advancements. *Honda Robotics* <http://www.world.honda.com/news/2011/c111108All-new-ASIMO/index.html> (2011).

# Acknowledgements

The authors thank the Office of Naval Research, grant no. N00014-20-1-2438, Air Force Office of Scientific Research, grant no. FA9550-20-1-0254, and the National Science Foundation, grant no. EFMA-1830924.

# Author information

## Author notes

1. These authors contributed equally: Cameron A. Aubin, Jennifer A. Lewis, Robert F. Shepherd

## Affiliations

1. Sibley School of Mechanical & Aerospace Engineering, Cornell University, Ithaca, NY, USA  
Cameron A. Aubin & Robert F. Shepherd
2. John A. Paulson School of Engineering & Applied Sciences, Harvard University, Cambridge, MA, USA  
Benjamin Gorissen & Jennifer A. Lewis
3. Department of Mechanical Engineering, KU Leuven, Leuven, Belgium  
Benjamin Gorissen & Edoardo Milana
4. Materials and Manufacturing Directorate, Air Force Research Laboratory, Wright-Patterson Air Force Base, OH, USA  
Philip R. Buskohl
5. Energy and Biotechnology Division, Army Research Laboratory, Adelphi, MD, USA

Nathan Lazarus

6. Autonomous Systems Division, Army Research Laboratory, Adelphi, MD, USA

Geoffrey A. Slipher

7. Robotic Materials Department, Max Planck Institute for Intelligent Systems, Stuttgart, Germany

Christoph Keplinger

8. Department of Computer Science, University of Vermont, Burlington, VT, USA

Josh Bongard

9. Department of Engineering, University of Cambridge, Cambridge, UK

Fumiya Iida

## Contributions

R.F.S. and J.A.L. conceived of the concept. C.A.A., J.A.L. and R.F.S. drafted key elements of the manuscript. C.A.A. researched, collected and analysed data. C.A.A., B.G. and E.M. drafted figures. P.R.B., N.L., G.A.S., C.K., J.B. and F.I. assisted in editing and refining the vision.

## Corresponding author

Correspondence to [Robert F. Shepherd](#).

## Ethics declarations

## Competing interests

The authors declare no competing interests.

# Peer review

## Peer review information

*Nature* thanks Milo Shaffer and the other, anonymous, reviewer(s) for their contribution to the peer review of this work.

## Additional information

**Publisher's note** Springer Nature remains neutral with regard to jurisdictional claims in published maps and institutional affiliations.

## Extended data figures and tables

**Extended Data Table 1 Energy density and power density of common energy storage and actuator technologies**

## Rights and permissions

[Reprints and Permissions](#)

## About this article

### Cite this article

Aubin, C.A., Gorissen, B., Milana, E. *et al.* Towards enduring autonomous robots via embodied energy. *Nature* **602**, 393–402 (2022).  
<https://doi.org/10.1038/s41586-021-04138-2>

- Received: 17 February 2021
- Accepted: 14 October 2021
- Published: 16 February 2022

- Issue Date: 17 February 2022
- DOI: <https://doi.org/10.1038/s41586-021-04138-2>

## Share this article

Anyone you share the following link with will be able to read this content:

[Get shareable link](#)

Sorry, a shareable link is not currently available for this article.

[Copy to clipboard](#)

Provided by the Springer Nature SharedIt content-sharing initiative

---

This article was downloaded by **calibre** from <https://www.nature.com/articles/s41586-021-04138-2>

| [Section menu](#) | [Main menu](#) |

- Article
- [Published: 16 February 2022](#)

# Thermal imaging of dust hiding the black hole in NGC 1068

- [Violeta Gámez Rosas](#) ORCID: [orcid.org/0000-0002-8830-6199<sup>1</sup>](https://orcid.org/0000-0002-8830-6199),
- [Jacob W. Isbell<sup>2</sup>](#),
- [Walter Jaffe<sup>1</sup>](#),
- [Romain G. Petrov<sup>3</sup>](#),
- [James H. Leftley<sup>3</sup>](#),
- [Karl-Heinz Hofmann<sup>4</sup>](#),
- [Florentin Millour<sup>3</sup>](#),
- [Leonard Burtscher](#) ORCID: [orcid.org/0000-0003-1014-043X<sup>1</sup>](https://orcid.org/0000-0003-1014-043X),
- [Klaus Meisenheimer<sup>2</sup>](#),
- [Anthony Meilland<sup>3</sup>](#),
- [Laurens B. F. M. Waters<sup>5,6</sup>](#),
- [Bruno Lopez<sup>3</sup>](#),
- [Stéphane Lagarde<sup>3</sup>](#),
- [Gerd Weigelt<sup>4</sup>](#),
- [Philippe Berio<sup>3</sup>](#),
- [Fatme Allouche<sup>3</sup>](#),
- [Sylvie Robbe-Dubois<sup>3</sup>](#),
- [Pierre Cruzalèbes<sup>3</sup>](#),
- [Felix Bettonvil<sup>7</sup>](#),
- [Thomas Henning](#) ORCID: [orcid.org/0000-0002-1493-300X<sup>2</sup>](https://orcid.org/0000-0002-1493-300X),
- [Jean-Charles Augereau<sup>8</sup>](#),
- [Pierre Antonelli<sup>3</sup>](#),
- [Udo Beckmann<sup>4</sup>](#),
- [Roy van Boekel<sup>2</sup>](#),

- [Philippe Bendjoya<sup>3</sup>](#),
- [William C. Danchi<sup>9</sup>](#),
- [Carsten Dominik<sup>10</sup>](#),
- [Julien Drevon<sup>3</sup>](#),
- [Jack F. Gallimore<sup>11</sup>](#),
- [Uwe Graser<sup>2</sup>](#),
- [Matthias Heininger<sup>4</sup>](#),
- [Vincent Hocdé<sup>3</sup>](#),
- [Michiel Hogerheijde](#) ORCID: [orcid.org/0000-0001-5217-537X<sup>1,10</sup>](https://orcid.org/0000-0001-5217-537X),
- [Josef Hron<sup>12</sup>](#),
- [Caterina M. V. Impellizzeri<sup>1</sup>](#),
- [Lucia Klarmann<sup>2</sup>](#),
- [Elena Kokoulina<sup>3</sup>](#),
- [Lucas Labadie<sup>13</sup>](#),
- [Michael Lehmitz<sup>2</sup>](#),
- [Alexis Matter<sup>3</sup>](#),
- [Claudia Paladini](#) ORCID: [orcid.org/0000-0003-4974-7239<sup>14</sup>](https://orcid.org/0000-0003-4974-7239),
- [Eric Pantin<sup>15</sup>](#),
- [Jörg-Uwe Pott<sup>2</sup>](#),
- [Dieter Schertl<sup>4</sup>](#),
- [Anthony Soulain<sup>16</sup>](#),
- [Philippe Stee](#) ORCID: [orcid.org/0000-0001-8220-0636<sup>3</sup>](https://orcid.org/0000-0001-8220-0636),
- [Konrad Tristram<sup>14</sup>](#),
- [Jozsef Varga<sup>1</sup>](#),
- [Julien Woillez](#) ORCID: [orcid.org/0000-0002-2958-4738<sup>17</sup>](https://orcid.org/0000-0002-2958-4738),
- [Sebastian Wolf<sup>18</sup>](#),
- [Gideon Yoffe<sup>2</sup>](#) &
- [Gerard Zins<sup>14</sup>](#)

*Nature* volume **602**, pages 403–407 (2022)

- 862 Accesses
- 672 Altmetric

- [Metrics details](#)

## Subjects

- [Astronomical instrumentation](#)
- [Astrophysical dust](#)
- [Galaxies and clusters](#)

## Abstract

In the widely accepted ‘unified model’<sup>1</sup> solution of the classification puzzle of active galactic nuclei, the orientation of a dusty accretion torus around the central black hole dominates their appearance. In ‘type-1’ systems, the bright nucleus is visible at the centre of a face-on torus. In ‘type-2’ systems the thick, nearly edge-on torus hides the central engine. Later studies suggested evolutionary effects<sup>2</sup> and added dusty clumps and polar winds<sup>3</sup> but left the basic picture intact. However, recent high-resolution images<sup>4</sup> of the archetypal type-2 galaxy NGC 1068<sup>5,6</sup>, suggested a more radical revision. The images displayed a ring-like emission feature that was proposed to be hot dust surrounding the black hole at the radius where the radiation from the central engine evaporates the dust. That ring is too thin and too far tilted from edge-on to hide the central engine, and ad hoc foreground extinction is needed to explain the type-2 classification. These images quickly generated reinterpretations of the dichotomy between types 1 and 2<sup>7,8</sup>. Here we present new multi-band mid-infrared images of NGC 1068 that detail the dust temperature distribution and reaffirm the original model. Combined with radio data (J.F.G. and C.M.V.I., manuscript in preparation), our maps locate the central engine that is below the previously reported ring and obscured by a thick, nearly edge-on disk, as predicted by the unified model. We also identify emission from polar flows and absorbing dust that is mineralogically distinct from that towards the Milky Way centre.

This is a preview of subscription content

## Access options

Subscribe to Nature+

Get immediate online access to the entire Nature family of 50+ journals

\$29.99

monthly

[Subscribe](#)

Subscribe to Journal

Get full journal access for 1 year

\$199.00

only \$3.90 per issue

[Subscribe](#)

All prices are NET prices.

VAT will be added later in the checkout.

Tax calculation will be finalised during checkout.

Buy article

Get time limited or full article access on ReadCube.

\$32.00

[Buy](#)

All prices are NET prices.

### **Additional access options:**

- [Log in](#)
- [Learn about institutional subscriptions](#)

**Fig. 1:** IRBis reconstructed images of NGC 1068.

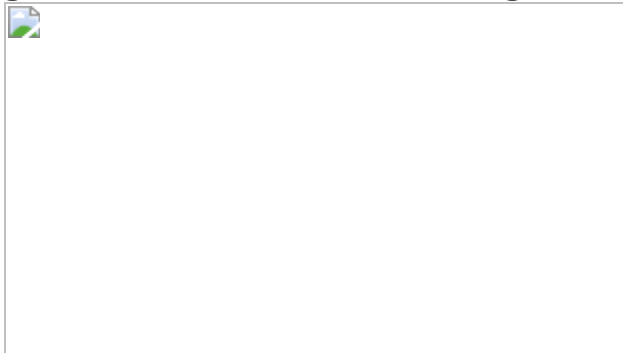


**Fig. 2:** Apertures for the extraction of infrared SEDs.

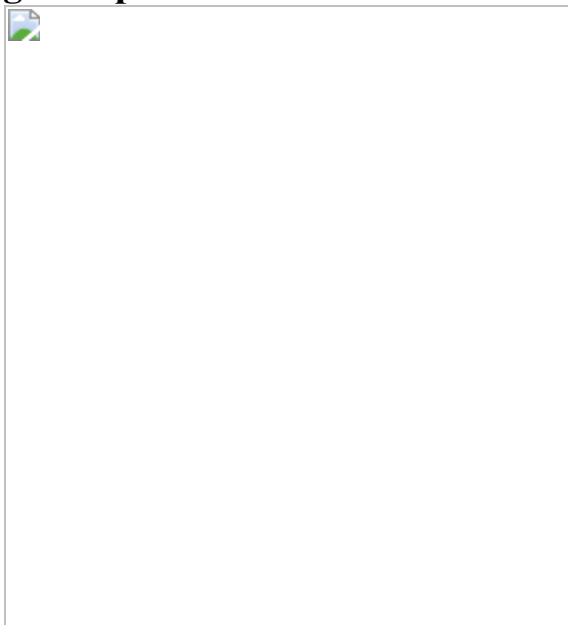


**Fig. 3:** Blackbody SED fits.



**Fig. 4:** Comparison of infrared and radio images.



## Data availability

The raw MATISSE data used in this article are available to qualified researchers at [http://archive.eso.org/eso/eso\\_archive\\_main.html](http://archive.eso.org/eso/eso_archive_main.html). Reduced data are available at [https://github.com/VioletaGamez/NGC1068\\_MATISSE](https://github.com/VioletaGamez/NGC1068_MATISSE).

## Code availability

The Python code for the emcee sampler is available via <https://emcee.readthedocs.io>. The Python code to fit multi-Gaussian models, and spectral energy distributions, is available at <https://doi.org/10.5281/zenodo.5599363>. The MiRA image reconstruction code is available at <https://github.com/emmt/MiRA>. The ESO MATISSE pipeline, including IRBis, is available from <https://www.eso.org/sci/software/pipelines/matisse/matisse-pipe-recipes.html>.

## References

1. Antonucci, R. Unified models for active galactic nuclei and quasars. *Ann. Rev. Astron. Astrophys.* **31**, 473–521 (1993).
2. López-Gonzaga, N. & Jaffe, W. Mid-infrared interferometry of Seyfert galaxies: challenging the standard model. *Astron. Astrophys.* **591**, A128 (2016).
3. Asmus, D., Höning, S. F. & Gandhi, P. The subarcsecond mid-infrared view of local active galactic nuclei. III. Polar dust emission. *Astrophys. J.* **822**, 109–121 (2016).
4. GRAVITY Collaboration. An image of the dust sublimation region in the nucleus of NGC 1068. *Astron. Astrophys.* **634**, A1 (2020).
5. Seyfert, C. K. Nuclear emission in spiral nebulae. *Astrophys. J.* **97**, 28–40 (1943).
6. Antonucci, R. R. J. & Miller, J. S. Spectropolarimetry and the nature of NGC 1068. *Astrophys. J.* **297**, 621–632 (1985).

7. Vermot, P. et al. The hot dust in the heart of NGC 1068's torus: a 3D radiative model constrained with GRAVITY/VLTI. *Astron. Astrophys.* **652**, A65 (2021).
8. Prieto, A., Nadolny, J., Fernández-Ontiveros, J. A. & Mezcua, M. Dust in the central parsecs of unobscured AGN: more challenges to the torus. *Mon. Not. R. Astron. Soc.* **506**, 562–580 (2020).
9. Hönig, S. F. Redefining the torus: a unifying view of AGNs in the infrared and submillimetre. *Astrophys. J.* **884**, 171 (2019).
10. Barvainis, R. Hot dust and the near-infrared bump in the continuum spectra of quasars and active galactic nuclei. *Astrophys. J.* **320**, 537–544 (1987).
11. Baskin, A. & Laor, A. Dust inflated accretion disc as the origin of the broad line region in active galactic nuclei. *Mon. Not. R. Astron. Soc.* **474**, 1970–1994 (2018).
12. Jaffe, W. et al. The central dusty torus in the active nucleus of NGC 1068. *Nature* **429**, 47–49 (2004).
13. Raban, D., Jaffe, W., Röttgering, H., Meisenheimer, K. & Tristram, K. R. W. W. Resolving the obscuring torus in NGC 1068 with the power of infrared interferometry: revealing the inner funnel of dust. *Mon. Not. R. Astron. Soc.* **394**, 1325–1337 (2009).
14. López-Gonzaga, N., Jaffe, W., Burtscher, L., Tristram, K. R. W. & Meisenheimer, K. Revealing the large nuclear dust structures in NGC 1068 with MIDI/VLTI. *Astron. Astrophys.* **565**, A71 (2014).
15. Lopez, B. et al. MATISSE, the VLTI mid-infrared imaging spectro-interferometer. Preprint at <https://arxiv.org/abs/2110.15556> (2021).
16. Hofmann, K.-H., Weigelt, G. & Schertl, D. An image reconstruction method (IRBis) for optical/infrared interferometry. *Astron. Astrophys.* **565**, A48 (2014).

17. Thiébaut, E. In *Proc. SPIE 7013: Optical and Infrared Interferometry* (eds Schöller, M. et al.) 70131I (SPIE, 2008).
18. Högbom, J. A. Aperture synthesis with a non-regular distribution of interferometer baselines. *Astron. Astrophys. Suppl. Ser.* **15**, 417–426 (1974).
19. Nenkova, M., Sirocky, M. M., Ivezić, Z. & Elitzur, M. AGN dusty tori. I. Handling of clumpy media. *Astrophys. J.* **685**, 147–159 (2008).
20. Fritz, T. K. et al. Line derived infrared extinction toward the Galactic center. *Astrophys. J.* **737**, 73 (2011).
21. Min, M., Hovenier, J. W. & de Koter, A. Modelling optical properties of cosmic dust grains using a distribution of hollow spheres. *Astron. Astrophys.* **432**, 909–920 (2005).
22. Impellizzeri, C. M. V. et al. Counter-rotation and high-velocity outflow in the parsec-scale molecular torus of NGC 1068. *Astrophys. J. Lett.* **884**, L28–L33 (2019).
23. Greenhill, L. J., Gwinn, C. R., Antonucci, R. & Barvainis, R. VLBI imaging of water maser emission from the nuclear torus of NGC 1068. *Astrophys. J.* **472**, L21–L24 (1996).
24. Gallimore, J. F., Baum, S. A. & O’Dea, C. P. The parsec-scale radio structure of NGC 1068 and the nature of the nuclear radio source. *Astrophys. J.* **613**, 794–810 (2004).
25. Das, V., Crenshaw, D. M., Kraemer, S. B. & Deo, R. P. Kinematics of the narrow-line region in the Seyfert 2 galaxy NGC 1068: dynamical effects of the radio jet. *Astron. J.* **132**, 620–632 (2006).
26. Poncelet, A., Sol, H. & Perrin, G. Dynamics of the ionization bicone of NGC 1068 probed in mid-infrared with VISIR. *Astron. Astrophys.* **481**, 305–317 (2008).

27. García-Burillo, S. et al. ALMA images the many faces of the NGC 1068 torus and its surroundings. *Astron. Astrophys.* **632**, A61 (2019).
28. Evans, I. N. et al. HST Imaging of the inner 3 arcseconds of NGC 1068 in the light of [O III] lambda 5007. *Astrophys. J.* **369**, L27 (1991).
29. Gallimore, J. F., Baum, S. A., O'Dea, C. P. & Pedlar, A. The subarcsecond radio structure in NGC 1068. I. Observations and results. *Astrophys. J.* **458**, 136 (1996).
30. Kishimoto, M. The location of the nucleus of NGC 1068 and the three-dimensional structure of its nuclear region. *Astrophys. J.* **518**, 676–692 (1999).
31. Antonucci, R., Hurt, T. & Miller, J. HST ultraviolet spectropolarimetry of NGC 1068. *Astrophys. J.* **430**, 210 (1994).
32. Leinert, C. et al. MIDI – the 10  $\mu\text{m}$  instrument on the VLTI. *Astrophys. Space Sci.* **286**, 73–83 (2003).
33. Cruzalèbes, P. et al. A catalogue of stellar diameters and fluxes for mid-infrared interferometry. *Mon. Not. R. Astron. Soc.* **490**, 3158–3176 (2019).
34. Burtscher, L., Tristram, K. R. W., Jaffe, W. J. & Meisenheimer, K. In *Proc. SPIE 8445: Optical and Infrared Interferometry III* (eds Delplancke, F. et al.) 494–506 (SPIE, 2012).
35. Jaffe, W. J. In *Proc. SPIE 5491: New Frontiers in Stellar Interferometry* (ed. Traub, W. A.) 715–724 (SPIE, 2004).
36. Millour, F. et al. In *Proc. SPIE 5491: New Frontiers in Stellar Interferometry* (ed. Traub, W. A.) 1222–1230 (SPIE, 2004).
37. Cohen, M. et al. Spectral irradiance calibration in the infrared. X. A self-consistent radiometric all-sky network of absolutely calibrated stellar spectra. *Astron. J.* **117**, 1864–1889 (1999).

38. Petrov, R. G. et al. Commissioning MATISSE: operation and performances. *Proc. SPIE 11446: Optical and Infrared Interferometry and Imaging VII* (eds Tuthill, P. G. et al.) 124–142 (SPIE, 2020).
39. Bourges, L. et al. JMMC stellar diameters catalogue – JSDC. Version 2. *VizieR Online Data Catalog* <https://cdsarc.cds.unistra.fr/viz-bin/cat/II/346> (2017).
40. Meilland, A. et al. The binary Be star δ Scorpii at high spectral and spatial resolution. I. Disk geometry and kinematics before the 2011 periastron. *Astron. Astrophys.* **532**, A80 (2011).
41. Leftley, J. H. et al. Resolving the hot dust disk of ESO323-G77. *Astrophys. J.* **912**, 92 (2021).
42. Lawson, P. R. et al. In *Proc. SPIE 5491: Frontiers in Stellar Interferometry* (ed. Traub, W. A.) 886–899 (SPIE, 2004).
43. Cotton, W. et al. In *Proc. SPIE 7013: Optical and Infrared Interferometry* (eds Schöller, M. et al.) 531–544 (SPIE, 2008).
44. Baron, F. et al. In *Proc. SPIE 8445: Optical and Infrared Interferometry III* (eds Delplancke, F. et al.) 470–483 (SPIE, 2012).
45. Sanchez-Bermudez, J. et al. In *Proc. SPIE 9907: Optical and Infrared Interferometry V* (eds Melbet, F. et al.) 372–389 (SPIE, 2016).
46. Hager, W. W. & Park, S. Global convergence of SSM for minimizing a quadratic over a sphere. *Math. Comput.* **74**, 1413–1423 (2005).
47. Byrd, R. H., Lu, P., Nocedal, J. & Zhu, C. A limited memory algorithm for bound constrained optimization. *SIAM J. Sci. Comput.* **16**, 1190–1208 (1995).
48. Zhu, C., Byrd, R. H., Lu, P. & Nocedal, J. Algorithm 778: L-BFGS-B: Fortran subroutines for large-scale bound-constrained optimization. *ACM Trans. Math. Softw.* **23**, 550–560 (1997).

49. Millour, F. et al. In *The 2007 ESO Instrument Calibration Workshop* (eds Kaufer, A. & Kerber, F.) 461–470 (Springer, 2008).
50. Lachaume, R. On marginally resolved objects in optical interferometry. *Astron. Astrophys.* **400**, 795–803 (2003).
51. López-Gonzaga, N., Jaffe, W., Burtscher, L., Tristram, K. R. W. & Meisenheimer, K. Revealing the large nuclear dust structures in NGC 1068 with MIDI/VLTI. *Astron. Astrophys.* **565**, A71 (2014).
52. Foreman-Mackey, D., Hogg, D. W., Lang, D. & Goodman, J. emcee: the MCMC hammer. *Publ. Astron. Soc. Pacif.* **125**, 306–312 (2013).
53. Wells, D. C. In *Data Analysis in Astronomy* (eds Di Gesù, V. et al.) 195–209 (Springer, 1985).
54. Greisen, E. W. In *Acquisition, Processing and Archiving of Astronomical Images* (eds Longo, G. & Sedmak, G.) 125–142 (OAC, FORMEZ, 1990).
55. Greisen, E. W. In *Information Handling in Astronomy – Historical Vistas* (ed. Heck, A.) 109–125 (Kluwer, 2003).
56. Cornwell, T. J. Multiscale CLEAN deconvolution of radio synthesis Images. *IEEE J. Sel. Top. Signal Process.* **2**, 793–801 (2008).
57. Cotton, W. D., Jaffe, W., Perrin, G. & Woillez, J. Observations of the inner jet in NGC 1068 at 43 GHz. *Astron. Astrophys.* **477**, 517–520 (2008).
58. Mathis, J. S., Rumpl, W. & Nordsieck, K. H. The size distribution of interstellar grains. *Astrophys. J.* **217**, 425–433 (1977).
59. Zasowski, G., et al. Lifting the dusty veil with near- and mid-infrared photometry. II. A large-scale study of the Galactic infrared extinction law. *Astrophys J.* **707**, 510–523 (2009).
60. Köhler, M. & Li, A. On the anomalous silicate absorption feature of the prototypical Seyfert 2 galaxy NGC1068. *Mon. Not. R. Astron. Soc.*

**406**, L6–L10 (2010).

61. Van Boekel, R., et al. The building blocks of planets within the ‘terrestrial’ region of protoplanetary disks. *Nature* **432**, 479–482 (2004).
62. Prieto, M. A. et al. The spectral energy distribution of the central parsecs of the nearest AGN. *Mon. Not. R. Astron. Soc.* **402**, 724–744 (2010).
63. Isbell, J. W. et al. Subarcsecond mid-infrared view of local active galactic nuclei. IV. The L- and M-band imaging atlas. *Astrophys. J.* **910**, 104 (2021).

## Acknowledgements

We thank ESO and particularly the Cerro Paranal staff for their support in obtaining these observations. The data presented here were taken as part of ESO projects 60.A-9257 (commissioning) and 0104.B-0322(A) (MATISSE Guaranteed Time Observations of AGNs). We thank the GRAVITY AGN team for useful scientific discussions and early access to digital versions of their data (programme IDs 0102.B-0667, 0102.C-0205 and 0102.C-0211). MATISSE was defined, funded and built in close collaboration with ESO, by a consortium composed of French (INSU-CNRS in Paris and OCA in Nice), German (MPIA, MPIfR and University of Kiel), Dutch (NOVA and University of Leiden), and Austrian (University of Vienna) institutes. The Conseil Départemental des Alpes-Maritimes in France, the Konkoly Observatory and Cologne University have also provided resources for the manufacture of the instrument. A thought goes to our two deceased OCA colleagues, Olivier Chesneau and Michel Dugué, with us at the origin of the MATISSE project, and with whom we shared many beautiful moments. V.G.R. was partially supported by the Netherlands Organisation for Scientific Research (NWO). J.H.L. acknowledges the support of the French government through the UCA JEDI Investment in the Future project managed by the National Research Agency (ANR) under the reference number ANR-15-IDEX-01.

# Author information

## Affiliations

1. Leiden Observatory, Leiden University, Leiden, Netherlands

Violeta Gámez Rosas, Walter Jaffe, Leonard Burtscher, Michiel Hogerheijde, Caterina M. V. Impellizzeri & Jozsef Varga

2. Max Planck Institute for Astronomy, Heidelberg, Germany

Jacob W. Isbell, Klaus Meisenheimer, Thomas Henning, Roy van Boekel, Uwe Graser, Lucia Klarmann, Michael Lehmitz, Jörg-Uwe Pott & Gideon Yoffe

3. Laboratoire Lagrange, Université Côte d'Azur, Observatoire de la Côte d'Azur, CNRS, Nice, France

Romain G. Petrov, James H. Leftley, Florentin Millour, Anthony Meiland, Bruno Lopez, Stéphane Lagarde, Philippe Berio, Fatme Allouche, Sylvie Robbe-Dubois, Pierre Cruzalèbes, Pierre Antonelli, Philippe Bendjoya, Julien Drevon, Vincent Hocdé, Elena Kokoulina, Alexis Matter & Philippe Stee

4. Max Planck Institute for Radio Astronomy, Bonn, Germany

Karl-Heinz Hofmann, Gerd Weigelt, Udo Beckmann, Matthias Heininger & Dieter Schertl

5. Department of Astrophysics, IMAPP, Radboud University, Nijmegen, Netherlands

Laurens B. F. M. Waters

6. SRON Netherlands Institute for Space Research, Leiden, Netherlands

Laurens B. F. M. Waters

7. ASTRON, Dwingeloo, Netherlands

Felix Bettonvil

8. Université Grenoble Alpes, CNRS, IPAG, Grenoble, France

Jean-Charles Augereau

9. Goddard Space Flight Center, NASA, Greenbelt, MD, USA

William C. Danchi

10. Anton Pannekoek Institute, University of Amsterdam, Amsterdam, Netherlands

Carsten Dominik & Michiel Hogerheijde

11. Department of Physics and Astronomy, Bucknell University, Lewisburg, PA, USA

Jack F. Gallimore

12. Department of Astrophysics University of Vienna, Vienna, Austria

Josef Hron

13. Physikalisches Institut der Universität zu Köln, Cologne, Germany

Lucas Labadie

14. European Southern Observatory, Santiago, Chile

Claudia Paladini, Konrad Tristram & Gerard Zins

15. Centre d'Etudes de Saclay, Gif-sur-Yvette, France

Eric Pantin

16. Sydney Institute for Astronomy, University of Sydney, Sydney, Australia

Anthony Soulain

17. European Southern Observatory, Garching, Germany

Julien Woillez

18. Institute of Theoretical Physics and Astrophysics, University of Kiel, Kiel, Germany

Sebastian Wolf

## Contributions

V.G.R., J.W.I., W.J., R.G.P., K.-H.H., F.M., J.H.L., A. Meilland: observing, data reduction, calibration, modelling, interpretation. B.L., S.L., F.A., S.R.-D., P.C., P. Berio, F.B., T.H., G.W., P.A., U.B., U.G., M. Heininger, M.L., A. Matter, D.S., P.S., J.W., G.Z., P. Bendjoya: MATISSE instrument design, fabrication, and commissioning, calibration. L.B., G.W., R.v.B., P.S., J.-C.A., M. Hogerheijde, J.-U.P.: scientific planning. J.F.G., C.M.V.I., K.T., L.B., C.P.: observing. W.C.D., C.D., J.D., V.H., J.H., L.K., E.K., L.L., E.P., A.S., J.V., S.W., L.B.F.M.W., G.Y.: interpretation.

## Corresponding author

Correspondence to [Violeta Gámez Rosas](#).

## Ethics declarations

## Competing interests

The authors declare no competing interests.

## Peer review

## Peer review information

*Nature* thanks Robert Antonucci and the other, anonymous, reviewer(s) for their contribution to the peer review of this work.

## Additional information

**Publisher's note** Springer Nature remains neutral with regard to jurisdictional claims in published maps and institutional affiliations.

## Extended data figures and tables

### [Extended Data Fig. 1 MATISSE faint calibrator data and \*uv\* coverage.](#)

**a**, Instrumental squared visibility (ISV) and **b**, non-calibrated closure phases (T3PHI) of calibrators observed during the months of September 2018, May 2019 and June 2019, at 3.4  $\mu$ m. Data points are colour-coded by their diameters, and the size of the circles correspond to the average coherence times of the observations. The vertical blue strip covers the approximate correlated flux of NGC 1068 at the same wavelength. Error bars show one standard deviation of data. **c**, *uv* coverage of MATISSE observations.

### [Extended Data Fig. 2 Comparison of photometry of the models and image reconstructions.](#)

The photometry between methods generally agrees in spectral shape between different methods. The most notable exceptions are SE and E3 which still produce similar temperatures from SED modelling between methods.

### [Extended Data Fig. 3 SED black body model fits to MATISSE aperture photometry.](#)

The figures are labelled with the aperture names defined in Fig. 2. The shaded areas show all models falling inside 1 sigma of the photometry, considering both pure amorphous olivine (magenta) and a mix of olivine and 20% amorphous carbon by weight (cyan). The plots for apertures E1 and SE are in the main article.

### Extended Data Fig. 4 NGC 1068 N-band data compared to best multi-Gaussian model.

**a**, Squared visibilities for NGC 1068. The blue lines show observed values, averaged over sub-exposures; the thin grey lines show individual sub-exposures in order to illustrate the measurement uncertainties, but are often hidden behind the blue lines. The green points with error bars show values predicted by the multi-Gaussian models from Methods. The error bars represent the r.m.s. sum of the measurement errors and the uncertainties of the model parameters. The distance between models and observations shows that a limited number of Gaussians cannot exactly represent the true sky or that we do not have a sufficient *uv* coverage and/or resolution. The grey bands mark the atmospheric non-transmission band. The labels indicate the telescope pairs for each baseline, the baseline length (m) and position angle (degrees), and the specific exposure label from the observation log described in the main paper. **b**, Closure phases (degrees) using the same colour code as above. The labels indicate the telescope triplets and the specific exposure label from the observing log.

### Extended Data Fig. 5 NGC 1068 spectra.

**a**, Average single telescope spectrum of NGC 1068 in LM-bands (black solid line) and N-band (blue solid line). The error bars represent uncertainties estimated from the differences between different dates and calibrators. The yellow stars refer to VLT/ISAAC L' -and M-band single-dish flux estimates from ref. <sup>63</sup>, while the green triangle corresponds to a VLT/NACO M-band flux from ref. <sup>62</sup>. **b**, The silicate absorption feature observed on two baselines at high spectral resolution ( $R \sim 300$ ) during a single MATISSE commissioning snapshot. The 85 m baseline shows the broader, double-peaked profile characteristic of crystalline, reprocessed

grains<sup>61</sup>. The difference between the curves shows that the crystallinity varies over the source.

### Extended Data Fig. 6 MATISSE N-band squared visibilities and closure phases.

The quantities plotted, and the symbols used are the same as Extended Data Fig. 4 for the N band.

### Extended Data Fig. 7 Comparison of reconstructed images at four wavelengths from four algorithms.

From left to right: the MIRA image reconstruction, the IRBis image reconstruction, the overfitted point source model (convolved with the beam), and Gaussian model for four selected wavelengths. The plot uses a 0.6 power colour scaling for visual purposes. Each method reveals similar structures and morphology.

### Extended Data Fig. 8 Evaluation of artefacts created by IRBis image reconstruction.

In order to quantify the fidelity of the reconstructions shown in Fig. 1, we performed analogous reconstruction on an artificial model. The model consisted of seven Gaussians, similar to our multi-Gaussian model for the dust emission (Methods). We simulated visibility and closure phase data for this model for our  $uv$  coverage; we added noise to the simulated data similar to that in the observations. We then performed image reconstruction using IRBis with identical reconstruction parameters to those used in Fig. 1.  
**a**, The input 7-Gaussian model. **b**, The IRBis reconstructed image. **c**, The reconstructed image minus the input model. In all cases the colour scale represents the fraction of the peak intensity of the original model. The r.m.s. errors in the residual maps were 2.3% of the peak brightness. This indicated that most of the artefacts present in Fig. 1 result from the  $uv$  coverage rather than noise on the observed quantities. In Fig. 1 we have drawn white contours at  $3\sigma = 6\%$  of the peak. Features brighter than this certainly represent true source emission.

## Extended Data Fig. 9 NGC 1068 image reconstruction data.

**a**, Image representation of models obtained from the Gaussian modelling approach described in Methods. We use square root intensity scale.  
**b**, Image reconstruction with MIRA using different methods (see Methods). From left to right: using total variation (TV) regularizer, on a large bandwidth ('grey' reconstruction); using the same regularizer, but independently reconstructing images at each wavelength, and computing a median over the wavelength interval; using maximum entropy regularizer (grey reconstruction); using smoothness regularizer (grey reconstruction).

## **Extended Data Table 1 Parameters for IRBis image reconstruction, Gaussian modelling and SED fitting**

## **Rights and permissions**

### Reprints and Permissions

## **About this article**

### **Cite this article**

Gámez Rosas, V., Isbell, J.W., Jaffe, W. *et al.* Thermal imaging of dust hiding the black hole in NGC 1068. *Nature* **602**, 403–407 (2022).  
<https://doi.org/10.1038/s41586-021-04311-7>

- Received: 17 May 2021
- Accepted: 06 December 2021
- Published: 16 February 2022
- Issue Date: 17 February 2022
- DOI: <https://doi.org/10.1038/s41586-021-04311-7>

## Share this article

Anyone you share the following link with will be able to read this content:

[Get shareable link](#)

Sorry, a shareable link is not currently available for this article.

[Copy to clipboard](#)

Provided by the Springer Nature SharedIt content-sharing initiative

### [The glowing dusty heart of a hidden quasar](#)

- Robert Antonucci

News & Views 16 Feb 2022

---

This article was downloaded by **calibre** from <https://www.nature.com/articles/s41586-021-04311-7>

| [Section menu](#) | [Main menu](#) |

- Article
- [Published: 16 February 2022](#)

# Nuclear spin-wave quantum register for a solid-state qubit

- [Andrei Ruskuc](#) [ORCID: orcid.org/0000-0001-7684-7409](#)<sup>1,2,3</sup>,
- [Chun-Ju Wu](#)<sup>1,2,3,4</sup>,
- [Jake Rochman](#)<sup>1,2,3</sup>,
- [Joonhee Choi](#) <sup>3,4</sup> &
- [Andrei Faraon](#) [ORCID: orcid.org/0000-0002-8141-391X](#)<sup>1,2,3</sup>

*Nature* volume **602**, pages 408–413 (2022)

- 2026 Accesses
- 51 Altmetric
- [Metrics details](#)

## Subjects

- [Quantum information](#)
- [Quantum optics](#)
- [Qubits](#)
- [Single photons and quantum effects](#)

## Abstract

Solid-state nuclear spins surrounding individual, optically addressable qubits<sup>1,2</sup> are a crucial resource for quantum networks<sup>3,4,5,6</sup>, computation<sup>7,8,9,10,11</sup> and simulation<sup>12</sup>. Although hosts with sparse nuclear

spin baths are typically chosen to mitigate qubit decoherence<sup>13</sup>, developing coherent quantum systems in nuclear-spin-rich hosts enables exploration of a much broader range of materials for quantum information applications. The collective modes of these dense nuclear spin ensembles provide a natural basis for quantum storage<sup>14</sup>; however, using them as a resource for single-spin qubits has thus far remained elusive. Here, by using a highly coherent, optically addressed  $^{171}\text{Yb}^{3+}$  qubit doped into a nuclear-spin-rich yttrium orthovanadate crystal<sup>15</sup>, we develop a robust quantum control protocol to manipulate the multi-level nuclear spin states of neighbouring  $^{51}\text{V}^{5+}$  lattice ions. Via a dynamically engineered spin-exchange interaction, we polarize this nuclear spin ensemble, generate collective spin excitations, and subsequently use them to implement a quantum memory. We additionally demonstrate preparation and measurement of maximally entangled  $^{171}\text{Yb} - ^{51}\text{V}$  Bell states. Unlike conventional, disordered nuclear-spin-based quantum memories<sup>16,17,18,19,20,21,22,23,24</sup>, our platform is deterministic and reproducible, ensuring identical quantum registers for all  $^{171}\text{Yb}^{3+}$  qubits. Our approach provides a framework for utilizing the complex structure of dense nuclear spin baths, paving the way towards building large-scale quantum networks using single rare-earth ion qubits<sup>15,25,26,27,28</sup>.

This is a preview of subscription content

## Access options

Subscribe to Nature+

Get immediate online access to the entire Nature family of 50+ journals

\$29.99

monthly

[Subscribe](#)

Subscribe to Journal

Get full journal access for 1 year

\$199.00

only \$3.90 per issue

[Subscribe](#)

All prices are NET prices.

VAT will be added later in the checkout.

Tax calculation will be finalised during checkout.

Buy article

Get time limited or full article access on ReadCube.

\$32.00

[Buy](#)

All prices are NET prices.

### **Additional access options:**

- [Log in](#)
- [Learn about institutional subscriptions](#)

**Fig. 1: Schematic of a many-body nuclear spin register for optically coupled  $^{171}\text{Yb}$  qubits in a nanophotonic cavity.**

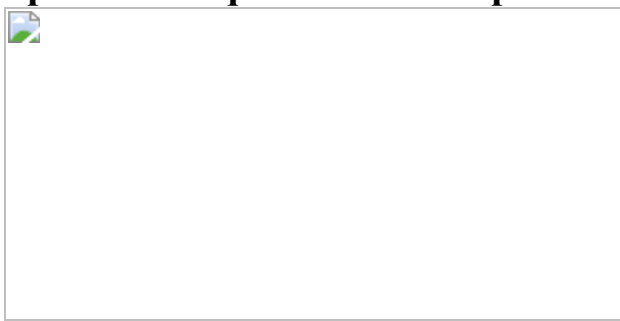


**Fig. 2: Pulse-based Hamiltonian engineering, nuclear register polarization and spin exchange between  $^{171}\text{Yb}$  and  $^{51}\text{V}$  ions.**

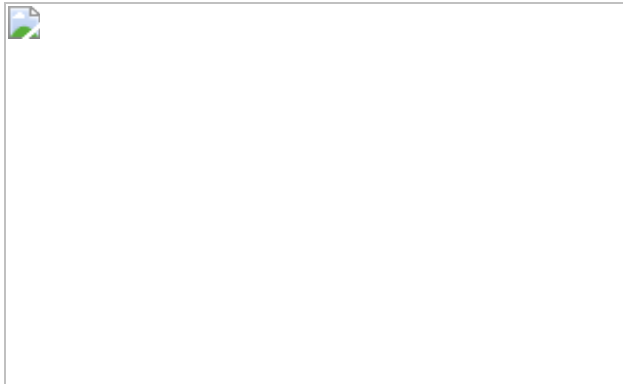


**Fig. 3: Quantum information storage in the nuclear spin-wave register.**

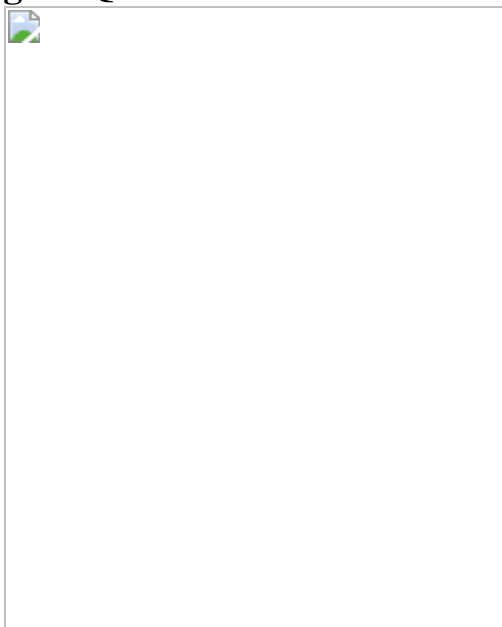
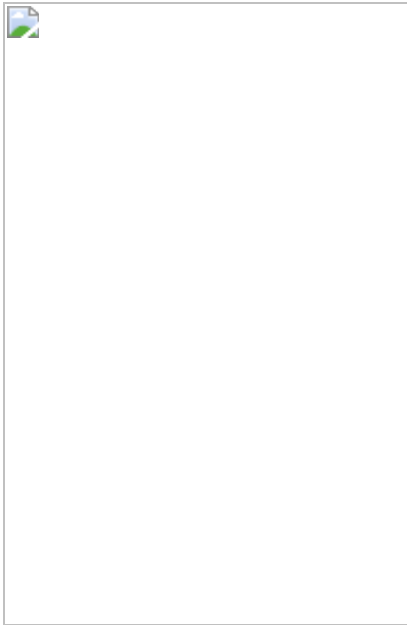


**Fig. 4: Characterization of maximally entangled  $^{171}\text{Yb}-^{51}\text{V}$  register Bell state.**



## Data availability

The data that support the findings of this study are available from the corresponding authors upon request.

## References

1. Awschalom, D. D., Hanson, R., Wrachtrup, J. & Zhou, B. B. Quantum technologies with optically interfaced solid-state spins. *Nat. Photonics* **12**, 516–527 (2018).
2. Chatterjee, A. et al. Semiconductor qubits in practice. *Nat. Rev. Phys.* **3**, 157–177 (2021).
3. Briegel, H.-J., Dür, W., Cirac, J. I. & Zoller, P. Quantum repeaters: the role of imperfect local operations in quantum communication. *Phys. Rev. Lett.* **81**, 5932–5935 (1998).
4. Hensen, B. et al. Loophole-free Bell inequality violation using electron spins separated by 1.3 kilometres. *Nature* **526**, 682–686 (2015).

5. Bhaskar, M. K. et al. Experimental demonstration of memory-enhanced quantum communication. *Nature* **580**, 60–64 (2020).
6. Pompili, M. et al. Realization of a multinode quantum network of remote solid-state qubits. *Science* **372**, 259–264 (2021).
7. Waldherr, G. et al. Quantum error correction in a solid-state hybrid spin register. *Nature* **506**, 204–207 (2014).
8. Taminiau, T. H., Cramer, J., van der Sar, T., Dobrovitski, V. V. & Hanson, R. Universal control and error correction in multi-qubit spin registers in diamond. *Nat. Nanotechnol.* **9**, 171–176 (2014).
9. Zhong, M., Ahlefeldt, R. L. & Sellars, M. J. Quantum information processing using frozen core  $\text{Y}^{3+}$  spins in  $\text{Eu}^{3+}:\text{Y}_2\text{SiO}_5$ . *New J. Phys.* **21**, 033019 (2019).
10. Bradley, C. E. et al. A ten-qubit solid-state spin register with quantum memory up to one minute. *Phys. Rev. X* **9**, 031045 (2019).
11. Kinoshita, A. et al. Roadmap for rare-earth quantum computing. Preprint at <https://arxiv.org/abs/2103.15743> (2021).
12. Randall, J. et al. Many-body-localized discrete time crystal with a programmable spin-based quantum simulator. *Science* **374**, 1474–1478 (2021).
13. Wolfowicz, G. et al. Quantum guidelines for solid-state spin defects. *Nat. Rev. Mater.* **6**, 906–925 (2021); correction **6**, 1191 (2021).
14. Taylor, J. M., Marcus, C. M. & Lukin, M. D. Long-lived memory for mesoscopic quantum bits. *Phys. Rev. Lett.* **90**, 206803 (2003).
15. Kindem, J. M. et al. Control and single-shot readout of an ion embedded in a nanophotonic cavity. *Nature* **580**, 201–204 (2020).
16. Gurudev Dutt, M. V. et al. Quantum register based on individual electronic and nuclear spin qubits in diamond. *Science* **316**, 1312–1316

(2007).

17. Kolkowitz, S., Unterreithmeier, Q. P., Bennett, S. D. & Lukin, M. D. Sensing distant nuclear spins with a single electron spin. *Phys. Rev. Lett.* **109**, 137601 (2012).
18. Taminiau, T. H. et al. Detection and control of individual nuclear spins using a weakly coupled electron spin. *Phys. Rev. Lett.* **109**, 137602 (2012).
19. Zhao, N. et al. Sensing single remote nuclear spins. *Nat. Nanotechnol.* **7**, 657–662 (2012).
20. Metsch, M. H. et al. Initialization and readout of nuclear spins via a negatively charged silicon-vacancy center in diamond. *Phys. Rev. Lett.* **122**, 190503 (2019).
21. Bourassa, A. et al. Entanglement and control of single nuclear spins in isotopically engineered silicon carbide. *Nat. Mater.* **19**, 1319–1325 (2020).
22. Hensen, B. et al. A silicon quantum-dot-coupled nuclear spin qubit. *Nat. Nanotechnol.* **15**, 13–17 (2020).
23. Kornher, T. et al. Sensing individual nuclear spins with a single rare-earth electron spin. *Phys. Rev. Lett.* **124**, 170402 (2020).
24. Wolfowicz, G. et al.  $^{29}\text{Si}$  nuclear spins as a resource for donor spin qubits in silicon. *New J. Phys.* **18**, 023021 (2016).
25. Utikal, T. et al. Spectroscopic detection and state preparation of a single praseodymium ion in a crystal. *Nat. Commun.* **5**, 3627 (2014).
26. Siyushev, P. et al. Coherent properties of single rare-earth spin qubits. *Nat. Commun.* **5**, 3895 (2014).
27. Zhong, T. et al. Optically addressing single rare-earth ions in a nanophotonic cavity. *Phys. Rev. Lett.* **121**, 183603 (2018).

28. Chen, S., Raha, M., Phenicie, C. M., Ourari, S. & Thompson, J. D. Parallel single-shot measurement and coherent control of solid-state spins below the diffraction limit. *Science* **370**, 592–595 (2020).
29. Gangloff, D. A. et al. Quantum interface of an electron and a nuclear ensemble. *Science* **364**, 62–66 (2019).
30. Gangloff, D. A. et al. Witnessing quantum correlations in a nuclear ensemble via an electron spin qubit. *Nat. Phys.* **17**, 1247–1253 (2021).
31. Kindem, J. M. et al. Characterization of  $^{171}\text{Yb}^{3+}$ : $\text{YVO}_4$  for photonic quantum technologies. *Phys. Rev. B* **98**, 024404 (2018).
32. Bleaney, B., Gregg, J. F., de Oliveira, A. C. & Wells, M. R. Nuclear magnetic resonance of  $^{51}\text{V}$  ( $I = 7/2$ ) in lanthanide vanadates: II. The nuclear electric quadrupole interaction. *J. Phys. C* **15**, 5293–5303 (1982).
33. Weimer, H., Yao, N. Y. & Lukin, M. D. Collectively enhanced interactions in solid-state spin qubits. *Phys. Rev. Lett.* **110**, 067601 (2013).
34. Hartmann, S. R. & Hahn, E. L. Nuclear double resonance in the rotating frame. *Phys. Rev.* **128**, 2042–2053 (1962).
35. Schwartz, I. et al. Robust optical polarization of nuclear spin baths using Hamiltonian engineering of nitrogen-vacancy center quantum dynamics. *Sci. Adv.* **4**, eaat8978 (2018).
36. Choi, J. et al. Robust dynamic Hamiltonian engineering of many-body spin systems. *Phys. Rev. X* **10**, 031002 (2020).
37. Bauch, E. et al. Ultralong dephasing times in solid-state spin ensembles via quantum control. *Phys. Rev. X* **8**, 031025 (2018).
38. Levine, H. et al. High-fidelity control and entanglement of Rydberg-atom qubits. *Phys. Rev. Lett.* **121**, 123603 (2018).

39. Gullion, T., Baker, D. B. & Conradi, M. S. New, compensated Carr–Purcell sequences. *J. Magn. Reson.* **89**, 479–484 (1990).
40. Kalb, N. et al. Entanglement distillation between solid-state quantum network nodes. *Science* **356**, 928–932 (2017).
41. Zhong, T., Rochman, J., Kindem, J. M., Miyazono, E. & Faraon, A. High quality factor nanophotonic resonators in bulk rare-earth doped crystals. *Opt. Express* **24**, 536–544 (2016).
42. Zhong, T. et al. Nanophotonic rare-earth quantum memory with optically controlled retrieval. *Science* **357**, 1392–1395 (2017).
43. Drever, R. W. P. et al. Laser phase and frequency stabilization using an optical resonator. *Appl. Phys. B* **31**, 97–105 (1983).
44. Slichter, C. P. *Principles of Magnetic Resonance* (Springer, 1990).
45. Degen, C. L., Reinhard, F. & Cappellaro, P. Quantum sensing. *Rev. Mod. Phys.* **89**, 035002 (2017).
46. Bernien, H. et al. Heralded entanglement between solid-state qubits separated by three metres. *Nature* **497**, 86–90 (2013).
47. Nguyen, C. T. et al. An integrated nanophotonic quantum register based on silicon-vacancy spins in diamond. *Phys. Rev. B* **100**, 165428 (2019).

## Acknowledgements

This work was funded by the Institute of Quantum Information and Matter, an NSF Physics Frontiers Center (PHY-1733907) with support from the Moore Foundation, NSF 1820790, Office of Naval Research award no. N00014-19-1-2182, Air Force Office of Scientific Research grant no. FA9550-18-1-0374 and no. FA9550-21-1-0055, Northrop Grumman, General Atomics, and Weston Havens Foundation. The device nanofabrication was performed in the Kavli Nanoscience Institute at the California Institute of Technology. J.R. acknowledges the support from the

Natural Sciences and Engineering Research Council of Canada (NSERC) (PGSD3-502844-2017). A.R. acknowledges the support from the Eddleman Graduate Fellowship. J.C. acknowledges support from the IQIM postdoctoral fellowship. We thank J. Kindem, J. G. Bartholomew, N. Yao, A. Sipahigil, M. Lei and T. Xie for discussion, and M. Shaw for help with superconducting photon detectors.

## Author information

### Affiliations

1. Thomas J. Watson, Sr., Laboratory of Applied Physics, California Institute of Technology, Pasadena, CA, USA

Andrei Ruskuc, Chun-Ju Wu, Jake Rochman & Andrei Faraon

2. Kavli Nanoscience Institute, California Institute of Technology, Pasadena, CA, USA

Andrei Ruskuc, Chun-Ju Wu, Jake Rochman & Andrei Faraon

3. Institute for Quantum Information and Matter, California Institute of Technology, Pasadena, CA, USA

Andrei Ruskuc, Chun-Ju Wu, Jake Rochman, Joonhee Choi & Andrei Faraon

4. Division of Physics, Mathematics and Astronomy, California Institute of Technology, Pasadena, CA, USA

Chun-Ju Wu & Joonhee Choi

### Contributions

A.R., J.C. and A.F. conceived the experiments. J.R. fabricated the device. A.R. and C.-J.W. performed the experiments and analysed the data. A.R.

and J.C. designed the control sequences. A.R., J.C. and A.F. wrote the manuscript with input from all authors. J.C. and A.F. supervised the project.

## Corresponding authors

Correspondence to [Joonhee Choi](#) or [Andrei Faraon](#).

## Ethics declarations

### Competing interests

The authors declare no competing interests.

## Peer review

### Peer review information

*Nature* thanks Fedor Jelezko and the other, anonymous, reviewer(s) for their contribution to the peer review of this work. Peer reviewer reports are available.

## Additional information

**Publisher's note** Springer Nature remains neutral with regard to jurisdictional claims in published maps and institutional affiliations.

## Extended data figures and tables

### [Extended Data Fig. 1 Experimental set-up and sequence detail.](#)

**a**, Energy level structure of  $^{171}\text{Yb}^{3+}$ : $\text{YVO}_4$   $^2\text{F}_{7/2}(0)$  and  $^2\text{F}_{5/2}(0)$ .

Initialization into  $|0_g\rangle$  involves repeated pulses on the F transition combined with consecutive pairs of  $\pi$  pulses applied to the A and  $f_e$  transitions leading to excitation into  $|1_e\rangle$ . Subsequently, decay via E leads to initialization into

$|0_g\rangle$ . Optical readout relies on repeated optical  $\pi$  pulses on the A transition, each followed by a photon detection window during which we measure cavity-enhanced emission via A. **b**, Experimental set-up. Optical control of the A and F transitions is realized via two frequency-stabilized lasers, each modulated using acousto-optic modulator (AOM) shutters. Microwave control is divided into two paths: a low-frequency path consisting of 675 MHz ground state control ( $f_g$  transition) and RF, both generated using a single arbitrary waveform generator (AWG) channel and a high-frequency path consisting of 3.4 GHz excited-state microwave control ( $f_e$  transition). Each path is independently amplified and combined using a diplexer. The device chip and a superconducting nanowire single photon detector (SNSPD) are cooled to  $\sim$ 500 mK in a cryostat. **c**, Detailed pulse sequence used for quantum state storage and retrieval. First, the  $^{51}\text{V}$  register and  $^{171}\text{Yb}$  qubit are initialized into  $|0_v\rangle$  and  $|0_g\rangle$ , respectively, as described in the text. Subsequently, the  $^{171}\text{Yb}$  is prepared in a superposition state via a  $\pi/2$  pulse, which is swapped onto the  $^{51}\text{V}$  register using a ZenPol sequence resonant with the 991 kHz  $\omega_c$   $^{51}\text{V}$  transition. After a wait time,  $t$ , the state is swapped back to  $^{171}\text{Yb}$  and measured in the  $x$  basis via a  $\pi/2$  pulse followed by optical readout.

## Extended Data Fig.2 Randomized benchmarking and $^{171}\text{Yb}$ qubit coherence.

**a**, We measure the average fidelity of single-qubit gates applied to the  $^{171}\text{Yb}$   $|0_g\rangle \leftrightarrow |1_g\rangle$  transition. We apply a series of  $M_{\text{gate}}$  randomly sampled Clifford gates followed by the inverse operation (top inset). When averaged over a sufficiently large number of samples (in our case 100) we can extract an average gate fidelity from the 1/e exponential decay constant, leading to  $f = 0.99975 \pm 0.00004$ . **b**, We also measure the coherence time of the qubit transition using an XY-8 dynamical decoupling pulse sequence (top inset) with a fixed inter- $\pi$ -pulse separation of 5.6  $\mu\text{s}$  and variable number of repetitions,  $M'$ . This leads to an exponential decay with 1/e time constant  $T_2 = 16 \pm 2 \text{ ms}$ .

## Extended Data Fig. 3 Hartmann Hahn spectroscopy.

**a**, Hartmann Hahn (HH) sequence used to perform spectroscopy of the nuclear spin environment. During the HH pulse (red), the  $^{171}\text{Yb} |0_g\rangle \leftrightarrow |1_g\rangle$  qubit transition is driven resonantly for duration  $t$  with  $y$ -phase leading to a pair of dressed states,  $\langle (\langle \text{pm} \rangle \rangle = \frac{1}{\sqrt{2}}) (|0\rangle_{\{\{\text{rm}\{g\}\}}}\rangle \pm |\text{rm}\{i\}\rangle) |1\rangle_{\{\{\text{rm}\{g\}\}}}\rangle$ , separated by energy splitting equal to the Rabi frequency,  $\Omega$ . An initial  $-x$ -phase  $\pi/2$  pulse prepares the  $^{171}\text{Yb}$  qubit in the  $|-\rangle$  dressed state. When the Rabi frequency of the HH pulse is tuned to equal one of the  $^{51}\text{V}$  transition frequencies, the  $^{171}\text{Yb}$  is transferred into the  $|+\rangle$  dressed state as a result of resonant population exchange (green arrows). The  $|+\rangle$  state population is mapped to  $|1_g\rangle$  with a final  $x$ -phase  $\pi/2$  pulse for readout. **b**, HH spectroscopy experimental results. To identify nuclear spin resonances, both the HH pulse amplitude and duration are varied. The three evenly spaced horizontal resonance features occurring at pulse amplitudes of 0.15, 0.3, and 0.45 (in arbitrary units, a.u.) correspond to interaction with the  $\omega_a$ ,  $\omega_b$  and  $\omega_c$  transitions, respectively. In the no-driving ( $\Omega = 0$ ) case, the sequence probes the decoherence dynamics of the prepared  $|-\rangle$  state; that is, it measures the Ramsey coherence time. **c**, HH spectroscopy simulation results. Simulation results agree well with the experiment, corroborating that  $^{171}\text{Yb}-^{51}\text{V}$  interactions are dominant in our system.

## Extended Data Fig. 4 ZenPol sequence detail.

**a**, ZenPol sequence with the toggling-frame transformation of the  $\langle (\widehat{\tilde{S}})_z \rangle$  operator for the  $^{171}\text{Yb}$  qubit. The ZenPol sequence consists of a series of  $\pi$  and  $\pi/2$  pulses about the  $x$  and  $y$  axes combined with a synchronously applied, square-wave RF magnetic field with period  $2\tau$ . The Overhauser- and RF-induced interactions are determined by the toggling-frame transformations of  $\langle (\widehat{\tilde{S}})_z \rangle$ , which are given by  $\langle (\widehat{\tilde{S}})_x f_x^z x^{\{\text{rm}\{OH\}\}} + \langle (\widehat{\tilde{S}})_y f_y^z y^{\{\text{rm}\{OH\}\}} \rangle \rangle$  and  $\langle (\widehat{\tilde{S}})_x f_x^z x^{\{\text{rm}\{RF\}\}} + \langle (\widehat{\tilde{S}})_y f_y^z y^{\{\text{rm}\{RF\}\}} \rangle \rangle$ .

\widehat{\tilde{S}}\}\_{y}\{f\}\_{y}^{\wedge\{\{\rm{RF}\}\}}), respectively (see yellow and purple lines for \langle f\_{x,y}^{\wedge\{\{\rm{OH}\}\}}\rangle and \langle f\_{x,y}^{\wedge\{\{\rm{RF}\}\}}\rangle, respectively). At the resonance condition  $1/2\tau = \omega/2\pi k$  for odd integer  $k$  with  $^{51}\text{V}$  spin precession frequency  $\omega_p$ , the sequence realizes noise-robust spin-exchange interaction with a time-averaged Hamiltonian that depends only on the RF magnetic field amplitude. **b**, ZenPol sequence filter functions corresponding to the Fourier transforms of \langle f\_{x}^{\wedge\{\{\rm{OH}\}\}}\rangle (yellow) and \langle f\_{x}^{\wedge\{\{\rm{RF}\}\}}\rangle (purple). For a sequence with fixed  $\tau$ , the peak positions determine the resonant frequencies at which  $^{171}\text{Yb}-^{51}\text{V}$  interactions can occur. Note that the incoherent Overhauser-induced interactions occur at even- $k$  resonances and are spectrally separated from the coherent RF-induced interactions occurring at odd- $k$  resonances.

### Extended Data Fig. 5 Polarization of multi-level nuclear register spins.

**a**, Polarization readout by polarization inversion (PROPI) experiments for the  $^{51}\text{V}$  register  $\omega_c$  transition. The PROPI sequence performs a repeated swap operation based on the ZenPol sequence, periodically interleaved with  $^{171}\text{Yb}$  qubit readout and reinitialization into  $|1_g\rangle$ . A total of 20 polarizing cycles are applied to the  $\omega_c$  transition to polarize the  $^{51}\text{V}$  register into  $|\pm 5/2\rangle$ . As a result of register polarization, the  $^{171}\text{Yb}$  population in  $|1_g\rangle$  increases over time, indicating the accumulation of the  $^{51}\text{V}$  population in  $|\pm 5/2\rangle$  (left). We observe that the register polarization saturates after approximately 10 cycles. Subsequently, we perform repolarization cycles where  $^{171}\text{Yb}$  is initialized into  $|0_g\rangle$  and  $^{51}\text{V}$  register spins are transferred to  $|\pm 7/2\rangle$  with similar saturation timescale (right). **b**, PROPI experiments for the  $^{51}\text{V}$  register  $\omega_b$  transition. Applying a ZenPol sequence resonant with the  $\omega_b$  transition, interleaved with  $^{171}\text{Yb}$  initialization into  $|1_g\rangle$  ( $|0_g\rangle$ ), results in  $^{51}\text{V}$  register polarization into  $|\pm 5/2\rangle$  ( $|\pm 3/2\rangle$ ), as indicated by an increase (decrease) in  $^{171}\text{Yb}$   $|1_g\rangle$  population. **c**, Experimental results of ZenPol spin-exchange dynamics with varying degree of  $^{51}\text{V}$  register polarization. As the number of polarization cycles used to prepare the  $|0_v\rangle$  state increases, the

subsequent spin-exchange oscillations become more pronounced. Note that these polarization cycles are interleaved between the  $\omega_b$  and  $\omega_c$  transitions.

### Extended Data Fig. 6 Spin-exchange dynamics.

**a**, ZenPol sequence schematic. The square-wave RF magnetic field amplitude  $B^{\text{RF}}$  determines the  $^{171}\text{Yb}$ – $^{51}\text{V}$  interaction strength, the pulse spacing  $\tau/4$  varies the sequence detuning from a specific  $^{51}\text{V}$  nuclear spin transition, and the number of ZenPol periods,  $M$ , determines the total interaction time. **b**, Simulated spin-exchange dynamics near the  $\omega_c$  transition at  $k = 5$ , probed as a function of sequence resonance frequency  $\omega$  and the number of ZenPol periods,  $M$ . **c**, Measured spin-exchange dynamics showing good agreement with the numerical simulation in **b**. **d**, Experimental demonstration of tunable spin-exchange rate by varying  $B^{\text{RF}}$ . When increasing  $B^{\text{RF}}$  from 0.8 G to 2.0 G, we observe a corresponding linear increase in the spin-exchange rate. In all cases, numerical simulations (solid lines), taking into account incomplete register polarization, control pulse imperfections and an exponential phenomenological decay, show reasonable agreement with the experimental data (markers). A simulation result without this phenomenological decay (dashed line) displays a discrepancy, which needs further investigation. See [Supplementary Information](#) for simulation details.

### Extended Data Fig. 7 Direct $^{51}\text{V}$ nuclear spin driving.

**a**, Details of  $^{51}\text{V}$  nuclear spin driving scheme. To directly drive the  $^{51}\text{V}$  nuclear spin  $\omega_c$  transition, a sinusoidal  $z$ -directed RF magnetic field,  $\langle\{B\}_z\rangle \propto \sin(\{\omega_c\}t)$ , is applied to the system at a frequency of  $\omega_c/2\pi = 991$  kHz after initializing the  $^{171}\text{Yb}$  and  $^{51}\text{V}$  register into  $|0_g\rangle$  and  $|0_v\rangle = |\downarrow\downarrow\downarrow\downarrow\rangle$ , respectively (drive protocol 1). This induces an oscillating magnetic dipole moment on the  $^{171}\text{Yb}$  qubit, which in turn generates an amplified transverse driving field at each  $^{51}\text{V}$  (Methods). Consequently, the four  $^{51}\text{V}$  register spins undergo independent Rabi oscillation between the  $|\uparrow\rangle = |\pm 5/2\rangle$  and  $|\downarrow\rangle = |\pm 7/2\rangle$  states. To probe the nuclear spin Rabi oscillation, the  $|\downarrow\rangle$  population is measured by preparing

the  $^{171}\text{Yb}$  in  $|1_g\rangle$  via an  $x$ -phase  $\pi$  pulse, performing a single swap gate and reading out the  $^{171}\text{Yb}$  population. **b**, Decoupling of magnetic field noise originating from the  $^{171}\text{Yb}$  Knight field. To improve the nuclear spin control fidelity, a train of equidistant  $\pi$  pulses are applied to the  $^{171}\text{Yb}$  during the driving period, thereby cancelling dephasing due to the  $^{171}\text{Yb}$  Knight field (drive protocol 2). Each  $\pi$  pulse is accompanied by a  $\pi$  phase shift of the sinusoidal field to ensure phase continuity of the nuclear Rabi driving, and an even number of  $\pi$  pulses ensures the  $^{171}\text{Yb}$  state is returned to  $|0_g\rangle$  at the end of the sequence (Methods). **c**, Measured  $^{51}\text{V}$  register Rabi oscillations using the aforementioned schemes. We observe coherent nuclear Rabi oscillations between the  $|\downarrow\rangle$  and  $|\uparrow\rangle$  states at a Rabi frequency of  $\Omega_D/2\pi = 7.65 \pm 0.05$  kHz. An exponential decay is observed with a 1/e time constant of  $280 \pm 30$   $\mu\text{s}$  without decoupling (blue). The additional  $\pi$  pulses applied to the  $^{171}\text{Yb}$  qubit lead to an enhancement in control fidelity, giving a 1/e Gaussian decay time of  $1040 \pm 70$   $\mu\text{s}$  (red). The black arrow at  $t \approx 69$   $\mu\text{s}$  indicates the  $^{51}\text{V}$   $\pi$  pulse used in Fig. 3c.

### Extended Data Fig. 8 $^{51}\text{V}$ spin register population relaxation.

**a**, Measured relaxation timescales,  $\langle\langle T \rangle\rangle_1^{\langle\langle W \rangle\rangle}$ , of the entangled register state,  $|W_v\rangle$ , under various conditions. Top, the  $^{51}\text{V}$  register is prepared in the  $|W_v\rangle$  state by swapping a single spin excitation from the  $^{171}\text{Yb}$  initialized into  $|1_g\rangle$ . After a variable wait time,  $t$ , the  $^{51}\text{V}$  state is swapped back onto  $^{171}\text{Yb}$  and measured (top inset). The resulting Gaussian decay shows a 1/e relaxation time of  $\langle\langle T \rangle\rangle_1^{\langle\langle W \rangle\rangle} = 39.5 \pm 1.3$   $\mu\text{s}$  (blue trace), limited by dephasing of the entangled  $|W_v\rangle$  state. Middle, the  $\langle\langle T \rangle\rangle_1^{\langle\langle W \rangle\rangle}$  lifetime can be extended by applying a series of equidistant  $\pi$  pulses to the  $^{171}\text{Yb}$  separated by  $2t_w = 6$   $\mu\text{s}$  (middle inset). This decouples the  $|W_v\rangle$  state from dephasing induced by the  $^{171}\text{Yb}$  Knight field, equivalent to the coherence time extension in Fig. 3b, leading to an extended 1/e lifetime of  $\langle\langle T \rangle\rangle_1^{\langle\langle W \rangle\rangle} = 127 \pm 8$   $\mu\text{s}$  (red trace). Bottom, further extension of the  $\langle\langle T \rangle\rangle_1^{\langle\langle W \rangle\rangle}$  lifetime is achieved by dynamical decoupling whereby additionally two  $^{51}\text{V}$   $\pi$  pulses are applied

during the wait time with a variable pulse separation  $2t_D$  (bottom inset). This gives rise to a substantially prolonged lifetime of  $\langle\{T\}_1^W\rangle = 640 \pm 20 \mu s$  (yellow trace), equivalent to the coherence time extension in Fig. 3c. **b**, Measured relaxation timescale,  $\langle\{T\}_1^{(0)}\rangle$ , of the polarized register state  $|0_v\rangle$ . The register is initialized in  $|0_v\rangle$  and after a variable wait time,  $t$ , the  $^{51}V$  state is swapped onto  $^{171}Yb$  and measured (inset). We observe an exponential decay with a 1/e relaxation time of  $\langle\{T\}_1^{(0)}\rangle = 0.54 \pm 0.08$  s, probably limited by incoherent population transfer to the bath. See [Supplementary Information](#) for detailed discussion of  $T_1$  relaxation mechanisms.

### [Extended Data Fig. 9 Population measurement histograms for register fidelity characterization.](#)

**a**, Sequential tomography protocol for characterizing  $^{171}Yb-^{51}V$  populations in the basis spanned by  $\{|0_g0_v\rangle, |0_gW_v\rangle, |1_g0_v\rangle, |1_gW_v\rangle\}$ . Reconstructing the population probability distribution utilizes readout sequences 1 and 2, each including three consecutive  $^{171}Yb$  state readouts interleaved with single-qubit gate operations and a swap gate. **b**, Table summarizing the post-processing criteria for state attribution. Readout sequences 1 and 2 measure the  $\{|0_g0_v\rangle, |0_gW_v\rangle\}$  and  $\{|1_g0_v\rangle, |1_gW_v\rangle\}$  populations, respectively, conditioned on the three measurement outcomes. See [Methods](#) for full details of the post-processing procedure. **c**, Reconstructed population distributions for estimating state preparation fidelity. The four basis states,  $\{|0_g0_v\rangle, |0_gW_v\rangle, |1_g0_v\rangle, |1_gW_v\rangle\}$ , are independently prepared by applying a combination of  $^{171}Yb$   $\pi$  pulses and swap gates to the initial  $|0_g0_v\rangle$  state (see insets). Subsequently, the sequential tomography protocol for state readout (RO) is applied iteratively, alternating between readout 1 and 2 sequences to fully reconstruct the population probability distributions. **d**, Reconstructed population distribution for the  $^{171}Yb-^{51}V$  Bell state (reproduced from Fig. 4c). The maximally entangled Bell state  $\langle|\Psi^+\rangle = \frac{1}{\sqrt{2}}(|1_g0_v\rangle - |\rm{i}|0_g\rangle)$  is prepared by applying a  $\sqrt{\rm{swap}}$  gate to  $|1_g0_v\rangle$  and measured using RO (inset). In **c**,

**d**, the uncorrected and readout-corrected measurement results are presented as dashed and solid filled histograms, respectively, with error bars indicating one standard deviation. Populations are corrected by accounting for the swap gate error during the readout sequences (Methods).

## **Extended Data Fig. 10 Experimental demonstration of deterministic nuclear spin register.**

To demonstrate the deterministic nature of the nuclear spin register, we perform the same measurements on two additional  $^{171}\text{Yb}$  ion qubits present in the device: ion 2 (red) and ion 3 (yellow). Results for ion 1 (blue) are reproduced from Figs. 2 and 3 for ease of comparison. **a**, ZenPol spectra near the  $\omega_c(k=5)$  resonance of the  $^{51}\text{V}$  register spins. Note that for all three ions, the bath and register transitions are identified at the same resonance frequencies of  $\{\omega\}_{\rm c} = 1,028 \text{ kHz}$  and  $\omega_c/2\pi = 991 \text{ kHz}$ , respectively. **b**, Dynamically engineered spin-exchange dynamics between the  $^{171}\text{Yb}$  qubit and  $^{51}\text{V}$  register. Using constant ZenPol square-wave RF amplitude we obtain equal spin-exchange rates for all three ions. **c**, Characterization of  $^{51}\text{V}$  register coherence times with decoupling from the  $^{171}\text{Yb}$  Knight field. The 1/e coherence times are measured to be  $225 \pm 9 \mu\text{s}$ ,  $273 \pm 12 \mu\text{s}$  and  $261 \pm 9 \mu\text{s}$  for ions 1, 2 and 3, respectively. All of these results demonstrate that our platform provides a nearly identical nuclear spin register for every  $^{171}\text{Yb}$  qubit in the system.

## **Supplementary information**

### **Supplementary Information**

This file contains Supplementary Text, Supplementary Equations 1–38 and Supplementary References.

### **Peer Review File**

## **Rights and permissions**

## [Reprints and Permissions](#)

## About this article

### Cite this article

Ruskuc, A., Wu, CJ., Rochman, J. *et al.* Nuclear spin-wave quantum register for a solid-state qubit. *Nature* **602**, 408–413 (2022).  
<https://doi.org/10.1038/s41586-021-04293-6>

- Received: 29 August 2021
- Accepted: 29 November 2021
- Published: 16 February 2022
- Issue Date: 17 February 2022
- DOI: <https://doi.org/10.1038/s41586-021-04293-6>

### Share this article

Anyone you share the following link with will be able to read this content:

[Get shareable link](#)

Sorry, a shareable link is not currently available for this article.

[Copy to clipboard](#)

Provided by the Springer Nature SharedIt content-sharing initiative

## [Clock qubit conducts nuclear ensemble](#)

- Claire Le Gall

News & Views 16 Feb 2022

---

This article was downloaded by **calibre** from <https://www.nature.com/articles/s41586-021-04293-6>

| [Section menu](#) | [Main menu](#) |

- Article
- Open Access
- [Published: 16 February 2022](#)

# Magnetic control of tokamak plasmas through deep reinforcement learning

- [Jonas Degrave](#) [ORCID: orcid.org/0000-0002-2738-6500<sup>1</sup>](#)<sup>na1</sup>,
- [Federico Felici](#) [ORCID: orcid.org/0000-0001-7585-376X<sup>2</sup>](#)<sup>na1</sup>,
- [Jonas Buchli](#) <sup>1</sup><sup>na1</sup>,
- [Michael Neunert](#) [ORCID: orcid.org/0000-0003-2080-8376<sup>1</sup>](#)<sup>na1</sup>,
- [Brendan Tracey](#) [ORCID: orcid.org/0000-0001-5724-5912<sup>1</sup>](#)<sup>na1</sup>,
- [Francesco Carpanese<sup>1,2</sup>](#)<sup>na1</sup>,
- [Timo Ewalds<sup>1</sup>](#)<sup>na1</sup>,
- [Roland Hafner](#) [ORCID: orcid.org/0000-0001-8061-8828<sup>1</sup>](#)<sup>na1</sup>,
- [Abbas Abdolmaleki<sup>1</sup>](#),
- [Diego de las Casas<sup>1</sup>](#),
- [Craig Donner<sup>1</sup>](#),
- [Leslie Fritz<sup>1</sup>](#),
- [Cristian Galperti<sup>2</sup>](#),
- [Andrea Huber](#) [ORCID: orcid.org/0000-0002-4431-8171<sup>1</sup>](#),
- [James Keeling<sup>1</sup>](#),
- [Maria Tsimpoukelli<sup>1</sup>](#),
- [Jackie Kay<sup>1</sup>](#),
- [Antoine Merle<sup>2</sup>](#),
- [Jean-Marc Moret<sup>2</sup>](#),
- [Seb Noury<sup>1</sup>](#),
- [Federico Pesamosca<sup>2</sup>](#),
- [David Pfau<sup>1</sup>](#),
- [Olivier Sauter<sup>2</sup>](#),
- [Cristian Sommariva<sup>2</sup>](#),
- [Stefano Coda<sup>2</sup>](#),
- [Basil Duval<sup>2</sup>](#),
- [Ambrogio Fasoli<sup>2</sup>](#),
- [Pushmeet Kohli<sup>1</sup>](#),

- [Koray Kavukcuoglu<sup>1</sup>](#),
- [Demis Hassabis ORCID: orcid.org/0000-0003-2812-9917<sup>1</sup>](#) &
- [Martin Riedmiller ORCID: orcid.org/0000-0002-8465-5690<sup>1</sup>](#)

*Nature* volume **602**, pages 414–419 (2022)

- 47k Accesses
- 1932 Altmetric
- [Metrics details](#)

## Subjects

- [Computer science](#)
- [Magnetically confined plasmas](#)
- [Nuclear fusion and fission](#)

## Abstract

Nuclear fusion using magnetic confinement, in particular in the tokamak configuration, is a promising path towards sustainable energy. A core challenge is to shape and maintain a high-temperature plasma within the tokamak vessel. This requires high-dimensional, high-frequency, closed-loop control using magnetic actuator coils, further complicated by the diverse requirements across a wide range of plasma configurations. In this work, we introduce a previously undescribed architecture for tokamak magnetic controller design that autonomously learns to command the full set of control coils. This architecture meets control objectives specified at a high level, at the same time satisfying physical and operational constraints. This approach has unprecedented flexibility and generality in problem specification and yields a notable reduction in design effort to produce new plasma configurations. We successfully produce and control a diverse set of plasma configurations on the Tokamak à Configuration Variable<sup>1,2</sup>, including elongated, conventional shapes, as well as advanced configurations, such as negative triangularity and ‘snowflake’ configurations. Our approach achieves accurate tracking of the location, current and shape for these configurations. We also demonstrate sustained ‘droplets’ on TCV, in which two separate plasmas are maintained simultaneously within the vessel. This represents a notable advance for tokamak feedback control, showing the potential of reinforcement learning to accelerate research in the fusion domain, and is one of the most challenging real-world systems to which reinforcement learning has been applied.

[Download PDF](#)

## Main

Tokamaks are torus-shaped devices for nuclear fusion research and are a leading candidate for the generation of sustainable electric power. A main direction of research is to study the effects of shaping the distribution of the plasma into different configurations<sup>3,4,5</sup> to optimize the stability, confinement and energy exhaust, and, in particular, to inform the first burning-plasma experiment, ITER. Confining each configuration within the tokamak requires designing a feedback controller that can manipulate the magnetic field<sup>6</sup> through precise control of several coils that are magnetically coupled to the plasma to achieve the desired plasma current, position and shape, a problem known as the tokamak magnetic control problem.

The conventional approach to this time-varying, non-linear, multivariate control problem is to first solve an inverse problem to precompute a set of feedforward coil currents and voltages<sup>7,8</sup>. Then, a set of independent, single-input single-output PID controllers is designed to stabilize the plasma vertical position and control the radial position and plasma current, all of which must be designed to not mutually interfere<sup>6</sup>. Most control architectures are further augmented by an outer control loop for the plasma shape, which involves implementing a real-time estimate of the plasma equilibrium<sup>9,10</sup> to modulate the feedforward coil currents<sup>8</sup>. The controllers are designed on the basis of linearized model dynamics, and gain scheduling is required to track time-varying control targets. Although these controllers are usually effective, they require substantial engineering effort, design effort and expertise whenever the target plasma configuration is changed, together with complex, real-time calculations for equilibrium estimation.

A radically new approach to controller design is made possible by using reinforcement learning (RL) to generate non-linear feedback controllers. The RL approach, already used successfully in several challenging applications in other domains<sup>11,12,13</sup>, enables intuitive setting of performance objectives, shifting the focus towards what should be achieved, rather than how. Furthermore, RL greatly simplifies the control system. A single computationally inexpensive controller replaces the nested control architecture, and an internalized state reconstruction removes the requirement for independent equilibrium reconstruction. These combined benefits reduce the controller development cycle and accelerate the study of alternative plasma configurations. Indeed, artificial intelligence has recently been identified as a ‘Priority Research Opportunity’ for fusion control<sup>14</sup>, building on demonstrated successes in reconstructing plasma-shape parameters<sup>15,16</sup>, accelerating simulations using surrogate models<sup>17,18</sup> and detecting impending plasma disruptions<sup>19</sup>. RL has not, however, been

used for magnetic controller design, which is challenging due to high-dimensional measurements and actuation, long time horizons, rapid instability growth rates and the need to infer the plasma shape through indirect measurements.

In this work, we present an RL-designed magnetic controller and experimentally verify its performance on a tokamak. The control policies are learned through interaction with a tokamak simulator and are shown to be directly capable of tokamak magnetic control on hardware, successfully bridging the ‘sim-to-real’ gap. This enables a fundamental shift from engineering-driven control of a pre-designed state to artificial-intelligence-driven optimization of objectives specified by an operator. We demonstrate the effectiveness of our controllers in experiments carried out on the Tokamak à Configuration Variable (TCV)<sup>1,2</sup>, in which we demonstrate control of a variety of plasma shapes, including elongated ones, such as those foreseen in ITER, as well as advanced configurations, such as negative triangularity and ‘snowflake’ plasmas. Additionally, we demonstrate a sustained configuration in which two separate plasma ‘droplets’ are simultaneously maintained within the vessel. Tokamak magnetic control is one of the most complex real-world systems to which RL has been applied. This is a promising new direction for plasma controller design, with the potential to accelerate fusion science, explore new configurations and aid in future tokamak development.

## Learning control and training architecture

Our architecture, depicted in Fig. 1, is a flexible approach for designing tokamak magnetic confinement controllers. The approach has three main phases. First, a designer specifies objectives for the experiment, potentially accompanied by time-varying control targets. Second, a deep RL algorithm interacts with a tokamak simulator to find a near-optimal control policy to meet the specified goals. Third, the control policy, represented as a neural network, is run directly (‘zero shot’) on tokamak hardware in real time.

**Fig. 1: Representation of the components of our controller design architecture.**

---

 **figure 1**

---

**a**, Depiction of the learning loop. The controller sends voltage commands on the basis of the current plasma state and control targets. These data are sent to the replay buffer, which feeds data to the learner to update the policy. **b**, Our environment interaction loop, consisting of a power supply model, sensing model, environment physical parameter variation and reward computation. **c**, Our control policy is an MLP with three hidden layers that takes measurements and control targets and outputs voltage commands. **d–f**, The interaction of TCV and the real-time-deployed control system implemented using either a conventional controller composed of many subcomponents (**f**) or our architecture using a single deep neural network to control all 19 coils directly (**e**). **g**, A depiction of TCV and the 19 actuated coils. The vessel is 1.5 m high, with minor radius 0.88 m and vessel half-width 0.26 m. **j**, A cross section of the vessel and plasma, with the important aspects labelled.

In the first phase, the experimental goal is specified by a set of objectives that can contain a wide variety of desired properties (Extended Data Table 4). These properties range from basic stabilization of position and plasma current to sophisticated combinations of several time-varying targets, including a precise shape outline with specified elongation, triangularity and X-point location. These objectives are then combined into a ‘reward function’ that assigns a scalar quality measure to the state at each time step. This function also penalizes the control policy for reaching undesired terminal states, as discussed below. Crucially, a well-designed reward function will be minimally specified, giving the learning algorithm maximum flexibility to attain the desired outcome.

In the second phase, a high-performance RL algorithm collects data and finds a control policy through interaction with an environment, as depicted in Fig. 1a,b. We use a simulator that has enough physical fidelity to describe the evolution of plasma shape and current, while remaining sufficiently computationally cheap for learning. Specifically, we model the dynamics governing the evolution of the plasma state under the influence of the poloidal field coil voltages using a free-boundary plasma-evolution model<sup>20</sup>. In this model, the currents in the coils and passive conductors evolve under the influence of externally applied voltages from the power supplies, as well as induced voltages from time-varying currents in other conductors and in the plasma itself. The plasma is, in turn, modelled by the Grad–Shafranov equation<sup>21</sup>, which results from the balance between the Lorentz force and the pressure gradient inside the plasma on the timescales of interest. The evolution of total plasma current  $I_p$  is modelled using a lumped-circuit equation. This set of equations is solved numerically by the FGE software package<sup>22</sup>.

The RL algorithm uses the collected simulator data to find a near-optimal policy with respect to the specified reward function. The data rate of our simulator is markedly slower than that of a typical RL environment due to the computational requirements of evolving the plasma state. We overcome the paucity of data by optimizing the policy using maximum a posteriori policy optimization (MPO)<sup>23</sup>, an actor-critic algorithm. MPO supports data collection across distributed parallel streams and learns in a data-efficient way. We additionally exploit the asymmetry inherent to the actor-critic design of MPO to overcome the constraints of magnetic control. In actor-critic algorithms, the ‘critic’ learns the discounted expected future reward for various actions using the available data and the ‘actor’ uses the predictions of the critic to set the control policy. The representation of the control policy of the actor is restricted, as it must run on TCV with real-time guarantees, whereas the critic is unrestricted, as it is only used during training. We therefore use a fast, four-layer feedforward neural network in the actor (Fig. 1c) and a much larger recurrent neural network in the critic. This asymmetry enables the critic to infer the underlying state from measurements, deal with complex state-transition dynamics over different timescales and assess the influence of system measurement and action delays. The information from the coupled dynamics is then distilled into a real-time-capable controller.

In the third phase, the control policy is bundled with the associated experiment control targets into an executable using a compiler tailored towards real-time control at 10 kHz that minimizes dependencies and eliminates unnecessary computations. This executable is loaded by the TCV control framework<sup>24</sup> (Fig. 1d). Each experiment begins with standard plasma-formation procedures, in which a traditional controller maintains the location of the plasma and total current. At a prespecified time, termed the ‘handover’, control is switched to our control policy, which then actuates the 19 TCV control coils to transform the plasma shape and current to the desired targets.

Experiments are executed without further tuning of the control-policy network weights after training, in other words, there is ‘zero-shot’ transfer from simulation to hardware.

The control policies reliably transfer onto TCV through several key attributes of the learning procedure, depicted in Fig. 1b. We identified an actuator and sensor model that incorporates properties affecting control stability, such as delays, measurement noise and control-voltage offsets. We applied targeted parameter variation during training across an appropriate range for the plasma pressure, current density profile and plasma resistivity through analysis of experiment data, to account for varying, uncontrolled experimental conditions. This provides robustness while ensuring performance. Although the simulator is generally accurate, there are known regions where the dynamics are known to be poorly represented. We built ‘learned-region avoidance’ into the training loop to avoid these regimes through the use of rewards and termination conditions (Extended Data Table 5), which halt the simulation when specified conditions are encountered. Termination conditions are also used to enforce operational limits. The control policies learn to stay within the specified limits, for example, on maximum coil current or the edge safety factor<sup>25</sup>.

The controllers designed by our architecture are greatly structurally simplified compared with conventional designs, as depicted in Fig. 1e,f. Instead of a series of controllers, RL-driven design creates a single network controller.

## Fundamental capability demonstration

We demonstrate the capability of our architecture on control targets in real-world experiments on TCV. We first show accurate control of the fundamental qualities of plasma equilibria. We then control a wide range of equilibria with complex, time-varying objectives and physically relevant plasma configurations. Finally, we demonstrate control of a configuration with several plasma ‘droplets’ in the vessel simultaneously.

We first test the fundamental tasks of plasma control through a series of changes representative of those required for a full plasma discharge. First, from the handover at 0.0872 s, take over and stabilize  $I_p$  at −110 kA. Next, ramp the plasma current to −150 kA and then elongate the plasma from 1.24 to 1.44, thereby increasing the vertical instability growth rate to 150 Hz. Next, demonstrate position control through shifting the vertical plasma position by 10 cm and then divert the plasma with control of the active X-point location (see Fig. 1h). Finally, return the plasma to the handover condition and ramp down  $I_p$  to −70 kA to shut down safely. Although accuracy requirements will generally depend on the exact experiment, a reasonable aim is to control  $I_p$  to within 5 kA (3% of the final 150-kA target) and the shape to within 2 cm

(8% of the vessel radial half width of 26 cm). Note that the equilibrium reconstruction used matches a visually reconstructed boundary with a typical accuracy<sup>26</sup> of 1 cm.

The performance of the control policy is depicted in Fig. 2. All tasks are performed successfully, with a tracking accuracy below the desired thresholds. In the initial limited phase (0.1 s to 0.45 s), the  $I_p$  root-mean-square error (RMSE) is 0.71 kA (0.59% of the target) and the shape RMSE is 0.78 cm (3% of the vessel half width). In the diverted phase (0.55 s to 0.8 s), the  $I_p$  and shape RMSE are 0.28 kA and 0.53 cm, respectively (0.2% and 2.1%), yielding RMSE across the full window (0.1 s to 1.0 s) of 0.62 kA and 0.75 cm (0.47% and 2.9%). This demonstrates that our RL architecture is capable of accurate plasma control across all relevant phases of a discharge experiment.

**Fig. 2: Fundamental capability demonstration.**

 figure 2

Demonstration of plasma current, vertical stability, position and shape control. Top, target shape points with 2 cm radius (blue circles), compared with the post-experiment equilibrium reconstruction (black continuous line in contour plot). Bottom left, target time traces (blue traces) compared with reconstructed observation (orange traces), with the window of diverted plasma marked (green rectangle). Bottom right, picture inside the vessel at 0.6 s showing the diverted plasma with its legs.

[Source data](#)

## Control demonstrations

We next demonstrate the capability of our architecture to produce complex configurations for scientific study. Each demonstration has its own time-varying targets but, otherwise, uses the same architectural setup to generate a control policy, including the training and environment configuration, with only minor adjustments to the reward function (shown in Extended Data Table 3). Recall that, in each experiment, the plasma has low elongation before the handover, and the control policy actively modulates the plasma to the configuration of interest. Selected time slices from these experiments are shown in Fig. 3, with further detail in Extended Data Fig. 1 and error metrics in Extended Data Table 1.

**Fig. 3: Control demonstrations.**

 [figure 3](#)



Control demonstrations obtained during TCV experiments. Target shape points with 2 cm radius (blue circles), compared with the equilibrium reconstruction plasma boundary (black continuous line). In all figures, the first time slice shows the handover condition. **a**, Elongation of 1.9 with vertical instability growth rate of 1.4 kHz. **b**, Approximate ITER-proposed shape with neutral beam heating (NBH) entering H-mode. **c**, Diverted negative triangularity of  $-0.8$ . **d**, Snowflake configuration with a time-varying control of the bottom X-point, where the target X-points are marked in blue. Extended traces for these shots can be found in Extended Data Fig. 2.

[Source data](#)

Elongating plasmas improves their thermal confinement properties, but their increased vertical-instability growth rate complicates control. We targeted a high elongation of 1.9 with a considerable growth rate. The controller was able to produce and stabilize this elongation, as shown in Fig. 3a. We obtained a good match between the targeted and the desired elongation, with an RMSE of 0.018. We also controlled shape and plasma current to their target values, with an  $I_p$  RMSE of 1.2 kA and shape RMSE of 1.6 cm. This demonstrates the capability to stabilize a high vertical-instability growth rate of more than 1.4 kHz, despite acting at only 10 kHz.

We next tested applying auxiliary heating through neutral beam injection to enter ‘H-mode’, which is desirable for having higher energy confinement time, but causes notable changes to the plasma properties. We were provided a time-varying trajectory on the basis of the proposed ITER configuration that uses such auxiliary heating. As the normalized pressure  $\beta_p$  increases to 1.12, seen in Fig. 3b, the plasma position and current were maintained accurately, with an  $I_p$  RMSE of 2.6 kA and shape RMSE of 1.4 cm. This shows that our controller can robustly adapt to a changing plasma state and can work with heated H-mode plasma under externally specified configurations.

Negative triangularity plasmas are attractive as they have favourable confinement properties without the strong edge pressure gradient typical of H-modes. We targeted a diverted configuration with triangularity of −0.8, and with X-points at both corners. We successfully achieved this configuration, shown in Fig. 3c. The triangularity was accurately matched, with an RMSE of 0.070, as were the plasma current and shape, with RMSE values of 3.5 kA and 1.3 cm, respectively. This demonstrates the ability to rapidly and directly create a configuration under active study<sup>27</sup>.

Snowflake configurations are researched<sup>28,29</sup>, as they distribute the particle exhaust across several strike points. A crucial parameter is the distance between the two X-points that form the divertor legs. We demonstrated our ability to control this distance, shown in Fig. 3d. The control policy first established a snowflake configuration with X-points separated by 34 cm. It then manipulated the far X-point to approach the limiting X-point, ending with a separation of 6.6 cm. The time-varying X-point targets were tracked with a combined RMSE of 3.7 cm. The plasma current and shape were maintained to high accuracy during this transition, with RMSE values of 0.50 kA and 0.65 cm, respectively. This demonstrates accurate control of a complex time-varying target with several coupled objectives.

In aggregate, these experiments demonstrate the ease with which new configurations can be explored, prove the ability of our architecture to operate in high-performance discharges and confirm the breadth of its capability. In the [Methods](#) section, we further investigate the control-policy behaviours.

## New multi-domain plasma demonstration

Lastly, we demonstrate the power of our architecture to explore new plasma configurations. We test control of ‘droplets’, a configuration in which two separate plasmas exist within the vessel simultaneously. It is probably possible that existing approaches could stabilize such droplets. Nonetheless, great investment would be required to develop feedforward coil-current programming, implement real-time estimators, tune controller gains and successfully take control after plasma creation. By contrast, with our approach, we simply adjust the simulated handover state to account for the different handover condition from single-axis plasmas and define a reward function to keep the position of each droplet component steady while ramping up the domain plasma currents. This loose specification gives the architecture the freedom to choose how to best adapt the droplet shapes as  $I_p$  increases to maintain stability. The architecture was able to successfully stabilize droplets over the entire 200 ms control window and ramp the current within each domain, as shown in Fig. 4. This highlights the advantage of a general, learning-based control architecture to adapt control for previously unknown configurations.

**Fig. 4: Droplets.**



Demonstration of sustained control of two independent droplets on TCV for the entire 200-ms control window. Left, control of  $I_p$  for each independent lobe up to the same target value. Right, a picture in which the two droplets are visible, taken from a camera looking into the vessel at  $t = 0.55$ .

## [Source data](#)

## Discussion

We present a new paradigm for plasma magnetic confinement on tokamaks. Our control design fulfils many of the hopes of the community for a machine-learning-based control approach<sup>14</sup>, including high performance, robustness to uncertain operating conditions, intuitive target specification and unprecedented versatility. This achievement required overcoming gaps in capability and infrastructure through scientific and engineering advances: an accurate, numerically robust simulator; an informed trade-off between simulation accuracy and computational complexity; a sensor and actuator model tuned to specific hardware control; realistic variation of operating conditions during training; a highly data-efficient RL algorithm that scales to high-dimensional problems; an asymmetric learning setup with an expressive critic but fast-to-evaluate policy; a process for compiling neural networks into real-time-capable code and deployment on a tokamak digital control system. This resulted in successful hardware experiments that demonstrate fundamental capability alongside advanced shape control without requiring fine-tuning on the plant. It additionally shows that a free-boundary equilibrium evolution model has sufficient fidelity to develop transferable controllers, offering a justification for using this approach to test control of future devices.

Efforts could further develop our architecture to quantify its robustness through analysis of the non-linear dynamics<sup>30,31,32</sup> and reduce training time through increased reuse of data and multi-fidelity learning<sup>33</sup>. Additionally, the set of control targets can be expanded, for example, to reduce target heat loads through flux expansion<sup>5</sup>, aided by the use of privileged information in the critic to avoid requiring real-time observers. The architecture can be coupled to a more capable simulator, for example, incorporating plasma pressure and current-density-evolution physics, to optimize the global plasma performance.

Our learning framework has the potential to shape future fusion research and tokamak development. Underspecified objectives can find configurations that maximize a desired performance objective or even maximize power production. Our architecture can be rapidly deployed on a new tokamak without the need to design and commission the complex system of controllers deployed today, and evaluate proposed designs before they are constructed. More broadly, our approach may enable the discovery of new reactor designs by jointly optimizing the plasma shape, sensing, actuation, wall design, heat load and magnetic controller to maximize overall performance.

## Methods

## Tokamak à Configuration Variable

The TCV [1,34](#), shown in Fig. [1](#), is a research tokamak at the Swiss Plasma Center, with a major radius of 0.88 m and vessel height and width of 1.50 m and 0.512 m, respectively. TCV has a flexible set of magnetic coils that enable the creation of a wide range of plasma configurations. Electron cyclotron resonance heating and neutral beam injection<sup>[35](#)</sup> systems provide external heating and current drive, as used in the experiment in Fig. [3b](#). TCV is equipped with several real-time sensors and our control policies use a subset of these sensors. In particular, we use 34 of the wire loops that measure magnetic flux, 38 probes that measure the local magnetic field and 19 measurements of the current in active control coils (augmented with an explicit measure of the difference in current between the ohmic coils). In addition to the magnetic sensors, TCV is equipped with other sensors that are not available in real time, such as the cameras shown in Figs. [2](#) and [4](#). Our control policy consumes the magnetic and current sensors of TCV at a 10-kHz control rate. The control policy produces a reference voltage command at each time step for the active control coils.

## Tokamak simulator

The coupled dynamics of the plasma and external active and passive conductors are modelled with a free-boundary simulator, FGE<sup>[22](#)</sup>. The conductors are described by a circuit model in which the resistivity is considered known and constant, and the mutual inductance is computed analytically.

The plasma is assumed to be in a state of toroidally symmetric equilibrium force balance (Grad–Shafranov equation<sup>[21](#)</sup>), in which the Lorentz force  $J \times B$  generated from the interaction of the plasma current density,  $J$ , and the magnetic field,  $B$ , balances the plasma pressure gradient  $\nabla p$ . The transport of radial pressure and current density caused by heat and current drive sources is not modelled. Instead, the plasma radial profiles are modelled as polynomials whose coefficients are constrained by the plasma current  $I_p$  plus two free parameters: the normalized plasma pressure  $\beta_p$ , which is the ratio of kinetic pressure to the magnetic pressure, and the safety factor at the plasma axis  $q_A$ , which controls the current density peakedness.

The evolution of the total plasma current  $I_p$ , is described as a lumped-parameter equation on the basis of the generalized Ohm's law for the magnetohydrodynamics model. For this model, the total plasma resistance,  $R_p$ , and the total plasma self-inductance,  $L_p$ , are free parameters. Finally, FGE produces the synthetic magnetic measurements that simulate the TCV sensors, which are used to learn the control policies, as discussed below.

## Specific settings for the droplets

In the experiment with the droplets (Fig. 4), the plasma is considered pressureless, which simplifies the numerical solution of the force balance equation. Moreover, the G coil was disabled in simulation, as it was placed in open circuit during experiments (the fast radial fields it generates were deemed unnecessary for these plasmas). This experiment used an earlier model for the  $I_p$  evolution designed for stationary-state plasma operation. This model has one free parameter, the radial profile of the neoclassical parallel plasma conductivity  $(\{\sigma\}_{\parallel})$  (ref. 22). This model was replaced with the one described above for the single-domain plasma experiment, as it better describes the evolution of  $I_p$ , especially when it is changing rapidly.

## Plasma parameter variation

We vary the plasma-evolution parameters introduced above during training to provide robust performance across the true but unknown condition of the plasma. The amount of variation is set within ranges identified from experimental data as shown in Extended Data Table 2. In the single-plasma experiments, we vary the plasma resistivity  $R_p$ , as well as the profile parameters  $\beta_p$  and  $q_A$ .  $L_p$  is not varied, as it can be computed from a simple relation<sup>36</sup>. These are all independently sampled from a parameter-specific log-uniform distribution. In the experiment with droplets, we vary the initial ohmic coil current values according to a uniform distribution. We set two different values for the droplet  $(\{\sigma\}_{\parallel})$  components. We sample the log of the difference between them from a scaled beta distribution and the overall shift in the combined geometric mean from a log-uniform distribution, and then solve for the individual  $(\{\sigma\}_{\parallel})$ . Parameter values are sampled at the beginning of each episode and kept constant for the duration of the simulation. The sampled value is deliberately not exposed to the learning architecture because it is not directly measurable. Therefore, the agent is forced to learn a controller that can robustly handle all combinations of these parameters. This informed and targeted domain-randomization technique proved to be effective to find policies that track time targets for shape and  $I_p$  while being robust to the injection of external heating and the edge-localized mode perturbations during high confinement mode.

## Sensing and actuation

The raw sensor data on TCV go through a low-pass filtering and signal-conditioning stage<sup>37</sup>. We model this stage in simulation by a time delay and a Gaussian noise model, identified from data during a stationary-plasma operation phase (Extended Data Table 2). This sensor model (shown in Fig. 1b) captures the relevant dynamics

affecting control stability. The power-supply dynamics (also shown in Fig. 1b) are modelled with a fixed bias and a fixed time delay identified from data, as well as a further offset varied randomly at the beginning of each episode. The values for these modifications can be found in Extended Data Table 2. This is a conservative approximation of the true thyristor-based power supplies<sup>37</sup>, but captures the essential dynamics for control purposes.

The control policy can learn to be robust against very non-linear hardware-specific phenomena. For example, when the current in the active coils changes polarity and the controller requests a too low voltage, the power supplies can get ‘stuck’, erroneously providing zero output current over an extended period of time (Extended Data Fig. 4b). This phenomenon might affect both the controller stability and the precision. To demonstrate the capability of our controller to deal with this issue, we applied ‘learned-region avoidance’ in the advanced control demonstration to indicate that currents near zero are undesirable. As a result, the control policy effectively learns to increase the voltages when changing the current polarity to avoid stuck coils on the plant (Extended Data Fig. 4c).

## Neural-network architecture

MPO<sup>23</sup> uses two neural-network architectures to design and optimize the policy: the critic network and the policy network. Both networks are adapted during training, but only the policy network is deployed on the plant.

For the critic network, the inputs are combined with the hyperbolic tangent function value of the last commanded action and fed to a long short-term memory (LSTM) layer 256 units wide. The outputs of the LSTM layer are then concatenated with its inputs and fed to a multilayer perceptron (MLP), that is, a stack of two densely connected hidden layers with 256 latents each. Each of the MLP layers uses an exponential linear unit non-linearity. Finally, we use a last linear layer to output the Q-value.

The policy network is restricted to a network architecture that can be evaluated on the target hardware within 50  $\mu$ s to obtain the necessary 10-kHz control rate. Additionally, the network needs to perform this inference to sufficient numerical accuracy on the control system, which uses a different processor architecture from the hardware used for training. Therefore, the policy network is built as follows. We feed the inputs to a stack of a linear layer with 256 outputs. The outputs of this linear layer are normalized with a LayerNorm<sup>38</sup> and bounded using a hyperbolic tangent function. After this, the output is fed through a three-layer MLP using exponential linear unit non-linearity and 256 latents each. The output of this stack is fed through a final linear layer that outputs two parameters per action: one mean of the Gaussian distribution and one standard

deviation of the Gaussian distribution. The standard deviation uses a softplus non-linearity to make sure it is always positive. The parameters of this Gaussian distribution over actions are the output of the neural network. Note that, for assessing the policy in simulation and executing on TCV, only the mean of the distribution is used. With this small neural network, we can perform inference within the L2 cache of the CPU on the control system.

These neural networks are initialized with the weights of a truncated normal distribution scaled with the number of inputs and a bias of zero. The exception is the last layer of the policy network, which is initialized the same way but scaled with 0.0001 (ref. [39](#)). These networks are trained with an unroll length of 64 steps. For training, we used a batch size of 256 and a discount of 0.99.

Extended Data Figure [5a](#) shows the importance of an asymmetric design between the actor network and the critic network. We compare the standard setup with a symmetric setup in which the critic is also limited by the control rate on the plant. In the standard setup, the critic network is much larger than the policy network (718,337 parameters compared with 266,280 parameters) and also uses a recurrent LSTM. In the symmetric setup, the critic is also an MLP that is about the same size as the policy (266,497 parameters). We see that the symmetric design notably underperforms the asymmetric design in learning an effective policy. We additionally find that the main benefit comes from the recurrent design in the critic to handle the non-Markovian properties of this environment. When we scale up the critic keeping the feedforward structure of the policy, we find that widening its width to 512 units (926,209 parameters) or even 1,024 units (3,425,281 parameters) still does not match the performance of the setup with the smaller but recurrent critic.

## Learning loop

Our approach uses an episodic training approach in which data are collected by running the simulator with a control policy in the loop, as shown in Fig. [1a](#). The data from these interactions are collected in a finite-capacity first-in-first-out buffer<sup>[40](#)</sup>. The interaction trajectories are sampled at random from the buffer by a ‘learner’, which executes the MPO algorithm to update the control-policy parameters. During training, the executed control policy is stochastic to explore successful control options. This stochastic policy is represented by a diagonal Gaussian distribution over coil actions.

Each episode corresponds to a single simulation run that terminates either when a termination condition is hit, which we will discuss below, or when a fixed simulation time has passed in the episode. This fixed time was 0.2 s for the droplets, 0.5 s in the case of Extended Data Fig. [2a, c](#), and 1 s otherwise. Each episode is initialized from an

equilibrium state at the preprogrammed handover time, which was reconstructed from a previous experiment on TCV.

Our training loop emulates the control frequency of 10 kHz. At each step, the policy is evaluated using the observation from the previous step. The resulting action is then applied to the simulator, which is then stepped. Observations and rewards are also collected at the 10-kHz control frequency, resulting in training data collected at 0.1 ms intervals. For our simulation, we chose a time step of 50 kHz. Hence, for each evaluation of the policy, five simulation time steps are computed. The action, that is, the desired coil voltage, is kept constant during these substeps. Data from intermediate steps are only used for checking termination conditions and are discarded afterwards. This enables choosing the control rate and simulator time step independently and, hence, setting the latter on the basis of numerical considerations.

We use a distributed architecture<sup>41</sup> with a single learner instance on a tensor processing unit and several actors each running an independent instance of the simulator. We used 5,000 actors in parallel for our experiments, generally resulting in training times of 1-3 days, although sometimes longer for complex target specifications. We ran a sweep on the number of actors required to stabilize a basic plasma and the results can be seen in Extended Data Fig. 5. We see that a similar level of performance can be achieved with a large reduction in the number of actors for a moderate cost in training time.

As RL only interacts sample-wise with the environment, the policy could be fine-tuned further with data from interacting with the plant. Alternatively, one might imagine leveraging the database of past experiments performed on TCV to improve the policy. However, it is unclear if the data are sufficiently diverse, given the versatility of TCV and the fact that the same plasma configuration can be achieved by various coil-voltage configurations. Especially for previously unknown plasma shapes, no data or only very limited data are available, rendering this approach ineffective. Conversely, the simulator can directly model the dynamics for the configurations of interest. This issue in which data collection requires a good policy becomes even more pronounced if one wants to optimize a policy de novo from data, without relying on a simulator model.

## Rewards and terminations

All of our experiments have several objectives that must be satisfied simultaneously. These objectives are specified as individual reward components that track an aspect of the simulation — typically, a physical quantity — and these individual components are combined into a single scalar reward value. Descriptions of the targets used are listed in Extended Data Table 4. The target values of the objectives are often time-varying

(for example, the plasma current and boundary target points), and are sent to the policy as part of the observations. This time-varying trace of targets is defined by a sequence of values at points in time, which are linearly interpolated for all time steps in between.

Shape targets for each experiment were generated using the shape generator<sup>42</sup> or specified manually. These points are then canonicalized to 32 equally spaced points along a spline, which are the targets that are fed to the policy. The spline is periodic for closed shapes but non-periodic for diverted shapes, ending at the X-points.

The process for combining these multiple objectives into a single scalar is as follows. First, for each objective, the difference between the actual and target values is computed, and then transformed with a non-linear function to a quality measure between 0 and 1. In the case of a vector-valued objective (for example, distance to each target-shape point), the individual differences are first merged into a single scalar through a ‘combiner’, a weighted non-linear function. Finally, a weighted combination of the individual objective-specific quality measures is computed into a single scalar reward value between 0 and 1 using a combiner as above. This (stepwise) reward is then normalized so that the maximum cumulative reward is 100 for 1 s of control. In cases in which the control policy has triggered a termination, a large negative reward is given. See Extended Data Table 5 for more details.

We typically compute the quality measure from the error using a softplus or sigmoid, which provides a non-zero learning signal early in training when the errors are large, while simultaneously encouraging precision as the policy improves. Similarly, we combine the rewards using a (weighted) smooth max or geometric mean, which gives a larger gradient to improving the worst reward, while still encouraging improving all objectives. The precise reward definitions used in each of our experiments are listed in Extended Data Table 3 and the implementations are available in the supplementary material.

## Further findings

Some controllers exhibited several interesting behaviours, which are briefly mentioned here. These control behaviours hint at further potential capabilities of learned-control approaches.

External heating was applied during the experiment shown in Fig. 3b. We first ran a test experiment without heating, but with the exact same controller and objectives. This provides a simple repeatability test in the control window before heating was applied. A performance comparison is depicted in Extended Data Fig. 3 and shows that, in these two experiments, the controller performed similarly.

When given the goal to maintain only the plasma position and current, our architecture autonomously constructed a low-elongation plasma that eliminates the vertical instability mode (Extended Data Fig. 4a), without being explicitly told to do so.

Our control architecture can naturally choose to use a varying combination of poloidal field and ohmic coils to drive the inductive voltage required for sustaining the plasma current (Extended Data Fig. 4b), in contrast to existing control architectures that typically assume a strict separation.

Our architecture can learn to include non-linear physical and control requests by adding objectives to the goal specification. It can, for example, avoid limitations in the power supplies that occasionally cause ‘stuck’ control-coil currents when reversing polarity (Extended Data Fig. 4c) and avoid X-points in the vessel but outside the plasma (Extended Data Fig. 4d) when requested with high-level rewards.

We see that, for some quantities, there is a steady-state error in the target value (for example,  $\kappa$  in Extended Data Fig. 3). Future development will be towards removing such errors, for example, by making the control policy recurrent rather than feedforward. Care must be taken to ensure that these more powerful recurrent policies do not overspecialize to the specific dynamics of the simulator and continue to transfer to TCV successfully.

## Deployment

As the stochastic nature of the training policy is only useful for exploration, the final control policy is taken to be the mean of the Gaussian policy at the conclusion of training. This gives a deterministic policy to execute on the plant. During training, we monitor the quality of this deterministic policy before deployment.

The control loop of TCV runs at 10 kHz, although only half of the cycle time, that is, 50  $\mu$ s, is available for the control algorithm due to other signal processing and logging. Therefore we created a deployment system that compiles our neural network into real-time-capable code that is guaranteed to run within this time window. To achieve this, we remove superfluous weights and computations (such as the exploration variance) and then use `tfcompile`<sup>43</sup> to compile it into binary code, carefully avoiding unnecessary dependencies. We tailored the neural network structure to optimize the use of the processor’s cache and enable vectorized instructions for optimal performance. The table of time-varying control targets is also compiled into the binary for ease of deployment. In future work, targets could easily be supplied at runtime to dynamically adjust the behaviour of the control policy. We then test all compiled policies in an automated, extensive benchmark before deployment to ensure that timings are met consistently.

## Post-experiment analysis

The plasma shape and position are not directly observed and need to be inferred from the available magnetic measurements. This is done with magnetic-equilibrium reconstruction, which solves an inverse problem to find the plasma-current distribution that respects the force balance (Grad–Shafranov equation) and best matches the given experimental magnetic measurements at a specific time in a least-squares sense.

In a conventional magnetic control design, a real-time-capable magnetic-equilibrium reconstruction is needed as a plasma-shape observer to close the shape-control feedback loop (shown as the ‘Plasma shape’ observer in Fig. 1f). In our approach, instead, we only make use of equilibrium reconstruction with LIUQE code<sup>10</sup> during post-discharge analysis to validate the plasma-shape controller performances and compute the physical initial conditions for the simulation during training.

After running the experiment, we use this equilibrium-reconstruction code to obtain an estimate of the plasma state and magnetic flux field. Using this approach is consistent with previous literature for evaluating performance<sup>9,10</sup>.

The plasma boundary is defined by the last closed-flux surface (LCFS) in the domain. We extract the LCFS as 32 equiangular points around the plasma axis and then canonicalize with splines to 128 equidistant points. The error distance is computed using the shortest distance between each of the points that defined the target shape and the polygon defined by the 128 points on the LCFS. The shape RMSE is computed across these 32 error distances over all time steps in the time range of interest.

Errors on scalar quantities, such as  $I_p$  or elongation, are computed from the error between the reference and the respective estimation from the equilibrium reconstruction over the time period of interest. The estimate of the growth rate of the vertical displacement instability<sup>6</sup> is computed from a spectral decomposition of the linearized system of equations of the simulator around the reconstructed equilibrium.

## Comparison with previous work

In recent years, advanced control techniques have been applied to magnetic confinement control. De Tommasi et al.<sup>44</sup> describe a model-based control approach for plasma-position control using a linear model and a cascaded feedback-control structure. Gerkšić and De Tommasi<sup>45</sup> propose a model predictive control approach, demonstrating linear model predictive control for plasma position and shape control in simulation, including a feasibility estimate for hardware deployment. Boncagni et al.<sup>46</sup> have proposed a switching controller, improving on plasma-current tracking on hardware but without demonstrating further capabilities. There has been other

previous work in which RL has learned on plasma models, for example, to control the safety factor<sup>47</sup> or to control the ion-temperature gradient<sup>48</sup>. Recently, Seo et al.<sup>49</sup> have developed feedforward signals for beta control using RL, which have then been verified on the KSTAR tokamak.

More generally, machine-learning-based approaches are being developed for magnetic-confinement control and fusion in general, not limited to control. A survey of this area is provided by Humphreys et al.<sup>14</sup>, who categorized approaches into seven Priority Research Opportunities, including accelerating science, diagnostics, model extraction, control, large data, prediction and platform development. Early use of neural networks in a control loop for plasma control is presented by Bishop et al.<sup>15</sup>, who used a small-scale neural network to estimate the plasma position and low-dimensional shape parameters, which were subsequently used as error signals for feedback control.

Our architecture constitutes an important step forward in terms of generality, in which a single framework is used to solve a broad variety of fusion-control challenges, satisfying several of the key promises of machine learning and artificial intelligence for fusion set out in ref. <sup>14</sup>.

## Application to alternative tokamaks

Our approach has been successfully demonstrated on TCV, and we are confident that, with a few basic modifications, our approach is directly applicable to other tokamaks that meet some assumptions and technical requirements laid out below. All present-day tokamaks have been confirmed to respect, from the magnetic control point of view, the coupled equations solved by free-boundary simulators. Equilibrium controllers have routinely been designed on the basis of these models, and — for future tokamaks — there is no reason as of yet to believe this model will no longer be valid. Naturally, we cannot predict the performance of our approach on other kinds of devices.

To simulate a different device, the free-boundary simulator parameters will need to be set appropriately. This includes the machine description with the locations and electrical properties of coils, vessel and limiter, the actuator and sensor characteristics, such as current and voltage ranges, noise and delay. Operational conditions such as the expected range of variation of profile parameters also need to be determined. Finally, rewards and targets need to be updated to match the geometry and desired shapes.

The aforementioned characteristics should be readily available, as these are typically part of the design process for a given tokamak. Indeed, Grad–Shafranov equilibrium calculations are routinely carried out for the general design and analysis of a new

tokamak, and these include all required parameters. These variations in vessel geometry and the number, placement and range of sensors and coils should not require changes to the learning algorithm beyond adjusting design bounds. The learning algorithm will automatically adjust input and output layer dimensions for the neural network and will automatically learn a policy suited to the new vessel and control system.

Further considerations are required for deployment. Our approach requires a centralized control system with sufficient computational power to evaluate a neural network at the desired control frequency, although a desktop-grade CPU is sufficient to meet this requirement. Also, an existing magnetic controller is needed to perform plasma breakdown and early ramp-up before handing over to the learned controller. Although our controllers are trained to avoid terminations in simulation corresponding to disruption criteria, they are not guaranteed to avoid plasma disruptions. Hence, if the target tokamak cannot tolerate certain kinds of disruptions, a machine-protection layer such as a simpler fallback controller or interlock system should be in place during experiments.

## Data availability

TCV experimental data from the images in this paper are available in the Supplementary information. [Source data](#) are provided with this paper.

## Code availability

The learning algorithm used in the actor-critic RL method is MPO<sup>23</sup>, a reference implementation of which is available under an open-source license<sup>41</sup>. Additionally, the software libraries launchpad<sup>50</sup>, dm\_env<sup>51</sup>, sonnet<sup>52</sup>, tensorflow<sup>53</sup> and reverb<sup>40</sup> were used, which are also available as open source. The code to compute the control targets, rewards and terminations is available in the Supplementary information. FGE and LIUQE are available subject to license agreement from the Swiss Plasma Center at EPFL (Antoine Merle [antoine.merle@epfl.ch](mailto:antoine.merle@epfl.ch), Federico Felici [federico.felici@epfl.ch](mailto:federico.felici@epfl.ch)).

## References

1. Hofmann, F. et al. Creation and control of variably shaped plasmas in TCV. *Plasma Phys. Control. Fusion* **36**, B277 (1994).
2. Coda, S. et al. Physics research on the TCV tokamak facility: from conventional to alternative scenarios and beyond. *Nucl. Fusion* **59**, 112023 (2019).

3. Anand, H., Coda, S., Felici, F., Galperti, C. & Moret, J.-M. A novel plasma position and shape controller for advanced configuration development on the TCV tokamak. *Nucl. Fusion* **57**, 126026 (2017).
4. Mele, A. et al. MIMO shape control at the EAST tokamak: simulations and experiments. *Fusion Eng. Des.* **146**, 1282–1285 (2019).
5. Anand, H. et al. Plasma flux expansion control on the DIII-D tokamak. *Plasma Phys. Control. Fusion* **63**, 015006 (2020).
6. De Tommasi, G. Plasma magnetic control in tokamak devices. *J. Fusion Energy* **38**, 406–436 (2019).
7. Walker, M. L. & Humphreys, D. A. Valid coordinate systems for linearized plasma shape response models in tokamaks. *Fusion Sci. Technol.* **50**, 473–489 (2006).
8. Blum, J., Heumann, H., Nardon, E. & Song, X. Automating the design of tokamak experiment scenarios. *J. Comput. Phys.* **394**, 594–614 (2019).
9. Ferron, J. R. et al. Real time equilibrium reconstruction for tokamak discharge control. *Nucl. Fusion* **38**, 1055 (1998).
10. Moret, J.-M. et al. Tokamak equilibrium reconstruction code LIUQE and its real time implementation. *Fusion Eng. Des.* **91**, 1–15 (2015).
11. Xie, Z., Berseth, G., Clary, P., Hurst, J. & van de Panne, M. Feedback control for Cassie with deep reinforcement learning. In *2018 IEEE/RSJ International Conference on Intelligent Robots and Systems (IROS)* 1241–1246 (IEEE, 2018).
12. Akkaya, I. et al. Solving Rubik’s cube with a robot hand. Preprint at <https://arxiv.org/abs/1910.07113> (2019).
13. Bellemare, M. G. et al. Autonomous navigation of stratospheric balloons using reinforcement learning. *Nature* **588**, 77–82 (2020).
14. Humphreys, D. et al. Advancing fusion with machine learning research needs workshop report. *J. Fusion Energy* **39**, 123–155 (2020).
15. Bishop, C. M., Haynes, P. S., Smith, M. E., Todd, T. N. & Trotman, D. L. Real time control of a tokamak plasma using neural networks. *Neural Comput.* **7**, 206–217 (1995).

16. Joung, S. et al. Deep neural network Grad-Shafranov solver constrained with measured magnetic signals. *Nucl. Fusion* **60**, 16034 (2019).
17. van de Plassche, K. L. et al. Fast modeling of turbulent transport in fusion plasmas using neural networks. *Phys. Plasmas* **27**, 022310 (2020).
18. Abbate, J., Conlin, R. & Kolemen, E. Data-driven profile prediction for DIII-D. *Nucl. Fusion* **61**, 046027 (2021).
19. Kates-Harbeck, J., Svyatkovskiy, A. & Tang, W. Predicting disruptive instabilities in controlled fusion plasmas through deep learning. *Nature* **568**, 526–531 (2019).
20. Jardin, S. *Computational Methods in Plasma Physics* (CRC Press, 2010).
21. Grad, H. & Rubin, H. Hydromagnetic equilibria and force-free fields. *J. Nucl. Energy* (1954) **7**, 284–285 (1958).
22. Carpanese, F. *Development of Free-boundary Equilibrium and Transport Solvers for Simulation and Real-time Interpretation of Tokamak Experiments*. PhD thesis, EPFL (2021).
23. Abdolmaleki, A. et al. Relative entropy regularized policy iteration. Preprint at <https://arxiv.org/abs/1812.02256> (2018).
24. Paley, J. I., Coda, S., Duval, B., Felici, F. & Moret, J.-M. Architecture and commissioning of the TCV distributed feedback control system. In *2010 17th IEEE-NPSS Real Time Conference* 1–6 (IEEE, 2010).
25. Freidberg, J. P. *Plasma Physics and Fusion Energy* (Cambridge Univ. Press, 2008).
26. Hommen, G. D. et al. Real-time optical plasma boundary reconstruction for plasma position control at the TCV Tokamak. *Nucl. Fusion* **54**, 073018 (2014).
27. Austin, M. E. et al. Achievement of reactor-relevant performance in negative triangularity shape in the DIII-D tokamak. *Phys. Rev. Lett.* **122**, 115001 (2019).
28. Kolemen, E. et al. Initial development of the DIII-D snowflake divertor control. *Nucl. Fusion* **58**, 066007 (2018).
29. Anand, H. et al. Real time magnetic control of the snowflake plasma configuration in the TCV tokamak. *Nucl. Fusion* **59**, 126032 (2019).

30. Wigbers, M. & Riedmiller, M. A new method for the analysis of neural reference model control. In *Proc. International Conference on Neural Networks (ICNN'97)* Vol. 2, 739–743 (IEEE, 1997).
31. Berkenkamp, F., Turchetta, M., Schoellig, A. & Krause, A. Safe model-based reinforcement learning with stability guarantees. In *2017 Advances in Neural Information Processing Systems* 908–919 (ACM, 2017).
32. Wabersich, K. P., Hewing, L., Carron, A. & Zeilinger, M. N. Probabilistic model predictive safety certification for learning-based control. *IEEE Tran. Automat. Control* **67**, 176–188 (2021).
33. Abdolmaleki, A. et al. On multi-objective policy optimization as a tool for reinforcement learning. Preprint at <https://arxiv.org/abs/2106.08199> (2021).
34. Coda, S. et al. Overview of the TCV tokamak program: scientific progress and facility upgrades. *Nucl. Fusion* **57**, 102011 (2017).
35. Karpushov, A. N. et al. Neutral beam heating on the TCV tokamak. *Fusion Eng. Des.* **123**, 468–472 (2017).
36. Lister, J. B. et al. Plasma equilibrium response modelling and validation on JT-60U. *Nucl. Fusion* **42**, 708 (2002).
37. Lister, J. B. et al. The control of tokamak configuration variable plasmas. *Fusion Technol.* **32**, 321–373 (1997).
38. Ulyanov, D., Vedaldi, A. & Lempitsky, V. Instance normalization: the missing ingredient for fast stylization. Preprint at <https://arxiv.org/abs/1607.08022> (2016).
39. Andrychowicz, M. et al. What matters in on-policy reinforcement learning? A large-scale empirical study. In *ICLR 2021 Ninth International Conference on Learning Representations* (2021).
40. Cassirer, A. et al. Reverb: a framework for experience replay. Preprint at <https://arxiv.org/abs/2102.04736> (2021).
41. Hoffman, M. et al. Acme: a research framework for distributed reinforcement learning. Preprint at <https://arxiv.org/abs/2006.00979> (2020).
42. Hofmann, F. FBT-a free-boundary tokamak equilibrium code for highly elongated and shaped plasmas. *Comput. Phys. Commun.* **48**, 207–221 (1988).

43. Abadi, M. et al. TensorFlow: a system for large-scale machine learning. In *Proc. 12th USENIX Symposium on Operating Systems Design and Implementation (OSDI '16)* 265–283 (2016).
44. De Tommasi, G. et al. Model-based plasma vertical stabilization and position control at EAST. *Fusion Eng. Des.* **129**, 152–157 (2018).
45. Gerkšič, S. & De Tommasi, G. ITER plasma current and shape control using MPC. In *2016 IEEE Conference on Control Applications (CCA)* 599–604 (IEEE, 2016).
46. Boncagni, L. et al. Performance-based controller switching: an application to plasma current control at FTU. In *2015 54th IEEE Conference on Decision and Control (CDC)* 2319–2324 (IEEE, 2015).
47. Wakatsuki, T., Suzuki, T., Hayashi, N., Oyama, N. & Ide, S. Safety factor profile control with reduced central solenoid flux consumption during plasma current ramp-up phase using a reinforcement learning technique. *Nucl. Fusion* **59**, 066022 (2019).
48. Wakatsuki, T., Suzuki, T., Oyama, N. & Hayashi, N. Ion temperature gradient control using reinforcement learning technique. *Nucl. Fusion* **61**, 046036 (2021).
49. Seo, J. et al. Feedforward beta control in the KSTAR tokamak by deep reinforcement learning. *Nucl. Fusion* **61**, 106010 (2021).
50. Yang, F. et al. Launchpad: a programming model for distributed machine learning research. Preprint at <https://arxiv.org/abs/2106.04516> (2021).
51. Muldal, A. et al. dm\_env: a Python interface for reinforcement learning environments. [http://github.com/deepmind/dm\\_env](http://github.com/deepmind/dm_env) (2019).
52. Reynolds, M. et al. Sonnet: TensorFlow-based neural network library. <http://github.com/deepmind/sonnet> (2017).
53. Martín A. et al. TensorFlow: large-scale machine learning on heterogeneous systems. Software available from <https://www.tensorflow.org/> 2015.
54. Hender, T. C. et al. Chapter 3: MHD stability, operational limits and disruptions. *Nucl. Fusion* **47**, S128–S202 (2007).

## Acknowledgements

We gratefully acknowledge the work and support of the TCV team (see the author list of Coda et al.<sup>2</sup>) in enabling these experimental results. We thank C. Wüthrich and Y. Andrebe for support with the diagnostics. We thank C. Jones and E. Smith for strategic help and inspiration at the start of the project. We thank R. Ahamed, P. Komarek, V. Panneershelvam and F. Song for their support in the preparation and during this research. This work was supported in part by the Swiss National Science Foundation.

## Author information

### Author notes

1. These authors contributed equally: Jonas Degrave, Federico Felici, Jonas Buchli, Michael Neunert, Brendan Tracey, Francesco Carpanese, Timo Ewalds, Roland Hafner, Martin Riedmiller

### Affiliations

#### 1. DeepMind, London, UK

Jonas Degrave, Jonas Buchli, Michael Neunert, Brendan Tracey, Francesco Carpanese, Timo Ewalds, Roland Hafner, Abbas Abdolmaleki, Diego de las Casas, Craig Donner, Leslie Fritz, Andrea Huber, James Keeling, Maria Tsipoukelli, Jackie Kay, Seb Noury, David Pfau, Pushmeet Kohli, Koray Kavukcuoglu, Demis Hassabis & Martin Riedmiller

#### 2. Swiss Plasma Center - EPFL, Lausanne, Switzerland

Federico Felici, Francesco Carpanese, Cristian Galperti, Antoine Merle, Jean-Marc Moret, Federico Pesamosca, Olivier Sauter, Cristian Sommariva, Stefano Coda, Basil Duval & Ambrogio Fasoli

### Contributions

B.T., F.C., F.F., J.B., J.D., M.N., M.R., R.H. and T.E. contributed equally. D.P., F.F., J.B., J.D., M.R. and R.H. conceived the project. A.H., B.T., F.F., J.B., J.D., L.F., M.N. and M.R. led the project. A.M., B.T., C.D., C.S., F.C., F.F., F.P., J.B., J.-M.M., M.N. and O.S. developed the physics simulations. B.T., C.D., D.C., F.F., J.D., J. Kay, M.N., M.T. and T.E. integrated the physics simulations with the learning framework. A.A., B.T., J.D., J. Keeling, R.H. and T.E. developed the learning framework and performed learning experiments. C.G., D.C., F.F., J.B., J.D., M.N., S.N. and T.E. developed the real-time neural network interface. C.G., F.C., F.F., J.D. and S.C. integrated the real-time neural network with the control system and ran tokamak experiments. C.D., D.C.,

F.C., F.F., J.B., J. Keeling, M.N. and T.E. developed data-curation tools. B.T., C.G., F.C., F.F., J.B., J. Keeling, M.N., R.H. and T.E. developed and ran the data analysis. A.F., B.D., D.H., S.C., K.K. and P.K. consulted for the project. B.T., F.C., F.F., J.B., J.D., M.N., M.R., R.H. and T.E. wrote the manuscript.

## Corresponding authors

Correspondence to [Federico Felici](#), [Jonas Buchli](#) or [Brendan Tracey](#).

## Ethics declarations

### Competing interests

B.T., F.C., F.F., J.B., J.D., M.N., R.H. and T.E. have filed a provisional patent application about the contents of this manuscript. The remaining authors declare no competing interests.

## Peer review

### Peer review information

*Nature* thanks Takuma Wakatsuki and the other, anonymous, reviewers for their contribution to the peer review of this work.

## Additional information

**Publisher's note** Springer Nature remains neutral with regard to jurisdictional claims in published maps and institutional affiliations.

## Extended data figures and tables

### [Extended Data Fig. 1 Pictures and illustration of the TCV.](#)

**a, b** Photographs showing the part of the TCV inside the bioshield. **c** CAD drawing of the vessel and coils of the TCV. **d** View inside the TCV (Alain Herzog/EPFL), showing the limiter tiling, baffles and central column.

### [Extended Data Fig. 2 A larger overview of the shots in Fig. 3.](#)

We plotted the reconstructed values for the normalized pressure  $\beta_p$  and safety factor  $q_A$ , along with the range of domain randomization these variables saw during training (in green), which can be found in Extended Data Table 2. We also plot the growth rate,  $\gamma$ , and the plasma current,  $I_p$ , along with the associated target value. Where relevant, we plot the elongation  $\kappa$ , the neutral beam heating, the triangularity  $\delta$  and the vertical position of the bottom X-point  $Z_X$  and its target.

[Source data](#)

### Extended Data Fig. 3 Control variability.

To illustrate the variability of the performance that our deterministic controller achieves on the environment, we have plotted the trajectories of one policy that was used twice on the plant: in shot 70599 (in blue) and shot 70600 (in orange). The dotted line shows where the cross sections of the vessel are illustrated. The trajectories are shown from the handover at 0.0872 s until 0.65 s after the breakdown, after which, on shot 70600, the neutral beam heating was turned on and the two shots diverge. The green line shows the RMSE distance between the LCFS in the two experiments, providing a direct measure of the shape similarity between the two shots. This illustrates the repeatability of experiments both in shape parameters such as elongation  $\kappa$  and triangularity  $\delta$  and in the error achieved with respect to the targets in plasma current  $I_p$  and the shape of the last closed-flux surface.

[Source data](#)

### Extended Data Fig. 4 Further observations.

**a**, When asked to stabilize the plasma without further specifications, the agent creates a round shape. The agent is in control from  $t = 0.45$  and changes the shape while trying to attain  $R_a$  and  $Z_a$  targets. This discovered behaviour is indeed a good solution, as this round plasma is intrinsically stable with a growth rate  $\gamma < 0$ . **b**, When not given a reward to have similar current on both ohmic coils, the algorithm tended to use the E coils to obtain the same effect as the OH001 coil. This is indeed possible, as can be seen by the coil positions in Fig. 1g, but causes electromagnetic forces on the machine structures. Therefore, in later shots, a reward was added to keep the current in both ohmic coils close together. **c**, Voltage requests by the policy to avoid the E3 coil from sticking when crossing 0 A. As can be seen in, for example, Extended Data Fig. 4b, the currents can get stuck on 0 A for low voltage requests, a consequence of how these requests are handled by the power system. As this behaviour was hard to model, we introduced a reward to keep the coil currents away from 0 A. The control policy produces a high voltage request to move through this region quickly. **d**, An illustration

of the difference in cross sections between two different shots, in which the only difference is that the policy on the right was trained with a further reward for avoiding X-points in vacuum.

[Source data](#)

### **Extended Data Fig. 5 Training progress.**

Episodic reward for the deterministic policy smoothed across 20 episodes with parameter variations enabled, in which 100 means that all objectives are perfectly met. **a** comparison of the learning curve for the capability benchmark (as shown in Fig. 2) using our asymmetric actor-critic versus a symmetric actor-critic, in which the critic is using the same real-time-capable feedforward network as the actor. In blue is the performance with the default critic of 718,337 parameters. In orange, we show the symmetric version, in which the critic has the same feedforward structure and size (266,497 parameters) as the policy (266,280 parameters). When we keep the feedforward structure of the symmetric critic and scale up the critic, we find that widening its width to 512 units (in green, 926,209 parameters) or even 1,024 units (in red, 3,425,281 parameters) does not bridge the performance gap with the smaller recurrent critic. **b** comparison between using various amounts of actors for stabilizing a mildly elongated plasma. Although the policies in this paper were trained with 5,000 actors, this comparison shows that, at least for simpler cases, the same level of performance can be achieved with much lower computational resources.

[Source data](#)

**Extended Data Table 1 Performance metrics of experiments**

**Extended Data Table 2 Simulation parameters for actuator, sensor and current diffusion models**

**Extended Data Table 3 Rewards used in the experiments**

**Extended Data Table 4 Reward components**

**Extended Data Table 5 Reward elements**

## **Supplementary information**

### **Supplementary Information**

This file contains an overview of the files located in the accompanying zipped Supplementary Data folder.

### **Supplementary Data**

## Source data

[Source Data Fig. 2](#)

[Source Data Fig. 3](#)

[Source Data Fig. 4](#)

[Source Data Extended Data Fig. 2](#)

[Source Data Extended Data Fig. 3](#)

[Source Data Extended Data Fig. 4](#)

[Source Data Extended Data Fig. 5](#)

## Rights and permissions

**Open Access** This article is licensed under a Creative Commons Attribution 4.0 International License, which permits use, sharing, adaptation, distribution and reproduction in any medium or format, as long as you give appropriate credit to the original author(s) and the source, provide a link to the Creative Commons license, and indicate if changes were made. The images or other third party material in this article are included in the article's Creative Commons license, unless indicated otherwise in a credit line to the material. If material is not included in the article's Creative Commons license and your intended use is not permitted by statutory regulation or exceeds the permitted use, you will need to obtain permission directly from the copyright holder. To view a copy of this license, visit <http://creativecommons.org/licenses/by/4.0/>.

[Reprints and Permissions](#)

## About this article

### Cite this article

Degrave, J., Felici, F., Buchli, J. *et al.* Magnetic control of tokamak plasmas through deep reinforcement learning. *Nature* **602**, 414–419 (2022).  
<https://doi.org/10.1038/s41586-021-04301-9>

- Received: 14 July 2021

- Accepted: 01 December 2021
- Published: 16 February 2022
- Issue Date: 17 February 2022
- DOI: <https://doi.org/10.1038/s41586-021-04301-9>

## Share this article

Anyone you share the following link with will be able to read this content:

[Get shareable link](#)

Sorry, a shareable link is not currently available for this article.

[Copy to clipboard](#)

Provided by the Springer Nature SharedIt content-sharing initiative

## [Machine learning helps control tokamak plasmas](#)

- Iulia Georgescu

Research Highlight 18 Feb 2022

---

This article was downloaded by **calibre** from <https://www.nature.com/articles/s41586-021-04301-9>

| [Section menu](#) | [Main menu](#) |

- Article
- [Published: 16 February 2022](#)

# Resolving the gravitational redshift across a millimetre-scale atomic sample

- [Tobias Bothwell](#) [ORCID: orcid.org/0000-0002-9532-1290<sup>1</sup>](#),
- [Colin J. Kennedy<sup>1 nAff2</sup>](#),
- [Alexander Aeppli<sup>1</sup>](#),
- [Dhruv Kedar](#) [ORCID: orcid.org/0000-0003-1117-8616<sup>1</sup>](#),
- [John M. Robinson<sup>1</sup>](#),
- [Eric Oelker](#) [ORCID: orcid.org/0000-0002-3916-1595<sup>1 nAff3</sup>](#),
- [Alexander Staron<sup>1</sup>](#) &
- [Jun Ye](#) [ORCID: orcid.org/0000-0003-0076-2112<sup>1</sup>](#)

[Nature](#) volume **602**, pages 420–424 (2022)

- 2604 Accesses
- 524 Altmetric
- [Metrics details](#)

## Subjects

- [Quantum metrology](#)
- [Optical spectroscopy](#)
- [Ultracold gases](#)

## Abstract

Einstein's theory of general relativity states that clocks at different gravitational potentials tick at different rates relative to lab coordinates—an effect known as the gravitational redshift<sup>1</sup>. As fundamental probes of space and time, atomic clocks have long served to test this prediction at distance scales from 30 centimetres to thousands of kilometres<sup>2,3,4</sup>. Ultimately, clocks will enable the study of the union of general relativity and quantum mechanics once they become sensitive to the finite wavefunction of quantum objects oscillating in curved space-time. Towards this regime, we measure a linear frequency gradient consistent with the gravitational redshift within a single millimetre-scale sample of ultracold strontium. Our result is enabled by improving the fractional frequency measurement uncertainty by more than a factor of 10, now reaching  $7.6 \times 10^{-21}$ . This heralds a new regime of clock operation necessitating intra-sample corrections for gravitational perturbations.

This is a preview of subscription content

## Access options

Subscribe to Nature+

Get immediate online access to the entire Nature family of 50+ journals

\$29.99

monthly

[Subscribe](#)

Subscribe to Journal

Get full journal access for 1 year

\$199.00

only \$3.90 per issue

[Subscribe](#)

All prices are NET prices.  
VAT will be added later in the checkout.  
Tax calculation will be finalised during checkout.

Buy article

Get time limited or full article access on ReadCube.

\$32.00

[Buy](#)

All prices are NET prices.

### **Additional access options:**

- [Log in](#)
- [Learn about institutional subscriptions](#)

**Fig. 1: Experimental system and quantum state control.**

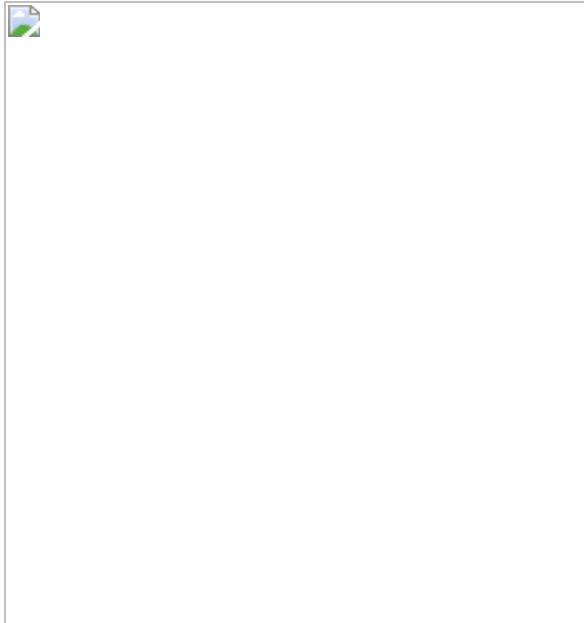


**Fig. 2: Atomic coherence.**

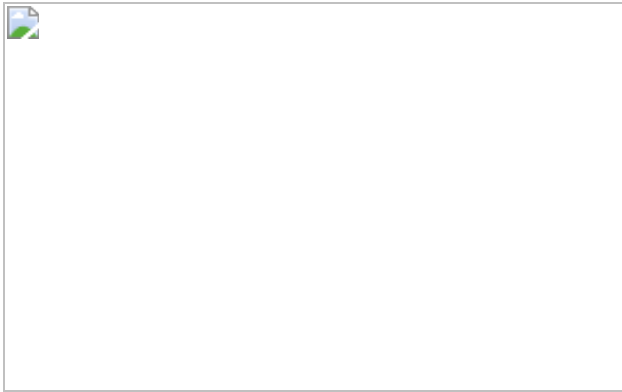


**Fig. 3: Evaluating frequency gradients.**

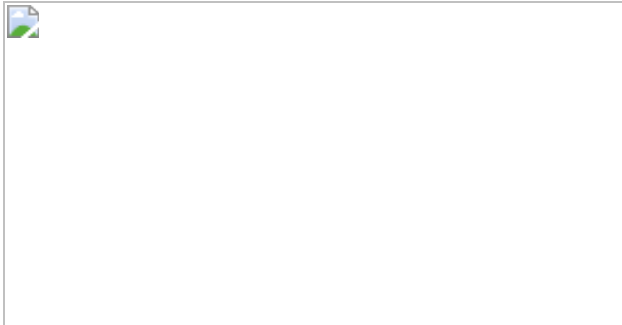


**Fig. 4: In situ synchronous clock comparison.**

## Data availability

The experimental data are available from the corresponding authors upon reasonable request.

## Code availability

The code used for the analysis is available from the corresponding authors upon reasonable request.

## References

1. Einstein, A. Grundgedanken der allgemeinen Relativitätstheorie und Anwendung dieser Theorie in der Astronomie. *Preuss. Akad. der Wissenschaften, Sitzungsberichte* **315**, 778–786 (1915).
2. Chou, C. W., Hume, D. B., Rosenband, T. & Wineland, D. J. Optical clocks and relativity. *Science* **329**, 1630–1633 (2010).
3. Herrmann, S. et al. Test of the gravitational redshift with Galileo satellites in an eccentric orbit. *Phys. Rev. Lett.* **121**, 231102 (2018).
4. Delva, P. et al. Gravitational redshift test using eccentric Galileo satellites. *Phys. Rev. Lett.* **121**, 231101 (2018).
5. Campbell, S. L. et al. A Fermi-degenerate three-dimensional optical lattice clock. *Science* **358**, 90–94 (2017).
6. Oelker, E. et al. Demonstration of  $4.8 \times 10^{-17}$  stability at 1 s for two independent optical clocks. *Nat. Photon.* **13**, 714–719 (2019).
7. Nicholson, T. et al. Systematic evaluation of an atomic clock at  $2 \times 10^{-18}$  total uncertainty. *Nat. Commun.* **6**, 6896 (2015).
8. McGrew, W. F. et al. Atomic clock performance enabling geodesy below the centimetre level. *Nature* **564**, 87–90 (2018).
9. Brewer, S. M. et al.  $^{27}\text{Al}^+$  quantum-logic clock with a systematic uncertainty below  $10^{-18}$ . *Phys. Rev. Lett.* **123**, 33201 (2019).
10. Bothwell, T. et al. JILA SrI optical lattice clock with uncertainty of  $2.0 \times 10^{-18}$ . *Metrologia* **56**, 065004 (2019).

11. Marti, G. E. et al. Imaging optical frequencies with 100  $\mu$ Hz precision and 1.1  $\mu$ m resolution. *Phys. Rev. Lett.* **120**, 103201 (2018).
12. Pedrozo-Peñaflor, E. et al. Entanglement on an optical atomic-clock transition. *Nature* **588**, 414–418 (2020).
13. Kaubruegger, R. et al. Variational spin-squeezing algorithms on programmable quantum sensors. *Phys. Rev. Lett.* **123**, 260505 (2019).
14. Kómár, P. et al. Quantum network of atom clocks: a possible implementation with neutral atoms. *Phys. Rev. Lett.* **117**, 060506 (2016).
15. Young, A. W. et al. Half-minute-scale atomic coherence and high relative stability in a tweezer clock. *Nature* **588**, 408–413 (2020).
16. Safronova, M. S. et al. Search for new physics with atoms and molecules. *Rev. Mod. Phys.* **90**, 25008 (2018).
17. Sanner, C. et al. Optical clock comparison for Lorentz symmetry testing. *Nature* **567**, 204–208 (2019).
18. Kennedy, C. J. et al. Precision metrology meets cosmology: improved constraints on ultralight dark matter from atom-cavity frequency comparisons. *Phys. Rev. Lett.* **125**, 201302 (2020).
19. Boulder Atomic Clock Optical Network. Frequency ratio measurements at 18-digit accuracy using an optical clock network. *Nature* **591**, 564–569 (2021).
20. Kolkowitz, S. et al. Gravitational wave detection with optical lattice atomic clocks. *Phys. Rev. D* **94**, 124043 (2016).
21. Hafele, J. C. & Keating, R. E. Around-the-world atomic clocks. *Science* **177**, 166 (1972).
22. Takamoto, M. et al. Test of general relativity by a pair of transportable optical lattice clocks. *Nat. Photon.* **14**, 411–415 (2020).

23. Laurent, P., Massonnet, D., Cacciapuoti, L. & Salomon, C. The ACES/PHARAO space mission. *C. R. Phys.* **16**, 540–552 (2015).
24. Tino, G. M. et al. SAGE: a proposal for a space atomic gravity explorer. *Eur. Phys. J. D* **73**, 228 (2019).
25. Grotti, J. et al. Geodesy and metrology with a transportable optical clock. *Nat. Phys.* **14**, 437–441 (2018).
26. Flechtner, F., Sneeuw, N. & Schuh, W.-D. (eds) Observation of the System Earth from Space: CHAMP, GRACE, GOCE and Future Missions (Springer, 2014).
27. Kolkowitz, S. et al. Spin–orbit-coupled fermions in an optical lattice clock. *Nature* **542**, 66–70 (2017).
28. Bromley, S. L. et al. Dynamics of interacting fermions under spin–orbit coupling in an optical lattice clock. *Nat. Phys.* **14**, 399–404 (2018).
29. Wilkinson, S. R., Bharucha, C. F., Madison, K. W., Niu, Q. & Raizen, M. G. Observation of atomic Wannier–Stark ladders in an accelerating optical potential. *Phys. Rev. Lett.* **76**, 4512–4515 (1996).
30. Lemonde, P. & Wolf, P. Optical lattice clock with atoms confined in a shallow trap. *Phys. Rev. A* **72**, 1–8 (2005).
31. Aepli, A. et al. Hamiltonian engineering of spin-orbit coupled fermions in a Wannier-Stark optical lattice clock. Preprint at <https://arxiv.org/abs/2201.05909> (2022).
32. Muniz, J. A., Young, D. J., Cline, J. R. K. & Thompson, J. K. Cavity-QED measurements of the  $^{87}\text{Sr}$  millihertz optical clock transition and determination of its natural linewidth. *Phys. Rev. Res.* **3**, 023152 (2021).
33. Ludlow, A. D., Boyd, M. M., Ye, J., Peik, E. & Schmidt, P. O. Optical atomic clocks. *Rev. Mod. Phys.* **87**, 637–701 (2015).

34. Zheng, X. et al. Differential clock comparisons with a multiplexed optical lattice clock. *Nature* <https://doi.org/10.1038/s41586-021-04344-y> (2022).
35. Matei, D. G. et al. 1.5  $\mu\text{m}$  lasers with sub-10 mHz linewidth. *Phys. Rev. Lett.* **118**, 263202 (2017).
36. Lemonde, P., Brusch, A., Targat, R. L., Baillard, X. & Fouche, M. Hyperpolarizability effects in a Sr optical lattice clock. *Phys. Rev. Lett.* **96**, 103003 (2006).
37. Lodewyck, J., Zawada, M., Lorini, L., Gurov, M. & Lemonde, P. Observation and cancellation of a perturbing dc Stark shift in strontium optical lattice clocks. *IEEE Trans. Ultrason. Ferroelectr. Freq. Control* **59**, 411–415 (2012).
38. Leibfried, D., Blatt, R., Monroe, C. & Wineland, D. Quantum dynamics of single trapped ions. *Rev. Mod. Phys.* **75**, 281–324 (2003).
39. Boyd, M. M. et al. Nuclear spin effects in optical lattice clocks. *Phys. Rev. A* **76**, 022510 (2007).
40. Martin, M. J. et al. A quantum many-body spin system in an optical lattice clock. *Science* **341**, 632–636 (2013).
41. Ushijima, I. et al. Operational magic intensity for Sr optical lattice clocks. *Phys. Rev. Lett.* **121**, 263202 (2018).
42. van Westrum, D. *Geodetic Survey of NIST and JILA Clock Laboratories, Boulder, Colorado* (NOAA, 2019).

## Acknowledgements

We acknowledge funding support from the Defense Advanced Research Projects Agency, National Science Foundation QLCI OMA-2016244, the DOE Quantum System Accelerator, the National Institute of Standards and Technology, National Science Foundation Phys-1734006 and the Air Force Office for Scientific Research. We are grateful for theory insight from A.

Chu, P. He and A. M. Rey. We acknowledge J. Zaris, J. Uhrich, J. Meyer, R. Hutson, C. Sanner, W. Milner, L. Sonderhouse, L. Yan, M. Miklos, Y. M. Tso and S. Kolkowitz for stimulating discussions and technical contributions. We thank J. Thompson, C. Regal, J. Hall and S. Haroche for careful reading of the manuscript.

## Author information

### Author notes

1. Colin J. Kennedy

Present address: Quantinuum, Broomfield, CO, USA

2. Eric Oelker

Present address: Physics Department, University of Glasgow, Glasgow, UK

## Affiliations

1. JILA, National Institute of Standards and Technology and University of Colorado, Department of Physics, University of Colorado, Boulder, CO, USA

Tobias Bothwell, Colin J. Kennedy, Alexander Aeppli, Dhruv Kedar, John M. Robinson, Eric Oelker, Alexander Staron & Jun Ye

## Contributions

All authors contributed to carrying out the experiments, interpreting the results and writing the manuscript.

## Corresponding authors

Correspondence to [Tobias Bothwell](#) or [Jun Ye](#).

# Ethics declarations

## Competing interests

The authors declare no competing interests.

## Peer review

### Peer review information

*Nature* thanks the anonymous reviewers for their contribution to the peer review of this work. Peer reviewer reports are available.

## Additional information

**Publisher's note** Springer Nature remains neutral with regard to jurisdictional claims in published maps and institutional affiliations.

## Extended data figures and tables

### Extended Data Table 1 Gradient Systematic Budget

## Supplementary information

### [Peer Review File](#)

## Rights and permissions

### [Reprints and Permissions](#)

## About this article

### Cite this article

Bothwell, T., Kennedy, C.J., Aepli, A. *et al.* Resolving the gravitational redshift across a millimetre-scale atomic sample. *Nature* **602**, 420–424 (2022). <https://doi.org/10.1038/s41586-021-04349-7>

- Received: 24 September 2021
- Accepted: 13 December 2021
- Published: 16 February 2022
- Issue Date: 17 February 2022
- DOI: <https://doi.org/10.1038/s41586-021-04349-7>

## Share this article

Anyone you share the following link with will be able to read this content:

[Get shareable link](#)

Sorry, a shareable link is not currently available for this article.

[Copy to clipboard](#)

Provided by the Springer Nature SharedIt content-sharing initiative

## [\*\*Atomic clouds stabilized to measure dilation of time\*\*](#)

- Ksenia Khabarova

News & Views 16 Feb 2022

---

This article was downloaded by **calibre** from <https://www.nature.com/articles/s41586-021-04349-7>

- Article
- [Published: 16 February 2022](#)

# Differential clock comparisons with a multiplexed optical lattice clock

- [Xin Zheng ORCID: orcid.org/0000-0003-4745-8070<sup>1</sup>](#),
- [Jonathan Dolde<sup>1</sup>](#),
- [Varun Lochab<sup>1</sup>](#),
- [Brett N. Merriman<sup>1</sup>](#),
- [Haoran Li<sup>1</sup>](#) &
- [Shimon Kolkowitz ORCID: orcid.org/0000-0001-7095-1547<sup>1</sup>](#)

[Nature](#) volume **602**, pages 425–430 (2022)

- 1242 Accesses
- 174 Altmetric
- [Metrics details](#)

## Subjects

- [Atomic and molecular physics](#)
- [Quantum metrology](#)
- [Optical spectroscopy](#)

## Abstract

Rapid progress in optical atomic clock performance has advanced the frontiers of timekeeping, metrology and quantum science<sup>1,2,3</sup>. Despite considerable efforts, the instabilities of most optical clocks remain limited

by the local oscillator rather than the atoms themselves<sup>4,5</sup>. Here we implement a ‘multiplexed’ one-dimensional optical lattice clock, in which spatially resolved strontium atom ensembles are trapped in the same optical lattice, interrogated simultaneously by a shared clock laser and read-out in parallel. In synchronous Ramsey interrogations of ensemble pairs we observe atom–atom coherence times of 26 s, a 270-fold improvement over the measured atom–laser coherence time, demonstrate a relative instability of  $\sqrt{9.7(4) \times 10^{-18} / \tau}$  (where  $\tau$  is the averaging time) and reach a relative statistical uncertainty of  $8.9 \times 10^{-20}$  after 3.3 h of averaging. These results demonstrate that applications involving optical clock comparisons need not be limited by the instability of the local oscillator. We further realize a miniaturized clock network consisting of 6 atomic ensembles and 15 simultaneous pairwise comparisons with relative instabilities below  $\sqrt{3 \times 10^{-17} / \tau}$ , and prepare spatially resolved, heterogeneous ensemble pairs of all four stable strontium isotopes. These results pave the way for multiplexed precision isotope shift measurements, spatially resolved characterization of limiting clock systematics, the development of clock-based gravitational wave and dark matter detectors<sup>6,7,8,9,10,11,12</sup> and new tests of relativity in the lab<sup>13,14,15,16</sup>.

This is a preview of subscription content

## Access options

Subscribe to Nature+

Get immediate online access to the entire Nature family of 50+ journals

\$29.99

monthly

[Subscribe](#)

Subscribe to Journal

Get full journal access for 1 year

\$199.00

only \$3.90 per issue

[Subscribe](#)

All prices are NET prices.

VAT will be added later in the checkout.

Tax calculation will be finalised during checkout.

Buy article

Get time limited or full article access on ReadCube.

\$32.00

[Buy](#)

All prices are NET prices.

### **Additional access options:**

- [Log in](#)
- [Learn about institutional subscriptions](#)

**Fig. 1: Multiplexed OLC configuration and procedure for loading two ensembles.**

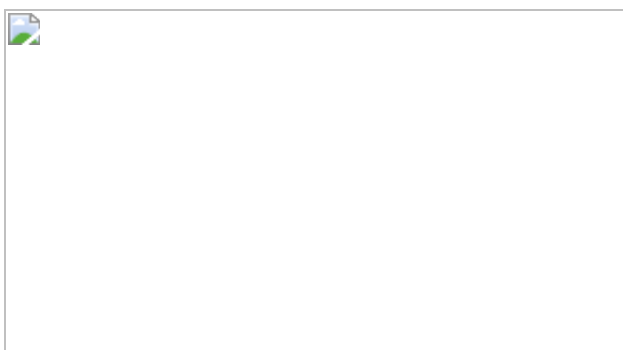


**Fig. 2: Characterization of atom–atom coherence time by synchronous clock comparisons.**

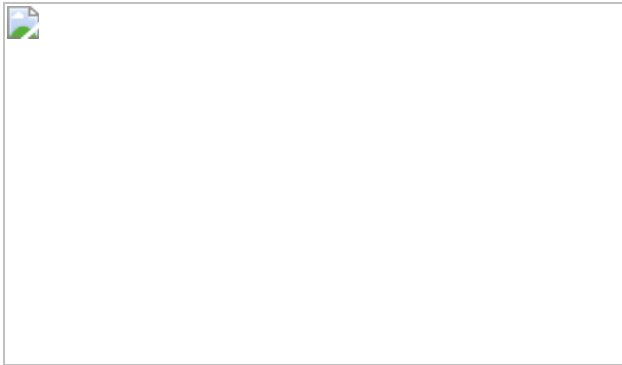


**Fig. 3: Low relative instability with multiplexed Ramsey interrogation.**

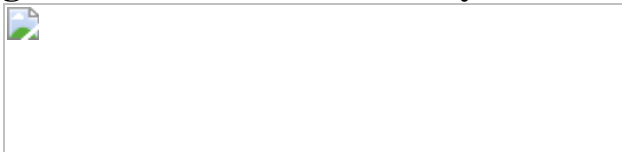
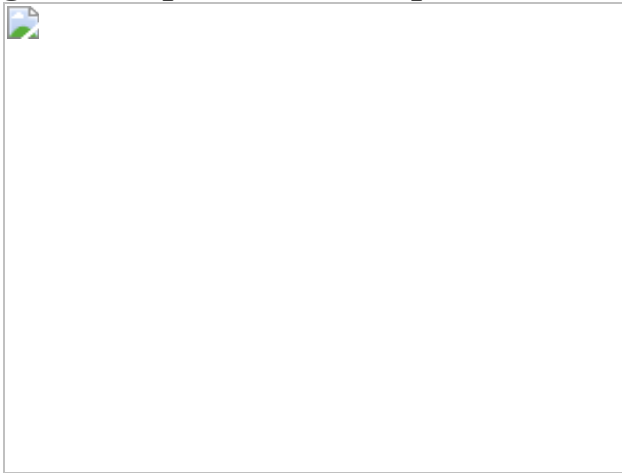


**Fig. 4: Prospects for multiplexed OLC comparisons.**



## Data availability

The experimental data presented in this manuscript are available from the corresponding author upon reasonable request. [Source data](#) are provided with this paper.

## Code availability

The code used for experimental control, data analysis and simulation in this work are available from the corresponding author upon reasonable request.

## References

1. Ludlow, A. D., Boyd, M. M., Ye, J., Peik, E. & Schmidt, P. O. Optical atomic clocks. *Rev. Mod. Phys.* **87**, 637–701 (2015).
2. Campbell, S. L. et al. A Fermi-degenerate three-dimensional optical lattice clock. *Science* **358**, 90–94 (2017).
3. McGrew, W. F. et al. Atomic clock performance enabling geodesy below the centimetre level. *Nature* **564**, 87–90 (2018).
4. Schioppo, M. et al. Ultrastable optical clock with two cold-atom ensembles. *Nat. Photon.* **11**, 48–52 (2017).
5. Oelker, E. et al. Demonstration of  $4.8 \times 10^{-17}$  stability at 1 s for two independent optical clocks. *Nat. Photon.* **13**, 714–719 (2019).
6. Safronova, M. S. et al. Search for new physics with atoms and molecules. *Rev. Mod. Phys.* **90**, 025008 (2018).
7. Kolkowitz, S. et al. Gravitational wave detection with optical lattice atomic clocks. *Phys. Rev. D* **94**, 124043 (2016).
8. Stadnik, Y. V. & Flambaum, V. V. Improved limits on interactions of low-mass spin-0 dark matter from atomic clock spectroscopy. *Phys. Rev. A* **94**, 022111 (2016).
9. Derevianko, A. & Pospelov, M. Hunting for topological dark matter with atomic clocks. *Nat. Phys.* **10**, 933–936 (2014).
10. Arvanitaki, A., Huang, J. W. & Van Tilburg, K. Searching for dilaton dark matter with atomic clocks. *Phys. Rev. D* **91**, 015015 (2015).
11. Wcisło, P. et al. New bounds on dark matter coupling from a global network of optical atomic clocks. *Sci. Adv.* **4**, eaau4869 (2018).
12. Kennedy, C. J. et al. Precision metrology meets cosmology: improved constraints on ultralight dark matter from atom-cavity frequency

- comparisons. *Phys. Rev. Lett.* **125**, 201302 (2020).
- 13. Chou, C. W., Hume, D. B., Rosenband, T. & Wineland, D. J. Optical clocks and relativity. *Science* **329**, 1630–1633 (2010).
  - 14. Takano, T. et al. Geopotential measurements with synchronously linked optical lattice clocks. *Nat. Photon.* **10**, 662–666 (2016).
  - 15. Grotti, J. et al. Geodesy and metrology with a transportable optical clock. *Nat. Phys.* **14**, 437–441 (2018).
  - 16. Takamoto, M. et al. Test of general relativity by a pair of transportable optical lattice clocks. *Nat. Photon.* **14**, 411–415 (2020).
  - 17. Hinkley, N. et al. An atomic clock with  $10^{-18}$  instability. *Science* **341**, 1215–1218 (2013).
  - 18. Bloom, B. J. et al. An optical lattice clock with accuracy and stability at the  $10^{-18}$  level. *Nature* **506**, 71–75 (2014).
  - 19. Marti, G. E. et al. Imaging optical frequencies with  $100 \mu\text{Hz}$  precision and  $1.1 \mu\text{m}$  resolution. *Phys. Rev. Lett.* **120**, 103201 (2018).
  - 20. Bothwell, T. et al. JILA SrI optical lattice clock with uncertainty of  $2.0 \times 10^{-18}$ . *Metrologia* **56**, 065004 (2019).
  - 21. Boulder Atomic Clock Optical Network (BACON) Collaboration. Frequency ratio measurements at 18-digit accuracy using an optical clock network. *Nature* **591**, 564–569 (2021).
  - 22. Itano, W. M. et al. Quantum projection noise: population fluctuations in two-level systems. *Phys. Rev. A* **47**, 3554 (1993).
  - 23. Dick, G. J., Prestage, J. D., Greenhall, C. A. & Maleki, L. Local oscillator induced degradation of medium-term stability in passive atomic frequency standards. In *Proc. 22nd Precise Time and Time Interval Meeting* (Ed. Sydnor, R. L.) 487–508 (NASA, 1990).

24. Kim, M. E. et al. Optical coherence between atomic species at the second scale: improved clock comparisons via differential spectroscopy. Preprint at <https://arxiv.org/abs/2109.09540> (2021).
25. Nicholson, T. L. et al. Comparison of two independent Sr optical clocks with  $1 \times 10^{-17}$  stability at  $10^3$  s. *Phys. Rev. Lett.* **109**, 230801 (2012).
26. Clements, E. R. et al. Lifetime-limited interrogation of two independent  $^{27}\text{Al}^+$  clocks using correlation spectroscopy. *Phys. Rev. Lett.* **125**, 243602 (2020).
27. Young, A. W. et al. Half-minute-scale atomic coherence and high relative stability in a tweezer clock. *Nature* **588**, 408–413 (2020).
28. Matei, D. G. et al.  $1.5\ \mu\text{m}$  lasers with sub-10 mHz linewidth. *Phys. Rev. Lett.* **118**, 263202 (2017).
29. Swallows, M. D. et al. Suppression of collisional shifts in a strongly interacting lattice clock. *Science* **331**, 1043–1046 (2011).
30. Martin, M. J. et al. A quantum many-body spin system in an optical lattice clock. *Science* **341**, 632–636 (2013).
31. Blatt, S. et al. Rabi spectroscopy and excitation inhomogeneity in a one-dimensional optical lattice clock. *Phys. Rev. A* **80**, 052703 (2009).
32. Hutson, R. B. et al. Engineering quantum states of matter for atomic clocks in shallow optical lattices. *Phys. Rev. Lett.* **123**, 123401 (2019).
33. Pedrozo-Peñafield, E. et al. Entanglement on an optical atomic-clock transition. *Nature* **588**, 414–418 (2020).
34. Beloy, K. et al. Faraday-shielded dc stark-shift-free optical lattice clock. *Phys. Rev. Lett.* **120**, 183201 (2018).
35. Zhang, W. et al. Ultrastable silicon cavity in a continuously operating closed-cycle cryostat at 4 K. *Phys. Rev. Lett.* **119**, 243601 (2017).

36. Milner, W. R. et al. Demonstration of a timescale based on a stable optical carrier. *Phys. Rev. Lett.* **123**, 173201 (2019).
37. Norcia, M. A. et al. Seconds-scale coherence on an optical clock transition in a tweezer array. *Science* **366**, 93–97 (2019).
38. Dörscher, S. et al. Lattice-induced photon scattering in an optical lattice clock. *Phys. Rev. A* **97**, 063419 (2018).
39. Boyd, M. M. et al. Nuclear spin effects in optical lattice clocks. *Phys. Rev. A* **76**, 022510 (2007).
40. Delaunay, C., Ozeri, R., Perez, G. & Soreq, Y. Probing atomic Higgs-like forces at the precision frontier. *Phys. Rev. D* **96**, 093001 (2017).
41. Berengut, J. C. et al. Probing new long-range interactions by isotope shift spectroscopy. *Phys. Rev. Lett.* **120**, 091801 (2018).
42. Takano, T., Mizushima, R. & Katori, H. Precise determination of the isotope shift of  $^{88}\text{Sr} - ^{87}\text{Sr}$  optical lattice clock by sharing perturbations. *Appl. Phys. Express* **10**, 072801 (2017).
43. Miyake, H., Pisenti, N. C., Elgee, P. K., Sitaram, A. & Campbell, G. K. Isotope-shift spectroscopy of the  $^1S_0 \rightarrow ^3P_1$  and  $^1S_0 \rightarrow ^3P_0$  transitions in strontium. *Phys. Rev. Res.* **1**, 033113 (2019).
44. Counts, I. & Hur, J. et al. Evidence for nonlinear isotope shift in  $\text{Yb}^+$  search for new boson. *Phys. Rev. Lett.* **125**, 123002 (2020).
45. Taichenachev, A. V. et al. Magnetic field-induced spectroscopy of forbidden optical transitions with application to lattice-based optical atomic clocks. *Phys. Rev. Lett.* **96**, 083001 (2006).
46. Madjarov, I. S. et al. An atomic-array optical clock with single-atom readout. *Phys. Rev. X* **9**, 041052 (2019).
47. Gil, L. I. R., Mukherjee, R., Bridge, E. M., Jones, M. P. A. & Pohl, T. Spin squeezing in a Rydberg lattice clock. *Phys. Rev. Lett.* **112**, 103601

(2014).

48. Van Damme, J., Zheng, X., Saffman, M., Vavilov, M. G. & Kolkowitz, S. Impacts of random filling on spin squeezing via Rydberg dressing in optical clocks. *Phys. Rev. A* **103**, 023106 (2021).
49. Bothwell, T. et al. Resolving the gravitational redshift within a millimeter atomic sample. *Nature* <https://doi.org/10.1038/s41586-021-04349-7> (2022).
50. Lemonde, P. & Wolf, P. Optical lattice clock with atoms confined in a shallow trap. *Phys. Rev. A* **72**, 033409 (2005).
51. Campbell, G. K. et al. The absolute frequency of the  $^{87}\text{Sr}$  optical clock transition. *Metrologia* **45**, 539 (2008).
52. Schmid, S., Thalhammer, G., Winkler, K., Lang, F. & Denschlag, J. H. Long distance transport of ultracold atoms using a 1D optical lattice. *New J. Phys.* **8**, 159 (2006).
53. Ma, L. S., Jungner, P., Ye, J. & Hall, J. L. Delivering the same optical frequency at two places: accurate cancellation of phase noise introduced by an optical fiber or other time-varying path. *Opt. Lett.* **19**, 1777–1779 (1994).
54. Falke, S., Misera, M., Sterr, U. & Lisdat, C. Delivering pulsed and phase stable light to atoms of an optical clock. *Appl. Phys. B* **107**, 301–311 (2012).
55. Swallows, M. D. et al. Operating a  $^{87}\text{Sr}$  optical lattice clock with high precision and at high density. *IEEE Trans. Ultrason. Ferroelectr. Freq. Control.* **59**, 416–425 (2012).

## Acknowledgements

We thank J. Ye, A. Kaufman, J. Thompson, T. Bothwell and A. Jayich for insightful discussions and helpful feedback on the manuscript. This work

was supported in part by the NIST Precision Measurement Grants program, the Northwestern University Center for Fundamental Physics and the John Templeton Foundation through a Fundamental Physics grant, the Wisconsin Alumni Research Foundation, the Army Research Office through agreement number W911NF-21-1-0012 and a Packard Fellowship for Science and Engineering.

## Author information

### Affiliations

1. University of Wisconsin-Madison, Madison, WI, USA

Xin Zheng, Jonathan Dolde, Varun Lochab, Brett N. Merriman, Haoran Li & Shimon Kolkowitz

### Contributions

X.Z. designed and built the experimental apparatus with assistance from J.D., V.L., H.L. and B.N.M., and with guidance from S.K. All authors contributed to maintenance and operation of the experimental apparatus, data collection, data analysis and writing of the manuscript.

### Corresponding author

Correspondence to [Shimon Kolkowitz](#).

### Ethics declarations

### Competing interests

The authors declare no competing interests.

### Peer review

## Peer review information

*Nature* thanks the anonymous reviewers who contributed to the peer review of this paper. Peer reviewer reports are available.

## Additional information

**Publisher's note** Springer Nature remains neutral with regard to jurisdictional claims in published maps and institutional affiliations.

## Extended data figures and tables

### Extended Data Fig. 1 Lattice and clock path.

Schematic diagram showing the lattice and clock beam paths for the interrogation the  $|{}^1S_0, m_F = \pm 1\rangle$  transition. To interrogate the  $|{}^1S_0, m_F = \pm 3\rangle$  transition, the first order diffraction clock beam is overlapped with the lattice by first using a long-pass dichroic beam splitter and subsequently transmitting through the polarized beam splitter, shown in the dashed blue box. The inset shows the corresponding orientations of the bias magnetic field ( $B$ ) and the lattice and clock polarizations ( $\varepsilon$ ). Abbreviations: PBS, polarized beam-splitter; DBS, dichroic beam-splitter; AOM, acousto-optic-modulator; PD, photo-diode; HWP, half-waveplate; QWP, quarter-waveplate.

### Extended Data Fig. 2 Energy levels diagram.

**a**, Energy level diagram for strontium. The double-arrow lines correspond to the relevant transitions, including the 461-nm  ${}^1S_0 \leftrightarrow {}^1P_1$  transition for the first-stage MOT and imaging, the 689-nm  ${}^1S_0 \leftrightarrow {}^3P_1$  transition for narrow-linewidth MOT, spin-polarization and in-lattice-cooling, the 679-nm  ${}^3P_0 \leftrightarrow {}^3S_1$  and 707-nm  ${}^3P_2 \leftrightarrow {}^3S_1$  transitions for repumping, and the 698-nm  ${}^1S_0$

$\leftrightarrow ^3P_0$  transition for clock interrogation. The wavy lines correspond to spontaneous emission. **b**, Hyperfine clock states. Red double arrows represent clock interrogation of the  $|{}^1S_0, m_F = \pm 1\rangle \leftrightarrow |{}^3P_0, m_F = \pm 1\rangle$  transition. Blue double arrows represent clock interrogation of the  $|{}^1S_0, m_F = \pm 1\rangle \leftrightarrow |{}^3P_0, m_F = \pm 3\rangle$  transition. Grey dashed lines stand for transitions for coherent transfer of atoms from  $|{}^1S_0, m_F = \pm 1\rangle$  states to  $|{}^3P_0, m_F = \pm 3\rangle$  states.

### Extended Data Fig. 3 Timing diagram.

**a**, Typical timing diagram for a Ramsey spectroscopy sequence, in which laser cooling, state preparation and camera imaging contribute to about 1.6 s dead time, with clock interrogation time ranging from 10 ms to 20 s. **b, c**, The corresponding lattice retro detuning, lattice velocity and lattice acceleration for loading two ensembles at 1 cm separation.

### Extended Data Fig. 4 Comparison of bias correction.

**a, b**, Comparison of ‘closed-loop’ analysis with **(a)** and without **(b)** bias correction. 197 unique ‘closed-loop’ combinations are shown, with each datum corresponds to the sum frequency within each loop. Shaded area represents a window of  $1 \times 10^{-18}$ .

[Source data](#)

### Extended Data Fig. 5 Differential density shift.

**a**, Measured differential density shift as a function of atom number difference between two symmetrically prepared ensembles at 1 cm separation. The data is taken at 20  $E_{\text{rec}}$  lattice trap depth with 6 s interrogation time. Dashed line is the linear fitting, in which the slope is extracted as  $-8.5(6) \times 10^{-19}$  shift per 100 atom number difference. **b**, Scaling of differential density shift per 100 atom number difference

between ensemble pairs with lattice trap depth  $U$ . The dashed line is a fit to the expected  $\alpha U^{5/4} + \beta$  scaling<sup>20</sup>, where  $\alpha$  and  $\beta$  are fit parameters.

## [Source data](#)

**Extended Data Table 1** Measured coherence times

**Extended Data Table 2** Differential frequencies from 6 ensemble measurement

# Supplementary information

## [Supplementary Information](#)

This file contains Supplementary Information, including Supplementary Figs. 1–8 and additional references.

## [Peer Review File](#)

## Source data

### [Source Data Fig. 2](#)

### [Source Data Fig. 3](#)

### [Source Data Fig. 4](#)

### [Source Data Extended Data Fig. 4](#)

### [Source Data Extended Data Fig. 5](#)

## Rights and permissions

### [Reprints and Permissions](#)

## About this article

### Cite this article

Zheng, X., Dolde, J., Lochab, V. *et al.* Differential clock comparisons with a multiplexed optical lattice clock. *Nature* **602**, 425–430 (2022). <https://doi.org/10.1038/s41586-021-04344-y>

- Received: 24 September 2021
- Accepted: 14 December 2021
- Published: 16 February 2022
- Issue Date: 17 February 2022
- DOI: <https://doi.org/10.1038/s41586-021-04344-y>

### Share this article

Anyone you share the following link with will be able to read this content:

[Get shareable link](#)

Sorry, a shareable link is not currently available for this article.

[Copy to clipboard](#)

Provided by the Springer Nature SharedIt content-sharing initiative

### [\*\*Atomic clouds stabilized to measure dilation of time\*\*](#)

- Ksenia Khabarova

News & Views 16 Feb 2022

| [Section menu](#) | [Main menu](#) |

- Article
- [Published: 16 February 2022](#)

# Scaling of the strange-metal scattering in unconventional superconductors

- [Jie Yuan<sup>1,2</sup>](#) na1,
- [Qihong Chen<sup>1,3</sup>](#) na1,
- [Kun Jiang<sup>1</sup>](#),
- [Zhongpei Feng<sup>1,3</sup>](#),
- [Zefeng Lin<sup>1</sup>](#),
- [Heshan Yu<sup>1</sup>](#),
- [Ge He<sup>1</sup>](#),
- [Jinsong Zhang<sup>1</sup>](#),
- [Xingyu Jiang<sup>1</sup>](#),
- [Xu Zhang<sup>1</sup>](#),
- [Yujun Shi<sup>1</sup>](#),
- [Yanmin Zhang<sup>1</sup>](#),
- [Mingyang Qin<sup>1</sup>](#),
- [Zhi Gang Cheng](#) ORCID: orcid.org/0000-0002-9449-6734<sup>1,3</sup>,
- [Nobumichi Tamura](#) ORCID: orcid.org/0000-0002-3698-2611<sup>4</sup>,
- [Yi-feng Yang](#) ORCID: orcid.org/0000-0002-6702-6091<sup>1</sup>,
- [Tao Xiang<sup>1,5</sup>](#),
- [Jiangping Hu](#) ORCID: orcid.org/0000-0002-4837-7742<sup>1,3</sup>,
- [Ichiro Takeuchi](#) ORCID: orcid.org/0000-0003-2625-0553<sup>6,7</sup>,
- [Kui Jin](#) ORCID: orcid.org/0000-0003-2208-8501<sup>1,2,3</sup> &
- [Zhongxian Zhao<sup>1,2,3</sup>](#)

[Nature](#) volume **602**, pages 431–436 (2022)

- 2157 Accesses
- 16 Altmetric
- [Metrics details](#)

## Subjects

- [Electronic properties and materials](#)
- [Phase transitions and critical phenomena](#)
- [Superconducting properties and materials](#)

## Abstract

Marked evolution of properties with minute changes in the doping level is a hallmark of the complex chemistry that governs copper oxide superconductivity as manifested in the celebrated superconducting domes and quantum criticality taking place at precise compositions<sup>1,2,3,4</sup>. The strange-metal state, in which the resistivity varies linearly with temperature, has emerged as a central feature in the normal state of copper oxide superconductors<sup>5,6,7,8,9</sup>. The ubiquity of this behaviour signals an intimate link between the scattering mechanism and superconductivity<sup>10,11,12</sup>. However, a clear quantitative picture of the correlation has been lacking. Here we report the observation of precise quantitative scaling laws among the superconducting transition temperature ( $T_c$ ), the linear-in- $T$  scattering coefficient ( $A_1$ ) and the doping level ( $x$ ) in electron-doped copper oxide  $\text{La}_{2-x}\text{Ce}_x\text{CuO}_4$  (LCCO). High-resolution characterization of epitaxial composition-spread films, which encompass the entire overdoped range of LCCO, has enabled us to systematically map its structural and transport properties with unprecedented accuracy and with increments of  $\Delta x = 0.0015$ . We have uncovered the relations  $T_c \sim (x_c - x)^{0.5} \sim (A_1^\square)^{0.5}$ , where  $x_c$  is the critical doping in which superconductivity disappears and  $A_1^\square$  is the coefficient of the linear resistivity per  $\text{CuO}_2$  plane. The striking similarity of the  $T_c$  versus  $A_1^\square$  relation among copper oxides, iron-based and organic superconductors may be an indication of a common mechanism of the

strange-metal behaviour and unconventional superconductivity in these systems.

This is a preview of subscription content

## Access options

Subscribe to Nature+

Get immediate online access to the entire Nature family of 50+ journals

\$29.99

monthly

[Subscribe](#)

Subscribe to Journal

Get full journal access for 1 year

\$199.00

only \$3.90 per issue

[Subscribe](#)

All prices are NET prices.

VAT will be added later in the checkout.

Tax calculation will be finalised during checkout.

Buy article

Get time limited or full article access on ReadCube.

\$32.00

[Buy](#)

All prices are NET prices.

### **Additional access options:**

- [Log in](#)
- [Learn about institutional subscriptions](#)

**Fig. 1: Combinatorial synthesis and multiscale structural characterization of LCCO.**

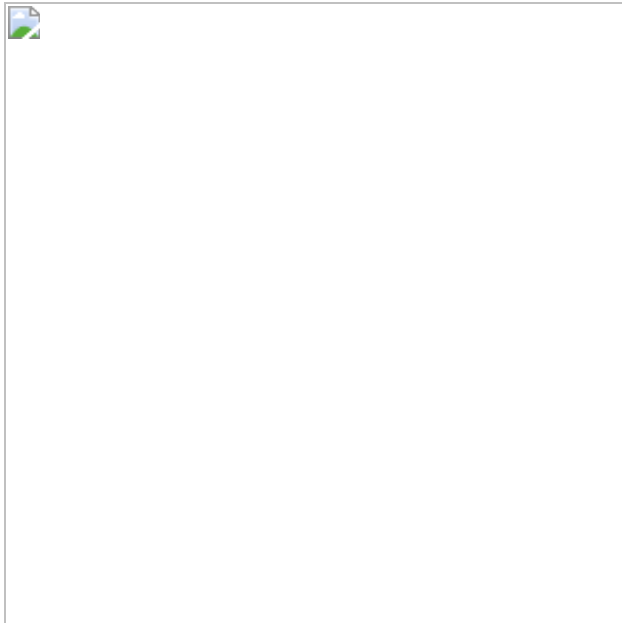


**Fig. 2: Microregion characterizations of electrical transport properties.**

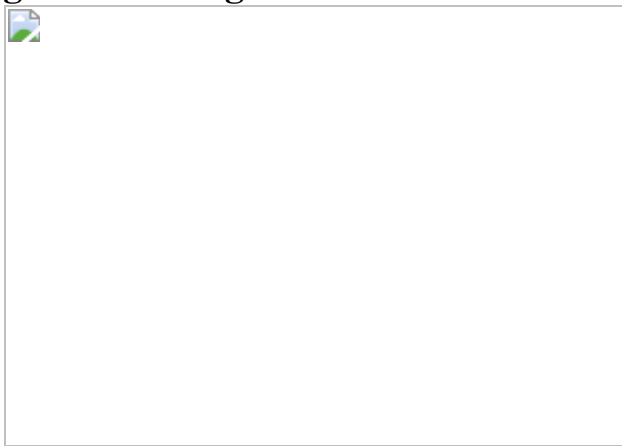
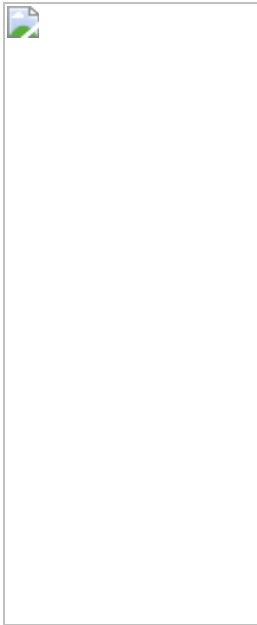


**Fig. 3: Quantitative scaling revealed from the systematic spread data and comparison of different unconventional superconductors.**



## Data availability

The data that support the findings of this study are available in the paper. Additional data are available from the corresponding authors upon reasonable request.

## References

1. Lee, P. A., Nagaosa, N. & Wen, X.-G. Doping a Mott insulator: physics of high-temperature superconductivity. *Rev. Mod. Phys.* **78**, 17–85 (2006).
2. Armitage, N. P., Fournier, P. & Greene, R. L. Progress and perspectives on electron-doped cuprates. *Rev. Mod. Phys.* **82**, 2421–2487 (2010).
3. Scalapino, D. J. A common thread: the pairing interaction for unconventional superconductors. *Rev. Mod. Phys.* **84**, 1383–1417 (2012).
4. Keimer, B., Kivelson, S. A., Norman, M. R., Uchida, S. & Zaanen, J. From quantum matter to high-temperature superconductivity in copper

- oxides. *Nature* **518**, 179–186 (2015).
5. Gurvitch, M. & Fiory, A. T. Resistivity of  $\text{La}_{1.825}\text{Sr}_{0.175}\text{CuO}_4$  and  $\text{YBa}_2\text{Cu}_3\text{O}_7$  to 1100 K: absence of saturation and its implications. *Phys. Rev. Lett.* **59**, 1337–1340 (1987).
  6. Takagi, H. et al. Systematic evolution of temperature-dependent resistivity in  $\text{La}_{2-x}\text{Sr}_x\text{CuO}_4$ . *Phys. Rev. Lett.* **69**, 2975–2978 (1992).
  7. Cooper, R. A. et al. Anomalous criticality in the electrical resistivity of  $\text{La}_{2-x}\text{Sr}_x\text{CuO}_4$ . *Science* **323**, 603–607 (2009).
  8. Fournier, P. et al. Insulator-metal crossover near optimal doping in  $\text{Pr}_{2-x}\text{Ce}_x\text{CuO}_4$ : anomalous normal-state low temperature resistivity. *Phys. Rev. Lett.* **81**, 4720–4723 (1998).
  9. Jin, K., Butch, N. P., Kirshenbaum, K., Paglione, J. & Greene, R. L. Link between spin fluctuations and electron pairing in copper oxide superconductors. *Nature* **476**, 73–75 (2011).
  10. Taillefer, L. Scattering and pairing in cuprate superconductors. *Annu. Rev. Condens. Matter Phys.* **1**, 51–70 (2010).
  11. Greene, R. L., Mandal, P. R., Poniatowski, N. R. & Sarkar, T. The strange metal state of the electron-doped cuprates. *Annu. Rev. Condens. Matter Phys.* **11**, 213–229 (2020).
  12. Varma, C. M. Colloquium: linear in temperature resistivity and associated mysteries including high temperature superconductivity. *Rev. Mod. Phys.* **92**, 031001 (2020).
  13. Sarkar, T. et al. Hidden strange metallic state in underdoped electron-doped cuprates. *Phys. Rev. B* **103**, 224501 (2021).
  14. Koinuma, H. & Takeuchi, I. Combinatorial solid-state chemistry of inorganic materials. *Nat. Mater.* **3**, 429–438 (2004).

15. Yuan, J., Stanev, V., Gao, C., Takeuchi, I. & Jin, K. Recent advances in high-throughput superconductivity research. *Supercond. Sci. Technol.* **32**, 123001 (2019).
16. Sarkar, T. et al. Ferromagnetic order beyond the superconducting dome in a cuprate superconductor. *Science* **368**, 532–534 (2020).
17. Schneider, T. & Singer, J. M. *Phase Transition Approach to High Temperature Superconductivity* (Imperial College Press, 2000).
18. Legros, A. et al. Universal T-linear resistivity and Planckian dissipation in overdoped cuprates. *Nat. Phys.* **15**, 142–147 (2019).
19. Ayres, J. et al. Incoherent transport across the strange-metal regime of overdoped cuprates. *Nature* **595**, 661–666 (2021).
20. Božović, I., He, X., Wu, J. & Bollinger, A. T. Dependence of the critical temperature in overdoped copper oxides on superfluid density. *Nature* **536**, 309–311 (2016).
21. Anderson, P. W. The resonating valence bond state in  $\text{La}_2\text{CuO}_4$  and superconductivity. *Sci. New Ser.* **235**, 1196–1198 (1987).
22. Varma, C. M., Littlewood, P. B., Schmitt-Rink, S., Abrahams, E. & Ruckenstein, A. E. Phenomenology of the normal state of Cu-O high-temperature superconductors. *Phys. Rev. Lett.* **63**, 1996–1999 (1989).
23. Sachdev, S. Quantum phase transitions. *Phys. World* **12**, 33–38 (1999).
24. Zaanen, J. Why the temperature is high. *Nature* **430**, 512–513 (2004).
25. Bruin, J. a. N., Sakai, H., Perry, R. S. & Mackenzie, A. P. Similarity of scattering rates in metals showing T-linear resistivity. *Science* **339**, 804–807 (2013).
26. Licciardello, S. et al. Electrical resistivity across a nematic quantum critical point. *Nature* **567**, 213–217 (2019).

27. Moriya, T. & Ueda, K. Spin fluctuations and high temperature superconductivity. *Adv. Phys.* **49**, 555–606 (2000).
28. Monthoux, P. & Pines, D. Spin-fluctuation-induced superconductivity and normal-state properties of  $\text{YBa}_2\text{Cu}_3\text{O}_7$ . *Phys. Rev. B* **49**, 4261–4278 (1994).
29. Bourbonnais, C. & Sedeki, A. Link between antiferromagnetism and superconductivity probed by nuclear spin relaxation in organic conductors. *Phys. Rev. B* **80**, 085105 (2009).
30. Doiron-Leyraud, N. et al. Correlation between linear resistivity and  $T_c$  in the Bechgaard salts and the pnictide superconductor  $\text{Ba}(\text{Fe}_{1-x}\text{Co}_x)_2\text{As}_2$ . *Phys. Rev. B* **80**, 214531 (2009).
31. Sedeki, A., Bergeron, D. & Bourbonnais, C. Extended quantum criticality of low-dimensional superconductors near a spin-density-wave instability. *Phys. Rev. B* **85**, 165129 (2012).
32. Fang, L. et al. Roles of multiband effects and electron-hole asymmetry in the superconductivity and normal-state properties of  $\text{Ba}(\text{Fe}_{1-x}\text{Co}_x)_2\text{As}_2$ . *Phys. Rev. B* **80**, 140508 (2009).
33. Fradkin, E., Kivelson, S. A. & Tranquada, J. M. Colloquium: theory of intertwined orders in high temperature superconductors. *Rev. Mod. Phys.* **87**, 457–482 (2015).
34. Rullier-Albenque, F., Alloul, H. & Tourbot, R. Influence of pair breaking and phase fluctuations on disordered high  $T_c$  cuprate superconductors. *Phys. Rev. Lett.* **91**, 047001 (2003).
35. Emery, V. J. & Kivelson, S. A. Superconductivity in bad metals. *Phys. Rev. Lett.* **74**, 3253–3256 (1995).
36. Hussey, N. E., Gordon-Moys, H., Kokalj, J. & McKenzie, R. H. Generic strange-metal behaviour of overdoped cuprates. *J. Phys. Conf. Ser.* **449**, 012004 (2013).

37. Maier, T. A., Karakuzu, S. & Scalapino, D. J. Overdoped end of the cuprate phase diagram. *Phys. Rev. Res.* **2**, 033132 (2020).
38. Zhang, X. et al. Quantum criticality tuned by magnetic field in optimally electron-doped cuprate thin films. *Phys. Rev. B* **103**, 014517 (2021).
39. Jin, K., Zhu, B. Y., Wu, B. X., Gao, L. J. & Zhao, B. R. Low-temperature Hall effect in electron-doped superconducting  $\text{La}_{2-x}\text{Ce}_x\text{CuO}_4$  thin films. *Phys. Rev. B* **78**, 174521 (2008).
40. Jin, K., Zhang, X. H., Bach, P. & Greene, R. L. Evidence for antiferromagnetic order in  $\text{La}_{2-x}\text{Ce}_x\text{CuO}_4$  from angular magnetoresistance measurements. *Phys. Rev. B* **80**, 012501 (2009).
41. Sarkar, T. et al. Fermi surface reconstruction and anomalous low-temperature resistivity in electron-doped  $\text{La}_{2-x}\text{Ce}_x\text{CuO}_4$ . *Phys. Rev. B* **96**, 155449 (2017).
42. Ando, Y., Komiya, S., Segawa, K., Ono, S. & Kurita, Y. Electronic phase diagram of high- $T_c$  cuprate superconductors from a mapping of the in-plane resistivity curvature. *Phys. Rev. Lett.* **93**, 267001 (2004).

## Acknowledgements

We thank R. Greene for many fruitful discussions and inspiring comments during the preparation of the manuscript. We thank T. Schneider for discussions surrounding the scaling relations. We thank G. Zhang, Z. Weng, Y. Li, Y. Zhou and E. Liu for fruitful discussions. We thank S. Tu and Y. Zou for experimental assistance. This work was supported by the National Key Basic Research Program of China (grant nos. 2017YFA0302900, 2017YFA0303003 and 2018YFB0704102), the National Natural Science Foundation of China (grant nos. 11888101, 11927808, 11834016 and 11961141008), Beijing Natural Science Foundation (grant no. Z190008), the Strategic Priority Research Program (B) of Chinese Academy of Sciences (grant nos. XDB25000000 and XDB33000000), the CAS

Interdisciplinary Innovation Team, Key-Area Research and Development Program of Guangdong Province (grant no. 2020B0101340002). The work at the University of Maryland was supported by grant nos. AFOSR FA9550-14-10332, AFOSR FA9550-22-10023, ONR N00014-13-1-0635 and ONR N00014-15-2-222, and NIST grant no. 60NANB19D027. This research used BL12.3.2 of the Advanced Light Source, a US Department of Energy Office of Science User Facility under contract no. DE-AC02-05CH11231.

## Author information

### Author notes

1. These authors contributed equally: Jie Yuan, Qihong Chen

### Affiliations

1. Beijing National Laboratory for Condensed Matter Physics, Institute of Physics, Chinese Academy of Sciences, Beijing, China

Jie Yuan, Qihong Chen, Kun Jiang, Zhongpei Feng, Zefeng Lin, Heshan Yu, Ge He, Jinsong Zhang, Xingyu Jiang, Xu Zhang, Yujun Shi, Yanmin Zhang, Mingyang Qin, Zhi Gang Cheng, Yi-feng Yang, Tao Xiang, Jiangping Hu, Kui Jin & Zhongxian Zhao

2. Key Laboratory of Vacuum Physics, School of Physical Sciences, University of Chinese Academy of Sciences, Beijing, China

Jie Yuan, Kui Jin & Zhongxian Zhao

3. Songshan Lake Materials Laboratory, Dongguan, Guangdong, China

Qihong Chen, Zhongpei Feng, Zhi Gang Cheng, Jiangping Hu, Kui Jin & Zhongxian Zhao

4. Advanced Light Source, Lawrence Berkeley National Laboratory,  
Berkeley, CA, USA

Nobumichi Tamura

5. Beijing Academy of Quantum Information Sciences, Beijing, China

Tao Xiang

6. Department of Materials Science and Engineering, University of  
Maryland, College Park, MD, USA

Ichiro Takeuchi

7. Maryland Quantum Materials Center, Department of Physics,  
University of Maryland, College Park, MD, USA

Ichiro Takeuchi

## Contributions

K. Jin conceived the project. K. Jin, J.Y. and Q.C. supervised the experiments. Z.F., Z.L. and H.Y. synthesized the composition-spread films. G.H., J.Z., X.Z. and M.Q. performed the transport measurements. N.T. and I.T. carried out the synchrotron XRD measurements. X.J., Y.S., Y.Z., Z.G.C., I.T., J.Y., Q.C., K. Jin and Z.Z. analysed the experimental data. K. Jiang, Y.-f.Y., T.X. and J.H. provided theoretical understanding. Q.C, J.Y., I.T. and K. Jin wrote the manuscript with input from all authors.

## Corresponding authors

Correspondence to [Jiangping Hu](#), [Ichiro Takeuchi](#) or [Kui Jin](#).

## Ethics declarations

## Competing interests

The authors declare no competing interests.

## Peer review information

### Peer review information

*Nature* thanks the anonymous reviewers for their contribution to the peer review of this work.

## Additional information

**Publisher's note** Springer Nature remains neutral with regard to jurisdictional claims in published maps and institutional affiliations.

## Extended data figures and tables

### [Extended Data Fig. 1 Temperature dependence of resistivity for different bridges \(100- \$\mu\text{m}\$ width\) across a combinatorial \$\text{La}\_{2-x}\text{Ce}\_x\text{CuO}\_4\$ \(LCCO\) film.](#)

**a**, The doping varies from 0.123 to 0.185 from the top to the bottom, as indicated by the arrow. These curves provide the raw data for extracting the  $A_1^\square$  vs.  $x$ , and  $A_1^\square$  vs.  $T_c$  dependences shown in Figs. 3a and 3b of the main text. **b**, The low-temperature range of the colored lines in panel **a**. The doping for each curve is (normal-state resistivity from top to bottom): 0.123, 0.129, 0.138, 0.144, 0.148, 0.152, 0.156, 0.160, 0.162, 0.165, 0.167, 0.168, 0.169, and 0.175.

### [Extended Data Fig. 2 Definition of \$T\_c\$ in the main text.](#)

The solid red curve is a typical  $\rho(T)$  curve of a 100- $\mu\text{m}$  bridge from the combinatorial  $\text{La}_{2-x}\text{Ce}_x\text{CuO}_4$  (LCCO) film. The black dashed line is a linear extension of the normal-state resistivity to lower temperatures. The arrow

indicates where the resistivity starts to deviate from the linear extension, which is defined as  $T_c$  in this work.

### Extended Data Fig. 3 Comparison of different $T_c$ definitions.

**a**,  $T_c$ (cross) is defined as the temperature where the linear extrapolation crosses extrapolation of the bulk of the resistance drop due to superconducting transition.  $T_c(90\%R_N)$  is defined as the temperature where the resistivity is 90% of the normal-state resistivity. The lower dashed line is obtained by maintaining the slope of the linear extrapolation of the normal-state resistivity, while multiplying the intercept by 0.9. **b**,  $T_c$  as a function of doping. The solid line shows the fit with the formula:  $T_c \propto (x_c - x)^{0.5}$ . **c**, Comparison of the scaling relation between  $(A_1^{\square})^{0.5}$  and different definitions of  $T_c$ . **d**,  $T_{c0}$  is extracted by extrapolating the bulk of the resistance drop to zero resistivity. **e**,  $T_c$  as a function of doping. The solid line shows the fit with the formula:  $T_c \propto (x_c - x)^{0.5}$ . **f**, Comparison of the scaling relation between  $(A_1^{\square})^{0.5}$  vs.  $T_c$ (onset) and  $(A_1^{\square})^{0.5}$  vs.  $T_{c0}$ . Although there are a few kelvins difference between different definitions of  $T_c$ , the parabolic relation between  $T_c$  and  $x$  and linear scaling relation between  $(A_1^{\square})^{0.5}$  and  $T_c$  are valid in all three.

### Extended Data Fig. 4 Linear-in- $T$ resistivity in superconducting LCCO.

**a–b**, Temperature dependence of resistivity  $\rho(T)$  in zero field (diamonds), fitted by  $\rho(T) = \rho_0 + A_1 T$  (red line), for  $x \approx 0.123$  (**a**) and  $0.146$  (**b**). **c**,  $\rho(T)$  of  $x \approx 0.160$  at  $B = 0$  (grey diamonds) and  $B = 5$  T (blue circles). The red line is the linear fit to the 5 T data. The insets show the fitting quality presented as  $\Delta\rho / \rho_0$  vs.  $T$ , where  $\Delta\rho = \rho - (\rho_0 + A_1 T)$ .

### Extended Data Fig. 5 Temperature dependence of resistivity for the LCCO film around optimal doping ( $x = 0.10$ ).

Magnetic fields are applied along the  $c$ -axis direction of the LCCO film: 0 T (black squares), 15 T (green circles) and 55 T (orange diamonds). The linear-in- $T$  resistivity is gradually recovered at high magnetic fields. Dashed lines mark the linear-in- $T$  resistivity region at  $B = 0$  and 55 T. Data adapted from ref. [38](#).

### Extended Data Fig. 6 Evolution of Hall signal as a function of doping measured on a combinatorial film.

**a–e**, The Hall resistivity ( $\rho_{xy}$ ) as a function of magnetic field (applied perpendicular to the  $ab$ -plane of the LCCO film) at different temperatures, for Ce doping  $x \approx 0.117$  (a), 0.132 (b), 0.145 (c), 0.157 (d), and 0.174 (e). **f**,  $\rho_{xy}$  vs.  $B$  at  $T = 2$  K for different Ce concentrations from 0.117 to 0.174. **g**, Temperature dependence of the Hall coefficient ( $R_H$ ) for different Ce concentrations from 0.117 to 0.174, measured at a magnetic field of 14 T. **h**,  $R_H$  at  $T = 2$  K and  $B = 14$  T as a function of Ce doping. **i**, The corresponding Ce doping dependence of Hall number  $n_H = V/eR_H$ .

### Extended Data Fig. 7 $T_c$ versus $x$ plots for different unconventional superconductors.

Symbols are data extracted from literature and solid curves are fits with the formula  $T_c \propto (x_c - x)^n$ , with  $n$  being a fitting parameter. **a**, Data for  $\text{Ba}(\text{Fe}_{1-x}\text{Co}_x)_2\text{As}_2$  extracted from ref. [10](#). **b**, Data for  $\text{La}_{2-x}\text{Sr}_x\text{CuO}_4$  (black squares: ref. [17](#); green dots: ref. [7](#); blue triangles: ref. [42](#)). **c**, Data for  $\text{La}_{2-x}\text{Sr}_x\text{CuO}_4$  extracted from the  $\rho(T)$  curves of ref. [20](#). The exponent  $n$  for different materials fall in the range of 0.4–0.6. For  $\text{Ba}(\text{Fe}_{1-x}\text{Co}_x)_2\text{As}_2$ , the data is scarce and the fitting uncertainty is relatively large.  $\text{La}_{2-x}\text{Sr}_x\text{CuO}_4$  is one of the most intensively studied hole-doped copper oxide, thus there are more data in literature. However, data from different studies (panel b) are quite scattered thus the fit is poor. In panel c, the data are extracted from a relatively comprehensive study of  $\text{La}_{2-x}\text{Sr}_x\text{CuO}_4$  (ref. [20](#)), which is in a relatively good fit to the formula  $T_c \propto (x_c - x)^n$  with  $n = 0.51 \pm 0.07$ ,

consistent with the value reported in this work, and the uncertainty is smaller compared to the other two panels.

### **Extended Data Fig. 8 Temperature dependence of the resistivity for a bridge with $T_c \sim 10$ K ( $x = 0.16$ ) at $B = 0$ T and $B = 5$ T.**

The red straight line indicates the extrapolation of the low-temperature linear fit to higher temperatures.

### **Extended Data Table 1 Doping, $c$ -axis, $T_c$ and linear-in- $T$ coefficients for the data shown in Fig. 3 of the main text**

## Rights and permissions

### Reprints and Permissions

## About this article

### Cite this article

Yuan, J., Chen, Q., Jiang, K. *et al.* Scaling of the strange-metal scattering in unconventional superconductors. *Nature* **602**, 431–436 (2022).  
<https://doi.org/10.1038/s41586-021-04305-5>

- Received: 30 March 2021
- Accepted: 29 November 2021
- Published: 16 February 2022
- Issue Date: 17 February 2022
- DOI: <https://doi.org/10.1038/s41586-021-04305-5>

## Share this article

Anyone you share the following link with will be able to read this content:

[Get shareable link](#)

Sorry, a shareable link is not currently available for this article.

[Copy to clipboard](#)

Provided by the Springer Nature SharedIt content-sharing initiative

---

This article was downloaded by **calibre** from <https://www.nature.com/articles/s41586-021-04305-5>

| [Section menu](#) | [Main menu](#) |

- Article
- Open Access
- [Published: 16 February 2022](#)

# Hydrogen trapping and embrittlement in high-strength Al alloys

- [Huan Zhao](#) [ORCID: orcid.org/0000-0001-8840-084X<sup>1</sup>](#),
- [Poulami Chakraborty<sup>1</sup>](#),
- [Dirk Ponge<sup>1</sup>](#),
- [Tilmann Hückel](#) [ORCID: orcid.org/0000-0003-0698-4891<sup>1,2</sup>](#),
- [Binhan Sun](#) [ORCID: orcid.org/0000-0001-9561-7019<sup>1,3</sup>](#),
- [Chun-Hung Wu<sup>1</sup>](#),
- [Baptiste Gault](#) [ORCID: orcid.org/0000-0002-4934-0458<sup>1,4</sup>](#) &
- [Dierk Raabe](#) [ORCID: orcid.org/0000-0003-0194-6124<sup>1</sup>](#)

[Nature](#) volume 602, pages 437–441 (2022)

- 3749 Accesses
- 32 Altmetric
- [Metrics details](#)

## Subjects

- [Atomistic models](#)
- [Mechanical properties](#)
- [Metals and alloys](#)

## Abstract

Ever more stringent regulations on greenhouse gas emissions from transportation motivate efforts to revisit materials used for vehicles<sup>1</sup>. High-strength aluminium alloys often used in aircrafts could help reduce the weight of automobiles, but are susceptible to environmental degradation<sup>2,3</sup>. Hydrogen ‘embrittlement’ is often indicated as the main culprit<sup>4</sup>; however, the exact mechanisms underpinning failure are not precisely

known: atomic-scale analysis of H inside an alloy remains a challenge, and this prevents deploying alloy design strategies to enhance the durability of the materials. Here we performed near-atomic-scale analysis of H trapped in second-phase particles and at grain boundaries in a high-strength 7xxx Al alloy. We used these observations to guide atomistic ab initio calculations, which show that the co-segregation of alloying elements and H favours grain boundary decohesion, and the strong partitioning of H into the second-phase particles removes solute H from the matrix, hence preventing H embrittlement. Our insights further advance the mechanistic understanding of H-assisted embrittlement in Al alloys, emphasizing the role of H traps in minimizing cracking and guiding new alloy design.

[Download PDF](#)

## Main

High-strength Al alloys of the 7xxx series are essential structural materials in aerospace, manufacturing, transportation and mobile communication<sup>5,6</sup>, owing to their high strength-to-weight ratio, which enables products with lower fuel consumption and environmental impact. The high strength is achieved through the formation of a high number density (approximately  $10^{24} \text{ m}^{-3}$ ) of nanosized precipitates via an aging thermal treatment<sup>6,7</sup>. Unfortunately, high-strength Al alloys are notoriously sensitive to environmentally assisted cracking<sup>2,8</sup>, and, like most high-strength materials, are subject to H embrittlement<sup>9,10</sup>. Overcoming these intrinsic limitations requires gaining a precise understanding of how H penetrates the material and of its interactions with ubiquitous microstructural features, for example, grain boundaries (GBs) or second phases, to ultimately cause a catastrophic deterioration of mechanical properties<sup>11</sup>. H uptake can occur during high-temperature heat treatments, as well as in service<sup>12,13</sup>. H has low solubility in Al<sup>14</sup>, yet crystal defects can assist H absorption<sup>15,16,17,18,19,20,21,22</sup>, leading, for instance, to a drop in the fatigue life<sup>23</sup>.

The enduring question remains of where the H is located in the microstructure and how such traps facilitate catastrophic failure. Several studies pointed to the critical role of GBs in the environmental degradation. GBs are locations of preferential electrochemical attack<sup>4</sup>, but also cracks propagate more easily via GB networks throughout the microstructure of the alloy<sup>24,25</sup>. An experimental validation of the H distribution in Al alloys is challenging, owing to its low solubility and to the experimental difficulty of performing spatially resolved characterization of H at relevant scales and at specific microstructural features. Recent efforts in atomic-scale H imaging in steels led to insights into the trapping behaviour of second phases and interfaces<sup>26,27,28</sup>.

Here we address these critical questions using the latest developments in cryo-atom probe tomography (APT)<sup>26,27,28</sup>, enabled by cryo-plasma focused-ion beam (PFIB) specimen preparation to investigate H associated with different microstructures in an Al alloy. Through isotope-labelling with deuterium (D), we partly avoid characterization artefacts associated with the introduction of H from the sample preparation<sup>28,29</sup> and from residual gas in the atom probe vacuum chamber. We studied a 7xxx Al alloy with a composition of Al–6.22Zn–2.46Mg–2.13Cu–0.155Zr (wt.%) in its peak-aged condition. For this alloy, electrochemical-charging with H leads to a critical drop in the ductility compared with uncharged samples (Fig. 1a). The H desorption spectra are shown in Extended Data Fig. 1. Figure 1b–d highlights the complexity of the microstructure across multiple length scales. First, Fig. 1b,c reveals the predominant role of GBs and GB networks in the crack formation and propagation during deformation of the H-charged material. Fig. 1d displays the typical distribution of fine precipitates in the bulk, coarse precipitates at GBs and precipitate-free zones (PFZs) adjacent to GBs. Intermetallic phases (for example, the Al<sub>2</sub>CuMg S phase) and Al<sub>3</sub>Zr dispersoids that act as grain refiners are also shown.

**Fig. 1: Heterogeneous microstructure of an aerospace Al–Zn–Mg–Cu alloy.**



**a**, Engineering stress–strain curves of uncharged and H-charged samples in the peak-aged condition (120 °C for 24 h). **b**, Backscattered electron imaging of an intergranular crack of the H-charged alloy subjected to tensile fracture. **c**, Electron backscatter diffraction imaging showing the crack along GBs. **d**, The microstructure of GBs, precipitates, PFZs<sup>31</sup> and main types of secondary phases (the S phase<sup>47</sup> and Al<sub>3</sub>Zr dispersoid). The colour schemes reflect the microstructures where specific APT analyses were performed. APT, atom probe tomography; GB, grain boundary; GBPs,

grain boundary precipitates; PFZs, precipitate-free zones. Scale bars: 20  $\mu\text{m}$  (**b**, **c**), 100 nm (**d**, top), 50 nm (**d**, top inset), 3 nm (**d**, middle and bottom).

Peak-aged specimens were electrochemically charged with D for subsequent APT analysis after validating that H and D show a similar embrittling effect on mechanical properties (Extended Data Fig. 2). D-charged specimens were prepared by PFIB at cryogenic temperatures to limit the introduction of H<sup>29</sup>, and immediately analysed by APT using voltage pulsing to minimize residual H from APT<sup>28,29</sup>. Figure 2a displays the APT analysis of Al<sub>3</sub>Zr dispersoids in the D-charged specimen, with the corresponding composition profile shown in Fig. 2b. H is strongly enriched, up to 9.5 at.% on average, within the dispersoids, contrasting with the much lower content of only 0.4 at.% H in the Al matrix. D is also enriched up to 2.8 at.% inside the dispersoids. H and D atoms partition preferably to sites inside the dispersoids, with a slightly higher content at the interface that may be due to the misfit strain (0.75%)<sup>30</sup>. We further analysed uncharged specimens prepared by PFIB and electrochemical polishing for reference (Extended Data Fig. 3). H appears consistently enriched inside Al<sub>3</sub>Zr dispersoids, up to 8.5 at.% on average. Only a peak at a mass-to-charge ratio at 1 Da, corresponding to H<sup>+</sup> atomic ions, is detected in the dispersoids in uncharged specimens. However, in the D-charged material, a distinct peak at 2 Da gives proof of efficient D-charging, with D partitioning into Al<sub>3</sub>Zr dispersoids.

**Fig. 2: APT analysis of second phases of the D-charged Al–Zn–Mg–Cu samples in the peak-aged condition (120 °C for 24 h).**

---

 **figure 2**

**a–d**, Atom map and composition profiles are presented along the red arrows respectively for  $\text{Al}_3\text{Zr}$  dispersoids (**a**, **b**) and S phase (**c**, **d**). The shaded bands of the traces correspond to the standard deviations of the counting statistics in each bin of the profile. The background colours in **b**, **d** show the locations of the dispersoid and the S phase, respectively. Scale bars: 30 nm (**a**, **c**).

Figure [2c](#) shows the APT analysis on an intermetallic particle in the D-charged sample. The composition profile indicates that the Mg-enriched region corresponds to the S phase ( $\text{Al}_2\text{CuMg}$ ). The S-particle contains 4.2 at.% H, whereas the matrix has only 0.3 at.% H, and 0.12 at.% D (right axis). Comparison with a similar S particle in an uncharged sample (Extended Data Fig. [4](#)) shows a 6.5-times higher peak ratio of 2 Da/1 Da in the D-charged sample, revealing that most of the signal at 2 Da comes from electrochemically charged D. Further evidence of an enrichment up to 9 at.% H within  $\text{Al}_7\text{Cu}_2\text{Fe}$ , and  $\text{Mg}_{32}(\text{Zn},\text{Al})_{49}$  T-phase particles, is provided for the uncharged material (Supplementary Figs. [1](#), [2](#)).

We then analysed the distribution of H and D at a high-angle GB. Following sharpening at cryo-temperature, the specimen was transferred through a cryo-suitcase into the APT to minimize out-diffusion of D<sup>28</sup>. The peak-aged sample contains 5-nm (Mg, Zn)-rich strengthening precipitates in the bulk and coarser 20–50-nm-sized precipitates at the GB<sup>31</sup>, as well as typical PFZs adjacent to the GB (Fig. [3a](#)). Atom

maps of H and D( $H_2^+$ ) in Fig. 3b reveal a higher concentration at the GB. Fig. 3c shows details of the precipitates and solutes populating the GB. Al<sub>3</sub>Zr dispersoids at the GB (Fig. 3d) contain 11 at.% H and 0.6 at.% D—that is, a lower D content compared to the Al<sub>3</sub>Zr dispersoids in the bulk (Fig. 2b). No enrichment in H and D( $H_2^+$ ) (right axis) is shown in (Mg, Zn)-rich precipitates distributed both at the GB (Fig. 3e) and in the bulk (Extended Data Fig. 5). Fig. 3f gives a composition profile through the GB between the particles, showing that the GB is enriched with 2 at.% Mg. We observe no enrichment in Zn and Cu (1 at.%, Extended Data Fig. 6), and in the peak-aged state this can be explained by the accelerated GB precipitation through the consumption of segregated solutes<sup>31</sup>. The locally increased content of D( $H_2^+$ ) implies that the solute-decorated GB (that is, devoid of precipitates) acts as a trap for H, and no enrichment in H and D is observed in the adjacent PFZs (that is, the regions next to the GB), an effect that amplifies the mechanical and electrochemical contrast in these regions. Comparison with a similar GB in an uncharged sample (Extended Data Fig. 7) shows a higher signal at 2 Da (by a factor of 3) in the D-charged sample, supporting that D is indeed enriched at the GB. We obtained seven APT datasets containing GBs in D-charged samples, and all show consistent enrichment of H and D at GBs (two additional datasets are shown in Supplementary Figs. 3, 4).

**Fig. 3: APT analysis of a D-charged peak-aged Al–Zn–Mg–Cu sample containing a GB (120 °C for 24 h).**

---

 **figure 3**

**a**, The iso-surfaces highlight the dispersion of fine (Mg, Zn)-rich precipitates in the matrix, coarse ones at the GB, and Al<sub>3</sub>Zr dispersoids. Scale bar: 30 nm. **b**, Atom maps of H and D(H<sub>2</sub><sup>+</sup>). **c**, Solute distribution at the GB plane. **d**, Composition profile across one Al<sub>3</sub>Zr dispersoid at the GB. **e**, Composition profile of one (Mg, Zn)-rich precipitate at the GB. **f**, Solute composition profile across the GB in between precipitates. The shaded bands of the traces correspond to the standard deviations of the counting statistics in each bin of the profile.

We note that the probability of detecting spurious H from residual gas in APT decreases as the strength of the electric field increases, which can be traced by the evolution of the charge-state ratio of Al (that is, Al<sup>2+</sup>/Al<sup>1+</sup>)<sup>32</sup>. For each microstructural feature studied herein, this ratio is reported in Extended Data Fig. 8, and in each H-enriched case, the electric field either does not change notably or increases compared to Al matrix. The content of H and D measured in each feature in the uncharged and D-charged conditions is compiled in Supplementary Table 1. These analyses indicate that the peak at 2 Da is extremely unlikely to be associated with H<sub>2</sub><sup>+</sup>, but with D in D-charged samples, and that most of the detected H was from initially trapped atoms

inside the specimen, either from its preparation or/and from the processing history of the material<sup>28</sup>. The electrolytical-charging with D reinforces our observation that H is trapped within the material itself<sup>28</sup>.

To better understand the effect of H in the intermetallic phases (for example, S phase Al<sub>2</sub>CuMg), Al<sub>3</sub>Zr dispersoids and at GBs, we used density functional theory (DFT). Solubility analysis of H in the S phase reveals that Al-rich octahedral sites provide the lowest solution enthalpy (0.014 eV). The calculated concentrations of H in these sites is 3 at.% at 300 K, substantially higher than  $5 \times 10^{-5}$  at.% assumed for the Al matrix, which explains the APT observations. In Al<sub>3</sub>Zr dispersoids, H prefers octahedral interstitial sites with Zr in the second nearest-neighbour shell and with a solution enthalpy of 0.128 eV and a H solubility of 0.2 at.%. However, the high experimental H concentrations may be explained by the presence of Zr antisites in the first nearest-neighbour positions of H, which reduces the solution enthalpy to -0.202 eV. The solubility of H in the GB was estimated for a symmetric  $\Sigma 5$  (210) [100] GB (Fig. 4a) as a representative high-angle GB<sup>33</sup>. The excess volume for all considered GB sites (Fig. 4b) explains the negative segregation energies given in Fig. 4c. Therefore, the corresponding solution enthalpies at these sites are lower than in the Al matrix, but still much higher than in the S phase or Al<sub>3</sub>Zr dispersoids.

**Fig. 4: Theoretical analysis based on DFT simulations.**

 figure 4

**a**, Schematic representation of the symmetric  $\Sigma 5$  (210) GB in Al shown with two GB planes. **b**, The projected and perspective views of delta-hedral packing units show the H adsorption sites of the calculations. Site number 1 is the substitutional site for a Mg atom nearby the H sites located inside the polyhedral packing units. **c**, The embrittling energy and segregation energy are compared in the absence and presence (patterned bars) of Mg as a solute atom at the GB for the different interstitial sites of H labelled in **b**. **d**, The Al (light grey) and Mg atoms (light green) in the enlarged figure belong to different adjacent (001) planes.

To explain why GBs, nevertheless, show higher susceptibility for H embrittlement, as documented in Fig. 1, we determine the embrittling energy associated with H (Fig. 4c). This quantity describes the thermodynamic driving force for fracture formation by comparing the impact of H on the energetics of the GB with that of the free surface. In the  $\Sigma 5$  GB, H when located at sites with the strongest segregation energy, also yields the strongest embrittlement. When distributing H atoms according to their nominal solubility over all these possible sites in a unit area of the GB, weighted by their respective segregation energy (Fig. 4c), the total contribution to the embrittling energy adds up to  $600 \text{ mJ m}^{-2}$  for this GB. This value is substantially more positive (that is, more detrimental) than the embrittling energy determined for  $\text{Al}_3\text{Zr}$  dispersoids ( $2 \text{ mJ m}^{-2}$ ) and the S phase ( $129 \text{ mJ m}^{-2}$ ).

We investigate the effect of Mg segregation on GBs revealed by APT and introduce in the simulation cell a Mg atom substituting one of four equivalent Al atoms in the GB plane (Fig. 4d). The negative segregation energy of Mg ( $-0.274 \text{ eV}$ ) indicates that it stabilizes the GB compared to defect-free Al<sup>34,35</sup>, whereas the small negative embrittling energy ( $-0.043 \text{ eV}$ ) yields almost no effect on the GB strength compared to the formation of free surfaces. However, for H added to the GB supercell into the interstitial sites at and near the segregated Mg atom (Fig. 4a), the embrittling energy changes greatly, as summarized in Fig. 4c. The solution enthalpy gives no indication that co-segregation of Mg and H is energetically favourable. In particular, H sitting at the capped trigonal prisms maintains its strong (that is, negative) segregation energy and has a strong (positive) embrittling energy that is considerably enhanced in the presence of Mg. In the same way, all other sites substantially contribute to embrittlement when a Mg atom is nearby and when H diffusion at the opening free surface is considered. This is even true for sites such as 1i and 1gb, for which an occupation by H is less probable. Overall, these effects increase the embrittling energy by H per unit GB area by approximately one order of magnitude with Mg compared to the Mg-free case. The opposite impact of Mg on the segregation and the embrittlement caused by H is explained by the interaction of Mg and H at the free surface resulting from the decohesion.

We can now rationalize the H-embrittlement mechanism as follows: as H penetrates the alloy, the equilibrium H concentration remains low in the Al matrix and also in the fine and coarse (Mg, Zn)-rich precipitates. However, H accumulates in intermetallic phases (for example, S or T phases),  $\text{Al}_3\text{Zr}$  dispersoids, and to a lesser extent, at GBs. The high H enrichment in the second-phase particles was explained by DFT calculations where H shows no clear decohesion or embrittlement effects. Upon H saturation of the second phases, further ingress of H will gradually lead to an accumulation of H at GBs. DFT predicts no strong increase in H concentrations in the presence of Mg, which agrees with APT where H is not strongly segregated at GBs compared to second phases. Yet DFT calculations suggest that when combined with

Mg, the strong driving force for H to segregate to a free surface with respect to a possible interstitial site at GBs favours GB decohesion and drives the system towards crack formation. This rationalizes that GBs are embrittled and explains that Mg can impact the H embrittlement without promoting the absorption of H to GBs<sup>11,36</sup>. Further investigation on the elemental distribution at a H-induced intergranular crack using scanning Auger electron microscopy reveals the enrichment of Mg at the cracked GB (Extended Data Fig. 9). The enrichment is even stronger (by a factor of 2) than the Mg concentration at the GB (Fig. 3f). To confirm the generality of the role of Mg we also show that no H-embrittlement features occurred in a Mg-free Al–5.41 (wt.%) Zn alloy that was used as reference material. The alloy was exposed to the same H-charging and tensile test conditions, but no sign of H embrittlement was found, neither in the tensile test results nor in the metallographic fractography (Extended Data Fig. 10). These findings support the result that the co-segregation of Mg and H to free surfaces provides the driving force for the embrittlement of GBs.

Generally, avoiding the ingress of H in the first place is extremely unlikely to work, and the best approach to mitigate H embrittlement is therefore to control its trapping to maximize the in-service lifetime of the components. Our results provide indications of H-trapping sites and their respective propensity to initiate damage in environmentally assisted degradation, thus contributing towards establishing a mechanistic understanding of H embrittlement in Al alloys. On this basis of this study, we propose specific measures that may be explored to enhance resistance to H-induced damage and improve the lifetime and sustainability of high-strength lightweight engineering components. The results on the high H enrichment in second-phase particles provide a potential mitigation strategy for improving H-embrittlement resistance, namely through introduction and manipulation of the volume fraction, dispersion and chemical composition of the second phases, despite their potentially harmful effects on mechanical properties. Other strategies could aim at designing and controlling GB segregation, for instance with the goal of eliminating Mg decoration of GBs by trapping it into precipitates and keeping it in bulk solution. A third and more general avenue against environmental degradation lies in reducing the size of PFZs in these alloys, with the goal to mitigate the H-enhanced contrast in mechanical and electrochemical response between the H-decorated GBs and the less H-affected adjacent regions.

## Methods

## Materials

The chemical composition of the Al alloy studied is Al–6.22Zn–2.46Mg–2.13Cu–0.16Zr–0.02Fe in wt.% (Al–2.69Zn–2.87Mg–0.95Cu–0.05Zr–0.01Fe in at.%). The as-cast ingot was homogenized at 475 °C and water quenched followed by hot rolling at

450 °C to 3 mm thickness. Samples were cut to the size of 12 mm × 10 mm × 2 mm and then they were solution treated at 475 °C for 1 h and quenched in water. Peak aging was immediately carried out by heat treatment at 120 °C for 24 h with water quenching. The detailed precipitation behaviour during aging is described in a previous work<sup>7</sup>.

An Al–5.41Zn–0.15Fe–0.02Si in wt.% (Al–2.31–0.08Fe–0.02Si in at.%) alloy was used as reference material, which contains a similar amount of Zn as in the studied Al–Zn–Mg–Cu alloy. The cast ingot was homogenized at 360 °C for 6 h and water quenched, followed by hot rolling at 345 °C from 20 to 3 mm thickness and solution treated at 360 °C for 1 h and a final quench in water.

## Microstructure observations

The microstructures of the cracks and the adjacent regions were characterized by the combined use of backscattered electron imaging (Zeiss-Merlin SEM) and electron backscatter diffraction (Sigma). For transmission electron microscopy (TEM), specimens were prepared by in situ lift-out, using a dual-beam PFIB instrument. The microstructures of specimens prepared for TEM probing were analysed using a JEOL-2200FS operated at 200 kV or an aberration-corrected FEI Titan Themis 80–300 operated at 300 kV. Auger analysis was performed on a JEOL JAMP 9500 F Auger spectrometer with a cylindrical mirror analyser and a thermal emission electron gun. The operating vacuum pressure of the chamber was about  $5 \times 10^{-7}$  Pa. The accelerating voltage ( $E_p$ ) of the electron beam is 25 kV and the probe current ( $I_p$ ) is about 10 nA, the Auger measurements were conducted at a working distance 23.2 mm, with the sample being tilt by 30°. Before the mapping started, the sample was pre-sputtered to remove surface contaminations. The scanning energy intervals of each element—O (495.6–518.4 eV), Al (1,453.2–1,504 eV), Mg (1,175.0–1,188.0 eV), Cu (896.0–930.0 eV), Zn (970.0–1,004.0 eV)—and the mapping settings (dwell time, 50  $\mu$ s, number of accumulations, 10) were identical for all elements. The intensity definition of the obtained map is  $(P - B)/B$  ( $P$ , peak,  $B$ , background).

## Deuterium charging method

Deuterium (D) charging was conducted on a three-electrode electrochemical cell as shown in a previous work<sup>28</sup>. A charging solution of 0.05M NaCl with 0.03 wt.% NH<sub>4</sub>SCN in D<sub>2</sub>O (Sigma-Aldrich) was used as the cathode electrolysis to create a D-rich environment around the Al samples. A platinum counter-electrode and reference ( $\mu$ -Ag/AgCl) were used. The D charging was conducted for 3 days to 1 week, followed by immediately transferring the samples to PFIB. For all charging experiments, a PalmSens EmStat3 potentiostat was used.

## TDS measurements

Thermal desorption spectroscopy (TDS) experiments were performed using a Hiden TPD Workstation to measure the H concentration in both H-charged and uncharged reference specimens. Specimens with a dimension of  $10 \times 15 \times 1.0 \text{ mm}^3$  were used, and the TDS spectra were measured at a constant heating rate of  $16 \text{ }^\circ\text{C min}^{-1}$ . Three samples were measured for each condition in the H-charged and uncharged state. The charging was conducted on a three-electrode electrochemical cell for 3 days. A charging solution of 0.05M NaCl with 0.03 wt.% NH<sub>4</sub>SCN in H<sub>2</sub>O was used, after which the tests were started within 15 min. The total H concentration was determined by measuring the cumulative desorbed H from room temperature to 400 °C.

## Tensile experiments

Tensile testing was conducted on a Kammrath & Weiss test stage coupled with the digital image correlation (DIC) technique. Tensile specimens with a gauge length of 8 mm and a width of 2 mm were used. The tests were performed at a strain rate of  $3 \times 10^{-4} \text{ s}^{-1}$ . At least five samples were tested for each condition (uncharged, H-charged and D-charged). Global and local strain distributions were measured by DIC. The data analysis was done using the ARAMIS software.

## APT sample preparation

For the APT specimens prepared by electrochemical polishing, samples were first cut into  $1 \text{ mm} \times 1 \text{ mm} \times 12 \text{ mm}$  bars. First rough polishing was conducted in a solution of 25% perchloric acid in glacial acetic acid at 10–30 V. Final polishing was done in 2% perchloric acid in 2-butoxyethanol under an optical microscope. For the APT specimens prepared by PFIB, bulk samples with the size of  $10 \text{ mm} \times 12 \text{ mm} \times 1 \text{ mm}$  were prepared on an FEI Helios PFIB instrument operated with a Xe source to avoid contamination by gallium.

For the APT specimens prepared from grain boundaries (GBs), GBs were first crystallographically characterized and then site-selected in the SEM, and trenches were cut from the GBs in the plate samples. D charging was then conducted in the bulk plate samples. After charging, the samples were immediately transferred to PFIB, lifted out from the pre-cut trenches, and mounted to the Si coupons. The sharpening processes were done at a cryo-stage fitted with a Dewar and a cold finger. More details on this specific setup can be found in previous works<sup>28,29,37</sup>. The cryo-prepared APT specimens were transferred from the PFIB into APT under cryogenic ultrahigh vacuum (UHV) conditions using our cryogenic UHV sample transfer protocols described previously<sup>37</sup>.

## APT experiments

Atom probe measurements were performed on the local electrode atom probe (LEAP 5000XS/LEAP 5000XR) at a cryogenic temperature of 25 K under UHV conditions of  $10^{-11}$  Torr. All APT measurements were carried out using voltage pulsing with a 20% pulse fraction and a 250 kHz pulse rate. Multiple APT datasets were obtained from multiple APT tips prepared from GBs and second-phase particles. APT datasets were analysed using the commercial software package IVAS 3.8.4. The APT reconstruction parameters were calibrated according to the crystallographic poles appearing on the detector hit maps<sup>38</sup>.

## Computational details

The DFT calculations were carried out using the projector augmented wave (PAW) potentials as implemented in VASP<sup>39,40</sup>. The exchange and correlation terms were described by the generalized gradient approximation (GGA) proposed by Perdew, Burke and Ernzerhof (PBE)<sup>41</sup>. A plane-wave cut-off of 500 eV was taken for all calculations. The convergence tolerance of atomic forces is 0.01 eV Å<sup>-1</sup> and of total energies is  $10^{-6}$  eV. The  $k$ -point sampling number was set large enough that the convergence of the total energies was within 2 meV per atom. Brillouin zone integration was made using Methfessel–Paxton smearing. Ionic relaxations were allowed in all calculations keeping the shape and volume fixed. The equilibrium structure for pure Al with a lattice parameter of 4.04 Å obtained within the convergence criteria is consistent with previous DFT-GGA calculations<sup>42</sup> and has been used to construct the supercells.

The H solubility across microstructural features, denoted as  $\sigma$ , can be calculated as:

$$\begin{array}{l} \text{\$\$}\backslash\begin{array}{ccc} \{c\}_{\{\{\rm{H}\}\}} & = & \exp[-\{H\}_{\{\{\rm{sol}\}\}}]^{\{\sigma\}} \\ (\{\rm{H}\})/\{k\}_{\{\{\rm{B}\}\}}T] & = & \exp[-(\{E\}_{\{\{\rm{Al}\}\}}X+ \\ \{\rm{H}\})^{\{\sigma\}}-\{E\}_{\{\{\rm{Al}\}\}}X]^{\{\sigma\}}-\{\mu \\ \}_{\{\{\rm{H}\}\}})/\{k\}_{\{\{\rm{B}\}\}}T], \end{array} \end{array} \backslash\end{array} \text{\$\$}$$

where  $(\{E\}_{\{\{\rm{Al}\}\}}X+\{\rm{H}\})^{\{\sigma\}}$  is the total DFT energy of the supercell,  $\{H\}_{\{\{\rm{sol}\}\}}^{\{\sigma\}}$  is the solution enthalpy of H in the phase  $\sigma$ ,  $X$  is an impurity as explained in the next section, and  $k_B$  is the Boltzmann constant. The chemical potential  $\mu_H$  is aligned such that a nominal solubility of  $\sim 5 \times 10^{-5}$  at.% is obtained at  $T=300$  K for the preferred tetrahedral interstitial positions in the face-centred cubic (fcc) Al matrix<sup>43,44</sup>. A  $2 \times 2 \times 4$  simulation cell is considered for Al<sub>2</sub>CuMg (256 atoms per cell) and the solution enthalpy of H is compared for all possible interstitial sites. Al<sub>3</sub>Zr has a L1<sub>2</sub> structure

with Al atoms at the fcc positions. A  $3 \times 3 \times 3$  cell is considered here with 108 atoms in total. The solution enthalpy of H is calculated for the two different octahedral sites in  $\text{Al}_3\text{Zr}$ . For each microstructure a consistent simulation cell is considered for bulk and the free surface. The free surface depicts the supercell after crack formation, thereby containing half the number of bulk atoms.

The  $\Sigma 5$  (210)[100] symmetric tilt grain boundary (STGB) is selected as a representative high-angle GB<sup>33</sup>. The supercell shown in Fig. 4a contains 40 atomic layers (4 atoms per layer, 160 atoms per cell) and represents a cell doubled along the [100] and [012] directions. The GB supercell includes two GBs where two Mg solute atoms are placed at the GB layer such that possible interactions between them are avoided. The free-surface supercell has exactly half the number of atoms, but the same dimensions as the GB supercell and the two Mg solute atoms are placed in symmetrically equivalent positions. The Mg atoms replace one of four equivalent host atoms in the GB plane and the H atom is inserted between host atoms and close to the substituted Mg atom in the GB2 plane as shown in Fig. 4. The dimension of all the models was fixed during structural optimizations, allowing relaxations only along the direction perpendicular to the GB plane. The  $2 \times 9 \times 9$  Monkhorst–Pack  $k$ -point mesh is used in all calculations of GB. All structures have been rendered using the OVITO<sup>45</sup> programme package and all GB structures were created using the software GB Code<sup>46</sup>.

## GB segregation

The ability of an impurity  $X$  to segregate to the GB can be characterized by the segregation energy given by,

$$\$ \$ \{E\}_{\{\{\rm seg\}\}}^{\{\{\rm GB\}\}} = (\{E\}_{\{\{\rm Al\}\}} + X)^{\{\{\rm GB\}\}} - \\ \{E\}_{\{\{\rm Al\}\}}^{\{\{\rm GB\}\}} - (\{E\}_{\{\{\rm Al\}\}} + X)^{\{\{\rm bulk\}\}} - \\ \{E\}_{\{\{\rm Al\}\}}^{\{\{\rm bulk\}\}} \$ \$$$

Here,  $(\{E\}_{\{\{\rm Al\}\}}^{\{\{\rm GB\}\}})$ ,  $(\{E\}_{\{\{\rm Al\}\}} + X)^{\{\{\rm GB\}\}}$ ,  $(\{E\}_{\{\{\rm Al\}\}}^{\{\{\rm bulk\}\}})$  and  $(\{E\}_{\{\{\rm Al\}\}} + X)^{\{\{\rm bulk\}\}}$  are the total energy of the pure Al GB, GB in presence of impurity atoms  $X = \text{Mg}$  or  $\text{H}$ , pure bulk Al and bulk Al with impurity atoms  $X$ , respectively. A negative segregation energy indicates that the impurity atoms prefer to segregate towards GB from the bulk environment.

## GB embrittlement

The changes in the mechanical strength of the GB with segregation of impurity atoms is characterized by the embrittling energy  $\eta$  within the framework of Rice–Thomson–Wang approach<sup>34,35</sup>

$$\eta = \{E\}_{\rm seg}^{\rm GB} - \{E\}_{\rm Al}^{\rm GB} + \{E\}_{\rm seg}^{\rm FS} - \{E\}_{\rm Al}^{\rm FS}$$

Here free-surface energies (FS) are defined similarly to the corresponding GB energies. A negative value of embrittling energy suggests that the impurity will enhance the GB strength, whereas a positive value indicates a detrimental effect on GB strength. The embrittling effect of H in presence of Mg in  $\Sigma 5$  (210) STGB is modified depending upon the H site at the GB. However, at the opening free surface, H is expected to immediately diffuse to the position with the lowest segregation energy. This yields a higher embrittling energy compared to H remaining at the specific site of the GB (thin horizontal lines in the bars of Fig. 4c).

## Data availability

All data to evaluate the conclusions are present in the manuscript, the Extended Data items and the [Supplementary Information](#). Raw data are available from the corresponding authors on reasonable request.

## Code availability

The code for this study can be found at ref. [46](#), which is also available on GitHub ([https://github.com/oekosheri/GB\\_code](https://github.com/oekosheri/GB_code)).

## References

- European Commission. CO<sub>2</sub> emission performance standards for cars and vans. European Commission – Climate Action (accessed 20 March 2021); [https://ec.europa.eu/clima/policies/transport/vehicles/regulation\\_en#tab-0-2](https://ec.europa.eu/clima/policies/transport/vehicles/regulation_en#tab-0-2).
- Holroyd, N. J. H. & Scamans, G. M. Crack propagation during sustained-load cracking of Al-Zn-Mg-Cu aluminum alloys exposed to moist air or distilled water. *Metall. Mater. Trans. A* **42**, 3979–3998 (2011).
- European Union Aviation Safety Agency. Environmentally Assisted Cracking in certain Aluminium Alloys. Safety Information Bulletin no. 2018-04R2 (EASA, 2021); <https://ad.easa.europa.eu/ad/2018-04R1>.
- Davis, J. R. (ed.) Corrosion of Aluminum and Aluminum Alloys (ASM International, 1999).

5. Chen, J. H., Costan, E., van Huis, M. A., Xu, Q. & Zandbergen, H. W. Atomic pillar-based nanoprecipitates strengthen AlMgSi alloys. *Science* **312**, 416–419 (2006).
6. Sun, W. et al. Precipitation strengthening of aluminum alloys by room-temperature cyclic plasticity. *Science* **363**, 972–975 (2019).
7. Zhao, H., Gault, B., Ponge, D., Raabe, D. & De Geuser, F. Parameter free quantitative analysis of atom probe data by correlation functions: application to the precipitation in Al-Zn-Mg-Cu. *Scr. Mater.* **154**, 106–110 (2018).
8. Scamans, G., Alani, R. & Swann, P. Pre-exposure embrittlement and stress corrosion failure in AlZnMg Alloys. *Corros. Sci.* **16**, 443–459 (1976).
9. Young, G. A. Jr & Scully, J. R. The effects of test temperature, temper, and alloyed copper on the hydrogen-controlled crack growth rate of an Al-Zn-Mg-(Cu) alloy. *Metall. Mater. Trans. A* **33**, 1167–1181 (2002).
10. Bond, G. M., Robertson, I. M. & Birnbaum, H. K. The influence of hydrogen on deformation and fracture processes in high-strength aluminum alloys. *Acta Metall.* **35**, 2289–2296 (1987).
11. Song, R. G. et al. Stress corrosion cracking and hydrogen embrittlement of an Al-Zn-Mg-Cu alloy. *Acta Mater.* **52**, 4727–4743 (2004).
12. Su, H. et al. Assessment of hydrogen embrittlement via image-based techniques in Al-Zn-Mg-Cu aluminum alloys. *Acta Mater.* **176**, 96–108 (2019).
13. Ishikawa, T. & McLellan, R. B. The diffusivity of hydrogen in aluminum. *Acta Metall.* **34**, 1091–1095 (1986).
14. Young, G. A. Jr & Scully, J. R. The diffusion and trapping of hydrogen in high purity aluminum. *Acta Mater.* **46**, 6337–6349 (1998).
15. Lu, G. & Kaxiras, E. Hydrogen embrittlement of aluminum: the crucial role of vacancies. *Phys. Rev. Lett.* **94**, 155501 (2005).
16. Itoh, G., Koyama, K. & Kanno, M. Evidence for the transport of impurity hydrogen with gliding dislocations in aluminum. *Scr. Mater.* **35**, 695–698 (1996).
17. Kamoutsi, H., Haidemenopoulos, G. N., Bontozoglou, V. & Pantelakis, S. Corrosion-induced hydrogen embrittlement in aluminum alloy 2024. *Corros. Sci.* **48**, 1209–1224 (2006).

18. Larignon, C. et al. Investigation of Kelvin probe force microscopy efficiency for the detection of hydrogen ingress by cathodic charging in an aluminium alloy. *Scr. Mater.* **68**, 479–482 (2013).
19. Charitidou, E., Papapolymerou, G., Haidemenopoulos, G., Hasiotis, N. & Bontozoglou, V. Characterization of trapped hydrogen in exfoliation corroded aluminium alloy 2024. *Scr. Mater.* **41**, 1327–1332 (1999).
20. Chao, P. & Karnesky, R. A. Hydrogen isotope trapping in Al–Cu binary alloys. *Mater. Sci. Eng. A* **658**, 422–428 (2016).
21. Saitoh, H., Iijima, Y. & Hirano, K. Behaviour of hydrogen in pure aluminium, Al–4 mass% Cu and Al–1 mass% Mg<sub>2</sub>Si alloys studied by tritium electron microautoradiography. *J. Mater. Sci.* **29**, 5739–5744 (1994).
22. Xie, D. et al. Hydrogenated vacancies lock dislocations in aluminium. *Nat. Commun.* **7**, 13341 (2016).
23. Scully, J. R., Young, G. A. & Smith, S. W. In Gaseous Hydrogen Embrittlement of Materials in Energy Technologies: Vol. 1 (eds Gangloff, R. P. & Somerday, B. P.) 707–768 (Woodhead, 2012).
24. Garner, A. et al. Multiscale analysis of grain boundary microstructure in high strength 7xxx Al alloys. *Acta Mater.* **202**, 190–210 (2021).
25. Christodoulou, L. & Flower, H. M. Hydrogen embrittlement and trapping in Al6%Zn-3%Mg. *Acta Metall.* **28**, 481–487 (1980).
26. Chen, Y.-S. et al. Direct observation of individual hydrogen atoms at trapping sites in a ferritic steel. *Science* **355**, 1196–1199 (2017).
27. Chen, Y.-S. et al. Observation of hydrogen trapping at dislocations, grain boundaries, and precipitates. *Science* **367**, 171–175 (2020).
28. Breen, A. J. et al. Solute hydrogen and deuterium observed at the near atomic scale in high-strength steel. *Acta Mater.* **188**, 108–120 (2020).
29. Chang, Y. et al. Ti and its alloys as examples of cryogenic focused ion beam milling of environmentally sensitive materials. *Nat. Commun.* **10**, 942 (2019).
30. Lefebvre, W., Masquelier, N., Houard, J., Patte, R. & Zapsolsky, H. Tracking the path of dislocations across ordered Al<sub>3</sub>Zr nano-precipitates in three dimensions. *Scr. Mater.* **70**, 43–46 (2014).

31. Zhao, H. et al. Segregation assisted grain boundary precipitation in a model Al-Zn-Mg-Cu alloy. *Acta Mater.* **156**, 318–329 (2018).
32. Lefebvre, W. et al. 3DAP measurements of Al content in different types of precipitates in aluminium alloys. *Surf. Interface Anal.* **39**, 206–212 (2007).
33. Tschopp, M. A., Coleman, S. P. & McDowell, D. L. Symmetric and asymmetric tilt grain boundary structure and energy in Cu and Al (and transferability to other fcc metals). *Integr. Mater. Manuf. Innov.* **4**, 176–189 (2015).
34. Rice, J. R. & Wang, J.-S. Embrittlement of interfaces by solute segregation. *Mater. Sci. Eng. A* **107**, 23–40 (1989).
35. Rice, J. R. & Thomson, R. Ductile versus brittle behaviour of crystals. *Philos. Mag. A* **29**, 73–97 (1974).
36. Scamans, G. M., Holroyd, N. J. H. & Tuck, C. D. S. The role of magnesium segregation in the intergranular stress corrosion cracking of aluminium alloys. *Corros. Sci.* **27**, 329–347 (1987).
37. Stephenson, L. T. et al. The Laplace Project: an integrated suite for preparing and transferring atom probe samples under cryogenic and UHV conditions. *PLoS ONE* **13**, e0209211 (2018).
38. Gault, B. et al. Advances in the calibration of atom probe tomographic reconstruction. *J. Appl. Phys.* **105**, 034913 (2009).
39. Kresse, G. & Hafner, J. Ab initio molecular dynamics for liquid metals. *Phys. Rev. B* **47**, 558–561 (1993).
40. Kresse, G. & Furthmüller, J. Efficient iterative schemes for ab initio total-energy calculations using a plane-wave basis set. *Phys. Rev. B* **54**, 11169–11186 (1996).
41. Perdew, J. P., Burke, K. & Ernzerhof, M. Generalized gradient approximation made simple. *Phys. Rev. Lett.* **77**, 3865–3868 (1996).
42. Benali, A., Lacaze-Dufaure, C. & Morillo, J. Density functional study of copper segregation in aluminum. *Surf. Sci.* **605**, 341–350 (2011).
43. Wolverton, C., Ozoliņš, V. & Asta, M. Hydrogen in aluminum: first-principles calculations of structure and thermodynamics. *Phys. Rev. B* **69**, 144109 (2004).
44. Lu, G., Orlikowski, D., Park, I., Politano, O. & Kaxiras, E. Energetics of hydrogen impurities in aluminum and their effect on mechanical properties. *Phys.*

*Rev. B* **65**, 064102 (2002).

45. Stukowski, A. Visualization and analysis of atomistic simulation data with OVITO—the Open Visualization Tool. *Model. Simul. Mater. Sci. Eng.* **18**, 015012 (2009).
46. Hadian, R., Grabowski, B. & Neugebauer, J. GB code: A grain boundary generation code. *J. Open Source Softw.* **3**, 900 (2018).
47. Zhao, H. et al. Interplay of chemistry and faceting at grain boundaries in a model Al alloy. *Phys. Rev. Lett.* **124**, 106102 (2020).

## Acknowledgements

We acknowledge A. Sturm for technical support with cryo-experiments in the PFIB and cryo-suitcase transfer in the atom probe. The help of L. Stephenson for the cryo-transfer in the atom probe is also appreciated. We are grateful to D. Wan for the initial TDS measurements, and M. Adamek for the tensile experiments. B.G. acknowledges financial support from the ERC-CoG-SHINE-771602. Plane vector image in Fig. 1 was obtained from <https://freesvg.org/plane-vector-image> (public domain).

## Funding

Open access funding provided by Max Planck Society.

## Author information

### Affiliations

1. Max-Planck-Institut für Eisenforschung, Düsseldorf, Germany

Huan Zhao, Poulami Chakraborty, Dirk Ponge, Tilmann Hickel, Binhan Sun, Chun-Hung Wu, Baptiste Gault & Dierk Raabe

2. BAM Federal Institute for Materials Research and Testing, Berlin, Germany

Tilmann Hickel

3. Key Laboratory of Pressure Systems and Safety, Ministry of Education, School of Mechanical and Power Engineering, East China University of Science and Technology, Shanghai, China

Binhan Sun

4. Department of Materials, Royal School of Mines, Imperial College London, London, UK

Baptiste Gault

## Contributions

H.Z., B.G., D.R. and D.P. developed the research concept; H.Z. was the lead experimental scientist of the study and interpreted the data; H.Z., B.G. and D.R. discussed and interpreted the APT results; P.C. and T.H. performed atomic calculations; B.S. conducted TDS measurements; C.-H.W. performed scanning Auger mapping measurements; H.Z., B.G., P.C. and T.H. wrote the manuscript. All authors contributed to the discussion of the results and commented on the manuscript.

## Corresponding authors

Correspondence to [Huan Zhao](#), [Baptiste Gault](#) or [Dierk Raabe](#).

## Ethics declarations

## Competing interests

The authors declare no competing interests.

## Peer review

## Peer review information

*Nature* thanks the anonymous reviewers for their contribution to the peer review of this work. Peer reviewer reports are available.

## Additional information

**Publisher's note** Springer Nature remains neutral with regard to jurisdictional claims in published maps and institutional affiliations.

## Extended data figures and tables

## Extended Data Fig. 1 Thermal desorption spectroscopy analysis.

The H desorption spectra of uncharged and H-charged Al–Zn–Mg–Cu samples in the peak-aged state. cum., cumulative; ppm, parts per million.

## Extended Data Fig. 2 Tensile properties of H-charged and D-charged samples.

Engineering stress–strain curves of H-charged and D-charged Al–Zn–Mg–Cu samples in the peak-aged state showing that H and D have a similar embrittling effect on mechanical properties.

## Extended Data Fig. 3 Atom probe analysis of Al<sub>3</sub>Zr dispersoids in peak-aged Al–Zn–Mg–Cu samples.

**a**, D-charged. **b**, Uncharged sample prepared by PFIB. **c**, Uncharged samples prepared by electropolishing. Associated H peaks in the mass-to-charge ratio within the local Al<sub>3</sub>Zr dispersoids (middle) and composition analysis across the Al<sub>3</sub>Zr dispersoids (right) are also shown for each condition.

## Extended Data Fig. 4 Atom probe analysis of S phase in Al–Zn–Mg–Cu samples.

**a**, D-charged; **b**, uncharged. Atom maps of Al, Mg, H and D are presented, with the S phase visualized by the Mg enriched regions. Associated H peaks in the mass-to-charge ratio within the S phases are also shown.

## Extended Data Fig. 5 Atom probe analysis of bulk precipitates.

Representative composition profile across the bulk precipitate in D-charged Al–Zn–Mg–Cu samples in the peak-aged state, showing no H enriched.

## Extended Data Fig. 6 Atom probe analysis of the GB composition.

The mean chemical composition profile of Zn, Cu, Al<sup>2+</sup> across the GB represented in Fig. 3. The composition profile of Al<sup>2+</sup> shows the evaporation field not changing.

## Extended Data Fig. 7 Atom probe analysis of GBs in peak-aged Al–Zn–Mg–Cu samples.

**a–c**, D-charged; **d–f**, uncharged. Associated H peaks in the mass-to-charge ratio within the GBs and composition analysis across the GB are also shown for each condition.

### [Extended Data Fig. 8 The local electrical field analysis for microstructural features.](#)

The local electrical field for each microstructural feature was tracked by the charge state ratio of Al<sup>2+</sup>/Al<sup>+</sup>.

### [Extended Data Fig. 9 Scanning Auger electron microscopy analysis of a H-induced intergranular crack in the Al–Zn–Mg–Cu sample.](#)

**a**, Scanning electron microscopy image of a crack at the grain boundary. **b**, Auger map of the overlay of Al, O and Mg showing Mg enriched at the crack. **c**, Elemental distribution images of Al, Zn, Mg, Cu at the crack.

### [Extended Data Fig. 10 Tensile properties and metallographic fractography of Al–5.41 wt.% Zn alloy.](#)

**a**, Engineering stress–strain curves of uncharged and H-charged Al–Zn samples. **b, c**, Typical scanning electron microscopy fractography of the uncharged (**b**), and H-charged (**c**) Al–Zn samples.

## Supplementary information

### [Supplementary Information](#)

This file contains Supplementary Figures 1–4 and Supplementary Table 1.

### [Peer Review File](#)

## Rights and permissions

**Open Access** This article is licensed under a Creative Commons Attribution 4.0 International License, which permits use, sharing, adaptation, distribution and reproduction in any medium or format, as long as you give appropriate credit to the original author(s) and the source, provide a link to the Creative Commons license, and indicate if changes were made. The images or other third party material in this article are included in the article's Creative Commons license, unless indicated otherwise in a credit line to the material. If material is not included in the article's Creative Commons

license and your intended use is not permitted by statutory regulation or exceeds the permitted use, you will need to obtain permission directly from the copyright holder. To view a copy of this license, visit <http://creativecommons.org/licenses/by/4.0/>.

## Reprints and Permissions

## About this article

### Cite this article

Zhao, H., Chakraborty, P., Ponge, D. *et al.* Hydrogen trapping and embrittlement in high-strength Al alloys. *Nature* **602**, 437–441 (2022). <https://doi.org/10.1038/s41586-021-04343-z>

- Received: 04 April 2021
- Accepted: 13 December 2021
- Published: 16 February 2022
- Issue Date: 17 February 2022
- DOI: <https://doi.org/10.1038/s41586-021-04343-z>

### Share this article

Anyone you share the following link with will be able to read this content:

[Get shareable link](#)

Sorry, a shareable link is not currently available for this article.

[Copy to clipboard](#)

Provided by the Springer Nature SharedIt content-sharing initiative

---

This article was downloaded by **calibre** from <https://www.nature.com/articles/s41586-021-04343-z>.

- Article
- [Published: 16 February 2022](#)

# Warming weakens the night-time barrier to global fire

- [Jennifer K. Balch](#) [ORCID: orcid.org/0000-0002-3983-7970<sup>1,2</sup>](#),
- [John T. Abatzoglou](#) [<sup>3 na1</sup>](#),
- [Maxwell B. Joseph](#) [ORCID: orcid.org/0000-0002-7745-9990<sup>1,4 na1</sup>](#),
- [Michael J. Koontz](#) [ORCID: orcid.org/0000-0002-8276-210X<sup>1 na1</sup>](#),
- [Adam L. Mahood](#) [ORCID: orcid.org/0000-0003-3791-9654<sup>1,2 na1</sup>](#),
- [Joseph McGlinchy](#) [<sup>1,5 na1</sup>](#),
- [Megan E. Cattau](#) [ORCID: orcid.org/0000-0003-2164-3809<sup>6</sup>](#) &
- [A. Park Williams](#) [<sup>7,8</sup>](#)

*Nature* volume **602**, pages 442–448 (2022)

- 1480 Accesses
- 311 Altmetric
- [Metrics details](#)

## Subjects

- [Climate-change impacts](#)
- [Environmental impact](#)

## Abstract

Night-time provides a critical window for slowing or extinguishing fires owing to the lower temperature and the lower vapour pressure deficit

(VPD). However, fire danger is most often assessed based on daytime conditions<sup>1,2</sup>, capturing what promotes fire spread rather than what impedes fire. Although it is well appreciated that changing daytime weather conditions are exacerbating fire, potential changes in night-time conditions—and their associated role as fire reducers—are less understood. Here we show that night-time fire intensity has increased, which is linked to hotter and drier nights. Our findings are based on global satellite observations of daytime and night-time fire detections and corresponding hourly climate data, from which we determine landcover-specific thresholds of VPD ( $VPD_t$ ), below which fire detections are very rare (less than 95 per cent modelled chance). Globally, daily minimum VPD increased by 25 per cent from 1979 to 2020. Across burnable lands, the annual number of flammable night-time hours—when VPD exceeds  $VPD_t$ —increased by 110 hours, allowing five additional nights when flammability never ceases. Across nearly one-fifth of burnable lands, flammable nights increased by at least one week across this period. Globally, night fires have become 7.2 per cent more intense from 2003 to 2020, measured via a satellite record. These results reinforce the lack of night-time relief that wildfire suppression teams have experienced in recent years. We expect that continued night-time warming owing to anthropogenic climate change will promote more intense, longer-lasting and larger fires.

This is a preview of subscription content

## Access options

Subscribe to Nature+

Get immediate online access to the entire Nature family of 50+ journals

\$29.99

monthly

[Subscribe](#)

Subscribe to Journal

Get full journal access for 1 year

\$199.00

only \$3.90 per issue

[Subscribe](#)

All prices are NET prices.

VAT will be added later in the checkout.

Tax calculation will be finalised during checkout.

Buy article

Get time limited or full article access on ReadCube.

\$32.00

[Buy](#)

All prices are NET prices.

### **Additional access options:**

- [Log in](#)
- [Learn about institutional subscriptions](#)

**Fig. 1: Large portions of the globe experience night-time fires.**

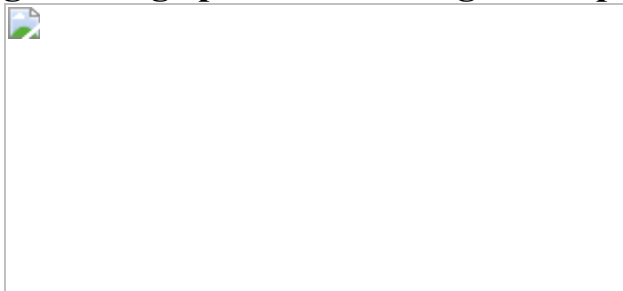


**Fig. 2: VPD provides a key metric for the atmospheric moisture conditions that can cause fire extinction.**

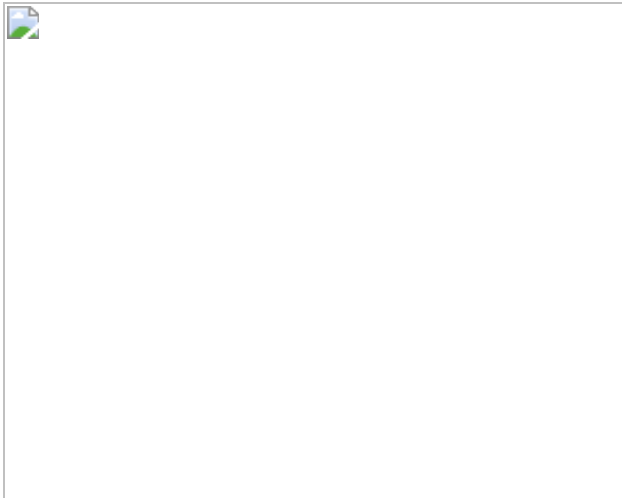


**Fig. 3: Two wildfires illustrate the relationship between night-time VPD and fire activity.**



**Fig. 4: The annual number of flammable night-time hours when  $VPD > VPD_t$  increased by over a third from 1979 to 2020.**

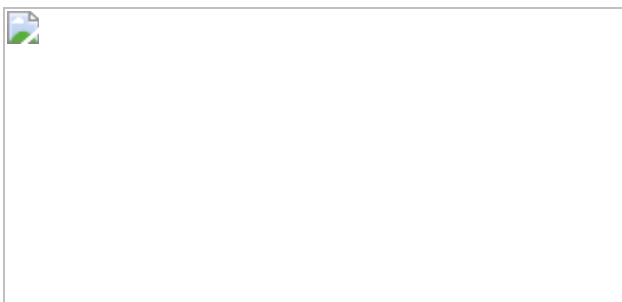
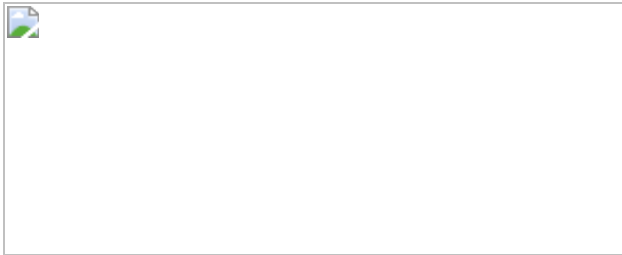


**Fig. 5: Night-time fires have become more intense across large portions of the globe in just the past 18 years.**



## Data availability

The datasets for conducting the analysis presented here are all publicly available, including: the MODIS active fire product (<https://earthdata.nasa.gov/earth-observation-data/near-real-time/firms/mcd14ml>); the GOES-16 full-disk active fire product (<https://registry.opendata.aws/noaa-goes/>); the ERA-5 hourly climate data (<https://www.ecmwf.int/en/forecasts/datasets/reanalysis-datasets/era5>); the MODIS GeoMeta Collection 6.1 product (<https://ladsweb.modaps.eosdis.nasa.gov/archive/geoMeta/61/>); the Köppen–Geiger climate classifications (<https://doi.org/10.6084/m9.figshare.6396959>); and the MODIS MCD12Q1v006 Landcover Type 1 product (<https://lpdaac.usgs.gov/products/mcd12q1v006/>). We also generated fire perimeters using the FIRED algorithm (<https://www.github.com/earthlab/firedpy>) for fire events in North America and South America from May 2017 to July 2020 (<https://scholar.colorado.edu/concern/datasets/d217qq78g>). [Source data](#) are provided with this paper.

## Code availability

The code for conducting the data integration and analysis is available at contributor and Earth Lab’s GitHub repositories, including code for: calculation of hourly VPD and the delineation of day and night hours (<https://github.com/abatz/VPD>) or at DOI (<https://doi.org/10.5281/zenodo.5911663>); quantifying monthly counts of day and night MODIS overpasses (<https://github.com/mikoontz/modis-overpass-correction>) or at DOI (<https://doi.org/10.5281/zenodo.5911671>); and the remainder of the workflow (<https://github.com/earthlab/warming->

[weakens-the-nighttime-barrier-to-global-fire](#)) or at DOI (<https://doi.org/10.5281/zenodo.5911673>). A Python software package, ‘firedpy’, recreates the FIRED event perimeters from the FIRED algorithm, available at <https://github.com/earthlab/firedpy>.

## References

1. Jolly, W. M. et al. Climate-induced variations in global wildfire danger from 1979 to 2013. *Nat. Commun.* **6**, 7537 (2015).
2. Abatzoglou, J. T., Williams, A. P. & Barbero, R. Global emergence of anthropogenic climate change in fire weather indices. *Geophys. Res. Lett.* **46**, 326–336 (2019).
3. Easterling, D. R. et al. Maximum and minimum temperature trends for the globe. *Science* **277**, 364–367 (1997).
4. Peterson, T. C. & Vose, R. S. An overview of the Global Historical Climatology Network temperature database. *Bull. Am. Meteorol. Soc.* **78**, 2837–2850 (1997).
5. Goens, D. W. *Forecast Guidelines for Fire Weather and Forecasters—How Nighttime Humidity Affects Wildland Fuels* Technical Memorandum NWS WR-205 (NOAA, 1989).
6. Byram, G. M. & Nelson Jr., R. M. *An Analysis of the Drying Process in Forest Fuel Material* General Technical Report SRS-200 (US Department of Agriculture Forest Service, Southern Research Station, 2015).
7. Seager, R. et al. Climatology, variability, and trends in the US vapor pressure deficit, an important fire-related meteorological quantity. *J. Appl. Meteorol. Climatol.* **54**, 1121–1141 (2015).
8. Krawchuk, M. A., Moritz, M. A., Parisien, M. A., Van Dorn, J. & Hayhoe, K. Global pyrogeography: the current and future distribution of wildfire. *PLoS ONE* **4**, e5102 (2009).

9. Forkel, M. et al. Recent global and regional trends in burned area and their compensating environmental controls. *Environ. Res. Commun.* **1**, 051005 (2019).
10. Ray, D., Nepstad, D. & Moutinho, P. Micrometeorological and canopy controls of fire susceptibility in a forested Amazon landscape. *Ecol. Appl.* **15**, 1664–1678 (2005).
11. Sedano, F. & Randerson, J. T. Multi-scale influence of vapor pressure deficit on fire ignition and spread in boreal forest ecosystems. *Biogeosciences* **11**, 3739–3755 (2014).
12. Abatzoglou, J. T. & Williams, A. P. The impact of anthropogenic climate change on wildfire across western US forests. *Proc. Natl Acad. Sci. USA* **113**, 11770–11775 (2016).
13. Williams, A. P. et al. Observed impacts of anthropogenic climate change on wildfire in California. *Earth's Future* **7**, 892–910 (2019).
14. Rothermel, R. C. *A Mathematical Model for Predicting Fire Spread in Wildland Fuels* Research Paper INT-115 (US Department of Agriculture Forest Service, Intermountain Forest and Range Experiment Station, 1972).
15. Nolan, R. H. et al. Predicting dead fine fuel moisture at regional scales using vapour pressure deficit from MODIS and gridded weather data. *Remote Sens. Environ.* **174**, 100–108 (2016).
16. Viney, N. & Catchpole, E. Estimating fuel moisture response times from field observations. *Int. J. Wildland Fire* **1**, 211–214 (1991).
17. Nemani, R. R. et al. Climate-driven increases in global terrestrial net primary production from 1982 to 1999. *Science* **300**, 1560–1563 (2003).
18. Barkhordarian, A., Saatchi, S. S., Behrang, A., Loikith, P. C. & Mechoso, C. R. A recent systematic increase in vapor pressure deficit over tropical South America. *Sci. Rep.* **9**, 15331 (2019).

19. Schmidt, C. C. & Prins, E. M. GOES wildfire ABBA applications in the Western Hemisphere. In *2nd International Wildland Fire Ecology and Fire Management Congress and 5th Symposium on Fire and Forest Meteorology* (Citeseer, 2003).
20. Giglio, L., Schroeder, W. & Justice, C. O. The collection 6 MODIS active fire detection algorithm and fire products. *Remote Sens. Environ.* **178**, 31–41 (2016).
21. Cahoon, D. R., Stocks, B. J., Levine, J. S., Cofer, W. R. & O'Neill, K. P. Seasonal distribution of African savanna fires. *Nature* **359**, 812–815 (1992).
22. Giglio, L., Csiszar, I. & Justice, C. O. Global distribution and seasonality of active fires as observed with the Terra and Aqua Moderate Resolution Imaging Spectroradiometer (MODIS) sensors. *J. Geophys. Res. Biogeosci.* **111**, G02016 (2006).
23. Giglio, L. Characterization of the tropical diurnal fire cycle using VIIRS and MODIS observations. *Remote Sens. Environ.* **108**, 407–421 (2007).
24. Amraoui, M., DaCamara, C. C. & Pereira, J. M. C. Detection and monitoring of African vegetation fires using MSG-SEVIRI imagery. *Remote Sens. Environ.* **114**, 1038–1052 (2010).
25. Andela, N., Kaiser, J. W., van der Werf, G. R. & Wooster, M. J. New fire diurnal cycle characterizations to improve fire radiative energy assessments made from MODIS observations. *Atmos. Chem. Phys.* **15**, 8831–8846 (2015).
26. Roberts, G., Wooster, M. J. & Lagoudakis, E. Annual and diurnal African biomass burning temporal dynamics. *Biogeosciences* **6**, 849–866 (2009).
27. Williamson, G. J. et al. Measurement of inter-and intra-annual variability of landscape fire activity at a continental scale: the Australian case. *Environ. Res. Lett.* **11**, 035003 (2016).

28. Balch, J. K. et al. The susceptibility of southeastern Amazon forests to fire: insights from a large-scale burn experiment. *BioScience* **65**, 893–905 (2015).
29. Gill, A. M., Hoare, J. R. L. & Cheney, N. P. In *Fire in the Tropical Biota: Ecosystem Processes and Global Challenges* (ed. Goldammer, J. G.) 159–178 (Springer, 1990); [https://doi.org/10.1007/978-3-642-75395-4\\_10](https://doi.org/10.1007/978-3-642-75395-4_10)
30. Daniels, J. Night-flying by fire agencies in California gains interest as state's wildfire threat grows. *CNBC* <https://www.cnbc.com/2018/08/09/night-flying-by-fire-agencies-in-california-gains-more-interest.html> (2018).
31. Pyne, S. J. *Fire in America: A Cultural History of Wildland and Rural Fire* (Univ. Washington Press, 1997).
32. St. Denis, L. A., Mietkiewicz, N. P., Short, K. C., Buckland, M. & Balch, J. K. All-hazards dataset mined from the US National Incident Management System 1999–2014. *Sci. Data* **7**, 64 (2020).
33. Alencar, A. et al. *Desmatamento na Amazônia: indo além da "emergência crônica"* Vol. **90** (Ipam Belém, 2004).
34. McCarty, J., Justice, C. & Korontzi, S. Agricultural burning in the southeastern United States detected by MODIS. *Remote Sens. Environ.* **108**, 151–162 (2007).
35. Kolden, C. A. We're not doing enough prescribed fire in the western United States to mitigate wildfire risk. *Fire* **2**, 30 (2019).
36. Huffman, M. R. The many elements of traditional fire knowledge: synthesis, classification, and aids to cross-cultural problem solving in fire-dependent systems around the world. *Ecol. Soc.* **18**, art3 (2013).
37. Balch, J. K. et al. FIRED (Fire Events Delineation): an open, flexible algorithm and database of US fire events derived from the MODIS burned area product (2001–2019). *Remote Sens.* **12**, 3498 (2020).

38. Hersbach, H. et al. The ERA5 global reanalysis. *Q. J. R. Meteorol. Soc.* **146**, 1999–2049 (2020).
39. Noble, I., Gill, A. & Bary, G. McArthur’s fire-danger meters expressed as equations. *Aust. J. Ecol.* **5**, 201–203 (1980).
40. Van Wagner, C. E. et al. *Development and Structure of the Canadian Forest Fire Weather Index System* Technical Report (Canadian Forestry Service, 1987).
41. Wooster, M. J., Roberts, G., Perry, G. L. W. & Kaufman, Y. J. Retrieval of biomass combustion rates and totals from fire radiative power observations: FRP derivation and calibration relationships between biomass consumption and fire radiative energy release. *J. Geophys. Res. Atmos.* **110**, D24311 (2005).
42. Andela, N. et al. A human-driven decline in global burned area. *Science* **356**, 1356–1362 (2017).
43. Libonati, R. et al. Twenty-first century droughts have not increasingly exacerbated fire season severity in the Brazilian Amazon. *Sci. Rep.* **11**, 4400 (2021).
44. Alencar, A., Nepstad, D. & Diaz, M. C. V. Forest understory fire in the Brazilian Amazon in ENSO and non-ENSO years: area burned and committed carbon emissions. *Earth Interact.* **10**, 1–17 (2006).
45. Balch, J. K. et al. Switching on the big burn of 2017. *Fire* **1**, 17 (2018).
46. Higuera, P. E. & Abatzoglou, J. T. Record-setting climate enabled the extraordinary 2020 fire season in the western United States. *Glob. Change Biol.* **27**, 1–2 (2021).
47. Chiodi, A. M., Potter, B. E. & Larkin, N. K. Multi-decadal change in western US nighttime vapor pressure deficit. *Geophys. Res. Lett.* **48**, e2021GL092830 (2021).

48. Joseph, M. B. et al. Spatiotemporal prediction of wildfire size extremes with Bayesian finite sample maxima. *Ecol. Appl.* **29**, 1266–1281 (2019).
49. Perkins, S. E., Alexander, L. V. & Nairn, J. R. Increasing frequency, intensity and duration of observed global heatwaves and warm spells. *Geophys. Res. Lett.* **39**, L20714 (2012).
50. Stone, D. A. & Weaver, A. J. Daily maximum and minimum temperature trends in a climate model. *Geophys. Res. Lett.* **29**, 70-1–70-4 (2002).
51. Kolden, C. A., Lutz, J. A., Key, C. H., Kane, J. T. & van Wagendonk, J. W. Mapped versus actual burned area within wildfire perimeters: characterizing the unburned. *For. Ecol. Manage.* **286**, 38–47 (2012).
52. Krawchuk, M. A. et al. Topographic and fire weather controls of fire refugia in forested ecosystems of northwestern North America. *Ecosphere* **7**, e01632 (2016).
53. Koontz, M. J., North, M. P., Werner, C. M., Fick, S. E. & Latimer, A. M. Local forest structure variability increases resilience to wildfire in dry western U.S. coniferous forests. *Ecol. Lett.* **23**, 483–494 (2020).
54. Saide, P. E. et al. Revealing important nocturnal and day-to-day variations in fire smoke emissions through a multiplatform inversion. *Geophys. Res. Lett.* **42**, 3609–3618 (2015).
55. Korontzi, S., McCarty, J., Loboda, T., Kumar, S. & Justice, C. Global distribution of agricultural fires in croplands from 3 years of Moderate Resolution Imaging Spectroradiometer (MODIS) data. *Glob. Biogeochem. Cycles* **20**, GB2021 (2006).
56. Schmit, T. J. et al. A closer look at the ABI on the GOES-R series. *Bull. Am. Meteorol. Soc.* **98**, 681–698 (2017).
57. Schmidt, C. In *The GOES-R Series* (eds Goodman, S. J. et al.) 145–163 (Elsevier, 2020).

58. Giglio, L., Boschetti, L., Roy, D. P., Humber, M. L. & Justice, C. O. The Collection 6 MODIS burned area mapping algorithm and product. *Remote Sens. Environ.* **217**, 72–85 (2018).
59. Hawbaker, T. J. et al. Mapping burned areas using dense time-series of Landsat data. *Remote Sens. Environ.* **198**, 504–522 (2017).
60. Schroeder, W. et al. Early characterization of the active fire detection products derived from the next generation NPOESS/VIIRS and GOES-R/ABI instruments. In *2010 IEEE International Geoscience and Remote Sensing Symposium* 2683–2686 <https://doi.org/10.1109/IGARSS.2010.5650863> (IEEE, 2010).
61. Schroeder, W. et al. Validation of GOES and MODIS active fire detection products using ASTER and ETM+ data. *Remote Sens. Environ.* **112**, 2711–2726 (2008).
62. Hall, J. V., Zhang, R., Schroeder, W., Huang, C. & Giglio, L. Validation of GOES-16 ABI and MSG SEVIRI active fire products. *Int. J. Appl. Earth Obs. Geoinf.* **83**, 101928 (2019).
63. Li, F., Zhang, X., Kondragunta, S., Schmidt, C. C. & Holmes, C. D. A preliminary evaluation of GOES-16 active fire product using Landsat-8 and VIIRS active fire data, and ground-based prescribed fire records. *Remote Sens. Environ.* **237**, 111600 (2020).
64. Li, F., Zhang, X., Roy, D. P. & Kondragunta, S. Estimation of biomass-burning emissions by fusing the fire radiative power retrievals from polar-orbiting and geostationary satellites across the conterminous United States. *Atmos. Environ.* **211**, 274–287 (2019).
65. Jordahl, K. *GeoPandas: Python tools for geographic data*; <https://github.com/geopandas/geopandas> (2020).
66. Gillies, S. et al. *Rasterio: Geospatial raster I/O for Python programmers*; <https://github.com/rasterio/rasterio> (2020).

67. Lyapustin, A. & Wang, Y. *MODIS Multi-angle Implementation of Atmospheric Correction (MAIAC) data user's guide*; [https://modis-land.gsfc.nasa.gov/pdf/MCD19\\_UserGuide\\_final\\_Feb-6-2018.pdf](https://modis-land.gsfc.nasa.gov/pdf/MCD19_UserGuide_final_Feb-6-2018.pdf) (2018).
68. Sulla-Menashe, D. & Friedl, M. A. *User guide to collection 6 MODIS land cover (MCD12Q1 and MCD12C1) product*; [https://lpdaac.usgs.gov/documents/101/MCD12\\_User\\_Guide\\_V6.pdf](https://lpdaac.usgs.gov/documents/101/MCD12_User_Guide_V6.pdf) (2018).
69. Beck, H. E. et al. Present and future Köppen–Geiger climate classification maps at 1-km resolution. *Sci. Data* **5**, 180214 (2018).
70. Siegel, A. F. Robust regression using repeated medians. *Biometrika* **69**, 242–244 (1982).
71. Cleveland, R. B., Cleveland, W. S., McRae, J. E. & Terpenning, I. STL: a seasonal-trend decomposition. *J. Stat.* **6**, 3–73 (1990).
72. Bolker, B. M. et al. Generalized linear mixed models: a practical guide for ecology and evolution. *Trends Ecol. Evol.* **24**, 127–135 (2009).
73. Wood, S. N., Pya, N. & Säfken, B. Smoothing parameter and model selection for general smooth models. *J. Am. Stat. Assoc.* **111**, 1548–1563 (2016).
74. Sen, P. K. Estimates of the regression coefficient based on Kendall's tau. *J. Am. Stat. Assoc.* **63**, 1379–1389 (1968).

## Acknowledgements

Funding for this work was provided by Earth Lab through CU Boulder's Grand Challenge Initiative and the Cooperative Institute for Research in Environmental Sciences (CIRES) at CU Boulder. J.K.B. was supported, in part, by the National Science Foundation's CAREER (grant number 1846384) and Macrosystems (grant number 2017889) programmes. A.P.W. was supported by the Zegar Family Foundation. M.E.C. was supported, in

part, by ‘RII Track-1: Linking Genome to Phenome to Predict Adaptive Responses of Organisms to Changing Landscapes’ under the National Science Foundation (grant number OIA-1757324).

## Author information

### Author notes

1. These authors contributed equally: John T. Abatzoglou, Maxwell B. Joseph, Michael J. Koontz, Adam L. Mahood, Joseph McGlinchy

### Affiliations

1. Earth Lab, CIRES, University of Colorado Boulder, Boulder, CO, USA

Jennifer K. Balch, Maxwell B. Joseph, Michael J. Koontz, Adam L. Mahood & Joseph McGlinchy

2. Department of Geography, University of Colorado Boulder, Boulder, CO, USA

Jennifer K. Balch & Adam L. Mahood

3. Management of Complex Systems Department, University of California-Merced, Merced, CA, USA

John T. Abatzoglou

4. NCX, San Francisco, CA, USA

Maxwell B. Joseph

5. Hydrosat Inc., Washington DC, USA

Joseph McGlinchy

6. Human–Environment Systems, College of Innovation and Design,  
Boise State University, Boise, ID, USA

Megan E. Cattau

7. Department of Geography, University of California, Los Angeles, Los Angeles, CA, USA

A. Park Williams

8. Lamont-Doherty Earth Observatory of Columbia University, Palisades, NY, USA

A. Park Williams

## Contributions

Conceptualization, J.K.B., J.T.A., M.E.C. and A.P.W.; data curation, J.T.A., M.B.J., M.J.K. and J.M.; formal analysis, J.T.A., M.E.C., M.B.J., M.J.K. and J.M.; funding acquisition, J.K.B. and A.P.W.; investigation, J.K.B., J.T.A., M.E.C., M.B.J., M.J.K., A.L.M. and J.M.; methodology, J.K.B., J.T.A., M.E.C., M.B.J., M.J.K., J.M. and A.P.W.; project administration, J.K.B.; resources, M.B.J.; software, M.B.J., M.J.K. and J.M.; supervision, J.K.B.; visualization, J.K.B., J.T.A., M.E.C., M.B.J., M.J.K., A.L.M., J.M. and A.P.W.; writing—original draft, J.K.B., M.B.J., M.J.K. and J.M.; writing—review and editing J.K.B., J.T.A., M.E.C., M.B.J., M.J.K., A.L.M., J.M. and A.P.W.

## Corresponding authors

Correspondence to [Jennifer K. Balch](#), [John T. Abatzoglou](#) or [A. Park Williams](#).

## Ethics declarations

## Competing interests

The authors declare no competing interests.

## Peer review

### Peer review information

*Nature* thanks Renata Libonati and the other, anonymous, reviewer(s) for their contribution to the peer review of this work. Peer reviewer reports are available.

## Additional information

**Publisher's note** Springer Nature remains neutral with regard to jurisdictional claims in published maps and institutional affiliations.

## Extended data figures and tables

### [Extended Data Fig. 1 Climate and landcover classifications used in VPD threshold analysis shown at 1° grid cell resolution.](#)

**a**, The Köppen–Geiger climate classifications<sup>69</sup>. **b**, The MODIS MOD12Q1 landcover<sup>68</sup>. **c**, Areas in red fill represent Köppen–Geiger landcover classes that were burnable (that is,  $\geq 100$  fire events in the FIRED data product<sup>37</sup> that also had GOES detections<sup>19</sup> between December 2017 and June 2020).

### [Source data](#)

### [Extended Data Fig. 2 Observed peak fire season \(dark lines\) based on MODIS active fire detections \(MCD14ML\)20.](#)

Each line, smoothed using a 31-day window, represents the expected number of day or night active fire detections per overpass per million km<sup>2</sup> (left facets) or the expected day or night FRP per detection (right facets) for each landcover type averaged across 2003–2020. Note the y axis is on the

$\log_{10}$  scale and the FRP facet  $y$  axis begins at 15. Facets are presented in ascending order of the derived  $VPD_t$  (Extended Data Table 2). Bimodality in the ‘peak’ is largely explained by landcover types that are split across the Northern and Southern hemispheres.

[Source data](#)

**Extended Data Fig. 3 Diurnal oscillations of weather and active fire counts, displaying hourly time series of GOES active fire detections<sup>19</sup> and ERA-5<sup>38</sup> VPD for two fire events in the United States.**

A dashed line marks the land-cover specific VPD threshold. The red points indicate observations made during the day and the blue points represent night-time observations.

[Source data](#)

**Extended Data Fig. 4 Estimated relationship between VPD (kPa) on GOES active fire detections by landcover type (facets).**

The posterior mean is shown as a solid line, with 1,000 posterior draws as transparent lines in the background to convey uncertainty. Facets are presented in ascending order of the derived VPD thresholds.

[Source data](#)

**Extended Data Fig. 5**

**Trends in flammable nights.** Change in daily minimum VPD (kPa) from 1979 to 2020<sup>38</sup> based on a linear trend.

**Extended Data Fig. 6 Global climatology of flammable hours and nights (1991–2020) and global trend in flammable hours**

## and nights (1979–2020), based on VPD38.

**a–d**, The average total of daytime hours (**a**), night-time hours (**b**), nights (days, 24-hour periods, when  $\text{VPD}_{\min} > \text{VPD}_t$ ; **c**) and consecutive nights (**d**) per year (1991–2020) where minimum VPD  $> \text{VPD}_t$  across the burnable globe. **e–h**, Change in annual number of daytime hours (**e**), night-time hours (Fig. 4 reproduced here for ease of comparison; **f**), nights (**g**) and consecutive nights (**h**) (1979–2019) where minimum VPD  $> \text{VPD}_t$  based on a linear trend across the burnable globe.

## Extended Data Fig. 7 Global trends in active fire detections from 2003 to 2020.

**a–c**, Day (**a**), night (**b**) and the percentage of night-time (**c**) detections out of total detections, Siegel-estimated slopes<sup>70</sup> of MODIS active fire detections<sup>20</sup> at  $1^\circ$  annual aggregations. Grey pixels are those defined as burnable but without a significant trend.

[Source data](#)

## Extended Data Fig. 8 Trends in fire radiative power and active fire detections from 2003 to 2020.

**a, b**, Trends (2003–2020) in MODIS fire radiative power (MW per detection) for detections that occurred during the day and night, and areas with increases and decreases in flammable night-time hours from 1979–2020 (**a**) and active fire detections (per overpass per  $M \text{ km}^2$ ) and percent of total detections that occurred at night, globally and by major Köppen–Geiger climate classification<sup>69</sup> (Siegel-estimated slopes<sup>70</sup> at monthly aggregations at  $1^\circ$ ; **b**). Bold lines surrounded by dotted confidence intervals indicate significant trends. The underlying data are the observed values with the seasonal oscillation removed, and smoothed to aid visualization.

[Source data](#)

**Extended Data Table 1** Observed aspects of the night-time fire regime from the MODIS-derived MCD14ML active fire product, with variables averaged across 2003–2020

**Extended Data Table 2** Estimated VPD<sub>t</sub> for each landcover class

## Supplementary information

### [Peer Review File](#)

### Source data

#### [Source Data Fig. 1](#)

#### [Source Data Fig. 2](#)

#### [Source Data Fig. 4](#)

#### [Source Data Fig. 5](#)

#### [Source Data Extended Data Fig. 1](#)

#### [Source Data Extended Data Fig. 2](#)

#### [Source Data Extended Data Fig. 3](#)

#### [Source Data Extended Data Fig. 4](#)

#### [Source Data Extended Data Fig. 7](#)

#### [Source Data Extended Data Fig. 8](#)

### Rights and permissions

#### [Reprints and Permissions](#)

## About this article

### Cite this article

Balch, J.K., Abatzoglou, J.T., Joseph, M.B. *et al.* Warming weakens the night-time barrier to global fire. *Nature* **602**, 442–448 (2022).  
<https://doi.org/10.1038/s41586-021-04325-1>

- Received: 03 July 2020
- Accepted: 09 December 2021
- Published: 16 February 2022
- Issue Date: 17 February 2022
- DOI: <https://doi.org/10.1038/s41586-021-04325-1>

### Share this article

Anyone you share the following link with will be able to read this content:

[Get shareable link](#)

Sorry, a shareable link is not currently available for this article.

[Copy to clipboard](#)

Provided by the Springer Nature SharedIt content-sharing initiative

### [The night brakes on fires are failing](#)

Research Briefing 16 Feb 2022

---

This article was downloaded by **calibre** from <https://www.nature.com/articles/s41586-021-04325-1>

- Article
- [Published: 26 January 2022](#)

# Evolution of inner ear neuroanatomy of bats and implications for echolocation

- [R. Benjamin Sulser](#)<sup>1</sup>,
- [Bruce D. Patterson](#)<sup>2</sup>,
- [Daniel J. Urban](#)<sup>3,4</sup>,
- [April I. Neander](#) [ORCID: orcid.org/0000-0001-6816-2872](#)<sup>5</sup> &
- [Zhe-Xi Luo](#) [ORCID: orcid.org/0000-0003-2170-8879](#)<sup>5</sup>

[Nature](#) volume **602**, pages 449–454 (2022)

- 4140 Accesses
- 1 Citations
- 238 Altmetric
- [Metrics details](#)

## Subjects

- [Animal behaviour](#)
- [Evolutionary theory](#)
- [Phylogenetics](#)

## Abstract

Phylogenomics of bats suggests that their echolocation either evolved separately in the bat suborders Yinpterochiroptera and Yangochiroptera, or had a single origin in bat ancestors and was later lost in some yinpterochiropterans<sup>1,2,3,4,5,6</sup>. Hearing for echolocation behaviour depends on the inner ear, of which the spiral ganglion is an essential structure. Here we report the observation of highly derived structures of the spiral ganglion in yangochiropteran bats: a *trans*-otic ganglion with a wall-less Rosenthal's canal. This neuroanatomical arrangement permits a larger ganglion with more neurons, higher innervation density of neurons and denser clustering of cochlear nerve fascicles<sup>7,8,9,10,11,12,13</sup>. This differs from the plesiomorphic neuroanatomy of Yinpterochiroptera and non-chiropteran mammals. The osteological correlates of these derived ganglion features can now be traced into bat phylogeny, providing direct evidence of how Yangochiroptera differentiated from Yinpterochiroptera in spiral ganglion neuroanatomy. These features are highly variable across major clades and between species of Yangochiroptera, and in morphospace, exhibit much greater disparity in Yangochiroptera than Yinpterochiroptera. These highly variable ganglion features may be a neuroanatomical evolutionary driver for their diverse echolocating strategies<sup>4,14,15,16,17</sup> and are associated with the explosive diversification of yangochiropterans, which include most bat families, genera and species.

This is a preview of subscription content

## Access options

Subscribe to Nature+

Get immediate online access to the entire Nature family of 50+ journals

\$29.99

monthly

[Subscribe](#)

Subscribe to Journal

Get full journal access for 1 year

\$199.00

only \$3.90 per issue

[Subscribe](#)

All prices are NET prices.

VAT will be added later in the checkout.

Tax calculation will be finalised during checkout.

Buy article

Get time limited or full article access on ReadCube.

\$32.00

[Buy](#)

All prices are NET prices.

### **Additional access options:**

- [Log in](#)
- [Learn about institutional subscriptions](#)

**Fig. 1: Major neuroanatomical configurations of the spiral ganglion and Rosenthal's canal in cochleas of bats.**

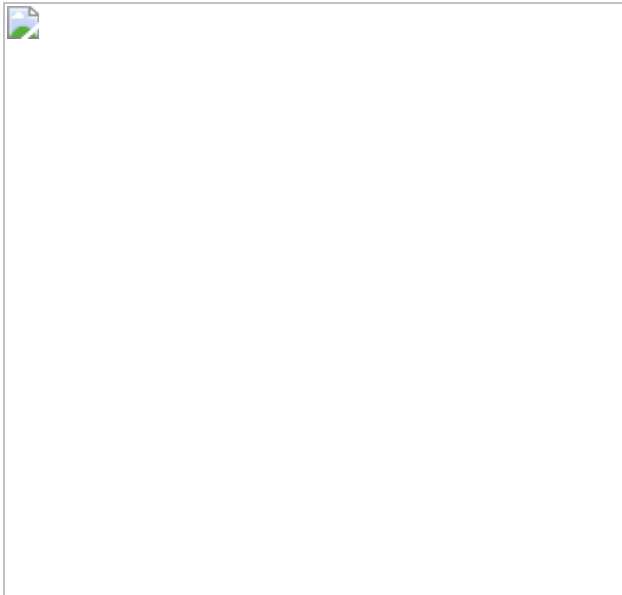


**Fig. 2: Evolutionary patterns and morphological disparity of Rosenthal's canal and spiral ganglion in inner ears of bats.**

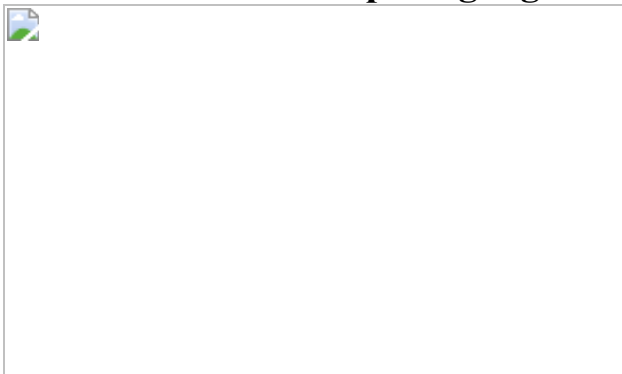
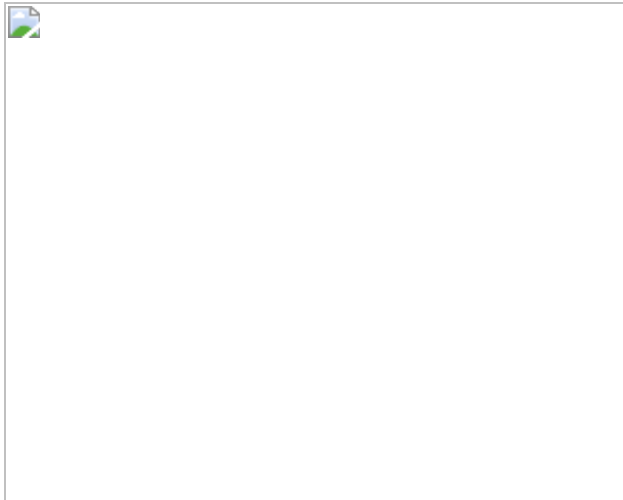


**Fig. 3: Apomorphic neuroanatomical configuration of wall-less Rosenthal's canal (RC) for *trans*-otic ganglion in most Yangochiroptera, corroborating CT scans and histology in *M. inflatus* (Miniopteridae).**



## Data availability

Skull specimens of bats and mammalian outgroups examined by CT scanning in this study are in the collection of Field Museum of Natural History, the teaching collections of UChicago, and the mammalogy collection of American Museum of Natural History. The specimen list is presented in Supplementary Table 2. CT scanning resolutions for all scanned specimens are listed in Supplementary Table 2. Metric measurements of CT visualization of the Rosenthal's Canal and cochlear canal turns of these specimens are presented in Supplementary Table 3. Photographs of histological sections are presented in the figures and extended data figures.

## Code availability

The metric measurements of the Rosenthal's canal and cochlear turns were obtained using the Mimics visualization package ([www.materialise.com](http://www.materialise.com)). Methods of morphological disparity analysis and ancestral state reconstruction are presented in the [Supplementary Information](#).

## References

1. Teeling, E. C. et al. Molecular evidence regarding the origin of echolocation and flight in bats. *Nature* **403**, 188–192 (2000).

2. Teeling, E. C. et al. A molecular phylogeny for bats illuminates biogeography and the fossil record. *Science* **307**, 580–584 (2005).
3. Maltby, A., Jones, K. E. & Jones, G. in *Handbook of Mammalian Vocalization—An Integrative Neuroscience Approach* (ed Brudzynski, S. M.) 37–50 (Elsevier, 2010).
4. Jones, G., Teeling, E. C. & Rossiter, S. J. From the ultrasonic to the infrared: molecular evolution and the sensory biology of bats. *Front. Physiol.* **4**, 117 (2013).
5. Jebb, D. et al. Six reference-quality genomes reveal evolution of bat adaptations. *Nature* **583**, 578–584 (2020).
6. Nojiri, T. et al. Embryonic evidence uncovers convergent origins of laryngeal echolocation in bats. *Curr. Biol.* **31**, 1353–1365.e3 (2021).
7. Bruns, V., Fielder, J. & Kraus, H. J. Structural diversity of the inner ear of bats. *Myotis* **21/22**, 52–61 (1984).
8. Ramprashad, F., Money, K. E., Landolt, J. P. & Laufer, J. A neuroanatomical study of the cochlea of the little brown bat (*Myotis lucifugus*). *J. Comp. Neurol.* **178**, 347–363 (1978).
9. Vater, M. in *Animal Sonar: Processes and Performance* (eds Nachtigall, P. E. & Moore, P. W. B.) 225–241 (Springer, 1988).
10. Henson, O. W. & Henson, M. M. in *Animal Sonar: Processes and Performance* (eds Nachtigall, P. E. & Moore, P. W. B.) 301–305 (Springer, 1988).
11. Echteler, S. M. & Nofsinger, Y. C. Development of ganglion cell topography in the postnatal cochlea. *J. Comp. Neurol.* **425**, 436–446 (2000).
12. Johnson, S. B., Schmitz, H. M. & Santi, P. A. TSLIM imaging and a morphometric analysis of the mouse spiral ganglion. *Hear. Res.* **278**, 34–42 (2011).

13. Gacek, R. R. Clustering is a feature of the spiral ganglion in the basal turn. *ORL* **74**, 22–27 (2012).
14. Fenton, M. B. Describing the echolocation calls and behavior of bats. *Acta Chiropterologica* **1**, 127–136 (1999).
15. Fenton, M. B., Faure, P. A. & Ratcliffe, J. M. Evolution of high duty cycle echolocation in bats. *J. Exp. Biol.* **215**, 2935–2944 (2012).
16. Lazure, L. & Fenton, M. B. High duty cycle echolocation and prey detection by bats. *J. Exp. Biol.* **214**, 1131–1137 (2011).
17. Neuweiler, G. Evolutionary aspects of bat echolocation. *J. Comp. Physiol. A* **189**, 245–256 (2003).
18. Teeling, E., Dool, S. & Springer, M. in *Evolutionary History of Bats: Fossils, Molecules and Morphology* (eds Gunnell, G. F. & Simmons, N. B.) 1–22 (Cambridge Univ. Press, 2012).
19. Dabdoub, A. & Fritzsch, B. in *The Primary Auditory Neurons of the Mammalian Cochlea. Springer Handbook of Auditory Research* (eds Dabdoub, A. et al.) 1–10 (Springer, 2016).
20. Goodrich, L. V. in *The Primary Auditory Neurons of the Mammalian Cochlea. Springer Handbook of Auditory Research* (eds Dabdoub, A. et al.) 11–48 (Springer, 2016).
21. Yang, T., Kersigo, J., Jahan, I., Pan, N. & Fritzsch, B. The molecular basis of making spiral ganglion neurons and connecting them to hair cells of the organ of Corti. *Hear. Res.* **278**, 21–33 (2011).
22. Luo, Z.-X., Ruf, I. & Martin, T. The petrosal and inner ear of the Late Jurassic cladotherian mammal *Dryolestes leiriensis* and implications for ear evolution in therian mammals. *Zool. J. Linn. Soc.* **166**, 433–463 (2012).
23. Luo, Z.-X. & Manley, G. A. in *The Senses—A Comprehensive Reference Vol. 2* 2nd edn (eds Fritzsch, B. & Grothe, B.) 207–252

(Elsevier, 2020).

24. Vater, M. & Siefer, W. The cochlea of *Tadarida brasiliensis*: specialized functional organization in a generalized bat. *Hear. Res.* **91**, 178–195 (1995).
25. Carter, R. T. & Adams, R. A. Ontogeny of the larynx and flight ability in Jamaican fruit bats (Phyllostomidae) with considerations for the evolution of echolocation. *Anatomical Rec.* **297**, 1270–1277 (2014).
26. Davies, K. T., Maryanto, I. & Rossiter, S. J. Evolutionary origins of ultrasonic hearing and laryngeal echolocation in bats inferred from morphological analyses of the inner ear. *Front. Zool.* **10**, 2 (2013).
27. Simmons, N. B., Seymour, K. L., Habersetzer, J. & Gunnell, G. F. Primitive Early Eocene bat from Wyoming and the evolution of flight and echolocation. *Nature* **451**, 818–821 (2008).
28. Ekdale, E. G. Comparative anatomy of the bony labyrinth (inner ear) of placental mammals. *PLoS ONE* **8**, e66624 (2013).
29. Spoedlin, H. Anatomy of cochlear innervation. *Am. J. Otolaryngology* **6**, 453–467 (1985).
30. Kössl, M. & Vater, M. The cochlear frequency map of the mustache bat, *Pteronotus parnellii*. *J. Comp. Physiol. A* **157**, 687–697 (1985).
31. Vater, M. in *Ontogeny, Functional Ecology, and Evolution of Bats* (eds Adams, R. A. & Pedersen, S. C.) 137–173 (Cambridge Univ. Press, 2000).
32. Simmons, J. A. & Stein, R. A. Acoustic imaging in bat sonar: echolocation signals and the evolution of echolocation. *J. Comp. Physiol. A* **135**, 61–84 (1980).
33. Simmons, N. B., Seymour, K. L., Habersetzer, J. & Gunnell, G. F. Inferring echolocation in ancient bats. *Nature* **466**, E8 (2010).

34. Veselka, N. et al. A bony connection signals laryngeal echolocation in bats. *Nature* **463**, 939–942 (2010).
35. Shi, J. J. & Rabosky, D. L. Speciation dynamics during the global radiation of extant bats. *Evolution* **69**, 1528–1545 (2015).
36. Jacobs, D. & Bastian, A. High duty cycle echolocation may constrain the evolution of diversity within horseshoe bats (Family: Rhinolophidae). *Diversity* **10**, 85 (2018).
37. Arbour, J. H., Curtis, A. A. & Santana, S. E. Signatures of echolocation and dietary ecology in the adaptive evolution of skull shape in bats. *Nat. Commun.* **10**, 2036–13 (2019).
38. Hedrick, B. P. et al. Morphological diversification under high integration in a hyper diverse mammal clade. *J. Mamm. Evol.* **27**, 563–575 (2020).
39. Rojas, D., Warsi, O. M. & Dávalos, L. M. Bats (Chiroptera: Noctilionoidea) challenge a recent origin of extant Neotropical diversity. *Syst. Biol.* **65**, 432–448 (2016).
40. Thiagavel, J. et al. Auditory opportunity and visual constraint enabled the evolution of echolocation in bats. *Nat. Commun.* **9**, 98 (2018).
41. Schnitzler, H.-U. & Kalko, E. K. V. Echolocation by insect-eating bats. *Bio Science* **51**, 557–569 (2001).
42. Denzinger, A. & Schnitzler, H.-J. Bat guilds, a concept to classify the highly diverse foraging and echolocation behaviors of microchiropteran bats. *Front. Physiol.* **4**, 1 (2013).
43. Schnitzler, H.-U., & Denzinger, A. Auditory fovea and Doppler shift compensation: adaptations for flutter detection in echolocating bats using CF-FM signals. *J. Comp. Physiol. A* **197**, 541–559 (2011).
44. Neuweiler, G. Auditory adaptations for prey capture in echolocating bats. *Physiol. Rev.* **70**, 615–641 (1990).

45. Revell, L. J. phytools: an R package for phylogenetic comparative biology (and other things): phytools: R package. *Methods Ecol. Evol.* **3**, 217–223 (2012).
46. Paradis, E. & Schliep, K. ape 5.0: an environment for modern phylogenetics and evolutionary analyses in R. *Bioinformatics* **35**, 526–528 (2019).
47. R Core Team. R: A Language and Environment for Statistical Computing. <http://www.R-project.org/> (R Foundation for Statistical Computing, 2013).
48. Hsiao, C. J., Jen, P. H.-S. & Wu C. H. The cochlear size of bats and rodents derived from MRI images and histology. *NeuroReport* **26**, 478–482 (2015).

## Acknowledgements

This research was supported by UChicago Metcalf Fellowship and Graduate Fellowships from NSF and AMNH (to R.B.S.), by Postdoctoral Fellowships from NSF and University of Illinois (to D.J.U.), Field Museum Brown Mammal Research Fund and grant from JRS Biodiversity Foundation (to B.D.P.) and UChicago Biological Sciences Division and NSF fundings (to Z.-X.L.). We thank J. Schultz, K. Sears, N. Simmons, G. Manley, R. MacPhee and J. Flynn for discussion; K. Sears and E. Rodriguez for access to histological sectioning facilities. Full acknowledgements are presented in the [Supplementary Information](#).

## Author information

### Affiliations

1. Richard Gilder Graduate School, American Museum of Natural History, New York, NY, USA

R. Benjamin Sulser

2. Negaunee Integrative Research Center, Field Museum of Natural History, Chicago, IL, USA

Bruce D. Patterson

3. Institute for Genomic Biology, University of Illinois at Urbana-Champaign, Urbana, IL, USA

Daniel J. Urban

4. The Sears Lab, Department of Ecology and Evolution, University of California Los Angeles, Los Angeles, CA, USA

Daniel J. Urban

5. Department of Organismal Biology and Anatomy, The University of Chicago, Chicago, IL, USA

April I. Neander & Zhe-Xi Luo

## Contributions

Conceptualization: R.B.S., Z.-X.L. and B.D.P. Data contribution: all authors. CT scanning: A.I.N. and R.B.S. CT visualization and morphometrical analysis: R.B.S. Histological sections: R.B.S. and D.J.U. Providing access to museum collections and histological specimens: B.D.P. Interpretation of anatomical data: R.B.S., Z.-X.L., B.D.P. and A.I.N. Compilation of Supplementary Information: R.B.S., Z.-X.L. and B.D.P. Graphics: R.B.S., A.I.N. and Z.-X.L. Writing: R.B.S., Z.-X.L. and BDP, and approved by all authors. The project was coordinated by Z.-X.L.

## Corresponding authors

Correspondence to [R. Benjamin Sulser](#) or [Zhe-Xi Luo](#).

## Ethics declarations

## Competing interests

The authors declare no competing interests.

## Peer review information

*Nature* thanks Brock Fenton, Amanda Lauer and the other, anonymous, reviewers for their contribution to the peer review of this work.

## Additional information

**Publisher's note** Springer Nature remains neutral with regard to jurisdictional claims in published maps and institutional affiliations.

## Extended data figures and tables

### [Extended Data Fig. 1 Phylogenetic evolution and systematic character distribution of the wall patterns of Rosenthal's canal for placement of the spiral ganglion among bats and outgroups, showing phylogeny and classification.](#)

**A** (left, cladogram): phylogeny of Chiroptera (tree topology based on Ref. [35](#).-Shi and Rabosky, 2015) Superfamilies are indicated by numbers: **1**- Rhinolophoidea, **2**- Emballonuroidea, **3** - Noctilionoidea, **4** - Vespertilionoidea. **B.-D.** (right columns), wall patterns of Rosenthal's canal (RC) from the basal  $\frac{1}{2}$  turn to the third (apical) turn of the entire cochlea (explanation: between the fenestra vestibuli and basal  $\frac{1}{2}$  turn landmark, the spiral ganglion canal has small foramina in all therian mammals, and no variation in the local area). The research here focuses on the structural and phylogenetic variations in ganglion canal wall between the basal  $\frac{1}{2}$  turn and the apex). **B.** RC wall pattern at the basal  $\frac{1}{2}$  cochlear turn; **C.** RC wall pattern at the 1.5 cochlear turn; **D.** RC wall pattern at the 2.5 cochlear turn. For taxa with less than 2.5 turns, the patterns in the remainder of coil from turn 1.5 onward is represented. The three major wall patterns (lower left panel) are explained in Fig. [1](#) and Extended Data Fig. [2](#). Structures of the

cochlear canal and the spiral ganglion canal are based on CT scanning (Supplementary Tables 1–3; n = 45). Of these, 15 bats and two outgroups are examined both by CT scans and then corroborated by original histological sections of this study, or from published histological literature (Supplementary Table 1). Symbol † - two taxa (*Homo sapiens* and *Crocidura russala*) that are based on published cochlear structure from literature. **E.** Echolocation duty cycle for bats in this study (LDC= Low Duty Cycle, HDC = High Duty Cycle). Foraging habitats and foraging modes of bats. Abbreviations for foraging habitats for echolocation: **E** – around the edges of open space; **Nc** – narrow space with cluttered background; **O** - open and uncluttered foraging space (Ref. [42](#).- Denzinger and Schnitzler 2013); **TC** - tongue-clicking echolocation. Abbreviations for foraging modes: **A** – aerial foraging of insects; **Fr** – frugivorous; **Fl** – foraging for fluttering insects; **G**- gleaning for prey; **Tw** – trawling over water.

**Extended Data Fig. 2 Ancestral state reconstruction for the wall configurations of Rosenthal's canal of bats and therian mammal outgroups. Each taxon is assigned a diagnostic character in one of the three major canal wall patterns.**

The assignments were based on one of the two alternative representation schemes. **A.** The wall structure of the ganglion canal of each taxon is represented by the most derived ganglion wall pattern for taxa with multiple patterns. **B.** The most extensive canal wall pattern (character state), ranked by the highest percentage to the total cochlear length, is assigned to be the diagnostic character of the taxon. The ancestral state reconstruction at the main nodes of the cladogram is estimated by utilizing the *phytools* (Ref. [45](#) - Revell 2012) and *ape* (Ref. [46](#) - Paradis and Schliep, 2019) programs in R (Ref. [47](#) - R core team, 2013). The foraminal wall with cis-otic ganglion (Blue - primitive); the fenestral wall and cis-otic ganglion (Green - intermediate); the wall-less canal and trans-otic ganglion (Red – most derived). Tree topology is adapted from Shi and Rabosky (2015) (Ref. [35](#).) and Teeling et al. (2016). **C.** Morphological disparity of the inner ear ganglion by the enclosure of the cochlear ganglion (measured via percent ossification, see main text) and cochlear turns. Symbols and plot are

identical to Fig. 2, but adjusted to show alternate groupings of Yangochiroptera (red) and Yinpterochiroptera + outgroups (blue). Source data in Supplementary Table 3.

### Extended Data Fig. 3 Three major neuroanatomical configurations of the spiral ganglion and Rosenthal's canal in bats and therian outgroups.

**A.** Schematic configuration of Rosenthal's canal, its tractus foraminosus (= foraminial wall), and their structural relationships to the cochlear nerve fiber fascicles and the cis-otic ganglion placement. **B.** Schematic model of the bony canal for the cis-otic ganglion and the foramina on the surface of internal auditory meatus (nerve structures omitted for clarity). **B1.** *Felis catus* (mammal outgroup; domestic cat): the foraminial canal wall structure as seen on the surface of the internal auditory meatus, visualized by CT. **B2.** *Hypsignathus monstrosus* (Yinpterochiroptera, Pteropodidae) – the hammer-headed bat: the foraminial RC wall in the internal auditory meatus. **B3.** *Rhinolophus blasii* (Yinpterochiroptera, Rhinolophidae) Blasius's horseshoe bat: the foraminial RC wall in the internal auditory meatus. The foraminial configuration (**B1 - B3**) is typical of therian mammals and plesiomorphic for Chiroptera as a group and for Yinpterochiroptera. **C** and **C1.** *Tadarida brasiliensis* (Yangochiroptera, Molossidae) – the Brazilian free-tailed bat: the fenestral configuration with large openings (tractus fenestralis) in the thinner wall with the cis-otic placement of the spiral ganglion. The large fenestra typically are present in the basal and near the  $\frac{1}{2}$  cochlear turns in bats having this pattern. The fenestral pattern is more derived than the plesiomorphic foraminial pattern, and it is an intermediate character state between the foraminial pattern and the most derived wall-less pattern. **D** and **D1.** *Miniopterus inflatus* (Yangochiroptera, Miniopteridae) – the greater long-fingered bat: the wall-less pattern of Rosenthal's canal, typically between the apex and the basal  $\frac{1}{2}$  cochlear turn, allows the trans-otic placement of the spiral ganglion, making ganglion space confluent with the space of the internal auditory meatus in the absence of RC wall. With the exception of the species of *Noctilio*, all Yangochiroptera show this pattern in the apical turn of the cochlea (Extended Data Fig. 1). Structurally, this is the most extreme neuroanatomical pattern of the ganglion and its canal. The confluence of spiral ganglion space and the internal auditory

meatus eliminates the constraint of many small foramina for the cochlear nerve fascicles to connect to the spiral ganglion and helps to shorten the ganglion's connection to cochlear nerve trunk. It also provides more space to accommodate greater numbers of ganglion neurons in higher density.

**Extended Data Fig. 4 Therian outgroup (*Felis catus*) and yinpterochiropteran bats (*Epomophorus wahlbergi* and *Rousettus aegyptiacus*): foraminal wall of the Rosenthal's canal (RC) for cis-otic ganglion placement.**

A. Schematic illustration of the cochlear nerve fiber fascicles and the cis-otic spiral ganglion, and their anatomical relationships to osteological structures. **A1.** The tractus foraminosus (foraminal wall) extends from the base to the apex of the cochlea, shown as dense foramina in the wall of internal auditory meatus in a schematic uncoiled cochlea.

Yinpterochiropteran bats (*Epomophorus* – non-echolocating and *Rousettus* – tongue-clicking echolocation) have the plesiomorphic foraminal wall and cis-otic ganglion placement, as in non-chiropteran therian mammals (represented by *Felis catus*, Carnivora, Laurasiatheria). **B.** *Epomophorus wahlbergi*: Histological section through modiolar section of the whole cochlea. **B1.** Histological details at basal  $\frac{1}{2}$  cochlear turn. **C.** *Epomophorus* - CT visualization of location of the ganglion in a transparent cochlea, with CT slice through to visualize the relationship of the ganglion. **C1.** Cut-away CT model the modiolar section of the cochlea to show the tractus foraminosus and ganglion (yellow) in Rosenthal's canal, relative to the cut-away internal auditory meatus. **D.** *Epomophorus* CT slice through the modiolar section of the cochlea to illustrate the osteological structures of the ganglion and cochlear nerve fibers (corresponding to histological section of **B**). **D1.** Details of the cochlea and Rosenthal's canal at the  $\frac{1}{2}$  cochlear turn. **E.** *Rousettus aegyptiacus* – CT slice across the modiolar plane of the cochlea to show the foraminal wall pattern of Rosenthal's Canal in the entire internal auditory meatus. **E1.** Details of ossified foraminal wall of the Rosenthal's canal at basal  $\frac{1}{2}$  turn of *Rousettus*. **F.** *Felis catus* (representative of laurasiatherian outgroup) - Cut-away CT visualization model of foramina on the ossified wall of the internal auditory meatus, and the inclusion of the ganglion (yellow) in Rosenthal's canal. **F1.**

*Felis* – CT slice through modiolar plane to show details of Rosenthal’s canal and its foraminal wall, relative to the internal auditory meatus. **G.** CT slice through the entire cochlea at the modiolar section. **G1.** *Felis* – enlarged details of Rosenthal’s canal and its structures at the basal 1.2 cochlear turn. The tractus foraminosus in the internal auditory meatus, the foraminal wall of the ganglion canal, and the internal placement of cis-otic ganglion are the ancestral pattern of therians, and their Mesozoic dryolestoid relatives (Ref. [22](#).- Luo et al. 2012). These are plesiomorphic for laurasiatherian placentals, including *Felis catus* and all yinpterochiropteran bats.

**Extended Data Fig. 5 Histology and CT scans of neuroanatomy of Rosenthal’s canal for the cis-otic spiral ganglion in *Hipposideros caffer* (Yinpterochiroptera, Hipposideridae).**

Sundevall’s roundleaf bat is a laryngeal echolocating bat. **A.** Diagram of the foraminal wall of Rosenthal’s canal for cis-otic placement of the ganglion, showing the tractus foraminosus (foraminal wall pattern) for the fascicles of cochlear nerve to connect with the ganglion in the Rosenthal’s canal; **A1.** Distribution of foramina along the length of cochlea. **B.** Histological section at the modiolus, to show internal auditory meatus, the canaliculi of tractus foraminosus in the entire cochlea; **B1,** Histological structures of the spiral ganglion in Rosenthal’s canal, the cochlear nerve fascicles through canaliculi of tractus foraminosus, and the radial fibers of the ganglion through the habenula perforata in the primary bony lamina, at the 1½ cochlear turn. **C.** and **C1.** CT scan slice through the modiolar section, corresponding to histology section of **B** and **B1:** to show the ganglion space in Rosenthal’s canal, the tractus foraminosus in canal wall, and the habenula perforata in primary bony lamina for radial ganglion fibers at the 1½ cochlear turn. **D** and **D1.** CT slice through transparent model, and cut-away section corresponding to histological section, to show the foraminal pattern on the surface of the internal auditory meatus near the 1½ to 2 cochlear turns. **E.** Cut-away CT visualization of the whole cochlea at the modiolar section. **E1.** Intact cochlea in the medial (endocranial) view of the internal auditory meatus to show the foraminal wall pattern.

**Extended Data Fig. 6 Foraminal Rosenthal's canal and cis-otic placement for two yinpterochiropteran LDC echolocators, *Rhinopoma hardwickii* and *Lyroderma lyra*.**

A. Anatomy of key neural and osteological structures. **A1.** Distribution of foramina for cochlear nerve fascicles from the base to the apex of the cochlea. **B.** *Rhinopoma* – uCT sections through the modiolar section of the whole cochlea. **B1.** Detail of Rosenthal's canal at the first  $\frac{1}{2}$  turn of the cochlea. **C.** Transparent inner ear model with the spiral ganglion (yellow) visible. **C1.** and **C2.** Cut-away section of the inner ear model to visualize the location of the spiral ganglion in relation to Rosenthal's canal. **D.** Details of the inner ear model in the medial (endocranial) view to visualize the extent of ossification within the modiolar region. **E.** *Lyroderma lyra* (“*Megaderma lyra*”)- transparent inner ear model with the spiral ganglion (yellow) visible. **E1.** and **E2.** Cut-away section of the inner ear model to visualize the location of the spiral ganglion in relation to Rosenthal's canal. **F** uCT sections through the modiolar section of the whole cochlea. **F1.** Detail of Rosenthal's canal at the first  $\frac{1}{2}$  turn of the cochlea. **G.** Details of the inner ear model in the medial (endocranial) view in order to visualize the extent of ossification within the modiolar region.

**Extended Data Fig. 7 Histology and CT scans of neuroanatomy of Rosenthal's canal for fenestral wall of Rosenthal's canal for the Cis-otic Spiral Ganglion in *Coleura afra* (Yangochiroptera, Emballonuridae).**

The African sheath-tailed bat *Coleura afra* is a laryngeal echolocating bat of Yangochiroptera. **A.** Diagram of the fenestral wall (tractus fenestralis) of Rosenthal's canal (RC); the large fenestrae of RC wall are well developed beyond the basal  $\frac{3}{4}$  turn, and the RC becomes wall-less in the apical  $\frac{1}{2}$  turn. The basal-most part of the cochlea retains the standard mammalian pattern of small foramina. **B.** Histology section through the modiolar plane and the internal auditory meatus to show the cis-otic placement of the ganglion, the tractus fenestralis that forms the canal wall. **B1.** Histological details of the fenestral openings of the  $1\frac{1}{2}$  cochlear turn. **C.** CT scan slice corresponding to the histological section of the whole cochlea. **C1.** CT visualization of the

ganglion space in Rosenthal's canal and the fenestral openings in canal wall at the 1½ cochlear turn. **D**. Transparent cochlea and **D1**. Cut-away section corresponding to histological sections (**B** and **B1**): the fenestras in the internal auditory meatus near the 1 to 1½ cochlear turns, and wall-less pattern of the apical turn. **E**. Intact cochlea in the medial (endocranial) view of the internal auditory meatus to show the fenestral wall pattern. **E1**. Cut-away CT visualization of the whole cochlea at the modiolar section.

**Extended Data Fig. 8 Fenestral wall of Rosenthal's canal and cis-otic placement of ganglion in *Tadarida brasiliensis* (Yangochiroptera, Molossidae) by CT scans.**

The Brazilian free-tailed bat *Tadarida brasiliensis* is a laryngeal echolocating bat. **A**. Diagram of the fenestral wall of Rosenthal's canal. **A1**. The canal wall shows large fenestrae between the basal ½ turn and 1½ turn, but it becomes wall-less in the apical ½ turn. **B**. and **C**. Outline illustration and CT scan slice across the modiolar section of the fenestral pattern up to ½ turn and the wall-less pattern in apical ½ turn. **C1**. Details of the large fenestral opening (tractus fenestralis) between the RC canal and the internal auditory meatus. **D** and **D1**. Transparent CT visualization and cut-away section of local details of fenestrae in the internal auditory meatus. **E**. Intact cochlea in the medial (endocranial) view of the internal auditory meatus to show the fenestral wall; and **E1**. Modiolar section to show the continuous variation of fenestral pattern (up to 1½ turn) and the wall less pattern (the apical ½ turn) along the length of the cochlea.

**Extended Data Fig. 9 Yangochiropteran vesper bats *Pipistrellus abramus* (Vespertilionidae) and *Myotis lucifugus* (Vespertilionidae): wall-less Rosenthal's canal with trans-otic placement of spiral ganglion.**

The Japanese pipistrelle bat (*P. abramus*) and the Little brown bat (*M. lucifugus*) are laryngeal echolocating bats. Their neuroanatomical RC and ganglionic patterns are the most derived characters among mammals, only known in yangochiropterans. **A**. Schematic diagram to show the absence of Rosenthal's canal wall and the confluence of the ganglion with cochlear

nerve in internal auditory meatus (IAM). **A1.** Rosenthal's canal has no wall between the basal  $\frac{1}{2}$  turn and apex, although the basal most  $\frac{1}{2}$  turn has foramina. **B** and **B1.** Histological section of *Pipistrellus* showing the spiral ganglion is placed in IAM, starting from near the base of the cochlea (Ref. [48](#) - Hsiao et al. 2015: fig. [2](#)). Histological section reproduced with permission/license from Copyright Clearance Center: [www.rightfind.com](http://www.rightfind.com)). **C.** and **C1.** CT slice through the modiolar section to show that Rosenthal's canal wall is entirely absent from the basal  $\frac{1}{2}$  to the apex; and the presumptive position of the ganglion is in IAM. **D.** Transparent model of cochlea to visualize the position of the ganglion. **D1.** Solid CT model of cochlea cut away at the modiolar section visualize the wall-less condition of Rosenthal's canal space and the placement of spiral ganglion in IAM. **E.** *Myotis* - Transparent cochlea to visualize the spiral ganglion space (yellow). **E1.** Cut-away surface to visualize that the ganglion space is open and confluent with the IAM. **E2.** Cut-away model to show the open and confluent condition of Rosenthal's canal of the entire internal auditory meatus. **E3.** Solid cochlea model of the internal auditory meatus to show the exposure of the spiral ganglion. **F.** *Myotis* - CT slice through the modiolar section. **F1.** Detailed osteological structures at  $1\frac{1}{2}$  turn. **F2.** Detailed osteological structure at the cochlear base. **F3.** Detailed osteological structures at  $1\frac{1}{2}$  turn. **C.** Transparent model of the cochlea. Abbreviations: **bm** – basilar membrane; **IAM** – internal auditory meatus; **RC** – Rosenthal's canal; **sg** – spiral ganglion; **sm** – scala media; **st** – scala tympani; **sv** – scala vestibuli; **tcm** – tectorial membrane; **TF** – tractus foraminosus; **vm** – vestibular membrane.

**Extended Data Fig. 10 Wall-less Rosenthal's canal for trans-otic placement of the spiral ganglion of *Pteronotus parnellii* (Yangochiroptera, Mormoopidae) - Parnell's mustached bat, a laryngeal echolocating bat.**

**A.** Schematic model of osteological structures. **A1.** Uncoiled schematic cochlea to visualize the wall-less part of Rosenthal's Canal between the basal  $\frac{1}{2}$  turn and the apical turn. **B.** Whole mount prepared nerve structures in the basal cochlear turn: cochlear nerve trunk, cochlear nerve fiber fascicles, spiral ganglion, and ganglion radial fibers to hair cells (image

redrawn from Henson and Henson 1988: fig. 1) (Ref. 10). **C.** CT slice corresponds to whole-mount cochlear nerve dissected (**B**) and visualizes the foraminal wall of Rosenthal's canal in the basal ½ turn, and the absence of the wall of Rosenthal's canal beyond basal ½ turn. The absence of Rosenthal's canal wall at ½ turn is corroborated by histology (Ref. 30 - Kössl and Vater 1985: fig. 1). **D.** Transparent inner ear model with location of the spiral ganglion (yellow). **D1.** Modiolar section of cochlea: Spiral ganglion is positioned in the internal auditory meatus between the basal ½ turn and the apex. **D2.** Details in modiolar section to visualize that the space of the ganglion is open and confluent with the IAM. **E.** CT visualization of the internal auditory meatus.

## Supplementary information

### Supplementary Information

This file contains Supplementary Information Parts 1–12, including a Figure, Tables 1–6 and references.

### Reporting Summary

## Rights and permissions

### Reprints and Permissions

## About this article

### Cite this article

Sulser, R.B., Patterson, B.D., Urban, D.J. *et al.* Evolution of inner ear neuroanatomy of bats and implications for echolocation. *Nature* **602**, 449–454 (2022). <https://doi.org/10.1038/s41586-021-04335-z>

- Received: 29 March 2021

- Accepted: 10 December 2021
- Published: 26 January 2022
- Issue Date: 17 February 2022
- DOI: <https://doi.org/10.1038/s41586-021-04335-z>

## Share this article

Anyone you share the following link with will be able to read this content:

[Get shareable link](#)

Sorry, a shareable link is not currently available for this article.

[Copy to clipboard](#)

Provided by the Springer Nature SharedIt content-sharing initiative

## Further reading

- [\*\*Ear anatomy traces a family tree for bats\*\*](#)

- M. Brock Fenton

*Nature* (2022)

## [\*\*Ear anatomy traces a family tree for bats\*\*](#)

- M. Brock Fenton

News & Views 26 Jan 2022

---

This article was downloaded by **calibre** from <https://www.nature.com/articles/s41586-021-04335-z>

- Article
- [Published: 09 February 2022](#)

# Genome-edited powdery mildew resistance in wheat without growth penalties

- [Shengnan Li<sup>1,na1</sup>](#),
- [Dexing Lin<sup>2,3,4 na1</sup>](#),
- [Yunwei Zhang<sup>2,3 na1</sup>](#),
- [Min Deng<sup>2,4 na1</sup>](#),
- [Yongxing Chen<sup>2</sup>](#),
- [Bin Lv<sup>1,5</sup>](#),
- [Boshu Li<sup>2,3,4</sup>](#),
- [Yuan Lei<sup>2,3,4</sup>](#),
- [Yanpeng Wang<sup>2,3</sup>](#),
- [Long Zhao<sup>2,4</sup>](#),
- [Yueting Liang<sup>1,5</sup>](#),
- [Jinxing Liu<sup>2,3</sup>](#),
- [Kunling Chen<sup>2,3</sup>](#),
- [Zhiyong Liu<sup>2,4</sup>](#),
- [Jun Xiao ORCID: orcid.org/0000-0002-6077-2155<sup>2,4,6</sup>](#),
- [Jin-Long Qiu ORCID: orcid.org/0000-0001-8054-2552<sup>1,5</sup>](#) &
- [Caixia Gao ORCID: orcid.org/0000-0003-3169-8248<sup>2,3,4</sup>](#)

[Nature](#) volume 602, pages 455–460 (2022)

- 9357 Accesses
- 1 Citations

- 356 Altmetric
- [Metrics details](#)

## Subjects

- [Agriculture](#)
- [Plant biotechnology](#)
- [Plant genetics](#)
- [Plant molecular biology](#)

## Abstract

Disruption of susceptibility (*S*) genes in crops is an attractive breeding strategy for conferring disease resistance<sup>1,2</sup>. However, *S* genes are implicated in many essential biological functions and deletion of these genes typically results in undesired pleiotropic effects<sup>1</sup>. Loss-of-function mutations in one such *S* gene, *Mildew resistance locus O* (*MLO*), confers durable and broad-spectrum resistance to powdery mildew in various plant species<sup>2,3</sup>. However, *mlo*-associated resistance is also accompanied by growth penalties and yield losses<sup>3,4</sup>, thereby limiting its widespread use in agriculture. Here we describe *Tamlo-R32*, a mutant with a 304-kilobase pair targeted deletion in the *MLO-B1* locus of wheat that retains crop growth and yields while conferring robust powdery mildew resistance. We show that this deletion results in an altered local chromatin landscape, leading to the ectopic activation of *Tonoplast monosaccharide transporter 3* (*TaTMT3B*), and that this activation alleviates growth and yield penalties associated with *MLO* disruption. Notably, the function of *TMT3* is conserved in other plant species such as *Arabidopsis thaliana*. Moreover, precision genome editing facilitates the rapid introduction of this *mlo* resistance allele (*Tamlo-R32*) into elite wheat varieties. This work demonstrates the ability to stack genetic changes to rescue growth defects caused by recessive alleles, which is critical for developing high-yielding crop varieties with robust and durable disease resistance.

This is a preview of subscription content

## **Access options**

Subscribe to Nature+

Get immediate online access to the entire Nature family of 50+ journals

\$29.99

monthly

[Subscribe](#)

Subscribe to Journal

Get full journal access for 1 year

\$199.00

only \$3.90 per issue

[Subscribe](#)

All prices are NET prices.

VAT will be added later in the checkout.

Tax calculation will be finalised during checkout.

Buy article

Get time limited or full article access on ReadCube.

\$32.00

[Buy](#)

All prices are NET prices.

**Additional access options:**

- [Log in](#)
- [Learn about institutional subscriptions](#)

**Fig. 1:** *Tamlo-R32* wheat exhibits immunity to powdery mildew without growth and yield penalties.



**Fig. 2:** Chromosomal rearrangement in *Tamlo-R32* leads to activation of *TaTMT3B* in leaves.

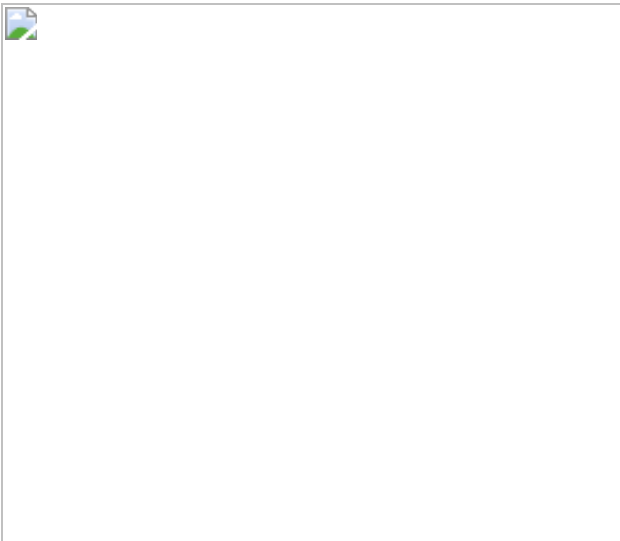
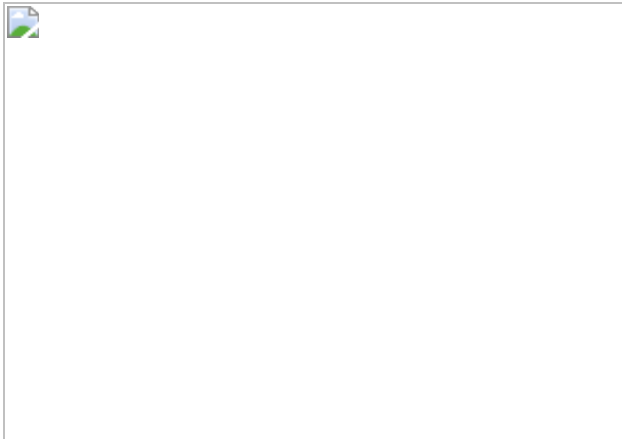


**Fig. 3:** Increased *TMT3* expression rescues growth phenotypes in *mlo* mutants of wheat and *Arabidopsis*.



**Fig. 4:** Introduction of the *Tamlo-R32* allele into elite wheat varieties.



## Data availability

The sequencing data obtained in this study have been deposited in the Genome Sequence Archive (GSA) database in the BIG Data Center (<https://ngdc.cncb.ac.cn/>) under accession number [PRJCA005687](#). Chinese Spring wheat reference genome RefSeq v1.1 is available on IWGSC (<http://www.wheatgenome.org/>). Transcriptome data from different wheat tissues are from ref. <sup>29</sup>. [Source data](#) are provided with this paper.

## References

1. van Schie, C. C. & Takken, F. L. Susceptibility genes 101: how to be a good host. *Annu. Rev. Phytopathol.* **52**, 551–581 (2014).
2. Schulze-Lefert, P. & Vogel, J. Closing the ranks to attack by powdery mildew. *Trends Plant Sci.* **5**, 343–348 (2000).
3. Büschges, R. et al. The barley *Mlo* gene: a novel control element of plant pathogen resistance. *Cell* **88**, 695–705 (1997).
4. Consonni, C. et al. Conserved requirement for a plant host cell protein in powdery mildew pathogenesis. *Nat. Genet.* **38**, 716–720 (2006).
5. van Esse, H. P., Reuber, T. L. & van der Does, D. Genetic modification to improve disease resistance in crops. *New Phytol.* **225**, 70–86 (2020).

6. Li, W., Deng, Y., Ning, Y., He, Z. & Wang, G.-L. Exploiting broad-spectrum disease resistance in crops: from molecular dissection to breeding. *Annu. Rev. Plant Biol.* **71**, 575–603 (2020).
7. Dangl, J. L., Horvath, D. M. & Staskawicz, B. J. Pivoting the plant immune system from dissection to deployment. *Science* **341**, 746–751 (2013).
8. Deng, Y. et al. Epigenetic regulation of antagonistic receptors confers rice blast resistance with yield balance. *Science* **355**, 962–965 (2017).
9. Saintenac, C. et al. Wheat receptor-kinase-like protein Stb6 controls gene-for-gene resistance to fungal pathogen *Zymoseptoria tritici*. *Nat. Genet.* **50**, 368–374 (2018).
10. Jones, J. D. & Dangl, J. L. The plant immune system. *Nature* **444**, 323–329 (2006).
11. Dangl, J. L. & Jones, J. D. Plant pathogens and integrated defence responses to infection. *Nature* **411**, 826–833 (2001).
12. Dodds, P. N. & Rathjen, J. P. Plant immunity: towards an integrated view of plant–pathogen interactions. *Nat. Rev. Genet.* **11**, 539–548 (2010).
13. Oliva, R. et al. Broad-spectrum resistance to bacterial blight in rice using genome editing. *Nat. Biotechnol.* **37**, 1344–1350 (2019).
14. Lapin, D. & Van den Ackerveken, G. Susceptibility to plant disease: more than a failure of host immunity. *Trends Plant Sci.* **18**, 546–554 (2013).
15. Vogel, J. P., Raab, T. K., Schiff, C. & Somerville, S. C. *PMR6*, a pectate lyase–like gene required for powdery mildew susceptibility in *Arabidopsis*. *Plant Cell* **14**, 2095–2106 (2002).
16. Eckardt, N. A. Plant disease susceptibility genes? *Plant Cell* **14**, 1983–1986 (2002).

17. Kim, M. C. et al. Calmodulin interacts with MLO protein to regulate defence against mildew in barley. *Nature* **416**, 447–451 (2002).
18. Devoto, A. et al. Topology, subcellular localization, and sequence diversity of the *Mlo* family in plants. *J. Biol. Chem.* **274**, 34993–35004 (1999).
19. Kusch, S. & Panstruga, R. *mlo*-based resistance: an apparently universal "weapon" to defeat powdery mildew disease. *Mol. Plant Microbe Interact.* **30**, 179–189 (2017).
20. Wang, Y. et al. Simultaneous editing of three homoeoalleles in hexaploid bread wheat confers heritable resistance to powdery mildew. *Nat. Biotechnol.* **32**, 947–951 (2014).
21. Bai, Y. et al. Naturally occurring broad-spectrum powdery mildew resistance in a Central American tomato accession is caused by loss of *Mlo* function. *Mol. Plant Microbe Interact.* **21**, 30–39 (2008).
22. Humphry, M., Consonni, C. & Panstruga, R. *mlo*-based powdery mildew immunity: silver bullet or simply non-host resistance? *Mol. Plant Pathol.* **7**, 605–610 (2006).
23. Piffanelli, P. et al. A barley cultivation-associated polymorphism conveys resistance to powdery mildew. *Nature* **430**, 887–891 (2004).
24. Acevedo-Garcia, J., Kusch, S. & Panstruga, R. Magical mystery tour: MLO proteins in plant immunity and beyond. *New Phytol.* **204**, 273–281 (2014).
25. Appiano, M. et al. Monocot and dicot MLO powdery mildew susceptibility factors are functionally conserved in spite of the evolution of class-specific molecular features. *BMC Plant Biol.* **15**, 257 (2015).
26. Singh, R. P. et al. Disease impact on wheat yield potential and prospects of genetic control. *Annu. Rev. Phytopathol.* **54**, 303–322 (2016).

27. Acevedo-Garcia, J. et al. *mlo*-based powdery mildew resistance in hexaploid bread wheat generated by a non-transgenic TILLING approach. *Plant Biotechnol. J.* **15**, 367–378 (2017).
28. Bogdanove, A. J. & Voytas, D. F. TAL effectors: customizable proteins for DNA targeting. *Science* **333**, 1843–1846 (2011).
29. Ramírez-González, R. H. et al. The transcriptional landscape of polyploid wheat. *Science* **361**, eaar6089 (2018).
30. Wormit, A. et al. Molecular identification and physiological characterization of a novel monosaccharide transporter from *Arabidopsis* involved in vacuolar sugar transport. *Plant Cell* **18**, 3476–3490 (2006).
31. Bieluszewski, T., Xiao, J., Yang, Y. & Wagner, D. PRC2 activity, recruitment, and silencing: a comparative perspective. *Trends Plant Sci.* **21**, S1360–S1385 (2021).
32. Kajimura, T., Mizuno, N. & Takumi, S. Utility of leaf senescence-associated gene homologs as developmental markers in common wheat. *Plant Physiol. Biochem.* **48**, 851–859 (2010).
33. Consonni, C. et al. Tryptophan-derived metabolites are required for antifungal defense in the *Arabidopsis mlo2* mutant. *Plant Physiol.* **152**, 1544–1561 (2010).
34. Gao, C. Genome engineering for crop improvement and future agriculture. *Cell* **184**, 1621–1635 (2021).
35. Zhang, Y. et al. Efficient and transgene-free genome editing in wheat through transient expression of CRISPR/Cas9 DNA or RNA. *Nat. Commun.* **7**, 12617–12624 (2016).
36. Liang, Z. et al. Efficient DNA-free genome editing of bread wheat using CRISPR/Cas9 ribonucleoprotein complexes. *Nat. Commun.* **8**, 14261–14265 (2017).

37. Jansen, M., Jarosch, B. & Schaffrath, U. The barley mutant *emrl* exhibits restored resistance against *Magnaporthe oryzae* in the hypersusceptible *mlo*-genetic background. *Planta* **225**, 1381–1391 (2007).
38. Li, S. et al. MYB75 phosphorylation by MPK4 is required for light-induced anthocyanin accumulation in *Arabidopsis*. *Plant Cell* **28**, 2866–2883 (2016).
39. Shan, Q. et al. Targeted genome modification of crop plants using a CRISPR–Cas system. *Nat. Biotechnol.* **31**, 686–688 (2013).
40. Liang, Z. et al. Genome editing of bread wheat using biolistic delivery of CRISPR/Cas9 in vitro transcripts or ribonucleoproteins. *Nat. Protoc.* **13**, 413–430 (2018).
41. Clough, S. J. & Bent, A. F. Floral dip: a simplified method for *Agrobacterium*-mediated transformation of *Arabidopsis thaliana*. *Plant J.* **16**, 735–743 (1998).
42. Wang, Z. et al. Genetic and physical mapping of powdery mildew resistance gene *MlHLT* in Chinese wheat landrace Hulutou. *Theor. Appl. Genet.* **128**, 365–373 (2015).
43. Shen, Q. H. et al. Nuclear activity of MLA immune receptors links isolate-specific and basal disease-resistance responses. *Science* **315**, 1098–1103 (2007).
44. Li, H. & Durbin, R. Fast and accurate short read alignment with Burrows–Wheeler transform. *Bioinformatics* **25**, 1754–1760 (2009).
45. Danecek, P. et al. Twelve years of SAMtools and BCFtools. *Gigascience* **10**, giab008 (2021).
46. Thorvaldsdóttir, H., Robinson, J. T. & Mesirov, J. P. Integrative Genomics Viewer (IGV): high-performance genomics data visualization and exploration. *Brief Bioinform.* **14**, 178–192 (2013).

47. Kim, D., Paggi, J. M., Park, C., Bennett, C. & Salzberg, S. L. Graph-based genome alignment and genotyping with HISAT2 and HISAT-genotype. *Nat. Biotechnol.* **37**, 907–915 (2019).
48. Liao, Y., Smyth, G. K. & Shi, W. featureCounts: an efficient general purpose program for assigning sequence reads to genomic features. *Bioinformatics* **30**, 923–930 (2014).
49. Robinson, M. D., McCarthy, D. J. & Smyth, G. K. edgeR: a Bioconductor package for differential expression analysis of digital gene expression data. *Bioinformatics* **26**, 139–140 (2010).
50. Weber, B., Jamge, S. & Stam, M. 3C in maize and *Arabidopsis*. *Methods Mol. Biol.* **1675**, 247–270 (2018).
51. Krijger, P. H., Geeven, G., Bianchi, V., Hilvering, C. R., & de Laat, W. 4C-seq from beginning to end: a detailed protocol for sample preparation and data analysis. *Methods* **170**, 17–32. (2020).
52. Ricci, W. A. et al. Widespread long-range *cis*-regulatory elements in the maize genome. *Nat. Plants* **5**, 1237–1249 (2019).
53. Rao, S. S. et al. A 3D map of the human genome at kilobase resolution reveals principles of chromatin looping. *Cell* **159**, 1665–1680 (2014).
54. Kim, D. & Sung, S. Vernalization-triggered intragenic chromatin-loop formation by long noncoding RNAs. *Dev. Cell* **40**, 302–312 (2017).
55. Paolacci, A. R., Tanzarella, O. A., Porceddu, E. & Ciaffi, M. Identification and validation of reference genes for quantitative RT-PCR normalization in wheat. *BMC Mol. Biol.* **10**, 11 (2009).
56. Bajic, M., Maher, K. A. & Deal, R. B. Identification of open chromatin regions in plant genomes using ATAC-seq. *Methods Mol. Biol.* **1675**, 183–201 (2018).
57. Zhang, Y. et al. Model-based analysis of ChIP-seq (MACS). *Genome Biol.* **9**, R137 (2008).

58. Ramírez, F., Dündar, F., Diehl, S., Grüning, B. A. & Manke, T. deepTools: a flexible platform for exploring deep-sequencing data. *Nucleic Acids Res.* **42**, W187–W191 (2014).
59. Kaya-Okur, H. S. et al. CUT&Tag for efficient epigenomic profiling of small samples and single cells. *Nat. Commun.* **10**, 1930 (2019).
60. Chen, S., Zhou, Y., Chen, Y. & Gu, J. fastp: an ultra-fast all-in-one FASTQ preprocessor. *Bioinformatics* **34**, i884–i890 (2018).
61. Xiao, J. et al. *Cis*- and *trans*-determinants of epigenetic silencing by Polycomb Repressive Complex 2 in *Arabidopsis*. *Nat. Genet.* **49**, 1546–1552 (2017).
62. Gou, J. Y. et al. Wheat stripe rust resistance protein WKS1 reduces the ability of the thylakoid-associated ascorbate peroxidase to detoxify reactive oxygen species. *Plant Cell* **27**, 1755–1770 (2015).
63. Qin, D. et al. Characterization and fine mapping of a novel barley *Stage Green-Revertible Albino* gene (*HvSGRA*) by bulked segregant analysis based on ssr assay and specific length amplified fragment sequencing. *BMC Genomics* **16**, 838–851 (2015).
64. Ni, Z. et al. Altered circadian rhythms regulate growth vigour in hybrids and allopolyploids. *Nature* **457**, 327–331 (2009).

## Acknowledgements

This work was supported by grants from the Strategic Priority Research Program of the Chinese Academy of Sciences (XDA24020101 to J.-L.Q., XDA24020102 to C.G., XDA24010204 to J.X., XDA24020310 to Y.W., XDPB16 to J.-L.Q.), the National Natural Science Foundation of China (31788103 to C.G., 32001891 to S.L., 31970529 to J.X. and 31971370 to K.C.) and the Key Research Program of Frontier Sciences (QYZDY-SSW-SMC030 to C.G.) and the Youth Innovation Promotion Association of the Chinese Academy of Sciences (2020000003 to Y.W.).

# **Author information**

## Author notes

1. These authors contributed equally: Shengnan Li, Dexing Lin, Yunwei Zhang, Min Deng

## Affiliations

1. State Key Laboratory of Plant Genomics, Institute of Microbiology, Innovation Academy for Seed Design, Chinese Academy of Sciences, Beijing, China

Shengnan Li, Bin Lv, Yueling Liang & Jin-Long Qiu

2. State Key Laboratory of Plant Cell and Chromosome Engineering, Institute of Genetics and Developmental Biology, Innovation Academy for Seed Design, Chinese Academy of Sciences, Beijing, China

Dexing Lin, Yunwei Zhang, Min Deng, Yongxing Chen, Boshu Li, Yuan Lei, Yanpeng Wang, Long Zhao, Jinxing Liu, Kunling Chen, Zhiyong Liu, Jun Xiao & Caixia Gao

3. Center for Genome Editing, Institute of Genetics and Developmental Biology, Chinese Academy of Sciences, Beijing, China

Dexing Lin, Yunwei Zhang, Boshu Li, Yuan Lei, Yanpeng Wang, Jinxing Liu, Kunling Chen & Caixia Gao

4. College of Advanced Agricultural Sciences, University of Chinese Academy of Sciences, Beijing, China

Dexing Lin, Min Deng, Boshu Li, Yuan Lei, Long Zhao, Zhiyong Liu, Jun Xiao & Caixia Gao

5. CAS Center for Excellence in Biotic Interactions, University of Chinese Academy of Sciences, Beijing, China

Bin Lv, Yueling Liang & Jin-Long Qiu

6. CAS-JIC Centre of Excellence for Plant and Microbial Science,  
Institute of Genetics and Developmental Biology, Chinese Academy of  
Sciences, Beijing, China

Jun Xiao

## Contributions

C.G. and J.-L.Q. conceived and conceptualized the study. C.G. and J.-L.Q. designed the experiments. S.L., D.L. and Y.Z. performed most of the experiments. S.L., Y.W. and J.X. prepared the figures. S.L. and Y.Z. performed the powdery mildew infection experiment. D.L., B. Li, Y. Lei, J.L. and K.C carried out genome-editing experiments and mutant identification. M.D. conducted the 4C and 3C experiments. L.Z. and J.X. conducted the CUT&Tag, ATAC-seq and bioinformatics analyses. B. Lv, and Y. Liang performed the marker-assisted selection (MAS) and powdery mildew microscopic analyses. S.L. and Y.W. characterized the phenotypes of mutant plants. Y.C. and Z.L. carried out traditional breeding and field trials. J.-L.Q., C.G., S.L. and J.X wrote the manuscript. All authors commented on the results and contributed to the manuscript.

## Corresponding authors

Correspondence to [Jun Xiao](#), [Jin-Long Qiu](#) or [Caixia Gao](#).

## Ethics declarations

## Competing interests

C.G., J.-L.Q., S.L. and Y.W. have filed patent applications based on the work published here.

## Peer review

## Peer review information

*Nature* thanks Wendy Harwood, Nian Wang and the other, anonymous, reviewers for their contribution to the peer review of this work. Peer review reports are available.

## Additional information

**Publisher's note** Springer Nature remains neutral with regard to jurisdictional claims in published maps and institutional affiliations.

## Extended data figures and tables

### [Extended Data Fig. 1 Genotyping by agarose gel electrophoresis and Sanger sequencing.](#)

**a**, Detection of the transgene in the *Tamlo-R32* mutants by PCR using five independent primer sets. Plasmid DNA of the TALEN vector was used as a positive control. **b**, Schematic diagram of the structure of the wheat *TaMLO1* gene. Green rectangles and solid black lines represent exons and introns, respectively. The conserved TALEN target site within *TaMLO1* is indicated by the red vertical line. Black arrows denote the positions and orientations of the three pairs of gene-specific primers (F1/R1, F2/R2, F3/R3) for amplifying *TaMLO-A1*, *TaMLO-B1* and *TaMLO-D1*, respectively. **c**, Agarose gel electrophoresis of *TaMLO1* amplicons from genomic DNA of the BW wild-type (upper) and *Tamlo-R32* mutant (lower) using gene-specific primers. **d**, Agarose gel electrophoresis of the PCR products amplified by the primer pairs F2/R2 (upper) and F4/R4 (lower) from genomic DNA of the wild type and *Tamlo-R32* mutants. The positions and orientations of the F4/R4 primer pairs are denoted by black arrows in Fig. 1g. **e**, DNA sequence of the edited sites in *Tamlo-R32*. Blue letters indicate inserted sequences. Red letters indicate the original sequence. Black vertical lines indicate the target site. The black dotted line indicates the deleted region. For **a**, **c**, **d**, experiments were repeated 3 times with the same results.

## Extended Data Fig. 2 The *Tamlo-R32* mutant displays no yield penalties when grown in the field.

**a–d**, The agronomic traits, including grain yield per plant (**a**), thousand kernel weight (**b**), tiller number per plant (**c**) and grain number per spike (**d**) were evaluated in field conditions in two wheat-growing areas in the North China Plain, Beijing and Zhaoxian in Hebei Province in 2019 and 2020. For box plots, the box limits indicate the twenty-fifth and seventy-fifth percentiles, the whiskers indicate the full range of the data, and the center line indicates the median. Individual data points are plotted. *n* represents the sample size. Statistical significance was determined by two-tailed Mann-Whitney tests or two-tailed Student's *t*-tests. *P* values are indicated

Source data

## Extended Data Fig. 3 Macroscopic powdery mildew infection phenotypes of F<sub>2</sub> plants from various crosses.

**a, b**, Representative detached leaves of the F<sub>2</sub> generations of *Tamlo-R32* × *Tamlo-aaBBdd* (**a**) and *Tamlo-R32* × *Tamlo-aabbdd* (**b**) are shown seven days after inoculation of *Bgt* isolate E09. Red triangles indicate resistant plants. Scale bar, 1 cm.

## Extended Data Fig. 4 Expression patterns and chromatin landscapes of genes around the large deletion.

**a**, Expression of *TaTMT3B* and 11 other nearby genes in different tissues; data are from a previous publication<sup>30</sup>. Genes within the deleted region are indicated. **b, c**, Amino acid sequence alignment between homeologs on the A, B and D genomes of downregulated genes in the deletion region. **d**, Expression levels of *TaTMT3B* in different tissues of *Tamlo-R32* and WT plants measured by quantitative RT-PCR. Results are normalized to *TaPAGE* gene. n.d., not detected. Data are means ± s.d., of three independent RNA preparations from biological replicates. **e**, Chromatin accessibility, and histone modification profiles in the *TaTMT3B-MLO-B1* region in leaf tissue of Chinese Spring wheat. The Integrative Genomics

Viewer (IGV) views show the various chromatin status profiles near *TaTMT3B*. The y-axis represents signal enrichment computed from reads at each position normalized to the total number of reads (RPKM). The dark shading indicates regions with either repressive (H3K27me3) or active (H3K4me3, H3K36me3, H3K27ac) histone modifications (a-f). **f**, Schematic illustration of a possible model for regulation of the activation of *TaTMT3B* expression in *Tamlo-R32*

[Source data](#)

**Extended Data Fig. 5 Expression levels of twenty genes around the large deletion measured by quantitative RT-PCR.**

**a**, Schematic diagram of the gene distribution around the large B-genome deletion identified in *Tamlo-R32*. **b**, Expression levels of twenty genes of the B genome were measured by quantitative RT-PCR in both wild-type Bobwhite and *Tamlo-R32* mutant leaves. Results are normalized to *TaPARG* gene and the expression level of gene in wild-type BW plants was set at one except *TaTMT3B*. n.d., not detected. Data are means ± s.d. of three independent RNA preparations from biological replicates

[Source data](#)

**Extended Data Fig. 6 Wheat and *Arabidopsis mlo* mutants overexpressing *TMT3* maintain powdery mildew resistance.**

**a**, Targeted knockout of *TaTMT3B* by CRISPR-Cas9 in the *Tamlo-R32* background. Blue letters indicate *TaTMT3B* sgRNA. The PAM sequence is highlighted in red. The numbers on the right show the type of mutation and how many nucleotides are involved, with “-” indicating deletion of the given number of nucleotides. **b**, Expression levels of *TaTMT3* in *TaTMT3B*-overexpressors in the *Tamlo-aabbdd* mutant background, assessed by quantitative RT-PCR. The primers were designed to detect complete *TaTMT3* transcripts. The results are normalized to *TaACTIN*, and expression of the gene in KN199 (wild type) is set at one. Data are means ± s.d., of three independent RNA preparations from biological replicates. **c**, Macroscopic infection phenotypes of representative detached leaves of the

indicated wheat plants seven days after inoculation with *Bgt* isolate E09. Scale bar, 1 cm. **d**, Micrographs of microcolony formation by *Bgt* on wheat leaves of the indicated genotypes three days postinoculation. Powdery mildew spores and colonies were stained with Coomassie blue. Scale bars, 100 µm. **e**, Percentages of microcolonies formed from the total number of germinated spores of *Bgt* on the leaves of the indicated wheat plants. **f**, Expression levels of *AtTMT3* in *TMT3*-overexpressors in the *Atmlo2/6/12* background measured by quantitative RT-PCR. The primers were designed to detect both transgenic and endogenous *AtTMT3* transcripts. The results are normalized to *Arabidopsis AtACTIN8*, and the expression level of the gene in WT was set at one. Data are means ± s.d. of three independent RNA preparations from biological replicates. **g**, Detached rosette leaves of the indicated 7-week-old *Arabidopsis* plants grown under long-day condition were laid out. Scale bar, 1 cm. **h**, Chlorophyll content of 6th rosette leaves of 7-week-old *Arabidopsis* plants grown under long-day conditions. The *Tamlo-aabbdd* mutants in **b–e** is in the KN199 background. Data are means of three biological replicates. Error bars represent means ± s.d. *P* values are indicated. **i**, Macroscopic infection phenotypes of representative detached leaves of the indicated *Arabidopsis* plants seven days after inoculation with *G. orontii*. Scale bar, 1 cm. **j**, Micrographs of microcolony formation by *G. orontii* on *Arabidopsis* leaves of the indicated genotypes three days post-inoculation. Powdery mildew spores and colonies were stained with Coomassie blue. Scale bars, 100 µm. **k**, Percentages of microcolonies formed from the total number of germinated spores of *G. orontii* on leaves of indicated *Arabidopsis* plants. More than 1000 germinated spores per genotype per experiment were examined 72 h after inoculation in **e** and **k**. Data are means of three independent experiments. Error bars represent means ± s.d. Statistical significance in **e**, **h**, **k** was determined by two-tailed Mann-Whitney tests or two-tailed Student's *t*-tests

[Source data](#)

[\*\*Extended Data Fig. 7 Detection of transgene-free mutants.\*\*](#)

Outcome of tests for transgene-free mutants using five primer sets in 31 mutant plants in Extended Data Table 2. Lanes labelled WT and plasmid show the PCR fragments amplified from a WT plant and plasmid constructs

pJIT163-Ubi-Cas9 and pU6-gRNA vector respectively. KN-WT, XN-WT, XY-WT and S-WT indicate elite wheat varieties KN199, XN511, XY60 and S4185. Experiments were repeated 3 times with the same results.

**Extended Data Table 1 Frequencies of mutations generated by genome editing with CRISPR-Cas9 DNA/RNP in the T<sub>0</sub> generation of four elite wheat varieties**

**Extended Data Table 2 Genotypes of the mutants generated by CRISPR-Cas9 DNA in terms of mutations in *TaMLO-A1*, *TaMLO-D1* and the large deletion in the B genome**

**Extended Data Table 3 Genotypes of the mutants generated by CRISPR-Cas9 RNP with respect to mutations in *TaMLO-A1*, *TaMLO-D1* and the large deletion in the B genome**

## Supplementary information

### Supplementary Information

This file contains the uncropped images of agarose gels (Supplementary Fig. 1) and a list of primers used in the study (Supplementary Table 1).

### Reporting Summary

## Source data

### Source Data Fig. 1

### Source Data Fig. 2

### Source Data Fig. 3

### Source Data Fig. 4

### Source Data Extended Data Fig. 2

[\*\*Source Data Extended Data Fig. 4\*\*](#)

[\*\*Source Data Extended Data Fig. 5\*\*](#)

[\*\*Source Data Extended Data Fig. 6\*\*](#)

## Rights and permissions

[Reprints and Permissions](#)

## About this article

### Cite this article

Li, S., Lin, D., Zhang, Y. *et al.* Genome-edited powdery mildew resistance in wheat without growth penalties. *Nature* **602**, 455–460 (2022).  
<https://doi.org/10.1038/s41586-022-04395-9>

- Received: 06 July 2021
- Accepted: 20 December 2021
- Published: 09 February 2022
- Issue Date: 17 February 2022
- DOI: <https://doi.org/10.1038/s41586-022-04395-9>

## Share this article

Anyone you share the following link with will be able to read this content:

[Get shareable link](#)

Sorry, a shareable link is not currently available for this article.

[Copy to clipboard](#)

Provided by the Springer Nature SharedIt content-sharing initiative

## Further reading

- [China's approval of gene-edited crops energizes researchers](#)

◦ Smriti Mallapaty

*Nature* (2022)

---

This article was downloaded by **calibre** from <https://www.nature.com/articles/s41586-022-04395-9>

| [Section menu](#) | [Main menu](#) |

- Article
- [Published: 09 February 2022](#)

# Moving bar of light evokes vectorial spatial selectivity in the immobile rat hippocampus

- [Chinmay S. Purandare](#)<sup>1,2</sup> na1,
- [Shonali Dhingra](#)<sup>1</sup> na1,
- [Rodrigo Rios](#)<sup>1</sup>,
- [Cliff Vuong](#)<sup>1</sup>,
- [Thuc To](#)<sup>1</sup>,
- [Ayaka Hachisuka](#)<sup>1</sup>,
- [Krishna Choudhary](#)<sup>1</sup> &
- [Mayank R. Mehta](#)    [ORCID: orcid.org/0000-0003-2005-2468](#)<sup>1,3,4</sup>

[Nature](#) volume 602, pages 461–467 (2022)

- 4111 Accesses
- 95 Altmetric
- [Metrics details](#)

## Subjects

- [Extrastriate cortex](#)
- [Hippocampus](#)
- [Striate cortex](#)

## Abstract

Visual cortical neurons encode the position and motion direction of specific stimuli retrospectively, without any locomotion or task demand<sup>1</sup>. The hippocampus, which is a part of the visual system, is hypothesized to require self-motion or a cognitive task to generate allocentric spatial selectivity that is scalar, abstract<sup>2,3</sup> and prospective<sup>4,5,6,7</sup>. Here we measured rodent hippocampal selectivity to a moving bar of light in a body-fixed rat to bridge these seeming disparities. About 70% of dorsal CA1 neurons showed stable activity modulation as a function of the angular position of the bar, independent of behaviour and rewards. One-third of tuned cells also encoded the direction of revolution. In other experiments, neurons encoded the distance of the bar, with preference for approaching motion.

Collectively, these demonstrate visually evoked vectorial selectivity (VEVS). Unlike place cells, VEVS was retrospective. Changes in the visual stimulus or its predictability did not cause remapping but only caused gradual changes. Most VEVS-tuned neurons behaved like place cells during spatial exploration and the two selectivities were correlated. Thus, VEVS could form the basic building block of hippocampal activity. When combined with self-motion, reward or multisensory stimuli<sup>8</sup>, it can generate the complexity of prospective representations including allocentric space<sup>9</sup>, time<sup>10,11</sup> and episodes<sup>12</sup>.

This is a preview of subscription content

## Access options

Subscribe to Nature+

Get immediate online access to the entire Nature family of 50+ journals

\$29.99

monthly

[Subscribe](#)

Subscribe to Journal

Get full journal access for 1 year

\$199.00

only \$3.90 per issue

[Subscribe](#)

All prices are NET prices.

VAT will be added later in the checkout.

Tax calculation will be finalised during checkout.

Buy article

Get time limited or full article access on ReadCube.

\$32.00

[Buy](#)

All prices are NET prices.

### **Additional access options:**

- [Log in](#)
- [Learn about institutional subscriptions](#)

**Fig. 1: Hippocampal response to a revolving bar of light.**

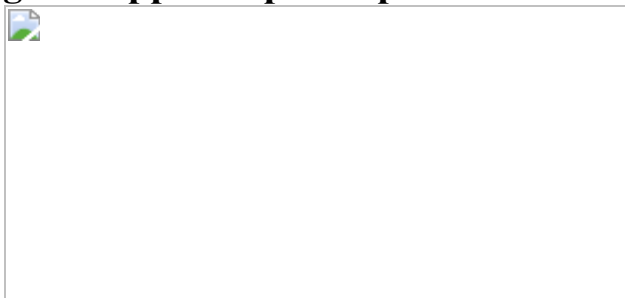


**Fig. 2: Directionality, stability and ensemble decoding of aVEVS.**

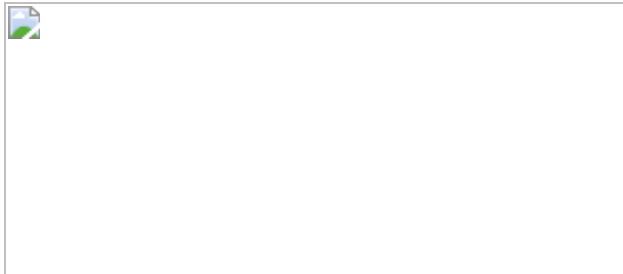


**Fig. 3: aVEVS is retrospective and changes gradually with stimulus pattern, colour, motion predictability and time.**

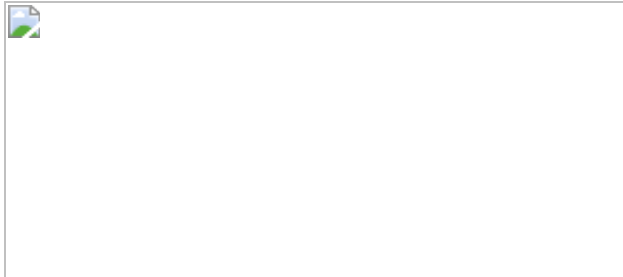


**Fig. 4: aVEVS cells are place cells and stimulus distance-encoding cells.**

## Data availability

The data that support the findings of this study are available from the corresponding author on reasonable request.

## Code availability

All analyses were performed using custom-written code in MATLAB version R2016a. Codes necessary to reproduce the figures in this study are available from the corresponding authors upon reasonable request.

## References

1. Hubel, D. H. & Wiesel, T. N. Receptive fields, binocular interaction and functional architecture in the cat's visual cortex. *J. Physiol.* **160**, 106–154 (1962).
2. O'Keefe, J. & Dostrovsky, J. The hippocampus as a spatial map. Preliminary evidence from unit activity in the freely-moving rat. *Brain Res.* **34**, 171–175 (1971).
3. O'Keefe, J. & Nadel, L. *The Hippocampus as a Cognitive Map* (Clarendon Press, 1978).
4. Muller, R. U. & Kubie, J. L. The firing of hippocampal place cells predicts the future position of freely moving rats. *J. Neurosci.* **9**, 4101–4110 (1989).
5. Mehta, M. R. Neuronal dynamics of predictive coding. *Neuroscience* **7**, 490–495 (2001).
6. Battaglia, F. P., Sutherland, G. R. & McNaughton, B. L. Local sensory cues and place cell directionality: additional evidence of prospective coding in the hippocampus. *J. Neurosci.* **24**, 4541–4550 (2004).
7. Resnik, E., McFarland, J. M., Sprengel, R., Sakmann, B. & Mehta, M. R. The effects of GluA1 deletion on the hippocampal population code for position. *J. Neurosci.* **32**, 8952–8968 (2012).
8. Ravassard, P. et al. Multisensory control of hippocampal spatiotemporal selectivity. *Science* **340**, 1342–1346 (2013).
9. Aghajan, Z. M. et al. Impaired spatial selectivity and intact phase precession in two-dimensional virtual reality. *Nat. Neurosci.* **18**, 121–128 (2015).
10. Pastalkova, E., Itskov, V., Amarasingham, A., Buzsaki, G. & Buzsáki, G. Internally generated cell assembly sequences in the rat hippocampus. *Science* **321**, 1322–1327 (2008).

11. MacDonald, C. J., Lepage, K. Q., Eden, U. T. & Eichenbaum, H. Hippocampal ‘time cells’ bridge the gap in memory for discontiguous events. *Neuron* **71**, 737–749 (2011).
12. Moore, J. J., Cushman, J. D., Acharya, L., Popeney, B. & Mehta, M. R. Linking hippocampal multiplexed tuning, Hebbian plasticity and navigation. *Nature* **599**, 442–448 (2021).
13. Fyhn, M., Molden, S., Witter, M. P., Moser, E. I. & Moser, M. B. Spatial representation in the entorhinal cortex. *Science* **305**, 1258–1264 (2004).
14. Taube, J. S., Muller, R. U. & Ranck, J. B. Jr Head-direction cells recorded from the postsubiculum in freely moving rats. II. Effects of environmental manipulations. *J. Neurosci.* **10**, 436–447 (1990).
15. Foster, T. C., Castro, C. A. & McNaughton, B. L. Spatial selectivity of rat hippocampal neurons: dependence on preparedness for movement. *Science* **244**, 1580–1582 (1989).
16. McNaughton, B. L. et al. Deciphering the hippocampal polyglot: the hippocampus as a path integration system. *J. Exp. Biol.* **199**, 173–185 (1996).
17. Sakurai, Y. Involvement of auditory cortical and hippocampal neurons in auditory working memory and reference memory in the rat. *J. Neurosci.* **14**, 2606–2623 (1994).
18. Itskov, P. M. et al. Sound sensitivity of neurons in rat hippocampus during performance of a sound-guided task sound sensitivity of neurons in rat hippocampus during performance of a sound-guided task. *J. Neurophysiol.* **107**, 1822–1834 (2012).
19. Aronov, D., Nevers, R. & Tank, D. W. Mapping of a non-spatial dimension by the hippocampal–entorhinal circuit. *Nature* **543**, 719–722 (2017).

20. Omer, D. B., Maimon, S. R., Las, L. & Ulanovsky, N. Social place-cells in the bat hippocampus. *Science* **359**, 218–224 (2018).
21. Danjo, T., Toyoizumi, T. & Fujisawa, S. Spatial representations of self and other in the hippocampus. *Science* **359**, 213–218 (2018).
22. von Heimendahl, M., Rao, R. P. & Brecht, M. Weak and nondiscriminative responses to conspecifics in the rat hippocampus. *J. Neurosci.* **32**, 2129–2141 (2012).
23. Mou, X. & Ji, D. Social observation enhances cross-environment activation of hippocampal place cell patterns. *eLife* **5**, 1–26 (2016).
24. Dotson, N. M. & Yartsev, M. M. Nonlocal spatiotemporal representation in the hippocampus of freely flying bats. *Science* **373**, 242–247 (2021).
25. Sakurai, Y. Coding of auditory temporal and pitch information by hippocampal individual cells and cell assemblies in the rat. *Neuroscience* **115**, 1153–1163 (2002).
26. Cushman, J. D. et al. Multisensory control of multimodal behavior: do the legs know what the tongue is doing? *PLoS ONE* **8**, e80465 (2013).
27. Malpeli, J. G. & Baker, F. H. The representation of the visual field in the lateral geniculate nucleus of *Macaca mulatta*. *J. Comp. Neurol.* **161**, 569–594 (1975).
28. Mehta, M. R., Quirk, M. C. & Wilson, M. A. Experience-dependent asymmetric shape of hippocampal receptive fields. *Neuron* **25**, 707–715 (2000).
29. Ahmed, O. J. & Mehta, M. R. The hippocampal rate code: anatomy, physiology and theory. *Trends Neurosci.* **32**, 329–338 (2009).
30. Acharya, L., Aghajan, Z. M., Vuong, C., Moore, J. J. & Mehta, M. R. Causal influence of visual cues on hippocampal directional selectivity. *Cell* **164**, 197–207 (2016).

31. de Vries, S. E. J. et al. A large-scale standardized physiological survey reveals functional organization of the mouse visual cortex. *Nat. Neurosci.* **23**, 138–151 (2020).
32. Wilson, M. A. & McNaughton, B. L. Dynamics of the hippocampal ensemble code for space. *Science* **261**, 1055–1058 (1993).
33. Stefanini, F. et al. A distributed neural code in the dentate gyrus and in CA1. *Neuron* **107**, 703–716.e4 (2020).
34. Muller, R. U., Kubie, J. L., Bostock, E. M., Taube, J. S. & Quirk, G. J. in *Brain and Space* (ed. Paillard, J.) 296–333 (Oxford Univ. Press, 1991).
35. Colgin, L. L., Moser, E. I. & Moser, M. B. Understanding memory through hippocampal remapping. *Trends Neurosci.* **31**, 469–477 (2008).
36. Suzuki, W. A., Miller, E. K. & Desimone, R. Object and place memory in the macaque entorhinal cortex. *J. Neurophysiol.* **78**, 1062–1081 (1997).
37. Saleem, A. B., Diamanti, E. M., Fournier, J., Harris, K. D. & Carandini, M. Coherent encoding of subjective spatial position in visual cortex and hippocampus. *Nature* **562**, 124–127 (2018).
38. Markus, E. J. et al. Interactions between location and task affect the spatial and directional firing of hippocampal neurons. *J. Neurosci.* **15**, 7079–7094 (1995).
39. Ziv, Y. et al. Long-term dynamics of CA1 hippocampal place codes. *Nat. Neurosci.* **16**, 264–266 (2013).
40. Nakazawa, K. et al. Requirement for hippocampal CA3 NMDA receptors in associative memory recall. *Science* **297**, 211–218 (2002).
41. Geiller, T., Fattah, M., Choi, J.-S. S. & Royer, S. Place cells are more strongly tied to landmarks in deep than in superficial CA1. *Nat.*

*Commun.* **8**, 14531 (2017).

42. Taube, J. S. & Muller, R. U. Comparisons of head direction cell activity in the postsubiculum and anterior thalamus of freely moving rats. *Hippocampus* **8**, 87–108 (1998).
43. Deacon, T. W., Eichenbaum, H., Rosenberg, P. & Eckmann, K. W. Afferent connections of the perirhinal cortex in the rat. *J. Comp. Neurol.* **220**, 168–190 (1983).
44. Lozano, Y. R. et al. Retrosplenial and postsubicular head direction cells compared during visual landmark discrimination. *Brain Neurosci. Adv.* **1**, 2398212817721859 (2017).
45. Felleman, D. J. & Van Essen, D. C. Distributed hierarchical processing in the primate cerebral cortex. *Cereb. Cortex* **1**, 1–47 (1991).
46. Hubel, D. H. & Wiesel, T. N. Receptive fields of single neurones in the cat's striate cortex. *J. Physiol.* **148**, 574–591 (1959).
47. Mehta, M. R. & Wilson, M. A. From hippocampus to V1: effect of LTP on spatio-temporal dynamics of receptive fields. *Neurocomputing* **32–33**, 905–911 (2000).
48. Quiroga, R. Q., Reddy, L., Kreiman, G., Koch, C. & Fried, I. Invariant visual representation by single neurons in the human brain. *Nature* **435**, 1102–1107 (2005).
49. Hahn, T. T., Sakmann, B. & Mehta, M. R. Phase-locking of hippocampal interneurons' membrane potential to neocortical up-down states. *Nat. Neurosci.* **9**, 1359–1361 (2006).
50. Hahn, T. T., Sakmann, B. & Mehta, M. R. Differential responses of hippocampal subfields to cortical up-down states. *Proc. Natl Acad. Sci. USA* **104**, 5169–5174 (2007).
51. Hahn, T. T. G., McFarland, J. M., Berberich, S., Sakmann, B. & Mehta, M. R. Spontaneous persistent activity in entorhinal cortex

- modulates cortico-hippocampal interaction in vivo. *Nat. Neurosci.* **15**, 1531–1538 (2012).
52. Beltramo, R. & Scanziani, M. A collicular visual cortex: neocortical space for an ancient midbrain visual structure. *Science* **363**, 64–69 (2019).
  53. Mehta, M. R., Barnes, C. A. & McNaughton, B. L. Experience-dependent, asymmetric expansion of hippocampal place fields. *Proc. Natl Acad. Sci. USA* **94**, 8918–8921 (1997).
  54. Berens, P. CircStat: a MATLAB toolbox for circular statistics. *J. Stat. Softw.* **31**, 1–21 (2009).
  55. Ringach, D. L., Shapley, R. M. & Hawken, M. J. Orientation selectivity in macaque V1: diversity and laminar dependence. *J. Neurosci.* **22**, 5639–5651 (2002).
  56. Ghodrati, M., Zavitz, E., Rosa, M. G. P. & Price, N. S. C. Contrast and luminance adaptation alter neuronal coding and perception of stimulus orientation. *Nat. Commun.* **10**, 941 (2019).

## Acknowledgements

We thank K. Delao, C. Polizu and S. Samant for help with data collection; V. Yuan, S. Ryklansky, A. Chorbajian and W. Zhu for help with single-unit clustering; and D. Dixit. This work was supported by grants to M.R.M. from the W.M. Keck Foundation, AT&T, NSF 1550678 and NIH 1U01MH115746.

## Author information

### Author notes

1. These authors contributed equally: Chinmay S. Purandare, Shonali Dhingra

## Affiliations

1. W.M. Keck Center for Neurophysics, Department of Physics and Astronomy, UCLA, Los Angeles, CA, USA

Chinmay S. Purandare, Shonali Dhingra, Rodrigo Rios, Cliff Vuong, Thuc To, Ayaka Hachisuka, Krishna Choudhary & Mayank R. Mehta

2. Department of Bioengineering, UCLA, Los Angeles, CA, USA

Chinmay S. Purandare

3. Department of Neurology, UCLA, Los Angeles, CA, USA

Mayank R. Mehta

4. Department of Electrical and Computer Engineering, UCLA, Los Angeles, CA, USA

Mayank R. Mehta

## Contributions

M.R.M. and C.S.P. designed the experiments. S.D., C.S.P., R.R., C.V., T.T., A.H. and K.C. performed the experiments. C.S.P. developed the stimuli and performed the analyses with input from M.R.M. M.R.M. and C.S.P. wrote the manuscript with critical input from S.D. and other authors.

## Corresponding author

Correspondence to [Mayank R. Mehta](#).

## Ethics declarations

## Competing interests

The authors declare no competing interests.

## Peer review

### Peer review information

*Nature* thanks the anonymous reviewers for their contribution to the peer review of this work. Peer reviewer reports are available.

## Additional information

**Publisher's note** Springer Nature remains neutral with regard to jurisdictional claims in published maps and institutional affiliations.

## Extended data figures and tables

### [Extended Data Fig. 1 Relationship between different properties of aVEVS.](#)

**a**, (top) aVEVS quantified by z-scored sparsity is significantly correlated ( $r = 0.82, p < 10^{-150}$ ) with, but significantly greater than the z-scored direction selectivity index (DSI) (41%  $z > 2$  for sparsity vs 31% for DSI, KS-test  $p = 9.3 \times 10^{-10}$ ). (Bottom) Cumulative histogram (cdf) of z-scored metric of sparsity and DSI. **b**, Similar as **a**, (1- (circular variance)) is significantly correlated ( $r = 0.84, p < 10^{-150}$ ) but significantly weaker (33%  $z > 2$  for (1- circular variance)) than sparsity. (KS-test  $p = 7 \times 10^{-6}$ ). **c**, Similar to **a** coherence is significantly correlated ( $r = 0.89 p < 10^{-150}$ ) but significantly weaker (26%  $z > 2$  for coherence KS-test  $p = 6.3 \times 10^{-16}$ ) than sparsity. **d**, Similar to **a**, but mutual information is significantly correlated ( $r = 0.47 p = 8.6 \times 10^{-132}$ ) but significantly smaller than sparsity (37%  $z > 2$  for mutual information, KS-test  $p = 7.2 \times 10^{-5}$ ).

### [Extended Data Fig. 2 Unimodality of aVEVS.](#)

Majority of (**a**) uni-directional as well as (**b**) bi-directional tuning curves were unimodal with only one significant peak (top row), whereas (**c**) untuned responses did not have significant peaks, as expected. Both tuned responses were used for the bi-directional cells, and only the tuned response was used for the uni-directional cells. Significant troughs, i.e. off-responses were not found for unidirectional or bidirectional cells (bottom row). Significance of a peak (or trough) was determined with the spike train shuffling analysis, similar to that performed to compute the z-scored sparsity. A peak (trough) was determined to be significant if it was larger (smaller) than the median value of peaks (troughs) in all shuffles and had a height of at least 20% of the range of firing rate variation in the shuffle data. These criteria resulted in zero significant peaks for some tuned responses.

### Extended Data Fig. 3 Trial-to-trial variability of mean vector angle but not mean firing rate determines aVEVS tuning.

For each cell, in each trial, we computed the mean firing rate (MFR), mean vector length (MVL) and mean vector angle (MVA) of aVEVS (see [Methods](#)). To enable comparison across metrics, this analysis was restricted to responsive trials (firing rate above 0.5 Hz) where MVL and MVA could be meaningfully computed. Qualitatively similar results were obtained when this restriction was removed. **a**, Trial to trial fluctuations of firing rate was qualitatively similar between tuned (maroon) and untuned (gray) cells (KS-test  $p = 0.25$ ). **b**, The variability was not significantly correlated with the degree of aVEVS tuning (*Pearson* partial correlation, after factoring out mean firing rate,  $p = 0.85$ ). **c, d**, The variance of MVL (see [Methods](#)) was significantly greater for untuned cells (KS-test  $p = 0.01$ ) than tuned cells (**c**) and was inversely related to aVEVS tuning strength ( $r = -0.19, p = 7.3 \times 10^{-10}$ ) (**d**). **e**, The circular standard deviation of MVA, which signifies the instability of aVEVS tuning from trial to trial, was significantly ( $p = 1.3 \times 10^{-72}$ ) smaller (11%) for tuned than untuned cells and (**f**) strongly anti-correlated with aVEVS ( $r = -0.77 p = 7.4 \times 10^{-192}$ ). **g**, This standard deviation of MVA was inversely correlated with MVL for tuned ( $r = -0.15 p = 0.004$ ), and for untuned cells ( $r = -0.12 p = 0.003$ ). **h**, It was also positively correlated with the preferred angle of tuning ( $r = 0.18 p = 3.5 \times 10^{-4}$ ), with lower variability for cells tuned to the front angles ( $0^\circ$ )

than behind ( $\pm 180^\circ$ ). Standard deviation of MVA was uncorrelated with preferred angle of tuning for untuned cells ( $r = 0.02, p = 0.67$ ). All correlations were computed as *Pearson* correlation coefficients.

### **Extended Data Fig. 4 Continuity of stability and sparsity measures and example cells.**

**a**, across all neurons, the z-scored sparsity, i.e., degree of tuning, and stability varied continuously, with no clear boundary between tuned and untuned neurons. **b**, Same distribution as **a**, with color-coding of stable and tuned responses separated. **c**, Detailed breakdown of aVEVS properties that had significant sparsity (i.e., tuned) or significant stability and whether these were observed in both directions (e.g., bidirectional stable) or only one direction (e.g. unidirectional tuned). If unidirectional, whether CW or CCW direction was significant. Nearly all cells that were significantly tuned in a given direction were also stable in that direction. **d**, For clarity, the CCW (blue) and CW (red) trials are stacked separately in all raster plot figures, even though these alternated every four trials. First five examples are of bi-directionally tuned cells (green y-axis); next four examples are of uni-directionally tuned cells (orange-yellow y-axis). **e**, These cells did not have significant sparsity ( $z < 2$ ) in either direction but had significant stability.

### **Extended Data Fig. 5 Firing rate differences between CW and CCW revolution direction.**

**a**, Percentage of tuned responses as a function of the absolute preferred angle, for bidirectional and unidirectional populations are significantly different from each other (KS-test  $p = 0.04$ ). **b**, Firing rate modulation index for uni-directional cells inside preferred zone was significantly different from zero (t-test,  $p = 4.1 \times 10^{-35}$ ), but not outside ( $p = 0.35$ ). **c**, Correlation coefficient of CCW and CW responses for different populations of cells, (KS-test green, bidirectional,  $p = 3.3 \times 10^{-27}$ , orange, unidirectional  $p = 7.0 \times 10^{-27}$ , lavender, untuned stable,  $p = 4.4 \times 10^{-4}$ ). Dashed curves indicate respective shuffles. **d**, Firing rate of unidirectional cells in tuned versus untuned directions shows significantly higher (KS-test  $p = 7.9 \times$

$10^{-9}$ ) firing rates in the tuned direction. **e**, Same as **d**, for bidirectional cells showing higher firing rate (KS-test,  $p = 2.4 \times 10^{-18}$ ) in the revolution direction with better tuning. **f**, Cumulative histogram of ratio between firing rate in untuned to tuned direction was less than one for 67% of cells. **g**, Same as **f**, but for bidirectional cells (other/better since both directions are tuned) showing 65% of firing rate ratios were less than one. **h**, To remove the contribution of firing rate to sparsity, the strength of tuning (z-score sparsity) difference was computed with spike thinning procedures (similar to Extended Data Fig. 6; see [Methods](#)) ensuring equal firing rate in both directions. The difference in tuning strength (z-scored sparsity) was not significantly correlated with firing rate ratio for unidirectional ( $r = -0.09 p = 0.16$ ) as well as (**i**) bidirectional ( $r = 0.005 p = 0.95$ ) populations. For bidirectionally tuned cells, aVEVS with higher z-scored sparsity was labeled as the “better” response, and the aVEVS with lower z-scored sparsity was called “other” response. All correlations were computed as *Pearson* correlation coefficients.

### **Extended Data Fig. 6 The relative number of bidirectional cells increases with mean firing rate, but not the fraction of tuned cells.**

To remove the effect of firing rate on z-scored sparsity computation, we randomly subsampled spike trains to have a firing rate of 0.5 Hz (see [Methods](#)). **a**, The fraction of cells with significant sparsity, i.e., fraction tuned, increased with the firing rate for the actual data ( $r = 0.11 p = 2.2 \times 10^{-6}$ ), but after spike thinning, there was no correlation ( $r = 0.01, p = 0.77$ ). Thus, the true probability of being tuned was independent of the firing rate of neurons. **b**, Proportion of bidirectional and uni-directional tuned neurons is comparable (10% vs 13%) with and without spike thinning. **c**, Fraction of bi-directional cells compared to uni-directional cells increases with original firing rate, even after spike train thinning. **d**, Spike thinning procedure reduces the sparsity of the tuning curves, as expected, due to loss of signal. After spike thinning, sparsity was significantly correlated in both directions of revolution ( $r = 0.39, p = 3.8 \times 10^{-31}$ ) and this was not due to the rate changes because sparsity was uncorrelated with firing rates ( $r = 0.01, p = 0.72$  for CCW sparsity and firing rate,  $r = 0.02, p = 0.54$  for CW sparsity

and firing rate). All correlations were computed as *Pearson* correlation coefficients.

### Extended Data Fig. 7 Population vector stability and decoding of visual cue angle.

**a**, Stability for CCW tuned responses (number of cells,  $n = 310$ ). Color indicates correlation coefficient between two non-overlapping groups of trials' population responses (see [Methods](#)). The maximum correlation values were pre-dominantly along the diagonal. Maxima along x-axis and y-axis were significantly correlated (Circular correlation coefficient  $r = 0.97, p < 10^{-150}$ ). **b**, Same as **a** but using untuned stable cells ( $n = 266$ ) showed significant ensemble stability ( $r = 0.91, p < 10^{-150}$ ). **c**, Same as **a** but using untuned and unstable cells ( $n = 306$ ). This was not significantly different than chance ( $r = -0.16, p = 0.09$ ). **d**, Same as **a**, using tuned cells with their spike trains circularly shifted in blocks of four trials, showed no significant stability ( $r = 1.1 \times 10^{-3}, p = 0.99$ ). **e–h**, Same as **a–d**, but for CW data. **i**, Decoding CW direction shows similar results as in CCW direction (shown earlier in Fig. 2). Similar analysis as shown in Fig. 2 for the stimulus movement in CW direction. (Left) Decoding cue angle in 10 trials of CW cue movement, using all other CW trials to build a population-encoding matrix. Gray trace indices movement of visual bar, colored trace is the decoded angle. (Right) Same as left, for shuffle data. **j**, Same as **i** but using the untuned-stable cells in CW movement direction. **k**, Median error between stimulus angle and decoded angle over 10 instantiations of decoding 10 trials each for actual and cell ID shuffle data. Green dashed line indicates width of the visual cue; black dashed line indicates median error expected by chance.

### Extended Data Fig. 8 Retrospective coding of aVEVS cells versus prospective coding in place cells.

**a**, (Top) A bidirectional cell responds with a latency after the stimulus goes past the angular position of the bar of light depicted by the green stripped bar. (Bottom) Population overlap is above the  $45^\circ$  line, indicating retrospective response. **b**, Same as **a** but for a prospective response, where

the neuron responds before the stimulus arrives in the receptive field. Such prospective responses are seen in place fields during navigation in the real world, where the population overlap is maximal below the 45° line (adapted from earlier work<sup>8</sup>). Prospective coding was seen in purely visual virtual reality, but those cells encoded prospective distance, not position.

### **Extended Data Fig. 9 Significant retrospective aVEVS in the unidirectional and untuned stable cells but not unstable cells.**

**a**, Stack plots of normalized population responses of cells, sorted according to the peak angle in the CCW (left). The corresponding responses of cells in the CW direction (right). **b**, The firing rate, averaged across the entire ensemble of bidirectional cells at -30° in the CCW direction was misaligned with the same in CW direction at the same angle (top), but better aligned with the response at -10° (bottom, vertical boxed in **a**), showing retrospective response. **c**, Same as **a** for uni-directional cells with CCW tuned cells (top row) and CW tuned cells (bottom row) sorted according to their aVEVS peak in the tuned direction. **d**, Same as in Fig. 3e for unidirectional cells. Majority (67%) of the cross correlations between CW and CCW responses had a significantly positive lag (median latency =  $19.9^\circ \pm 86.1^\circ$ , circular median t-test at 0°,  $p = 1.8 \times 10^{-10}$ ). The larger range of latencies and weaker correlations for unidirectional cells compared to the bidirectional cells could arise because significant tuning is present in only one direction. **e**, Same as Fig. 3f for unidirectional cells. For all angles the population vector cross correlation coefficients had a peak at a positive lag (CW peak–CCW peak, median =  $+56.2^\circ \pm 23.7^\circ$  circular median t-test,  $p = 1.5 \times 10^{-36}$ ), which was not significantly different from the retrospective lag in bidirectional cells (KS-test,  $p = 0.28$ ). **f**, Average strength of tuning in CCW and CW direction is inversely related to the peak angular lag between the two aVEVS for bidirectional (*Pearson's r* = -0.19  $p = 0.04$ ) as well as unidirectional cells (*Pearson's r* = -0.16  $p = 0.02$ ). **g**, Absolute difference between strengths of tuning between CCW and CW directions was not significantly correlated with the peak angular lag in their cross correlation for bidirectional ( $r = 0.13 p = 0.14$ ) or unidirectional cells ( $r = 0.03 p = 0.64$ ). This analysis was restricted to cells with retrospective lags, which were in majority. **h**, Untuned stable cells too show significant retrospective

bias, quantified using the cross correlation between the tuning curves in CCW and CW directions (median lag =  $13.6^\circ$  circular median t-test at  $0^\circ, p = 0.02$ ). **i**, This is not seen for the untuned unstable population (median =  $4.6^\circ$ , circular median t-test at  $0^\circ, p = 0.39$ ). **j**, Cross-correlations between CCW and CW tuning curves were averaged across all the bidirectional cells (green curves) for the systematic (latency for peak =  $25.7^\circ$ ) and random ( $16.7^\circ$ ) condition and showed a similar pattern of retrospective coding. (two sample KS-Test to ascertain if the distribution of latencies was significantly different,  $p = 0.75$ ). Unidirectional cells showed similar pattern for systematic ( $19.7^\circ$ ) and random ( $31.8^\circ$ ) conditions, but correlations were weaker than bidirectional cells. **k**, Cumulative distributions show that under systematic and random conditions comparable number of cells had positive latency (80% each) for bidirectional cells, and (67% and 68%) unidirectional cells respectively.

### **Extended Data Fig. 10 Photodiode experiment to measure the latency introduced by the equipment.**

Instead of a rat, we placed a photodiode where the rat sat. **a, b**, The signal from the photodiode (purple trace) synchronized with bar position (black) was extracted (**a**) and cross correlation computed between the CW and CCW tuning curves of photodiode response (**b**). The cross correlation had maxima at a latency of  $-2.8^\circ$ , which corresponds to a temporal lag of 38.9 ms. This was much smaller than the latency between neural spike trains (median latency  $22.7^\circ$ , corresponding to a temporal latency of 315.3 ms before accounting for the recording apparatus latency). For all the latency numbers reported in the main text, this small latency introduced by the recording apparatus was removed.

### **Extended Data Fig. 11 Additional properties of aVEVS invariance.**

**a**, (Row 1) For same cells recorded in response to the movement of a green striped and green checkered bars of light, mean firing rates during stationary epochs (running speed < 5 cm/sec), were significantly correlated (*Pearson's r* = 0.48  $p = 2 \times 10^{-5}$ ). Preferred angles of aVEVS between the

two stimulus patterns were also significantly correlated (circular correlation coefficient,  $r = 0.32$   $p = 5 \times 10^{-3}$ ). Solid red dots denote preferred angles of cells tuned (sparsity ( $z$ )  $> 2$ ) in both conditions; gray dots are for cells with significant tuning in one of the conditions. (Row 2) Same as **a** (Row 1), but for responses to changes of stimulus color, green and blue. Firing rate ( $r = 0.45$   $p = 1 \times 10^{-4}$ ) & preferred angle ( $r = 0.36$   $p = 0.01$ ) were correlated. (Row 3) Same as **a** (Row 1), but for changes to predictability of the stimulus, also called “random” vs “systematic”. Firing rate ( $r = 0.55$   $p = 2 \times 10^{-13}$ ) & preferred angle ( $r = 0.27$   $p = 0.01$ ) were significantly correlated between systematic and random stimuli movement. (Row 4) Same as **a** (Row 1), but for responses recorded across 2 days. Firing rate ( $r = 0.28$   $p = 3.2 \times 10^{-5}$ ) & preferred angle ( $r = 0.22$   $p = 0.006$ ) were correlated. **b**, Similar to Fig. 3, we computed the population remapping indices based on sparsity difference, preferred angle difference and peak value of cross correlation. The sparsity difference did not show a systematic pattern, but the other two metrics generally showed increasing remapping going from pattern (correlation = 0.68, angle difference =  $30^\circ$ ) to color (correlation = 0.64, angle difference =  $46.5^\circ$ ) to predictability (correlation = 0.55, angle difference =  $66^\circ$ ) and across days (correlation = 0.63, angle difference =  $66^\circ$ ).  $n$  indicates the number of responses measured in both conditions for each comparison, similar to Fig. 3h. Thick line – median, box – sem. **c**, Percentage of tuned responses in the random stimulus experiments, showing, comparable bi-directionality (10% here vs 13% for systematically moving bar). **d**, For same cells recorded in random and systematic stimulus experiments, the distributions of firing rates and selectivity, quantified by z-scored sparsity, were not significantly different (cyan-systematic, purple-random, KS-test for z-scored sparsity  $p = 0.14$ , for firing rate  $p = 0.27$ ). **e**, Cross correlation between CCW and CW tuning curves showing lagged response for the majority of bidirectional cells in the random condition. **f**, Same as **e**, but for unidirectional cells. **g**, Cross correlation of tuning curves (for tuned cells in the random stimulus experiment) between fast- and slow-moving stimulus was calculated from the subsample of data for a particular speed in CW and CCW direction separately and stacked together after flipping the CCW data and was not significantly biased from zero (Circular median test at  $0^\circ$ ,  $p = 0.56$ ). **h**, Example cell showing similar aVEVS for data within 1 s of stimulus direction change (top), or an equivalent, late

subsample (bottom). **i**, Firing rate (KS-test  $p = 0.73$ ) and sparsity (KS-test  $p = 0.87$ ) were not significantly different for these two subsamples of experimental recordings. **j**, In the randomly moving stimulus experiments, we computed a stimulus speed modulation index (see [Methods](#)). This distribution was not significantly biased away from zero. **k**, This modulation index was z-scored (see [Methods](#)), and only 5.2% of cells had significant firing rate modulation beyond z of  $\pm 2$ .

### [Extended Data Fig. 12 Relationship between place cells, stimulus angle \(aVEVS\) and distance \(dVEVS\) tuned cells.](#)

**a**, The mean firing rates of cells was significantly correlated (*Pearson's r* =  $0.43 p = 4.5 \times 10^{-10}$ ) between the aVEVS and place cell (spatial exploration) experiments. **b**, Majority of cells active during the aVEVS experiments were also active during random foraging in real world. **c**, Almost all of the aVEVS cells were also spatially selective during spatial exploration. **d**, Between the approaching and receding directions, the mean firing rates, computed when the rats were immobile, were highly correlated (*Pearson's r* =  $0.96 p = 4 \times 10^{-81}$ ) and not significantly different (KS-test  $p = 0.99$ ). **e**, Firing rates, computed when rats were stationary, during the stimulus angle and stimulus distance experiments were significantly correlated ( $r = 0.22 p = 0.008$ ). **f**, Population vector decoding of the stimulus distance (similar to stimulus angle decoding, Fig. [2](#)), was significantly better than chance. (KS-test  $p = 5.5 \times 10^{-10}$  for approaching and  $p = 4.7 \times 10^{-9}$  for receding data). Approaching stimulus decoding error (median = 194 cm) was significantly lesser than that for receding (median = 237 cm) (KS-test  $p = 4.2 \times 10^{-5}$ ). These errors were 59% and 82% of the error expected from shuffled data, which was greater than that for aVEVS decoding, where the error was 33% of the shuffles, when controlling for the number of cells. **g**, More than twice as many cells were unidirectional tuned for approaching (coming closer) movement direction, as compared to receding (moving away). **h**, For bidirectional cells, location of peak firing in the approaching and receding direction shows bimodal response, with most cells preferring either the locations close to the rat, i.e., 0 cm or far away, ~500 cm. Unidirectional cells preferred locations close to the rat. **i**, Population vector overlap (Fig. [4j](#)), was further quantified by comparing the

values along the diagonal for actual tuning curves, with the spike train shuffles. The actual overlap was significantly above two standard deviations of the shuffles for distances close to the rat (around 0) and far away (beyond 400 cm).

### Extended Data Fig. 13 Rewards and reward related licking are uncorrelated with VEVS.

**a**, Example cells showing aVEVS from Fig. 1, with reward times overlaid (black dots), showing random reward dispensing at all stimulus angles. **b**, The average rate of rewards was uncorrelated with visual stimulus angle (circular test for uniformity  $p = 0.99$ ). **c**, Rat's consumption of rewards, estimated by the reward tube lick rate, was measured by an infrared detector attached to the reward tube<sup>26</sup>. As expected, lick rate increased after reward delivery by ~4 fold and remained high for about five seconds (green shaded area). This duration is termed the “reward zone”. **d**, Lick rate inside the reward zone (green) was significantly larger than that outside (red, KS-test  $p = 2.3 \times 10^{-54}$ ). Inside as well as outside reward-zone lick rates were uncorrelated with visual stimulus angle (circular test for uniformity  $p = 0.99$  for both).

### Extended Data Fig. 14 Behavioral controls of VEVS.

To ascertain whether systematic changes in behavior caused VEVS, we employed a ‘behavioral clamp’ approach and estimated tuning strength using only the subset of data where the hypothesized behavioral variable was held constant. **a**, Example aVEVS tuned cells maintained its tuning even if we used only the data when the rat was (**b**) stationary (running speed <5 cm/sec, blue, left). This was comparable to a random subsample of behavior, obtained by shuffling the indices of spikes and behavior when the animal was stationary (orange, middle) (see [Methods](#)). 38% of cells were aVEVS tuned (sparsity  $z > 2$ ) when using only the stationary data which is significantly greater than chance, whereas 42% were significantly tuned in the equivalent, random subsample and this difference was significant (KS-test  $p = 0.02$ ). **c**, Similar to **b** but using only the data when the rat's head was immobile (head movement velocity <10 mm/sec). 43% and 42% of

cells were significant tuned in actual behavioral clamp and equivalent subsample, and these were not significantly different (KS-test  $p = 0.93$ ). **d**, Similar to **b**, but removing data within 5 s after reward dispensing, called void post-reward. 43% cells were tuned in “void post-reward” data, 43% for equivalent subsample (KS-test  $p = 0.56$ ). **e**, Similar to **d**, but removing data within 5 s before reward dispensing, called void pre-reward. 39% cells were tuned for void pre-reward, 42% for equivalent subsample (KS-test  $p = 0.43$ ). **f**, Using a subsample of data, from when the rat’s head was within the central 20 percentile of head positions (typically  $<10^\circ$ ), rat was stationary and there were no rewards in the last 5 s. This condition was called “analytical head fixation”. 28% of cells were aVEVS tuned under this behavioral clamp, which was lesser than that in an equivalent subsample (31%, KS-test  $p = 0.05$ ), but significantly greater than chance. **g**, Tuning curves for head positions to the leftmost 20 percentile and rightmost 20 percentile were similar, with 31% and 32% cells tuned in the two conditions (KS-test  $p = 0.67$ ). The preferred angles of tuning were highly correlated (circular correlation  $r = 0.67 p = 1.3 \times 10^{-11}$ ) and not significantly different (circular KS-test  $p > 0.1$ ). **h**, aVEVS tuning was recomputed in the head centric frame, by accounting for the rat’s head movements (obtained by tracking overhead LEDs attached to the cranial implant) and obtaining a relative stimulus angle, with respect to the body centric head angle. Overall tuning levels were comparable, between allocentric and this head centric estimation. First panel of **h** is the same as that in **a** since all aVEVS tuning reported earlier was in the allocentric or body centric frame. Using a subset of data when both overhead LEDs were reliably detected, 25% and 26% of cells were significantly tuned for the stimulus angle in the allocentric and egocentric frames (KS-test  $p = 0.9$ ). Preferred angle of aVEVS tuning for tuned cells was highly correlated ( $r = 0.81 p = 1.8 \times 10^{-15}$ ) and not significantly different between the two frames (circular KS-test  $p > 0.1$ ).

### **Extended Data Fig. 15 GLM estimate of aVEVS tuning.**

To estimates the independent contribution of stimulus angle to neural activity, while factoring out the contribution of head position and running speed, we used the generalized linear model (GLM) technique (see [Methods](#)<sup>30</sup>). **a**, Tuning curves obtained by binning methods were comparable with those from GLM estimation, including for the cells used in

Fig. 1 (first 2 examples in row 1 & 2). **b**, Sparsity levels were comparable (KS-test  $p = 0.07$ ) and 40% of cells were found to be significantly tuned for stimulus angle using GLM based estimated, compared to 43% from binning in this subset of data where head and leg movements were reliably captured (cell count,  $n = 991$ ). **c**, Preferred angle of firing between GLM and binning based estimates of aVEVS were highly correlated (circular correlation test  $r = 0.86 p < 10^{-150}$ ). **d**, Correlation between the aVEVS tuning curves from the two methods was significantly greater than that expected by chance, computed by randomly shuffling the pairing of cell ID across binning and GLM (KS-test  $p < 10^{-150}$ ). **e–h**, Properties of aVEVS tuning responses based on GLM estimates were similar to those based on binning method, as shown in Fig. 1. **e**, Distribution of tuned cells as a function of the preferred angle (angle of maximal firing). There were more tuned cells at forward angles than behind. **f**, Median  $\pm$  SEM z-scored sparsity and its variability (SEM, shaded area, here and subsequently) of tuned cells as a function of their preferred angle. (Pearson's  $r = -0.17 p = 0.004$ ). **g**, Median  $\pm$  SEM full width at quarter maxima across the ensemble of tuned responses increased as a function of preferred angle of tuning. (Pearson's  $r = +0.33 p < 10^{-150}$ ). **h**, CDF of firing rate modulation index within versus outside the preferred zone (see [Methods](#)) for tuned cells were significantly different (Two-sample KS test  $p = 2.9 \times 10^{-37}$ ).

### [Extended Data Fig. 16 Simultaneously recorded cells span all angles.](#)

16 simultaneously recorded cells showed significant aVEVS. Their preferred angles are indicated on top. Only cells selective for CCW direction shown for clarity. While the forward direction ( $0^\circ$ ) is overrepresented, these cells span all angles of the visual field including angles behind him ( $180^\circ$ ).

### [Extended Data Fig. 17 Simultaneously recorded cells show very weak co-fluctuation of aVEVS tuning across trials.](#)

**a, b**, Two simultaneously recorded cells showing significant aVEVS in the CCW direction (**a**), and zoomed in for a subset of trials, showing mostly

uncorrelated fluctuations in the two cells' spiking (**b**). **c**, For the same cell-pair, mean firing rate across trials was broadly uncorrelated. Only trials with non-zero spikes were used here, and henceforth, to ensure comparison with aVEVS tuning (see below). **d**, Same as **c** but showing uncorrelated fluctuations in the depth of modulation of aVEVS response of the two cells across trials, quantified by the Mean Vector Length (MVL, see [Methods](#)). **e**, Same as **c** but showing uncorrelated fluctuation of aVEVS response across trials, quantified by Mean Vector Angles (MVA, see [Methods](#)). **f**, Same as **c** but showing largely independent fluctuations in the overall aVEVS tuning (measured by correlation between the trial-averaged aVEVS tuning curve and the aVEVS tuning curve in a given trial) for this cell-pair. The significance of co-fluctuations in cell-pairs were quantified by bootstrapping methods, by employing trial id shuffles (see [Methods](#)). CCW and CW tuning curves were treated as separate responses throughout these analyses. **g**, 21% (14%) of simultaneously recorded, tuned (untuned) cell-pairs showed significant ( $z > 2$ ) co-fluctuation of mean firing rates across trials which provides an estimate of the non-specific effects such as running, reward consumption etc. **h**, Only 7% (5%) of tuned (untuned) cell pairs showed significant co-fluctuation of MVL across trials indicating little effect of nonspecific variables on the depth of aVEVS tuning. **i**, Similarly, only 10% (6%) of tuned (untuned) cell pairs showed significant co-fluctuation of MVA across trials. **j**, Only 14% (5%) of tuned (untuned) cell pairs showed significant co-fluctuation of aVEVS. Notably, the number of cell pairs showing significant co-fluctuations in any of the aVEVS tuning properties (**h–j**) was smaller than the number of cell pairs showing significant co-fluctuation of firing rates; and there was little qualitative difference between the significantly aVEVS tuned vs untuned populations.

## Supplementary information

### [Reporting Summary](#)

### [Peer Review File](#)

## Rights and permissions

## [Reprints and Permissions](#)

## About this article

### Cite this article

Purandare, C.S., Dhingra, S., Rios, R. *et al.* Moving bar of light evokes vectorial spatial selectivity in the immobile rat hippocampus. *Nature* **602**, 461–467 (2022). <https://doi.org/10.1038/s41586-022-04404-x>

- Received: 01 May 2020
- Accepted: 04 January 2022
- Published: 09 February 2022
- Issue Date: 17 February 2022
- DOI: <https://doi.org/10.1038/s41586-022-04404-x>

### Share this article

Anyone you share the following link with will be able to read this content:

[Get shareable link](#)

Sorry, a shareable link is not currently available for this article.

[Copy to clipboard](#)

Provided by the Springer Nature SharedIt content-sharing initiative

---

This article was downloaded by **calibre** from <https://www.nature.com/articles/s41586-022-04404-x>

- Article
- [Published: 26 January 2022](#)

# Sensory representation and detection mechanisms of gut osmolality change

- [Takako Ichiki](#)<sup>1</sup>,
- [Tongtong Wang](#) [ORCID: orcid.org/0000-0002-0408-2571](#)<sup>1</sup>,
- [Ann Kennedy](#)<sup>1,2</sup>,
- [Allan-Hermann Pool](#)<sup>1</sup>,
- [Haruka Ebisu](#)<sup>1</sup>,
- [David J. Anderson](#) [ORCID: orcid.org/0000-0001-6175-3872](#)<sup>1,3</sup> &
- [Yuki Oka](#) [ORCID: orcid.org/0000-0003-2686-0677](#)<sup>1</sup>

[Nature](#) volume **602**, pages 468–474 (2022)

- 8149 Accesses
- 1 Citations
- 346 Altmetric
- [Metrics details](#)

## Subjects

- [Cellular neuroscience](#)
- [Feeding behaviour](#)

## Abstract

Ingested food and water stimulate sensory systems in the oropharyngeal and gastrointestinal areas before absorption<sup>1,2</sup>. These sensory signals modulate brain appetite circuits in a feed-forward manner<sup>3,4,5</sup>. Emerging evidence suggests that osmolality sensing in the gut rapidly inhibits thirst neurons upon water intake. Nevertheless, it remains unclear how peripheral sensory neurons detect visceral osmolality changes, and how they modulate thirst. Here we use optical and electrical recording combined with genetic approaches to visualize osmolality responses from sensory ganglion neurons. Gut hypotonic stimuli activate a dedicated vagal population distinct from mechanical-, hypertonic- or nutrient-sensitive neurons. We demonstrate that hypotonic responses are mediated by vagal afferents innervating the hepatic portal area (HPA), through which most water and nutrients are absorbed. Eliminating sensory inputs from this area selectively abolished hypotonic but not mechanical responses in vagal neurons. Recording from forebrain thirst neurons and behavioural analyses show that HPA-derived osmolality signals are required for feed-forward thirst satiation and drinking termination. Notably, HPA-innervating vagal afferents do not sense osmolality itself. Instead, these responses are mediated partly by vasoactive intestinal peptide secreted after water ingestion. Together, our results reveal visceral hypoosmolality as an important vagal sensory modality, and that intestinal osmolality change is translated into hormonal signals to regulate thirst circuit activity through the HPA pathway.

This is a preview of subscription content

## Access options

Subscribe to Nature+

Get immediate online access to the entire Nature family of 50+ journals

\$29.99

monthly

[Subscribe](#)

[Subscribe to Journal](#)

Get full journal access for 1 year

\$199.00

only \$3.90 per issue

[Subscribe](#)

All prices are NET prices.

VAT will be added later in the checkout.

Tax calculation will be finalised during checkout.

[Buy article](#)

Get time limited or full article access on ReadCube.

\$32.00

[Buy](#)

All prices are NET prices.

### **Additional access options:**

- [Log in](#)
- [Learn about institutional subscriptions](#)

**Fig. 1: The vagus nerve responds to visceral osmolality changes.**

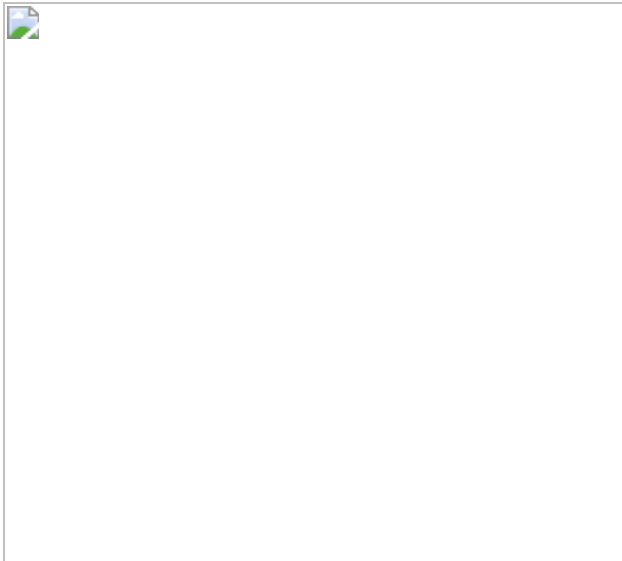


**Fig. 2: Visceral hypotonic stimuli activate a dedicated vagal population.**



**Fig. 3: Vagal sensory inputs from the HPA transmits gut-to-brain osmolality signals.**

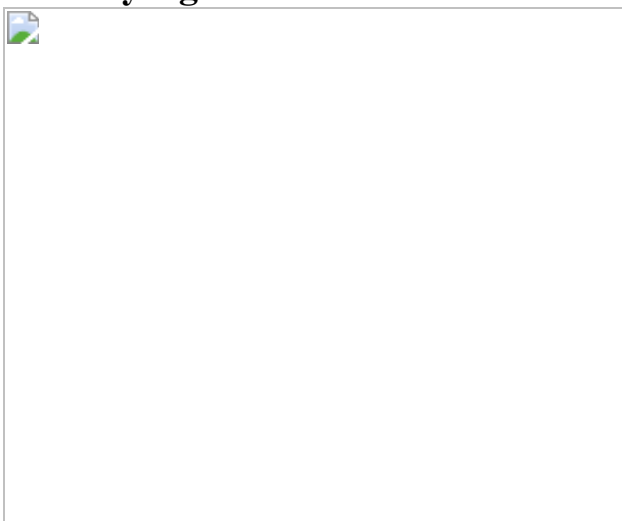


**Fig. 4: HPA vagal afferents are required for pre-absorptive thirst satiation.**

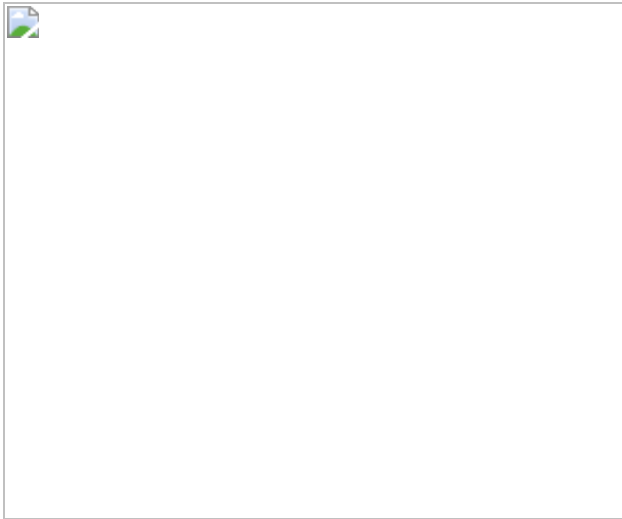
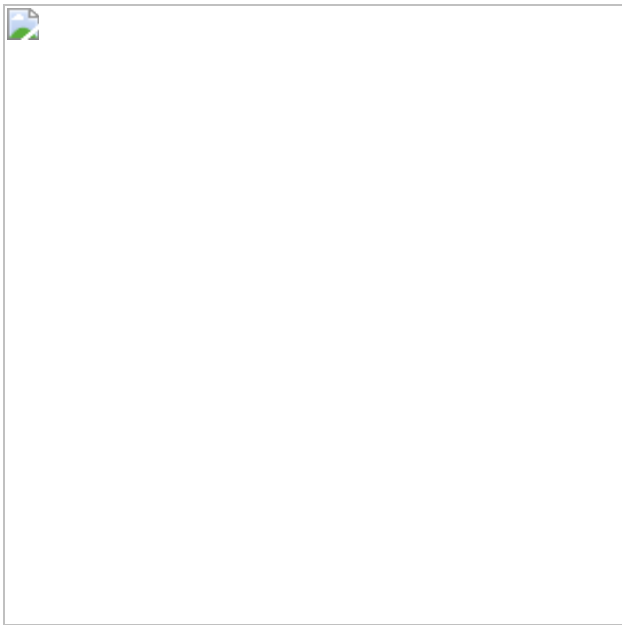


**Fig. 5: Visceral osmolality sensing recruits VIP–VIPR2 signalling in the HPA.**



## Data availability

Additional data that support the finding of this study are available from the corresponding author upon reasonable request. [Source data](#) are provided with this paper.

## Code availability

The MATLAB code used to perform the imaging analysis is modified from the CalmAn code at <https://github.com/flatironinstitute/CalmAn-MATLAB>, and is available at <https://github.com/Oka-Lab/Imaging-analysis>.

## References

1. Browning, K. N., Verheijden, S. & Boeckxstaens, G. E. The vagus nerve in appetite regulation, mood, and intestinal inflammation. *Gastroenterology* **152**, 730–744 (2017).
2. Kim, K. S., Seeley, R. J. & Sandoval, D. A. Signalling from the periphery to the brain that regulates energy homeostasis. *Nat. Rev. Neurosci.* **19**, 185–196 (2018).
3. Andermann, M. L. & Lowell, B. B. Toward a wiring diagram understanding of appetite control. *Neuron* **95**, 757–778 (2017).
4. Augustine, V., Lee, S. & Oka, Y. Neural control and modulation of thirst, sodium appetite, and hunger. *Cell* **180**, 25–32 (2020).
5. Zimmerman, C. A., Leib, D. E. & Knight, Z. A. Neural circuits underlying thirst and fluid homeostasis. *Nat. Rev. Neurosci.* **18**, 459–469 (2017).
6. Augustine, V. et al. Hierarchical neural architecture underlying thirst regulation. *Nature* **555**, 204–209 (2018).
7. Ichiki, T., Augustine, V. & Oka, Y. Neural populations for maintaining body fluid balance. *Curr. Opin. Neurobiol.* **57**, 134–140 (2019).
8. Zimmerman, C. A. & Knight, Z. A. Layers of signals that regulate appetite. *Curr. Opin. Neurobiol.* **64**, 79–88 (2020).
9. Lowell, B. B. New neuroscience of homeostasis and drives for food, water, and salt. *N. Engl. J. Med.* **380**, 459–471 (2019).
10. Augustine, V., Gokce, S. K. & Oka, Y. Peripheral and central nutrient sensing underlying appetite regulation. *Trends Neurosci.* **41**, 526–539

(2018).

11. Thrasher, T. N., Nistal-Herrera, J. F., Keil, L. C. & Ramsay, D. J. Satiety and inhibition of vasopressin secretion after drinking in dehydrated dogs. *Am. J. Physiol.* **240**, E394–E401 (1981).
12. Zimmerman, C. A. et al. A gut-to-brain signal of fluid osmolarity controls thirst satiation. *Nature* **568**, 98–102 (2019).
13. Augustine, V. et al. Temporally and spatially distinct thirst satiation signals. *Neuron* **103**, 242–249.e244 (2019).
14. Lechner, S. G. et al. The molecular and cellular identity of peripheral osmoreceptors. *Neuron* **69**, 332–344 (2011).
15. Brierley, S. M. et al. Selective role for TRPV4 ion channels in visceral sensory pathways. *Gastroenterology* **134**, 2059–2069 (2008).
16. Zimmer, L. J., Meliza, L. & Hsiao, S. Effects of cervical and subdiaphragmatic vagotomy on osmotic and volemic thirst. *Physiol. Behav.* **16**, 665–670 (1976).
17. Smith, G. P. & Jerome, C. Effects of total and selective abdominal vagotomies on water intake in rats. *J. Auton. Nerv. Syst.* **9**, 259–271 (1983).
18. Kim, D. Y. et al. A neural circuit mechanism for mechanosensory feedback control of ingestion. *Nature* **580**, 376–380 (2020).
19. Williams, E. K. et al. Sensory neurons that detect stretch and nutrients in the digestive system. *Cell* **166**, 209–221 (2016).
20. Kaelberer, M. M. et al. A gut–brain neural circuit for nutrient sensory transduction. *Science* **361**, eaat523 (2018).
21. Tan, H. E. et al. The gut–brain axis mediates sugar preference. *Nature* **580**, 511–516 (2020).

22. Kupari, J., Haring, M., Agirre, E., Castelo-Branco, G. & Ernfors, P. An atlas of vagal sensory neurons and their molecular specialization. *Cell Rep.* **27**, 2508–2523.e2504 (2019).
23. Bai, L. et al. Genetic identification of vagal sensory neurons that control feeding. *Cell* **179**, 1129–1143.e1123 (2019).
24. Prescott, S. L., Umans, B. D., Williams, E. K., Brust, R. D. & Liberles, S. D. An airway protection program revealed by sweeping genetic control of vagal afferents. *Cell* **181**, 574–589.e514 (2020).
25. Adachi, A., Nijima, A. & Jacobs, H. L. An hepatic osmoreceptor mechanism in the rat: electrophysiological and behavioral studies. *Am. J. Physiol.* **231**, 1043–1049 (1976).
26. Baertschi, A. J. & Vallet, P. G. Osmosensitivity of the hepatic portal vein area and vasopressin release in rats. *J. Physiol.* **315**, 217–230 (1981).
27. Morita, H., Fujiki, N., Hagiike, M., Yamaguchi, O. & Lee, K. Functional evidence for involvement of bumetanide-sensitive  $\text{Na}^+\text{K}^+2\text{Cl}^-$  cotransport in the hepatoportal  $\text{Na}^+$  receptor of the Sprague–Dawley rat. *Neurosci. Lett.* **264**, 65–68 (1999).
28. Nijima, A. Glucose-sensitive afferent nerve fibres in the hepatic branch of the vagus nerve in the guinea-pig. *J. Physiol.* **332**, 315–323 (1982).
29. McKinley, M. J. & Johnson, A. K. The physiological regulation of thirst and fluid intake. *News Physiol Sci* **19**, 1–6 (2004).
30. Gribble, F. M. & Reimann, F. Function and mechanisms of enteroendocrine cells and gut hormones in metabolism. *Nat. Rev. Endocrinol.* **15**, 226–237 (2019).
31. Christofides, N. D. et al. Release of gastrointestinal hormones following an oral water load. *Experientia* **35**, 1521–1523 (1979).

32. Costa, M. & Furness, J. B. The origins, pathways and terminations of neurons with VIP-like immunoreactivity in the guinea-pig small intestine. *Neuroscience* **8**, 665–676 (1983).
33. Talbot, J. et al. Feeding-dependent VIP neuron–ILC3 circuit regulates the intestinal barrier. *Nature* **579**, 575–580 (2020).
34. Furness, J. B. The enteric nervous system and neurogastroenterology. *Nat. Rev. Gastroenterol. Hepatol.* **9**, 286–294 (2012).
35. Giovannucci, A. et al. CaImAn an open source tool for scalable calcium imaging data analysis. *eLife* **8**, e38173 (2019).
36. Kennedy, A. et al. Stimulus-specific hypothalamic encoding of a persistent defensive state. *Nature* **586**, 730–734 (2020).
37. Zocchi, D., Wennemuth, G. & Oka, Y. The cellular mechanism for water detection in the mammalian taste system. *Nat. Neurosci.* **20**, 927–933 (2017).
38. Xie, C., Wei, W., Zhang, T., Dirsch, O. & Dahmen, U. Monitoring of systemic and hepatic hemodynamic parameters in mice. *J. Vis. Exp.* **92**, e51955 (2014).
39. McHugh, J. et al. Portal osmopressor mechanism linked to transient receptor potential vanilloid 4 and blood pressure control. *Hypertension* **55**, 1438–1443 (2010).
40. Lerner, T. N. et al. Intact-brain analyses reveal distinct information carried by SNC dopamine subcircuits. *Cell* **162**, 635–647 (2015).
41. Han, W. et al. A neural circuit for gut-induced reward. *Cell* **175**, 665–678.e623 (2018).
42. Hama, H. et al. ScaleS: an optical clearing palette for biological imaging. *Nat. Neurosci.* **18**, 1518–1529 (2015).
43. L'Heureux-Bouron, D. et al. Total subdiaphragmatic vagotomy does not suppress high protein diet-induced food intake depression in rats.

*J. Nutr.* **133**, 2639–2642 (2003).

44. Lee, S. et al. Chemosensory modulation of neural circuits for sodium appetite. *Nature* **568**, 93–97 (2019).

## Acknowledgements

We thank the members of the Oka laboratory, S. D. Liberles and C. S. Zuker for helpful discussion and comments; B. Ho and A. Koranne for maintaining and genotyping mouse lines; T. Zhang, W. Han and I. E. Araujo for technical advice on surgical techniques; L. Luebbert for initial imaging analysis; T. Karigo for technical help; X. Chen and V. Gradinaru for advice on virus development and tissue clearing; and J. Parker for sharing the qPCR machine. This work was supported by Startup funds from the President and Provost of California Institute of Technology and the Biology and Biological Engineering Division of California Institute of Technology. Y.O. is also supported by New York Stem Cell Foundation, NIH (R01NS109997, R01NS123918), Alfred P. Sloan Foundation, and Heritage Medical Research Institute. T.I. is supported by the Japan Society for the Promotion of Science.

## Author information

### Affiliations

1. Division of Biology and Biological Engineering, California Institute of Technology, Pasadena, CA, USA

Takako Ichiki, Tongtong Wang, Ann Kennedy, Allan-Hermann Pool, Haruka Ebisu, David J. Anderson & Yuki Oka

2. Department of Physiology, Northwestern University, Chicago, IL, USA

Ann Kennedy

3. Howard Hughes Medical Institute, California Institute of Technology,  
Pasadena, CA, USA

David J. Anderson

## Contributions

T.I. and Y.O. conceived the research programme and designed experiments. T.I. performed the experiments and analysed the data, with help from T.W. A.K., and D.J.A. wrote the code for the imaging analysis and provided advice on the data analysis. A.-H.P. analysed the single-cell RNA sequencing data. H.E. performed and analysed chemogenetic experiments. T.I. and Y.O. wrote the paper. Y.O. supervised the entire work.

## Corresponding author

Correspondence to [Yuki Oka](#).

## Ethics declarations

## Competing interests

The authors declare no competing interests.

## Peer review information

*Nature* thanks Richard Palmiter and the other, anonymous reviewers for their contribution to the peer review of this work.

## Additional information

**Publisher's note** Springer Nature remains neutral with regard to jurisdictional claims in published maps and institutional affiliations.

## Extended data figures and tables

## Extended Data Fig. 1 Responses of vagal and thoracic DRG neurons *in vivo*.

**a**, Schematic of intestinal infusion during electrophysiological and optical recording. Isotonic (0.9%) saline was continuously perfused using a peristaltic pump. Stimulus was delivered using a solenoid valve at the same flow rate (800  $\mu$ L/min). **b**, Integrated vagal nerve responses during stimulation (AUC) were quantified ( $n = 8$  mice for saline and water, and  $n = 6$  for other stimuli). **c**, Quantification of vagal water response at different flow rates ( $n = 5$  mice). **d**, Number of WGA-positive cells in DRG (thoracic, T5-lumber, L3) retrogradely tracing from HPA, intestine or stomach. Representative images from 3 mice for each tracing site are shown in the right. Scale bar, 100  $\mu$ m. **e**, Schematic diagram of DRG imaging. GRIN lens was placed on a thoracic DRG (T12 or 13). Calcium dynamics of individual neurons was visualized in *Slc17a6-Cre;Ai96* mice. **f**, Response heatmaps to skin pinch, intestinal infusion of 4% acetic acid, water, 1M NaCl and Ensure from individual DRG neurons ( $\Delta F/F(\sigma)$ , left) and percentage of responding neurons (right,  $n = 3$  mice for acetic acid, water and NaCl, 4 mice for other stimuli). \* $P < 0.05$ , \*\* $P < 0.01$ , \*\*\* $P < 0.001$  by Kruskal–Wallis test (with Dunn’s post test). Data are shown as mean  $\pm$  s.e.m.

### Source data

## Extended Data Fig. 2 Osmolality and mechanical responses under vagal ganglia imaging.

**a**, Calcium dynamics during saline (blue), first (red) and second (purple) intestinal water infusion (*Slc17a6-Cre;Ai96* mice). Representative images and a heatmap of individual vagal responses from 4 animal are shown. 64% of neurons activated by one trial were also activated by another trial. **b**, After subdiaphragmatic vagotomy (SVx), responses to intestinal water, 500 mM NaCl infusion, and distension were abolished (left). The number of total responding neurons was quantified (right, *Slc17a6-Cre;Ai96*,  $n = 4$  mice). **c**, Heatmap of individual vagal activity during short- (20 s) and long- (2 min) term of intestinal water infusion (*Slc17a6-Cre;Ai96*,  $n = 3$  mice). **d**, Osmotic-stimuli and mechanical distension activated largely non-

overlapping neurons. Venn diagrams indicate the number of responding neurons (right, *Slc17a6-Cre*; Ai96, n = 3 mice). **e**, Representative vagal ganglia responses to water infusion and distension in the intestine (red) and stomach (green, n = 4 mice). **f**, Total number of vagal neurons responding to the indicated stimuli in the intestine (red, n = 4 mice) and stomach (green, n = 4 mice). Scale bar, 200  $\mu$ m. Data are presented as mean  $\pm$  s.e.m.

[Source data](#)

**Extended Data Fig. 3 Transcriptomic analyses of the vagal ganglia.**

**a**, Vagal ganglia contain 27 transcriptomic neuron types shown in a t-SNE embedding with color-coded cell identity. **b**, Violin plot of log-normalized expression of marker genes in vagal ganglia, including *Tac1* and *Nts* with maximum counts per million (max CPM) above. t-SNE embedding for *Nts* (**c**) and *Tac1* (**d**) shows log-normalized expression in vagal neuron types. These data are reanalyzed and plotted from a previous study (Prescott *et al*, 2020)<sup>24</sup>. **e**, Two-color RNA *in situ* hybridization for validating *Cre* expression in *Tac1-Cre* lines. 91.2% of *Tac1-Cre* expression matched endogenous gene expression. Scale bar, 20  $\mu$ m.

**Extended Data Fig. 4 Functional manipulation of TAC1+ and NTS+ vagal neurons.**

**a**, TAC1+ neurons that responded to intestinal water or 500 mM NaCl are shown (*Tac1-Cre*; Ai162D, n = 4 mice). Same datasets from Fig. 3a are shown. **b**, Chemogenetic activation of TAC1+ vagal neurons significantly inhibited water intake after deprivation. AAV-hSyn-DIO-hM3D(Gq)-mCherry was injected into the vagal ganglia of *Nts-Cre*, *Tac1-Cre*, *Slc17a6-Cre*, or wild type (WT) mice. Water intake after 24-h water deprivation, 300 mM sucrose or chow consumption after 24-h food deprivation were measured after intraperitoneal PBS (vehicle) or clozapine N-oxide (CNO) administration (n = 7, 7, 5, and 4 mice (water and sucrose), and 5, 5, 4, and 4 mice (chow) were analyzed for *Nts-Cre*, *Tac1-Cre*, *Slc17a6-Cre* and WT animals, respectively.). **c**, Loss-of-function of TAC1+ vagal neurons. *Cre*-dependent taCasp3-encoding AAV was injected into the vagal ganglia of

*Tac1-Cre* mice (left, n = 6) or WT mice (right, n = 6). After 2 weeks of recovery period, water intake was measured under water-deprived state. \*P < 0.05, \*\*P < 0.01, \*\*\*P < 0.001, ns, not significant by two-way ANOVA (Šídák multiple comparisons) or two-tailed paired t-test. Data are presented as mean ± s.e.m.

[Source data](#)

[Extended Data Fig. 5 Anatomical projection patterns of TAC1+ and NTS+ vagal sensory neurons.](#)

Whole-mount cleared tissue or sliced brain sections showing vagal terminals (AAV-Flex-tdTomato, red) and cell bodies (counterstained with DAPI or NeuN for Vagal ganglia and DRG, blue). Enteric neurons are labeled by Fluoro-Gold (green). A magnified image of stomach IGLE in a *Slc17a6-Cre* mouse is presented (bottom, left). The expression patterns in *Slc17a6-Cre*, *Tac1-Cre* and *Nts-Cre* mice are summarized (bottom, right, n = 3 animals for each mouse line). NTS, nucleus of the solitary tract; CG-SMG, celiac ganglion and superior mesenteric ganglion complex. Scale bar, 200 µm.

[Extended Data Fig. 6 Anatomical projection patterns of vagal sensory neurons in the liver.](#)

**a**, Whole-mount staining of innervation of SLC17A6+, TAC1+, NTS+ vagal populations in the hepatic area (n = 2 animals for each mouse line). Sensory terminals were visualized by AAV-Flex-tdTomato (red). Scale bar, 100 µm. **b**, Cell bodies of vagal sensory neurons were retrogradely labeled by WGA 555 (magenta) from the different liver parts (#2, #4, or all parts except #2 and #4, referred from **a**), and by WGA 647 (green) from HPV. The vagal innervation to the hilus and HPV mostly overlapped due to their proximity (84%), while the majority of the liver lacked innervation except a limited area in the left lobe (n = 3 mice). Scale bar, 200 µm. **c**, Hepatic branch denervation with intact liver branch abolished intestinal hypoosmotic responses (*Slc17a6-Cre*;Ai96, n = 3 mice).

## Extended Data Fig. 7 Hepatic-branch-specific vagal denervation and its physiological significance.

**a**, Heatmap of individual vagal activity during long-term intestinal water infusion before and after HVx (*Slc17a6-Cre;Ai96*, n = 3 mice). **b**, Distinct vagal populations project to different organs. Whole-mount vagal sensory neurons retrogradely labeled by WGA 555 (magenta) and WGA 647 (green) from the same organ (HPA vs HPA) or different organs (HPA vs intestine, HPA vs stomach). Percentage of overlapping neurons is quantified (right, n = 3 mice). **c**, Validation of hepatic-branch-specific denervation. Vagal sensory neurons were retrogradely labeled by WGA 555 from intestine (magenta) and WGA 647 from HPA (green). After HPA denervation, the number of labeled neurons from HPA was drastically reduced (n = 3 mice). **d**, Reversible inhibition of water responses by a local anesthesia to HPA. Vagal responses to intestinal water infusion before and after application of 5% lidocaine (left, *Slc17a6-Cre;Ai96*, n = 4 mice). Responses recovered after the drug wore off. The number of the responded cells and mean  $\Delta F/F(\sigma)$  values in neurons responded after 100 min are shown in the bottom. By contrast, the same anesthesia treatment did not affect intestinal distension responses (right, *Slc17a6-Cre;Ai96*, n = 3 mice). **e**, Duodenum and pancreas denervation using 85% phenol did not affect vagal activity during intestinal water infusion (left, *Slc17a6-Cre;Ai96*, n = 2 mice). Denervation was verified by injecting WGA 555 to pancreas (magenta) and WGA 647 to duodenum (green). After denervation, the number of retrogradely labeled neurons was drastically reduced (right, n = 3 mice). Scale bar, 200  $\mu$ m. \*P < 0.05, \*\*\*P < 0.001, ns, not significant by two-way or one-way ANOVA (Šídák multiple comparisons) or by Friedman test (Dunn's multiple comparisons). Data are presented as mean  $\pm$  s.e.m.

[Source data](#)

## Extended Data Fig. 8 Functional and anatomical analyses of the hepatic vagal branch.

**a**, Vagal responses to intestinal water stimuli were abolished after HPA denervation using 85% phenol (*Slc17a6-Cre;Ai96*, n = 4 mice). **b** and **c**, Vagal response heatmaps to 500 mM NaCl or 300 mM glucose stimuli

before and after HVx (**b**, n = 3 mice), or after injecting WGA 647 into the HPA (**c**, n = 3 mice). **d**, A minor population of intestine-innervating neurons (labeled by WGA 647) responded to intestinal acute water stimulus (*Slc17a6-Cre;Ai96*, n = 3 mice).

### **Extended Data Fig. 9 The effects of vagal manipulation on nutrient consumption and SFO neuron activity.**

**a**, Water intake after 24-h deprivation during a 20-min session after HVx (n = 9 mice for sham and HVx, left) and HPA denervation using 85% phenol (n = 4 for sham, n = 7 mice for denervation, right). The same dataset from Fig. 4a for HVx experiments is presented. **b**, No change was observed for daily *ad libitum* water intake in sham (grey) and HPA denervation (red) animals (n = 5 mice). **c**, The vagus nerve does not contribute to water absorption. Plasma osmolality was measured in water-deprived mice after intestinal water infusion with or without SVx (n = 3 for sham, n = 3 for water-deprived SVx mice, n = 4 for water-infused SVx mice). **d**, Water (left) or food (normal chow, middle) intake after 24-h deprivation during a 20-min (water) or 1-h (food) session. Consistent with previous studies<sup>17,43</sup>, no difference was observed between sham (grey) and SVx (red) mice, or pre- and post-operation (n = 5 and 11 mice for pre- and post-op water intake measurement, n = 5 mice for food consumption measurement). Spontaneous daily water intake under sated states was not affected (right, n = 5 mice). **e**, Representative stomach and intestine samples after SVx (left) or HVx (right), with sham as a comparison. Stomach weight was significantly increased in the SVx animals but not in the HVx animals (n = 5 mice for sham, n = 6 mice for SVx and HVx). **f**, A diagram of vagal sensory circuits transmitting thirst satiation signals. **g**, Simultaneous photometry recording from SFO<sup>NOS1</sup> neurons and chemogenetic stimulation of vagal ganglion neurons. AAV-hSyn-hM3D(Gq)-mCherry was injected into the vagal ganglia while SFO<sup>NOS1</sup> neurons were infected with AAV-Flex-GCaMP6s in *Nos1-Cre* animals. **h**, Calcium dynamics of thirst neurons after PBS (vehicle) or CNO administration (n = 5 mice). Chemogenetic activation of vagal ganglia induced strong feed-forward inhibition in thirst neurons in sated- (left, red trace) and water-deprived condition (right, red trace). AUC was quantified between 300 to 600 s after CNO injection. \*P < 0.05, \*\*P < 0.01, \*\*\*P < 0.001, ns, not significant by two-way ANOVA (Šídák multiple

comparisons), two-tailed Mann-Whitney *U*-test, or two-tailed paired *t*-test. Data are presented as mean ± s.e.m.

### [Source data](#)

### **Extended Data Fig. 10 Contribution of hormones to HPA-innervating vagal responses and fluid balance.**

**a**, Representative responses of vagal neurons to hormones infused into the HPV before (red) and after (green) HVx (*Slc17a6-Cre;Ai96* mice, n = 3 mice). Scale bar, 200 µm. **b**, Vagal responses to intestinal water infusion and HPV GLP1 infusion (n = 3 mice). **c**, Vagal responses to a near-physiological concentration of VIP and intestinal hypoosmotic stimuli (n = 3 mice). **d**, VIP concentration in the HPV plasma was measured by ELISA from water-deprived (W.D.) animals and water-repleted animals with 10 min or 20 min water access (left, n = 9 mice for W.D., n = 8 mice for +water 10 min, and n = 6 mice for +water 20 min). No change in the systemic VIP level was observed in the retro-orbital sinus after water consumption (right, n = 9 mice for W.D., n = 8 mice for +water 10 min). **e**, After VIPR antagonist application, water and VIP dual-responding neurons were suppressed. **f**, qPCR analysis of VIPR1 and VIPR2 expression in the HPA, liver, duodenum, and colon. The same dataset from Fig. 5e is presented. \**P* < 0.05 by one-way ANOVA (Šídák multiple comparisons) or two-tailed unpaired *t*-test. Data are presented as mean ± s.e.m.

### [Source data](#)

## Supplementary information

### [Reporting Summary](#)

### [Supplementary Dataset](#)

Statistics Summary.

### Source data

[\*\*Source Data Fig. 1\*\*](#)

[\*\*Source Data Fig. 4\*\*](#)

[\*\*Source Data Fig. 5\*\*](#)

[\*\*Source Data Extended Data Fig. 1\*\*](#)

[\*\*Source Data Extended Data Fig. 2\*\*](#)

[\*\*Source Data Extended Data Fig. 4\*\*](#)

[\*\*Source Data Extended Data Fig. 7\*\*](#)

[\*\*Source Data Extended Data Fig. 9\*\*](#)

[\*\*Source Data Extended Data Fig. 10\*\*](#)

## Rights and permissions

[\*\*Reprints and Permissions\*\*](#)

## About this article

### Cite this article

Ichiki, T., Wang, T., Kennedy, A. *et al.* Sensory representation and detection mechanisms of gut osmolality change. *Nature* **602**, 468–474 (2022).  
<https://doi.org/10.1038/s41586-021-04359-5>

- Received: 15 April 2021
- Accepted: 15 December 2021
- Published: 26 January 2022

- Issue Date: 17 February 2022
- DOI: <https://doi.org/10.1038/s41586-021-04359-5>

## Share this article

Anyone you share the following link with will be able to read this content:

[Get shareable link](#)

Sorry, a shareable link is not currently available for this article.

[Copy to clipboard](#)

Provided by the Springer Nature SharedIt content-sharing initiative

## Further reading

- [\*\*Detecting gut osmolality changes to quench thirst\*\*](#)
  - Katrina Ray

*Nature Reviews Gastroenterology & Hepatology* (2022)

## [\*\*Detecting gut osmolality changes to quench thirst\*\*](#)

- Katrina Ray

Research Highlight 11 Feb 2022

---

This article was downloaded by **calibre** from <https://www.nature.com/articles/s41586-021-04359-5>

- Article
- [Published: 20 December 2021](#)

# VLDLR and ApoER2 are receptors for multiple alphaviruses

- [Lars E. Clark](#) [ORCID: orcid.org/0000-0002-6093-7597](#)<sup>1 nal</sup>,
- [Sarah A. Clark](#) [ORCID: orcid.org/0000-0001-9944-0919](#)<sup>1 nal</sup>,
- [ChieYu Lin](#)<sup>1 nal</sup>,
- [Jianying Liu](#)<sup>2,3 nal</sup>,
- [Adrian Coscia](#) [ORCID: orcid.org/0000-0002-6836-9993](#)<sup>1</sup>,
- [Katherine G. Nabel](#) [ORCID: orcid.org/0000-0002-4429-7075](#)<sup>1</sup>,
- [Pan Yang](#)<sup>1</sup>,
- [Dylan V. Neel](#) [ORCID: orcid.org/0000-0001-6964-9842](#)<sup>4</sup>,
- [Hyo Lee](#)<sup>5</sup>,
- [Vesna Brusic](#)<sup>1</sup>,
- [Iryna Stryapunina](#)<sup>6</sup>,
- [Kenneth S. Plante](#) [ORCID: orcid.org/0000-0002-7485-3167](#)<sup>2,3,7</sup>,
- [Asim A. Ahmed](#)<sup>8</sup>,
- [Flaminia Catteruccia](#) [ORCID: orcid.org/0000-0003-3295-6683](#)<sup>6</sup>,
- [Tracy L. Young-Pearse](#) [ORCID: orcid.org/0000-0001-7846-1542](#)<sup>5</sup>,
- [Isaac M. Chiu](#) [ORCID: orcid.org/0000-0002-0723-4841](#)<sup>4</sup>,
- [Paula Montero Llopis](#) [ORCID: orcid.org/0000-0002-5983-2296](#)<sup>1,9</sup>,
- [Scott C. Weaver](#) [ORCID: orcid.org/0000-0001-8016-8556](#)<sup>2,3,7</sup> &
- [Jonathan Abraham](#) [ORCID: orcid.org/0000-0002-7937-3920](#)<sup>1,10,11</sup>

[Nature](#) volume **602**, pages 475–480 (2022)

- 6543 Accesses
- 1 Citations
- 95 Altmetric
- [Metrics details](#)

## Subjects

- [Alphaviruses](#)
- [Virus–host interactions](#)

## Abstract

Alphaviruses, like many other arthropod-borne viruses, infect vertebrate species and insect vectors separated by hundreds of millions of years of evolutionary history. Entry into evolutionarily divergent host cells can be accomplished by recognition of different cellular receptors in different species, or by binding to receptors that are highly conserved across species. Although multiple alphavirus receptors have been described<sup>1,2,3</sup>, most are not shared among vertebrate and invertebrate hosts. Here we identify the very low-density lipoprotein receptor (VLDLR) as a receptor for the prototypic alphavirus Semliki forest virus. We show that the E2 and E1 glycoproteins (E2–E1) of Semliki forest virus, eastern equine encephalitis virus and Sindbis virus interact with the ligand-binding domains (LBDs) of VLDLR and apolipoprotein E receptor 2 (ApoER2), two closely related receptors. Ectopic expression of either protein facilitates cellular attachment, and internalization of virus-like particles, a VLDLR LBD–Fc fusion protein or a ligand-binding antagonist block Semliki forest virus E2–E1-mediated infection of human and mouse neurons in culture. The administration of a VLDLR LBD–Fc fusion protein has protective activity against rapidly fatal Semliki forest virus infection in mouse neonates. We further show that invertebrate receptor orthologues from mosquitoes and worms can serve as functional alphavirus receptors. We propose that the ability of some alphaviruses to infect a wide range of hosts is a result of their engagement of evolutionarily conserved lipoprotein receptors and contributes to their pathogenesis.

[Download PDF](#)

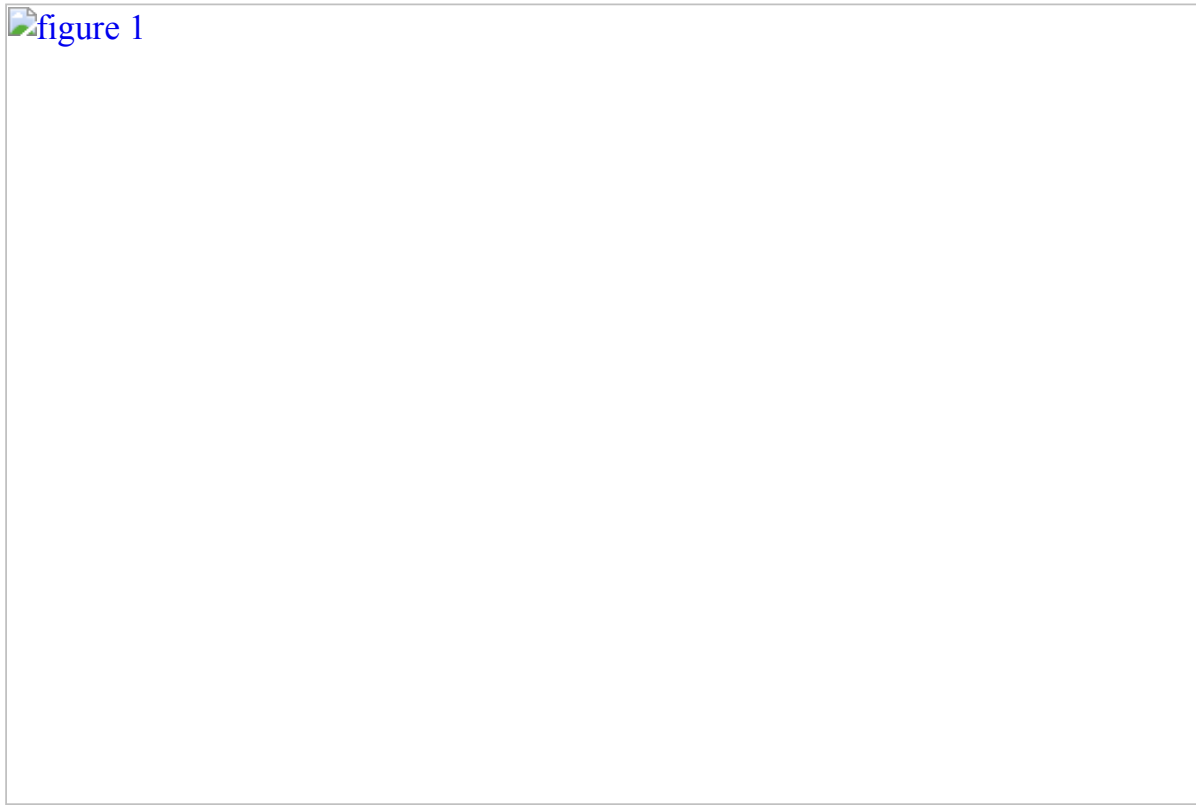
## Main

Alphaviruses are enveloped RNA viruses that cause disease in humans ranging from acute febrile illness with rash and arthralgia to lethal encephalitis. Their genomes encode four nonstructural proteins, nsP1–nsP4, and structural proteins, capsid and E3–E2–(6K/TF)–E1. The viral envelope proteins are arranged with icosahedral symmetry and E2–E1 glycoproteins form heterodimers that assemble as 80 trimers that mediate receptor binding and fusion of viral and cellular membranes<sup>4,5,6</sup>. To use a system that accurately mimics E2–E1 organization, we converted an alphavirus replicon system<sup>7</sup> into a DNA-based reporter virus particle (RVP) system in which one plasmid encodes heterologous E3–E2–(6K/TF)–E1 proteins and a second plasmid encodes Ross River virus (RRV) nonstructural proteins, capsid and a reporter (Extended Data Fig. [1a, b](#)). We also generated a library of single guide RNAs (sgRNAs) that target membrane-

associated proteins in the human genome (Extended Data Fig. 1c, Supplementary Table 1). We used the library to perform a CRISPR–Cas9 screen for cellular viral receptors using HEK 293T (human kidney epithelial) cells expressing Cas9 (HEK 293T-Cas9) infected with Semliki forest virus (SFV) RVPs. The screen identified *VLDLR* as the top candidate (Fig. 1a, Supplementary Table 2). VLDLR is a part of the low-density lipoprotein receptor (LDLR) family and mediates endocytosis of lipoproteins and other ligands<sup>8</sup>.

**Fig. 1: A CRISPR–Cas9 screen identifies VLDLR as a host factor for SFV E2–E1-mediated infection.**

 figure 1



**a**, Results of MAGeCK<sup>49</sup> analysis for the screen performed with SFV RVPs in HEK 293T-Cas9 cells showing enriched genes on the basis of top robust rank aggregation (RRA) scores. **b**, Wild-type (WT) cells, VLDLR-knockout (KO) cells and VLDLR-knockout cells transiently transfected with cDNA encoding VLDLR with an N-terminal Flag tag (VLDLR–Flag) were infected with SFV single-cycle RVPs expressing GFP, and infection was measured by fluorescence-activated cell sorting (FACS). VLDLR cell surface expression was monitored by immunostaining (Extended Data Fig. 2b). **c**, Infection of HEK 293T cells with single-cycle SFV RVPs in the presence of an antibody against VLDLR or a control antibody against human leukocyte antigen (HLA), measured by FACS. **d**, Infection of Vero cells with SFV or CHIKV single-cycle RVPs expressing GFP in the presence of the indicated antibodies. Cells were imaged by fluorescence microscopy. Scale bar, 100 µm. The experiment

was performed twice with representative images shown. **e**, Infection of Vero cells with replication-competent SINV chimeras expressing GFP and the structural proteins of SFV (SINV-SFV) or CHIKV (SINV-CHIKV) at a multiplicity of infection (MOI) of 1 in the presence of the indicated antibodies. GFP expression was measured by FACS 24 h after infection. **f**, Infection of HEK 293T cells with GFP-expressing single-cycle RVPs in the presence of receptor-associated protein (RAP) or transferrin (Tf) control, measured by FACS. Data are mean  $\pm$  s.d. from two experiments ( $n = 6$ ) (**b, c, e, f**). One-way ANOVA with Tukey's multiple comparisons test, \*\*\* $P < 0.0001$  (**b, e**). Two-way ANOVA with Šídák's multiple comparison test, \*\*\* $P < 0.0001$  (**c, f**).

### Source data

Guide RNAs targeting *HSP90B1* and *STT3A* were also enriched in the screen (Fig. [1a](#)). *HSP90B1* encodes an endoplasmic reticulum-resident chaperone that binds the proprotein convertase subtilisin/kexin type 9 serine protease (PCSK9) and prevents PCSK9 from inducing the degradation of LDLR family members<sup>9</sup>. *STT3A* encodes the catalytic subunit of the *N*-oligosaccharyltransferase complex and is also involved in cellular infection by flaviviruses, another group of arthropod-borne viruses that, like alphaviruses, carry positive-sense RNA genomes<sup>10,11</sup>. *STT3A* has a role in flavivirus RNA replication and binds to viral nonstructural proteins<sup>10,11</sup>. Genetic disruption of *STT3A* in our screen may have, therefore, affected replication through the RRV component of the RVP system and may act downstream of SFV E2–E1-mediated entry.

We focused on exploring the role of human VLDLR as a cellular receptor for SFV. Clonal VLDLR-knockout HEK 293T cells became resistant to infection by GFP-expressing SFV RVPs, and this resistance could be reverted by VLDLR overexpression (Fig. [1b](#), Extended Data Fig. [2a, b](#)). An antibody against VLDLR, but not a control antibody, blocked infection of HEK 293T cells by SFV RVPs (Fig. [1c](#)). In an experiment using African green monkey kidney (Vero) cells, an anti-VLDLR antibody inhibited the entry of SFV, but not of control RVPs for Chikungunya virus (CHIKV) (Fig. [1d](#)), an alphavirus that uses MXRA8 as a cellular receptor<sup>2</sup>. The anti-VLDLR antibody also blocked SFV RVP infection of immortalized human cell lines derived from brain, lung, liver, lymphoid, bone and kidney tissues (Extended Data Fig. [2c, d](#)). We generated replication-competent chimeric alphaviruses expressing Sindbis virus (SINV) nonstructural proteins with heterologous structural proteins (capsid and E3–E2–(6K/TF)–E1) and GFP as a reporter. The anti-VLDLR antibody, but not a control antibody, inhibited chimeric SINV–SFV infection of Vero cells (Fig. [1e](#)). Receptor-associated protein (RAP) is a chaperone that binds to some LDLR-related receptors in the endoplasmic reticulum and blocks ligand engagement<sup>12</sup>. Addition of RAP blocked SFV RVP infection of HEK 293T cells, whereas addition of a control protein did not (Fig. [1f](#)).

We used on K562 cells<sup>13</sup> to determine whether a cell line that is highly resistant to infection could be rendered susceptible by ectopic expression of VLDLR. VLDLR was not detected on the plasma membrane of K562 cells (Extended Data Fig. 2c), which were resistant to SFV RVP infection (Fig. 2a, b). Transduction with VLDLR, however, rendered K562 cells highly susceptible to SFV RVP infection, but not to CHIKV RVP infection (Fig. 2a, b, Extended Data Fig. 3a). Conversely, transduction of K562 cells with MXRA8 rendered them highly susceptible to CHIKV but not to SFV RVP infection (Fig. 2a, b, Extended Data Fig. 3a). Transduction of cells with a control membrane protein had no effect in this assay (Fig. 2b).

**Fig. 2: The VLDLR ligand-binding domain supports SFV E2–E1-mediated infection.**

 figure 2

**a**, Infection of wild-type K562 cells or K562 cells expressing indicated proteins infected with SFV or CHIKV single-cycle RVPs expressing GFP. Cells were imaged by fluorescence microscopy. Scale bar, 100  $\mu$ m. The experiment was performed twice independently with similar results and representative images are shown. **b**, Infection of wild-type or transduced K562 cells with GFP-expressing SFV or CHIKV single-cycle RVPs measured by FACS. NRP2 is a control membrane protein. **c**, VLDLR ectodomain and deletion constructs. LBD LA repeats are numbered. **d**, Infection of

K562 cells transduced to express the constructs shown in **c** or NRP2 with GFP-expressing SFV single-cycle RVPs, measured by FACS. **e**, Infection of HEK 293T cells with SFV single-cycle RVPs after pre-incubation with VLDLR<sub>LBD</sub>-Fc or a control NRP2 a1 domain (NRP2<sub>a1</sub>)-Fc fusion protein, measured by FACS. Cell surface expression of NRP2-Flag, VLDLR-Flag and MXRA8 (**a**) and VLDLR-Flag variants (**d**) was confirmed with immunostaining (see Extended Data Fig. [3a](#)). Data are mean  $\pm$  s.d. from two experiments performed in triplicate ( $n = 6$ ) (**b**) or three experiments performed in duplicate (**d, e**) ( $n = 6$ ). One-way ANOVA with Tukey's multiple comparisons test,  $****P < 0.0001$  (**b, d**). Two-way ANOVA with Šídák's multiple comparison test,  $****P < 0.0001$  (**e**).

### Source data

Like other LDLR family members, VLDLR contains an N-terminal ligand-binding domain (LBD) with cysteine-rich repeats (LDLR class A (LA) repeats), a cluster of EGF modules containing a  $\beta$ -propeller domain, and a membrane-proximal *O*-linked sugar domain<sup>8</sup> (Fig. [2c](#)). A construct in which the EGF module containing the  $\beta$ -propeller domain was deleted supported SFV RVP infection, but one in which the LBD was deleted did not (Fig. [2c, d](#), Extended Data Fig. [3a](#)). Further supporting a role for the LBD as a site of E2-E1 attachment, a VLDLR LBD-Fc fusion protein (VLDLR<sub>LBD</sub>-Fc), but not an Fc fusion protein comprising a subdomain of an unrelated protein, inhibited SFV RVP infection of HEK 293T cells (Fig. [2e](#), Extended Data Fig. [4a](#)).

We next sought to determine whether other alphaviruses could bind human VLDLR for cellular entry. Infection by SINV, eastern equine encephalitis virus (EEEV), Venezuelan equine encephalitis (VEEV), western equine encephalitis (WEEV) or CHIKV RVPs was not decreased in VLDLR-knockout HEK 293T cells compared with wild-type cells (Extended Data Fig. [5a](#)). An anti-VLDLR antibody blocked the entry of SFV RVPs into Vero cells but had no effect on the other alphaviruses we tested (Extended Data Fig. [5b](#)). This suggested that some alphaviruses may be able to bind multiple LDLR family members. LDLR, VLDLR and ApoER2 are highly conserved and have superimposable structures, indicating that their corresponding genes evolved from a single ancestor<sup>14</sup>. ApoER2 and VLDLR have critical roles in brain development and modulate synaptic plasticity in adults<sup>14,15,16</sup>. ApoER2 is enriched in the brain and can undergo a large number of alternative splicing events that alter the number of LA repeats and ligand-binding properties<sup>14,17,18,19,20</sup>. We cloned an ApoER2 isoform that contains all seven possible LA repeats (LA1-LA7) (ApoER2<sub>iso1</sub>) and another that contains only LA1-LA3 (ApoER2<sub>iso2</sub>), which is thought to be the predominant form<sup>14,20</sup> (Extended Data Fig. [6](#)). K562 cells expressed LDLR, but not VLDLR or ApoER2 at the plasma membrane (Extended Data Figs. [2c](#), [3b](#)). SFV, EEEV and SINV RVPs infected K562 cells transduced with VLDLR or

ApoER2 isoforms to varying degrees (Extended Data Fig. 5c, d). Addition of RAP or a soluble VLDLR LBD (sVLDLR<sub>LBD</sub>) protein that does not contain an Fc segment (which we avoided because K562 cells express Fc receptors) blocked E2–E1-mediated infection of K562 cells expressing VLDLR or ApoER2<sub>iso2</sub>, confirming that infection was a result of ectopic lipoprotein receptor expression (Extended Data Fig. 5e). VLDLR or ApoER2 expression did not affect CHIKV, VEEV or WEEV RVP infection of K562 cells (Extended Data Fig. 5f). sVLDLR<sub>LBD</sub> blockade of SFV, EEEV and SINV RVP infection of K562 cells overexpressing ApoER2<sub>iso2</sub> (Extended Data Fig. 5e) suggest that VLDLR and ApoER2 bind an overlapping site on the E2–E1 proteins of these alphaviruses.

To confirm the interaction of alphavirus E2–E1 proteins with the VLDLR LBD, we transfected HEK 293T cells with plasmids encoding different alphavirus E3–E2–(6K/TF)–E1 proteins and conducted cell surface staining experiments with Fc fusion proteins (Fig. 3a, Extended Data Fig. 4a). VLDLR<sub>LBD</sub>–Fc-bound cells transfected with the E3–E2–(6K/TF)–E1 proteins of SFV, EEEV and SINV, but not cells transfected with CHIKV E3–E2–(6K/TF)–E1 (Fig. 3a). Conversely, the MXRA8 ectodomain (MXRA8<sub>ect</sub>)–Fc fusion protein, but not VLDLR<sub>LBD</sub>–Fc, bound cells transfected with CHIKV E3–E2–(6K/TF)–E1 (Fig. 3a).

**Fig. 3: Human VLDLR and ApoER2 support E2–E1-mediated entry of divergent alphaviruses.**

 **figure 3**

**a**, Cell surface expression of VLDLR<sub>LBD</sub>–Fc or MXRA8<sub>ect</sub>–Fc in HEK 293T cells transfected with plasmids encoding alphavirus E3–E2–(6K/TF)–E1 proteins. PE, *R*-phycoerythrin. **b**, BLI-based binding analysis of VLPs to sensor tips coated with

VLDLR<sub>LBD</sub>-Fc or MXRA8<sub>ect</sub>-Fc after pre-dipping into buffer or solution containing RAP or transferrin (Tf). The maximal response value is plotted. Sensorgrams are shown in Extended Data Fig. 4c. c, xy slice and 3D volume renderings of representative images of WGA (green)-stained transduced K562 cells incubated with fluorescently labelled VLPs (pink) imaged by live-cell confocal microscopy after co-incubation of cells and VLPs at the indicated temperatures (see Extended Data Fig. 6). Scale bars, 5 μm. d, Number of VLPs bound to individual cell membranes (membr.) or found in the cytoplasm (cyto.) of individual cells at the indicated temperatures (see Extended Data Fig. 8). Data are mean ± s.d. from two experiments performed in triplicate ( $n = 6$ ); two-way ANOVA with Šídák's multiple comparison test, \*\*\*\* $P < 0.0001$  (a). Mean of values obtained from two experiments; one-way ANOVA with Tukey's multiple comparisons test, \*\*\*\* $P < 0.0001$ ; \*\*\* $P = 0.0003$  (d).

### Source data

To determine whether alphavirus E2–E1 proteins directly bind the LBDs of VLDLR and ApoER2 without a requirement for associated lipoproteins, we generated and purified virus-like particles (VLPs), which replicate the structure of native virions<sup>21,22</sup> (Extended Data Fig. 1d). When we examined VLPs by negative-stain electron microscopy, we observed no associated lipoproteins (Extended Data Fig. 4b). Mass spectrometry did not reveal substantial amounts of lipoprotein-associated peptides in purified VLP samples as compared to a VLDL control (Supplementary Table 3). In biolayer interferometry (BLI)-based experiments, VLDLR<sub>LBD</sub>-Fc, but not MXRA8<sub>ect</sub>-Fc, captured SFV, SINV and EEEV VLPs (Fig. 3b, Extended Data Fig. 4c). We also generated an ApoER2<sub>iso1</sub> LBD-Fc fusion protein (ApoER2<sub>LBDIso1</sub>-Fc) (Extended Data Fig. 4a). ApoER2<sub>LBDIso1</sub>-Fc captured SFV, EEEV and SINV VLPs (Fig. 3b, Extended Data Fig. 4c). Addition of RAP, but not a control protein, specifically blocked VLP binding to VLDLR<sub>LBD</sub>-Fc and ApoER2<sub>LBDIso1</sub>-Fc (Fig. 3b, Extended Data Fig. 4c). Thus the LBDs of VLDLR and ApoER2 interact directly with alphavirus E2–E1 proteins.

We next turned to confocal microscopy to determine whether the expression of VLDLR or ApoER2<sub>iso2</sub> (chosen because this shorter form is predominant<sup>14,20</sup>) enables cell surface binding and internalization of fluorescently labelled VLPs. We incubated labelled VLPs with transduced K562 cells that had also been treated with heparinase and stained with wheat germ agglutinin (WGA) to visualize cell membranes (Fig. 3c, Extended Data Figs. 7, 8). Expression of VLDLR, but not MXRA8, promoted the binding of labelled SFV VLPs to cell surface membranes, and more particles were detected in the cytoplasm of cells at 37 °C than at 4 °C, suggesting internalization (Fig. 3c,d). We also observed an increased number of SFV VLPs in the cytoplasm of cells expressing ApoER2<sub>iso2</sub> at 37 °C. The expression of VLDLR and

ApoER2<sub>iso2</sub> promoted cell surface binding of EEEV VLPs, and more particles were again detected in the cytoplasm of cells expressing VLDLR or ApoER2<sub>iso2</sub> at 37 °C (Fig. 3d). We detected cell surface binding and internalization of SINV VLPs on cells expressing VLDLR and ApoER2, but the magnitude of the effects was more modest than those observed with SFV and EEEV VLPs (Fig. 3d).

SFV is neuropathogenic in young laboratory mice<sup>23</sup> and has also caused fatal encephalitis in an exposed laboratory worker, although this individual had chronic purulent bronchitis and may have been immunocompromised<sup>24</sup>. We sought to determine whether VLDLR<sub>LBD</sub>–Fc or RAP could prevent SFV RVP infection of mouse primary cortical neurons and of human neurons differentiated from induced pluripotent stem (iPS) cells<sup>25</sup>. VLDLR<sub>LBD</sub>–Fc and RAP, but not a control protein, blocked SFV RVP infection of mouse cortical neurons and human iPS cell-derived neurons (Fig. 4a,b, Extended Data Fig. 9a–d).

**Fig. 4: Lipoprotein receptors mediate neuronal infection and divergent receptor orthologues support E2–E1 mediated entry.**

 figure 4

**a**, Infection of mouse primary cortical neurons with GFP-expressing SFV single-cycle RVPs in the presence of the indicated proteins. Cells were imaged by fluorescence microscopy. Scale bars, 100  $\mu$ m. Phase-contrast images are shown in Extended Data Fig. 9c. The experiment was performed twice, and representative images are shown. **b**, Quantification of infection in the experiment shown in **a** using a live cell imaging system (see Methods). **c, d**, Ten-day-old mice were administered a VLDLR<sub>LBD</sub>-Fc fusion protein or an isotype control antibody intraperitoneally 6 h before intraperitoneal inoculation with 100 PFU (**c**) or 1,000 PFU (**d**) of SFV A774. Survival of the mice was monitored daily. **e**, Infection of wild-type K562 or K562 cells transduced with VLDLR orthologues with single-cycle RVPs expressing GFP. **f**, Infection of wild-type K562 cells or K562 cells transduced with ApoER2 orthologues with single-cycle RVPs expressing GFP. Cell surface expression of constructs used in **e** and **f**, was confirmed by immunostaining (Extended Data Fig. 3). Data are mean  $\pm$  s.d. from two experiments performed in triplicate ( $n = 6$ ), except for the RAP experiment in **b**, which was performed once in triplicate and once in duplicate ( $n = 5$ ). One-way ANOVA with Tukey's multiple comparisons test, \*\*\* $P < 0.0001$  (**b, e, f**). Survival data (**c, d**) are from two independent experiments; in **c**: PBS  $n = 10$ , VLDLR<sub>LBD</sub>-Fc  $n = 10$  isotype control  $n = 9$  mice; in **d**: PBS,  $n = 11$ , VLDLR<sub>LBD</sub>-Fc  $n = 12$ , isotype control  $n = 11$  mice. log-rank (Mantel–Cox) test comparing VLDLR<sub>LBD</sub>-Fc or isotype control to PBS, \*\*\* $P < 0.0001$  (**c, d**); or isotype control to PBS,  $P = 0.4745$  (**c**) or  $P > 0.9999$  (**d**); NS, not significant. *H. sapiens*, *Homo sapiens*.

### Source data

We next tested wild-type, replication-competent strains of SFV (A774), EEEV (FL-939-39, and SINV (Ar Mg812) in a multi-step viral replication assay using transduced K562 cells. Ectopic expression of VLDLR and ApoER2 isoforms resulted in faster kinetics and increased levels of viral replication, and we observed a three-log increase in viral replication for SFV and an almost five-log increase with EEEV (Extended Data Fig. 9e). The effect was less pronounced but nonetheless significant with SINV infection, consistent with the moderate phenotype we observed with SINV RVPs in infectivity assays with K562 cells expressing VLDLR and ApoER2 (Extended Data Fig. 5c, d) or VLP cell binding and internalization assays (Fig. 3c, d).

When infected with SFV strain A774, neonatal mice, but not adult mice, rapidly die from fulminant encephalitis<sup>26,27,28,29,30</sup>. Because VLDLR and ApoER2 are important for the development of the central nervous system, mice that are deficient in both receptors have ataxia, severe cognitive deficits and early lethality<sup>31</sup>, thus limiting our ability to carry out in vivo studies in double-knockout mice. We instead used VLDLR<sub>LBD</sub>-Fc as a blocking agent for in vivo studies. This protein should block VLDLR- and ApoER2-dependent cellular entry, as sVLDLR<sub>LBD</sub> blocking experiments suggest that alphavirus E2–E1 proteins use the same surface to bind to both receptors

(Extended Data Fig. 5e). VLDLR<sub>LBD</sub>-Fc neutralized SFV A774 in a plaque assay (Extended Data Fig. 5g). When ten-day-old mice were inoculated with SFV A774 six hours after receiving phosphate-buffered saline or an isotype control IgG, all mice rapidly succumbed to infection within three days of viral challenge. However, 100% of mice treated with VLDLR<sub>LBD</sub>-Fc 6 h before viral challenge were still alive 3 days after challenge (Fig. 4c,d). Although all VLDLR<sub>LBD</sub>-Fc-treated mice eventually succumbed to infection (became moribund, meeting euthanasia criteria) on day 8 (100 plaque-forming units (PFU) challenge dose group) or day 7 (1,000 PFU challenge dose group), the isotype control-treated mice all became moribund significantly faster, by day three. Because VLDLR<sub>LBD</sub>-Fc could have, in principle, been cleared from circulation by associating with lipoproteins (in addition to binding virus), further studies will be required to determine whether repeated administration would provide additional therapeutic benefit in this model system for otherwise rapidly fatal viral encephalitis.

The LBDs of VLDLR and ApoER2 are mostly conserved even among highly divergent species (Extended Data Figs. 6, 10). We transduced K562 cells with various VLDLR and ApoER2 orthologues and—taking advantage of the ability of RAP to interact with highly divergent lipoprotein receptor orthologues<sup>32,33</sup> but not with LDLR when added exogenously<sup>34</sup>—we used RAP to monitor orthologue cell surface expression (Extended Data Fig. 3c). SFV RVPs infected K562 cells that expressed equine (*Equus caballus*) and avian (*Sturnus vulgaris*) VLDLR orthologues (Fig. 4e). SFV and EEEV infected cells that expressed mosquito (*Aedes aegypti* and *Aedes albopictus*) VLDLR orthologues (lipophorin receptor 1) (Fig. 4e). Remarkably, SFV RVPs could also infect cells overexpressing a *Caenorhabditis elegans* VLDLR orthologue, a receptor with a role in regulating the worm's intestinal lipid content<sup>35,36</sup> (Fig. 4e). Murine, equine and avian ApoER2 orthologues supported entry of SFV, EEEV and SINV RVPs to varying degrees (Fig. 4f, Extended Data Fig. 10c).

ApoER2 is almost exclusively expressed in the central nervous system<sup>14</sup>. Accordingly, we did not detect ApoER2 on the surface of HEK 293T, Vero or K562 cells (Extended Data Fig. 3b). These findings may explain why incubation with an antibody against VLDLR is sufficient to block SFV E2-E1-mediated infection of multiple cell lines (Fig. 1c–e, Extended Data Fig. 2d). Whereas SFV primarily depends on VLDLR for entry into several cell types, EEEV and SINV—although they can bind VLDLR and ApoER2—can enter HEK 293T and Vero cells through independent pathways, as genetic disruption of VLDLR in HEK 293T cells, or treatment of Vero cells with an antibody against VLDLR, did not decrease EEEV or SINV RVP infection of these cells (Extended Data Fig. 5a,b). NRAMP2 is a possible alternative receptor for SINV<sup>1</sup>. Other LDLR-family members that we did not test, including LRP1, LRP1b, LRP2 and LRP4, could also have roles in alphavirus entry. An anti-VLDLR antibody

had a modest effect on SFV entry into U2OS cells, a human bone-derived cell line (Extended Data Fig. 2d), also suggesting the presence of alternative SFV receptors on this cell type. SFV is reported to partially depend on MXRA8 for entry into mouse cells<sup>2</sup>. Human MXRA8, however, is an unlikely alternative receptor for SFV on U2OS cells, as we did not detect SFV RVP entry into K562 cells overexpressing human MXRA8 (Fig. 2a, b, Extended Data Fig. 5c, d), nor did we detect SFV VLP binding to these cells (Fig. 3d) or to human MXRA8<sub>ect</sub>-Fc in BLI experiments (Fig. 3b).

SFV causes encephalitis in horses, mice, rats, rabbits and guinea pigs, and SINV also causes age-dependent encephalitis in mice<sup>26,37,38</sup>. Because SFV, SINV and EEEV can cause encephalitis in humans or animals, binding to VLDLR or ApoER2 could contribute to their neuropathogenesis. VEEV has recently been shown to bind low-density lipoprotein receptor class A domain-containing 3 (LDLRAD3) as a receptor<sup>3</sup>. While LDLRAD3A is found in vertebrates, it does not have an apparent orthologue in mosquitos<sup>3</sup>. However, every VLDLR orthologue we tested supported SFV E2-E1-mediated infection, including that of *C. elegans*, which is separated by 10<sup>9</sup> years of evolutionary divergence from humans (Fig. 4e, Extended Data Fig. 10c). Furthermore, only the entry of VEEV RVPs, but not that of SFV, EEEV or SINV RVPs, was enhanced by overexpression of LDLRAD3 on K562 cells, suggesting that the VEEV E2-E1 proteins evolved the ability to only recognize this specific receptor that is structurally homologous to LDLR family members (Extended Data Fig. 5h). Our data, therefore, reveal that similarities in alphavirus E2-E1 protein structure correlate with structural homology in receptors from organisms as evolutionarily distant from humans as worms.

The lipoprotein receptor gene family appeared in an evolutionary burst at the advent of multicellular life and has maintained a remarkable degree of conservation throughout evolutionary history<sup>36</sup>. The ability of some alphaviruses to bind LDLR family members probably accounts for their extensive tissue and species tropism. Many viruses, including vesicular stomatitis virus<sup>34</sup>, minor group rhinoviruses<sup>39,40</sup>, subgroup A Rous sarcoma virus<sup>41</sup>, several *Flaviviridae* family members<sup>42,43,44</sup>, VEEV<sup>3</sup> and Rift Valley fever virus<sup>45</sup>, have been reported to bind LDLR-repeat-containing receptors to enter cells. LDLR is also a receptor for *Clostridium difficile* toxin A<sup>46</sup>. LDLR family members may, therefore, represent evolutionary conserved ‘hotspots’ for interfacing with pathogens. Pathogens, in turn, may be driving sequence divergence of the receptor LBDs. A similar evolutionary arms race has been described with the iron-uptake protein transferrin receptor 1, which is also recurrently targeted by pathogens for cellular entry<sup>47,48</sup>.

Our studies help answer, in part, the longstanding question of how some alphaviruses can infect a wide range of organisms. They further suggest that strategies targeting

multiple cellular receptors, and possibly multiple receptor binding sites on virions, may be required to effectively limit the cellular entry of some pathogenic alphaviruses.

## Methods

### Cells and viruses

We maintained HEK 293T (human kidney epithelial, ATCC CRL-11268), 293FT (Thermo Fisher Scientific R70007), Vero (*Cercopithecus aethiops* kidney, ATCC CCL-81), U2OS (human bone, ATCC HTB-96), A549 (human lung epithelial, ATCC CCL-185), SVG-A (human astroglial, provided by T. Kirchhausen), and Huh7 cells (provided by F. Zhang) in Dulbecco's modified Eagle's medium (DMEM, Gibco) supplemented with 10% (v/v) fetal bovine serum (FBS), 25 mM HEPES (Thermo Fisher Scientific), and 1% (v/v) penicillin-streptomycin (Thermo Fisher Scientific). We maintained Jurkat clone E6-1 (human lymphoblast, ATCC TIB-152) and K562 (human chronic myelogenous leukemia, ATCC CCL-243) cells in RPMI (Thermo Fisher Scientific) supplemented with 10% (v/v) FBS, 25 mM HEPES, and 1% (v/v) penicillin-streptomycin. We maintained SK-N-SH (human brain, ATCC HTB-11) and EBC-1 (human squamous cell lung carcinoma, provided by T. Kirchhausen) in Eagle's minimum essential medium (EMEM, Sigma) supplemented with 10% (v/v) FBS, 25 mM HEPES, and 1% (v/v) penicillin-streptomycin. We maintained Expi293F cells (Thermo Fisher Scientific A14527) in Expi293 Expression Medium (Thermo Fisher Scientific) supplemented with 1% (v/v) penicillin-streptomycin. We maintained BHK-21 cells (ATCC CCL-10) in DMEM supplemented with 10% (v/v) fetal bovine serum and 1% (v/v) penicillin-streptomycin. Cell lines were not authenticated. We confirmed the absence of mycoplasma in all cell lines through monthly testing using an e-Myco PCR detection kit (Bulldog Bio 25234).

The following wild-type replication-competent alphaviruses were used: SINV (strain DAK Ar Mg812) and EEEV (strain FL-93-939). These viruses were propagated in Vero CCL-81 cells and titrated by standard plaque assays. For work with unmodified replication-competent SFV, we rescued a molecular clone using a plasmid encoding SFV A774 (pCMV-A774wt)<sup>50</sup> obtained from A. Merits. The SFV clone was rescued by electroporating 10 µg of pCMV-A774wt plasmid into BHK-21 cells (220 V, 975 µF, one pulse in a cuvette with a 4-mm electrode gap) using a BTX-Harvard Apparatus ECM 830 Square Wave Electroporator (Harvard Apparatus). After incubation for 24 h at 37 °C, the stock of rescued virus (P<sub>0</sub> stock) was collected and titrated in a plaque assay on Vero cells. To obtain P<sub>1</sub> stock, confluent BHK-21 cells grown on T75 flasks were infected with P<sub>0</sub> stock at an MOI of 5. At 24 h post infection, the supernatant (P<sub>1</sub> stock) was collected, and virus titre was determined on Vero cells.

## **Primary mouse cortical neuron culture and infection assays**

Mouse experiments were approved at Harvard Medical School under the Harvard Medical School Institutional Animal Care and Use Committee protocol number IS00000054. Mouse (C57BL/6J) primary cortical neurons were dissociated and cultured using the Papain Dissociation System (Worthington Biochemical LK003153) as previously described<sup>51</sup>. In brief, postnatal day 0 (P0) C57BL/6J mice were euthanized and mouse cortices were collected in cold Earle's balanced salt solution (EBSS) and resuspended in 2.5 ml of warmed EBSS supplemented with papain (20 units ml<sup>-1</sup>) and DNase (2000 units ml<sup>-1</sup>). Following a 12 min incubation at 37 °C, cortices were triturated using fire polished glass Pasteur pipettes. Samples were centrifuged (2,000g for 5 min) to pellet cells, and then resuspended in 1.6 ml of suspension media (1.375 ml EBSS, 150 µl albumin-ovomucoid inhibitor (10 mg ml<sup>-1</sup> in EBSS), and 75 µl DNase (2,000 units ml<sup>-1</sup>)). This solution was then layered on top of a 2.5 ml solution of albumin-ovomucoid inhibitor (10 mg ml<sup>-1</sup> in EBSS) to create a continuous density gradient and the samples were centrifuged at 1,000 rpm for 5 min. The supernatant (gradient) was discarded, and pelleted neurons were collected in pre-warmed Neurobasal Plus medium (Thermo Fisher Scientific) supplemented with 200 mM l-glutamine (Thermo Fisher Scientific) and 1× B-27 (Thermo Fisher Scientific) with 1% (v/v) penicillin-streptomycin (Thermo Fisher Scientific). Cells were plated in 24 well glass bottom dishes (Cellvis 24 well plate 1.5 glass bottom cover dish) (P241.5HN) for imaging experiments at a density of  $4 \times 10^5$  cells per well. After neurons had been cultured for 7 d, we pre-incubated SFV RVPs with VLDLR<sub>LBD</sub>-Fc fusion proteins or RAP in culture media containing 5 µg ml<sup>-1</sup> polybrene for 30 min at 37 °C. We then added SFV RVP and Fc fusion proteins or SFV RVP and RAP mixtures to cells. Cells were imaged every 2 h for 24 h using the Incucyte S3 Live Cell Imaging system (Sartorius) with Incucyte S3 Software v2018B (Sartorius) using the following objectives: 20×/0.45 Plan Fluor (4465), 10×/0.3 Plan Fluor (4464). GFP-positive neurons were scored as cells with a threshold signal greater than 5 green calibrated units (GCU) above background, using a Top-hat background subtraction method. To calculate the percent positive cells, at the time point of 22 h post-infection, the area of GFP signal above background was divided by the total area covered by cells under phase contrast and was multiplied by 100. We calculated relative infection as follows: Relative infection (%) = (% GFP-positive cells in the presence of antibody or Fc fusion protein or RAP)/(% GFP-positive cells in the absence of antibody or Fc fusion or RAP) × 100%.

## **Induced pluripotent stem cell lines**

The generation of cell lines from human iPS cells was approved by the institutional review board (IRB) of Brigham & Women's Hospital (IRB protocol 2015P001676).

iPSCs were generated from peripheral blood mononuclear cells (PBMCs) from the Religious Order Study (ROS) and Memory and Aging Project (MAP) cohort using the Sendai virus reprogramming method as previously described<sup>25</sup>. iPS cells underwent a rigorous quality check procedure that includes a sterility check, mycoplasma testing, karyotyping and pluripotency assays performed by the New York Stem Cell Foundation (NYSCF). iPS cells were maintained using StemFlex Medium (Thermo Fisher Scientific). For this study, two cell lines (one male and one female) were used for induced neuron differentiation.

## Induced neuron differentiation

Induced neurons were generated as previously described<sup>52</sup> with minor modifications that have also been previously described<sup>25</sup>. In brief, iPS cells were plated at a density of 95,000 cells per cm<sup>2</sup> on a growth factor reduced Matrigel basement membrane matrix (Corning) coated plate, then were transduced with three lentiviruses: pTet-O-NGN2-puro (Addgene plasmid #52047, a gift from M. Wernig)<sup>52</sup>, Tet-O-FUW-EGFP (Addgene plasmid 30130, a gift from M. Wernig)<sup>53</sup>, and FUDeltaGW-rtTA (Addgene plasmid 19780, a gift from K. Hochedlinger)<sup>54</sup>. The cells were then dissociated with StemPro Accutase Cell Dissociation Reagent (Thermo Fisher Scientific) plated at 200,000 cells per cm<sup>2</sup> using StemFlex and ROCK inhibitor Y-27632 (Stemcell Technologies) (10 µM) (day 0). From day 1 to day 3, the media was gradually switched from KSR media (KnockOut DMEM (Thermo Fisher Scientific), 15% (v/v) KnockOut Serum Replacement (Thermo Fisher Scientific), 1× MEM non-essential amino acids solution (Thermo Fisher Scientific), 55 µM β-mercaptoethanol (Thermo Fisher Scientific), 1× GlutaMAX (Life Technologies)) to N2B media (DMEM: Nutrient Mixture F-12 (DMEM/F12) (Thermo Fisher Scientific), 1× GlutaMAX (Life Technologies), 1× N2 Supplement-B (Stemcell Technologies), 0.3% (v/v) dextrose (d-(+)-glucose) (Sigma)). Day 1 media contained 100% (v/v) KSR, day 2 media contained 50% (v/v) KSR and 50% (v/v) N2B, and day 3 media contained 100% (v/v) N2B. Doxycycline (2 µg ml<sup>-1</sup>) (Sigma) was added from day 1 to the end of the differentiation, and puromycin (5 µg ml<sup>-1</sup>) (Gibco) was added from day 2 to the end of the differentiation. On day 3, B27 supplement (1:100) (Life Technologies) was added. On day 4, cells were replated at 50,000 cells per cm<sup>2</sup> and from day 4 to the end of differentiation (day 21), cells were cultured with NBM media (Neurobasal medium (Thermo Fisher Scientific), 0.5× MEM-NEAA (Thermo Fisher Scientific), 1× GlutaMAX 0.3% dextrose (d-(+)-glucose) (Sigma) supplemented with 1:50 B27 + BDNF, GDNF, CNTF (10 ng ml<sup>-1</sup>) (PeproTech)) with media replaced every 2 to 3 days. After neurons had been cultured for an additional 14 d, we pre-incubated SFV RVPs with VLDLR<sub>LBD</sub>-Fc fusion proteins or RAP in culture media containing 5 µg ml<sup>-1</sup> polybrene for 30 min at 37 °C. We then added SFV RVP and Fc fusion proteins or SFV RVP and RAP mixtures to cells. Cells were imaged every 2 h for 24 h using

the Incucyte S3 Live Cell Imaging system and relative infection based on GFP expression at the time point of 22 h post-infection was calculated as described above in experiments performed with primary mouse cortical neuron cultures.

## Reporter virus particle generation

To create a two-component RVP system, we used elements from an RRV replicon plasmid (pRR64)<sup>7</sup> provided by R. Kuhn (Purdue University). We removed the SP6 promoter and replaced it with a CMV/T7 promoter cassette. We also removed RRV E3–E2–(6K/TF)–E1 sequence from pRR64 and replaced it with reporter gene (CD20) or turbo GFP downstream of the capsid gene sequence and preceded by a 2A ‘self-cleaving’ peptide derived from porcine teschovirus-1, and included a bGH termination signal after the 3'UTR poly-A tail. RVPs were generated by providing in *trans* the modified pRR64 plasmid and a pCAGGS vector expressing the heterologous alphavirus E3–E2–(6K/TF)–E1 proteins with a start codon upstream of E3. pCAGGS E3–E2–(6K/TF)–E1 expressor plasmids for CHIKV (strain 37997, GenBank AY726732.1) and EEEV (Florida 91-469, Q4QXJ7.1) have been previously described<sup>55</sup>. pCAGGS E3–E2–(6K/TF)–E1 expressor plasmids for SFV (SFV4, AKC01668.1), SINV (Toto1101 T6P144, AKZ17594.1), WEEV (71V-1658, NP\_640331.1), and VEEV (TC-83, AAB02517.1) were subcloned for this study. We used Lipofectamine 3000 (Invitrogen) to transfect 293FT cells using the manufacturer’s protocol and replaced media with Opti-MEM (Thermo Fisher Scientific) supplemented with 5% (v/v) FBS, 25 mM HEPES, and 5 mM sodium butyrate 1 d post-transfection. We collected supernatants 3 d post-transfection. Supernatants were then centrifuged at 1,000 rpm for 5 min, filtered using a 0.45 µm filter, and frozen at –80 °C for storage.

To purify RVPs for SDS–PAGE analysis, we collected supernatants 24 and 48 h (EEEV and SINV) or 48 h (SFV) post-transfection. We clarified supernatants by centrifugation at 3,000g for 10 min. We then performed polyethylene glycol (PEG)-precipitation by mixing clarified supernatants to a final concentration of 7% (v/v) PEG 6000 and 2.3% (v/v) NaCl and incubated samples at 4 °C for 4 h. Precipitates were pelleted by centrifugation at 4,000g for 30 min and resuspended in phosphate-buffered saline (PBS). We loaded resuspended RVPs onto a 20–70% continuous sucrose gradient and centrifuged samples at 210,000g for 1.5 h. We collected VLP bands and then used 100-kDa Amicon filters (Sigma UFC910096) to buffer exchange samples into PBS and to concentrate samples. Samples were analysed by SDS–PAGE using a 4–15% Mini-PROTEAN TGX Stain-Free Protein Gel (Bio-Rad 4568083), with proteins visualized using a stain-free gel imaging system (Bio-Rad ChemiDoc). Uncropped, unprocessed images of scanned gels are provided in Supplementary Fig. 1.

## sgRNA library design, screening, and data analysis

We generated a list of membrane or membrane-associated proteins by examining list of proteins determined to be on the cell surface by mass spectrometry<sup>56</sup> or predicted bioinformatically to be cell surface associated<sup>57,58</sup>. We also obtained a list of genes that encode proteins predicted to be on endosomes, lysosomes, vesicles or the cell surface by UniProt (<https://www.uniprot.org>). To compile a comprehensive list of genes using these resources, we included genes encoding proteins that were identified to be cell surface associated by mass spectrometry and then added any other gene that was predicted to be on cell surface by at least one of the other resources. The final list of genes is included in Supplementary Table 1. A CRISPR knockout library containing 10 sgRNAs per gene was generated by Desktop Genetics. We amplified the library in Endura ElectroCompetent cells (Lucigen 60242) as previously described<sup>59</sup>. We packaged the sgRNA plasmid library in HEK 293T cells through co-transfection of the lentiGuide-Puro vector (provided by F. Zhang, Addgene #52963)<sup>60</sup>, psPAX2 (provided by D. Trono, Addgene #12260) and pMD2.G (provided by D. Trono, Addgene #12259) using Lipofectamine 3000 (Invitrogen) and following the manufacturer's instructions. Supernatants were collected 1 and 2 d post-transfection, pooled, clarified by centrifugation (1,200 rpm for 5 min), filtered through a 0.45 µm membrane, and stored at -80 °C.

To generate a clonal HEK 293T cell line that expresses *Streptococcus pyogenes* Cas9 (HEK 293T-Cas9), we transduced cells with lentiCas9-blast (provided by F. Zhang, Addgene #52962)<sup>60</sup>, selected transduced cells with blasticidin, and isolated clones by limiting dilution. We selected a HEK 293T-Cas9 clone with high Cas9 activity after clonal dilution by transfecting cells with pXPR\_011 vector (provided by J. Doench and D. Root, Addgene #59702)<sup>61</sup>, which expresses GFP and an sgRNA against GFP, and monitoring for low GFP expression by FACS. We selected a clone that had roughly an 80% decrease in GFP signal as compared to WT HEK 293T cells. We expanded the HEK 293T-Cas9 cells and transduced cells ( $150 \times 10^7$ ) with the CRISPR sgRNA lentivirus library at a multiplicity of infection (MOI) of 0.3. We began selection of sgRNA containing cells with puromycin at  $1 \mu\text{g ml}^{-1}$  1 d post-transduction. Seven to 10 d post-selection, we infected cells with SFV RVPs expressing CD20, aiming for 80–90% infected cells as monitored by an anti-CD20 APC conjugate antibody (Miltenyi Biotec Clone LT20 130-113-370) used at 1:50 dilution using separate HEK 293T-Cas9 cells that had not been exposed to sgRNAs. Three days post RVP infection, we depleted infected cells using anti-CD20 MicroBeads (Miltenyi Biotec 130-091-104) and following the manufacturer's protocol. We chose to use anti-CD20 MicroBeads to deplete infected cells, instead of flow cytometry to separate cells based on GFP expression, because the former isolation strategy could be performed in a biosafety cabinet rather than requiring several hours of instrument time on a flow cytometer. To improve the signal-to-noise ratio, we expanded non-infected cells and repeated infection with SFV RVPs expressing CD20 for an additional two rounds. We extracted genomic DNA from

uninfected cells and control HEK 293T-Cas9 cells that had been exposed to sgRNAs and puromycin for the duration of the experiment but had not been infected with RVPs. We amplified sgRNA sequences and determined sgRNA content using next generation sequencing on an Illumina MiSeq. We determined sgRNA sequences targeting specific genes after removing tag sequences. We analysed sequences for gene enrichment using MAGeCK<sup>49</sup>.

## Genetic knockout validation

For disrupting genes using CRISPR–Cas9, we used paired sgRNAs<sup>62</sup> with a nuclease to introduce ~200-bp deletions in target genes. We used Lipofectamine 3000 (Invitrogen) and followed the manufacturer’s protocol to co-transfect HEK 293T cells with the lentiGuide-Puro vector (Addgene #52963)<sup>60</sup> expressing sgRNAs and the lentiCas9-blast plasmid (Addgene #52962)<sup>60</sup>. Two days post-transfection, we split cells and started selection with blasticidin at 10 µg ml<sup>-1</sup> and puromycin at 1 µg ml<sup>-1</sup>. We returned cells to normal media for replication 3 d post-transfection and isolated individual clones using clonal dilution. We isolated genomic DNA from clonal cells and used a genotyping PCR to confirm successful deletion and confirmed lack of cell surface VLDLR expression using the mouse anti-human VLDLR antibody 1H10 (GeneTex GTX79552).

sgRNA sequences for *VLDLR* disruption were as follows: *VLDLR* sgRNA-1: 5'-CACCGCGACCAATCTGATGAGTCCC-3'; *VLDLR* sgRNA-2: 5'-AACACGGGACTCATCAGATTGGTCGC-3'; *VLDLR* sgRNA-3: 5'-CACCGACTGGAGCAGGTGAACTCGT-3'; *VLDLR* sgRNA-4: 5'-AACACACGAGTTCACCTGCTCCAGTC-3'.

Genotyping primer sequences were as follows: primer 1: 5'-CCATTGTAGCCTTAAGTTGGG-3'; primer 2: 5'-TCCTCACATTCAAATTGGTCAG-3'.

## SINV chimera generation

A plasmid encoding infectious SINV expressing GFP (pTE3'2J)<sup>63</sup> was provided by R. Andino. To generate plasmid launched SINV chimeric recombinant alphaviruses, we replaced the Sp6 promoter located at the 5' end of the SINV insert with a CMV/T7 promoter cassette and introduced at the 3' end the hepatitis delta virus (HDV) ribozyme and SV40 poly(A) sequences. To generate replication-competent SINV chimeric viruses, we then replaced the genes encoding SINV structural proteins (capsid and E3–E2–(6K/TF)–E1) with the structural proteins of CHIKV (strain 37997, GenBank AY726732.1) or SFV (SFV4, AKC01668.1). We transfected HEK 293T cells using Lipofectamine 3000 (Invitrogen) following the manufacturer’s protocol.

We replaced media 12 h post-transfection with Opti-MEM (Thermo Fisher Scientific) with 5% (v/v) FBS and 25 mM HEPES. We collected the supernatant 48 h after transfection, filtered these through a 0.45  $\mu$ m filters, and froze supernatants at -80 °C for storage. Chimeras were titred on Vero (CCL-81) cells by plaque assay.

## Expression and purification of virus-like particles

To produce SINV and SFV VLPs, we subcloned the structural proteins (capsid and E3–E2–(6K/TF)–E1) of SINV (Strain T6P144, GenBank AKZ17594.1) and SFV (SFV4, AKC01668.1) into the mammalian expression vector pHLSec<sup>64</sup>. We used previously described vectors to produce CHIKV<sup>21</sup> and EEEV<sup>22</sup> VLPs. We transfected HEK 293T cells with Lipofectamine 3000 (Invitrogen) according to the manufacturer's instructions. We purified VLPs as previously described<sup>65</sup>. In brief, we collected supernatant 24 h and 48 h post-transfection and clarified these by centrifugation at 3,000g for 10 min. We then performed PEG precipitation by mixing clarified supernatants to a final concentration of 7% (v/v) PEG 6000 and 2.3% (v/v) NaCl and incubated at 4 °C overnight. Precipitates were pelleted by centrifugation at 4,000g for 30 min and resuspended in PBS. We loaded resuspended VLPs onto a 20–70% continuous sucrose gradient and centrifuged samples at 210,000g for 1.5 h. We collected VLP bands and buffer exchanged using a 100-kDa Amicon filter (Sigma). VLPs were stored at 4 °C in Tris buffered saline (TBS), pH 7.4, containing 2 mM CaCl<sub>2</sub> (for BLI experiments) or in PBS (for electron microscopy experiments) and not frozen. We confirmed particle integrity and the absence of degradation products using SDS–PAGE (Extended Data Fig. 1d) in addition to negative-stain electron microscopy (Extended Data Fig. 4b). VLPs were always used within seven days of purification.

## Protein sequence analysis by LC–MS/MS

Protein sequence analysis by LC–MS/MS of purified alphavirus VLPs and human VLDL (Sigma LP1) was performed at the Taplin Biological Mass Spectrometry Facility at Harvard Medical School. Prior to analysis, samples were digested in trypsin followed by a reverse phase clean up. Samples were then dried in a Vacufuge (Eppendorf) concentrator for ~1 h and stored at 4 °C until analysis. On the day of analysis, samples were reconstituted in 10  $\mu$ l of high-performance liquid chromatography (HPLC) solvent A (2.5% (v/v) acetonitrile, 0.1% (v/v) formic acid). A nano-scale reverse-phase HPLC capillary column was created by packing Accucore 2.6  $\mu$ m C<sub>18</sub> spherical silica beads (Thermo Fisher Scientific) into a fused silica capillary (100  $\mu$ m inner diameter  $\times$  ~30 cm length) (Polymicro Technologies) with a flame-drawn tip<sup>66</sup>. After equilibrating the column each sample was loaded using a FAMOS autosampler (LC Packings) onto the column. A gradient was formed, and peptides were eluted with increasing concentrations of solvent B (97.5% (v/v)

acetonitrile, 0.1% (v/v) formic acid). As peptides eluted, they were subjected to electrospray ionization and then entered into an LTQ Orbitrap Velos Pro ion-trap mass spectrometer (Thermo Fisher Scientific). Peptides were detected, isolated, and fragmented to produce a tandem mass spectrum of specific fragment ions for each peptide. Peptide sequences (and hence, protein identity) were determined by matching protein databases with the acquired fragmentation pattern using the software program SEQUEST version 28 rev 13 (Thermo Fisher Scientific)<sup>67</sup>. All databases include a reversed version of all the sequences and the data was filtered to between a one and two percent peptide false discovery rate.

## Labelling of virus-like particles

We purified VLPs as described above with the exception that we first buffer exchanged particles into 0.1 M Sodium Bicarbonate (pH 8.3) and diluted them to a concentration of 1 mg ml<sup>-1</sup> for labeling. Immediately before use, Alexa Fluor 647 (AF647) NHS ester (succinimidyl ester) (Invitrogen A37573) was dissolved into dimethyl sulfoxide (DMSO) at a final concentration of 1 mg ml<sup>-1</sup>. While stirring, we added 25 µg of the amine reactive dye to 1 mg of VLP and incubated the mixture for 1 h at room temperature. We removed excess dye from the solution with a Zeba Spin Desalting Column (Thermo Fisher Scientific) and buffer exchanged labelled VLPs into PBS and stored these at 4 °C. Labelled VLPs were used for confocal microscopy experiments within 12 h of labelling.

## Ectopic expression experiments

cDNA encoding full length human VLDLR (GenBank NP\_003374.3), human LDLR (GenBank AAP88892) and MXRA8 (clone ID: NM\_032348.3) were obtained from GenScript. cDNA encoding human NRP2 (GenBank NM\_201267.2)<sup>68</sup> was provided by S. Whelan. Codon-optimized versions of the following *H. sapiens* VLDLR (GenBank NP\_003374.3), *H. sapiens* ApoER2 isoform 1 (GenBank NM\_004631.5), *H. sapiens* ApoER2 isoform 2 (GenBank NM\_004631.5), *M. musculus* ApoER2 (GenBank XP\_036019651), *E. caballus* VLDLR (GenBank XP\_023483037), *E. caballus* ApoER2 (GenBank XP\_023485552), *S. vulgaris* VLDLR (GenBank XM\_014880599.1), *S. vulgaris* ApoER2 (GenBank XM\_014870608.1), *A. aegypti* lipophorin receptor 1 (GenBank JN411069.1), *A. albopictus* lipophorin receptor 1 (GenBank JAC13440) and *C. elegans* VLDLR (GenBank NM\_182223.6). For constructs containing a Flag tag, we used the SignalP server<sup>69</sup> to predict signal peptidase processing sites and introduced sequence encoding a glutamic acid residue followed by a Flag tag (DYKDDDDK) and a short linker (GSG) at the N-terminus of each construct to monitor cell surface expression. We subcloned untagged or Flag-tagged versions of these constructs into the backbone of the lentiGuide-Puro vector

(Addgene #52963)<sup>60</sup>. We packaged lentivirus in HEK 293T cells by co-transfected this vector with psPAX2 (Addgene #12260), and a previously described pCAGGs vector expressing vesicular stomatitis virus (VSV) G<sup>70</sup> in a ratio of 3:2:1 using Lipofectamine 3000 (Invitrogen). We exposed K562 cells to filtered (0.45 µm) supernatants containing lentivirus for 48 h. We selected transduced cell populations with puromycin (2 µg ml<sup>-1</sup>). For all Flag-tagged constructs, we used a FACS sorting step to select subpopulations of positive cells and confirmed construct cell surface expression using cell surface antibody staining (Extended Data Figs. 2b, 3a).

## Generation of Fc fusion proteins and RAP

We subcloned the LBD of human VLDLR (residues 31–355, GenBank NP\_003374.3), the LBD of human ApoER2 isoform 1 (46–334, GenBank NM\_004631.5), the ectodomain of human MXRA8 (residues 20–337, GenBank NP\_001269511.1), or the a1 subdomain of NRP2 (NRP2a1, residues 32–146, GenBank NM\_201267.2) into a pVRC expression vector encoding the human IgG1 Fc provided by A. Schmidt<sup>71</sup>. We expressed these Fc fusion proteins in HEK 293T cells grown in suspension using linear polyethylenimine (PEI) according to the manufacturer’s protocol. We collected supernatants five days post-transfection and purified Fc fusion proteins with MabSelect SuRe LX protein A affinity resin (GE Healthcare) using the manufacturer’s protocol and further by size-exclusion chromatography using a Superdex 200 increase column. The Fc fusion proteins were stored in TBS containing 2 mM CaCl<sub>2</sub>.

VLDLR<sub>LBD</sub>–Fc fusion protein purification yields were poor when the protein was expressed alone. To increase VLDLR<sub>LBD</sub>–Fc fusion protein purification yields, we cloned full length human RAP (residues 1–353, including the signal sequence) (GenBank NP\_002328) into the pCAGGs vector. Co-transfection of HEK 293T cells grown in suspension with vectors encoding VLDLR<sub>LBD</sub>–Fc and human RAP in a 1:1 ratio drastically improved expression yields. VLDLR<sub>LBD</sub>–Fc fusion protein and RAP co-eluted as a stable complex when purified using protein A affinity chromatography and subsequent size-exclusion chromatography on a Superdex 200 Increase column. We separated the VLDLR<sub>LBD</sub>–Fc from RAP by binding the complex to protein A resin and washing with 100 column volumes of 10 mM EDTA in TBS, followed by a wash with 50 column volumes of 10 mM EDTA and 500 mM NaCl in TBS. The washes were collected, buffer exchanged in TBS containing 2 mM CaCl<sub>2</sub>, and concentrated. RAP eluted as a single peak by size-exclusion chromatography using a Superdex 200 Increase column. The VLDLR<sub>LBD</sub>–Fc fusion protein was refolded on the column by washing with 100 column volumes of TBS containing 2 mM CaCl<sub>2</sub> and eluted using the manufacturers protocol.

Prior to mouse studies and after size exclusion, the VLDLR<sub>LBD</sub>-Fc fusion protein was bound to a protein A resin and washed with 100 column volumes of 10 mM EDTA in TBS, followed by a wash with 100 column volumes of 0.5 M l-Arginine in TBS. The VLDLR<sub>LBD</sub>-Fc fusion protein was washed with 100 column volumes of TBS containing 2 mM CaCl<sub>2</sub> and eluted. Endotoxin levels were <4 endotoxin units ml<sup>-1</sup> for both the VLDLR<sub>LBD</sub>-Fc fusion protein and the control IgG used in mouse studies as quantified using a Pierce Chromogenic Endotoxin Quantification Kit (Thermo Fisher Scientific).

To generate Flag-tagged RAP (RAP<sub>Flag</sub>), we cloned RAP (residues 1–353) with a C-terminal Flag tag in place of the endoplasmic reticulum retention signal into the pCAGGS vector. We co-transfected HEK 293T cells in suspension with vectors encoding VLDLR<sub>LBD</sub>-Fc and human RAP<sub>Flag</sub> in a 1:1 ratio and purified the protein as described earlier.

To generate soluble VLDLR-LBD (sVLDLR<sub>LBD</sub>), we cloned VLDLR residues 31–355 with an N-terminal twin-Strep tag (WSHPQFEKGGGGSGGGSGGSAAWSHPQFEK) followed by a Factor Xa cleavage site (IEGR) followed by a SGSG linker into the pHLsec vector<sup>64</sup>. We co-transfected HEK 293T cells grown in suspension with plasmids encoding sVLDLR<sub>LBD</sub> and RAP in a 1:1 ratio using PEI and by following the manufacturer's protocol. We collected supernatants five days post-transfection and treated the supernatant with BioLock (Iba Lifesciences 2-0205-050), according to the manufacturer's protocol, to sequester biotin from the media. We bound the sVLDLR<sub>LBD</sub>-RAP complex to Strep-Tactin XT Resin (IBA-Lifesciences 2-4030-010) and washed the column with 150 column volumes of 10 mM EDTA in TBS to remove RAP, followed by washing with 50 column volumes of 2 mM CaCl<sub>2</sub> in TBS to refold sVLDLR<sub>LBD</sub>. We eluted the protein with buffer containing 50 mM biotin, 2 mM CaCl<sub>2</sub> in TBS followed by dialysis in 2 mM CaCl<sub>2</sub> in TBS. We removed the Twin-Strep-tag by adding Factor Xa protease (NEB P8010L) to the sVLDLR<sub>LBD</sub> solution in a 1:50 ratio for 3 h, at which point we inactivated the reaction by adding 1,5-dansyl-Glu-Gly-Argchloromethyl ketone, dihydrochloride Calbiochem (Sigma 251700-5MG) to a final concentration of 2 µM. We separated sVLDLR<sub>LBD</sub> from the cleaved Twin-Strep tag by size-exclusion chromatography on a preparation grade Superdex 200 16/600 column.

### **Entry blocking assays with Fc fusion proteins, anti-VLDLR antibody, and RAP with immortalized cell lines**

We pre-incubated alphavirus RVPs with Fc fusion proteins or RAP in culture media containing 5 µg ml<sup>-1</sup> polybrene for 30 min at 37 °C. We then added RVP/Fc fusion protein or RVP/RAP mixtures to cells. For blocking studies with SINV-SFV and

SINV–CHIKV chimeras, we pre-mixed chimeras at an MOI of 1 with monoclonal antibodies anti-human VLDLR 1H10 (GeneTex GTX79552) or anti-HLA (BD Biosciences 560187) for 30 min at 37 °C, then added the mixture to Vero (CCL-81) cells and incubated for 1 h at 37 °C, and then replaced media. We visualized cells by fluorescence microscopy (using a LAXCO LMC4-FL8 microscope, Olympus UPLFNL Semi-Apo Phase objectives, with a 470 nm LED fluorescence lamp fluorescence filter set) or measured GFP expression by FACS using an iQue3 Screener PLUS (Intellicyt) with IntelliCyt ForeCyt Standard Edition version 8.1.7524 (Sartorius) software or a BD LSR II Flow Cytometer (BD Biosciences) with BD FACSDiva (BD Biosciences) software 30 h post infection for RVPs and 24 h post infection for SINV chimeras, after washing cells twice with PBS then fixing with PBS containing 2% (v/v) formalin. We used IntelliCyt ForeCyt Standard Edition version 8.1.7524 (Sartorius) or FlowJo (BD Biosciences) version 10.6.2 to analyze data. An example of the flow cytometry gating scheme used to quantify GFP-expressing RVP infection is provided in Extended Data Fig. 1b. We calculated relative infection as follows: Relative infection (%) = (%GFP positive cells in the presence of antibody or Fc fusion protein or RAP)/(%GFP-positive cells in the absence of antibody or Fc fusion or RAP) × 100%.

For plaque-neutralization assays with infectious SFV A774, the VLDLR<sub>LBD</sub>–Fc fusion protein or an isotype control IgG (C1A-H12, a previously described SARS-CoV-2 non-neutralizing IgG1 antibody)<sup>72</sup> were serially diluted tenfold in PBS with a starting concentration of 100 µg ml<sup>-1</sup>. Fifty PFUs of SFV A774 were mixed with the serially diluted VLDLR<sub>LBD</sub>–Fc fusion protein, isotype control antibody, or PBS. After incubation at 37 °C for 1 h, the protein–virus mixtures were inoculated onto 12-well plates with a monolayer of Vero cells (which had been seeded the previous day). The cells were incubated at 37 °C with 5% CO<sub>2</sub> for 1 h with gentle shaking every 15 min. After 1 h, 1 ml of overlay medium (DMEM, 2% (v/v) FBS, 0.8% (v/v) methyl cellulose, and 1% penicillin/streptomycin) was added onto each well. The plates were cultured at 37 °C with 5% CO<sub>2</sub> for 2 d until clear plaques formed. The plates were fixed in 4% (v/v) formaldehyde solution for 2 h and stained with 1% (v/v) crystal violet. Plaques were counted. We calculated relative infection as follows: Relative infection (%) = (number of plaques in the presence of antibody or Fc fusion protein)/(number of plaques in the absence of antibody or Fc fusion) × 100%.

## Cell surface Fc fusion protein binding assays

We transfected HEK 293T cells with pCAGGS alphavirus E3–E2–(6K/TF)–E1 expressor plasmids using Lipofectamine 3000 (Invitrogen) or an empty pCAGGS vector. We detached cells 48 h post-transfection with TrypLE Express (Thermo Fisher Scientific) and washed them in 50 mM Tris HCl pH 7.5, 150 mM NaCl, 2 mM CaCl<sub>2</sub>,

2% (w/v) bovine serum albumin (BSA) (binding buffer) followed by incubation in 50 mM Tris HCl pH 7.5, 150 mM NaCl, 2 mM CaCl<sub>2</sub>, 4% (w/v) BSA (blocking buffer). Cells were then incubated with increasing concentrations of MXRA8<sub>ect</sub>-Fc or VLDLR<sub>LBD</sub>-Fc fusion protein in binding buffer with 3% (v/v) goat serum for 1 h at 4 °C. We then washed cells three times in binding buffer and incubated them with a phycoerythrin (PE)-coupled goat anti-human F(ab')<sub>2</sub> fragment (Jackson ImmunoResearch, 109-116-098) at 1:200 dilution in binding buffer for 1 h at 4 °C. We washed cells three times with binding buffer, then twice with binding buffer without BSA, and fixed cells with 2% (v/v) formalin. We measured cell binding by monitoring PE-intensity and percent positivity by FACS. To control for non-specific cell surface binding, we subtracted the percent positive cells detected in staining experiments with untransfected cells incubated with the same Fc fusion proteins.

## Confocal microscopy with labelled virus-like particles

We spun down  $10 \times 10^6$  K562 cells transduced for ectopic expression of membrane proteins in a 15 ml conical tube at 1200 RPM for 3 min. We removed supernatant and treated the cells with a Heparinase I and III mixture (Sigma H3917) at 2 units ml<sup>-1</sup> and Heparinase II (Sigma H8891) at 1 unit ml<sup>-1</sup> for 1 h at 37 °C. Cells were washed and resuspended in 1.5 ml microcentrifuge tube at a concentration of  $0.5 \times 10^6$  cells ml<sup>-1</sup> in culture medium. Twenty-five micrograms of VLPs were added to  $0.5 \times 10^6$  cells. For cells kept at 4 °C, after virus was added, 1.5 ml microcentrifuge tubes were immediately placed on ice and incubated for 15 min. Cells were then washed twice with PBS and kept at 4 °C before imaging. For the 37 °C condition, after adding virus to 1.5 ml microcentrifuge tubes, these were immediately placed at 37 °C and incubated for 15 min. Cells were then washed twice with PBS, and then kept at 4 °C. Just prior to imaging, 500 µl of WGA conjugated to Alexa Fluor 488 (WGA-AF488) (Invitrogen W11261) at 1 µg ml<sup>-1</sup> was added to the cell mixture and incubated for 4 min on ice. Cells were then washed twice in PBS, resuspended in 80 µl of PBS, and placed in glass bottom microwell dishes (MatTek P35G-1.5-14-C) for immediate imaging. Samples were imaged with a Yokogawa CSU-W1 single disk (50 µm pinhole size) spinning disk confocal unit attached to either a fully motorized Nikon Ti or a Nikon Ti2 inverted microscope equipped with a Nikon linear-encoded motorized stage with a PI 250 mm range or a MadLabs 500 Z mm range piezo insert, an Andor Zyla 4.2 plus (6.5 µm photodiode size) sCMOS camera using a Nikon Plan Apo λS SR HP 100×C/1.45 Silicon DIC silicone immersion objective with Nikon Silicone oil. The final digital resolution of the image was 0.065 µm per pixel. Fluorescence from WGA-AF488 and VLPs conjugated to AF647 was collected by illuminating the sample with a solid-state directly modulated 488 nm diode 100 mW (at the fibre tip) laser line or a solid state, directly modulated 640 nm diode 100 mW (laser tip) laser line in a Toptica iChrome MLE laser launch, respectively. A hard-coated Semrock Di01-

T405/488/568/647 multi-bandpass dichroic mirror was used for both channels. Signal from each channel was acquired sequentially with either a hard-coated Chroma ET525/36m or Chroma ET700/75m emission filters in a filter wheel placed within the scan unit, respectively. Z-stacks were set by determining the top and bottom of the cell, using WGA-AF488 fluorescence as a reference. The approximate volume was 20  $\mu\text{m}$ , and the step size was set to 0.2  $\mu\text{m}$ , using the piezo drive. Fluorescence from each fluorophore was acquired sequentially at each z-step of the confocal to improve the precision of the measurements. Nikon NIS-Elements Advanced Research (AR) 5.02 acquisition software was used to acquire the data, and the files were exported in ND2 file format. Figures were generated in Fiji<sup>73</sup>. A median filter of 1.0 pixels was applied to both channels (VLP and WGA). Gamma of 0.7 or 1.2 gamma was set for WGA and VLP filtered images, respectively, before adjusting brightness and contrast. Top views of stacks were created by using the (Stacks>Reslice>Top) function with an output spacing of 0.3  $\mu\text{m}$ . 3D renderings were created by using the 3D projection function (Stacks>3D Project). The starting angle was set to 30° with 10° increments and interpolation selected to smooth the 3D rendering.

For VLP quantification of confocal images, 3D image analysis was performed using custom pipelines built in Arivis 4DFusion 3.4 analysis software. Viral particles were detected using a particle enhancement filter of 0.65  $\mu\text{m}$  followed by a dilation morphology filter of diameter 0.52  $\mu\text{m}$  (sphere shaped) and a Blob Finder segmentation filter set to 0/52  $\mu\text{m}$  diameter, 3% probability threshold and split sensitivity of 70%. To segment cells, the signal from WGA-488 was first enhanced using the enhance edges filter within the membrane detection operation, selecting a membrane width of 0.6  $\mu\text{m}$  and a gap size of 0.13  $\mu\text{m}$ . A discrete gaussian filter of diameter 0.65  $\mu\text{m}$  was applied to the resulting enhanced image. Finally, the membrane-based segmentation operation was used to segment the processed image to obtain the whole cell masks. The two compartments, cytoplasm and membrane, were created by eroding the cell mask by two pixels (cytoplasm) and by performing object math between the cell masks and the eroded cytoplasm masks, producing the membrane masks. The number of viruses in each compartment was then calculated by combining all masks.

## Biolayer interferometry binding assays

We performed BLI experiments with an Octet RED96e (Sartorius) and analyzed data using ForteBio Data Analysis HT version 12.0.1.55 software. MXRA8<sub>ect</sub>-Fc, VLDLR<sub>LBD</sub>-Fc, or ApoER2<sub>LBDiso1</sub>-Fc were loaded onto Anti-Human IgG Fc Capture (AHC) Biosensors (Sartorius 18-5063) at 250 nM in kinetic buffer (TBS containing 2 mM CaCl<sub>2</sub> and 0.1% (w/v) BSA) for 80 s. After a baseline measurement for 60 s in kinetic buffer, Fc fusion protein coated sensor-tips surfaces were incubated with RAP or transferrin at 100  $\mu\text{g ml}^{-1}$  for 50 s, or kinetic buffer alone for 50 s. After an

additional baseline measurement for 20 s in kinetic buffer, VLPs were associated for 300 s at 20 nM. We plotted total response nm change at the end of the 300 s association in Fig. 3b, and raw sensorgrams are provided in Extended Data Fig. 4c.

## Cell surface staining of receptors and receptor orthologues

We incubated cells for 30 min at 4 °C in PBS containing 5% (v/v) goat serum (blocking buffer), prior to incubating them with an anti-human VLDLR monoclonal antibody 1H10 (GeneTex GTX79552) at 10 µg ml<sup>-1</sup>, anti-human ApoER2 (LRP8) antibody (clone 3H2) (Sigma WH0007804M1-100) at 10 µg ml<sup>-1</sup>, anti-human LDLR monoclonal antibody (R&D Systems MAB2148-100) at 10 µg ml<sup>-1</sup>, anti-human MXRA8 antibody (clone 2H2G12A) (MBL International W040-3) at 10 µg ml<sup>-1</sup>, or no antibody in PBS containing 2% (v/v) goat serum (binding buffer) for 1 h. Following incubation, we washed cells three times in binding buffer and then incubated cells for 30 min with a PE-conjugated donkey anti-mouse F(ab')<sub>2</sub> fragment (Jackson ImmunoResearch 715-116-150) at 1:200 dilution according to the manufacturer's recommended binding buffer. We washed cells twice with binding buffer, fixed them with 2% (v/v) formalin, and detected cell surface receptor expression by FACS using an iQue3 Screener PLUS (Intelicyt) with ForeCyt (Sartorius) software.

For staining of cells expressing Flag-tagged receptors, we added an APC conjugated anti-DYKDDDDK (Flag) antibody (BioLegend 637307) at 1:200 dilution in binding buffer, according to the manufacturer's recommendation. We washed cells three times with binding buffer, fixed them with 2% (v/v) formalin, and detected cell surface receptor expression by FACS. For staining using Flag-tagged RAP, we incubated cells with RAP<sub>Flag</sub> at 10 µg ml<sup>-1</sup>, or no protein in binding buffer for 30 min. Following incubation, we washed cells three times with binding buffer and added an APC conjugated anti-DYKDDDDK (BioLegend 637307) at 1:200 dilution and carried out the steps described above for antibody staining of Flag-tagged receptors.

## Negative-stain electron microscopy

We collected negative-stain micrographs of VLPs at the Molecular Electron Microscopy Core Facility at Harvard Medical School. We buffer-exchanged VLPs into buffer containing 50 mM Tris HCl pH 7.4, 100 mM NaCl, 1 mM EDTA using a 100-kDa Amicon filter (Sigma). VLPs were adsorbed to glow-discharged Formvar carbon film grids (Electron Microscopy Sciences), rinsed twice with water, and stained with 1.5% uranyl formate. Multiple fields of view were inspected to confirm VLP integrity and the absence of associated lipoproteins. Representative micrographs shown in

Extended Data Fig. 4b were collected using a Tecnai T12 (ThermoScientific) at 120 kV with a Gatan UltraScan 895 4k CCD camera.

## Replication-competent virus replication kinetics assays

Transduced K562 cells ( $2.5 \times 10^6$ ) were spun in a 15 ml polypropylene conical tube at 1200 RPM for 5 mins; SFV (A774), SINV (DAK Ar Mg812), or EEEV (FL93-939) were used to inoculate cells at a multiplicity of infection (MOI) of 0.01. Cells were incubated with virus for 2 h in a 15 ml polypropylene conical tube in a CO<sub>2</sub> incubator at 37 °C, washed three times with D-PBS (Lonza), and resuspended to a final concentration of  $5 \times 10^5$  cells ml<sup>-1</sup> with culture medium in T25 flasks (Corning). At indicated time points (0, 6, 12, 24 or 48 h), 500 µl of culture supernatants were collected for plaque assays, with 500 µl of fresh culture medium added back to the flask. Virus titres were then determined on Vero cells by plaque assay.

## In vivo study

Mouse studies were performed in accordance with the NIH Guidance for the Care and Use of Laboratory Animals. The study protocol was approved by the University of Texas Medical Branch Institutional Animal Care and Use Committee under protocol 1708051. Pregnant mice were received by the dedicated animal research personnel at the University of Texas Medical Branch, who randomly assigned animals to one mouse per cage with no additional knowledge of the study design. Mice were fed a 19% protein diet (Teklad, 2919, Irradiated), had a 12 h light:dark cycle (0600–1800 h), and were housed in a facility maintained at a temperature range of 20 to 26 °C with a humidity range of 30 to 70%. Food and water were provided ad libitum. The offspring were too young to be randomly separated into different cages, and no further randomization was performed by study personnel. Pups were taken as mixed groups and were not sexed (that is, both sexes were used). All mouse manipulations were performed under anesthesia with isoflurane. Ten-day-old CD-1 mice (Charles River) were administered 125 µg VLDLR<sub>LBD</sub>–Fc fusion protein or IgG1 isotype control monoclonal antibody through the intraperitoneal route 6 h before intraperitoneal inoculation with 100 PFU or 1,000 PFU of SFV A774. Survival rate of mice was monitored daily.

## Statistical analysis

Data were deemed statistically significant when *P* values were <0.05 using version 9 of GraphPad Prism. Experiments were analysed by one-way or two-way ANOVA with multiple comparison correction or by log-rank (Mantel–Cox) test in GraphPad Prism. *P* values are indicated in each of the figure legends.

## Reporting summary

Further information on research design is available in the [Nature Research Reporting Summary](#) linked to this paper.

## Data availability

All data that support the findings of this study are available within the Article and its Supplementary Information. Confocal microscopy images that support the findings of this study are available at <https://omero.hms.harvard.edu/webclient/?show=project-8752>. Any other relevant data are available from the corresponding author upon reasonable request. [Source data](#) are provided with this paper.

## Code availability

Custom pipelines built in Arivis 4DFusion 3.4 analysis software used for this study are available at [https://github.com/paulamonterollopis/Viral\\_Particle\\_on\\_Cells\\_Arivis](https://github.com/paulamonterollopis/Viral_Particle_on_Cells_Arivis).

## References

1. Rose, P. P. et al. Natural resistance-associated macrophage protein is a cellular receptor for Sindbis virus in both insect and mammalian hosts. *Cell Host Microbe* **10**, 97–104 (2011).
2. Zhang, R. et al. Mxra8 is a receptor for multiple arthritogenic alphaviruses. *Nature* **557**, 570–574 (2018).
3. Ma, H. et al. LDLRAD3 is a receptor for Venezuelan equine encephalitis virus. *Nature* **588**, 308–314 (2020).
4. Cheng, R. H. et al. Nucleocapsid and glycoprotein organization in an enveloped virus. *Cell* **80**, 621–630 (1995).
5. Paredes, A. M. et al. Three-dimensional structure of a membrane-containing virus. *Proc. Natl Acad. Sci. USA* **90**, 9095–9099 (1993).
6. Paredes, A. M., Simon, M. N. & Brown, D. T. The mass of the Sindbis virus nucleocapsid suggests it has  $T = 4$  icosahedral symmetry. *Virology* **187**, 329–332 (1992).

7. Kuhn, R. J., Niesters, H. G., Hong, Z. & Strauss, J. H. Infectious RNA transcripts from Ross River virus cDNA clones and the construction and characterization of defined chimeras with Sindbis virus. *Virology* **182**, 430–441 (1991).
8. Nimpf, J. & Schneider, W. J. From cholesterol transport to signal transduction: low density lipoprotein receptor, very low density lipoprotein receptor, and apolipoprotein E receptor-2. *Biochim. Biophys. Acta* **1529**, 287–298 (2000).
9. Poirier, S., Mamarbachi, M., Chen, W. T., Lee, A. S. & Mayer, G. GRP94 regulates circulating cholesterol levels through blockade of PCSK9-induced LDLR degradation. *Cell Rep.* **13**, 2064–2071 (2015).
10. Marceau, C. D. et al. Genetic dissection of Flaviviridae host factors through genome-scale CRISPR screens. *Nature* **535**, 159–163 (2016).
11. Zhang, R. et al. A CRISPR screen defines a signal peptide processing pathway required by flaviviruses. *Nature* **535**, 164–168 (2016).
12. Willnow, T. E., Armstrong, S. A., Hammer, R. E. & Herz, J. Functional expression of low density lipoprotein receptor-related protein is controlled by receptor-associated protein in vivo. *Proc. Natl Acad. Sci. USA* **92**, 4537–4541 (1995).
13. Lozzio, C. B. & Lozzio, B. B. Human chronic myelogenous leukemia cell-line with positive Philadelphia chromosome. *Blood* **45**, 321–334 (1975).
14. Dlugosz, P. & Nimpf, J. The reelin receptors apolipoprotein E receptor 2 (ApoER2) and VLDL receptor. *Int. J. Mol. Sci.* **19**, 3090 (2018).
15. D'Arcangelo, G. et al. Reelin is a ligand for lipoprotein receptors. *Neuron* **24**, 471–479 (1999).
16. D'Arcangelo, G. et al. A protein related to extracellular matrix proteins deleted in the mouse mutant reeler. *Nature* **374**, 719–723 (1995).
17. Brandes, C. et al. Avian and murine LR8B and human apolipoprotein E receptor 2: differentially spliced products from corresponding genes. *Genomics* **42**, 185–191 (1997).
18. Kim, D. H. et al. Human apolipoprotein E receptor 2. A novel lipoprotein receptor of the low density lipoprotein receptor family predominantly expressed in brain. *J. Biol. Chem.* **271**, 8373–8380 (1996).

19. Clatworthy, A. E. et al. Expression and alternate splicing of apolipoprotein E receptor 2 in brain. *Neuroscience* **90**, 903–911 (1999).
20. Lane-Donovan, C. & Herz, J. The ApoE receptors Vldlr and Apoer2 in central nervous system function and disease. *J. Lipid Res.* **58**, 1036–1043 (2017).
21. Akahata, W. et al. A virus-like particle vaccine for epidemic Chikungunya virus protects nonhuman primates against infection. *Nat. Med.* **16**, 334–338 (2010).
22. Ko, S. Y. et al. A virus-like particle vaccine prevents equine encephalitis virus infection in nonhuman primates. *Sci. Transl. Med.* **11**, eaav3113 (2019).
23. Fazakerley, J. K. Semliki forest virus infection of laboratory mice: a model to study the pathogenesis of viral encephalitis. *Arch. Virol. Suppl.* **2004**, 179–190 (2004).
24. Willems, W. R. et al. Semliki forest virus: cause of a fatal case of human encephalitis. *Science* **203**, 1127–1129 (1979).
25. Lagomarsino, V. N. et al. Stem cell-derived neurons reflect features of protein networks, neuropathology, and cognitive outcome of their aged human donors. *Neuron* **109**, 3402–3420 e3409 (2021).
26. Bradish, C. J., Allner, K. & Maber, H. B. The virulence of original and derived strains of Semliki forest virus for mice, guinea-pigs and rabbits. *J. Gen. Virol.* **12**, 141–160 (1971).
27. Bradish, C. J. & Allner, K. The early responses of mice to respiratory or intraperitoneal infection by defined virulent and avirulent strains of Semliki forest virus. *J. Gen. Virol.* **15**, 205–218 (1972).
28. Pattyn, S. R., De Vleesschauwer, L. & van der Groen, G. Replication of arboviruses in mouse organ cultures. II. Multiplication of virulent and avirulent Semliki Forest and western equine encephalitis viruses in mouse organ cultures. *Arch. Virol.* **49**, 33–37 (1975).
29. Fleming, P. Age-dependent and strain-related differences of virulence of Semliki Forest virus in mice. *J. Gen. Virol.* **37**, 93–105 (1977).
30. Woodward, C. G., Marshall, I. D. & Smith, H. Investigations of reasons for the avirulence of the A7 strain of Semliki Forest virus in adult mice. *Br. J. Exp. Pathol.* **58**, 616–624 (1977).

31. Trommsdorff, M. et al. Reeler/Disabled-like disruption of neuronal migration in knockout mice lacking the VLDL receptor and ApoE receptor 2. *Cell* **97**, 689–701 (1999).
32. Van Hoof, D., Rodenburg, K. W. & Van der Horst, D. J. Insect lipoprotein follows a transferrin-like recycling pathway that is mediated by the insect LDL receptor homologue. *J. Cell Sci.* **115**, 4001–4012 (2002).
33. Van der Horst, D. J., Roosendaal, S. D. & Rodenburg, K. W. Circulatory lipid transport: lipoprotein assembly and function from an evolutionary perspective. *Mol. Cell. Biochem.* **326**, 105–119 (2009).
34. Finkelshtein, D., Werman, A., Novick, D., Barak, S. & Rubinstein, M. LDL receptor and its family members serve as the cellular receptors for vesicular stomatitis virus. *Proc. Natl Acad. Sci. USA* **110**, 7306–7311 (2013).
35. Ashrafi, K. et al. Genome-wide RNAi analysis of *Caenorhabditis elegans* fat regulatory genes. *Nature* **421**, 268–272 (2003).
36. Dieckmann, M., Dietrich, M. F. & Herz, J. Lipoprotein receptors—an evolutionarily ancient multifunctional receptor family. *Biol. Chem.* **391**, 1341–1363 (2010).
37. Atkins, G. J., Sheahan, B. J. & Mooney, D. A. Pathogenicity of Semliki Forest virus for the rat central nervous system and primary rat neural cell cultures: possible implications for the pathogenesis of multiple sclerosis. *Neuropathol. Appl. Neurobiol.* **16**, 57–68 (1990).
38. Johnson, R. T., McFarland, H. F. & Levy, S. E. Age-dependent resistance to viral encephalitis: studies of infections due to Sindbis virus in mice. *J. Infect. Dis.* **125**, 257–262 (1972).
39. Hofer, F. et al. Members of the low density lipoprotein receptor family mediate cell entry of a minor-group common cold virus. *Proc. Natl Acad. Sci. USA* **91**, 1839–1842 (1994).
40. Marlovits, T. C., Abrahamsberg, C. & Blaas, D. Very-low-density lipoprotein receptor fragment shed from HeLa cells inhibits human rhinovirus infection. *J. Virol.* **72**, 10246–10250 (1998).
41. Bates, P., Young, J. A. & Varmus, H. E. A receptor for subgroup A Rous sarcoma virus is related to the low density lipoprotein receptor. *Cell* **74**, 1043–1051 (1993).

42. Yamamoto, S. et al. Lipoprotein receptors redundantly participate in entry of Hepatitis C virus. *PLoS Pathog.* **12**, e1005610 (2016).
43. Ujino, S. et al. Hepatitis C virus utilizes VLDR as a novel entry pathway. *Proc. Natl Acad. Sci. USA* **113**, 188–193 (2016).
44. Agnello, V., Abel, G., Elfahal, M., Knight, G. B. & Zhang, Q. X. Hepatitis C virus and other Flaviviridae viruses enter cells via low density lipoprotein receptor. *Proc. Natl Acad. Sci. USA* **96**, 12766–12771 (1999).
45. Ganaie, S. S. et al. Lrp1 is a host entry factor for Rift Valley fever virus. *Cell* **184**, 5163–5178.e5124 (2021).
46. Tao, L. et al. Sulfated glycosaminoglycans and low-density lipoprotein receptor contribute to *Clostridium difficile* toxin A entry into cells. *Nat. Microbiol.* **4**, 1760–1769 (2019).
47. Demogines, A., Abraham, J., Choe, H., Farzan, M. & Sawyer, S. L. Dual host-virus arms races shape an essential housekeeping protein. *PLoS Biol.* **11**, e1001571 (2013).
48. Gruszczak, J. et al. Transferrin receptor 1 is a reticulocyte-specific receptor for *Plasmodium vivax*. *Science* **359**, 48–55 (2018).
49. Li, W. et al. MAGeCK enables robust identification of essential genes from genome-scale CRISPR/Cas9 knockout screens. *Genome Biol.* **15**, 554 (2014).
50. Saul, S. et al. Differences in processing determinants of nonstructural polyprotein and in the sequence of nonstructural protein 3 affect neurovirulence of Semliki Forest virus. *J. Virol.* **89**, 11030–11045 (2015).
51. Finkbeiner, S. & Stevens, C. F. Applications of quantitative measurements for assessing glutamate neurotoxicity. *Proc. Natl Acad. Sci. USA* **85**, 4071–4074 (1988).
52. Zhang, Y. et al. Rapid single-step induction of functional neurons from human pluripotent stem cells. *Neuron* **78**, 785–798 (2013).
53. Vierbuchen, T. et al. Direct conversion of fibroblasts to functional neurons by defined factors. *Nature* **463**, 1035–1041 (2010).
54. Maherali, N. et al. A high-efficiency system for the generation and study of human induced pluripotent stem cells. *Cell Stem Cell* **3**, 340–345 (2008).

55. Jemielity, S. et al. TIM-family proteins promote infection of multiple enveloped viruses through virion-associated phosphatidylserine. *PLoS Pathog.* **9**, e1003232 (2013).
56. Bausch-Fluck, D. et al. A mass spectrometric-derived cell surface protein atlas. *PLoS ONE* **10**, e0121314 (2015).
57. Almen, M. S., Nordstrom, K. J., Fredriksson, R. & Schioth, H. B. Mapping the human membrane proteome: a majority of the human membrane proteins can be classified according to function and evolutionary origin. *BMC Biol.* **7**, 50 (2009).
58. da Cunha, J. P. Et al. Bioinformatics construction of the human cell surfaceome. *Proc. Natl Acad. Sci. USA* **106**, 16752–16757 (2009).
59. Joung, J. et al. Genome-scale CRISPR–Cas9 knockout and transcriptional activation screening. *Nat. Protoc.* **12**, 828–863 (2017).
60. Sanjana, N. E., Shalem, O. & Zhang, F. Improved vectors and genome-wide libraries for CRISPR screening. *Nat. Methods* **11**, 783–784 (2014).
61. Doench, J. G. et al. Rational design of highly active sgRNAs for CRISPR–Cas9-mediated gene inactivation. *Nat. Biotechnol.* **32**, 1262–1267 (2014).
62. Ran, F. A. et al. Double nicking by RNA-guided CRISPR Cas9 for enhanced genome editing specificity. *Cell* **154**, 1380–1389 (2013).
63. Saleh, M. C. et al. Antiviral immunity in *Drosophila* requires systemic RNA interference spread. *Nature* **458**, 346–350 (2009).
64. Aricescu, A. R., Lu, W. & Jones, E. Y. A time- and cost-efficient system for high-level protein production in mammalian cells. *Acta Crystallogr. D* **62**, 1243–1250 (2006).
65. Erasmus, J. H. et al. Novel insect-specific Eilat virus-based chimeric vaccine candidates provide durable, mono- and multivalent, single-dose protection against lethal alphavirus challenge. *J. Virol.* **92**, e01274-17 (2018).
66. Peng, J. & Gygi, S. P. Proteomics: the move to mixtures. *J. Mass Spectrom.* **36**, 1083–1091 (2001).
67. Eng, J. K., McCormack, A. L. & Yates, J. R. An approach to correlate tandem mass spectral data of peptides with amino acid sequences in a protein database. *J. Am. Soc. Mass. Spectrom.* **5**, 976–989 (1994).

68. Raaben, M. et al. NRP2 and CD63 are host factors for Lujo virus cell entry. *Cell Host Microbe* **22**, 688–696.e685 (2017).
69. Petersen, T. N., Brunak, S., von Heijne, G. & Nielsen, H. SignalP 4.0: discriminating signal peptides from transmembrane regions. *Nat. Methods* **8**, 785–786 (2011).
70. Radoshitzky, S. R. et al. Transferrin receptor 1 is a cellular receptor for New World haemorrhagic fever arenaviruses. *Nature* **446**, 92–96 (2007).
71. Bajic, G. et al. Influenza antigen engineering focuses immune responses to a subdominant but broadly protective viral epitope. *Cell Host Microbe* **25**, 827–835.e826 (2019).
72. Clark, S. A. et al. SARS-CoV-2 evolution in an immunocompromised host reveals shared neutralization escape mechanisms. *Cell* **184**, 2605–2617.e2618 (2021).
73. Schindelin, J. et al. Fiji: an open-source platform for biological-image analysis. *Nat. Methods* **9**, 676–682 (2012).
74. Robert, X. & Gouet, P. Deciphering key features in protein structures with the new ENDscript server. *Nucleic Acids Res.* **42**, W320–W324 (2014).

## Acknowledgements

J.A. is a recipient of a William Randolph Hearst Foundation and Brigham and Women's Hospital Young Investigator in Medicine Award, and a Burroughs Wellcome Fund Career Award for Medical Scientists. This work was also supported by a Harvard Milton Fund Award (J.A.), Vallee Scholar Award (J.A.), NIH grant T32 AI007061 (J.A.), NIH grant R24 AI120942 (S.C.W.), NIH grant T32 GM007753 (A.C., K.G.N. and D.V.N.), NIH grant R01 DK127257 (I.M.C.), Burroughs Wellcome Fund Pathogenesis Award (I.M.C.), and NIH T32 CA009216-40 (C.L.), and in part by a grant to Harvard Medical School from the Howard Hughes Medical Institute through the James H. Gilliam Fellowships for Advanced Study program (L.E.C.). The authors acknowledge the MicRoN (Microscopy Resources on the North Quad) Core at Harvard Medical School and the Molecular Electron Microscopy Core Facility at Harvard Medical School for their support and assistance in this work. Additionally, the authors thank A. Burdyniuk and M. Burdyniuk for support in building custom image analysis pipelines; and R. Tomaino from the Taplin Biological Mass Spectrometry Facility at Harvard Medical School for assistance with mass spectrometry of VLPs and data analysis.

# **Author information**

## Author notes

1. These authors contributed equally: Lars E. Clark, Sarah A. Clark, ChieYu Lin, Jianying Liu

## Affiliations

1. Department of Microbiology, Blavatnik Institute, Harvard Medical School, Boston, MA, USA

Lars E. Clark, Sarah A. Clark, ChieYu Lin, Adrian Coscia, Katherine G. Nabel, Pan Yang, Vesna Brusic, Paula Montero Llopis & Jonathan Abraham

2. Institute for Human Infections and Immunity, University of Texas Medical Branch, Galveston, TX, USA

Jianying Liu, Kenneth S. Plante & Scott C. Weaver

3. Department of Microbiology and Immunology, University of Texas Medical Branch, Galveston, TX, USA

Jianying Liu, Kenneth S. Plante & Scott C. Weaver

4. Department of Immunology, Blavatnik Institute, Harvard Medical School, Boston, MA, USA

Dylan V. Neel & Isaac M. Chiu

5. Ann Romney Center for Neurologic Diseases, Department of Neurology, Brigham & Women's Hospital, Harvard Medical School, Boston, MA, USA

Hyo Lee & Tracy L. Young-Pearse

6. Department of Immunology and Infectious Diseases, Harvard T.H. Chan School of Public Health, Boston, MA, USA

Iryna Stryapunina & Flaminia Catteruccia

7. World Reference Center for Emerging Viruses and Arboviruses, University of Texas Medical Branch, Galveston, TX, USA

Kenneth S. Plante & Scott C. Weaver

8. Division of Infectious Diseases, Boston Children's Hospital, Boston, MA, USA

Asim A. Ahmed

9. MicRoN Core, Harvard Medical School, Boston, MA, USA

Paula Montero Llopis

10. Department of Medicine, Division of Infectious Diseases, Brigham and Women's Hospital, Boston, MA, USA

Jonathan Abraham

11. Broad Institute of Harvard and MIT, Cambridge, MA, USA

Jonathan Abraham

## Contributions

C.L. designed the sgRNA library and the RVP system and performed the CRISPR–Cas9 genetic screen and initial validation. L.E.C. generated cell lines, RVPs and recombinant proteins, and performed infectivity studies for validation with RVPs with assistance from S.A.C., A.C., K.G.N., D.V.N., H.L. and V.B. S.A.C. produced recombinant proteins, and generated cell lines, SINV chimeras and VLPs, and performed experiments with VLPs and SINV chimeras. S.A.C. additionally performed mass spectrometry experiments, BLI experiments and confocal microscopy experiments, the latter of which were performed with assistance from P.M.L. P.M.L. developed the imaging workflow and analysed confocal microscopy data with S.A.C. S.A.C., A.C., P.Y. and V.B. purified RVPs and VLPs for characterization, and A.C. performed negative-stain electron microscopy with VLPs. J.L., K.S.P. and S.C.W. designed and executed experiments with wild-type, replication-competent viruses including in vitro and in vivo studies. D.V.N. and I.M.C. provided mouse cortical neurons and assisted with RVP infectivity studies of mouse and human cortical neurons. H.L. and T.L.Y.-P. provided human iPS cell-derived neurons. I.S., A.A.A. and F.C. participated in study conceptualization or provided critical reagents. I.M.C., S.C.W. and J.A. acquired funding. J.A. wrote the original draft of the manuscript and all authors participated in reviewing and editing.

## Corresponding author

Correspondence to [Jonathan Abraham](#).

# Ethics declarations

## Competing interests

The authors declare no competing interests.

## Peer review information

*Nature* thanks Laurie Silva and the other, anonymous, reviewer(s) for their contribution to the peer review of this work.

## Additional information

**Publisher's note** Springer Nature remains neutral with regard to jurisdictional claims in published maps and institutional affiliations.

## Extended data figures and tables

### [Extended Data Fig. 1 Screening strategy, reporter virus particle system, and gating strategy.](#)

**a**, Ross River (RRV) reporter virus particle (RVP) system. Cells are transfected with two plasmids. *CD20* or *GFP* is included as a reporter downstream of the capsid (C) after a 2A peptide sequence. The arrow indicates a subgenomic promoter. **b**, SDS-PAGE gel of purified RVPs imaged with a stain-free imaging system. The experiment was performed twice independently, and a representative gel image is shown. **c**, Screening strategy. HEK 293T-Cas9 cells are first transduced with the guide (sgRNA) library using vesicular stomatitis virus (VSV) glycoprotein G pseudotyped lentiviruses and are then infected with RVPs expressing CD20. Infected cells are depleted using magnetic beads against CD20. Selection is repeated iteratively to improve the signal-to-noise ratio of the screen. Non-infected, CD20 negative cells are sequenced using next generation sequencing at the final step. See Methods for additional details. **d**, Coomassie-stained SDS-

PAGE gel of purified virus-like particles (VLPs). The experiment was performed twice independently, and a representative gel image is shown. **e**, Flow cytometry gating strategy for quantification of GFP-expressing cells after RVP infection. K562 cells expressing human VLDLR (top panels) or wild-type (WT) K562 cells (bottom panels) were infected with GFP-expressing SFV RVPs. The percentage of cells falling within each gate is shown. The example is from an experiment shown in Fig. 4e. **f**, Flow cytometry gating strategy for detection of receptor cell surface staining. K562 cells overexpressing VLDLR (top panels) or WT K562 cells (bottom panels) were stained with RAP<sub>FLAG</sub> and a FLAG-APC antibody was used for detection. In the rightmost panel, the staining of each cell type is overlaid to allow for comparison. The example is from an experiment shown in Extended Data Fig. 3c. M: molecular weight marker. For gel source data, see Supplementary Fig. 1.

**Extended Data Fig. 2 Knockout cell line validation and antibody blocking of SFV E2–E1-mediated entry into multiple cell lines.**

**a**, Genotyping DNA gel (left panel) and anti-VLDLR ( $\alpha$ -VLDLR) antibody cell surface staining of WT HEK 293T (middle panel) or HEK 293T VLDLR clonal knockout (K.O.) cells (right panel) as monitored by FACS. The experiment was performed at least twice independently, and a representative gel image is shown. **b**, Anti-VLDLR ( $\alpha$ -VLDLR) cell surface staining of WT HEK 293T, HEK 293T VLDLR K.O., and HEK 293T VLDLR K.O. cells transiently transfected with cDNA encoding VLDLR-Flag (VLDLR<sub>FLAG</sub>) as monitored by FACS. **c**,  $\alpha$ -VLDLR cell surface staining of the indicated cell types as monitored by FACS. **d**, The indicated cell types were infected with GFP-expressing SFV single-cycle RVPs in the presence or absence of a  $\alpha$ -VLDLR or an anti-HLA control antibody ( $\alpha$ -HLA) and infection was measured by FACS. Means  $\pm$  standard deviation from two experiments performed in triplicate ( $n=6$ ) are shown. One-way ANOVA with Tukey's multiple comparisons test, \*\*\* $P<0.0001$  (**d**). For gel source data, see Supplementary Fig. 1.

[Source data](#)

**Extended Data Fig. 3 Immunostaining to monitor cell surface receptor expression.**

**a**, Anti-FLAG ( $\alpha$ -FLAG) and anti-MXRA8 ( $\alpha$ -Mxra8), staining of WT K562 cells or K562 cells expressing the indicated constructs as monitored by FACS. **b**, Anti-ApoER2 ( $\alpha$ -ApoER2) and anti-LDLR ( $\alpha$ -LDLR) staining of the indicated cell types as monitored by FACS. **c**, RAP<sub>FLAG</sub> staining of WT K562 cells or K562 cells transduced with the indicated constructs as monitored by  $\alpha$ -FLAG-tag staining and FACS.

**Extended Data Fig. 4 VLDLR and ApoER2 ligand binding domains directly bind alphavirus E2–E1 proteins.**

**a**, Size exclusion chromatography traces of the indicated purified proteins. Insets are SDS-PAGE gels of the peak fraction. Molecular weight markers are indicated. Each experiment was performed at least twice, and representative traces are shown. **b**, Electron micrographs of negatively stained purified VLPs. Scale bar is 100 nm. The experiment was performed twice, and representative micrographs are shown. **c**, Sensorgrams for binding of the indicated alphavirus VLPs to tips coated with VLDLR<sub>LBD</sub>-Fc, ApoER2<sub>LBDiso1</sub>-Fc, or Mxra8<sub>ect</sub>-Fc fusion proteins as measured by biolayer interferometry. Fc fusion protein coated sensor-tips surfaces were incubated with RAP or transferrin, or kinetic buffer alone, and VLPs were associated followed by dissociation. The experiment was performed twice and representative results from one experiment are shown.

[Source data](#)

**Extended Data Fig. 5 Role of VLDLR and ApoER2 in E2–E1-mediated cellular infection by divergent alphaviruses.**

**a**, Wild-type (WT) or clonal VLDLR knockout (K.O.) HEK 293T cells were infected with GFP-expressing single-cycle alphavirus RVPs with relative infection measured by FACS. EEEV RVPs more efficiently entered VLDLR K.O. cells, which we suspect could be related to clonal variability, as the cell line was generated by clonal dilution. **b**, Vero cells were infected

with GFP-expressing alphavirus single-cycle RVPs in the presence of the indicated antibodies with relative infection measured by FACS. **c**, Infection of WT or transduced K562 cells with GFP-expressing single-cycle RVPs. Cells were imaged by fluorescence microscopy. Scale bar is 100  $\mu$ m. The experiment was performed twice, and representative images are shown. **d**, Infection of WT or transduced K562 cells with GFP-expressing single-cycle RVPs measured by FACS. NRP2 is a control membrane protein. **e**, K562 cells expressing VLDLR or ApoER2<sub>iso2</sub> were infected with the indicated single-cycle RVPs in the presence of RAP, soluble VLDLR LBD (sVLDLR<sub>LBD</sub>), or a control protein (transferrin, Tf) with infection measured by FACS. **f**, WT or transduced K562 cells were infected with the indicated GFP-expressing single-cycle RVPs with infection measured by FACS. **g**, SFV A774 plaque reduction neutralization test with the indicated proteins performed on Vero cells. **h**, WT K562 cells or K562 cells transduced to express LDLRAD3 were infected with the indicated GFP-expressing single-cycle RVPs with infection measured by FACS. Means  $\pm$  standard deviation from an experiment performed once in triplicate ( $n = 3$ ) (**a**), or experiments performed twice in triplicate ( $n = 6$ ) with similar results (**b**, **d–h**). One-way ANOVA with Tukey's multiple comparisons test, \*\*\* $P < 0.0001$  (**a**, **b**, **d–h**). Two-way ANOVA with Šídák's multiple comparison test, \*\*\* $P < 0.0001$  (**g**). Cell surface expression of constructs used in (**c**), (**d**), and (**f**) was confirmed with immunostaining (see Extended Data Fig. 3).

#### [Source data](#)

#### [Extended Data Fig. 6 Ligand-binding domain sequence alignment and domain organization of ApoER2 constructs.](#)

**a**, Sequence alignment of the *Homo sapiens*, *Mus musculus*, *Equus caballus*, and *Sturnus vulgaris* ApoER2 ligand binding domains. The LDR class A (LA) repeats contained in each protein are shown in parentheses. The domain numbering is based on the human sequence shown. **b**, Schematic representation of the ectodomains of ApoER2 constructs used in this study. In mammals, exon regions encoding LA repeats 4–6 are almost

exclusively spliced out, while the predominant avian isoforms retain these repeats<sup>14</sup>. Panel (a) was generated using ESPrit 3.0<sup>74</sup>.

### Extended Data Fig. 7 Representative confocal microscopy images for virus-like particle cell binding and internalization.

K562 cells transduced with human VLDLR, human ApoER2<sub>iso2</sub>, or human MXRA8 were incubated with fluorescently labeled VLPs at 4 °C or 37 °C and then imaged by live cell confocal microscopy. WGA: wheat germ agglutinin. Scale bar is 10 μm. The experiment was performed twice independently, and representative images are shown.

### Extended Data Fig. 8 Workflow diagram of the 3-dimensional quantification of virus-like particle cell surface membrane binding and internalization.

**a**, 3D analysis of multi-colored stacks (*pink*, VLPs; *green*, cell membranes) using Arivis 4DFusion. Two custom-made pipelines were used to detect VLPs and cellular compartments. **b**, VLPs: left panel shows 3D rendering of VLP stacks, and right panel shows 3D rendering of detected VLPs. **c**, Cellular compartments: left panel shows 3D rendering of cellular membranes stacks; right, top panel shows 3D rendering of the detected cytoplasms (red) overlayed with an enhanced-membrane filter (white); right, bottom panel shows 3D rendering of the detected membranes (yellow). Objects obtained in each pipeline were combined to quantify the number of VLPs in each cellular compartment. **d**, Top: single plane representation of the detected objects, showing VLPs in the cytoplasm and the membrane. Bottom: 3D-view of the same cell. Related to Fig. 3c and 3d.

### Extended Data Fig. 9 Effects of VLDLR<sub>LBD</sub>-Fc and RAP on E2–E1-mediated neuron infection and viral replication assays.

**a**, Infection of human neurons derived from induced pluripotent stem cell (iPSCs) with GFP-expressing SFV single-cycle RVPs in the presence of the indicated proteins. Cells were imaged by fluorescence microscopy. The

experiment was performed twice with representative images shown. **b**, Quantification of single-cycle SFV RVP infection of human iPSC-derived neurons for the experiment shown in **(a)** using a live cell imaging system (see Methods for additional details). **c**, Merged phase contrast and fluorescent microscopy for the experiment with mouse cortical neurons shown in Fig. 4a. Scale bars are 100  $\mu$ m. Magnification is 20X. **d**, Merged phase contrast and fluorescent microscopy images for the experiment with human neurons shown in **(a)**. Scale bars are 100  $\mu$ m. Magnification is 10X. **e**, Viral replication curve for SFV, EEEV, and SINV strains in transduced K562 cells. Means  $\pm$  standard deviation from two experiments done in triplicate ( $n = 6$ ) with one-way ANOVA with Tukey's multiple comparisons test, \*\*\* $P < 0.0001$  (**b**). Means  $\pm$  standard deviation from two experiments done in triplicate ( $n = 6$ ) with two-way ANOVA with Tukey's multiple comparisons test, \* $P = 0.0233$ , \*\*\* $P < 0.0001$  (**e**).

#### Source data

#### Extended Data Fig. 10 Sequence alignment and domain organization of VLDLR constructs and summary of observed effects with alphavirus RVPs.

**a**, Sequence alignment of the *Homo sapiens*, *Mus musculus*, *Equus caballus*, *Sturnus vulgaris*, *Aedes aegypti*, *Aedes albopictus*, and *C. elegans* VLDLR ortholog ligand binding domains. The LDLR class A (LA) repeats contained in each protein are shown in parentheses. The domain numbering is based on the human sequence shown. **b**, Schematic representation of the ectodomains of VLDLR constructs used in this study. **c**, Summary of effects observed with GFP-expressing RVP infection of K562 cells transduced to express various VLDLR or ApoER2 orthologs derived from data shown in Extended Data Fig. 5d and Fig. 4e and 4f. +++, RVP infection with greater than 50% GFP positive cells achieved with overexpression. ++: RVP infection with 20–50% GFP positive cells achieved with overexpression. +: RVP infection with 5–20% GFP positive cells achieved with overexpression. +/-: RVP infection with less than 5% GFP positive cells of unclear biological significance. -: no enhancement. Panel **(a)** was generated using ESPrit 3.0<sup>74</sup>.

# **Supplementary information**

## **Supplementary Figure 1**

Uncropped gels for the indicated Extended Data Figures.

## **Reporting Summary**

## **Supplementary Table 1**

List of genes encoding membrane-associated proteins targeted by the CRISPR–Cas9 library.

## **Supplementary Table 2**

List of genes and scores from the CRISPR–Cas9 screen after MAGeCK analysis.

## **Supplementary Table 3**

Results of mass spectrometry analysis of purified virus-like particles.

# **Source data**

## **Source Data Fig. 1**

## **Source Data Fig. 2**

## **Source Data Fig. 3**

## **Source Data Fig. 4**

## **Source Data Extended Data Fig. 2**

[\*\*Source Data Extended Data Fig. 4\*\*](#)

[\*\*Source Data Extended Data Fig. 5\*\*](#)

[\*\*Source Data Extended Data Fig. 9\*\*](#)

## Rights and permissions

[Reprints and Permissions](#)

## About this article

### Cite this article

Clark, L.E., Clark, S.A., Lin, C. *et al.* VLDLR and ApoER2 are receptors for multiple alphaviruses. *Nature* **602**, 475–480 (2022).  
<https://doi.org/10.1038/s41586-021-04326-0>

- Received: 26 November 2020
- Accepted: 09 December 2021
- Published: 20 December 2021
- Issue Date: 17 February 2022
- DOI: <https://doi.org/10.1038/s41586-021-04326-0>

## Share this article

Anyone you share the following link with will be able to read this content:

[Get shareable link](#)

Sorry, a shareable link is not currently available for this article.

[Copy to clipboard](#)

Provided by the Springer Nature SharedIt content-sharing initiative

## Further reading

- [Identification of human and mosquito receptors for alphaviruses](#)

- Caroline K. Martin
- Margaret Kielian

*Nature* (2022)

## [Identification of human and mosquito receptors for alphaviruses](#)

- Caroline K. Martin
- Margaret Kielian

News & Views 19 Jan 2022

---

This article was downloaded by **calibre** from <https://www.nature.com/articles/s41586-021-04326-0>

| [Section menu](#) | [Main menu](#) |

- Article
- [Published: 23 December 2021](#)

# SARS-CoV-2 infection in free-ranging white-tailed deer

- [Vanessa L. Hale](#)<sup>1</sup> na1,
- [Patricia M. Dennis](#)<sup>1,2</sup> na1,
- [Dillon S. McBride](#) [ORCID: orcid.org/0000-0002-7408-3959](#)<sup>1</sup>,
- [Jacqueline M. Nolting](#) [ORCID: orcid.org/0000-0002-2705-4805](#)<sup>1</sup>,
- [Christopher Madden](#) [ORCID: orcid.org/0000-0001-9194-4143](#)<sup>1</sup>,
- [Devra Huey](#)<sup>1</sup>,
- [Margot Ehrlich](#) [ORCID: orcid.org/0000-0001-5855-3212](#)<sup>3</sup>,
- [Jennifer Grieser](#)<sup>4</sup>,
- [Jenessa Winston](#)<sup>5</sup>,
- [Dusty Lombardi](#)<sup>6</sup>,
- [Stormy Gibson](#)<sup>6</sup>,
- [Linda Saif](#)<sup>1,7</sup>,
- [Mary L. Killian](#)<sup>8</sup>,
- [Kristina Lantz](#)<sup>8</sup>,
- [Rachel M. Tell](#)<sup>8</sup>,
- [Mia Torchetti](#)<sup>8</sup>,
- [Suelee Robbe-Austerman](#) [ORCID: orcid.org/0000-0002-3794-3040](#)<sup>8</sup>,
- [Martha I. Nelson](#) [ORCID: orcid.org/0000-0003-4814-0179](#)<sup>9</sup> nAff11,
- [Seth A. Faith](#)<sup>10</sup> &
- [Andrew S. Bowman](#) [ORCID: orcid.org/0000-0002-0738-8453](#)<sup>1</sup>

[Nature](#) volume 602, pages 481–486 (2022)

- 43k Accesses
- 3 Citations
- 1396 Altmetric
- [Metrics details](#)

## Subjects

- [Ecological epidemiology](#)
- [Phylogenetics](#)
- [SARS-CoV-2](#)
- [Viral infection](#)

## Abstract

Humans have infected a wide range of animals with SARS-CoV-2<sup>1,2,3,4,5</sup>, but the establishment of a new natural animal reservoir has not been observed. Here we document that free-ranging white-tailed deer (*Odocoileus virginianus*) are highly susceptible to infection with SARS-CoV-2, are exposed to multiple SARS-CoV-2 variants from humans and are capable of sustaining transmission in nature. Using real-time PCR with reverse transcription, we detected SARS-CoV-2 in more than one-third (129 out of 360, 35.8%) of nasal swabs obtained from *O. virginianus* in northeast Ohio in the USA during January to March 2021. Deer in six locations were infected with three SARS-CoV-2 lineages (B.1.2, B.1.582 and B.1.596). The B.1.2 viruses, dominant in humans in Ohio at the time, infected deer in four locations. We detected probable deer-to-deer transmission of B.1.2, B.1.582 and B.1.596 viruses, enabling the virus to acquire amino acid substitutions in the spike protein (including the receptor-binding domain) and ORF1 that are observed infrequently in humans. No spillback to humans was observed, but these findings demonstrate that SARS-CoV-2 viruses have been transmitted in wildlife in the USA, potentially opening new pathways for evolution. There is an urgent need to establish comprehensive ‘One Health’ programmes to monitor the environment, deer and other wildlife hosts globally.

[Download PDF](#)

## Main

As of 9 November 2021, SARS-CoV-2, the virus responsible for coronavirus disease 2019 (COVID-19), has caused more than 5 million deaths globally<sup>6</sup>. The zoonotic origins of SARS-CoV-2 are not fully resolved<sup>7</sup>, exposing large gaps in our knowledge of susceptible host species and potential new reservoirs. Natural infections of SARS-CoV-2 linked to human exposure have been reported in domestic animals such as cats, dogs and ferrets, and in wildlife under human care, including several species of big cats, Asian small-clawed otters, western lowland gorillas and mink<sup>1</sup>. Detection of SARS-CoV-2 by PCR in free-ranging wildlife has been limited to small numbers of mink in Spain and in Utah in the USA, which were thought to have escaped from nearby farms<sup>8,9</sup>. An in silico study modelling SARS-CoV-2 binding sites on the

angiotensin-converting enzyme 2 (ACE2) receptor across host species predicted that cetaceans, rodents, primates and several species of deer are at high risk of infection<sup>10</sup>. Experimental infections have identified additional animal species susceptible to SARS-CoV-2, including hamsters, North American raccoons, striped skunks, white-tailed deer, raccoon dogs, fruit bats, deer mice, domestic European rabbits, bushy-tailed woodrats, tree shrews and multiple non-human primate species<sup>11,12,13,14,15,16,17,18,19,20</sup>. Moreover, several species are capable of intraspecies SARS-CoV-2 transmission<sup>13,14,15,17,21,22,23</sup>, including cats, ferrets, fruit bats, hamsters, raccoon dogs, deer mice and white-tailed deer. Vertical transmission has also been documented in experimentally infected white-tailed deer<sup>23</sup>. In July 2021, antibodies for SARS-CoV-2 were reported in 152 free-ranging white-tailed deer (seroprevalence 40%) sampled across Michigan, Pennsylvania, Illinois and New York in the USA<sup>24</sup>, raising the possibility that SARS-CoV-2 has infected deer in the Midwest and northeast regions.

In this study, we report the detection of SARS-CoV-2 in 129 out of 360 (35.8%) free-ranging white tailed deer (*O. virginianus*) from northeast Ohio using real-time PCR with reverse transcription (rRT–PCR) between January and March 2021. SARS-CoV-2 is a reportable disease in animals, and per international health regulations, these results were reported immediately to the World Organisation for Animal Health (OIE) on 31 August 2021 (Report ID: FUR\_151387, Outbreak ID: 89973)<sup>25</sup>; this was the first PCR-confirmed report of natural infection of SARS-CoV-2 in a cervid globally. Whole-genome sequences of 14 SARS-CoV-2 viruses were deposited in GISAID on 5 October 2021 (Extended Data Table 4). Additionally, we recovered two viable SARS-CoV-2 isolates from our samples, providing evidence that naturally infected deer shed infectious SARS-CoV-2 virus. We used genetic sequence data to estimate the number of human-to-deer transmission events, characterize the genetic diversity of the virus in deer and identify phylogenetic clades of deer-only viruses arising from deer-to-deer transmission.

## High infection rate of SARS-CoV-2

We sampled 360 free-ranging white-tailed deer across from 9 locations (Fig. 1a) in northeast Ohio between January and March 2021. Across all sites, SARS-CoV-2 was detected by rRT–PCR in 35.8% of nasal swabs from white-tailed deer (129 out of 360, 95% confidence interval 30.9–41.0%) (Supplementary Table 1). Each site was sampled 1–3 times during the study period, for a total of 18 collection dates (Extended Data Table 1). At least 1 rRT–PCR-positive sample was identified from 17 out of 18 collection dates, with the majority of positive sample  $C_t$  values being below 31 (Fig. 1b). Prevalence estimates varied from 13.5% to 70% across the nine sites (Fig. 1c). The highest prevalence estimates of SARS-CoV-2 were observed at four sites (sites 2,

5, 7 and 9) situated in the northern section of the sampled area, adjacent to urban areas with high human population densities (Fig. [1a, c](#)). Male deer ( $\chi^2 = 25.45, P < 0.0005$ ) and heavier deer (Wilcoxon–Mann–Whitney  $P = 0.0056$ ) were more likely to test positive for SARS-CoV-2 (Extended Data Table [2](#)).

**Fig. 1: SARS-CoV-2 viral RNA in white-tailed deer across the study locations.**

 figure 1

**a**, The nine study sites were spread across a 1,000-km<sup>2</sup> landscape of varying population density in northeast Ohio. Darker shading corresponds to higher human population density (people per square mile). Sampling sites 1, 2, 5, 7 and 9 are in close proximity to human populations and are indicated as urban sites with an asterisk in **b**, **c**. **b**, Nasal swabs from white-tailed deer were tested for the presence of SARS-CoV-2 viral RNA using real-time reverse transcriptase PCR (rRT–PCR). Estimates of amount of SARS-CoV-2 viral RNA are represented by (40 –  $C_t$  value of the N1 rRT–PCR target). Negative samples are represented with a value of zero. **c**, The prevalence of SARS-CoV-2 in the white-tailed deer at each study site was estimated using rRT–PCR. The proportion of positive samples is shown with Clopper–Pearson exact 95% confidence interval bars. The number of samples collected at each site is indicated in parentheses. Map created with ArcMap v.10.8.1, using base layers and data from Esri, Garmin, OpenStreetMap, GIS user community, Infogroup and the US Census Bureau.

## Three SARS-CoV-2 lineages identified

We sequenced the complete genome of 14 viruses collected from 6 of the 9 sites, collected at 7 time points spanning from 26 January 2021 to 25 February 2021 ([Supplementary Table 1](#)). The deer samples were collected approximately six weeks after the peak of Ohio's 2020–2021 winter epidemic of SARS-CoV-2 in humans, which was dominated by B.1.2 viruses (more than 50% of human viruses) (Fig. [2a](#), Extended Data Table [3](#)). B.1.2 viruses genetically similar to human viruses were detected in deer at sites 4, 7, 8 and 9 (Fig. [2b](#)). B.1.596, a minor lineage (accounting for around 11% of human viruses), was identified in seven deer samples at site 1, spanning two collection times (2 February and 25 February 2021). A rarer lineage, B.1.582 (present in approximately 1% of human samples), was identified in two deer samples at site 6. No sequences belonging to the Alpha (B.1.1.7) or Delta (B.1.617.2) lineages were identified in the deer samples, as these variants became widespread in the human population only after February 2021.

**Fig. 2: Three SARS-CoV-2 lineages identified in white-tailed deer.**

---

 **figure 2**

---

**a**, The number of weekly COVID-19 cases in humans from October 2020 to September 2021 in Ohio. Shading indicates the proportion of viruses sequenced each week in Ohio that belong to one of five Pango lineages (or ‘other’). **b**, Summary of six human-to-deer transmission events observed in Ohio, with putative deer-to-deer transmission. **c**, Maximum-likelihood tree inferred for SARS-CoV-2 viruses in humans and white-tailed deer in Ohio during January to March 2021. Tips are shaded by Pango

lineage and major lineages are boxed, labelled and shaded similar to Fig. 2b. Viruses found in white-tailed deer (clusters or singletons) are shaded red and labelled by location (the B.1.2 virus identified at site 4 is not shown owing to lower sequence coverage). All branch lengths are drawn to scale.

## Six human-to-deer transmission events

Although B.1.2 was identified in deer at 4 sites, our phylogenetic analysis found no evidence of B.1.2 viruses transmitting in deer across sites. Rather, each site experienced a separate human-to-deer transmission event of a slightly genetically different B.1.2 virus positioned in a different section of the B.1.2 clade on the phylogenetic tree (Fig. 2c). In total, six human-to-deer transmission events were observed: B.1.582 (site 6), B.1.596 (site 1) and B.1.2 (sites 4, 7, 8 and 9). There is a degree of uncertainty about the timing of each viral entry into the deer population, owing to long branch lengths that separate the deer viruses from the ancestral human viruses on the phylogenetic tree. To estimate the timing and location of human-to-deer transmission for the larger cluster of B.1.596 deer viruses, a time-scale Bayesian maximum clade credibility (MCC) tree was inferred using a phylogeographic approach (Fig. 3a). The MCC tree is consistent with human-to-deer transmission occurring geographically in Ohio (posterior probability = 0.98) and temporally during the winter epidemic when viral loads in humans (and the environment) would be peaking. The MCC tree indicates that B.1.596 viruses were introduced into humans in Ohio multiple times from other US states during the autumn of 2020 and winter of 2020–2021, forming three co-circulating Ohio clades in humans. The largest Ohio clade then seeded the deer outbreak. Deer viruses in this cluster were collected on 2 February and 25 February 2021, and the MCC tree estimates that human-to-deer transmission occurred several weeks, or possibly months, earlier (Fig. 3a). Gaps in sampling in both humans and deer make it difficult to narrow this time estimate further.

**Fig. 3: Evolution of B.1.596 viruses in white-tailed deer.**

---

 **figure 3**

**a**, Bayesian time-scale MCC tree inferred for the cluster of 7 B.1.596 viruses identified in white-tailed deer at site 1, the 46 most closely related human B.1.596 viruses, and a random sampling of other B.1.596 viruses observed in the USA during November 2020 to March 2021. Tips are shaded by location state (host species and

geography). Branches are shaded by the location state inferred from an ancestral reconstruction. Posterior probabilities are provided for key nodes. Cartoons indicate the host-switch branch where human-to-deer transmission may have occurred, followed by putative deer-to-deer transmission within site 1. The estimated timing and location state probability is provided for key nodes defining the host-switch branch. **b**, Clade-defining amino acid changes observed in all 7 B.1.596 deer viruses are listed. **c**, The E484D substitution in the spike protein's receptor-binding motif (RBM) is shown in one of the B.1.596 deer viruses (OH-OSU-340). NTD, N-terminal domain; RBD, receptor-binding domain.

## Deer-to-deer transmission and evolution

Viable SARS-CoV-2 virus was recovered from two of the deer samples (Extended Data Table 4). Deer-to-deer transmission may have occurred within the three study sites where more than 1 deer sample was sequenced: site 1 (B.1.596), site 6 (B.1.582) and site 9 (B.1.2). Only two viruses were collected from sites 6 and 9, both from the same sampling date (Fig. 2b), limiting what can be inferred about transmission. Instead, our analysis of deer-to-deer transmission and evolution focused on the larger deer cluster of 7 B.1.596 viruses observed in site 1 that spans two collection dates (Fig. 3a). A number of uncommon amino acid substitutions were observed in all seven deer viruses in this clade (that is, all site 1 sequences) that were not observed in the most closely related human viruses. Five clade-defining mutations were observed in ORF1ab: a five-residue deletion in nsp1 ( $\Delta$ 82–86), nsp2 T434I, nsp2 P597L, nsp12 A382V and nsp13 M474I (numbering in Fig. 3b refers to ORF1a and ORF1b). A clade-defining deletion ( $\Delta$ 141–144) was also observed in the S1 domain of the spike protein in the 7 deer viruses. All 6 clade-defining mutations observed in these deer are uncommon among human viruses (<0.05% frequency globally; <https://outbreak.info/>).

Uncommon amino acid changes in the spike protein S1 domain also were observed in singleton deer viruses. A B.1.2 virus from site 7 (hCoV-19/deer/USA/OH-OSU-0212/2021) has a substitution in the N-terminal domain of the spike protein (H245Y). A single B.1.596 virus from site 1 (hCoV-19/deer/USA/OH-OSU-0340/2021) has a substitution in the spike protein receptor-binding motif (E484D) (Fig. 3c). Both mutations are relatively rare in humans, being found in less than 0.5% of all SARS-CoV-2 viruses sequenced globally. In experimental studies, viruses with the E484D substitution are less sensitive to neutralization by convalescent sera<sup>26</sup>. The E484D substitution has been detected only in 201 SARS-CoV-2 sequences from humans globally, 71 of which were in the USA, but none of the B.1.596 viruses in humans that were most closely related to the deer virus have this mutation. It is therefore impossible to differentiate whether the E484D mutation arose in an unsampled human virus and was transmitted to deer or arose de novo in deer. Additionally, owing to low

availability of sequence data from deer it is not possible to determine whether these spike mutations have been transmitted to other deer.

## Discussion

Our finding that white-tailed deer are frequently infected with SARS-CoV-2 viruses raises profound questions about the future trajectory of SARS-CoV-2. The potential establishment of a new reservoir of SARS-CoV-2 viruses in white-tailed deer could open new pathways for evolution, transmission to other wildlife species and potential spillback of novel variants to humans that the human immune system has not previously encountered. SARS-CoV-2 viruses have a high capacity for adaptive evolution when infection rates are high in a community or population. It is therefore concerning that more than one-third of deer in our study tested positive for SARS-CoV-2 by PCR, suggesting an active or recent infection during the major wave the previous winter. A number of mutations were observed in white-tailed deer that occur at very low frequency in humans, including a mutation in the receptor-binding motif. Such mutations could potentially be amplified in a new reservoir host with high infection rates and different constraints on evolution. There is an urgent need to expand monitoring of SARS-CoV-2 viruses in potential wildlife hosts to document the breadth of the problem in white-tailed deer nationally, understand the ecology of transmission and track evolutionary trajectories going forward, including in other potential host species.

The impact of urban sprawl on disease ecology is well documented for Lyme disease and other multihost zoonotic systems that include white-tailed deer, rodents and other species that have become ubiquitous and well adapted in expanding US urban and semi-urban environments, creating opportunities for pathogen exchange.

Approximately 30 million free-ranging white-tailed deer are distributed broadly across urban, suburban, and rural environments in the USA, and can live at densities of greater than 45 deer per square mile in some areas<sup>27</sup>. Ohio is home to more than 700,000 free-ranging white-tailed deer<sup>28</sup> and another 440 commercial deer farms<sup>29</sup>. Estimates of deer density in and around our sites range from approximately  $8 \text{ km}^{-2}$  to upwards of  $30 \text{ km}^{-2}$ . There are no deer farms in the study area and public feeding of deer is prohibited. There is ample forage available around urban and suburban residences in gardens and plantings, drawing deer into close proximity with humans and their companion animals. Therefore, it is unsurprising that deer in urban sites were at higher risk for infection in our study. Urban settings provide ample opportunities for deer to have direct and indirect contact with human-contaminated sources (for example, trash, backyard feeders, bait stations and wildlife hospitals) that could serve as a pathway for viral spillover into wildlife. Additionally, urban and suburban environments include waterways that could be contaminated by multiple sources<sup>18,30</sup>.

Viable SARS-CoV-2 is shed in human stool. SARS-CoV-2 RNA has also been detected in wastewater<sup>31,32</sup> and urban runoff<sup>33</sup>, although the infectivity of SARS-CoV-2 from these sources is undetermined. The recent detection of genetically distinct SARS-CoV-2 virus fragments in New York City wastewater introduces an intriguing hypothesis that SARS-CoV-2 could be transmitting cryptically in rodents<sup>34</sup>. However, although sensitive techniques for detecting viral RNA in wastewater have vastly improved, providing a potentially useful tool for early detection of outbreaks, isolating or whole-genome sequencing viruses to characterize their genetic diversity remains challenging.

A major outstanding question is how the virus is transmitted between deer. Deer are social animals that live in small herds and frequently touch noses. It is unclear whether baiting the deer before collection contributed the increased frequency of SARS-CoV-2 in this study, but concentrating deer with bait could potentially have facilitated pathogen transmission through a population. However, baiting is regularly used in deer population-management programmes and the practice is commonly employed by deer hunters, which makes understanding the effect of baiting on SARS-CoV-2 transmission in free-ranging deer paramount for future studies. The increased rate of infection in males in this study could reflect sex-linked differences in behaviour that increase disease transmission. The higher prevalence of chronic wasting disease and tuberculosis in male white-tailed deer is attributed to larger male home ranges, increased movement and contact with other deer during breeding season (autumn–winter), and dynamic male social group composition and size<sup>35</sup>. Deer may experience high levels of viraemia and shedding that may be conducive to environmental or aerosol transmission. Another question is whether deer experience clinical disease and whether clinical signs such as sneezing or nasal discharge increase the risk of transmission. Two previous experimental studies reported only subclinical infections in white-tailed deer challenged with SARS-CoV-2, but these studies had very small sample sizes<sup>14,23</sup>.

Although extensive measures were taken to prevent cross-contamination during sample collection and testing, the nature of field work makes it impossible to completely exclude the possibility. Cross-contamination during sample collection would not invalidate the detection of SARS-CoV-2 in white-tailed deer, but would artificially inflate prevalence estimates. However, the extent of genomic diversity among the sequences recovered on a single sampling day (for example, site 1, sampling 2) indicates cross-contamination during sample collection was probably minimal.

Although our study was limited to northeast Ohio, these findings have implications for other US states, including Michigan, Pennsylvania, New York and Illinois, where high rates of exposure to SARS-CoV-2 in white-tailed deer have been reported on the basis

of serology<sup>24</sup>. Serological assays are notoriously difficult to interpret and many animal health experts had hoped that those results were an artefact. Moreover, the detection of antibodies does not prove active infection. However, the present study suggests that the antibodies observed in deer in other US states may have arisen from active infection, and that the true extent of infections may remain underestimated.

Moreover, it is worth noting that white-tailed deer are a relatively convenient surveillance target because of their abundance and accessibility. The detection of SARS-CoV-2 in free-ranging white-tailed deer naturally raises the question of whether less accessible species are also being infected through viral spillover from humans, which calls for broader surveillance efforts.

## Methods

### Sample collection

Between January and March 2021, 360 free-ranging white-tailed deer originating from 9 study sites in northeast Ohio (USA) were euthanized as part of a deer population-management programme. Collection occurred at locations that were baited with whole kernel corn for up to two weeks prior to each culling session, and additional deer were collected opportunistically when they were observed away from the bait on a culling session day. In the field, once a deer was collected, the head was wrapped in a plastic bag and an identification tag was attached to a leg. Each day of the programme, collected deer carcasses were transported to a central processing point where samples were collected. All samples were collected by one experienced veterinarian who wore a facemask and gloves that were changed or washed between each sample. A nasal swab was collected from each deer and placed into a tube with brain heart infusion broth (BHIB). After collection, samples were immediately chilled on ice packs then transferred into a -80 °C freezer within 12 h, where they remained until testing was initiated. Samples were collected post mortem, which was exempt from oversight by The Ohio State University Institutional Animal Care and Use Committee.

### Diagnostic testing

Samples were initially tested using the Charité/Berlin (WHO) assay<sup>36</sup>. Viral RNA was extracted from 200 µl of BHIB using Omega Bio-tek Mag-Bind Viral DNA/RNA kit (catalogue (cat.) no. M6246-03). Xeno Internal Control (Life Technologies cat. no. A29763) was included in the extraction to ensure the accuracy of negative results. Five microlitres of extracted RNA was added to Path-ID MPX One-Step Kit master mix (Life Technologies cat. no. 4442135) containing 12.5 µl 2× Multiplex RT-PCR buffer, 2.5 µl enzyme mix, 1.5 µl nuclease free water, 4.5 µl E assay primer/probe panel

(Integrated DNA Technologies cat. no. 1006804), and 1 µl XENO VIC Internal Control Assay (Life Technologies cat. no. A29765) for each sample. The cycling parameters for the rRT–PCR were 48 °C for 10 min, 95 °C for 10 min, 45 cycles of 95 °C 15 s and 58 °C 45 s. Samples with a cycle threshold ( $C_t$ ) of  $\leq 40$  were considered positive. If the E assay was positive, the RdRp confirmatory and discriminatory assays were completed using the above master mix formulation and thermocycler parameters, replacing the E assay primer–probe panel with the confirmatory and discriminatory primer–probe panel (Integrated DNA Technologies cat. no. 10006805 and 10006806). The RNA from all samples that tested positive with the E assay, was retested with the CDC rRT–PCR protocol<sup>37</sup>. Samples that were 2019-nCoV N1 and N2 positive were classified as presumptive positive. A subset of presumptive positive samples was selected for retesting, in which RNA was re-extracted from original samples to verify the rRT–PCR result.

## Genomic sequencing

Original sample material for 76 representative presumptive positive samples were sent to the National Veterinary Services Laboratories (NVSL) for confirmatory rRT–PCR testing using the CDC protocol and whole-genome sequencing. Viral RNA was amplified by PCR<sup>38</sup> and cDNA libraries were prepared using the Nextera XT DNA Sample Preparation Kit according to manufacturer instructions. Sequencing was performed using the 500-cycle MiSeq Reagent Kit v2. Sequences were assembled using IRMA v.0.6.7 and DNAStar SeqMan NGen v.14.0.1. Additional sequencing was attempted at Ohio State’s Applied Microbiology Services Laboratory using a modified ARTIC V3 method (<https://www.protocols.io/view/ncov-2019-sequencing-protocol-v3-locost-bh42j8ye>). Extracted RNA was reverse transcribed and amplified by PCR with the ARTIC SARS-CoV-2 FS Library Prep Kit (New England Biolabs) according to the manufacturer’s recommended protocol. Amplified products were converted to Illumina sequencing libraries using the RNA Prep with Enrichment (L) Tagmentation Kit protocol (Illumina) with unique dual indexes and 10 cycles of TagPCR. Sequencing libraries were pooled and quantified using ProNex NGS Library Quant Kit (NG1201, Promega). The 650 pM libraries were loaded on P2 sequencing cartridges and analysed with the NextSeq2000 (Illumina) with  $2 \times 101$  bp cycles. Data were transmitted to the BaseSpace Cloud platform (Illumina) and converted to FASTQ file format using DRAGEN FASTQ Generation v3.8.4 (Illumina). DRAGEN COVID Lineage app v.3.5.3 (Illumina) was used to align sequence data and produce quality metrics and consensus genome sequences.

## Data analysis

Pangolin v.3.1.11, 2021-09-17 was used to assign lineage<sup>39,40</sup>. Prevalence was estimated using the number of presumptive positive nasal swabs based upon the final

CDC rRT–PCR results. Prevalence estimates, confidence intervals, and other descriptive statistics were calculated using STATA 14.2 (StataCorp).

## Virus isolation

In brief, at the NVSL, the samples were diluted between 1:2 and 1:3 in minimum essential medium with Earle’s balanced salt solution (MEM-E). Vero 76 cells that were mycoplasma-free were inoculated with 1.5 ml diluted sample material and adsorbed for 1 h at 37 °C. After adsorption, a replacement medium containing 2 µg ml<sup>-1</sup> *N*-*p*-tosyl-l-phenylalanine chloromethyl ketone-treated trypsin was added, and cells were incubated at 37 °C for up to 7 days. Cell cultures with exhibiting no cytopathic effects (CPE) were frozen, thawed, and subjected to two blind passages, inoculating the fresh cultures with those lysates as described above. At the end of two blind passages or upon observation of CPE, cell culture material was tested by rRT–PCR for SARS-CoV-2 using the CDC N1 and N2 primer and probe sets.

## Phylogenetic analysis

First, a background dataset was compiled from GISAID that included all SARS-CoV-2 sequences available from humans in Ohio, USA during the study period (1 January to 31 March 2021), downloaded on 27 September 2021 ( $n = 4,801$  sequences). To our knowledge, these are the first SARS-CoV-2 viruses sequenced from white-tailed deer globally and no additional sequences from white-tailed deer were available in any public repository for comparison. Pangolin was used to assign a lineage to each human virus. In total, 102 lineages were identified in this dataset, with the most common being B.1.2 ( $n = 1,766$ ), B.1.1.7 ( $n = 833$ ), B.1.1.519 ( $n = 411$ ), B.1.429 ( $n = 307$ ) and B.1.596 ( $n = 274$ ). The dataset was aligned using NextClade with Wuhan-Hu-1 as a reference. The alignment was manually trimmed at the 5' and 3' ends. The final alignment included only coding regions and was manually edited to be in frame, with stop codons present only at the terminus of genes. A phylogenetic tree was inferred from this dataset using maximum-likelihood methods available in IQ-TREE version 1.6.12 with a GTR + G model of nucleotide substitution and 1,000 bootstrap replicates, using the high-performance computational capabilities of the Biowulf Linux cluster at the National Institutes of Health (<http://biowulf.nih.gov>). The inferred tree was visualized in FigTree v.1.4.4. Outlier sequences were removed with long branch lengths and incongruence between genetic divergence and sampling date, as assessed using TempEst v.1.5.3, typically arising from poor sequence coverage. One of the 14 sequences obtained from deer in our study (hCoV-19/deer/USA/OH-OSU-0025/2021, site 4) was lower in coverage and had a very long branch length and was excluded from the final phylogenetic analysis. To examine the evolutionary origins of the cluster of 7 B.1.596 viruses obtained from deer at site 1 in more granular detail, a second phylogenetic tree was inferred that included all B.1.596 sequences available

globally from NCBI's GenBank ( $n = 5,586$ ), nearly all (99.8%) from the USA, using similar methods as above. For purposes of visualization a separate phylogenetic tree was inferred that was limited to the sub-clade of B.1.596 viruses ( $n = 46$ ) most closely related to the 7 deer viruses. This clade, plus 100 viruses randomly sampled from other sections of the tree as background, was used in a subsequent Bayesian phylogeographic analysis. A time-scaled Bayesian analysis using the Markov chain Monte Carlo (MCMC) method was performed the BEAST v.1.10.4 package<sup>41</sup>, again using the Biowulf Linux cluster. A relaxed uncorrelated lognormal (UCLN) molecular clock was used with a flexible Bayesian skyline population, and a general-time reversible (GTR) model of nucleotide substitution with gamma-distributed rate variation among sites. Each sample was assigned to one of three categories based on host and geography: (1) viruses collected in humans in all US states except Ohio, (2) viruses collected in humans in Ohio, and (3) viruses collected in deer in Ohio. The MCMC chain was run separately three times for each of the datasets for at least 100 million iterations with subsampling every 10,000 iterations, using the BEAGLE 3 library to improve computational performance<sup>42</sup>. All parameters reached convergence, as assessed visually using Tracer v.1.7.1, with statistical uncertainty reflected in values of the 95% highest posterior density (HPD). At least 10% of the chain was removed as burn-in and runs were combined using LogCombiner v1.10.4 and a MCC tree was summarized using TreeAnnotator v.1.10.4 and visualized in FigTree v.1.4.4. The NVSL vSNP pipeline ((<https://github.com/USDA-VS/vSNP>) was applied for SNP based phylogenetic analysis using Wuhan-Hu-1 (NC\_045512) as a reference.

## Epidemiological data

The epidemiological curve of SARS-CoV-2 cases in Ohio from April 2020 to September 2020 was generated using the number of daily reported COVID-19 cases in the state of Ohio (all age groups), available from the US Centers for Disease Control and Prevention (<https://data.cdc.gov/Case-Surveillance/COVID-19-Case-Surveillance-Public-Use-Data-with-Ge/n8mc-b4w4>). All SARS-CoV-2 genetic sequences from Ohio were downloaded from GISAID on 8 October 2021 ( $n = 18,052$ ) to estimate the proportion of viruses belonging to different Pango lineages during each week of the epidemic. To account for the intensity of surveillance not being even over time the number of viruses per lineage per week was normalized against the epidemiological curve derived from COVID-19 case counts and visualized using R. To further minimize biases only sequences categorized in the GISAID submission as obtained using a 'baseline surveillance' sampling strategy were included in the analysis. The dataset was further trimmed to include only submissions with complete collection dates and sufficient coverage to assign a Pango lineage, resulting in a final dataset of 9,947 sequences from Ohio. For simplicity sub-lineages of B.1.617.2 (for example, AY.3) were consolidated into the Delta category and sub-lineages of B.1.1.7 (for example, Q.3) were consolidated into the Alpha category. Baseline surveillance data

before 20 December 2020 was too thinly sampled to reliably estimate the proportion of viruses from different lineages from this time period, so a second figure was generated using all available sequence data. As the proportions of Pango lineages over time proved to be very similar in the baseline data and the complete dataset, the larger dataset that dated back to October 2020 was used in the final figure.

## Reporting summary

Further information on research design is available in the [Nature Research Reporting Summary](#) linked to this paper.

## Data availability

Sequence data from the 14 SARS-CoV-2 viruses from white-tailed deer sequenced in this study are available at NCBI Sequence Read Archive (SRA) under accessions [SRR17187542](#), [SRR17187543](#), [SRR17187544](#), [SRR17187545](#), [SRR17187546](#), [SRR17187547](#), [SRR17187548](#), [SRR17187549](#), [SRR17187550](#), [SRR17187551](#), [SRR17187552](#), [SRR17187553](#), [SRR17187554](#) and [SRR17187555](#) and assembled genome sequences are on GISAID (Extended Data Table 4).

## References

1. *Confirmed Cases of SARS-CoV-2 in Animals in the United States*, <https://www.aphis.usda.gov/aphis/dashboards/tableau/sars-dashboard> (USDA APHIS, 2021).
2. McAloose. D. et al. From people to *Panthera*: natural SARS-CoV-2 infection in tigers and lions at the Bronx Zoo. *mBio* **11**, e02220 (2020).
3. Oude Munnink, B. B. et al. Transmission of SARS-CoV-2 on mink farms between humans and mink and back to humans. *Science* **371**, 172–177 (2021).
4. Schulz, C. et al. SARS-CoV-2-specific antibodies in domestic cats during first COVID-19 wave, Europe. *Emerg. Infect. Dis.* **27**, 3115–3118 (2021).
5. Sit, T. H. C., et al. Infection of dogs with SARS-CoV-2. *Nature* **586**, 776–778 (2020).
6. World Health Organization coronavirus (COVID-19) dashboard. *WHO* <https://covid19.who.int/> (2021).

7. Andersen, K. G., Rambaut, A., Lipkin, W. I., Holmes, E. C. & Garry, R. F. The proximal origin of SARS-CoV-2. *Nat. Med.* **26**, 450–452 (2020).
8. Shriner, S. A. et al. SARS-CoV-2 exposure in escaped mink, Utah, USA. *Emerg. Infect. Dis.* **27**, 988–990 (2021).
9. Aguiló-Gisbert, J. et al. First description of SARS-CoV-2 infection in two feral American mink (*Neovison vison*) caught in the wild. *Animals* **11**, 1422 (2021).
10. Damas, J. et al. Broad host range of SARS-CoV-2 predicted by comparative and structural analysis of ACE2 in vertebrates. *Proc. Natl Acad. Sci. USA* **117**, 22311–22322 (2020).
11. Francisco, R. et al. Experimental susceptibility of North American raccoons (*Procyon lotor*) and striped skunks (*Mephitis mephitis*) to SARS-CoV-2. Preprint at <https://doi.org/10.1101/2021.03.06.434226> (2021).
12. Schlottau, K. et al. SARS-CoV-2 in fruit bats, ferrets, pigs, and chickens: an experimental transmission study. *Lancet Microbe* **1**, e218–e225 (2020).
13. Freuling, C. et al. Susceptibility of raccoon dogs for experimental SARS-CoV-2 infection. *Emerg. Infect. Dis.* **26**, 2982–2985 (2020).
14. Palmer, M. V. et al. Susceptibility of white-tailed deer (*Odocoileus virginianus*) to SARS-CoV-2. *J. Virol.* **95**, e00083 (2021).
15. Fagre, A. et al. SARS-CoV-2 infection, neuropathogenesis and transmission among deer mice: implications for spillback to New World rodents. *PLoS Pathog.* **17**, e1009585 (2021).
16. Lu, S. et al. Comparison of nonhuman primates identified the suitable model for COVID-19. *Signal Transduct. Target. Ther.* **5**, 157 (2020).
17. Sia, S. F. et al. Pathogenesis and transmission of SARS-CoV-2 in golden hamsters. *Nature* **583**, 834–838 (2020).
18. Bosco-Lauth, A. et al. Peridomestic mammal susceptibility to severe acute respiratory syndrome coronavirus 2 infection. *Emerg. Infect. Dis.* **27**, 2073–2080 (2021).
19. Mykytyn, A. Z. et al. Susceptibility of rabbits to SARS-CoV-2. *Emerg. Microbes Infect.* **10**, 1–7 (2021).

20. Zhao, Y. et al. Susceptibility of tree shrew to SARS-CoV-2 infection. *Sci. Rep.* **10**, 16007 (2020).
21. Kim, Y.-I. et al. Infection and rapid transmission of SARS-CoV-2 in ferrets. *Cell Host Microbe* **27**, 704–709.e702 (2020).
22. Shi, J. et al. Susceptibility of ferrets, cats, dogs, and other domesticated animals to SARS-coronavirus 2. *Science* **368**, 1016–1020 (2020).
23. Cool, K. et al. Infection and transmission of ancestral SARS-CoV-2 and its Alpha variant in pregnant white-tailed deer. Preprint at <https://doi.org/10.1101/2021.08.15.456341> (2021).
24. Chandler, J. C. et al. SARS-CoV-2 exposure in wild white-tailed deer (*Odocoileus virginianus*). *Proc. Natl Acad. Sci. USA* **118**, e2114828118 (2021).
25. *Follow-Up Report 18, SARS-CoV-2 in Animals, United States of America*, FUR\_151387, <https://wahis.oie.int/#/report-info?reportId=38714> (World Organisation for Animal Health (OIE), 2021).
26. Liu, Z. et al. Identification of SARS-CoV-2 spike mutations that attenuate monoclonal and serum antibody neutralization. *Cell Host Microbe* **29**, 477–488.e474 (2021).
27. Walters, B. F., Woodall, C. W. & Russell, M. B. White-tailed deer density estimates across the eastern United States, 2008. *Data Repository for the University of Minnesota* (2016).
28. ODNR. *Managing Ohio's Deer Herd* <https://ohiodnr.gov/static/documents/wildlife/wildlife-management/Managing%20Ohio's%20Deer%20Herd%20pub087.pdf>
29. Shepstone Management Company (ed. Inc. *Whitetail Deer Farmers of Ohio*) (2010).
30. Franklin, A. B. & Bevins, S. N. Spillover of SARS-CoV-2 into novel wild hosts in North America: a conceptual model for perpetuation of the pathogen. *Sci. Total Environ.* **733**, 139358 (2020).
31. Bivins, A. et al. Persistence of SARS-CoV-2 in water and wastewater. *Environ. Sci. Technol. Lett.* **7**, 937–942 (2020).
32. Ai, Y. et al. Wastewater-based epidemiology for tracking COVID-19 trend and variants of concern in Ohio, United States. Preprint at

<https://doi.org/10.1101/2021.06.08.21258421> (2021).

33. Bernard, K. et al. Detection of SARS-CoV-2 in urban stormwater: An environmental reservoir and potential interface between human and animal sources. *Sci. Total Environ.* **807**, 151046 (2021).
34. Smyth, D. S. et al. Tracking cryptic SARS-CoV-2 lineages detected in NYC wastewater. Preprint at <https://doi.org/10.1101/2021.07.26.21261142> (2021).
35. O'Brien, D. J. et al. Epidemiology of *Mycobacterium bovis* in free-ranging white-tailed deer, Michigan, USA, 1995–2000. *Prev. Vet. Med.* **54**, 47–63 (2002).
36. Corman, V. M. et al. Detection of 2019 novel coronavirus (2019-nCoV) by real-time RT-PCR. *Euro Surveill.* **25**, 2000045 (2020).
37. *CDC 2019-Novel Coronavirus (2019-nCoV) Real-Time RT-PCR Diagnostic Panel*, <https://www.fda.gov/media/134922/download> (CDC, 2021).
38. Paden, C. R. et al. Rapid, sensitive, full-genome sequencing of severe acute respiratory syndrome coronavirus 2. *Emerg. Infect. Dis.* **26**, 2401–2405 (2020).
39. O'Toole, A. et al. Assignment of epidemiological lineages in an emerging pandemic using the pangolin tool. *Virus Evol.* **7**, veab064 (2021).
40. Rambaut, A. et al. A dynamic nomenclature proposal for SARS-CoV-2 lineages to assist genomic epidemiology. *Nat. Microbiol.* **5**, 1403–1407 (2020).
41. Suchard, M. A. et al. Bayesian phylogenetic and phylodynamic data integration using BEAST 1.10. *Virus Evol.* **4**, vey016 (2018).
42. Ayres, D. L. et al. BEAGLE 3: improved performance, scaling, and usability for a high-performance computing library for statistical phylogenetics. *Syst. Biol.* **68**, 1052–1061 (2019).

## Acknowledgements

This work was supported by The Ohio State University Infectious Diseases Institute and The Ohio State University Center of Microbiome Science (Targeted Investment: eSCOUT – Environmental Surveillance for COVID-19 in Ohio: Understanding Transmission), Centers of Excellence for Influenza Research and Surveillance, National Institute of Allergy and Infectious Diseases, National Institutes of Health, Department of Health and Human Services under contract HHSN272201400006C and HHSN272201400008C, and the NIAID Intramural Research Program. We thank H.

Cochran, E. Ohl, A. Cleggett, S. Treglia, A. M. Williams, F. Savona, J. W. Smith, D. Sizemore and the Cleveland Metroparks Deer Management Team. The content does not necessarily reflect the views or policies of the U.S. Government or imply endorsement of any products.

## Author information

### Author notes

1. Martha I. Nelson

Present address: National Center for Biotechnology Information, National Library of Medicine, National Institutes of Health, Bethesda, MD, USA

2. These authors contributed equally: Vanessa L. Hale, Patricia M. Dennis

### Affiliations

1. Veterinary Preventive Medicine, The Ohio State University College of Veterinary Medicine, Columbus, OH, USA

Vanessa L. Hale, Patricia M. Dennis, Dillon S. McBride, Jacqueline M. Nolting, Christopher Madden, Devra Huey, Linda Saif & Andrew S. Bowman

2. Cleveland Metroparks Zoo, Cleveland, OH, USA

Patricia M. Dennis

3. The Ohio State University College of Veterinary Medicine, Columbus, OH, USA

Margot Ehrlich

4. Cleveland Metroparks, Cleveland, OH, USA

Jennifer Grieser

5. Veterinary Clinical Sciences, The Ohio State University College of Veterinary Medicine, Columbus, OH, USA

Jenessa Winston

6. Ohio Wildlife Center, Powell, OH, USA

Dusty Lombardi & Stormy Gibson

7. Center for Food Animal Health, The Ohio State University College of Food, Agriculture, and Environmental Sciences, Wooster, OH, USA

Linda Saif

8. National Veterinary Services Laboratories, Animal and Plant Health Inspection Service, United States Department of Agriculture, Ames, IA, USA

Mary L. Killian, Kristina Lantz, Rachel M. Tell, Mia Torchetti & Suelee Robbe-Austerman

9. Division of Intramural Research, National Institute of Allergy and Infectious Diseases, National Institutes of Health, Bethesda, MD, USA

Martha I. Nelson

10. Infectious Diseases Institute, The Ohio State University, Columbus, OH, USA

Seth A. Faith

## Contributions

Conceptualization: V.L.H., P.M.D., J.M.N., D.L., S.G., L.S., S.A.F. and A.S.B.

Methodology: V.L.H., P.M.D., J.M.N., S.A.F., M.I.N. and A.S.B. Investigation:

P.M.D., J.G., C.M., D.H., M.E., R.M.T., M.L.K., K.L., S.R.-A., M.T. and A.S.B.

Visualization: M.I.N., D.S.M. and A.S.B. Funding acquisition: V.L.H., J.M.N., J.W.,

S.A.F. and A.S.B. Project administration: V.L.H., P.M.D., J.M.N. and A.S.B.

Supervision: V.L.H., P.M.D., J.G., M.T. and A.S.B. Writing, original draft: V.L.H.,

M.I.N., D.S.M., M.L.K., S.A.F. and A.S.B. Writing, review and editing: P.M.D., C.M., D.H., J.G., J.M.N., D.L., J.W., S.G., L.S., M.E., R.T., K.L., S.R.-A. and M.T.

## Corresponding author

Correspondence to [Andrew S. Bowman](#).

## Ethics declarations

## Competing interests

The authors declare no competing interests.

## Peer review

### Peer review information

*Nature* thanks Malik Peiris and the other, anonymous, reviewer(s) for their contribution to the peer review of this work. Peer reviewer reports are available.

## Additional information

**Publisher's note** Springer Nature remains neutral with regard to jurisdictional claims in published maps and institutional affiliations.

## Extended data figures and tables

**Extended Data Table 1** SARS-CoV-2 prevalence stratified by site and sampling date.

**Extended Data Table 2** Covariate data recorded for each deer sample

**Extended Data Table 3** Proportion of SARS-CoV-2 viruses identified in Ohio in humans during January 1 – February 28, 2021

**Extended Data Table 4** Whole genome sequence data

## Supplementary information

### [Reporting Summary](#)

### [Peer Review File](#)

### [Supplementary Table 1](#)

rRT–PCR testing results. The cycle threshold ( $C_t$ ) value results for the E assay screen, N1 and N2 rRT–PCR targets are shown for the 360 nasal swabs collected from white-tailed deer as a part of this study. Final SARS-CoV-2 rRT–PCR result was considered presumptive positive if  $C_t$  values for all three targets were  $< 40$ . For the 76 samples sent to NVSL, confirmatory rRT–PCR results are listed in addition to the samples for which whole-genome sequencing was successfully completed. See Extended Data Table 4 for GISAID accession numbers for the 14 sequences generated.

## Rights and permissions

## [Reprints and Permissions](#)

## About this article

### Cite this article

Hale, V.L., Dennis, P.M., McBride, D.S. *et al.* SARS-CoV-2 infection in free-ranging white-tailed deer. *Nature* **602**, 481–486 (2022). <https://doi.org/10.1038/s41586-021-04353-x>

- Received: 12 November 2021
- Accepted: 14 December 2021
- Published: 23 December 2021
- Issue Date: 17 February 2022
- DOI: <https://doi.org/10.1038/s41586-021-04353-x>

### Share this article

Anyone you share the following link with will be able to read this content:

[Get shareable link](#)

Sorry, a shareable link is not currently available for this article.

[Copy to clipboard](#)

Provided by the Springer Nature SharedIt content-sharing initiative

---

This article was downloaded by **calibre** from <https://www.nature.com/articles/s41586-021-04353-x>

- Article
- Open Access
- [Published: 23 December 2021](#)

# Evolution of enhanced innate immune evasion by SARS-CoV-2

- [Lucy G. Thorne](#) [ORCID: orcid.org/0000-0001-7358-6047](#)<sup>1</sup> na1,
- [Mehdi Bouhaddou](#)<sup>2,3,4,5</sup> na1,
- [Ann-Kathrin Reusch](#)<sup>1</sup> na1,
- [Lorena Zuliani-Alvarez](#)<sup>2,3,4,5</sup> na1,
- [Ben Polacco](#) [ORCID: orcid.org/0000-0003-1570-9234](#)<sup>2,3,4,5</sup>,
- [Adrian Pelin](#)<sup>2,3,4,5</sup>,
- [Jyoti Batra](#)<sup>2,3,4,5</sup>,
- [Matthew V. X. Whelan](#)<sup>1</sup>,
- [Myra Hosmillo](#)<sup>6</sup>,
- [Andrea Fossati](#) [ORCID: orcid.org/0000-0001-5170-4903](#)<sup>2,3,4,5</sup>,
- [Roberta Ragazzini](#) [ORCID: orcid.org/0000-0003-2186-293X](#)<sup>7</sup> nAffl,
- [Irwin Jungreis](#) [ORCID: orcid.org/0000-0002-3197-5367](#)<sup>8,9</sup>,
- [Manisha Ummadi](#)<sup>2,3,4,5</sup>,
- [Ajda Rojc](#)<sup>2,3,4,5</sup>,
- [Jane Turner](#)<sup>1</sup>,
- [Marie L. Bischof](#)<sup>1</sup>,
- [Kirsten Obernier](#) [ORCID: orcid.org/0000-0002-4025-1299](#)<sup>2,3,4,5</sup>,
- [Hannes Braberg](#) [ORCID: orcid.org/0000-0002-7070-2257](#)<sup>2,3,4,5</sup>,
- [Margaret Soucheray](#)<sup>2,3,4,5</sup>,
- [Alicia Richards](#)<sup>2,3,4,5</sup>,
- [Kuei-Ho Chen](#) [ORCID: orcid.org/0000-0001-6541-0578](#)<sup>2,3,4,5</sup>,
- [Bhavya Harjai](#)<sup>2,3,4,5</sup>,
- [Danish Memon](#) [ORCID: orcid.org/0000-0002-1365-0710](#)<sup>10</sup>,
- [Joseph Hiatt](#)<sup>2,3,4,5</sup>,
- [Romel Rosales](#)<sup>11,12</sup>,
- [Briana L. McGovern](#) [ORCID: orcid.org/0000-0002-0492-9904](#)<sup>11,12</sup>,
- [Aminu Jahun](#) [ORCID: orcid.org/0000-0002-4585-1701](#)<sup>6</sup>,
- [Jacqueline M. Fabius](#)<sup>2,3,4,5</sup>,

- [Kris White](#) ORCID: [orcid.org/0000-0003-0889-0506<sup>11,12</sup>](https://orcid.org/0000-0003-0889-0506),
- [Ian G. Goodfellow](#) ORCID: [orcid.org/0000-0002-9483-510X<sup>6</sup>](https://orcid.org/0000-0002-9483-510X),
- [Yasu Takeuchi](#)<sup>1</sup> nAff15,
- [Paola Bonfanti](#) ORCID: [orcid.org/0000-0001-9655-3766<sup>7</sup>](https://orcid.org/0000-0001-9655-3766) nAff1,
- [Kevan Shokat](#) ORCID: [orcid.org/0000-0001-8590-7741<sup>2,3,4,5,13</sup>](https://orcid.org/0000-0001-8590-7741),
- [Natalia Jura](#) ORCID: [orcid.org/0000-0001-5129-641X<sup>2,3,5,14,15</sup>](https://orcid.org/0000-0001-5129-641X),
- [Klim Verba](#) ORCID: [orcid.org/0000-0002-2238-8590<sup>2,3,5</sup>](https://orcid.org/0000-0002-2238-8590),
- [Mahdad Noursadeghi](#) ORCID: [orcid.org/0000-0002-4774-0853<sup>1</sup>](https://orcid.org/0000-0002-4774-0853),
- [Pedro Beltrao](#)<sup>2,10</sup>,
- [Manolis Kellis](#) ORCID: [orcid.org/0000-0001-7113-9630<sup>8,9</sup>](https://orcid.org/0000-0001-7113-9630),
- [Danielle L. Swaney](#) ORCID: [orcid.org/0000-0001-6119-6084<sup>2,3,4,5</sup>](https://orcid.org/0000-0001-6119-6084),
- [Adolfo García-Sastre](#) ORCID: [orcid.org/0000-0002-6551-1827<sup>11,12,16,17,18</sup>](https://orcid.org/0000-0002-6551-1827),
- [Clare Jolly](#) ORCID: [orcid.org/0000-0002-4603-2281<sup>1</sup>](https://orcid.org/0000-0002-4603-2281),
- [Greg J. Towers](#) ORCID: [orcid.org/0000-0002-7707-0264<sup>1</sup>](https://orcid.org/0000-0002-7707-0264) &
- [Nevan J. Krogan](#) ORCID: [orcid.org/0000-0003-4902-337X<sup>2,3,4,5</sup>](https://orcid.org/0000-0003-4902-337X)

*Nature* volume 602, pages 487–495 (2022)

- 46k Accesses
- 1 Citations
- 780 Altmetric
- [Metrics details](#)

## Subjects

- [SARS-CoV-2](#)
- [Systems biology](#)

## Abstract

The emergence of SARS-CoV-2 variants of concern suggests viral adaptation to enhance human-to-human transmission<sup>1,2</sup>. Although much effort has focused on the characterization of changes in the spike protein in variants of concern, mutations outside of spike are likely to contribute to adaptation. Here, using unbiased abundance proteomics, phosphoproteomics, RNA sequencing and viral replication assays, we show that isolates of the Alpha (B.1.1.7) variant<sup>3</sup> suppress innate immune responses in airway epithelial cells more effectively than first-wave isolates. We found that the Alpha variant has markedly increased subgenomic RNA and protein levels of the

nucleocapsid protein (N), Orf9b and Orf6—all known innate immune antagonists. Expression of Orf9b alone suppressed the innate immune response through interaction with TOM70, a mitochondrial protein that is required for activation of the RNA-sensing adaptor MAVS. Moreover, the activity of Orf9b and its association with TOM70 was regulated by phosphorylation. We propose that more effective innate immune suppression, through enhanced expression of specific viral antagonist proteins, increases the likelihood of successful transmission of the Alpha variant, and may increase *in vivo* replication and duration of infection<sup>4</sup>. The importance of mutations outside the spike coding region in the adaptation of SARS-CoV-2 to humans is underscored by the observation that similar mutations exist in the N and Orf9b regulatory regions of the Delta and Omicron variants.

[Download PDF](#)

## Main

Innate immunity exerts strong selective pressure during viral transmission<sup>5,6,7</sup> and affects COVID-19 outcomes<sup>8,9,10</sup>. We hypothesized that the Alpha variant evolved enhanced innate immune escape through adaptations outside the spike proteins. Naturally permissive Calu-3 human lung epithelial cells infected with first-wave (early-lineage) SARS-CoV-2 induce a delayed innate response, which is driven by the activation of the RNA sensors RIG-I and MDA5 (ref. <sup>11</sup>). Delayed responses, compared to rapid viral RNA replication, suggest effective early innate immune antagonism and evasion<sup>12,13</sup>. Here, we evaluated differences in replication and host responses to Alpha and first-wave isolates: B lineage BetaCoV/Australia/VIC01/2020 (VIC) and B.1.13 hCoV-19/England/IC19/2020 (IC19) (Fig. <sup>1a</sup>). Input dose was normalized using viral genomic and subgenomic copies of envelope (E) RNA (quantitative PCR with reverse transcription; RT-qPCR). Dose normalization is critical because input viral genome levels correspond with innate immune activation at 24 hours post-infection (hpi) in Calu-3 cells<sup>11</sup>. Equalizing input genomes also allows assessment of infectivity per genome, which may vary between variants. We therefore confirmed that measurements of E copies and infectious virions in inocula correlate, and that the infectivity (infectious units per E copy), is comparable between Alpha and first-wave isolates, supporting our dosing approach (Extended Data Fig. <sup>1a</sup>).

**Fig. 1: The SARS-CoV-2 Alpha variant antagonizes innate immune activation more efficiently than early-lineage isolates.**

---

 **figure 1**

**a**, Protein-coding changes in SARS-CoV2 Alpha (red), early-lineage IC19 (grey) and early-lineage VIC (blue) are indicated in comparison to the Wuhan-Hu-1 reference genome (MN908947). **b–e**, Viral replication after infection of Calu-3 cells with 5,000 E copies per cell. LOD, limit of detection. **b**, Intracellular viral RNA. **c**, Nucleocapsid (N)<sup>+</sup> cells. **d**, Infectious virions (TCID<sub>50</sub>, 50% tissue culture infectious dose). **e**, Negative-sense viral RNA. **f**, Total area of dsRNA area per cell measured by single-cell immunofluorescence in Calu-3 cells infected with 2,000 E copies per cell. **g**, Expression and secretion of IFN $\beta$  by cells in **b**. **h**, Replication (intracellular viral RNA; 24 h) and IFN $\beta$  expression (24 h) and secretion (48 h) after infection of Calu-3 cells with 250 E copies per cell. **i, j**, Measurements of infection in primary differentiated HAE cells infected with 2,000 E copies per cell (**j**, 72 h). **k**, Expression of IFN $\beta$  and ISGs in cells from **j**. Mean  $\pm$  s.e.m. of one of three representative experiments performed in triplicate. For **i–k**,  $n = 6$ , two independent donors. For **f**, one

of two independent experiments with one data point per cell is shown. Two-way ANOVA (**b–e**) with Dunn's multiple comparison test (**f**), one-way ANOVA with Tukey's post-hoc test (**g, h, i**) or Wilcoxon matched-pairs signed rank test (**j, k**). Blue asterisks, Alpha versus VIC (blue lines and symbols); grey stars, Alpha versus IC19 (grey lines and symbols). \* $P < 0.05$ , \*\* $P < 0.01$ , \*\*\* $P < 0.001$ , \*\*\*\* $P < 0.0001$ ; NS, not significant.

## Alpha shows reduced interferon induction

We found that the replication of Alpha and first-wave isolates was comparable at a high and a low multiplicity of infection (MOI), measuring intracellular E copies, N positivity and infectious virion production (Fig. [1b–d](#), Extended Data Fig. [1b–d](#)). We observed a small but significant increase in N positivity after Alpha infection (Fig. [1c](#), Extended Data Fig. [1c](#)), which we explain later. As double-stranded RNA (dsRNA) intermediates are important pathogen-associated molecular patterns (PAMPs) sensed by the cell<sup>[11,14](#)</sup>, we also confirmed equivalent negative-sense RNA synthesis for Alpha and first-wave isolates (Fig. [1e](#), Extended Data Fig. [1f](#)), using strand-specific RT–qPCR (Extended Data Fig. [1e](#)). All isolates reached comparable levels of dsRNA-positive cells from 8 hpi (Extended Data Fig. [1g, h](#)). However, Alpha isolates exhibited a reduction in the total area of dsRNA per cell from 6 hpi, despite replication being otherwise comparable (Fig. [1f](#)). One possibility is that increased levels of the Alpha N protein (Fig. [1c](#), Extended Data Fig. [1c](#), Fig. [3](#)) contribute to innate immune evasion by sequestering dsRNA, causing epitope masking. Alternatively, Alpha may induce less endogenous dsRNA production from the expression of transposable elements that can contribute PAMPs to innate immune sensing<sup>[15,16,17](#)</sup>.

Identical levels of replication of each isolate enabled direct comparison of innate immune responses without confounding differences in the amount of virus. We found that Alpha infection led to lower expression and secretion of interferon- $\beta$  (IFN $\beta$ ) (Fig. [1g](#), Extended Data Fig. [2a](#)), a result that was confirmed with three independent Alpha isolates (Fig. [1h](#)). Differences in innate immune activation between variants did not translate to differences in viral replication in Calu-3 cells (Fig. [1](#)). We therefore compared replication and innate immune activation in primary human airway epithelial (HAE) cells differentiated at an air–liquid interface. Alpha showed enhanced replication in HAE cells (Fig. [1i,j](#)); the replication of VIC was particularly limited (Extended Data Fig. [2b](#)), probably owing to the absence of the D614G mutation in the spike protein, which confers a replication advantage in HAE cells and animal models<sup>[18,19,20](#)</sup>.

Thus, we compared innate replication and immune activation between Alpha and IC19 and found that innate activation was similar at 72 hpi (Fig. [1k](#)), despite substantially enhanced Alpha replication (Fig. [1i,j](#)). Viral replication was not increased beyond

input levels at early time points (24 hpi; Fig. 1*i*), therefore interferon-stimulated genes (ISGs) were not induced (data not shown). However, when innate immune activation was normalized for viral replication at 72 hpi, with the caveat that E copies may not fully represent the amount of viral dsRNA PAMPs, we found that Alpha induced less expression of IFN $\beta$  and ISGs than did IC19 per E copy (Extended Data Fig. 2*d*). This is consistent both with enhanced innate immune antagonism by Alpha and with similar innate immune activation in Fig. 1*k*, as Alpha replicates more efficiently in primary HAE cells.

As IFN sensitivity correlates with the transmission of other pandemic viruses<sup>5,6</sup>, we measured IFN $\beta$  sensitivity. Alpha was consistently less sensitive to IFN $\beta$  over a wide range of doses compared to VIC (Extended Data Fig. 2*c*). Notably, IC19 showed a similar reduction in IFN $\beta$  sensitivity to Alpha (Extended Data Fig. 2*c*), perhaps owing to the D614G change in the spike protein, which is shared between IC19 and Alpha; this mutation is associated with IFN resistance and enhanced entry efficiency<sup>18,21,22,23</sup>. Thus Alpha not only induces less IFN $\beta$  (Fig. 1*g, h, k*, Extended Data Fig. 2*a*), but is also less sensitive to inhibition.

## Enhanced innate antagonism by Alpha

To compare global host responses to SARS-CoV-2 variants, we performed mass spectrometry protein abundance and phosphorylation profiling and total RNA sequencing (RNA-seq) in Calu-3 cells at 10 and 24 hpi (Fig. 2*a*, [Supplementary Table 1](#)). We observed infection-driven changes in RNA abundance and protein phosphorylation, with fewer differences in protein abundance (Extended Data Fig. 3*a*). We also observed poor correlation between protein phosphorylation and protein or mRNA abundance, suggesting that phosphorylation is driven independently from changes in protein abundance (Extended Data Fig. 3*h*).

**Fig. 2: Global RNA-seq and proteomics reveal innate immune suppression by Alpha.**

---

 **figure 2**

**a**, Schematic of the experimental workflow. Calu-3 cells were infected with 5,000 E copies per cell of SARS-CoV-2 Alpha (red), early-lineage VIC (blue) or early-lineage IC19 (grey) or mock-infected (biological triplicates were performed for each time point). Phosphoproteomics and abundance proteomics analysis using a data-independent acquisition (DIA) and total RNA-seq were performed at 10 and 24 h. **b**, Unbiased pathway enrichment analysis. The  $-\log_{10}(P)$  values were averaged for enrichments using Alpha/VIC and Alpha/IC19 at 10 and 24 hpi to rank terms. The top five terms are shown. Innate immune system terms are shown in bold. ECM, extracellular matrix; AMI, acute myocardial infarction. **c**, Heat map depicting the  $\log_2$ -transformed fold change ( $\log_2\text{FC}$ ; colour) of ISGs<sup>25</sup> (by RNA-seq) comparing Alpha

to VIC or IC19. Black outlines indicate  $P < 0.01$ . **d**, Box plots show  $\log_2 FC$  of ISGs between Alpha/VIC, Alpha/IC19 or IC19/VIC. Dots indicate different ISGs. Boxes indicate median (middle line) and interquartile range (upper and lower lines). Blue indicates comparisons with Alpha; black indicates comparisons between early-lineage viruses (IC19 and VIC). **e**, RT-qPCR analysis of bolded ISGs from **c** in cells infected with 2,000 E copies per cell. Mean  $\pm$  s.e.m. **f**, Number of phosphorylation sites significantly dysregulated for Alpha, VIC or IC19 versus mock at an absolute  $\log_2 FC > 1$  and adjusted  $P < 0.05$ . **g**, Kinase activities for the top enriched terms for the phosphoproteomics dataset ‘Reactome innate immune system’ (**b**, right). Two-tailed student’s *t*-test (**d**) or two-way ANOVA with Tukey’s multiple comparisons post-hoc test (**e**). Blue asterisks, Alpha versus VIC (blue bars); grey stars, Alpha versus IC19 (grey bars). \* $P < 0.05$ , \*\* $P < 0.01$ , \*\*\* $P < 0.001$ , \*\*\*\* $P < 0.0001$ , or exact  $P$  value (**d**); NS, not significant.

Gene set enrichment analysis<sup>24</sup> (GSEA) comparing Alpha to first-wave isolates highlighted pathways that relate to the innate immune system among the top five terms for RNA, protein abundance and phosphorylation (Fig. **2b**, Extended Data Fig. **4a–c**, [Supplementary Table 2](#)). The highest-scoring terms were related to IFN $\alpha$ , IFN $\beta$ , cytokine and chemokine signalling, and were most enriched for the RNA and protein phosphorylation datasets (Fig. **2b**). In addition to lower production of IFN $\beta$  (Fig. **1g, h**, Extended Data Fig. **2a, d**), infection with Alpha resulted in reduced expression of ISGs in RNA-seq data (10 and 24 hpi) and protein abundance data (24 hpi) using an ISG set<sup>25</sup> (Methods, [Supplementary Table 3](#), Fig. **2c, d**, Extended Data Fig. **4d–f**). For a subset of genes (*CXCL10*, *IFIT2*, *MX1*, *IFIT1* and *RSAD2*) (Fig. **2e**), as well as type III IFN $\lambda 1$  and IFN $\lambda 3$  (Extended Data Fig. **5a**), we confirmed reduced induction by multiple Alpha isolates (RT-qPCR).

We observed lower overall changes in protein phosphorylation early in infection for Alpha (Fig. **2f**). Accordingly, GSEA revealed that pathways with reduced phosphorylation at 10 hpi—that is, decreased activation—are related to innate immune responses (Extended Data Fig. **4c**), consistent with enhanced antagonism by Alpha. Notably, this was reversed at 24 hpi as Alpha caused enhanced phosphorylation later in infection (Extended Data Fig. **4c**). This led us to investigate the differential regulation of kinase signalling cascades, especially with respect to innate immune signalling. We used the phosphoproteomics data to estimate kinase activities for 191 kinases on the basis of regulation of their known substrates<sup>26,27</sup> ([Supplementary Table 4](#)), and grouped kinases according to their temporal dynamics (Extended Data Fig. **6a**). Of note, we did not observe any correlation between kinase activity and abundance in protein and RNA datasets (Extended Data Fig. **6b**), suggesting that changes in kinase activity are not driven by corresponding changes in kinase abundance. We identified 24 kinases from the top enriched term (‘Reactome innate immune system’; Fig. **2b**), which we clustered by similar pathway membership (Fig. **2g**, Methods). At 10 hpi, we

observed decreased activity of TBK1, as well as protein kinase A, PRKDC, RET, AKT–mTOR, ERK and JNK pathways. Given the central role of TBK1 in nucleic acid sensing, we evaluated known TBK1 substrates in greater detail to support the kinase analysis (Fig. 2g), and confirmed the lower levels of phosphorylation of known TBK1 substrates, including OPTN (ref. 28) and Ser72 in RAB7A (ref. 29), for Alpha compared to first-wave isolates at 10 hpi (Extended Data Fig. 6c). At 24 hpi, the activity of TBK1 and PRKDC kinases, as well as that of JNK, ERK and PKA pathway kinases, was increased for Alpha compared to VIC (Fig. 2g), consistent with the increased phosphorylation in innate-immune-system-enriched pathway terms (Extended Data Fig. 4c). Persistently lower induction of IFN by Alpha at 24 and 48 hpi (Figs. 1, 2, Extended Data Fig. 1), despite higher activation of TBK1 at 24 hpi, suggests antagonism downstream of TBK1; for example, by increased expression of SARS-CoV-2 Orf6 (Fig. 3), which suppresses the nuclear transport of inflammatory transcription factors<sup>13</sup>. Concordantly, pro-inflammatory mRNA induction (*IL6*, *IL8*, *CCL2* and *TNF*) and cytokine release (CXCL10, IL6 and CCL5) were significantly lower after infection with Alpha, compared to first-wave isolates (Extended Data Fig. 5b–d). This is consistent with a sustained reduction in cellular activation driven by inhibition of pathways upstream and downstream of TBK1 by Alpha. We did not observe differences in CCL3 induction, suggesting that not all inflammatory pathways are differentially regulated between viruses (Extended Data Fig. 5c, d). Thus, Alpha-enhanced innate immune antagonism, as judged by decreased protein phosphorylation, is only observed at early time points after infection, suggesting a delayed activation of signalling pathways involved in viral recognition compared to early-lineage viruses.

**Fig. 3: The SARS-CoV-2 Alpha variant upregulates innate immune antagonists at the subgenomic RNA and protein level.**

---

 **figure 3**

**a**, Top, the  $\log_2$  ratio of Alpha to VIC sgRNA normalized to total genomic RNA per time point and virus (from RNA-seq). Bottom, the  $\log_2$  ratio of summed peptide intensities per viral protein comparing Alpha to VIC (from proteomics analysis) ( $n = 3$ ). Orf3a–d refers to Orf3a, Orf3b, Orf3c and Orf3d. S, spike protein; E, envelope protein; M, membrane protein. ND, not detected. **b–d**, Quantification of Orf9b (**b**), Orf6 (**c**) and N (**d**) sgRNA from the RNA-seq dataset (top) and summed peptides per viral protein (bottom). **e**, Quantification of Orf9b and N (left) or Orf6 (right) sgRNA abundance by RT–qPCR (24 hpi). **f**, Representative western blot of Orf6, N and S expression in infected Calu-3 cells (2,000 E copies per cell) at 24 hpi ( $n = 3$ ). **g**, Pie

chart depicting the proportion (shown as percentages) of total sgRNA mapping to each viral sgRNA for Alpha at 24 hpi. VIC percentages in parentheses. **h**, sgRNA log<sub>2</sub>-normalized counts (dot height) projected onto their identified start sites on the SARS-CoV-2 genome (24 hpi). Canonical and two non-canonical sgRNAs (Orf9b and N\*) are depicted. **i**, Scatter plot of sgRNA abundance in Alpha or VIC at 24 hpi. Grey dots indicate other non-canonical sgRNAs containing a leader sequence but no clear start codon. Mean  $\pm$  s.e.m. (**a–e**). Two-way ANOVA with Tukey's multiple comparisons post-hoc test (**c–e**). \* $P < 0.05$ , \*\* $P < 0.01$ , \*\*\* $P < 0.001$ , \*\*\*\* $P < 0.0001$ ; NS, not significant.

## Higher expression of innate antagonists by Alpha

We next examined the viral RNA-seq and proteomic data, seeking to understand the differences between Alpha and first-wave isolates that underlie the contrasting host responses (Fig. 3a, Extended Data Fig. 7a, b, Supplementary Tables 6, 7). As RNA replication, measured by the levels of genomic and subgenomic (sgRNA) E, was similar between variants (Fig. 1, Extended Data Fig. 1), we determined the levels of each sgRNA by selecting transcripts with the 5' leader sequence, derived from the 5' genomic RNA during sgRNA synthesis (Fig. 3a, Extended Data Fig. 7). We observed similar levels of Nsp1, Nsp2 and Nsp3 proteins (Orf1ab) translated from genomic RNA (Fig. 3a), which is again consistent with comparable levels of infection, and thus enables effective comparisons of transcription and protein expression between variants.

Notably, we found a large increase in the innate immune antagonist Orf9b (97-amino-acid version<sup>30</sup>, encoded by an alternative reading frame within N) in Alpha compared to first-wave isolates (Fig. 3a, b Extended Data Fig. 7b), with a corresponding increase in Orf9b sgRNA<sup>31</sup> (an increase of more than 80-fold for Alpha sgRNA compared to VIC, and 64.5-fold for Alpha compared to IC19, at 24 hpi; Fig. 3a, b, Extended Data Fig. 7a). The increase in Orf9b transcription in Alpha is likely to be influenced by nucleotide changes 28,280 GAT>CTA (conferring the D3L substitution in the N protein), which introduces an enhanced transcriptional regulatory sequence (TRS) upstream of Orf9b<sup>31</sup> (Extended Data Fig. 8a–c). However, the overall amount of Alpha Orf9b sgRNA remains low (Fig. 3g). Thus, it is possible that increased expression of the Orf9b protein also derives from enhanced leaky scanning of the N sgRNA owing to a single-nucleotide deletion that weakens the Alpha N Kozak translation initiation context (position 28,271 in VIC and IC19; Fig. 6). The three-nucleotide mutation leading to N(D3L) also modifies the Alpha Orf9b Kozak context, which could influence Orf9b translation efficiency<sup>32</sup>. We predict a complex interplay between mutations that results in the enhancement of both Orf9b and N expression.

We also found that Alpha had a significant increase in sgRNA and protein expression (24 hpi) for a second innate immune regulator, Orf6<sup>12,13</sup> (Fig. 3a,c, Extended Data Fig. 7a, [Supplementary Table 6](#)). The specific mutations that influence Orf6 expression remain unclear. In addition, we detected increased sgRNA and protein levels in Alpha of N, a third innate immune regulator<sup>33</sup> (Fig. 3a,d). This is consistent with the increase in N-positive cells measured during Calu-3 infection (Fig. 1c, Extended Data Fig. 1c). We also observed enhancement of Orf3a, membrane (M) and Orf7b proteins at 24 hpi for Alpha, with only very modest changes observed at the RNA level (Fig. 3a, Extended Data Fig. 7a,c,d). We confirmed the upregulation of Alpha Orf9b, N and Orf6 sgRNA using RT-qPCR (Fig. 3e) and the increased expression of Alpha Orf6 and N proteins by immunoblot (Fig. 3f). These findings are consistent with the reported enhanced expression of Alpha Orf9b, Orf6 and N sgRNA in clinical samples<sup>31</sup>. The proportion of each sgRNA of the total sgRNA reads is summarized for each variant in Fig. 3g and Extended Data Fig. 7g. Of note, we observed an additional sgRNA in Alpha, called N\* (ref. 31), with an in-frame start codon at N M210 encoding the C terminus of the N protein (Fig. 3h, [Supplementary Table 7](#)). N\* synthesis is likely driven by the triple nucleotide mutations (encoding the R203K/G204R substitutions in the Alpha N protein) just upstream of the N\* start codon, which create a new TRS for N\* transcription, as previously suggested<sup>31</sup>. Accordingly, we did not detect N\* sgRNA in VIC or IC19 above background levels, while it accounted for 0.9% of the total sgRNA in Alpha (Fig. 3g). Indeed, measurements of sgRNA abundance were consistent with Orf9b and N\* being the most differentially expressed sgRNA between Alpha and first-wave isolates (Fig. 3i, Extended Data Fig. 7c). We note that Alpha sgRNA synthesis is not universally increased (Fig. 3a), because M and spike sgRNAs are not enhanced.

## Phosphorylation regulates Orf9b activity

To further understand differences in host responses to Alpha, we used the RNA-seq dataset to estimate transcription factor activities by mapping target genes to corresponding transcriptional regulators (Extended Data Fig. 6d, [Supplementary Table 5](#)). We extracted significantly regulated transcription factors within the top five most enriched terms from the unbiased RNA-seq pathway enrichment analysis (Fig. 2b). This revealed that IRF and STAT transcription factor families are significantly less activated by Alpha than by first-wave viruses (Fig. 4a). Consistently, measuring IRF3 nuclear translocation by single-cell immunofluorescence showed reduced activation of IRF3 after infection with Alpha compared to infection with VIC (Fig. 4b). STAT1, STAT2 and IRF9 lie downstream of the type I IFN receptor, and potent inhibition by Alpha is consistent with increased levels of Orf6, which is known to inhibit the nuclear translocation of STAT1 and IRF3 (refs. 12,13).

**Fig. 4: Orf9b binds TOM70 and antagonizes innate immune activation downstream of RNA sensing.**

 figure 4

**a**, Transcription factor (TF) activities in the five top enriched terms for the RNA-seq dataset (Fig. 2b, left); rows clustered hierarchically based on activity magnitude. Black outlines show activities  $>1.5$  or  $<-1.5$ . **b**, IRF3 nuclear to cytoplasmic ratio measured by single-cell immunofluorescence at 24 h in cells infected at 2,000 E copies per cell; 1,000 randomly sampled cells per condition (cut-off of  $0.1 \geq <5$ ). **c**, Cryo-electron microscopy of SARS-CoV-2 Orf9b (yellow) in complex with TOM70 (blue) (Protein Data bank (PDB) code: 7KDT)<sup>40</sup>. Serine residues (Ser50 and Ser53) in Orf9b in the TOM70-binding site are shown in red. **d**, Co-immunoprecipitation of Orf9b wild type (WT) or point mutants with TOM70 in HEK293T cells. **e**, ISG56-reporter activation by poly I:C in the presence of Orf9b WT, S50E/S53E or empty vector (EV) in HEK293T cells. **f**, Schematic of proposed innate immune antagonism by Orf9b. (i) When S53 is unphosphorylated, Orf9b binds TOM70 to inhibit innate immune signalling. (ii) When S53 is phosphorylated, Orf9b can no longer interact or antagonize innate immune activation. **g**, Ratio between the intensity of Orf9b peptide phosphorylated on Ser53 (S53p) and total Orf9b (as calculated in Fig. 3b, bottom) from phospho- and abundance proteomics of Calu-3 cells (Fig. 2). **h**, ISG56-reporter activation by poly:IC in the presence of N (VIC), N (Alpha) or EV in HEK293T cells. Mean  $\pm$  s.e.m. Mann–Whitney test (**b**) or two-way ANOVA with Tukey’s post-hoc test (**e, h**). For **e**, Orf9b WT versus Orf9b(S50E/S53E). For **h**, blue stars: VIC versus EV; red stars, Alpha versus EV.  $P < 0.05$ , \*\* $P < 0.01$ , \*\*\* $P < 0.001$ , \*\*\*\* $P < 0.0001$ .

Decreased activation of TBK1 by Alpha (Fig. 2g) also suggests antagonism upstream of IRF3 by additional mechanisms. The N protein is reported to antagonize the activation of RNA sensors<sup>33</sup>. Alpha N has four coding changes as compared to first-wave viruses (Fig. 1a). However, the antagonism of poly I:C activation of an *ISG56*-luciferase reporter by Alpha N was comparable to antagonism by the N protein of first-wave viruses, suggesting that these coding changes do not enhance the potency of innate antagonism for Alpha N (Fig. 4h). Nonetheless, increased levels of Alpha N during infection may facilitate innate antagonism and evasion through enhanced sequestration of viral and host-derived PAMPs<sup>34</sup> (Fig. 1f).

We have previously reported that SARS-CoV-2 Orf9b, which is expressed to significantly higher levels by Alpha (Fig. 3), interacts with human TOM70<sup>35</sup>, a mitochondrial import receptor that is required for the MAVS activation of TBK1 and IRF3 and subsequent RNA-sensing responses<sup>36,37</sup>. We previously found that two serine residues buried within the Orf9b-TOM70-binding pocket, Orf9b Ser50 and Ser53, are phosphorylated during SARS-CoV-2 infection<sup>38,39,40</sup> (Fig. 4c). Here we discovered that mutating Ser53 alone or both Ser50 and Ser53 in Orf9b to the phosphomimetic glutamic acid residue disrupted the co-immunoprecipitation of Orf9b and TOM70 (Fig. 4d) and abolished Orf9b antagonism of *ISG56*-luciferase reporter gene activation by poly I:C (Fig. 4e), presumably by preventing interaction with TOM70 (Fig. 4c). In addition, although the S53A mutation compromised protein stability (evidenced by immunoblot density, Extended Data Fig. 9), it confirmed the contribution of Ser53 to TOM70 binding, because S53A immunoprecipitated less TOM70 when normalized for Orf9b protein levels (Fig. 4d, Extended Data Fig. 9). Although it is unclear which kinases are responsible for Orf9b phosphorylation, our data are consistent with Orf9b suppressing signalling downstream of MAVS, by targeting TOM70, and also the regulation of Orf9b by host-mediated phosphorylation (Fig. 4f). Notably, we detected lower levels of Alpha Orf9b Ser53 phosphorylation at 10 hpi, but higher levels at 24 hpi, compared to first-wave isolates (Fig. 4g). This suggests that not only does Alpha express more Orf9b early in infection, but it may also be regulated more effectively by unknown host kinases to manipulate host innate immunity, consistent with enhanced host adaptation by Alpha.

## Discussion

Our data reveal that changes outside the spike protein—including noncoding changes—are important in SARS-CoV-2 adaptation through influencing sgRNA and protein expression. For Alpha, we discovered an upregulation of key viral innate antagonists, Orf9b, Orf6 and N, leading to enhanced innate immune evasion (Fig. 5). We propose that *in vivo*, enhanced innate immune antagonism by Alpha contributes to its transmission advantage, by enhancing replication through reducing or delaying early

host innate responses, which otherwise protect airway cells from infection and limit viral dissemination. This is also consistent with reports of prolonged viral shedding of Alpha<sup>41,42</sup>, suggesting less effective control of replication. Enhanced innate evasion has also been linked to transmission of HIV<sup>5,6</sup>.

**Fig. 5: Antagonism of innate immune activation by Alpha.**

 figure 5

SARS-CoV-2 Alpha has evolved more effective innate immune antagonisms. First-wave isolates activate a delayed innate response in airway epithelial cells relative to rapid viral replication, indicative of viral innate immune antagonism early in infection. The known innate immune antagonists Orf9b, Orf6 and N act at different levels to

inhibit RNA sensing. Orf6 inhibits IRF3 and STAT1 nuclear translocation<sup>12,13</sup>; N prevents activation of the RNA sensor RIG-I<sup>33</sup>; and Orf9b inhibits RNA sensing through interaction with TOM70, regulated by phosphorylation. Alpha has evolved to produce more sgRNA for these key innate immune antagonists, which leads to increased protein levels and enhanced innate immune antagonism as compared to first-wave isolates. gRNA, genomic RNA.

The SARS-CoV-2 Delta (B.1.617.2) variant of concern (VOC) contains the same noncoding deletion in the N Kozak sequence as Alpha, and the recently identified Omicron (B.1.1.529) VOC has a nucleotide substitution (28271A>T) at the same position, which would be predicted to confer a similar effect on the N Kozak context and on translation initiation (Fig. 6). Therefore, we suggest that these changes could represent key human adaptations that influence Orf9b levels, which, in turn, would dampen the immune response. Of note, the three-nucleotide change (28881–28883 GGG->AAC) that confers N\* sgRNA synthesis is also present in both the Gamma (P.1/B.1.1.28.1) and the Omicron VOCs (Fig. 6). However, more work is needed to determine whether N\* is involved in dsRNA sequestration or innate antagonism. Our data do not rule out coding changes in other innate antagonists being important for Alpha adaptation to humans, but highlight the need for quantitative sequencing of sgRNAs with future VOCs.

**Fig. 6: VOCs present similar nucleotide mutations in N and Orf9b.**

 figure 6

**a, b,** Genomic alignment of first-wave isolates and five VOCs showing sections of N and its 5' region, codonized by CodAlignView in the reading frames of N (**a**) and Orf9b (**b**). The alignment includes TRS for N sgRNA present in all genomes; partial TRS for Orf9b sgRNA only in Alpha; TRS for N\* sgRNA in Gamma and partial TRS in Alpha and Omicron. All mutations in Orf9b are colour-coded to indicate

conservative (dark green) and radical (red) amino acid changes in Orf9b protein. We also highlighted a one-base deletion at 5' of the N start codon in Alpha and Delta and an A to T substitution in Omicron, which change their adequate (A in -3, T in +4) Kozak initiation context to the weak (T in -3, T in +4) context, and could lead to more leaky scanning translation of Orf9b from the N sgRNA.

It is noteworthy that host phosphorylation regulates Orf9b activity. We hypothesize that unphosphorylated Orf9b is maximally active early after infection to permit effective innate antagonism and viral production, but that as host innate activation begins, Orf9b becomes phosphorylated and switched off, which drives subsequent innate immune activation. Such an inflammatory switch may have evolved to enhance transmission by increasing inflammation at the site of infection once virus production is high. This switch is enhanced in Alpha, as evidenced by a greater differential in Orf9b phosphorylation between early and late time points, consistent with a delayed onset of symptoms for Alpha, and enhanced inflammatory disease<sup>43,44</sup>. Understanding Orf9b phosphorylation mechanisms will be key to understanding this switch. We previously identified MARK1, MARK2 and MARK3 kinases as interaction partners of Orf9b<sup>35</sup> and ongoing studies will reveal their role in infection and the innate response.

The importance of Alpha adaptation to avoid innate immunity is also underlined by identification of the first recombinant VOC<sup>45</sup>. This variant has recombined around the Orf6–Orf7 junction, combining the spike protein adaptations of enhanced entry, furin cleavage and antibody escape of the Delta variant<sup>46,47,48,49</sup> with the enhanced innate immune antagonism of the Alpha variant, mediated by increased expression of N, N\* and Orf9b proteins. Inter-VOC recombination is a key development in the pandemic, consistent with the known importance of recombination in the generation of coronavirus diversity<sup>50</sup>—in this instance linking Alpha and Delta adaptations. Our findings highlight the importance of studying changes outside the spike protein to predict the behaviour of current and future VOCs, and emphasize the importance of innate immune evasion in the ongoing process of SARS-CoV-2 adaptation to humans.

## Methods

### Cell culture

Calu-3 cells were purchased from ATCC (HTB-55) and Caco-2 cells were a gift from D. Bailey. Hela-ACE2 cells were a gift from J. E Voss<sup>51</sup>. HEK293T cells were a gift from J. Luban. Cells were cultured in Dulbecco's modified Eagle's medium (DMEM) supplemented with 10% heat-inactivated FBS (Labtech) and 100 U ml<sup>-1</sup> penicillin–streptomycin, with the addition of 1% sodium pyruvate (Gibco) and 1% Glutamax. All

cells were passaged at 80% confluence and they were frequently monitored for mycoplasma contamination. For infections, adherent cells were trypsinized, washed once in fresh medium and passed through a 70- $\mu$ m cell strainer before seeding at  $0.2 \times 10^6$  cells per ml into tissue-culture plates. Calu-3 cells were grown to 60–80% confluence before infection as described previously<sup>52</sup>. Primary normal human bronchial/tracheal epithelial cells (ATCC PCS-300-010) were expanded at the density of 6,000 cells per cm<sup>2</sup> on a layer of lethally irradiated mouse 3T3-J2 cells<sup>53</sup> with keratinocyte culture medium cFAD (3:1 DMEM (Gibco) to F-12 Nut Mix (Ham) (Gibco)), 10% FBS (Sigma), 1% penicillin–streptomycin (100 $\times$ , Sigma), 0.4  $\mu$ g ml<sup>-1</sup> hydrocortisone (Calbiochem), 5  $\mu$ g ml<sup>-1</sup> insulin,  $10 \times 10^{-10}$  M cholera toxin (Sigma) and  $2 \times 10^{-9}$  M triiodothyronine (Sigma). Cells were stimulated with 10 ng ml<sup>-1</sup> hEGF (PeproTech) at day 3 and 5 of culture. Sub-confluent cultures were trypsinized with 0.25% Trypsin-EDTA (Sigma) and seeded at  $0.05 \times 10^6$  cells into 0.4- $\mu$ m transparent 12-well transwell inserts (Greiner) in CFAD. When cells reached confluence, basal medium was replaced with complete PneumaCult-ALI medium (StemCell) and apical medium was removed completely. Cells were cultured at the air–liquid interface for 21–24 days and basal medium was replaced every 2–3 days.

## Viruses

SARS-CoV-2 isolate VIC was provided by NISBC, and IC19, Alpha, Alpha (B) and Alpha (C) have been described previously<sup>54</sup>; full isolate names and GISAID references are listed below. Viruses were propagated by infecting Caco-2 cells at MOI 0.01 TCID<sub>50</sub> per cell, in culture medium at 37 °C. Virus was collected at 72 hpi and clarified by centrifugation at 4,000 rpm for 15 min at 4 °C to remove any cellular debris. We have previously shown that infection of Caco-2 cells in these conditions does not result in activation of the innate response or cytokine carryover<sup>52</sup>. Virus stocks were aliquoted and stored at –80 °C. Virus stocks were quantified by extracting RNA from 100  $\mu$ l of supernatant with 1  $\mu$ g carrier RNA using Qiagen RNeasy clean-up RNA protocol, before measuring viral E RNA copies per ml by RT–qPCR as described below. VIC virus refers to isolate BetaCoV/Australia/VIC01/2020 and PANGO lineage B. IC19 virus refers to isolate hCoV-19/England/IC19/2020, PANGO lineage B.1.13 and GISAID accession ID EPI\_ISL\_475572. Alpha virus refers to isolate hCoV-19/England/204690005/2020, PANGO lineage Alpha and GISAID accession ID EPI\_ISL\_693401. Alpha (B) virus refers to isolate hCoV-19/England/205090256/2020, PANGO lineage Alpha and GISAID accession ID EPI\_ISL\_747517. Alpha (C) refers to isolate hCoV-19/England/205080610/2020, PANGO lineage Alpha and GISAID accession ID EPI\_ISL\_723001.

## Viral sequencing and assembly

Viral stocks were sequenced to confirm each stock was the same at consensus level to the original isolate. Sequencing was performed using a multiplex PCR-based approach using the ARTIC LoCost protocol and v3 primer set as described<sup>55,56</sup>. Amplicon libraries were sequenced using MinION flow cells v.9.4.1 (Oxford Nanopore Technologies). Genomes were assembled using reference-based assembly to the MN908947.3 sequence and the ARTIC bioinformatic pipeline using 20× minimum coverage cut-off for any region of the genome and 50.1% cut-off for calling single-nucleotide polymorphisms.

## Infection of human cells

For infections, MOIs were calculated using E copies per cell quantified by RT–qPCR. Cells were inoculated with diluted virus stocks for 2 h at 37 °C, subsequently washed once with PBS and fresh culture medium was added. At the indicated time points, cells were collected for analysis. For primary HAE infections, virus was added to the apical side for 2 h at 37 °C. Supernatant was then removed and cells were washed twice with PBS. All liquid was removed from the apical side and basal medium was replaced with fresh Pneumacult ALI medium for the duration of the experiment. Virus release was measured at the indicated time points by extracting viral RNA from apical PBS washes.

## Virus quantification by TCID50

Virus titres were determined by TCID50 in Hela-ACE2 cells. In brief, 96-well plates were seeded at  $5 \times 10^3$  cells per well in 100 µl. Eight 10-fold serial dilutions of each virus stock or supernatant were prepared and 50 µl added to four replicate wells. Cytopathic effect (CPE) was scored at 2–3 days after infection. TCID50 per ml was calculated using the Reed & Muench method, and an Excel spreadsheet created by B. D. Lindenbach was used for calculating TCID50 per ml values<sup>57</sup>.

## RT–qPCR of viral proteins in infected cells

RNA was extracted using RNeasy Micro Kits (Qiagen) and residual genomic DNA was removed from RNA samples by on-column DNase I treatment (Qiagen). Both steps were performed according to the manufacturer's instructions. cDNA was synthesized using SuperScript III with random hexamer primers (Invitrogen). RT–qPCR was performed using Fast SYBR Green Master Mix (Thermo Fisher Scientific) for host gene expression and subgenomic RNA expression or TaqMan Master mix (Thermo Fisher Scientific) for viral RNA quantification, and reactions were performed on the QuantStudio 5 Real-Time PCR systems (Thermo Fisher Scientific). Viral E RNA copies were determined by a standard curve, using primers and a Taqman probe specific for E, as described elsewhere<sup>58</sup> and below. The primers used for quantification

of viral subgenomic RNA are listed below; the same forward primer against the leader sequence was used for all reactions, and is as described by the Artic Network<sup>31,55</sup>. Using the  $2^{-\Delta\Delta C_t}$  method, sgRNA levels were normalized to GAPDH to account for differences in RNA loading and then normalized to the level of Orf1a gRNA quantified in the same way for each variant to account for differences in the level of infection. Host gene expression was determined using the  $2^{-\Delta\Delta C_t}$  method and normalized to *GAPDH* expression using the primers listed below.

The following primers and probes were used:

SARS-CoV-2 E\_Sarboco\_Fwd: 5'-ACAGGTACGTTAATAGTTAATAGCGT-3';  
SARS-CoV-2 E\_Sarboco\_Probe1: 5'-FAM-  
ACACTAGCCATCCTTACTGCGCTTCG-TAMRA-3'; SARS-CoV-2  
E\_Sarboco\_Rev: 5'-ATATTGCAGCAGTACGCACACA-3'; 5'\_Leader\_Fwd:  
ACCAACCAACTTCGATCTCTTGT; Orf1a\_Rev:  
CCTCCACGGAGTCTCCAAAG;  
Orf6\_sg\_Rev:GAGGTTATGATGTAATCAAGATT; Orf9b\_N\_sgRNA\_Rev:  
CACTGCGTTCTCCATTCTGG; S\_sgRNA\_Rev:  
GTCAGGGTAATAAACACCACGTG; Orf3a\_sgRNA\_Rev:  
GCAGTAGCGCGAACAAAACTTG; CCL2: Fwd 5'-  
CAGCCAGATGCAATCAATGCC-3'; Rev 5'-TGGAATCCTGAACCCACTTCT-3';  
CCL3: Fwd 5'-CAGCCAGATGCAATCAATGCC-3'; Rev 5'-  
TGGAATCCTGAACCCACTTCT-3'; CXCL10: Fwd 5'-  
TGGCATTCAAGGAGTACCTC-3'; Rev 5'-TTGTAGCAATGATCTAACACAG-3';  
GAPDH: Fwd 5'-GGGAAACTGTGGCGTGAT-3'; Rev 5'-  
GGAGGAGTGGGTGTCGCTGTT-3'; IFIT1: Fwd 5'-  
CCTCCTGGTTCGTCTACA-3'; Rev 5'-GGCTGATATCTGGGTGCCTA-3';  
IFIT2: Fwd 5'-CAGCTGAGAATTGCACTGCAA-3'; Rev 5'-  
CGTAGGCTGCTCTCCAAGGA-3'; IFNB1: Fwd 5'-  
AGGACAGGATGAACTTGAC-3'; Rev 5'-TGATAGACATTGCCAGGAG-3';  
IFNL1: Fwd 5'-CACATTGGCAGGTTCAAATCTCT-3'; Rev 5'-  
CCAGCGGACTCCTTTGG-3'; IFNL3: Fwd 5'-  
TAAGAGGGCCAAAGATGCCTT-3'; Rev 5'-CTGGTCCAAGACATCCCC-3'; IL-  
6: Fwd 5'-AAATTCCGGTACATCCTCGACG-3'; Rev 5'-  
GGAAGGTTCAGGTTTTCT-3'; IL-8: Fwd 5'-  
ATGACTTCCAAGCTGGCCGTGGCT-3'; Rev 5'-  
TCTCAGCCCTCTCAAAAACCTCTC-3'; MX1: Fwd 5'-  
ATCCTGGATTGGGGCTT-3'; Rev 5'-CCGCTGTCGCTGGTGTGCG-3';  
RSAD2: Fwd 5'-CTGTCCGCTGGAAAGTG-3'; Rev 5'-  
GCTTCTTCTACACCAACATCC-3'; TNF: Fwd 5'-  
AGCCTCTCTCCTTGATCGT-3'; Rev 5'-  
GGCTGATTAGAGAGAGGTCCTGG-3'.

## Negative-sense-specific RT–qPCR

A negative-sense-strand-specific assay for the SARS-CoV-2 E gene was designed and established. A standard reference for the E gene was generated using fragment 11 (genome positions 25,595–28,779)<sup>59</sup> provided by V. Thiel. The strand-specific RNA standards were synthesized by in vitro transcription using T7 RNA polymerase, in which each RNA template is flanked with a specific non-viral sequence tag. Reverse transcription was performed using  $10^{10}$  copies of either positive- or negative-strand RNA with or without addition of excess copies ( $10^7$ ) of the opposite strand to test the assay specificity. Negative-sense-specific qPCR reactions were performed using cDNA templates of the negative-strand templates serially diluted by 10-fold from  $10^7$  to  $10^2$ . The qPCR reactions were conducted as follows: 95 °C for 2 min, followed by 45 cycles of 95 °C for 10 s and 60 °C for 60 s on a ViiA 7 real time PCR machine (Applied Biosystems). Results were analysed using the ViiA 7 software v.1.1 (Applied Biosystems). To evaluate the specificity of the assay, the qPCR was performed using the primers of the opposite strand side-by-side or in the presence of excess copies of the opposite strand.

## Western blot for viral proteins in infected cells

For detection of N, Orf6, spike and tubulin expression, whole-cell protein lysates were extracted with RIPA buffer, and then separated by SDS-PAGE, transferred onto nitrocellulose and blocked in PBS with 0.05% Tween 20 and 5% skimmed milk. Membranes were probed with rabbit-anti-SARS spike (Invitrogen, PA1-411-1165, 0.5 µg ml<sup>-1</sup>), rabbit-anti-Orf6 (Abnova, PAB31757, 4 µg ml<sup>-1</sup>), Cr3009 SARS-CoV-2 cross-reactive human-anti-N antibody (1 µg ml<sup>-1</sup>) (a gift from L. McCoy) and mouse-anti-α-tubulin (SIGMA, clone DM1A), followed by IRDye 800CW or 680RD secondary antibodies (Abcam, goat anti-rabbit, goat anti-mouse or goat anti-human). Blots were imaged using an Odyssey Infrared Imager (LI-COR Biosciences) and analysed with Image Studio Lite software.

## Flow cytometry of infected cells

For flow cytometry analysis, adherent cells were recovered by trypsinization and washed in PBS with 2 mM EDTA (PBS/EDTA). Cells were stained with fixable Zombie UV Live/Dead dye (BioLegend) for 6 min at room temperature. Excess stain was quenched with FBS-complemented DMEM. Unbound antibody was washed off thoroughly and cells were fixed in 4% PFA before intracellular staining. For intracellular detection of SARS-CoV-2 nucleoprotein, cells were permeabilized for 15 min with intracellular staining perm wash buffer (BioLegend). Cells were then incubated with 1 µg ml<sup>-1</sup> CR3009 SARS-CoV-2 cross-reactive antibody (a gift from L.

McCoy) in permeabilization buffer for 30 min at room temperature, washed once and incubated with secondary Alexa Fluor 488-donkey-anti-human IgG (Jackson Labs). All samples were acquired on a BD Fortessa X20 using BD FACSDiva software. Data were analysed using FlowJo v.10 (Tree Star).

## Innate immune sensing assay

HEK293T cells were seeded in 48-well plates ( $5 \times 10^4$  cells per well) the day before transfection. For viral protein expression, cells were transfected with 100 ng of empty vector or vector encoding Orf9b, Orf9b(S50E/S53E), VIC N or Alpha N (pLVX-EF1alpha-IRES-Puro backbone), alongside 10 ng of ISG56-firefly luciferase reporter plasmid (provided by A. Bowie) and 2.5 ng of a Renilla luciferase under control of a thymidine kinase promoter (Promega), as a control for transfection. Transfections were performed with 0.75  $\mu$ l fugene (Promega) and 25  $\mu$ l Optimem (Gibco) per well. Cells were stimulated 24 h after plasmid transfection with the poly I:C (Invivogen), concentrations stated in the figures (final 250  $\mu$ l volume per well), using Lipofectamine 2000 (Invitrogen) at a 3:1 ratio and 25  $\mu$ l optimem. Cells were lysed with 100  $\mu$ l passive lysis buffer (Promega) 24 h after stimulation, 30  $\mu$ l of cell lysis was transferred to a white 96-well assay plate and firefly and renilla activities were measured using the Dual-Glo Luciferase Assay System (Promega), reading luminescence on a GloMax -Multi Detection System (Promega). For each condition, data were normalized by dividing the firefly luciferase activity by renilla luciferase activity and then compared to the empty-vector-transfected mock-treated control to generate a fold induction.

## Immunofluorescence staining and microscopy imaging

Cells were fixed using 4% PFA-PBS for 1h and subsequently washed with PBS. A blocking step was carried out for 1 h at room temperature with 10% goat serum/1% BSA in PBS. N protein detection was performed by primary incubation with human anti-N antibody (Cr3009, 1  $\mu$ g ml<sup>-1</sup>) for 18 h, and washing thoroughly in PBS. Where appropriate, N protein staining was followed by incubation with mouse anti-IRF3 (sc-33641, Santa Cruz) for 1 h. dsRNA was detected by primary incubation with mouse anti-dsRNA (MABE1134, Millipore) for 18 h. Primary antibodies were detected by labelling with secondary anti-human AlexaFluor-568 and anti-mouse AlexaFluor 488 conjugates (Jackson Immuno Research) for 1 h. All cells were then labelled with either HCS CellMask DeepRed (H32721, Thermo Fisher Scientific) or Phalloidin-AlexaFluor 568 (Thermo Fisher Scientific) and Hoechst33342 (H3570, Thermo Fisher Scientific). Images were acquired using the WiScan Hermes High-Content Imaging System (IDEA Bio-Medical) at magnification 10 $\times$ /0.4NA or 40 $\times$ /0.75NA. Four-channel automated acquisition was carried out sequentially (DAPI/TRITC, GFP/Cy5). For the nuclear translocation assay, images were acquired at 40 $\times$  magnification, 35%

density and 30% well area, resulting in 102 fields of view (FOVs) per well. For dsRNA quantification, images were acquired at 10 $\times$  magnification, 100% density and 80% well area, resulting in 47 FOVs per well.

## Image analysis of immunofluorescence experiments

All image channels were pre-processed using a batch rolling ball background correction in the Fiji ImageJ software package<sup>60</sup> before 514 quantification. For nuclear translocation analysis, automated image analysis was carried out using CellProfiler<sup>61</sup>. First, nuclei were identified as primary objects by segmentation of the Hoechst33342 channel. Cells were identified as secondary objects by nucleus-dependent segmentation of the CellMask channel. Cell cytoplasm was segmented by subtracting the nuclear objects mask from the cell masks. Nucleocapsid-positive cells were identified by identifying the nucleocapsid signal as primary objects followed by generation of a nucleocapsid mask that was then applied to filter the segmented cell population. Intensity properties were calculated for the nuclei, cytoplasm and cell object populations. Nuclear:cytoplasmic ratio was calculated as part of the pipeline by dividing the integrated intensity of the nuclei object by the integrated intensity of corresponding cytoplasm object. Plotted are 1,000 randomly sampled cells selected for each condition using the ‘Pandas’ data processing package in Python 3 with a filter of  $0.1 >= <5$ . dsRNA was quantified using the Athena software (IDEA Bio-Medical) using the ‘Intracellular Granules’ module. In short, dsRNA granules within segmented cells were thresholded on the basis of the background intensity of the mock-infected population. Infected cell populations were identified as having a minimum of two segmented dsRNA objects. For dsRNA-positive cells, intensity and area properties were calculated.

## Co-immunoprecipitation of TOM70 with Orf9b

HEK293T cells were transfected with the indicated mammalian expression plasmids using Lipofectamine 2000 (Invitrogen). Twenty-four hours after transfection, cells were collected and lysed in NP-40 lysis buffer (0.5% Nonidet P 40 Substitute (NP-40; Fluka Analytical), 50 mM Tris-HCl, pH 7.4 at 4 °C, 150 mM NaCl and 1 mM EDTA) supplemented with cOmplete mini EDTA-free protease and PhosSTOP phosphatase inhibitor cocktails (Roche). Clarified cell lysates were incubated with streptactin sepharose beads (IBA) for 2 h at 4 °C, followed by five washes with NP-40 lysis buffer. Protein complexes were eluted in the SDS loading buffer and were analysed by western blotting with the indicated antibodies. Antibodies: rabbit anti-Strep-tag II (Abcam ab232586); rabbit anti-β-actin (Cell Signaling Technology 4967); monoclonal mouse anti-Flag M2 antibody (Sigma Aldrich, F1804); and polyclonal rabbit anti-Flag antibody (Sigma Aldrich, F7425).

## **Cell lysis and digestion for proteomics**

Following the infection time course, cells in six-well plates were washed quickly three times in ice cold 1× PBS. Next, cells were lysed in 250 µl per well of 6M guanidine hydrochloride (Sigma) in 100 mM Tris-HCl (pH 8.0) and scraped with a cell spatula for complete collection of the sample. Samples were then boiled for 5 min at 95 °C to inactivate proteases, phosphatases and virus. Samples were frozen at –80 °C and shipped to UCSF on dry ice. On arrival, samples were thawed, an additional 250 µl per sample of 6M guanidine hydrochloride buffer was added, and samples were sonicated for 3× for 10 s at 20% amplitude. Insoluble material was pelleted by spinning samples at maximum speed for 10 min. Supernatant was transferred to a new protein lo-bind tube and protein was quantified using a Bradford assay. The entire sample (approximately 600 µg of total protein) was subsequently processed for reduction and alkylation using a 1:10 sample volume of tris-(2-carboxyethyl) (TCEP) (10 mM final) and 2-chloroacetamide (4.4 mM final) for 5 min at 45 °C with shaking. Before protein digestion, the 6M guanidine hydrochloride was diluted 1:6 with 100 mM Tris-HCl pH8 to enable the activity of trypsin and LysC proteolytic enzymes, which were subsequently added at a 1:75 (wt/wt) enzyme/substrate ratio and placed in a 37 °C water bath for 16–20 h. After digestion, 10% trifluoroacetic acid (TFA) was added to each sample to a final pH of around 2. Samples were desalted under vacuum using 50 mg Sep Pak tC18 cartridges (Waters). Each cartridge was activated with 1 ml 80% acetonitrile (ACN)/0.1% TFA, then equilibrated with 3 × 1 ml of 0.1% TFA. After sample loading, cartridges were washed with 4 × 1 ml of 0.1% TFA, and samples were eluted with 2 × 0.4 ml 50% ACN/0.25% formic acid (FA). Sixty micrograms of each sample was kept for protein abundance measurements, and the remainder was used for phosphopeptide enrichment. Samples were dried by vacuum centrifugation. The same sample was used for abundance proteomics and phosphoproteomics analysis.

## **Phosphopeptide enrichment for proteomics**

IMAC beads (Ni-NTA from Qiagen) were prepared by washing 3× with HPLC water, incubating for 30 min with 50 mM EDTA pH 8.0 to strip the Ni, washing 3× with HPLC water, incubating with 50 mM FeCl<sub>3</sub> dissolved in 10% TFA for 30 min at room temperature with shaking, washing 3× with and resuspending in 0.1% TFA in 80% ACN. Peptides were enriched for phosphorylated peptides using a King Fisher Flex. For a detailed protocol, please contact the authors. Phosphorylated peptides were found to make up more than 90% of every sample, indicating high-quality enrichment.

## **Mass spectrometry data acquisition for proteomics**

Digested samples were analysed on an Orbitrap Exploris 480 mass spectrometry system (Thermo Fisher Scientific) equipped with an Easy nLC 1200 ultra-high

pressure liquid chromatography system (Thermo Fisher Scientific) interfaced via a Nanospray Flex nanoelectrospray source. For all analyses, samples were injected on a C18 reverse phase column (25 cm × 75 µm packed with ReproSilPur 1.9-µm particles). Mobile phase A consisted of 0.1% FA, and mobile phase B consisted of 0.1% FA/80% ACN. Peptides were separated by an organic gradient from 5% to 30% mobile phase B over 112 min followed by an increase to 58% B over 12 min, then held at 90% B for 16 min at a flow rate of 350 nl min<sup>-1</sup>. Analytical columns were equilibrated with 6 µl of mobile phase A. To build a spectral library, one sample from each set of biological replicates was acquired in a data-dependent manner. Data-dependent analysis (DDA) was performed by acquiring a full scan over a *m/z* range of 400–1,000 in the Orbitrap at 60,000 resolving power (200 *m/z*) with a normalized AGC target of 300%, an RF lens setting of 40% and a maximum ion injection time of 60 ms. Dynamic exclusion was set to 60 s, with a 10-ppm exclusion width setting. Peptides with charge states 2–6 were selected for MS/MS interrogation using higher-energy collisional dissociation (HCD), with 20 MS/MS scans per cycle. For phosphopeptide-enriched samples, MS/MS scans were analysed in the Orbitrap using isolation width of 1.3 *m/z*, normalized HCD collision energy of 30% and normalized AGC of 200% at a resolving power of 30,000 with a 54-ms maximum ion injection time. Similar settings were used for DDA of samples used to determine protein abundance, with an MS/MS resolving power of 15,000 and a 22-ms maximum ion injection time. Data-independent analysis (DIA) was performed on all samples. An MS scan at 60,000 resolving power over a scan range of 390–1010 *m/z*, a normalized AGC target of 300%, an RF lens setting of 40% and a maximum injection time of 60 ms was acquired, followed by DIA scans using 8 *m/z* isolation windows over 400–1,000 *m/z* at a normalized HCD collision energy of 27%. Loop control was set to All. For phosphopeptide-enriched samples, data were collected using a resolving power of 30,000 and a maximum ion injection time of 54 ms. Protein abundance samples were collected using a resolving power of 15,000 and a maximum ion injection time of 22 ms.

## Spectral library generation and raw data processing for proteomics

Raw mass spectrometry data from each DDA dataset were used to build separate libraries for DIA searches using the Pulsar search engine integrated into Spectronaut v. 14.10.201222.47784 by searching against a database of Uniprot *Homo sapiens* sequences (downloaded 28 February 2020) and 29 SARS-CoV-2 protein sequences translated from genomic sequence downloaded from GISAID (accession EPI\_ISL\_406596, downloaded 5 March 2020) including mutated tryptic peptides corresponding to the variants assessed in this study. For protein abundance samples, data were searched using the default Biognosys (BGS) settings, variable modification of methionine oxidation, static modification of carbamidomethyl cysteine, and filtering to a final 1% false discovery rate (FDR) at the peptide, peptide spectrum match (PSM) and protein level. For phosphopeptide-enriched samples, BGS settings

were modified to include phosphorylation of S, T and Y as a variable modification. The generated search libraries were used to search the DIA data. For protein abundance samples, default BGS settings were used, with no data normalization performed. For phosphopeptide-enriched samples, the significant post-translational modification (PTM) default settings were used, with no data normalization performed, and the DIA-specific PTM site localization score in Spectronaut was applied.

## Mass spectrometry data pre-processing

Quantitative analysis was performed in the R statistical programming language (v.3.6.1, 2019-07-05). Initial quality control analyses, including inter-run clusterings, correlations, principal component analysis (PCA), peptide and protein counts and intensities were completed with the R package artMS (v. 1.8.1). On the basis of obvious outliers in intensities, correlations and clusterings in PCA analysis, one run was discarded from the protein phosphorylation dataset (IC19 24 h replicate 2). Statistical analysis of phosphorylation and protein abundance changes between mock and infected runs, as well as between infected runs from different variants (for example, Kent versus VIC) were computed using peptide ion fragment data output from Spectronaut and processed using artMS. Specifically, quantifications of phosphorylation based on peptide ions were processed using artMS as a wrapper around MSstats, via functions artMS::doSiteConversion and artMS::artmsQuantification with default settings. All peptides containing the same set of phosphorylated sites were grouped and quantified together into phosphorylation site groups. For both phosphopeptide and protein abundance MSstats pipelines, MSstats performs normalization by median equalization, imputation of missing values and median smoothing to combine intensities for multiple peptide ions or fragments into a single intensity for their protein or phosphorylation site group, and statistical tests of differences in intensity between infected and control time points. When not explicitly indicated, we used defaults for MSstats for adjusted *P* values, even in cases of *n* = 2. By default, MSstats uses the Student's *t*-test for *P* value calculation and the Benjamini–Hochberg method of FDR estimation to adjust *P* values. After quality control data filtering, PCA (Extended Data Fig. 3b) and Pearson's correlation (Extended Data Fig. 3c) confirmed strong correlation between biological replicates, time points and conditions. On average, we quantified 33,000–40,000 peptides mapping to 3,600–4,000 proteins for protein abundance (Extended Data Fig. 3e), and 22,000–30,000 phosphorylated peptides mapping to 3,200–3,800 proteins (Extended Data Fig. 3f). On average we find that biological replicates had 61%–82% peptide detection overlap for protein abundance and 62%–93% phosphorylation site overlap (Extended Data Fig. 3g).

## Refining and filtering phosphorylation and abundance data

MSstats phosphorylation results had to be further simplified to effects at single sites. The results of artMS and MSstats are fold changes of specific phosphorylation site groups detected within peptides, so one phosphorylation site can have multiple measurements if it occurs in different phosphorylation site groups. This complex dataset was reduced to a single fold change per site by choosing the fold change with the lowest *P* value, favouring those detected in both conditions being compared (that is, non-infinite log<sub>2</sub>-transformed fold change values). This single-site dataset was used as the input for kinase activity analysis and enrichment analysis. Protein abundance data were similarly simplified when a single peptide was mapped to multiple proteins; that is, by choosing the fold change with the lowest *P* value, favouring those detected in both conditions being compared (see [Supplementary Table 1](#) for final refined data).

## Targeted proteomics for Orf9b phosphorylation

A spectral library was constructed from the DIA data to obtain Orf9b-specific transitions. We used four proteotypic Orf9b peptides to unbiasedly assess Orf9 abundance, and for Orf9b phosphorylation we included both Ser50 (LGS(+80)PLSLNMAR) and Ser53 (LGSPLS(+80)LNMR) and two phosphosites from heat shock proteins as internal controls for normalization and to remove any bias due to the IMAC enrichment. All samples were acquired on a Orbitrap Tribrid Lumos (Thermo Fisher Scientific) connected to a nanoLC easy 1200 (Thermo Fisher Scientific). For the whole-cell lysate samples, the peptides were separated in 50 min at 0.3  $\mu\text{l min}^{-1}$  with the following gradient: 2% B (0.1% FA in MeCN) to 33% B for 40 min, followed by another linear gradient from 33% to 90% of B (1 min) and an isocratic wash at 90% was performed for 10 min. Peptides were injected through self-packed columns (25 cm) packed with 1.9- $\mu\text{m}$  beads (ReproSil, Waters). The column tip was kept at 2 kV and 275 °C. The mass spectrometer was operated in positive mode (OT/OT) and each MS1 scan was performed with a resolution of 120,000 at 400  $m/z$  between 350 and 1,100  $m/z$ . Peptide ions were accumulated for 50 ms or until the ion population reached an AGC of  $5 \times 10^5$ . Orf9b peptides ( $n = 4$ ) within the inclusion list were fragmented using stepped HCD with a normalized energy of 33 and a spread of  $\pm 3\%$ . For precursor ion selection an isolation window of 1.4 Da was used and the fragments after HCD were analysed in the Orbitrap at 60,000 resolution (400  $m/z$ ). For targeted analysis of Orf9b phosphorylation we used the enriched samples with identical LC, source and MS configuration. The samples were separated in 40 min at 0.3  $\mu\text{l min}^{-1}$  to concentrate the analytes in narrower peaks and increase the signal. The gradient used was from 2% B to 25% in 30 min, then B was increased to 90% in 10 min and the column was washed for 10 min. The mass spectrometer was operated in positive mode and targeted acquisition (PRM). Specifically, one MS1 scan (120,000 resolution at 400  $m/z$ ,  $1 \times 10^6$  AGC, 256 ms IT and mass range 500–800  $m/z$ ) was followed by four unscheduled targeted scans per cycle. An isolation width of 1.6 Da was used per precursor and isolated peptides were

fragmented using stepped HCD ( $33\% \pm 3\%$ ). Each MS2 was acquired with a resolution of 60,000 and ions were accumulated for 118 ms or until reaching an AGC of  $5 \times 10^5$ . After acquisition, each experiment was analysed separately in Skyline. Under transition settings the MS1 filter was set to count and three precursors were used (10 ppm mass error). The MS2 filtering was set to Orbitrap and the resolution was set to 60,000 ( $400 m/z$ ). For the phosphorylation site experiments both b/y and a/z ions were used, whereas for the abundance experiments only y ions were included. Peaks were manually inspected for integration and boundaries refined if necessary. For Orf9b Ser50/Ser53 the presence of the proline in the peptide sequence resulted in a split chromatographic peak between the two isomers and the second peak was used for integration for all samples. For both phosphoisomers, only phosphosite-specific ions were used for quantification (that is, y5-y9/b6-b10 for Ser53 and y9-y5/b2-b6 for Ser50). After export of the transition-level intensities, fragments having an S/N < 10 (for the abundance data) and an S/N < 2 (for the phosphorylation data) were removed.

## RNA quality control

Thirty total RNA samples were submitted for RNA quality control. Total RNA samples were run on the Agilent Bioanalyzer, using the Agilent RNA 6000 Nano Kit. Three samples were excluded from library preparation owing to severe degradation and/or low amounts of RNA present.

## Library preparation for RNA-seq

Twenty-seven total RNA samples were processed using the Illumina Stranded Total RNA w/Ribo-Zero Plus assay. One-hundred nanograms of each total RNA sample (quantitated on the Invitrogen Qubit 2.0 Fluorometer using the Qubit RNA HS Assay Kit) was subjected to ribosomal RNA (rRNA) depletion through an enzymatic process, which includes reduction of human mitochondrial and cytoplasmic rRNAs. After rRNA depletion and purification, RNA was primed with random hexamers for first-strand cDNA synthesis, then second-strand cDNA synthesis. During second-strand cDNA synthesis, deoxyuridine triphosphate (dUTP) was incorporated in place of deoxythymidine triphosphate (dTTP) to achieve strand specificity in a subsequent amplification step. Next, adenine (A) nucleotide was added to the 3' ends of the blunt fragments to prevent ends from ligating to each other. The A-tail also provides a complementary overhang to the thymine (T) nucleotide on the 3' end of the adapter. During adapter ligation and amplification, indexes and adapters were added to both ends of the fragments, resulting in 10-bp, dual-indexed libraries, ready for cluster generation and sequencing. The second strand was quenched during amplification owing to the incorporation of dUTP during second-strand cDNA synthesis, allowing for only the antisense strand to be sequenced in read 1. Thirteen cycles of amplification were performed.

## **Library quality control and quantification for RNA-seq**

Each library was run on the Agilent Bioanalyzer, using the Agilent High Sensitivity DNA Kit, to assess the size distribution of the libraries. They were quantitated by qPCR using a Roche KAPA Library Quantification Complete Kit (ABI Prism), and run on the Applied Biosystems QuantStudio 5 Real-Time PCR System.

## **Sequencing for RNA-seq**

Each library was normalized to 10 nM, then pooled equimolarly for a final concentration of 10 nM. Pooled libraries were submitted to the University of California San Francisco Center for Advanced Technology (UCSF CAT) for one lane of sequencing on the Illumina NovaSeq 6000 S4 flow cell. The run parameter was  $100 \times 10 \times 10 \times 100$  bp.

## **Viral RNA quantification from the RNA-seq dataset**

Viral RNA was characterized by the junction of the leader with the downstream subgenomic sequence. Reads containing possible junctions were extracted by filtering for exact matches to the 3' end of the leader sequence 'CTTCGATCTCTGTAGATCTGTTCTC' using the bbdsk program in the BBTools package (BBTools - Bushnell B. - sourceforge.net/projects/bbmap/). This subset of leader-containing reads was left-trimmed to remove the leader, also using bbdsk. The filtered and trimmed reads were matched against SARS2 genomic sequence with the bbmap program from BBtools with settings (maxindel = 100, strictmaxindel = t, local = t). The leftmost mapped position in the reference was used as the junction site. All strains were mapped against a reference SARS-CoV-2 sequence (accession NC\_045512.2), except Alpha was mapped against an Alpha-specific sequence (GISaid: EPI\_ISL\_693401) and the resultant positions adjusted to the reference on the basis of a global alignment. Junction sites were labelled on the basis of locations of TRS sequences, or other known sites with a  $\pm$  5 base pair window as follows (genomic = 67, S = 21,553, orf3 = 25,382, E = 26,237, M = 26,470, orf6 = 27,041, orf7 = 27,385, orf8 = 27,885, N = 28,257, orf9b = 28,280, N\* = 28,878). Junction reads were counted per position, a pseudocount of 0.5 was added at all positions, counts between replicates and strains were normalized to have equal 'genomic' reads and counts were averaged across replicate samples. Means and standard errors of counts averaged across replicates were subsequently calculated. To calculate the ratios between Alpha and VIC, counts averaged across replicates from Alpha were divided in a condition and time-point-matched manner by values from VIC or IC19. The standard error (s.e.) of the ratios was calculated as  $(A/B) \times \sqrt{((s.e.A/A)^2 + (s.e.B/B)^2)}$ .

## Host RNA analysis

All reads were mapped to the human host genome (ensembl 101) using HISAT2 aligner<sup>62</sup>. Host transcript abundances were estimated using human annotations (ensembl 101) using StringTie<sup>63</sup>. Differential gene expression was calculated on the basis of read counts extracted for each protein-coding gene using featureCount and significance was determined by the DESeq2 R package<sup>64</sup>. On average, we quantified 15,000–16,000 mRNA transcripts above background levels (Extended Data Fig. 3d).

## Viral protein quantification

Median normalized peptide feature (peptides with unique charge states and elution times) intensities (on a linear scale) were refined to the subset that mapped to SARS-CoV-2 protein sequences using Spectronaut (see Methods). Peptide features found in the same biological replicate (that is, owing to different elution times, for example) were averaged. Next, for each time point separately, we selected the subset of peptides that were consistently detected in all biological replicates across all conditions (no missing values), isolating the set of peptides with the best comparative potential. We then summed all peptides mapping to each viral protein for each time point separately, which resulted in our final protein intensity per viral protein per time point per biological replicate. Resulting protein intensities were averaged across biological replicates and standard errors were calculated for each condition. To calculate the ratios between Alpha and VIC, averaged intensities for Alpha were divided in a condition and time-point-matched manner by values from VIC or IC19. The standard error (s.e.) of the ratios was calculated as  $(A/B) \times \sqrt{((s.e.A/A)^2 + (s.e.B/B)^2)}$ .

## Kinase activity analysis of phosphoproteomics data

Kinase activities were estimated using known kinase–substrate relationships in the literature<sup>65</sup>. The resource comprises a comprehensive collection of phosphosite annotations of direct substrates of kinases obtained from six databases—PhosphoSitePlus, SIGNOR, HPRD, NCI-PID, Reactome and the BEL Large Corpus—and using three text-mining tools: REACH, Sparser and RLIMS-P. Kinase activities were inferred as a *z*-score calculated using the mean  $\log_2 FC$  of phosphorylated substrates for each kinase in terms of standard error ( $z = (M - u)/s.e.$ ), comparing fold changes in phosphosite measurements of the known substrates against the overall distribution of fold changes across the sample. A *P* value was also calculated using this approach using a two-tailed *z*-test method. This statistical approach has been previously shown to perform well at estimating kinase activities<sup>27,66</sup>. We collected substrate annotations for 400 kinases with available data. Kinase activities for kinases with 3 or more measured substrates were considered, leaving us with 191 kinases with

activity estimates in at least 1 or more infection time points. Kinases were clustered on the basis of pathway similarity by constructing a kinase tree based on co-membership in pathway terms (from the CP ('Canonical Pathways') category of the Molecular Signature Database (MSigDBv7.1)).

## Pathway enrichment analysis

The pathway gene sets were obtained from the CP (that is, 'Canonical Pathways') category of MSigDBv7.1 (ref. [24](#)). We used the same approach for this pathway enrichment analysis as we used for the kinase activity analysis. Namely, we inferred pathway regulation as *z*-score and an FDR-corrected (0.05) *P* value calculated from a *z*-test (two-tailed) comparing fold changes in phosphosite, protein abundance or RNA abundance measurements of genes designated for a particular pathway against the overall distribution of fold changes in the sample. All resulting terms were further refined to select non-redundant terms by first constructing a pathway term tree based on distances (1-Jaccard similarity coefficients of shared genes in MSigDB) between the terms. The pathway term tree was cut at a specific level ( $h = 0.8$ ) to identify clusters of non-redundant gene sets. For results with multiple significant terms belonging to the same cluster, we selected the most significant term (that is, lowest adjusted *P* value). Next, we filtered out terms that were not significant (FDR-corrected *P* value  $< 0.05$ ) for at least one contrast. Terms were ranked according to either the absolute value *z*-score across contrasts that included Alpha (see Extended Data Fig. [4a–c](#)) or by average  $-\log_{10}(P)$  values across time-matched contrasts involving Alpha (see Fig. [2b](#)).

## Transcription factor activity analysis

Transcription factor activities were estimated from RNA-seq data using DoRothEA<sup>[67](#)</sup> which provides a comprehensive resource of transcription factor–target gene interactions and annotations indicating confidence level for each interaction on the basis of the amount of supporting evidence. We restricted our analysis to A, B and C levels that comprise the most reliable interactions. For the transcription factor activity enrichment analysis, VIPER<sup>[68](#)</sup> was executed with the *t*-statistic derived from the differential gene expression analysis between variant infected and controls (wild-type) infected cells. Transcription factor activity is defined as the normalized enrichment scores (NES) derived from the VIPER algorithm. VIPER algorithm was run with default parameters except for the eset.filter parameter, which was set to FALSE and considered regulons with at least five targets.

## Selection of ISGs

ISGs were taken from a previous study<sup>25</sup> and annotated as ISGs. To this list of 38 genes, we added the following based on manual curation from the literature: *IFI16*, *IFI35*, *IFIT5*, *LGALS9*, *OASL*, *CCL2*, *CCL7*, *IL6*, *IFNB1*, *CXCL10* and *ADAR*.

## Reporting summary

Further information on research design is available in the [Nature Research Reporting Summary](#) linked to this paper.

## Data availability

Abundance proteomics and phosphoproteomics datasets have been deposited to the ProteomeXchange Consortium through the PRIDE partner repository with the dataset identifier [PXD026302](#). Raw RNA-seq data files are available under the accession number [E-MTAB-11275](#). Processed proteomics and RNA-seq data are available as [Supplementary Information](#).

## Code availability

No new algorithms were developed for this project and previous algorithms used are cited in the methods.

## References

1. Volz, E. et al. Assessing transmissibility of SARS-CoV-2 lineage B.1.1.7 in England. *Nature* **593**, 266–269 (2021).
2. Davies, N. G. et al. Estimated transmissibility and impact of SARS-CoV-2 lineage B.1.1.7 in England. *Science* **372** eabg3055 (2021).
3. Galloway, S. E. et al. Emergence of SARS-CoV-2 B.1.1.7 lineage—United States, December 29, 2020–January 12, 2021. *MMWR Morb.*

*Mortal. Wkly Rep.* **70**, 95–99 (2021).

4. Calistri, P. et al. Infection sustained by lineage B.1.1.7 of SARS-CoV-2 is characterised by longer persistence and higher viral RNA loads in nasopharyngeal swabs. *Int. J. Infect. Dis.* **105**, 753–755 (2021).
5. Foster, T. L. et al. Resistance of transmitted founder HIV-1 to IFITM-mediated restriction. *Cell Host Microbe* **20**, 429–442 (2016).
6. Gondim, M. V. P. et al. Heightened resistance to host type 1 interferons characterizes HIV-1 at transmission and after antiretroviral therapy interruption. *Sci. Transl. Med.* **13**, eabd8179 (2021).
7. Sumner, R. P. et al. Are evolution and the intracellular innate immune system key determinants in HIV transmission? *Front. Immunol.* **8**, 1246 (2017).
8. Zhang, Q. et al. Inborn errors of type I IFN immunity in patients with life-threatening COVID-19. *Science* **370**, eabd4570 (2020).
9. Bastard, P. et al. Autoantibodies against type I IFNs in patients with life-threatening COVID-19. *Science* **370**, eabd4585 (2020).
10. Pairo-Castineira, E. et al. Genetic mechanisms of critical illness in COVID-19. *Nature* **591**, 92–98 (2021).
11. Thorne, L. G. et al. SARS-CoV-2 sensing by RIG-I and MDA5 links epithelial infection to macrophage inflammation. *EMBO J.* **40**, e107826 (2021).
12. Lei, X. et al. Activation and evasion of type I interferon responses by SARS-CoV-2. *Nat. Commun.* **11**, 3810 (2020).
13. Miorin, L. et al. SARS-CoV-2 Orf6 hijacks Nup98 to block STAT nuclear import and antagonize interferon signaling. *Proc. Natl Acad. Sci. USA* **117**, 28344–28354 (2020).
14. Hackbart, M., Deng, X. & Baker, S. C. Coronavirus endoribonuclease targets viral polyuridine sequences to evade activating host sensors.

*Proc. Natl Acad. Sci. USA* **117**, 8094–8103 (2020).

15. Ferrarini, M. G. et al. Genome-wide bioinformatic analyses predict key host and viral factors in SARS-CoV-2 pathogenesis. *Commun. Biol.* **4**, 590 (2021).
16. Sorek, M., Meshorer, E. & Schlesinger, S. Transposable elements as sensors of SARS-CoV-2 infection. Preprint at <https://doi.org/10.1101/2021.02.25.432821> (2021).
17. Rookhuizen, D. C., Bonte, P. E., Ye, M., Hoyler, T. & Gentili, M. Induction of transposable element expression is central to innate sensing. Preprint at <https://doi.org/10.1101/2021.09.10.457789> (2021).
18. Zhang, L. et al. SARS-CoV-2 spike-protein D614G mutation increases virion spike density and infectivity. *Nat. Commun.* **11**, 6013 (2020).
19. Hou, Y. J. et al. SARS-CoV-2 D614G variant exhibits efficient replication ex vivo and transmission in vivo. *Science* **370**, 1464–1468 (2020).
20. Plante, J. A. et al. Spike mutation D614G alters SARS-CoV-2 fitness. *Nature* **592**, 116–121 (2021).
21. Volz, E. et al. Evaluating the effects of SARS-CoV-2 spike mutation D614G on transmissibility and pathogenicity. *Cell* **184**, 64–75 (2021).
22. Ozono, S. et al. SARS-CoV-2 D614G spike mutation increases entry efficiency with enhanced ACE2-binding affinity. *Nat. Commun.* **12**, 848 (2021).
23. Guo, K., Barrett, B. S., Mickens, K. L., Hasenkrug, K. J. & Santiago, M. L. Interferon resistance of emerging SARS-CoV-2 variants. Preprint at <https://doi.org/10.1101/2021.03.20.436257> (2021).
24. Subramanian, A. et al. Gene set enrichment analysis: a knowledge-based approach for interpreting genome-wide expression profiles. *Proc. Natl Acad. Sci. USA* **102**, 15545–15550 (2005).

25. Liu, H. et al. Tumor-derived IFN triggers chronic pathway agonism and sensitivity to ADAR loss. *Nat. Med.* **25**, 95–102 (2019).
26. Ochoa, D. et al. An atlas of human kinase regulation. *Mol. Syst. Biol.* **12**, 888 (2016).
27. Hernandez-Armenta, C., Ochoa, D., Gonçalves, E., Saez-Rodriguez, J. & Beltrao, P. Benchmarking substrate-based kinase activity inference using phosphoproteomic data. *Bioinformatics* **33**, 1845–1851 (2017).
28. Clark, K., Plater, L., Peggie, M. & Cohen, P. Use of the pharmacological inhibitor BX795 to study the regulation and physiological roles of TBK1 and I $\kappa$ B kinase  $\epsilon$ . *J. Biol. Chem.* **284**, 14136–14146 (2009).
29. Heo, J.-M. et al. RAB7A phosphorylation by TBK1 promotes mitophagy via the PINK–PARKIN pathway. *Sci. Adv.* **4**, eaav0443 (2018).
30. Jungreis, I. et al. Conflicting and ambiguous names of overlapping ORFs in the SARS-CoV-2 genome: a homology-based resolution. *Virology* **558**, 145–151 (2021).
31. Parker, M. D., Lindsey, B. B., Shah, D. R., Hsu, S. & Keeley, A. J. Altered sub-genomic RNA expression in SARS-CoV-2 B.1.1.7 infections. Preprint at <https://doi.org/10.1101/2021.03.02.433156> (2021).
32. Jungreis, I., Sealfon, R. & Kellis, M. SARS-CoV-2 gene content and COVID-19 mutation impact by comparing 44 *Sarbecovirus* genomes. *Nat. Commun.* **12**, 2642 (2021).
33. Oh, S. J. & Shin, O. S. SARS-CoV-2 nucleocapsid protein targets RIG-I-like receptor pathways to inhibit the induction of interferon response. *Cells* **10**, 530 (2021).
34. Schmidt, N. Novel functions of host TRIM28 in restricting influenza virus infections. Dissertation, University of Zurich (2019).

35. Gordon, D. E. et al. A SARS-CoV-2 protein interaction map reveals targets for drug repurposing. *Nature* **583**, 459–468 (2020).
36. Liu, X.-Y., Wei, B., Shi, H.-X., Shan, Y.-F. & Wang, C. Tom70 mediates activation of interferon regulatory factor 3 on mitochondria. *Cell Res.* **20**, 994–1011 (2010).
37. Jiang, H.-W. et al. SARS-CoV-2 Orf9b suppresses type I interferon responses by targeting TOM70. *Cell. Mol. Immunol.* **17**, 998–1000 (2020).
38. Gao, X. et al. Crystal structure of SARS-CoV-2 Orf9b in complex with human TOM70 suggests unusual virus–host interactions. *Nat. Commun.* **12**, 2843 (2021).
39. Bouhaddou, M. et al. The global phosphorylation landscape of SARS-CoV-2 infection. *Cell* **182**, 685–712 (2020).
40. Gordon, D. E. et al. Comparative host–coronavirus protein interaction networks reveal pan-viral disease mechanisms. *Science* **370**, eabe9403 (2020).
41. Calistri, P. et al. Infection sustained by lineage B.1.1.7 of SARS-CoV-2 is characterised by longer persistence and higher viral RNA loads in nasopharyngeal swabs. *Int. J. Infect. Dis.* **105**, 753–755 (2021).
42. Kissler, S. M. et al. Densely sampled viral trajectories suggest longer duration of acute infection with B. 1.1. 7 variant relative to non-B. 1.1. 7 SARS-CoV-2. Preprint at <https://doi.org/10.1101/2021.02.16.21251535> (2021).
43. Davies, N. G. et al. Increased mortality in community-tested cases of SARS-CoV-2 lineage B.1.1.7. *Nature* **593**, 270–274 (2021).
44. Scientific Advisory Group for Emergencies. NERVTAG: Update Note on B.1.1.7 Severity.  
<https://assets.publishing.service.gov.uk/government/uploads/system/up>

[loads/attachment\\_data/file/982640/Feb\\_NERVTAG\\_update\\_note\\_on\\_B.1.1.7\\_severity.pdf](https://www.ncbi.nlm.nih.gov/pmc/articles/PMC8083332/) (2021).

45. Sekizuka, T. et al. Genome recombination between Delta and Alpha variants of severe acute respiratory syndrome Coronavirus 2 (SARS-CoV-2). Preprint at <https://doi.org/10.1101/2021.10.11.21264606> (2021).
46. Saito, A. et al. Enhanced fusogenicity and pathogenicity of SARS-CoV-2 Delta P681R mutation. *Nature* <https://doi.org/10.1038/s41586-021-04266-9> (2021).
47. Mlcochova, P. et al. SARS-CoV-2 B.1.617.2 Delta variant replication and immune evasion. *Nature* **599**, 114–119 (2021).
48. Planas, D. et al. Reduced sensitivity of SARS-CoV-2 variant Delta to antibody neutralization. *Nature* **596**, 276–280 (2021).
49. Escalera, A. et al. SARS-CoV-2 variants of concern have acquired mutations associated with an increased spike cleavage. Preprint at <https://doi.org/10.1101/2021.08.05.455290> (2021).
50. Gribble, J. et al. The coronavirus proofreading exoribonuclease mediates extensive viral recombination. *PLoS Pathog.* **17**, e1009226 (2021).
51. Rogers, T. F. et al. Isolation of potent SARS-CoV-2 neutralizing antibodies and protection from disease in a small animal model. *Science* **369**, 956–963 (2020).
52. Thorne, L. G., Reuschl, A. K. & Zuliani-Alvarez, L. SARS-CoV-2 sensing by RIG-I and MDA5 links epithelial infection to macrophage inflammation. *EMBO J.* **40**, e107826 (2020).
53. Rheinwald, J. G. & Green, H. Serial cultivation of strains of human epidermal keratinocytes: the formation of keratinizing colonies from single cells. *Cell* **6**, 331–343 (1975).

54. Brown, J. C. et al. Increased transmission of SARS-CoV-2 lineage B.1.1.7 (VOC 202012/01) is not accounted for by a replicative advantage in primary airway cells or antibody escape. Preprint at <https://doi.org/10.1101/2021.02.24.432576> (2021).
55. Meredith, L. W. et al. Rapid implementation of SARS-CoV-2 sequencing to investigate cases of health-care associated COVID-19: a prospective genomic surveillance study. *Lancet Infect. Dis.* **20**, 1263–1271 (2020).
56. Tyson, J. R. et al. Improvements to the ARTIC multiplex PCR method for SARS-CoV-2 genome sequencing using nanopore. Preprint at <https://doi.org/10.1101/2020.09.04.283077> (2020).
57. Lindenbach, B. D. Measuring HCV infectivity produced in cell culture and in vivo. *Methods Mol. Biol.* **510**, 329–336 (2009).
58. Corman, V. M. et al. Detection of 2019 novel coronavirus (2019-nCoV) by real-time RT–PCR. *Eurosurveillance* **25**, 23 (2020).
59. Thao, T. T. N. et al. Rapid reconstruction of SARS-CoV-2 using a synthetic genomics platform. *Nature* **582**, 561–565 (2020).
60. Schindelin, J. et al. Fiji: an open-source platform for biological-image analysis. *Nat. Methods* **9**, 676–682 (2012).
61. Carpenter, A. E. et al. CellProfiler: image analysis software for identifying and quantifying cell phenotypes. *Genome Biol.* **7**, R100 (2006).
62. Kim, D., Paggi, J. M., Park, C., Bennett, C. & Salzberg, S. L. Graph-based genome alignment and genotyping with HISAT2 and HISAT-genotype. *Nat. Biotechnol.* **37**, 907–915 (2019).
63. Kovaka, S. et al. Transcriptome assembly from long-read RNA-seq alignments with StringTie2. *Genome Biol.* **20**, 278 (2019).

64. Love, M. I., Huber, W. & Anders, S. Moderated estimation of fold change and dispersion for RNA-seq data with DESeq2. *Genome Biol.* **15**, 550 (2014).
65. Bachman, J. A., Gyori, B. M. & Sorger, P. K. Assembling a phosphoproteomic knowledge base using ProtMapper to normalize phosphosite information from databases and text mining. Preprint at <https://doi.org/10.1101/822668> (2019).
66. Casado, P. et al. Kinase-substrate enrichment analysis provides insights into the heterogeneity of signaling pathway activation in leukemia cells. *Sci. Signal.* **6**, rs6 (2013).
67. Garcia-Alonso, L., Holland, C. H., Ibrahim, M. M., Turei, D. & Saez-Rodriguez, J. Benchmark and integration of resources for the estimation of human transcription factor activities. *Genome Res.* **29**, 1363–1375 (2019).
68. Alvarez, M. J. et al. Functional characterization of somatic mutations in cancer using network-based inference of protein activity. *Nat. Genet.* **48**, 838–847 (2016).

## Acknowledgements

This research was funded by grants from the National Institutes of Health (P50AI150476, U19AI135990, U19AI135972, R01AI143292, R01AI120694 and P01AI063302 to N.J.K.; F32CA239333 to M.B.; R01GM133981 to D.L.S.); by the Excellence in Research Award (ERA) from the Laboratory for Genomics Research (LGR), a collaboration between UCSF, UCB and GSK (133122P); by the Roddenberry Foundation; by funding from F. Hoffmann-La Roche and Vir Biotechnology; and through gifts from QCRG philanthropic donors. This research was also partly funded by the Center for Research on Influenza Pathogenesis (CRIP), a NIAID funded Center of Excellence for Influenza Research and Surveillance (CEIRS, contract no. HHSN272201400008C), and the Center for Research on Influenza Pathogenesis and Transmission (CRIPT), a NIAID funded Center of Excellence for Influenza Research and Response

(CEIRR, contract no. 75N93021C00014); by NCI SeroNet grant U54CA260560; and by the support of the JPB Foundation, the Open Philanthropy Project (research grant 2020-215611 (5384)) and anonymous donors to A.G.-S. This work was also supported by the Defense Advanced Research Projects Agency (DARPA) under Cooperative Agreement no. HR0011-19-2-0020. The views, opinions, and/or findings contained in this material are those of the authors and should not be interpreted as representing the official views or policies of the Department of Defense or the U.S. Government. G.J.T. was funded by Wellcome Senior Fellowship 108183 followed by Wellcome Investigator Award 220863. C.J. was funded by Wellcome Investigator Award 108079 followed by 223065. G.J.T. and C.J. were funded by MRC/UKRI G2P-UK National Virology consortium (MR/W005611/1) and the UCL COVID-19 fund. M.N. was funded by Wellcome Investigator Award 207511. I.G.G. is a Wellcome Senior Fellow and this work was supported by grants from the Wellcome Trust (refs: 207498 and 206298). P. Bonfanti received funding from the European Research Council (ERC-Stg no. 639429), the Rosetrees Trust (M362-F1; M553) and the CF Trust (SRC006; SRC020); R. Ragazzini is supported by a Marie Skłodowska-Curie Individual Fellowships no. 896014. Funds were also obtained from the National Institutes of Health Research UCL/UCLH Biomedical Research Centre. M.V.X.W. is supported by the NIHR Biomedical Research Centre at UCLH and IDEA Bio-Medical. We are grateful to the National Institute of Health Research Health Protection Research Unit in Respiratory Infections (NIHR 200927) and the Assessment of Transmission and Contagiousness of COVID-19 in Contacts (ATACCC) Study funded by the DHSC COVID-19 Fighting Fund. We are also grateful to the ATACCC investigators, in particular A. Lalvani, J. Dunning, J. Fenn, R. Kundu, R. Varro, S. Hammett, J. Cutajaar, E. McDermott, J. Samuel, S. Bremang, A. Koycheva, N. Fernandez Derqui, S. Janakan, E. Conibear, L. Wang, S. Hakki, M. Zambon, J. Ellis, A. Lackenby, S. Miah and colleagues at Public Health England, G. Mattiuzzo at the National Institute for Biological Standards and Controls and W. Barclay and J. Brown at Imperial College London for provision of variant isolates, reagents and advice. We are grateful to R. Milne for discussions and critical reading of the manuscript.

## Author information

## Author notes

1. Roberta Ragazzini & Paola Bonfanti

Present address: Division of Infection and Immunity, University College London, London, UK

2. Yasu Takeuchi

Present address: Cardiovascular Research Institute, University of California San Francisco, San Francisco, CA, USA

3. These authors contributed equally: Lucy G. Thorne, Mehdi Bouhaddou, Ann-Kathrin Reuschl, Lorena Zuliani-Alvarez

## Affiliations

1. Division of Infection and Immunity, University College London, London, UK

Lucy G. Thorne, Ann-Kathrin Reuschl, Matthew V. X. Whelan, Jane Turner, Marie L. Bischof, Yasu Takeuchi, Mahdad Noursadeghi, Clare Jolly & Greg J. Towers

2. QBI Coronavirus Research Group (QCRG), University of California San Francisco, San Francisco, CA, USA

Mehdi Bouhaddou, Lorena Zuliani-Alvarez, Ben Polacco, Adrian Pelin, Jyoti Batra, Andrea Fossati, Manisha Ummadi, Ajda Rojc, Kirsten Obernier, Hannes Braberg, Margaret Soucheray, Alicia Richards, Kuei-Ho Chen, Bhavya Harjai, Joseph Hiatt, Jacqueline M. Fabius, Kevan Shokat, Natalia Jura, Klim Verba, Pedro Beltrao, Danielle L. Swaney & Nevan J. Krogan

3. Quantitative Biosciences Institute (QBI), University of California San Francisco, San Francisco, CA, USA

Mehdi Bouhaddou, Lorena Zuliani-Alvarez, Ben Polacco, Adrian Pelin, Jyoti Batra, Andrea Fossati, Manisha Ummadi, Ajda Rojc, Kirsten Obernier, Hannes Braberg, Margaret Soucheray, Alicia Richards, Kuei-Ho Chen, Bhavya Harjai, Joseph Hiatt, Jacqueline M. Fabius, Kevan Shokat, Natalia Jura, Klim Verba, Danielle L. Swaney & Nevan J. Krogan

4. J. David Gladstone Institutes, San Francisco, CA, USA

Mehdi Bouhaddou, Lorena Zuliani-Alvarez, Ben Polacco, Adrian Pelin, Jyoti Batra, Andrea Fossati, Manisha Ummadi, Ajda Rojc, Kirsten Obernier, Hannes Braberg, Margaret Soucheray, Alicia Richards, Kuei-Ho Chen, Bhavya Harjai, Joseph Hiatt, Jacqueline M. Fabius, Kevan Shokat, Danielle L. Swaney & Nevan J. Krogan

5. Department of Cellular and Molecular Pharmacology, University of California San Francisco, San Francisco, CA, USA

Mehdi Bouhaddou, Lorena Zuliani-Alvarez, Ben Polacco, Adrian Pelin, Jyoti Batra, Andrea Fossati, Manisha Ummadi, Ajda Rojc, Kirsten Obernier, Hannes Braberg, Margaret Soucheray, Alicia Richards, Kuei-Ho Chen, Bhavya Harjai, Joseph Hiatt, Jacqueline M. Fabius, Kevan Shokat, Natalia Jura, Klim Verba, Danielle L. Swaney & Nevan J. Krogan

6. Division of Virology, Department of Pathology, Addenbrooke's Hospital, University of Cambridge, Cambridge, UK

Myra Hosmillo, Aminu Jahun & Ian G. Goodfellow

7. Epithelial Stem Cell Biology and Regenerative Medicine Laboratory, The Francis Crick Institute, London, UK

Roberta Ragazzini & Paola Bonfanti

8. MIT Computer Science and Artificial Intelligence Laboratory, MIT, Cambridge, MA, USA

Irwin Jungreis & Manolis Kellis

9. Broad Institute of MIT and Harvard, Cambridge, MA, USA

Irwin Jungreis & Manolis Kellis

10. European Molecular Biology Laboratory (EMBL), European Bioinformatics Institute, Wellcome Genome Campus, Hinxton, UK

Danish Memon & Pedro Beltrao

11. Department of Microbiology, Icahn School of Medicine at Mount Sinai, New York, NY, USA

Romel Rosales, Briana L. McGovern, Kris White & Adolfo García-Sastre

12. Global Health and Emerging Pathogens Institute, Icahn School of Medicine at Mount Sinai, New York, NY, USA

Romel Rosales, Briana L. McGovern, Kris White & Adolfo García-Sastre

13. Howard Hughes Medical Institute, San Francisco, CA, USA

Kevan Shokat

14. Division of Advanced Therapies, National Institute for Biological Standards and Control, South Mimms, UK

Natalia Jura

15. Cardiovascular Research Institute, University of California San Francisco, San Francisco, CA, USA

Natalia Jura

16. The Tisch Cancer Institute, Icahn School of Medicine at Mount Sinai, New York, NY, USA

Adolfo García-Sastre

17. Department of Medicine, Division of Infectious Diseases, Icahn School of Medicine at Mount Sinai, New York, NY, USA

Adolfo García-Sastre

18. Department of Pathology, Molecular and Cell-Based Medicine, Icahn School of Medicine at Mount Sinai, New York, NY, USA

Adolfo García-Sastre

## Contributions

Conceptualization: L.G.T., M.B., A.-K.R., L.Z.-A., C.J., G.J.T. and N.J.K.  
Experimental set-up, investigation and analysis: L.G.T., M.B., A.-K.R., L.Z.-A., B.P., A.P., J.B., M.V.X.W., M.H., A.F., R. Ragazzini, I.J., M.U., A. Rojc, J.T., M.L.B., K.O., H.B., M.S., A. Richards, K.-H.C., B.H., D.M., J.H., R. Rosales, B.L.M., A.J., K.W., I.G.G., P. Bonfanti, J.M.F., K.S., N.J., K.V., M.N., P. Beltrao, D.L.S., A.G.-S, C.J., G.J.T. and N.J.K. Writing, review and editing: L.G.T., M.B., A.-K.R., L.Z.-A., B.P., A.P., J.B., M.V.X.W., M.H., R. Ragazzini, I.J., M.U., A. Rojc, J.T., K.O., H.B., M.S., A. Richards, K.-H.C., B.H., D.M., J.H., A.J., I.G.G., P. Bonfanti, K.S., N.J., K.V., M.N., P. Beltrao, D.L.S., A.G.-S., C.J., G.J.T. and N.J.K. Coordination and supervision: K.W., I.G.G., Y.T., P. Bonfanti, M.K., J.M.F., K.S., N.J., K.V., M.N., P. Beltrao, D.L.S., A.G.-S., C.J., G.J.T. and N.J.K.

## Corresponding authors

Correspondence to [Clare Jolly](#), [Greg J. Towers](#) or [Nevan J. Krogan](#).

## Ethics declarations

## Competing interests

The N.J.K. laboratory has received research support from Vir Biotechnology and F. Hoffmann-La Roche. N.J.K. has consulting agreements with the Icahn School of Medicine at Mount Sinai, New York, Maze Therapeutics and Interline Therapeutics. He is a shareholder in Tenaya Therapeutics, Maze Therapeutics and Interline Therapeutics, has received stocks from Maze Therapeutics and Interline Therapeutics and is a financially compensated Scientific Advisory Board Member for GEn1E Lifesciences. The A.G.-S. laboratory has received research support from Pfizer, Senhwa Biosciences, Kenall Manufacturing, Avimex, Johnson & Johnson, Dynavax, 7Hills Pharma, Pharmamar, ImmunityBio, Accurius, Nanocomposix, Hexamer, N-fold, Model Medicines, Atea Pharma and Merck. A.G.-S. has consulting agreements for the following companies involving cash and/or stock: Vivaldi Biosciences, Contrafект, 7Hills Pharma, Avimex, Vaxalto, Pagoda, Accurius, Esperovax, Farmak, Applied Biological Laboratories, Pharmamar, Paratus and Pfizer. A.G.-S. is inventor on patents and patent applications on the use of antivirals and vaccines for the treatment and prevention of virus infections, owned by the Icahn School of Medicine at Mount Sinai, New York.

## Peer review

### Peer review information

*Nature* thanks Ellen Foxman and the other, anonymous, reviewer(s) for their contribution to the peer review of this work.

## Additional information

**Publisher's note** Springer Nature remains neutral with regard to jurisdictional claims in published maps and institutional affiliations.

## Extended data figures and tables

[Extended Data Fig. 1 The SARS-CoV-2 Alpha variant replicates similarly to early-lineage isolates in Calu-3 cells.](#)

**a**, E copies/ml (left), TCID50/ml (centre) and infectious units per genome (TCID50/E copies) (right) were measured in viral stocks. **b-d**, Calu-3 cell infection with 5 E copies/cell. Viral replication (b), % infection (c), and infectious virion production (d) are shown. **e**, Quantification of E gene negative sense standard RNA in the presence and absence of  $10^7$  positive sense E RNA copies. Positive sense E primer set run with negative sense standards, observed at the limit of detection. **f**, Negative sense E copies in cells from (b). **g, h**, dsRNA detection by single cell immunofluorescence in cells infected with 2,000 E copies/cell. Representative images at 24 hpi (g) and quantification of dsRNA-positive cells (h) are shown. Shown are mean  $\pm$  s.e.m. of one of three representative experiments performed in triplicate. For (g) representative images from two independent experiments, quantified in (h), are shown. Scale bars are 50  $\mu$ m. Two Way ANOVA (b,c,d,f) or One Way ANOVA with a Tukey post-hoc test were used. Blue stars indicate comparison between Alpha and VIC (blue lines and symbols), grey stars indicate comparison between Alpha and IC19 (grey lines and symbols). \* ( $p < 0.05$ ), \*\* ( $p < 0.01$ ), \*\*\* ( $p < 0.001$ ), \*\*\*\* ( $p < 0.0001$ ). ns: non-significant. E: viral envelope gene. LOD, limit of detection.

## Extended Data Fig. 2 The SARS-CoV-2 Alpha variant antagonizes innate immune activation more efficiently than early-lineage isolates.

**a**, IFN $\beta$  gene expression (left) and protein secretion (right) from cells in Extended Data Fig 1b. **b**, HAE cells were infected with 2,000 E copies/cell of VIC. E copies were measured in apical washes of infected cultures. **c**, Calu-3 infection at 2,000 E copies/cell after 8h pre-treatment with IFN $\beta$ . Infection levels are shown normalized to untreated controls at 24 hpi. **d**, IFN $\beta$  and ISGs expression in HAE cells infected with 2,000 E copies/cell of IC19 or Alpha variant normalized to intracellular E copies for each sample. Shown are mean  $\pm$  s.e.m. of one of three representative experiments performed in triplicate. For d, n = 6, two independent donors. Two Way ANOVA (a,c) or One Way ANOVA (d) with Wilcoxon matched-pairs signed rank test were used. Blue stars indicate comparison between Alpha and VIC (blue lines and symbols), grey stars indicate comparison between Alpha and IC19 (grey lines and symbols). \* ( $p < 0.05$ ), \*\* ( $p < 0.01$ ), \*\*\* ( $p < 0.001$ ), \*\*\*\* ( $p < 0.0001$ ). ns: non-significant. E: viral envelope gene.

### Extended Data Fig. 3 Omics data quality control and pathway enrichments.

**a**, Significantly changing genes for RNA, proteins for protein abundance, and phosphorylation sites for phosphoproteomics data. Significance was defined as  $\text{abs}(\log_{2}\text{FC}) > 1$  and adjusted p-value  $< 0.05$ . Red depicts positive log<sub>2</sub> fold changes whereas blue depicts negative log<sub>2</sub> fold changes. **b**, Principal components analysis (PCA) on normalized RNA transcripts per million (TPM), protein intensities, or phosphorylation site intensities. Non-finite values were removed and detections (transcripts, proteins, or phosphorylation sites) not shared (non-finite) between all conditions were discarded prior to analysis. Coloured numbers indicate biological replicates. **c**, Pairwise Pearson's correlation between RNA, protein, or phosphorylation site abundance among replicates within the same condition (red) or between distinct conditions (black). **d**, Number of genes expressed above baseline in RNA-seq dataset per replicate. **e**, Number of peptides and proteins detected per replicate in the abundance proteomics dataset. **f**, Number of phosphorylated peptides and corresponding proteins from the phosphoproteomics dataset. **g**, Fraction of peptides from protein abundance (left) or phosphoproteomics (right; phosphorylated peptides) that overlap between two replicates. **h**, Correlation between Log<sub>2</sub> fold-change ( $\log_{2}\text{FC}$ ) phosphorylation sites and  $\log_{2}\text{FC}$  abundance of the corresponding protein. Dots are coloured according to the comparison between conditions.

### Extended Data Fig. 4 Omics data highlight the recruitment of innate immune signalling.

**a**, Gene set enrichment analysis based on  $\log_{2}\text{FC}$  method using RNA dataset (as in Fig. 2b). Ranking is based on the average of the absolute value z-scores across the indicated contrasts involving Alpha (per row). Black borders indicate an adjusted p-value  $< 0.05$ . **b**, Same as in a, but for abundance proteomics dataset. **c**, Same as in a, but for phosphoproteomics dataset. If a protein possessed multiple phosphorylation sites, the maximum absolute value  $\log_{2}\text{FC}$  was used as the representative value for the protein. Finite values (non-infinite) were prioritized over quantitative values. **d**, Expression of interferon-stimulated genes from Lui et al (2018)<sup>25</sup> (see

Methods) using the RNA-seq dataset. Significant fold changes with an adjusted p-value < 0.05 are indicated with black borders. **e**, Same as in (a) using the abundance proteomics dataset. N.D. indicates proteins either not detected in one condition (thus, Inf or -Inf) or not detected in both conditions. **f**, RNA expression per biological replicate of interferon-stimulated genes (ISGs) for each virus versus mock.

**Extended Data Fig. 5 Infection with the SARS-CoV-2 Alpha variant results in lower IFN III and pro-inflammatory responses than first wave isolates.**

**a**, Calu-3 cells were infected with 250 E copies/cell and *IFNL1* and *IFNL3* expression measured at 24 hpi. **b**, Secretion of CXCL10, IL6 and CCL5 by infected cells at 48 hpi. **c**, **d**, Calu-3 cells were infected with (c) 5,000 E copies/cell or (d) 5 E copies/cell. Expression of *TNF*, *CCL2*, *IL6*, *IL8* and *CCL3* were measured. Data shown are mean ± s.e.m. of one of three representative experiments performed in triplicate. One Way ANOVA with a Tukey post-comparison test (a, b) or two Way ANOVA (c,d) were used. Blue stars indicate comparison between Alpha and VIC (blue lines and symbols), grey stars indicate comparison between Alpha and IC19 (grey lines and symbols). \* (p < 0.05), \*\* (p < 0.01), \*\*\* (p < 0.001), \*\*\*\* (p < 0.0001). ns: non-significant. E: viral envelope gene.

**Extended Data Fig. 6 Kinase and transcription factor activity analysis.**

**a**, Full kinase activity analysis of indicated contrasts with z-score>2. Kinases were separated using k-means clustering, which naturally reveals groups depicting kinases downregulated for the entire time course (“Down”), downregulated early and upregulated late (“Down-Up”), upregulated early and downregulated late (“Up-Down”), or upregulated or constant throughout the time course (“Up”). Panel on the right depicts the average Z-score for each distinct cluster per time point, collapsing across Alpha/VIC and Alpha/IC19 comparisons. **b**, Correlation between the calculated kinase activity Z-score and protein (left) or RNA (right) abundance log2FC for kinases with estimated activities in our dataset.

Vertical dashed lines indicate kinase activity of  $\pm 2$ , horizontal dashed lines indicate protein log2FC of  $\pm 1$ . Colours represent comparisons between viruses and time points as indicated. **c**, Detected substrates known to be phosphorylated by TBK1. Log2FC of each phosphorylation site is depicted. Those not detected are indicated in grey. **d**, Transcription factor (TF) activities were estimated from the RNA-seq dataset using known TF-target gene interactions. Included are TFs with a NES $>2.5$ . TFs are clustered using ward hierarchical clustering based on similar activity patterns across time.

### Extended Data Fig. 7 Expression of viral RNA and protein for SARS-CoV-2 variants.

**a**, Log2 ratio of Alpha to IC19 subgenomic RNA (sgRNA) abundance as determined from the RNA-seq dataset. **b**, Log2 ratio of Alpha to IC19 viral proteins. Peptide intensities are summed per viral protein ( $n = 3$ ). **c**, Quantification of sgRNAs for M, S, Orf8, Orf7a, Orf3a, E and N\* from the RNA-seq dataset. Counts are normalized to genomic RNA abundance at each time point and virus. **d**, Quantification of Orf3a (left) or S (right) sgRNA abundance via RT-qPCR. **e**, Summed peptides per viral protein for M, S, Nsp1, Orf7b, and Orf3b. **f**, Western blot quantification of Orf6 and N protein in infected cells at 24 hpi ( $n = 3$ ). **g**, Pie chart depicting proportion of total sgRNA mapping to each viral sgRNA for IC19. **h**, Mean  $\pm$  s.e.m. are shown. Comparison of percentages of total sgRNA mapping to each viral sgRNA across Alpha, VIC, and IC19. \* ( $p < 0.05$ ), \*\* ( $p < 0.01$ ), \*\*\* ( $p < 0.001$ ), \*\*\*\* ( $p < 0.0001$ ). ns: non-significant, ND, not detected.

### Extended Data Fig. 8 Examples of leader-containing reads for Orf9b and N from the RNA-seq dataset.

**a–c**, Representative sequence for Orf9b (top) and N (bottom) sgRNA from Alpha (a), VIC (b) and IC19 (c). Leader sequences to identify sgRNAs are highlighted in yellow. The following sequence is used to differentiate Orf9b versus N sgRNAs. Orf9b and N start codons shown in maroon. The site of the N-protein D3L mutation is indicated in green, resulting in increased similarity to the transcriptional regulatory sequence (TRS) for Alpha. Read

counts of Orf9b and N are indicated to the right. Counts are normalized to mean genomic reads per replicate.

## [Extended Data Fig. 9 Western blot densitometry quantification for Orf9b immunoprecipitation with TOM70.](#)

Densitometry quantification of two western blot experimental repeats of Orf9b immunoprecipitation with TOM70 (as in Fig. [4d](#)).

## **Supplementary information**

### [Supplementary Figures](#)

This file contains Supplementary Figure 1: Raw western blot image for viral proteins Orf6 and N; and Supplementary Figure 2. Raw western blot image of quantification for Orf9b immunoprecipitation with TOM70.

### [Reporting Summary](#)

### [Supplementary Table 1](#)

Fold changes and *P* values for RNA-seq, abundance proteomics, and phosphoproteomics datasets.

### [Supplementary Table 2](#)

Full pathway enrichment results of RNA-seq, abundance proteomics, and phosphoproteomics datasets (i.e. Figures 2b and Extended Data Fig. 4a-c).

### [Supplementary Table 3](#)

Fold changes and p-values for interferon stimulated genes from RNA-seq and abundance proteomics datasets (i.e. Figures 2c-d).

### [Supplementary Table 4](#)

Full table of calculated kinase activities for comparisons between Alpha, VIC, and IC19 (i.e. Figures 2g and Extended Data Fig. 6a).

### **Supplementary Table 5**

Full table of calculated transcription factor activities for comparisons between Alpha, VIC, and IC19 (i.e. Figures 4a and Extended Data Fig. 6d).

### **Supplementary Table 6**

Viral RNA and protein quantities and ratios for Alpha to VIC and IC19 (i.e. Figure 3 and Extended Data Fig. 7).

### **Supplementary Table 7**

Read counts of subgenomic RNA mapped to SARS-CoV-2 genome (i.e. Figure 3i).

## **Rights and permissions**

**Open Access** This article is licensed under a Creative Commons Attribution 4.0 International License, which permits use, sharing, adaptation, distribution and reproduction in any medium or format, as long as you give appropriate credit to the original author(s) and the source, provide a link to the Creative Commons license, and indicate if changes were made. The images or other third party material in this article are included in the article's Creative Commons license, unless indicated otherwise in a credit line to the material. If material is not included in the article's Creative Commons license and your intended use is not permitted by statutory regulation or exceeds the permitted use, you will need to obtain permission directly from the copyright holder. To view a copy of this license, visit <http://creativecommons.org/licenses/by/4.0/>.

### **Reprints and Permissions**

## **About this article**

## Cite this article

Thorne, L.G., Bouhaddou, M., Reuschl, AK. *et al.* Evolution of enhanced innate immune evasion by SARS-CoV-2. *Nature* **602**, 487–495 (2022). <https://doi.org/10.1038/s41586-021-04352-y>

- Received: 31 May 2021
- Accepted: 14 December 2021
- Published: 23 December 2021
- Issue Date: 17 February 2022
- DOI: <https://doi.org/10.1038/s41586-021-04352-y>

## Share this article

Anyone you share the following link with will be able to read this content:

[Get shareable link](#)

Sorry, a shareable link is not currently available for this article.

[Copy to clipboard](#)

Provided by the Springer Nature SharedIt content-sharing initiative

## Further reading

- [\*\*Executable network of SARS-CoV-2-host interaction predicts drug combination treatments\*\*](#)
  - Rowan Howell
  - Matthew A. Clarke
  - Jasmin Fisher

---

This article was downloaded by **calibre** from <https://www.nature.com/articles/s41586-021-04352-y>.

| [Section menu](#) | [Main menu](#) |

- Article
- [Published: 02 February 2022](#)

# Streptococcal pyrogenic exotoxin B cleaves GSDMA and triggers pyroptosis

- [Wanyan Deng](#)<sup>1,2,3 na1</sup>,
- [Yang Bai](#)<sup>1,4 na1</sup>,
- [Fan Deng](#)<sup>1,4 na1</sup>,
- [Youdong Pan](#)<sup>5,6 na1</sup>,
- [Shenglin Mei](#)<sup>7</sup>,
- [Zengzhang Zheng](#)<sup>1,2,3</sup>,
- [Rui Min](#)<sup>1,4</sup>,
- [Zeyu Wu](#)<sup>1,4</sup>,
- [Wu Li](#)<sup>1,2,3</sup>,
- [Rui Miao](#)<sup>8,9</sup>,
- [Zhibin Zhang](#) [ORCID: orcid.org/0000-0003-1349-2713](#)<sup>8,9</sup>,
- [Thomas S. Kupper](#) [ORCID: orcid.org/0000-0002-4229-2916](#)<sup>5,6</sup>,
- [Judy Lieberman](#) [ORCID: orcid.org/0000-0002-6200-4715](#)<sup>8,9</sup> &
- [Xing Liu](#) [ORCID: orcid.org/0000-0002-6277-3856](#)<sup>1,2,3</sup>

[Nature](#) volume 602, pages 496–502 (2022)

- 5395 Accesses
- 56 Altmetric
- [Metrics details](#)

## Subjects

- [Infection](#)
- [Pathogens](#)
- [Pattern recognition receptors](#)

## Abstract

Gasdermins, a family of five pore-forming proteins (GSDMA–GSDME) in humans expressed predominantly in the skin, mucosa and immune sentinel cells, are key executioners of inflammatory cell death (pyroptosis), which recruits immune cells to infection sites and promotes protective immunity<sup>1,2</sup>. Pore formation is triggered by gasdermin cleavage<sup>1,2</sup>. Although the proteases that activate GSDMB, C, D and E have been identified, how GSDMA—the dominant gasdermin in the skin—is activated, remains unknown. *Streptococcus pyogenes*, also known as group A *Streptococcus* (GAS), is a major skin pathogen that causes substantial morbidity and mortality worldwide<sup>3</sup>. Here we show that the GAS cysteine protease SpeB virulence factor triggers keratinocyte pyroptosis by cleaving GSDMA after Gln246, unleashing an active N-terminal fragment that triggers pyroptosis. *Gsdma1* genetic deficiency blunts mouse immune responses to GAS, resulting in uncontrolled bacterial dissemination and death. GSDMA acts as both a sensor and substrate of GAS SpeB and as an effector to trigger pyroptosis, adding a simple one-molecule mechanism for host recognition and control of virulence of a dangerous microbial pathogen.

This is a preview of subscription content

## Access options

Subscribe to Nature+

Get immediate online access to the entire Nature family of 50+ journals

\$29.99

monthly

## Subscribe

Subscribe to Journal

Get full journal access for 1 year

\$199.00

only \$3.90 per issue

## Subscribe

All prices are NET prices.

VAT will be added later in the checkout.

Tax calculation will be finalised during checkout.

Buy article

Get time limited or full article access on ReadCube.

\$32.00

## Buy

All prices are NET prices.

## **Additional access options:**

- [Log in](#)
- [Learn about institutional subscriptions](#)

**Fig. 1: The GAS virulence factor SpeB triggers lytic death of skin epithelial cells.**

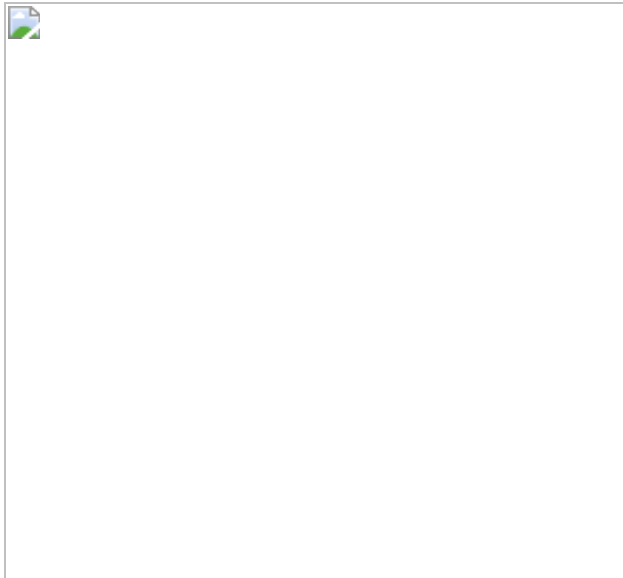


**Fig. 2: SpeB triggers pyroptosis in a GSDMA-dependent manner.**



**Fig. 3: SpeB directly cleaves GSDMA after Gln246.**

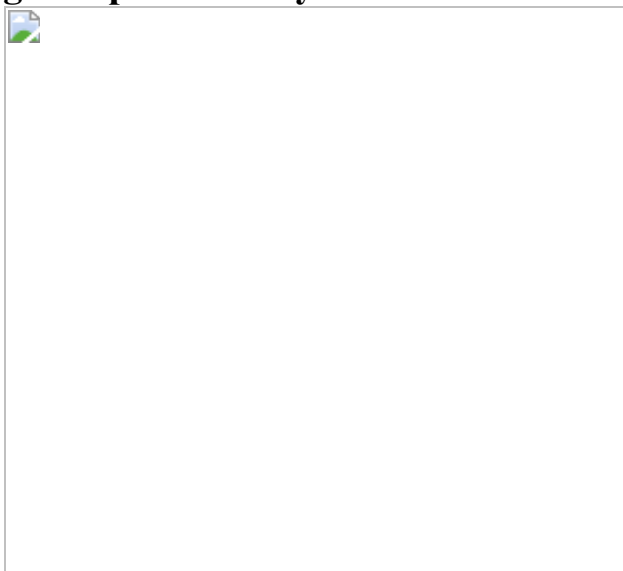
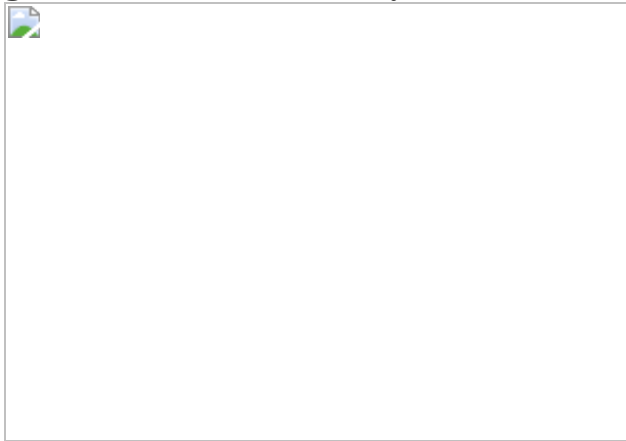


**Fig. 4: Gsdma1 deficiency blunts host anti-GAS immunity.**



## Data availability

All data supporting the findings of this study are included in this manuscript and its supplementary information. [Source data](#) are provided with this paper.

## References

1. Broz, P., Pelegrin, P. & Shao, F. The gasdermins, a protein family executing cell death and inflammation. *Nat. Rev. Immunol.* **20**, 143–157 (2020).
2. Liu, X., Xia, S., Zhang, Z., Wu, H. & Lieberman, J. Channelling inflammation: gasdermins in physiology and disease. *Nat. Rev. Drug Discov.* **20**, 384–405 (2021).
3. Cole, J. N., Barnett, T. C., Nizet, V. & Walker, M. J. Molecular insight into invasive group A streptococcal disease. *Nat. Rev. Microbiol.* **9**, 724–736 (2011).
4. Musser, J. M., Stockbauer, K., Kapur, V. & Rudgers, G. W. Substitution of cysteine 192 in a highly conserved *Streptococcus pyogenes* extracellular cysteine protease (interleukin 1beta convertase) alters proteolytic activity and ablates zymogen processing. *Infect. Immun.* **64**, 1913–1917 (1996).

5. Svensson, M. D. et al. Role for a secreted cysteine proteinase in the establishment of host tissue tropism by group A streptococci. *Mol. Microbiol.* **38**, 242–253 (2000).
6. Cole, J. N. et al. Trigger for group A streptococcal M1T1 invasive disease. *FASEB J.* **20**, 1745–1747 (2006).
7. Shelburne, S. A., 3rd et al. Growth characteristics of and virulence factor production by group A Streptococcus during cultivation in human saliva. *Infect. Immun.* **73**, 4723–4731 (2005).
8. Aziz, R. K. et al. Invasive M1T1 group A *Streptococcus* undergoes a phase-shift in vivo to prevent proteolytic degradation of multiple virulence factors by SpeB. *Mol. Microbiol.* **51**, 123–134 (2004).
9. Liu, X. et al. Inflammasome-activated gasdermin D causes pyroptosis by forming membrane pores. *Nature* **535**, 153–158 (2016).
10. Ding, J. et al. Pore-forming activity and structural autoinhibition of the gasdermin family. *Nature* **535**, 111–116 (2016).
11. Aglietti, R. A. et al. GsdmD p30 elicited by caspase-11 during pyroptosis forms pores in membranes. *Proc. Natl Acad. Sci. USA* **113**, 7858–7863 (2016).
12. Sborgi, L. et al. GSDMD membrane pore formation constitutes the mechanism of pyroptotic cell death. *EMBO J.* **35**, 1766–1778 (2016).
13. Sumitomo, T. et al. Streptococcal cysteine protease-mediated cleavage of desmogleins is involved in the pathogenesis of cutaneous infection. *Front. Cell Infect. Microbiol.* **8**, 10 (2018).
14. Saouda, M., Wu, W., Conran, P. & Boyle, M. D. Streptococcal pyrogenic exotoxin B enhances tissue damage initiated by other *Streptococcus pyogenes* products. *J. Infect. Dis.* **184**, 723–731 (2001).
15. Paz, I. et al. Galectin-3, a marker for vacuole lysis by invasive pathogens. *Cell Microbiol.* **12**, 530–544 (2010).

16. Doran, J. D. et al. Autocatalytic processing of the streptococcal cysteine protease zymogen: processing mechanism and characterization of the autoproteolytic cleavage sites. *Eur. J. Biochem.* **263**, 145–151 (1999).
17. Gerwin, B. I., Stein, W. H. & Moore, S. On the specificity of streptococcal proteinase. *J. Biol. Chem.* **241**, 3331–3339 (1966).
18. Nomizu, M. et al. Substrate specificity of the streptococcal cysteine protease. *J. Biol. Chem.* **276**, 44551–44556 (2001).
19. Carroll, R. K. & Musser, J. M. From transcription to activation: how group A *Streptococcus*, the flesh-eating pathogen, regulates SpeB cysteine protease production. *Mol. Microbiol.* **81**, 588–601 (2011).
20. Lichtenberger, B. M. et al. Epidermal EGFR controls cutaneous host defense and prevents inflammation. *Sci. Transl. Med.* **5**, 199ra111 (2013).
21. Sawada, Y. et al. Cutaneous innate immune tolerance is mediated by epigenetic control of MAP2K3 by HDAC8/9. *Sci. Immunol.* **6**, eabe1935 (2021).
22. Kolaczkowska, E. & Kubes, P. Neutrophil recruitment and function in health and inflammation. *Nat. Rev. Immunol.* **13**, 159–175 (2013).
23. Barnett, T. C. et al. The globally disseminated M1T1 clone of group A *Streptococcus* evades autophagy for intracellular replication. *Cell Host Microbe* **14**, 675–682 (2013).
24. LaRock, C. N. et al. IL-1 $\beta$  is an innate immune sensor of microbial proteolysis. *Sci. Immunol.* **1**, eaah3539 (2016).
25. Nitsche-Schmitz, D. P., Rohde, M. & Chhatwal, G. S. Invasion mechanisms of Gram-positive pathogenic cocci. *Thromb. Haemost.* **98**, 488–496 (2007).

26. Rohde, M. & Chhatwal, G. S. Adherence and invasion of streptococci to eukaryotic cells and their role in disease pathogenesis. *Curr. Top. Microbiol. Immunol.* **368**, 83–110 (2013).
27. Hynes, W. & Sloan, M. in *Streptococcus pyogenes: Basic Biology to Clinical Manifestations* (eds Ferretti, J. J. et al.) (2016).
28. Zhang, W., Rong, C., Chen, C. & Gao, G. F. Type-IVC secretion system: a novel subclass of type IV secretion system (T4SS) common existing in gram-positive genus *Streptococcus*. *PLoS ONE* **7**, e46390 (2012).
29. Richter, J. et al. Streptolysins are the primary inflammasome activators in macrophages during *Streptococcus pyogenes* infection. *Immunol. Cell Biol.* **99**, 1040–1052 (2021).
30. Richter, J., Brouwer, S., Schroder, K. & Walker, M. J. Inflammasome activation and IL-1 $\beta$  signalling in group A *Streptococcus* disease. *Cell Microbiol.* **23**, e13373 (2021).
31. Brouwer, S., Barnett, T. C., Rivera-Hernandez, T., Rohde, M. & Walker, M. J. *Streptococcus pyogenes* adhesion and colonization. *FEBS Lett.* **590**, 3739–3757 (2016).
32. Carothers, K. E. et al. The streptococcal protease SpeB antagonizes the biofilms of the human pathogen *Staphylococcus aureus* USA300 through cleavage of the staphylococcal SdrC protein. *J. Bacteriol.* **202**, e00008-e00020 (2020).
33. Zhou, W. et al. Structure of the human cGAS–DNA complex reveals enhanced control of immune surveillance. *Cell* **174**, 300–311.e311, (2018).
34. Kranzusch, P. J. et al. Ancient origin of cGAS–STING reveals mechanism of universal 2',3' cGAMP signaling. *Mol. Cell* **59**, 891–903 (2015).

35. Orzalli, M. H. & Kagan, J. C. A one-protein signaling pathway in the innate immune system. *Sci. Immunol.* **1**, eah6184 (2016).
36. Mitchell, P. S., Sandstrom, A. & Vance, R. E. The NLRP1 inflammasome: new mechanistic insights and unresolved mysteries. *Curr. Opin. Immunol.* **60**, 37–45 (2019).
37. Whatmore, A. M. & Kehoe, M. A. Horizontal gene transfer in the evolution of group A streptococcal *emm*-like genes: gene mosaics and variation in Vir regulons. *Mol. Microbiol.* **11**, 363–374 (1994).
38. Zheng, Z. Z. et al. The lysosomal Rag–Ragulator complex licenses RIPK1-and caspase-8-mediated pyroptosis by *Yersinia*. *Science* **372**, eabg0269(2021).
39. Li, W. et al. Quality control, modeling, and visualization of CRISPR screens with MAGeCK-VISPR. *Genome Biol.* **16**, 281, (2015).
40. Shepard, L. A., Shatursky, O., Johnson, A. E. & Tweten, R. K. The mechanism of pore assembly for a cholesterol-dependent cytolysin: formation of a large preporo complex precedes the insertion of the transmembrane β-hairpins. *Biochemistry* **39**, 10284–10293 (2000).

## Acknowledgements

We thank V. Nizet for sharing *S. pyogenes* isolate M1T1 strain 5448 and its isogenic mutant strains ( $\Delta speB$ ,  $covR/S^-$ ,  $\Delta cepA$  and  $\Delta mac$  variants) as well as SpeB constructs, Z. Zhang for providing *S. pyogenes* M9, M12 and M73 strains, C. Wang for providing Phage-Flag vector, and Y. Chen for providing a modified pET vector with an N-terminal 6×His-SUMO tag. This work was supported by National Key R&D Program of China (2020YFA0509600), National Natural Science Foundation of China (32122034, 31972897), Key Research Program of the Chinese Academy of Sciences (ZDBS-LY-SM008), Shanghai Pilot Program for Basic Research—Chinese Academy of Sciences, Shanghai Branch (JCYJ-SHFY-2021-009), Strategic Priority Research Program of Chinese Academy of Sciences (XDB29030300), Shanghai Municipal Science and Technology Major

Project (2019SHZDZX02) (X.L.), NIH R01CA240955 and R01AI39914 (J.L.), NIH R01AI127654 (T.S.K.) and China Postdoctoral Science Foundation (2019M650193), Guangzhou Science and Technology Project (202102020093) (W.D.).

## Author information

### Author notes

1. These authors contributed equally: Wanyan Deng, Yang Bai, Fan Deng, Youdong Pan

### Affiliations

1. The Center for Microbes, Development and Health, Key Laboratory of Molecular Virology and Immunology, Institut Pasteur of Shanghai, Chinese Academy of Sciences, Shanghai, China

Wanyan Deng, Yang Bai, Fan Deng, Zengzhang Zheng, Rui Min, Zeyu Wu, Wu Li & Xing Liu

2. The Joint Center for Infection and Immunity, Guangzhou Institute of Pediatrics, Guangzhou Women and Children's Medical Center, Guangzhou, China

Wanyan Deng, Zengzhang Zheng, Wu Li & Xing Liu

3. The Joint Center for Infection and Immunity, Institut Pasteur of Shanghai, Chinese Academy of Sciences, Shanghai, China

Wanyan Deng, Zengzhang Zheng, Wu Li & Xing Liu

4. University of Chinese Academy of Sciences, Beijing, China

Yang Bai, Fan Deng, Rui Min & Zeyu Wu

5. Department of Dermatology, Brigham and Women's Hospital, Boston, MA, USA

Youdong Pan & Thomas S. Kupper

6. Harvard Skin Disease Research Center, Harvard Medical School, Boston, MA, USA

Youdong Pan & Thomas S. Kupper

7. Department of Biomedical Informatics, Harvard Medical School, Boston, MA, USA

Shenglin Mei

8. Program in Cellular and Molecular Medicine, Boston Children's Hospital, Boston, MA, USA

Rui Miao, Zhibin Zhang & Judy Lieberman

9. Department of Pediatrics, Harvard Medical School, Boston, MA, USA

Rui Miao, Zhibin Zhang & Judy Lieberman

## Contributions

W.D., Y.B., F.D., Y.P., J.L. and X.L. conceived the study. W.D., Y.B., F.D. and Y.P. designed and performed most experiments with assistance from R. Min, Z.W. and W.L. Z. Zheng and S.M. performed the CRISPR screen and sequencing data analysis, respectively. R. Miao and Z. Zhang provided technical support. W.D., Y.B., F.D., Y.P. and X.L. analysed the data. All authors discussed the results and commented on the manuscript. W.D., Y.B., F.D., Y.P., T.S.K., J.L. and X.L. wrote the manuscript. X.L. supervised the study.

## Corresponding author

Correspondence to [Xing Liu](#).

## Ethics declarations

## Competing interests

The authors declare no competing interests.

## Peer review information

*Nature* thanks Dario Zamboni and the other, anonymous, reviewer(s) for their contribution to the peer review of this work.

## Additional information

**Publisher's note** Springer Nature remains neutral with regard to jurisdictional claims in published maps and institutional affiliations.

## Extended data figures and tables

### [Extended Data Fig. 1 SpeB-deficient GAS triggers systemic infection.](#)

**a**, DNA sequence comparison of GAS isolate M1T1 strain 5448 and its isogenic mutant strains ( $\Delta cepA$ ,  $\Delta mac$ ,  $covR/S^-$  and  $\Delta speB$  variants). **b, c**, RT-PCR (**b**) and immunoblot analysis (**c**) of the expression of SpeB in the indicated GAS strains. **d–f**, mice were infected or not with the indicated GAS strains. **d**, IHC analysis of neutrophil infiltration at infection site on day 1. Scale bar: 100  $\mu$ m. **e**, Bacteria load measured from skin lesions, spleens and livers of mice infected or not with GAS. **f**, Survival rate of mice challenged or not with the indicated GAS ( $n = 18$  mice per group). **e**, box plots show all points, min to max ( $n = 5$  mice per group). The center line, upper limit and lower limit of the box denote median, 25th and 75th percentiles and the whiskers denote the minimum and maximum values of data. **e**, Two-tailed Student's *t*-test; **f**, Mantel-Cox log-rank test. Data are representative of at least three independent experiments. For gel source data, see Supplementary Fig. 1.

### [Source data](#)

## Extended Data Fig. 2 SpeB contributes to local tissue destruction.

**a, b**, The re-expression of SpeB in  $\Delta speB$  GAS was confirmed by both RT-PCR (**a**) and immunoblot analysis (**b**). **c–h**, mice were infected or not with the indicated GAS strains. **c**, Representative image of skin lesions of mice challenged with GAS or not for 1 day. **d**, Quantification of skin lesion size. **e**, Histopathology of skin biopsies analysed by H&E staining. **f, g**, IHC analysis and quantification of neutrophil infiltration at infection site. **h**, Bacteria load measured from skin lesions, spleens and livers of mice infected or not with GAS. Scale bar: 100  $\mu$ m. **d, g**, show mean  $\pm$  s.d. ( $n = 5$  mice per group); **h**, box plots show all points, min to max ( $n = 5$  mice per group). The center line, upper limit and lower limit of the box denote median, 25th and 75th percentiles and the whiskers denote the minimum and maximum values of data. **d, g, h**, Two-tailed Student's *t*-test. Data are representative of at least three independent experiments. For gel source data, see Supplementary Fig. 1.

[Source data](#)

## Extended Data Fig. 3 SpeB triggers lytic death of primary mouse keratinocytes and A431 cells.

**a**, Primary mouse keratinocytes were infected with GAS isolate M1T1 strain 5448 or its isogenic mutant strains for the indicated times. Percentage of internalized GAS was shown by counting intracellular CFUs relative to the inoculum (left panel). Cell cytotoxicity of all the cells in a well was measured by LDH release assay (right panel). **b–d**, Primary keratinocytes infected with FITC-labeled GAS strains were washed with PBS before cells were stained and analyzed by confocal fluorescence imaging. Cell borders are outlined with dashed lines. Cells with intracellular GAS were quantified from 700 cells ( $n = 5$ , mean  $\pm$  s.d.) (**b**). **e**, Levels of hyaluronic acid capsule at logarithmic and stationary growth phases. **f**, RT-PCR (left panel) and immunoblot analysis (right panel) of the expression of SpeB in the indicated GAS strains. **g, h** Primary keratinocytes infected or not with the indicated GAS strains for 2.5 h were analysed by phase-contrast microscopy (**g**), LDH release (**h**). **i, j**, A431 cells infected or not with GAS isolate

M1T1 strain 5448 or its isogenic mutant strains for 2.5 h were analysed by phase-contrast microscopy (**i**) and LDH release (**j**). **k, l**, Equal amounts of recombinant of WT SpeB or protease activity-deficient mutant mSpeB were respectively electroporated into A431 cells for 1 h or directly added into cell culture medium for 2.5 h, followed by cell morphology observation by phase-contrast microscopy (**k**), cell viability assessment by CellTiter-Glo luminescent assay (**l**). **g, i**, Arrowheads indicate pyroptotic cells. **c, d, g, i, k**, scale bar: 10  $\mu$ m. Graphs show mean  $\pm$  s.d. of triplicate wells. **h, j**, One-way ANOVA; **l**, Two-tailed Student's *t*-test. Data are representative of at least three independent experiments. For gel source data, see Supplementary Fig. [1](#).

[Source data](#)

[\*\*Extended Data Fig. 4 Validation of additional hits identified from CRISPR screen of SpeB-triggered lytic cell death.\*\*](#)

**a**, List of top hits from CRISPR screen of SpeB-triggered lytic cell death. **b**, GSDMA-knockout cells used in this study. Gene coding sequences were present as black boxes. Top sequence track is the gene wild-type allele. Location of gRNAs is indicated with blue bars and PAM sequences were underscored. **c–l**, WT and the indicated gene knockout A431 cells were transfected or not with recombinant SpeB by electroporation, followed by cell morphology observation by phase-contrast microscopy (**c, e, g, i, k**), cell viability assessment by CellTiter-Glo luminescent assay (**d, f, h, j, l**). Scale bar: 10  $\mu$ m. Graphs show mean  $\pm$  s.d. of triplicate wells. Data are representative of at least three independent experiments.

[Source data](#)

[\*\*Extended Data Fig. 5 SpeB specifically targets and cleaves GSDMA.\*\*](#)

**a, b**, *In vitro* cleavage assay of recombinant GSDMA, GSDMD (**a**) or GSDME (**b**) by incubation with recombinant WT SpeB (100 nM) or mSpeB (250 nM) for 0.5 h. **c**, Whole cell lysates of A431 cells infected or not with the indicated GAS strains were subjected to immunoblot analysis for the

indicated proteins. **d–f**, 293T cells were transfected with the indicated plasmids (Flag-tagged GSDMA, Myc-tagged bacterial proteases) before analysed by phase-contrast microscopy (**d**), LDH release (**e**) and immunoblot of whole cell lysates with the indicated antibodies (**f**). **g, h**, Flag-tagged GSDMA was treated or not with SpeB, staphopains (ScpA, SspB), or cathepsins (Cathepsin B, L, D) before subjected to immunoblot analysis with the indicated antibodies. **i**, GSDMA N-terminal and C-terminal cleavage products (p27 and p23) were analysed by mass spectrometry (MS) and Edman sequencing, respectively. Individual peptides identified by MS and shown in black bars were mapped against N-terminal GSDMA (upper right panel). Middle right panel shows the N-terminal sequence of p23 determined by Edman sequencing, the diagram of GSDMA two-domain architecture, and SpeB cleavage site Gln246 highlighted in green. Bottom panel shows the positions (P) on the substrate of SpeB (GSDMA) which are counted and numbered (P3-P2-P1-P1'-P2'-P3') from the point of cleavage. **j**, Whole cell lysates of 293T cells transfected with the indicated plasmids were collected and subjected to immunoblot analysis. Scale bar: 10 μm. Data are representative of at least three independent experiments. Graphs show mean ± s.d. of triplicate wells. **e**, One-way ANOVA. Data are representative of at least three independent experiments. For gel source data, see Supplementary Fig. 1.

[Source data](#)

[Extended Data Fig. 6 GSDMA-NT produced by SpeB cleavage is sufficient to initiate pyroptosis, but does not injure bystander cells.](#)

**a**, Coomassie Blue-stained SDS-PAGE gel showing purified recombinant GSDMA, GSDMA-NT and GSDMA-CT. **b–d**, Equal amounts of recombinant full-length GSDMA, GSDMA-NT (1–246aa), GSDMA-CT, full-length GSDMD, Caspase-11 or full-length GSDMD plus Caspase-11 were electroporated into 293T cells respectively, followed by cell morphology observation by phase-contrast microscopy (**b**), cell viability analysis by CellTiter-Glo luminescent assay (**c**), and cell death assessment by PI uptake (**d**). **e–g**, Equal amounts of recombinant of full-length GSDMA, GSDMA-NT (1–246aa), GSDMA-CT, full-length GSDMD,

Caspase-11 or full-length GSDMD plus Caspase-11 were respectively added directly into cell culture medium, followed by cell morphology observation by phase-contrast microscopy (**e**), cell viability analysis by CellTiter-Glo luminescent assay (**f**), and cell death assessment by PI uptake (**g**). Pyroptotic cells form large ballooning bubbles; Scale bar: 20  $\mu$ m. Graphs show mean  $\pm$  s.d. of triplicate wells (**c, f**) or mean  $\pm$  s.e.m. of quadruplicate wells (**d, g**). **c**, Two-tailed Student's *t*-test. Data are representative of at least three independent experiments. For gel source data, see Supplementary Fig. 1.

[Source data](#)

**Extended Data Fig. 7 GSDMA 1-246aa, but not 1-214aa possesses pyroptosis-inducing activity.**

**a**, Coomassie Blue-stained SDS-PAGE gel showing recombinant engineered GSDMA with Flag tag-3C protease cleavage sequence inserted immediately after residue G214, Q246, treated with 3C protease. **b-d**, 293T cells were transfected with the indicated plasmids (Empty vector or Flag-tagged Gasdermin) before cell death was observed by phase-contrast microscopy (**b**) and determined by LDH release assay (**c**), whole cell lysates were collected for immunoblot analysis (**d**). Arrowheads indicate pyroptotic cells; Scale bar: 10  $\mu$ m. Graphs show mean  $\pm$  s.d. of triplicate wells. **c**, Two-tailed Student's *t*-test. Data are representative of at least three independent experiments. For gel source data, see Supplementary Fig. 1.

[Source data](#)

**Extended Data Fig. 8 Phospholipid binding property and liposome-disrupting activity of GSDMA-NT.**

**a**, Lipid strips dotted with indicated phospholipids (left panel) were incubated with noncovalent complex of cleaved GSDMA with a Flag-tag inserted right before the cleavage site, unprocessed full-length GSDMA, or 3C protease, followed by immunoblot analysis with an anti-Flag antibody (right panel). **b**, Indicated liposomes incubated with noncovalent complex of cleaved GSDMA (NT + CT) and full-length GSDMA (FL) were

subjected to sedimentation by ultracentrifugation. Proteins in both liposome-free supernatant (S) and liposome-containing pellet (P) were analysed by SDS-PAGE. **c**, Indicated recombinant proteins incubated or not with CL liposomes and glutaraldehyde were analyzed by SDS-agarose gel electrophoresis and subsequent Coomassie Blue staining. **d–h**, Leakage of PC-PE liposomes containing additional PS or CL was monitored in real-time by terbium ( $Tb^{3+}$ ) fluorescence after incubation with recombinant gasdermins proteins in the presence or absence of recombinant SpeB or enzymatically inactive SpeB C192S (mSpeB) as indicated, or cysteine protease inhibitor E64 if necessary. Data are representative of at least three independent experiments. For gel source data, see Supplementary Fig. [1](#).

#### [Source data](#)

#### [Extended Data Fig. 9 GSDMA proteins in different species.](#)

Multiple sequences alignment of human (h), chimpanzee (cp), monkey (mk), rat (r), dog (dg) GSDMA and mouse Gsdma1, Gsdma2 and Gsdma3 was performed using the ClustalW2 algorithm and plotted by ESPript program. Identical residues are highlighted by red background, and similar residues are indicated in red. Ile 245 and Gln246 (\*) in human GSDMA are highly conserved in chimpanzee, monkey, rat, dog GSDMA as well as mouse Gsdma1.

#### [Extended Data Fig. 10 SpeB cleaves mouse Gsdma1 and releases its N-terminal pyroptosis-inducing activity.](#)

**a**, Whole cell lysates of 293T cells transfected with the indicated plasmids were collected and subjected to immunoblot analysis with the indicated antibodies. **b**, Coomassie Blue-stained SDS-PAGE gel showing in vitro cleavage of recombinant WT Gsdma1 or mutant Gsdma1 I246N/Q247E (1  $\mu$ M) incubated with or without recombinant WT SpeB (100 nM) for 0.5 h. **c**, Whole cell lysates of 293T cells transfected with the indicated plasmids were collected and subjected to immunoblot analysis. **d**, Leakage of PC-PE liposomes containing additional PS or CL was monitored in real-time by terbium ( $Tb^{3+}$ ) fluorescence after incubation with recombinant gasdermins proteins in the presence or absence of recombinant SpeB as indicated. **e, f**,

293T cells transfected with the indicated plasmids were analysed by phase-contrast microscopy (**e**), LDH release (**f**). Arrowheads indicate pyroptotic cells; Scale bar: 10 µm. Graphs show mean ± s.d. of triplicate wells. **f**, One-way ANOVA. Data are representative of at least three independent experiments. For gel source data, see Supplementary Fig. [1](#).

### [Source data](#)

### [Extended Data Fig. 11 Gsdma1 deficiency affects host immune responses against subcutaneous but not intraperitoneal infection of GAS WT.](#)

**a**, WT and *Gsdma1*<sup>-/-</sup> mice were subcutaneously infected or not with GAS isolate M1T1 strain 5448 or its isogenic mutant strain ( $\Delta speB$  variant). IHC analysis of neutrophil infiltration at infection site on day 1. Scale bar: 100 µm. **b**, Quantification of neutrophil infiltration at infection site. **c**, Cutaneous sections from *Gsdma1*<sup>-/-</sup> mice infected or not for 18 h with FITC-labelled GAS WT were subjected to immunofluorescence staining with anti-keratin 14. Nucleus was stained with DAPI. Dashed lines delineate the boundaries of epidermis. Scale bar: 10 µm. **d**, Survival rate of mice intraperitoneally administrated with the indicated GAS (n = 12 mice per group). **e**, Model of SpeB-triggered GSDMA activation and subsequent pyroptosis of skin epithelial cells during GAS infection. **b**, show mean ± s.d. (n = 5 mice per group); Two-tailed Student's *t*-test. Data are representative of at least three independent experiments.

### [Source data](#)

## Supplementary information

### [Supplementary Figure 1](#)

Uncropped blots used to prepare main and extended data figures.

### [Reporting Summary](#)

## **Supplementary Table 1**

Oligonucleotide primers used in this study for cloning DNA fragments containing *cepA*, *mac*, *covR/S*, *speB*, *emm*, *Rgg* and *RocA* genes from the GAS genome.

## **Source data**

**Source Data Fig. 1**

**Source Data Fig. 2**

**Source Data Fig. 3**

**Source Data Fig. 4**

**Source Data Extended Data Fig. 1**

**Source Data Extended Data Fig. 2**

**Source Data Extended Data Fig. 3**

**Source Data Extended Data Fig. 4**

**Source Data Extended Data Fig. 5**

**Source Data Extended Data Fig. 6**

**Source Data Extended Data Fig. 7**

**Source Data Extended Data Fig. 8**

**Source Data Extended Data Fig. 10**

## [Source Data Extended Data Fig. 11](#)

## Rights and permissions

### [Reprints and Permissions](#)

## About this article

### Cite this article

Deng, W., Bai, Y., Deng, F. *et al.* Streptococcal pyrogenic exotoxin B cleaves GSDMA and triggers pyroptosis. *Nature* **602**, 496–502 (2022). <https://doi.org/10.1038/s41586-021-04384-4>

- Received: 13 April 2021
- Accepted: 23 December 2021
- Published: 02 February 2022
- Issue Date: 17 February 2022
- DOI: <https://doi.org/10.1038/s41586-021-04384-4>

## Share this article

Anyone you share the following link with will be able to read this content:

[Get shareable link](#)

Sorry, a shareable link is not currently available for this article.

[Copy to clipboard](#)

Provided by the Springer Nature SharedIt content-sharing initiative

---

This article was downloaded by **calibre** from <https://www.nature.com/articles/s41586-021-04384-4>

| [Section menu](#) | [Main menu](#) |

- Article
- [Published: 02 February 2022](#)

# Decade-long leukaemia remissions with persistence of CD4<sup>+</sup> CAR T cells

- [J. Joseph Melenhorst](#) ORCID: [orcid.org/0000-0001-7677-537X](https://orcid.org/0000-0001-7677-537X)<sup>1,2,3,4,5 na1 na2</sup>,
- [Gregory M. Chen](#)<sup>6 na1</sup>,
- [Meng Wang](#) ORCID: [orcid.org/0000-0002-3453-7805](https://orcid.org/0000-0002-3453-7805)<sup>1,2,3 na1</sup>,
- [David L. Porter](#)<sup>3,7 na1</sup>,
- [Changya Chen](#)<sup>8,9</sup>,
- [McKensie A. Collins](#)<sup>1,2,3,10</sup>,
- [Peng Gao](#)<sup>8,9</sup>,
- [Shovik Bandyopadhyay](#)<sup>10</sup>,
- [Hongxing Sun](#)<sup>1,2,3</sup>,
- [Ziran Zhao](#)<sup>1,2,3</sup>,
- [Stefan Lundh](#)<sup>1,2,3</sup>,
- [Iulian Pruteanu-Malinici](#)<sup>11</sup>,
- [Christopher L. Nobles](#)<sup>12</sup>,
- [Sayantan Maji](#)<sup>1,2,3</sup>,
- [Noelle V. Frey](#)<sup>3</sup>,
- [Saar I. Gill](#)<sup>3</sup>,
- [Lifeng Tian](#) ORCID: [orcid.org/0000-0001-9740-5327](https://orcid.org/0000-0001-9740-5327)<sup>1,3</sup>,
- [Irina Kulikovskaya](#)<sup>1,2,3</sup>,
- [Minnal Gupta](#)<sup>1,2,3</sup>,
- [David E. Ambrose](#)<sup>1,2,3</sup>,
- [Megan M. Davis](#)<sup>1,2,3</sup>,

- [Joseph A. Fraietta](#)<sup>1,2,3,12</sup>,
- [Jennifer L. Brogdon](#)<sup>11</sup>,
- [Regina M. Young](#)<sup>1,2,3</sup>,
- [Anne Chew](#)<sup>1,2,3</sup>,
- [Bruce L. Levine](#) [ORCID: orcid.org/0000-0001-6971-8465](#)<sup>1,2,3</sup>,
- [Donald L. Siegel](#) [ORCID: orcid.org/0000-0003-2098-2251](#)<sup>1,2,13</sup>,
- [Cécile Alanio](#) [ORCID: orcid.org/0000-0003-2785-7445](#)<sup>4,5,14</sup>,
- [E. John Wherry](#) [ORCID: orcid.org/0000-0003-0477-1956](#)<sup>4,5,14</sup>,
- [Frederic D. Bushman](#) [ORCID: orcid.org/0000-0003-4740-4056](#)<sup>12</sup>,
- [Simon F. Lacey](#)<sup>1,2,3</sup>,
- [Kai Tan](#) <sup>2,4,6,9,10 na2</sup> &
- [Carl H. June](#) [ORCID: orcid.org/0000-0003-0241-3557](#)<sup>1,2,3,4,5 na2</sup>

*Nature* volume **602**, pages 503–509 (2022)

- 24k Accesses
- 2 Citations
- 2207 Altmetric
- [Metrics details](#)

## Subjects

- [Immunotherapy](#)
- [Translational immunology](#)

## Abstract

The adoptive transfer of T lymphocytes reprogrammed to target tumour cells has demonstrated potential for treatment of various cancers<sup>1,2,3,4,5,6,7</sup>. However, little is known about the long-term potential and clonal stability of the infused cells. Here we studied long-lasting CD19-redirected chimeric antigen receptor (CAR) T cells in two patients with chronic lymphocytic leukaemia<sup>1,2,3,4</sup> who achieved a complete remission in 2010. CAR T cells

remained detectable more than ten years after infusion, with sustained remission in both patients. Notably, a highly activated CD4<sup>+</sup> population emerged in both patients, dominating the CAR T cell population at the later time points. This transition was reflected in the stabilization of the clonal make-up of CAR T cells with a repertoire dominated by a small number of clones. Single-cell profiling demonstrated that these long-persisting CD4<sup>+</sup> CAR T cells exhibited cytotoxic characteristics along with ongoing functional activation and proliferation. In addition, longitudinal profiling revealed a population of gamma delta CAR T cells that prominently expanded in one patient concomitant with CD8<sup>+</sup> CAR T cells during the initial response phase. Our identification and characterization of these unexpected CAR T cell populations provide novel insight into the CAR T cell characteristics associated with anti-cancer response and long-term remission in leukaemia.

This is a preview of subscription content

## Access options

Subscribe to Nature+

Get immediate online access to the entire Nature family of 50+ journals

\$29.99

monthly

[Subscribe](#)

Subscribe to Journal

Get full journal access for 1 year

\$199.00

only \$3.90 per issue

[Subscribe](#)

All prices are NET prices.  
VAT will be added later in the checkout.  
Tax calculation will be finalised during checkout.

Buy article

Get time limited or full article access on ReadCube.

\$32.00

[Buy](#)

All prices are NET prices.

### **Additional access options:**

- [Log in](#)
- [Learn about institutional subscriptions](#)

**Fig. 1: Molecular tracking of effectors and targets in long-term responders to anti-CD19 CAR T cell therapy for CLL.**

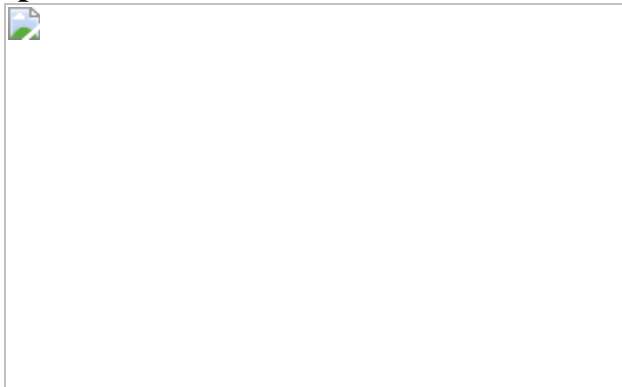


**Fig. 2: Analysis of CD3<sup>+</sup> CAR<sup>+</sup> T cells using CyTOF across multiple time points.**

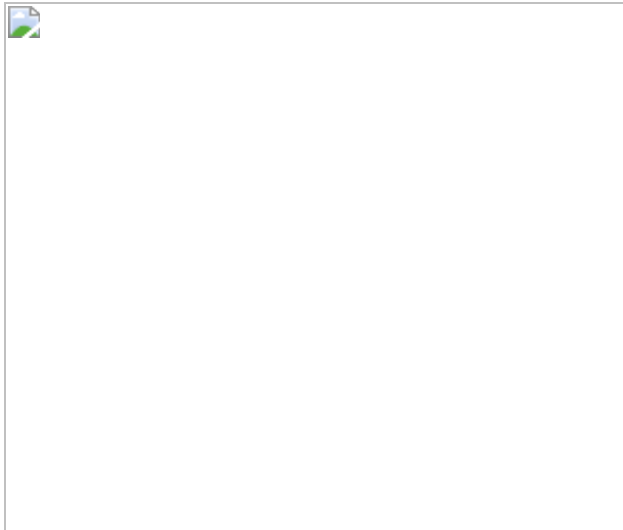


**Fig. 3: Multi-omic single-cell analysis reveals clonal expansion, proliferation and activation in CAR T cells from patient 1 at year 9.3.**

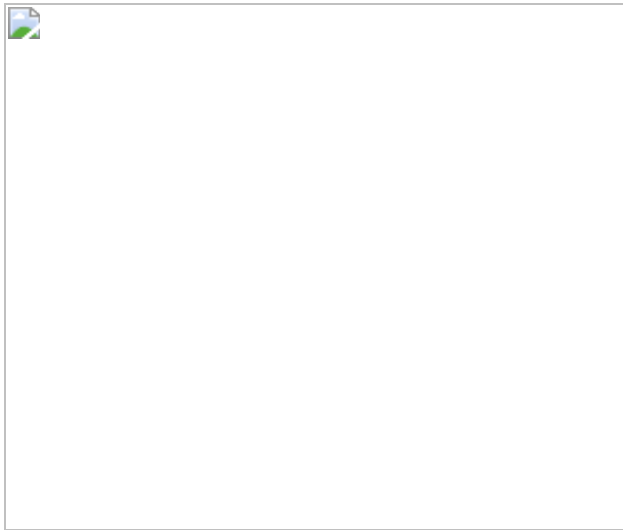
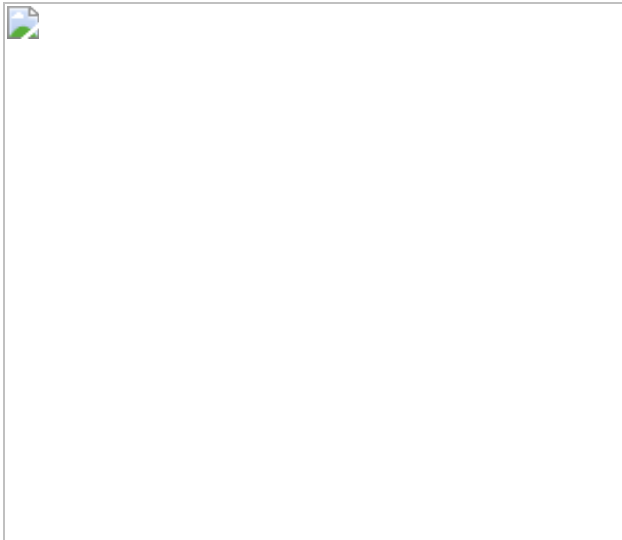


**Fig. 4: Evidence of functional activation, metabolic reprogramming and antigen-driven signalling in CAR T cells from patient 1 at year 9.3.**



## Data availability

Raw sequencing data for this study are in preparation for submission to dbGaP (accession number pending).

## Code Availability

Analysis code are available on request.

## References

1. Kalos, M. et al. T cells with chimeric antigen receptors have potent antitumor effects and can establish memory in patients with advanced leukemia. *Sci. Transl. Med.* **3**, 95ra73 (2011).
2. Fraietta, J. A. et al. Determinants of response and resistance to CD19 chimeric antigen receptor (CAR) T cell therapy of chronic lymphocytic leukemia. *Nat. Med.* **24**, 563–571 (2018).
3. Porter, D. L. et al. Chimeric antigen receptor T cells persist and induce sustained remissions in relapsed refractory chronic lymphocytic leukemia. *Sci. Transl. Med.* **7**, 303ra139 (2015).

4. Frey, N. V. et al. Long-term outcomes from a randomized dose optimization study of chimeric antigen receptor modified T cells in relapsed chronic lymphocytic leukemia. *J. Clin. Oncol.* Jco1903237 (2020).
5. Brentjens, R. J. et al. Safety and persistence of adoptively transferred autologous CD19-targeted T cells in patients with relapsed or chemotherapy refractory B-cell leukemias. *Blood* **118**, 4817–4828 (2011).
6. Geyer, M. B. et al. Safety and tolerability of conditioning chemotherapy followed by CD19-targeted CAR T cells for relapsed/refractory CLL. *JCI Insight* **4** (2019).
7. Turtle, C. J. et al. Durable molecular remissions in chronic lymphocytic leukemia treated with CD19-specific chimeric antigen receptor-modified T cells after failure of ibrutinib. *J. Clin. Oncol.* **35**, 3010–3020 (2017).
8. Maude, S. et al. Chimeric antigen receptor T cells for sustained remissions in leukemia. *N. Engl. J. Med.* **371**, 1507–1517 (2014).
9. Turtle, C. J. et al. CD19 CAR-T cells of defined CD4<sup>+</sup>:CD8<sup>+</sup> composition in adult B cell ALL patients. *J. Clin. Invest.* **126**, 2123–2138 (2016).
10. Fry, T. J. et al. CD22-targeted CAR T cells induce remission in B-ALL that is naive or resistant to CD19-targeted CAR immunotherapy. *Nat. Med.* **24**, 20 (2018).
11. Nobles, C. L. et al. CD19-targeting CAR T cell immunotherapy outcomes correlate with genomic modification by vector integration. *J. Clin. Invest.* **130**, 673–685 (2019).
12. Fraietta, J. A. et al. Disruption of TET2 promotes the therapeutic efficacy of CD19-targeted T cells. *Nature* **558**, 307–312 (2018).

13. Tirosh, I. et al. Dissecting the multicellular ecosystem of metastatic melanoma by single-cell RNA-seq. *Science* **352**, 189–196 (2016).
14. Fuertes Marraco, S. A., Neubert, N. J., Verdeil, G. & Speiser, D. E. Inhibitory receptors beyond T cell exhaustion. *Front. Immunol.* **6**, 310 (2015).
15. ElTanbouly, M. A. & Noelle, R. J. Rethinking peripheral T cell tolerance: checkpoints across a T cell's journey. *Nat. Rev. Immunol.* **21**, 257–267 (2021).
16. Irrthum, A., Wehenkel, L. & Geurts, P. Inferring regulatory networks from expression data using tree-based methods. *PLoS ONE* **5**, e12776 (2010).
17. Oh, D. Y. et al. Intratumoral CD4<sup>+</sup> T cells mediate anti-tumor cytotoxicity in human bladder cancer. *Cell* **181**, 1612–1625.e1613 (2020).
18. Porter, D. L., Levine, B. L., Kalos, M., Bagg, A. & June, C. H. Chimeric antigen receptor-modified T cells in chronic lymphoid leukemia. *N. Engl. J. Med.* **365**, 725–733 (2011).
19. Birsoy, K. et al. An essential role of the mitochondrial electron transport chain in cell proliferation is to enable aspartate synthesis. *Cell* **162**, 540–551 (2015).
20. Scholler, J. et al. Decade-long safety and function of retroviral-modified chimeric antigen receptor T cells. *Sci. Transl. Med.* **4**, 132ra153 (2012).
21. Berry, C. C. et al. Estimating abundances of retroviral insertion sites from DNA fragment length data. *Bioinformatics* **28**, 755–762 (2012).
22. Cavalcante, R. G. & Sartor, M. A. annotatr: genomic regions in context. *Bioinformatics* **33**, 2381–2383 (2017).

23. Kotecha, N., Krutzik, P. O. & Irish, J. M. Web-based analysis and publication of flow cytometry experiments. *Curr. Protoc. Cytometry* **53**, 10.17. 11–10.17. 24 (2010).
24. Bandyopadhyay, S., Fisher, D. A. C., Malkova, O. & Oh, S. T. Analysis of signaling networks at the single-cell level using mass cytometry. *Methods Mol. Biol.* **1636**, 371–392 (2017).
25. Butler, A., Hoffman, P., Smibert, P., Papalexi, E. & Satija, R. Integrating single-cell transcriptomic data across different conditions, technologies, and species. *Nat. Biotechnol.* **36**, 411–420 (2018).
26. Raudvere, U. et al. g: Profiler: a web server for functional enrichment analysis and conversions of gene lists (2019 update). *Nucleic Acids Res.* **47**, W191–W198 (2019).
27. Aibar, S. et al. SCENIC: single-cell regulatory network inference and clustering. *Nat. Methods* **14**, 1083–1086 (2017).

## Acknowledgements

We acknowledge the contributions of the following research cores at the University of Pennsylvania and Children's Hospital of Philadelphia: the Translational and Correlative Studies Laboratory for providing standardized flow cytometric, quantitative PCR and cytokine multiplexing analyses, and biobanking of patient specimens on CAR T cell trials; the Clinical Cell and Vaccine Production Facility for cell processing and biobanking; the Human Immunology Core for providing healthy donor cells and analytical support; the Flow Cytometry Core for flow cytometry equipment maintenance and access to electronic sorters; the Stem Cell and Xenograft Core for providing de-identified patient specimens; and the High-Performance Computing Facility. This work was supported by Novartis Institute for Biomedical Research (to J.J.M. and C.H.J.), NIH grant R01-CA-241762-01 (to J.J.M. and F.D.B.); NIH grant CA233285 (to K.T.); CIHR Doctoral Foreign Study Award no. 433117 (to G.M.C.); and NIH Medical Scientist Training Program T32 GM07170 (to S.B.).

# Author information

## Author notes

1. These authors contributed equally: J. Joseph Melenhorst, Gregory M. Chen, Meng Wang, David L. Porter
2. These authors jointly supervised this work: J. Joseph Melenhorst, Kai Tan, Carl H. June

## Affiliations

1. Center for Cellular Immunotherapies, Perelman School of Medicine, University of Pennsylvania, Philadelphia, PA, USA

J. Joseph Melenhorst, Meng Wang, McKensie A. Collins, Hongxing Sun, Ziran Zhao, Stefan Lundh, Sayantan Maji, Lifeng Tian, Irina Kulikovskaya, Minnal Gupta, David E. Ambrose, Megan M. Davis, Joseph A. Fraietta, Regina M. Young, Anne Chew, Bruce L. Levine, Donald L. Siegel, Simon F. Lacey & Carl H. June

2. Abramson Cancer Center, Perelman School of Medicine, University of Pennsylvania, Philadelphia, PA, USA

J. Joseph Melenhorst, Meng Wang, McKensie A. Collins, Hongxing Sun, Ziran Zhao, Stefan Lundh, Sayantan Maji, Irina Kulikovskaya, Minnal Gupta, David E. Ambrose, Megan M. Davis, Joseph A. Fraietta, Regina M. Young, Anne Chew, Bruce L. Levine, Donald L. Siegel, Simon F. Lacey, Kai Tan & Carl H. June

3. Department of Pathology and Laboratory Medicine, Perelman School of Medicine, University of Pennsylvania, Philadelphia, PA, USA

J. Joseph Melenhorst, Meng Wang, David L. Porter, McKensie A. Collins, Hongxing Sun, Ziran Zhao, Stefan Lundh, Sayantan Maji, Noelle V. Frey, Saar I. Gill, Lifeng Tian, Irina Kulikovskaya, Minnal Gupta, David E. Ambrose, Megan M.

Davis, Joseph A. Fraietta, Regina M. Young, Anne Chew, Bruce L. Levine, Simon F. Lacey & Carl H. June

4. Institute for Immunology, Perelman School of Medicine, University of Pennsylvania, Philadelphia, PA, USA

J. Joseph Melenhorst, Cécile Alanio, E. John Wherry, Kai Tan & Carl H. June

5. Parker Institute for Cancer Immunotherapy, University of Pennsylvania, Philadelphia, USA

J. Joseph Melenhorst, Cécile Alanio, E. John Wherry & Carl H. June

6. Graduate Group in Genomics and Computational Biology, University of Pennsylvania, Philadelphia, PA, USA

Gregory M. Chen & Kai Tan

7. Department of Medicine, University of Pennsylvania, Philadelphia, PA, USA

David L. Porter

8. Center for Childhood Cancer Research, The Children's Hospital of Philadelphia, Philadelphia, PA, USA

Changya Chen & Peng Gao

9. Department of Pediatrics, Perelman School of Medicine, University of Pennsylvania, Philadelphia, USA

Changya Chen, Peng Gao & Kai Tan

10. Graduate Group in Cell & Molecular Biology, University of Pennsylvania, Philadelphia, PA, USA

McKensie A. Collins, Shovik Bandyopadhyay & Kai Tan

11. Novartis Institute for Biomedical Research, Cambridge, MA, USA

Iulian Pruteanu-Malinici & Jennifer L. Brogdon

12. Department of Microbiology, Perelman School of Medicine,  
University of Pennsylvania, Philadelphia, PA, USA

Christopher L. Nobles, Joseph A. Fraietta & Frederic D. Bushman

13. Department of Transfusion Medicine, Perelman School of Medicine,  
University of Pennsylvania, Philadelphia, PA, USA

Donald L. Siegel

14. Department of Systems Pharmacology and Translational Therapeutics,  
Perelman School of Medicine, University of Pennsylvania,  
Philadelphia, PA, USA

Cécile Alanio & E. John Wherry

## Contributions

J.J.M., G.M.C., M.W., D.L.P., C.C., M.A.C., P.G., S.B., H.S., Z.Z., S.L., I.P.-M., C.L.N., S.M., L.T., I.K., M.G., D.E.A., F.D.B., S.F.L., K.T. and C.H.J. performed experiments or analysed the data. All authors helped design the experiments and contribute to data interpretation. J.J.M., G.M.C., M.W., D.L.P., K.T. and C.H.J. wrote the manuscript.

## Corresponding authors

Correspondence to [J. Joseph Melenhorst](#), [Kai Tan](#) or [Carl H. June](#).

## Ethics declarations

## Competing interests

J.J.M., D.L.P., J.A.F., S.F.L. and C.H.J. hold patents related to CAR T cell manufacturing and biomarker discovery. I.P.-M. and J.B. are employees of Novartis. The remaining authors declare no competing interests.

## Peer review

### Peer review information

*Nature* thanks Marcela Maus and the other, anonymous, reviewer(s) for their contribution to the peer review of this work. Peer review reports are available.

## Additional information

**Publisher's note** Springer Nature remains neutral with regard to jurisdictional claims in published maps and institutional affiliations.

## Extended data figures and tables

### [Extended Data Fig. 1 Clonal evolution for patient 1 and 2 based on TCR sequencing data.](#)

Pairwise Morisita's overlap index was computed between all timepoints (row and column labels) for patient 1 (**a**) and 2 (**b**). TCR clones (rows) with maximum abundance > 1% across time points were retained and tracked over time for patient 1 (**c**) and 2 (**d**).

### [Extended Data Fig. 2 Genomic annotation of integration sites for infusion product, post infusion timepoints < 60d and > 60d.](#)

**a**, graphic of the annotation scheme. The integration sites from patient 1 (**b**) and 2 (**c**) were annotated based on its position relative to known genes (UCSC hg38) and permissive enhancers (FANTOM 5). The counts of integration sites that fall into each annotation category in infusion product were summarized (left). The mean and standard deviation of the number of

sites for each category were also computed for 1–60 days post infusion (middle) and > 60 days post infusion (right).

**Extended Data Fig. 3 Gating strategy and CyTOF marker expression profiles.**

**a**, Gating strategy performed computationally on CyTOF data to filter to CD3<sup>+</sup>CAR<sup>+</sup> T cells for downstream analysis. **b**, Protein expression of our CyTOF panel depicted on a single-cell basis on our UMAP.

**Extended Data Fig. 4 CITE-Seq with 5' TCR profiling reveals the presence of double-negative gamma-delta CAR T-cells in patient 2 at month 3 and year 3.**

**a**, UMAP showing expression of key marker genes and TCR $\alpha\beta$  clonotype for patient 2 at month 3, and **(b)** patient 2 at year 3. Aliquots of peripheral blood were sorted for CD3<sup>+</sup>CD14<sup>-</sup>CAR<sup>+</sup> cells, and 5' CITE-Seq with TCR $\alpha\beta$  clonotyping was performed. High-quality cells were computationally identified by retaining cells with 200–5000 genes detected and less than 5% mitochondrial RNA, and shown are the 552 (month 3) and 242 (year 3) cells that were verified as CAR T-cells with at least one read aligned to the 5' CAR construct. UMAP plots showing normalized RNA expression are colored in shades of blue; plots showing protein expression via CITE-Seq antibody-derived tags are colored in shades of green; TCR $\alpha\beta$  clonotype plots (bottom-right of panels **a** and **b**) are colored using a spectral color scheme, with cells with no detected TCR $\alpha\beta$  clonotype colored light grey. Red arrows indicate the double-negative CAR T-cell population in both time points, with gamma-delta identity demonstrated by protein expression of the  $\gamma\delta$  TCR, lack of protein expression of the  $\alpha\beta$  TCR, specific RNA expression of *TRDV1* and *TRGV4*, and non-detection of the TCR $\alpha\beta$  clonotype.

**Extended Data Fig. 5 Re-analysis of previous published flow cytometry data performed on patient 2 demonstrates the**

## functional capacity of CD4 $\pm$ , CD8 $\pm$ , and double-negative CAR T-cells.

**a**, Gating strategy for the identification of CD4 $^+$ , CD8 $^+$ , and double-negative CAR T-cells. Flow cytometry data are from the functional experiment described by Porter et al. Sci Transl Med (2015), in which the authors stimulated cells from patient 2 with CD19 expressing K562 cells. Re-examination of the flow cytometry data identified prominent CD4 $^+$ , CD8 $^+$ , and double-negative CAR T-cell populations. Shown is representative gating at day 259, in which 31.2% of CAR T-cells were double-negative CAR T-cells. **b**, Line plots and box plots showing CAR-specific activation of CD4 $^+$ , CD8 $^+$ , and double-negative CAR T-cells supported by greater proportions of CAR $^+$  T-cells expression MIP-1B and CD107a compared to CAR $^-$  cells in response to CAR specific stimulation. Pairwise statistical testing was performed using the two-sided Welch's t-test.

## Extended Data Fig. 6 Analysis of CAR T-cell clonotype, cell cycle, and differential gene expression from patient 1 at year 9.3.

**a**, Heatmap showing the relative frequencies of TCR clonotypes at the 2-month, 3-month, 15-month, 18-month, 21-month, and 9-year time points. Note that the first five columns were estimated from bulk TCR sequencing, whereas the rightmost column was estimated from the single-cell TCR/CITE-Seq data from year 9. **b**, UMAPs indicating strong up-regulation of RNA expression of cell cycle genes. **c**, UMAP colored by cell cycle phase using Seurat. **d**, Proportions of cells in each cell cycle phase, compared between CAR $^-$  T and CAR $^+$  T cells. Chi-squared p-value = 8.97e-15. **e**, Proportions of cells in each cell cycle phase, compared between the top six CAR T-cell clonotypes. Pairwise statistical significance was assessed with the Chi-Squared test, and multiple-testing correction was performed using the Benjamini-Hochberg method. Numbers within the bars indicate the number of cells observed. **f**, Volcano plot indicating genes up-regulated in CAR T-cells compared to normal CD4 $^+$  T cells (rightward

direction) and genes down-regulated in CAR T-cells compared to normal CD4<sup>+</sup> T cells (leftward direction). Differentially expressed genes were determined using the Wilcoxon rank-sum test with a Bonferroni-adjusted p-value cutoff of 0.001 (dark red) and 0.05 (red). **g**, Gene Set Enrichment Analysis plot for the effector CD4<sup>+</sup> gene signature. **h**, Heatmap indicating normalized gene expression values for the 32 differentially expressed genes with a Bonferroni-adjusted p-value cutoff of 0.001.

**Extended Data Fig. 7 CITE-Seq protein expression and correlation for patient 1 at year 9.3.**

**a**, UMAP colored by normalized expression of CITE-Seq protein expression determined by antibody-derived tags. **b**, Pairwise Spearman correlations between CITE-Seq protein expression values across cells.

**Extended Data Fig. 8 Flow cytometry analysis of functional experiment on CAR T-cells from patient 1 year 9.3.**

**a**, Representative gating strategy to identify CD4<sup>+</sup> CAR T-cells from the functional assay. **b**, Identification of populations expressing functional markers CD107a, MIP-1 $\beta$ , Perforin, and Granzyme A. Gates were defined based on FMO controls.

**Extended Data Fig. 9 Transcriptional regulation of CAR T-cells in patient 1 at year 9.**

**a**, Volcano plot indicating transcription factors (TFs) up-regulated in CAR T-cells compared to normal CD4<sup>+</sup> T cells (rightward direction) and TFs down-regulated in CAR T-cells compared to normal CD4<sup>+</sup> T cells (leftward direction). Differentially expressed TFs were determined using the Wilcoxon rank-sum test with a Bonferroni-adjusted p-value cutoff of 0.001 (dark red) and 0.05 (red). **b**, Pairwise correlation of TF regulon scores determined by GENIE3 and AUCell in the comparison between CAR T-cells and CD4<sup>+</sup> CAR<sup>-</sup> T cells. **c**, UMAP indicating RNA expression of selected differentially expressed TFs *TCF7*, *TOX*, *IKZF3*, and *PRDM1*. **d**,

UMAP indicating RNA expression of differentially expressed AP-1 TFs, *FOS*, *JUNB*, *JUN*, and *BATF*.

**Extended Data Fig. 10 CITE-Seq with 5' TCR profiling reveals the presence of CD4<sup>±</sup> CAR T-cells with characteristic expression of *GZMA* and *GZMK* in patients 1 and 2.**

**a**, UMAP embeddings showing expression of key marker genes for patient 2 at year 6.5 post-infusion, as well as **(b)** patient 1 at month 12 and **(c)** patient 1 at month 15. Sample processing and data analysis was the same as in Extended Data Fig. 4. Shown are high-quality cells that were verified as CAR T-cells with at least one read aligned to the 5' CAR construct. UMAP plots showing normalized RNA expression are colored in shades of blue; plots showing protein expression via CITE-Seq antibody-derived tags are colored in shades of green. Red arrows in panel **a** indicate a CD4<sup>+</sup> CAR T-cell population with high expression of *GZMA* and *GZMK*, similar to the long-persisting CAR T-cell population in patient 1 at year 9.3 described in Figs. 3–4 and Extended Data Figs. 6, 7, and 9. The CAR T-cells from patient 1 at months 12 and 15 characteristically expressed *GZMA* and *GZMK* at high levels, with the observation of cells expressing CD4 at a protein and RNA level, and cells that expressed *CD8B* at the RNA level.

**Extended Data Table 1 Immunoglobulin heavy chain rearrangement deep sequencing shows persistent deep molecular remission for both patients**

## **Supplementary information**

**Reporting Summary**

**Peer Review File**

**Supplementary Table 1.**

**Supplementary Table 2.**

# Rights and permissions

[Reprints and Permissions](#)

## About this article

### Cite this article

Melenhorst, J.J., Chen, G.M., Wang, M. *et al.* Decade-long leukaemia remissions with persistence of CD4<sup>+</sup> CAR T cells. *Nature* **602**, 503–509 (2022). <https://doi.org/10.1038/s41586-021-04390-6>

- Received: 07 May 2021
- Accepted: 29 December 2021
- Published: 02 February 2022
- Issue Date: 17 February 2022
- DOI: <https://doi.org/10.1038/s41586-021-04390-6>

### Share this article

Anyone you share the following link with will be able to read this content:

[Get shareable link](#)

Sorry, a shareable link is not currently available for this article.

[Copy to clipboard](#)

Provided by the Springer Nature SharedIt content-sharing initiative

## Further reading

- Last-resort cancer therapy holds back disease for more than a decade

- Heidi Ledford

*Nature* (2022)

- Cytotoxic CD4+ CAR T cells implicated in long-term leukaemia remission

- Alexandra Flemming

*Nature Reviews Immunology* (2022)

## Cytotoxic CD4 $\pm$ CAR T cells implicated in long-term leukaemia remission

- Alexandra Flemming

Research Highlight 09 Feb 2022

---

This article was downloaded by **calibre** from <https://www.nature.com/articles/s41586-021-04390-6>

- Article
- Open Access
- [Published: 09 February 2022](#)

# Mapping clustered mutations in cancer reveals APOBEC3 mutagenesis of ecDNA

- [Erik N. Bergstrom](#)<sup>1,2,3</sup>,
- [Jens Luebeck](#)<sup>4,5</sup>,
- [Mia Petljak](#)<sup>6</sup>,
- [Azhar Khandekar](#)<sup>1,2,3,4</sup>,
- [Mark Barnes](#) [ORCID: orcid.org/0000-0002-5650-780X](#)<sup>1,2,3</sup>,
- [Tongwu Zhang](#) [ORCID: orcid.org/0000-0003-2124-2706](#)<sup>7</sup>,
- [Christopher D. Steele](#)<sup>8</sup>,
- [Nischalan Pillay](#) [ORCID: orcid.org/0000-0003-0579-4105](#)<sup>8,9</sup>,
- [Maria Teresa Landi](#) [ORCID: orcid.org/0000-0003-4507-329X](#)<sup>7</sup>,
- [Vineet Bafna](#) [ORCID: orcid.org/0000-0002-5810-6241](#)<sup>5,10</sup>,
- [Paul S. Mischel](#) [ORCID: orcid.org/0000-0002-4560-2211](#)<sup>11,12</sup>,
- [Reuben S. Harris](#) [ORCID: orcid.org/0000-0002-9034-9112](#)<sup>13,14,15,16</sup> &
- [Ludmil B. Alexandrov](#) [ORCID: orcid.org/0000-0003-3596-4515](#)<sup>1,2,3</sup>

*Nature* volume 602, pages 510–517 (2022)

- 9876 Accesses
- 166 Altmetric
- [Metrics details](#)

## Subjects

- [Cancer](#)
- [Cancer genetics](#)
- [Cancer genomics](#)

## Abstract

Clustered somatic mutations are common in cancer genomes and previous analyses reveal several types of clustered single-base substitutions, which include doublet- and multi-base substitutions<sup>1,2,3,4,5</sup>, diffuse hypermutation termed omikli<sup>6</sup>, and longer strand-coordinated events termed kataegis<sup>3,7,8,9</sup>. Here we provide a comprehensive characterization of clustered substitutions and clustered small insertions and deletions (indels) across 2,583 whole-genome-sequenced cancers from 30 types of cancer<sup>10</sup>. Clustered mutations were highly enriched in driver genes and associated with differential gene expression and changes in overall survival. Several distinct mutational processes gave rise to clustered indels, including signatures that were enriched in tobacco smokers and homologous-recombination-deficient cancers. Doublet-base substitutions were caused by at least 12 mutational processes, whereas most multi-base substitutions were generated by either tobacco smoking or exposure to ultraviolet light. Omikli events, which have previously been attributed to APOBEC3 activity<sup>6</sup>, accounted for a large proportion of clustered substitutions; however, only 16.2% of omikli matched APOBEC3 patterns. Kataegis was generated by multiple mutational processes, and 76.1% of all kataegis events exhibited mutational patterns that are associated with the activation-induced deaminase (AID) and APOBEC3 family of deaminases. Co-occurrence of APOBEC3 kataegis and extrachromosomal DNA (ecDNA), termed kyklonas (Greek for cyclone), was found in 31% of samples with ecDNA. Multiple distinct kyklonic events were observed on most mutated ecDNA. ecDNA containing known cancer genes exhibited both positive selection and kyklonic hypermutation. Our results reveal the diversity of clustered mutational processes in human cancer and the role of APOBEC3 in recurrently mutating and fuelling the evolution of ecDNA.

[Download PDF](#)

## Main

Cancer genomes contain somatic mutations that are imprinted by different mutational processes<sup>1,11</sup>. Most single-base substitutions and small indels are independently scattered across the genome; however, a subset of substitutions and indels tend to cluster<sup>12,13</sup>. This clustering has been attributed to a combination of heterogeneous mutation rates across the genome, biophysical characteristics of exogenous carcinogens, dysregulation of endogenous processes and larger mutational events associated with genome instability—amongst others<sup>2,3,6,7,8,10,13,14,15,16,17,18,19</sup>. Previous analyses of clustered mutations have focused on single-base substitutions and revealed several classes of clustered events, including doublet- and multi-base substitutions<sup>1,2,3,4,5</sup> (DBSs and MBSs, respectively), diffuse hypermutation (omikli)<sup>6</sup>

and longer events (kataegis)<sup>3,7,8,9</sup>. Most kataegic events were found to be strand-coordinated, defined as sharing the same strand and reference allele<sup>3,11</sup>. Previous studies have also revealed nine clustered signatures<sup>13</sup> and clustered driver substitutions due to APOBEC3-associated mutagenesis<sup>6</sup> or carcinogenic-triggered *POLH* mutagenesis<sup>13</sup>.

DBSs have been extensively examined, revealing multiple endogenous and exogenous processes that can cause these events, including failure of DNA repair pathways and exposure to environmental mutagens<sup>1,3,11</sup>. By contrast, MBSs have not been comprehensively investigated, presumably owing to their small numbers in cancer genomes. Moreover, only a handful of processes have been associated with omikli and kataegis events, with most processes attributed to the AID and APOBEC3 family of deaminases<sup>3,6,7,8,13,14,20,21,22,23</sup>. Specifically, the APOBEC3 enzymes, which are typically responsible for antiviral responses<sup>24,25,26,27,28,29,30</sup>, give rise to omikli and kataegis by requiring single-stranded DNA as a substrate<sup>6,8,23,31</sup>. Omikli were found to be enriched in early replicating regions and more prevalent in microsatellite stable tumours, indicating that mismatch repair has a role in exposing short single-stranded DNA regions<sup>6</sup>. The differential activity of mismatch repair towards gene-rich regions results in increased omikli events within cancer genes<sup>6</sup>. Kataegis is less prevalent than omikli as it is likely to depend on longer tracks of single-stranded DNA<sup>7,8,19</sup>. Such tracks are typically available during the repair of double-strand breaks and most kataegis has been observed within 10 kb of detected breakpoints<sup>10</sup>.

Amplification of known cancer genes is known to drive tumorigenesis in many types of cancer<sup>32</sup>. Studies have shown high copy-number states of circular ecDNAs, which often contain known cancer genes and are found in most cancers<sup>32,33,34,35</sup>. The circular nature of ecDNAs and their rapid replication mimic double-stranded DNA viral pathogens, which indicates that they could be substrates for APOBEC3 mutagenesis; this may contribute to the evolution of tumours that contain ecDNA through accelerated diversification of extrachromosomal oncoproteins.

## The landscape of clustered mutations

To identify clustered mutations, a sample-dependent intra-mutational distance (IMD) cut-off was derived in which mutations below the cut-off were unlikely to occur by chance (*q*-value < 0.01). A statistical approach using the IMD cut-off, variant allele frequencies (VAFs) and corrections for local sequence context was applied to each specimen ([Methods](#), Extended Data Fig. [1a](#)). Clustered mutations with consistent VAFs were subclassified into four categories (Extended Data Fig. [1b](#)). DBSs and MBSs were characterized as two adjacent mutations (DBSs) and as three or more adjacent mutations (MBSs) (IMD = 1). Multiple substitutions each with IMD > 1 bp

and below the sample-dependent cut-off were characterized as either omikli (two to three substitutions) or kataegis (four or more substitutions) (Supplementary Fig. 1). Clustered substitutions with inconsistent VAFs were classified as ‘other’. Although clustered indels were not subclassified into different categories, most events resembled diffuse hypermutation, with 92.3% of events having only two indels (Extended Data Fig. 1c).

Examining 2,583 whole-genome-sequenced cancers from the Pan-Cancer Analysis of Whole Genomes (PCAWG) project revealed a total of 1,686,013 clustered single-base substitutions and 21,368 clustered indels (Fig. 1, Extended Data Fig. 1d). DBSs, MBSs, omikli and kataegis comprised 45.7%, 0.7%, 37.2% and 7.0% of clustered substitutions across all samples, respectively, and their distributions varied greatly within and across cancer types. For example, melanoma had the highest clustered substitution burden, with ultraviolet light associated doublets (CC>TT) accounting for 74.2% of clustered mutations; however, these contributed only 5.3% of all substitutions in melanoma (Fig. 1a). By contrast, 11.5% of all substitutions in bone leiomyosarcomas were clustered, and omikli and kataegis constituted 43.8% and 46.7% of these mutations, respectively (Fig. 1a). Clustered indels exhibited similarly diverse patterns within and across cancer types (Fig. 1b). For example, the highest mutational burden of clustered indels was observed in lung and ovarian cancers. Clustered indels in lung cancer accounted for only 2.6% of all indels and were characterized by 1-bp deletions. By contrast, clustered long indels at microhomologies were commonly found in ovarian and breast cancers and contributed more than 10% of all indels in a subset of samples (Fig. 1b). Correlations between the total number of mutations and the number of clustered mutations were observed for DBSs and omikli but not for MBSs, kataegis or indels (Extended Data Fig. 1e). In most cancers, DBSs and omikli had VAFs consistent with those of non-clustered mutations, whereas MBSs and kataegis tended to have lower VAFs (Extended Data Fig. 1f). Kataegic events contained 4 to 44 mutations and 81% of events were strand-coordinated, indicative of damage or enzymatic changes on a single DNA strand.

**Fig. 1: The landscape of clustered mutations across human cancer.**

---

 **figure 1**

**a**, Pan-cancer distribution of clustered substitutions subclassified into DBSs, MBSs, omikli, kataegis and other clustered mutations. Top, each black dot represents a single cancer genome. Red bars reflect the median clustered TMB (mutations (mut) per Mb) for cancer types. Middle, the clustered TMB normalized to the genome-wide TMB reflecting the contribution of clustered mutations to the overall TMB of a given sample. Red bars reflect the median contribution for cancer types. Bottom, the proportion of each subclass of clustered events for a given cancer type with the total number of samples having at least a single clustered event over the total number of samples within a given cancer cohort. **b**, Pan-cancer distribution of clustered small indels. The top and middle panels have the same information as **a**. Bottom, the proportion of each cluster type of indel for a given cancer type with the total number of samples having at least a single clustered indel over the total number of samples within a given cancer cohort. All 2,583 whole-genome-sequenced samples from PCAWG are included in the analysis; however, cancers with fewer than 10 samples were removed from the main figure and included in Extended Data Fig. [1d](#). For definitions of abbreviations for cancer types used in the figures, see 'Cancer-type abbreviations' in Methods.

The overall survival was compared between patients with cancers containing high and low numbers of clustered mutations within whole-genome-sequenced PCAWG and whole-exome sequenced The Cancer Genome Atlas (TCGA) cancer types<sup>[36](#)</sup>. Better overall survival was observed only in whole-genome-sequenced ovarian cancers that contained high-levels of clustered substitutions or clustered indels (*q*-values < 0.05) (Extended Data Fig. [1g, h](#)). Conversely, whole-exome-sequenced adrenocortical carcinomas containing clustered substitutions were associated with a worse overall survival (*q*-value =  $7.2 \times 10^{-5}$ ) (Extended Data Fig. [1i-k](#)).

## **Signatures of clustered mutations**

Mutational signature analysis was performed for each category of clustered events, which enabled the identification of 12 DBS, 5 MBS, 17 omikli, 9 kataegic and 6 clustered indel signatures (Fig. 2, Supplementary Tables 1–5). Although DBS signatures have previously been described<sup>1</sup>, previous analysis combined DBSs and MBSs into a single class<sup>1</sup>. Separating these events into individual classes showed that a multitude of processes can give rise to DBSs, whereas most MBSs are attributable to signatures associated with tobacco smoking (SBS4) or ultraviolet light (SBS7). Additional DBS and MBS signatures were found within a small subset of cancer types (Extended Data Fig. 2).

**Fig. 2: Mutational processes that underlie clustered events.**

---

 **figure 2**

Each circle represents the activity of a signature for a given cancer type. The radius of the circle determines the proportion of samples with greater than a given number of mutations specific to each subclass; the colour reflects the median number of

mutations per cancer type. A minimum of two samples are required per cancer type for visualization ([Methods](#)).

In cancer genomes, omikli were previously attributed to APOBEC3 mutagenesis<sup>6</sup> with some indirect evidence from experimental models<sup>23,37,38</sup>. Our analysis of sequencing data<sup>39</sup> from the clonally expanded breast cancer cell line BT-474 with active APOBEC3 mutagenesis experimentally confirmed the existence of APOBEC3-associated omikli events (cosine similarity: 0.99) (Extended Data Fig. [3a](#)). Only 16.2% of omikli events across the 2,583 cancer genomes matched the APOBEC3 mutational pattern, suggesting that a variety of other processes can give rise to diffuse clustered hypermutation. Notably, our analysis revealed omikli due to tobacco smoking (SBS4), clock-like mutational processes (SBS5), ultraviolet light (SBS7), both direct and indirect mutations from AID (SBS9 and SBS85), and multiple mutational signatures with unknown aetiology in different cancer types (SBS8, SBS12, SBS17a/b, SBS28, SBS40 and SBS41) (Fig. [2](#)). Cell lines previously exposed to benzo[*a*]pyrene<sup>40</sup> and ultraviolet light<sup>41</sup> confirmed the generation of omikli events as a result of these two environmental exposures (cosine similarities: 0.86 and 0.84, respectively) (Extended Data Fig. [3a](#)).

Of the nine kataegic signatures, four have been reported previously, including two associated with APOBEC3 deaminases (SBS2 and SBS13) and two associated with canonical or non-canonical AID activities (SBS84 and SBS85) (Fig. [2](#)). SBS5 (clock-like mutagenesis) accounted for 15.0% of kataegis, with most events occurring in the vicinity of AID kataegis within B cell lymphomas. The remaining four kataegic signatures accounted for only 8.9% of kataegic mutations and included SBS7a/b (ultraviolet light), SBS9 (indirect mutations from AID) and SBS37 (unknown aetiology). Most kataegic signatures were strand-coordinated (Extended Data Fig. [3b](#)). Some samples exhibited consistent whereas others exhibited distinct signatures of clustered and non-clustered mutagenesis (Extended Data Fig. [4](#)). For example, in SP56533 (lung squamous cell carcinoma), most non-clustered and omikli substitutions were caused by tobacco signature SBS4, whereas kataegic events were generated by the APOBEC3 signatures (Extended Data Fig. [4a](#)). By contrast, the pattern of non-clustered substitutions in SP24815 (glioblastoma) was due to clock-like signatures SBS1 and SBS5, whereas omikli and kataegic events were mostly attributable to APOBEC3 (Extended Data Fig. [4a](#)).

The remaining ‘other’ clustered substitutions exhibited inconsistent VAFs that probably represent mutations at highly mutable genomic regions or the effects of co-occurring large mutational events such as copy number alterations (Extended Data Fig. [3d](#), Supplementary Table [6](#)).

Different cancers showed distinct tendencies of clustered indel mutagenesis (Fig. 2). For instance, clustered indels attributed to ID3 (tobacco smoking; characterized by 1-bp deletions) were found predominately in lung cancers and were significantly increased in smokers compared to non-smokers ( $P = 0.0014$ ) (Extended Data Figs. 3c, 4b). Clustered indels due to signatures ID6 and ID8—both attributed to homologous recombination deficiency and characterized by long indels at microhomologies—were found in breast and ovarian cancers and were highly increased in cancers with known deficiencies in homologous recombination genes ( $P = 4.9 \times 10^{-11}$ ) (Extended Data Figs. 3c, 4b).

## Panorama of clustered driver mutations

The PCAWG project elucidated a constellation of mutations that putatively drive cancer development<sup>10</sup>. Our current analysis reveals significant enrichments of clustered substitutions and clustered indels amongst these driver mutations. Specifically, whereas only 3.7% of all substitutions and 0.9% of all indels are clustered events, they contribute 8.4% and 6.9% of substitution and indel drivers, respectively ( $q$ -values  $< 1 \times 10^{-5}$ ; Fisher's exact tests) (Fig. 3a, b). Omikli accounted for 50.5% of all clustered substitution drivers, whereas DBSs, kataegis and other clustered events each contributed between 14% and 18% (Fig. 3c). Clustered driver substitutions varied greatly between genes and across different cancers (Fig. 3c, Extended Data Fig. 5a) with a 2.4-fold enrichment of clustered events within oncogenes compared to tumour suppressors ( $P = 5.79 \times 10^{-3}$ ) (Extended Data Fig. 5b, c). In some cancer genes, only a small percentage of driver events are due to clustered substitutions; examples include *TP53* (4.5% clustered driver substitutions), *KRAS* (3.7%) and *PIK3CA* (2.2%). In other genes, most detected substitution drivers were clustered events; examples include: *BTG1* (73.1%), *SGK1* (66.6%), *EBF1* (60.0%) and *NOTCH2* (38.5%). Notably, the contribution from each class of clustered events varied across driver substitutions in different genes (Fig. 3c). For instance, ultraviolet-light-associated DBSs comprised 93% of clustered *BRAF* driver events, omikli contributed 63% of clustered *BTG1* driver events and kataegis accounted for 100% of clustered *NOTCH2* driver substitutions (Fig. 3c). Similar behaviour was observed for clustered indel drivers, with 48.7% being single-base pair indels (Fig. 3d). In some cancer genes, clustered indel drivers were rare (for example, 2.4% of indel drivers in *TP53* were clustered), whereas in others they were common (for example, 76.6% in *ALB*) (Fig. 3d). Clustered driver substitutions were enriched in stop-lost mutations ( $q$ -value =  $1.9 \times 10^{-2}$ ) and depleted in stop-gained mutations ( $q$ -value =  $3.3 \times 10^{-3}$ ) when compared to non-clustered drivers (Fig. 3e). Furthermore, driver genes that contained clustered events were often differentially expressed compared to those containing non-clustered events (Extended Data Fig. 5d). For instance, clustered events within *CTNNB1* and *BTG1* associated with an increased expression compared to both non-clustered and wild-type expression levels for each gene ( $q$ -values  $< 0.05$ ). Opposite effects were

observed in *STAT6* and *RFTN1* ( $q$ -values  $< 0.05$ ). Collectively, these driver events were induced by the activity of multiple mutational processes including exposure to ultraviolet light, tobacco smoke, platinum chemotherapy and AID and APOBEC3 activity; amongst others (Extended Data Fig. 5e).

**Fig. 3: Panorama of clustered driver mutations in human cancer.**

 figure 3

**a, b**, Percentage of clustered mutations (top) compared to the percentage of clustered driver events (bottom) for substitutions (**a**) and indels (**b**). **c**, The frequency of clustered driver events across known cancer genes. The radius of the circle is proportional to the number of samples with a clustered driver mutation within a gene; the colour reflects the clustered mutational burden. All clustered driver events are classified into one of the five clustered classes, with the number of clustered driver substitutions and the total number of driver substitutions shown on the right. **d**, Clustered indel drivers are shown in a similar manner to **c**. **e**, The odds ratio of clustered substitutions (top) and indels (bottom) resulting in deleterious ( $n = 192$  clustered substitutions;  $n = 54$  clustered indels) or synonymous changes ( $n = 5$  clustered substitutions;  $n = 5$  clustered indels) within a given driver gene compared to non-clustered driver mutations ( $n = 771$  deleterious and  $n = 237$  synonymous substitutions;  $n = 111$  deleterious and  $n = 50$  synonymous indels). All events were overlapped with the PCAWG consensus list of driver events and were annotated using the ENSEMBL Variant Effect Predictor (VEP). The odds ratios are shown with their 95% confidence intervals. **f**, Kaplan–Meier survival curves comparing the outcome of samples with clustered versus non-clustered mutations in *BRAF* (top),

*TP53* (middle) and *EGFR* (bottom) across TCGA cohorts. Only cohorts with more than five samples containing a clustered mutation within the given gene were included. **g**, Kaplan–Meier survival curves comparing the outcome of samples with clustered versus non-clustered mutations in the same genes across the MSK-IMPACT cohort. The  $\log_{10}$ -transformed hazards ratios ( $\log_{10}(\text{HR})$ ) are shown with their 95% confidence intervals in **f**, **g**. Cox regressions were corrected for age (TCGA only), mutational burden and cancer type ([Methods](#)). *Q* values in **a**, **b**, **e** were calculated using a two-tailed Fisher’s exact test and corrected for multiple hypothesis testing.

The clinical utility of detecting clustered events in driver genes was evaluated by comparing the survival amongst individuals with clustered mutations versus individuals with non-clustered mutations within each driver gene across all whole-exome-sequenced samples in TCGA. For each of these comparisons, we performed Cox regressions considering the effects from age and tumour mutational burden (TMB) while correcting for cancer type and multiple hypothesis testing. These results were validated in targeted panel sequencing data from the Memorial Sloan Kettering-Integrated Mutation Profiling of Actionable Cancer Targets (MSK-IMPACT) cohort<sup>42,43</sup>. These analyses revealed a significant difference in survival between individuals with clustered and individuals with non-clustered mutations detected in *TP53*, *EGFR* and *BRAF*. Specifically, individuals with clustered events within *BRAF* had a better overall survival compared to individuals with non-clustered events (*q*-values < 0.05) (Fig. [3f,g](#)). Conversely, in both TCGA and MSK-IMPACT, individuals with clustered mutations in *TP53* or *EGFR* exhibited a significantly worse outcome compared to individuals with non-clustered mutations in each of these genes (*q*-values < 0.05) (Fig. [3f,g](#)).

## Kataegic events and focal amplifications

In each sample, kataegic mutations were separated into distinct events on the basis of consistent VAFs across adjacent mutations and IMD distances greater than the sample-dependent IMD threshold ([Methods](#)). Our analysis revealed that 36.2% of all kataegic events occurred within 10 kb of a structural breakpoint but not on detected focal amplifications (Fig. [4a](#)). In addition, 21.8% of all kataegic events occurred either on a detected focal amplification or within 10 kb of a focal amplification’s structural breakpoints: 9.6% on circular ecDNA, 6.3% on linear rearrangements, 3.3% within heavily rearranged events and 2.6% associated with breakage–fusion–bridge cycles (BFBs) (Fig. [4a](#)). Finally, 42.0% of kataegic events were neither within 10 kb of a structural breakpoint nor on a detected focal amplification. Modelling the distribution of the distances between kataegic events and the nearest structural variations revealed a multi-modal distribution with three components (Fig. [4b](#)): kataegis within 10 kb, around 1 Mb, or more than 1.5 Mb of a detected breakpoint. Of note, ecDNA-associated kataegis—termed kyklonas (Greek for cyclone)—had an average distance

from the nearest breakpoint of around 750 kb, with only 0.35% of kyklonic events occurring both on ecDNA and within 10 kb of a breakpoint (Fig. 4b). These results indicate that kyklonic events are not likely to have occurred because of structural rearrangements during the formation of ecDNA. In most cancer types, DBSs, MBSs, omikli and other cluster events were not found in the vicinity of structural variations (Extended Data Fig. 6a, b).

**Fig. 4: Kataegic events co-locate with most forms of structural variation.**

 figure 4

**a**, Proportion of all kataegic events per cancer type overlapping different amplifications or structural variations. **b**, Distance to the nearest breakpoint for all kataegic mutations (teal), kyklonas (gold) and non-clustered mutations (red). Kataegic distances were modelled as a Gaussian mixture with three components (blue line). **c**, Left, volcano plot depicting samples that are statistically enriched for kyklonas (red;  $q$ -values from a false discovery rate (FDR)-corrected  $z$ -test; not significant (NS)). Middle left, proportion of samples with ecDNA co-occurring with kataegis. Middle right, mutational spectrum of all kyklonas. Right, proportion of kyklonic events attributed to SBS2 and SBS13. Cosine similarity was calculated between the kyklonic and the reconstructed spectra composed using SBS2 and SBS13 ( $P$  value from a  $Z$ -score test). **d**, Rainfall plots illustrating the IMD distribution for a given sample with the genomic locations of ecDNA breakpoints (maroon). **e**, Top, YTCA versus RTCA enrichments per sample with kyklonas, in which YTCA or RTCA enrichment is suggestive of higher APOBEC3A or APOBEC3B activity, respectively. Genic mutations were divided into transcribed (template strand) and coding mutations. The RTCA/YTCA fold enrichments were compared to those of non-clustered mutations (bottom). **f**, Relative expression of APOBEC3A and APOBEC3B in samples containing ecDNA ( $n = 157$ ) compared to samples without ecDNA ( $n = 1,364$ ) (left),

and in samples with ecDNA that have kyklonas ( $n = 59$ ) compared to samples without kyklonas ( $n = 98$ ) (right). Expression values were normalized using fragments per kilobase of exon per million mapped fragment (FPKM) and upper quartile (UQ) normalization obtained from the PCAWG release.  $Q$  values in **e**, **f** were calculated using a two-tailed Mann–Whitney  $U$ -test and FDR corrected using the Benjamini–Hochberg procedure. For box plots, the middle line reflects the median, the lower and upper bounds of the box correspond to the first and third quartiles, and the lower and upper whiskers extend from the box by  $1.5 \times$  the interquartile range.

## Recurrent kyklonic mutagenesis of ecDNA

Although only 9.6% of kataegic events occur within ecDNA regions, more than 30% of ecDNAs had one or more associated kyklonic events (Fig. [4c](#)). The mutations within these ecDNA regions were dominated by the APOBEC3 patterns, which are characterized by strand-coordinated C>G and C>T mutations in the TpCpW context and attributed to signatures SBS2 and SBS13 ( $P < 1 \times 10^{-5}$ ) (Fig [4c, d](#), Extended Data Fig. [6c](#)). These APOBEC3-associated events contributed 97.8% of all kyklonic events, whereas the remaining mutations were attributed to clock-like signature SBS5 (1.2%) and other signatures (1.0%) (Extended Data Fig. [6c](#)). Furthermore, kyklonic events exhibited an enrichment of C>T and C>G mutations at APOBEC3B-preferred RTCA compared to APOBEC3A-preferred YTCA contexts (underlining reflects the mutated nucleotide)<sup>7</sup>, indicating that APOBEC3B is likely to have an important role in the mutagenesis of circular DNA bodies (Fig. [4e](#)). Similar levels of enrichment for RTCA contexts were also observed in both non-ecDNA kataegis and non-structural variant (SV)-associated kataegis, suggesting that APOBEC3B generally gives rise to many of the strand-coordinated kataegic events (Extended Data Fig. [6d](#)). An increase in the expression of APOBEC3B—but not APOBEC3A—was observed in cancers with ecDNA compared to samples without ecDNA (3.1-fold;  $q$ -value  $< 1 \times 10^{-5}$ ) (Fig. [4f](#)). Within cancers containing ecDNA, no differences were observed in the expression of APOBEC3A or APOBEC3B between samples with and without kyklonic events (Fig. [4f](#)).

More recurrent APOBEC3 kataegis was observed across circular ecDNA regions compared to other forms of structural variation (Fig. [5a](#)). An average of 2.5 kyklonic events were observed within ecDNA regions (range: 0–64 kyklonic events; 0–505 mutations). Recurrent kyklonas was widespread across cancer types (Extended Data Fig. [7a, b](#)). For example, glioblastomas and sarcomas exhibited an average of 5 and 86 kyklonic mutations, respectively. The average VAF of kyklonas was significantly lower than both non-ecDNA associated kataegis and all other clustered events ( $q$ -values  $< 1 \times 10^{-5}$  Fig. [5b](#)). Notably, a subset of kyklonas exhibited VAFs above 0.80, which is likely to reflect early mutagenesis of genomic regions that have subsequently amplified as ecDNA. Moreover, kyklonic events with high VAFs occurred more

commonly on ecDNA that contained known cancer genes, suggesting a mechanism of positive selection (Fig. 5b). Approximately 7.2% of kyklonas occurred early in the evolution of a given ecDNA population within a tumour ( $\text{VAF} > 0.80$ ), whereas the majority of kyklonic events (around 82.5%;  $\text{VAF} < 0.5$ ) have probably occurred after clonal amplification by recurrent APOBEC3 mutagenesis.

**Fig. 5: Recurrent APOBEC3 hypermutation of ecDNA.**

 figure 5



**a**, Number of clustered events overlapping a single amplicon or SV event; each dot represents an amplicon or SV ( $n = 84$  circular;  $n = 275$  linear;  $n = 111$  heavily rearranged;  $n = 62$  BFB; and  $n = 11,139$  SV). A 10-kb window was used to determine the co-occurrence of kataegis with SV breakpoints (\*\* $q < 0.01$ , \*\*\* $q < 0.0001$ ). **b**, Left, normalized distributions of the VAFs for all clustered mutations excluding kataegis (orange), all non-ecDNA kataegis (teal), and kyklonas (red). Right, normalized VAF distributions for kyklonic ecDNA containing cancer genes and for kyklonic ecDNA without cancer genes. **c**, Frequency of recurrence for all kataegis (teal) and kyklonas (red) using a sliding genomic window of 10 Mb. **d**, Number of kyklonic events and kyklonic mutations per ecDNA region containing cancer genes ( $n = 137$ ) or without cancer genes ( $n = 134$ ; left and right, respectively). **e**, Total number

of clustered and kataegis mutations found in samples with ecDNAs containing cancer genes ( $n = 67$  samples) compared to samples with ecDNAs without cancer genes ( $n = 44$ ; left and right, respectively).  $Q$  values in **a**, **d**, **e** were calculated using a two-tailed Mann–Whitney  $U$ -test and FDR-corrected using the Benjamini–Hochberg procedure. Box plot parameters as in Fig. 4.

Recurrent kyklonic events were increased within or near known cancer-associated genes including *TP53*, *CDK4* and *MDM2*, amongst others (Fig. 5c). These recurrent kyklonas were observed across many cancers including glioblastomas, sarcomas, head and neck carcinomas and lung adenocarcinomas (Extended Data Fig. 7c,d). For example, in a sarcoma sample (SP121828), 10 distinct kyklonic events overlapped a single ecDNA region with recurrent APOBEC3 activity in proximity to *MDM2*, resulting in a missense L230F mutation (Extended Data Fig. 7c). The same ecDNA region contained additional kyklonic events occurring within intergenic regions that have distinguishable VAF distributions, implicating recurrent mutagenesis (Extended Data Fig. 7c). Similarly, two distinct kyklonic events occurred on an ecDNA containing *EGFR*, resulting in a missense mutation D191N within a head and neck cancer (Extended Data Fig. 7d). Of note, ecDNA regions with known cancer-associated genes had significantly higher numbers of kyklonic events and mutational burdens of kyklonas compared to ecDNA regions without any known cancer-associated genes ( $q$ -values  $< 1 \times 10^{-5}$ ) (Fig. 5d). Furthermore, we observed a higher co-occurrence of kyklonas with known cancer-associated genes, which were mutated 2.5 times more than ecDNA without cancer-associated genes ( $P = 1.2 \times 10^{-5}$ ; Fisher's exact test). Overall, 41% of kyklonic events were found within the footprints of known cancer driver genes ( $P < 1 \times 10^{-5}$ ). These enrichments cannot be accounted for either by an increase in the overall mutations or by an increase in the overall clustered mutations in these samples (Fig. 5e). To understand the functional effect of kyklonas, we annotated the predicted consequence of each mutation. In total, 2,247 kyklonic mutations overlapped putative cancer-associated genes, of which 4.3% occur within coding regions (Extended Data Fig. 7e). Specifically, 63 resulted in missense mutations, 29 resulted in synonymous mutations, 4 introduced premature stop codons and 1 removed a stop codon (Supplementary Table 7). These downstream consequences of APOBEC3 mutagenesis suggest a contribution to the oncogenic evolution of specific ecDNA populations.

## Validation of kyklonic events in ecDNA

Kyklonic events were further investigated across 3 additional independent cohorts, including 61 sarcomas<sup>44</sup>, 280 lung cancers<sup>45</sup> and 186 oesophageal squamous cell carcinomas<sup>46</sup>. Comparable rates of clustered mutagenesis were found for both substitutions and indels to the rates reported in PCAWG, with a 2.4- and 5.0-fold enrichment of clustered substitutions and indels within driver events, respectively

(Extended Data Fig. 8a). Across the three cohorts, 31% of samples with ecDNA exhibited kyklonas within the sarcomas, 14% within the oesophageal cancers and 28% within the lung cancers, supporting the rates observed in PCAWG (Fig. 4c, Extended Data Figs. 7b, 8c). Similar to the rate observed in PCAWG (36.2%), approximately 30.1% of all kataegis occurred within 10 kb of the nearest breakpoint in the validation cohort (Extended Data Fig. 9a). In addition, only 0.34% of kyklonic events in the validation dataset occurred closer to SVs than expected by chance, which closely resembles the observations in the PCAWG data (0.35%) (Extended Data Fig. 9b). Kyklonic mutations were predominantly attributed to APOBEC3 signatures SBS2 and SBS13 ( $P < 1 \times 10^{-5}$ ) (Extended Data Fig. 8b, Methods) with an enrichment of mutations at the RTCA context supporting the role of APOBEC3B (Extended Data Fig. 8d). A widespread recurrence of kyklonic events was observed across the sarcomas, oesophageal and lung cancers, with 45%, 28% and 46% of samples with ecDNA containing multiple, distinct kyklonic events (Extended Data Fig. 8e). An example from each cohort was selected to illustrate multiple kyklonic events occurring within single ecDNAs, validating the recurrent APOBEC3 hypermutation of ecDNA (Extended Data Fig. 10).

## Discussion

Clustered mutagenesis in cancer can occur through different mutational processes, with AID and APOBEC3 deaminases having the most prominent role. In addition to enzymatic deamination, other endogenous and exogenous sources imprint many of the observed clustered indels and substitutions. A multitude of mutational processes can give rise to omikli events, including tobacco carcinogens and exposure to ultraviolet light. Clustered substitutions and indels were highly enriched in driver events and associated with differential gene expression, implicating them in cancer development and cancer evolution. Some clustered mutational signatures are associated with known cancer risk factors or the activity or failure of DNA repair processes. Notably, clustered mutations in *TP53*, *EGFR* and *BRAF* associated with changes in overall survival and can be detected in most types of sequencing data, including clinically actionable targeted panels such as MSK-IMPACT.

A large proportion of kataegis events occur within 10 kb of detected SV breakpoints with a mutational pattern, suggesting the activity of APOBEC3. Multiple distinct kataegis events, independent of detected breakpoints, were observed on circular ecDNA; such events—termed kyklonas—suggest recurrent APOBEC3 mutagenesis. The circular topology of ecDNAs<sup>47</sup> and their rapid replication patterns are reminiscent of the structure and behaviour of the circular genomes of several double-stranded-DNA based, pathogens including herpesviruses, papillomaviruses and polyomaviruses<sup>32,33,34,35</sup>. Previous pan-virome studies have shown that these double-stranded DNA viral genomes often manifest mutations from APOBEC3

enzymes<sup>48,49,50</sup>. As such, recurrent APOBEC3 mutagenesis on ecDNA is likely to be representative of an antiviral response in which the ecDNA viral-like structure is treated as an infectious agent and attacked by APOBEC3 enzymes. ecDNAs contain a plethora of cancer-associated genes and are responsible for many gene amplification events that can accelerate tumour evolution. Repeated mutagenic attacks of these ecDNAs reveal functional effects within known oncogenes and implicate additional modes of oncogenesis that may ultimately contribute to subclonal tumour evolution, subsequent evasion of therapy and clinical outcome. Further investigations with large-scale clinically annotated whole-genome-sequenced cancers are required to fully understand the clinical implications of clustered mutations and kyklonas.

## Methods

### Data sources

Somatic variant calls of single-base substitutions, small indels and structural variations were downloaded for the 2,583 white-listed whole-genome-sequenced samples from PCAWG along with the corresponding list of consensus driver events<sup>10</sup>.

Epidemiological and clinical features for all available samples were downloaded from the official PCAWG release (<https://dcc.icgc.org/releases/PCAWG>). The collection of whole-exome-sequenced samples from TCGA along with all available clinical features were downloaded from the Genomic Data Commons (GDC; <https://gdc.cancer.gov/>). The MSK-IMPACT Clinical Sequencing Cohort<sup>43</sup> composed of 10,000 clinical cases was downloaded from cBioPortal ([https://www.cbioportal.org/study/summary?id=msk\\_impact\\_2017](https://www.cbioportal.org/study/summary?id=msk_impact_2017)). The subclassification of focal amplifications comprised circular ecDNA, linear amplifications, BFBs and heavily rearranged events, and their corresponding genomic locations were obtained for a subset of samples ( $n = 1,291$ ) as reported<sup>34</sup>.

Experimental models used to validate clustered events were derived from previous studies using primary Hupki mouse embryonic fibroblasts (MEFs) exposed to ultraviolet light<sup>41</sup>, human induced pluripotent stem cells (iPS cells) exposed to benzo[*a*]pyrene<sup>40</sup>, and a clonally expanded BT-474 human breast cancer cell line with episodically active APOBEC3<sup>39</sup>.

Independent cohorts used to validate kyklonic events were collected from multiple sources. The 61 undifferentiated sarcomas<sup>44</sup> and 187 high-confidence oesophageal squamous cell carcinomas<sup>46</sup> were downloaded from the European Genome-phenome Archive (EGAD00001004162 and EGAD00001006868, respectively). The 280 lung adenocarcinomas<sup>45</sup> were downloaded from dbGaP under the accession number

(phs001697.v1.p1). Clustered mutations in validation samples were analysed using the same approach as the one used in the original cohort.

## Detection of clustered events

SigProfilerSimulator (v.1.0.2) was used to derive an IMD cut-off<sup>51</sup> that is unlikely to occur by chance based on the TMB and the mutational patterns for a given sample. Specifically, each tumour sample was simulated while maintaining the sample's mutational burden on each chromosome, the  $\pm 2$  bp sequence context for each mutation and the transcriptional strand bias ratios across all mutations. All mutations in each sample were simulated 100 times and the IMD cut-off was calculated such that 90% of the mutations below this cut-off could not appear by chance ( $q$ -value  $< 0.01$ ). For example, in a sample with an IMD threshold of 500bp, one may observe 1,000 mutations within this threshold with no more than 100 mutations expected based on the simulated data ( $q$ -value  $< 0.01$ ).  $P$  values were calculated using  $z$ -tests by comparing the number of real mutations and the distribution of simulated mutations that occur below the same IMD threshold. A maximum cut-off of 10 kb was used for all IMD thresholds. By generating a background distribution that reflects the random distribution of events used to reduce the false positive rate, this model also considers regional heterogeneities of mutation rates, partially attributed to replication timing and expression, and variances in clonality by correcting for mutation-rich regions and mutation-poor regions within 1-Mb windows. The 1-Mb window size has been used and established as an appropriate scale when considering the variability in mutation rates associated with chromatin structure, replication timing and genome architecture<sup>14,52,53</sup>. The 1-Mb window ensures that subsequent mutations are likely to have occurred as single events using a maximum cut-off of 0.10 for differences in the VAFs. The regional IMD cut-off was determined using a sliding window approach that calculated the fold enrichment between the real and simulated mutation densities within 1-Mb windows across the genome. The IMD cut-offs were further increased, for regions that had higher than ninefold enrichments of clustered mutations and where more than 90% of the clustered mutations were found within the original data, to capture additional clustered events while maintaining the original criteria (less than 10% of the mutations below this cut-off appear by chance;  $q$ -value  $< 0.01$ ). Last, as VAF of mutations may confound the definition of clustered events in ecDNA, we calculated the distribution of inter-event distances within recurrently mutated ecDNA while disregarding the VAF of individual mutations. This resulted in the exact same separation of kataegis events using only the inter-event distances as a criterion for the grouping of mutations into a single event.

Subsequently, all clustered mutations with consistent VAFs were classified into one of four categories (Extended Data Fig. 1a). Two adjacent mutations with an IMD of 1 were classified as DBSs. Three or more adjacent mutations each with an IMD of 1

were classified as MBSs. Two or three mutations with IMDs less than the sample-dependent threshold and with at least a single IMD greater than 1 were classified as omikli. Four or more mutations with IMDs less than the sample-dependent threshold and with at least a single IMD greater than 1 were classified as kataegis. A cut-off of four mutations for kataegis was chosen by fitting a Poisson mixture model to the number of mutations involved in a single event across all extended clustered events excluding DBSs and MBSs (Supplementary Note 1). This model comprised two distributions with  $C_1 = 2.08$  and  $C_2 = 4.37$  representing omikli and kataegis, respectively. A cut-off of four mutations was used for kataegis on the basis of a contribution of greater than 95% from the kataegis-associated distribution with events of four or more mutations. Note that there is certain ambiguity for events with two or three mutations. Although the majority of these events are omikli, some of these events are likely to be short kataegic events (Supplementary Note 1). All remaining clustered mutations with inconsistent VAFs were classified as other. Clustered indels were not classified into different classes. We also performed additional quality-checks to ensure that the majority of clustered indels were mapped to high confidence regions of the genome (Supplementary Fig. 2). Specifically, all clustered indels were aligned against a consensus list of blacklisted genomic regions developed by ENCODE<sup>54</sup> revealing that only 0.5% of all clustered indels overlapped regions with low mappability scores.

## Clustered mutational signatures analysis

The clustered mutational catalogues of the examined samples were summarized in SBS288 and ID83 matrices using SigProfilerMatrixGenerator<sup>55</sup> (v.1.2.0) for each tissue type and each category of clustered events. For example, six matrices were constructed for clustered mutations found in Breast-AdenoCA: one matrix for DBSs, one matrix for MBSs, one matrix for omikli, one matrix for kataegis, one matrix for other clustered substitutions and one matrix for clustered indels. The SBS288 classification considers the 5' and 3' bases immediately flanking each single-base substitution (referred to using the pyrimidine base in the Watson–Crick base pair) resulting in 96 individual mutation channels. In addition, this classification considers the strand orientation for mutations that occur within genic regions resulting in three possible categories: (1) transcribed; pyrimidine base occurs on the template strand; (2) untranscribed; pyrimidine base occurs on the coding strand; or (3) non-transcribed; pyrimidine base occurs in an intergenic region. Mutations in genic regions that are bidirectionally transcribed were evenly split amongst the coding and template strand channels. Combined, this results in a classification consisting of 288 mutation channels, which were used as input for de novo signature extraction of clustered substitutions. The ID83 mutational classification has previously been described<sup>55</sup>.

Mutational signatures were extracted from the generated matrices using SigProfilerExtractor (v.1.1.0), a Python-based tool that uses non-negative matrix factorization to decipher both the number of operative processes within a given cohort and the relative activities of each process within each sample<sup>56</sup>. The algorithm was initialized using random initialization and by applying multiplicative updates using the Kullback–Leibler divergence with 500 replicates. Each de novo extracted mutational signature was subsequently decomposed into the COSMIC (v.3) set of signatures (<https://cancer.sanger.ac.uk/signatures/>) requiring a minimum cosine similarity of 0.80 for all reconstructed signatures. All de novo extractions and subsequent decomposition were visually inspected and, as previously done<sup>1</sup>, manual corrections were performed for 2.2% of extractions (4 out of 180 extractions) in which the total number of operative signatures was adjusted  $\pm 1$ . Consistent with prior visualizations<sup>10</sup>, we have included all cancer types within the PCAWG cohort, which may comprise as few as one sample for certain cancer types. Similarly, consistent with prior visualizations<sup>1</sup>, decomposed signature activity plots required that each cancer type have more than 2 samples and used mutation thresholds for each clustered category; 25 mutations per sample were required for DBSs, omikli events and other clustered mutations; 15 mutations per sample were required for MBSs and kataegic events; and 10 mutations were required per sample for clustered indels.

## Experimental validation

A subset of clustered mutational signatures was validated using previously sequenced in vitro cell line models. As done for PCAWG samples, we generated a background model using SigProfilerSimulator<sup>51</sup> to calculate the clustered IMD cut-off for each sample and partitioned each substitution into the appropriate category of clustered events. Mutational spectra were generated for each subclass within each sample using SigProfilerMatrixGenerator<sup>55</sup> and were compared against the de novo signatures extracted from human cancer. The cosine similarity between the in vitro mutational spectra and de novo observed clustered signatures was calculated to assess the degree of similarity. The average cosine similarity between two random non-negative vectors is 0.75, and the cosine similarities above 0.81 reflect *P* values below 0.01 (ref. <sup>51</sup>).

## Associations with cancer risk factors

Homologous recombination (HR) deficiency was defined for breast cancers using the status of *BRCA1*, *BRCA2*, *RAD51C* and *PALB2*<sup>57</sup>. Samples with a germline, somatic or epigenetic alteration in one of these genes were considered HR-deficient, whereas samples without any known alterations in these genes were considered HR-proficient. The number of clustered indels was compared between HR-deficient and HR-proficient samples. The smoking status of lung cancers was determined using the

clinical annotation from TCGA (<https://portal.gdc.cancer.gov/repository>). The number of clustered indels associated with tobacco smoking (ID6) was compared between samples annotated as lifelong non-smokers and samples annotated as current and reformed smokers. The status of alcohol consumption was determined using the annotations from the official PCAWG release (<https://dcc.icgc.org/releases/PCAWG>). The total number of clustered indels was compared in samples annotated with no alcohol consumption and those annotated as daily and weekly drinkers.

## Expression of driver genes

All RNA-seq expression data were downloaded as a part of the official PCAWG release (<https://dcc.icgc.org/releases/PCAWG>). The relative expression data found within this release were normalized using FPKM normalization and upper quartile normalization. The relative expression of a gene was compared between those containing clustered or non-clustered events. Each distribution was then normalized to the average expression of the wild-type gene. Only genes with at least 10 total events (that is, clustered and non-clustered mutations) including at least 5 clustered events were considered for examination.

## SVs and clustered events

The distance to the nearest structural variation breakpoint was calculated for each mutation in each subclass using the minimum distance to the nearest adjacent upstream or downstream breakpoint. Each distribution was modelled using a Gaussian mixture with an automatic selection criterion for the number of components ranging between one and five components using the minimum Bayesian information criteria (BIC) across all iterations. Modelling of kataegic events resulted in an optimal fit of three components, which was used to separate kataegic substitutions into SV-associated and non-SV associated mutations. DBSs and MBSs were both modelled using a single Gaussian distribution relating to non-SV associated mutations, whereas omikli and other clustered mutations were modelled using a mixture of two components, probably reflecting leakage of smaller kataegic events contributing to a weak SV-associated distribution. To account for the frequency of breakpoints across each sample, we normalized the minimum distance of each mutation to the nearest SV by calculating the expected distance between a mutation and SV for each sample using the total number of breakpoints and the overall length of a given chromosome (Extended Data Fig. [9a, b](#)). After normalizing the kataegic events, we observed an optimal solution of two components with one SV-associated distribution (on average each mutation occurs within one-thousandth of the expected distance to nearest structural variation) and one non-SV associated distribution (on average occurring within the expected distance to the nearest structural variation). The normalized

kyklonic events are consistent with the non-SV associated distribution reflecting kataegic events that occur on ecDNA typically of lengths 1–10 Mb (ref. [35](#)).

## APOBEC3A and APOBEC3B enrichment analysis

The enrichment score of RTCA and YTCA penta-nucleotides quantifies the frequency for which each TpCpA>TpKpA mutation occurs at either an RTCA or a YTCA context. To account for motif availability, this score is calculated using the  $\pm 20$  bp sequence context around each mutation and normalized by the number of cytosine bases and C>N mutations within the set of 41-mers surrounding each mutation of interest<sup>[7](#)</sup>.

## APOBEC3 gene expression and kyklonas

All RNA-seq expression data were downloaded as a part of the official PCAWG release (<https://dcc.icgc.org/releases/PCAWG>). The relative expression data found within this release were normalized using FPKM normalization and upper quartile normalization. The APOBEC3A/B normalized expression was compared between samples containing ecDNA versus samples with no detected ecDNA and between samples with kyklonas and without kyklonas. All *P* values were generated using a Mann–Whitney *U*-test and were corrected for multiple hypothesis testing using the Benjamini–Hochberg FDR procedure.

## Circular ecDNA and kataegis

The collection of ecDNA ranges was intersected with the catalogue of clustered mutations, which was used to determine the overlapped mutational burden for each subclass of clustered event and the mutational spectra of overlapping kataegic events. Enrichments of events were calculated using statistical background models generated using SigProfilerSimulator<sup>[51](#)</sup> that shuffled the dominant mutation in each clustered event across the genome (that is, the most frequent mutation type in a single event). The decomposed kyklonic mutational spectra were generated using the decomposition module within SigProfilerExtractor<sup>[56](#)</sup>. Only mutational signatures that increased the overall cosine similarity by at least 0.01 were used. In both the original and validation cohorts, SBS2 and SBS13 were sufficient to explain the kyklonic mutational spectra with no other known mutational signature increasing the cosine similarity by more than 0.01. Comparisons between ecDNA with and without cancer genes were performed using the set of cancer genes from the Cancer Gene Census (CGC)<sup>[58](#)</sup>. All statistical comparisons and *P* values were calculated using a two-tailed Mann–Whitney *U*-test unless otherwise specified. For each set of tests, *P* values were corrected for multiple hypothesis testing using the Benjamini–Hochberg FDR procedure. The

predicted effect of each overlapping variant was determined using ENSEMBL's Variant Effect Predictor tool by reporting only the most severe consequence<sup>59</sup>.

## Overall survival and clustered mutations

All survival analyses, including the generation of Kaplan–Meier curves, Cox regressions and log-rank tests, were performed using the Lifelines Python package (v.0.24.4). Across the 30 distinct whole-genome-sequenced cancer types included in the PCAWG study, only 6 cancer types contained enough samples to examine the associations between survival and overall number of clustered mutations. The sufficient sample size criteria required more than 50 samples with survival end-points with at least 30 of the samples with an observed clustered event. Each cancer type was analysed separately by comparing the survival of samples with a high clustered mutational burden (top 80th percentile across a given cancer type) to the survival of samples with a low clustered mutational burden (bottom 20th percentile across a given cancer type).

Analysis of whole-exome-sequenced samples from TCGA was altered to reflect the limited resolution for identifying clustered mutations within the exome. Specifically, SigProfilerSimulator (v.1.0.2)<sup>51</sup> was used to derive an IMD cut-off for each sample based on the TMB within the exome and the mutational patterns for a given sample. Mutations were randomly shuffled while maintaining the mutational burden within the exome of each chromosome, the  $\pm 2$  bp sequence context for each mutation and the transcriptional strand bias ratios across all mutations. Each sample was simulated 100 times and an IMD cut-off was calculated using the same methods as outlined for the detection of clustered events within PCAWG. Owing to the limited number of detected events, 22 cancer types had sufficient data to perform survival analysis. Each cancer type was analysed separately by comparing samples with at least a single clustered event to samples with no detected clustered events within the exome.

For both PCAWG and TCGA analyses, survival distributions within a given cancer type were compared using a log-rank test. Cox regressions were performed to determine hazards ratios and to correct for age and total mutational burden. All *P* values were also corrected for multiple hypothesis testing using the Benjamini–Hochberg FDR procedure.

To investigate differential survival associated with the detection of clustered events within cancer driver genes, Kaplan–Meier survival curves were compared between individuals with clustered versus non-clustered mutations within a given cancer driver gene. The distributions were compared using a log-rank test. Cox regressions were performed to determine the hazards ratios and to correct for age, total mutational burden and cancer type across TCGA. Cox regressions performed for the MSK-

IMPACT cohort were corrected for total mutational burden and cancer type. No corrections were performed for age as these metadata were not available for the MSK-IMPACT cohort. All *P* values were also corrected for multiple hypothesis testing using the Benjamini–Hochberg FDR procedure.

## Validation of kyklonas in three cohorts

All three validation cohorts were analysed analogous to the PCAWG cohorts. Specifically, clustered mutations were classified by calculating a sample-dependent IMD threshold for clustered versus non-clustered mutations using a background model generated by SigProfilerSimulator<sup>51</sup>. All clustered mutations were subclassified into DBS, MBS, omikli, kataegis or other mutations. AmpliconArchitect (v.1.2) was used to determine regions of focal amplifications<sup>60</sup>, which were used for subsequent validation of kyklonic events by overlapping kataegic events with all detected focal amplifications. The decomposed kyklonic mutational spectra were generated using the decomposition module within SigProfilerExtractor<sup>56</sup>. Only mutational signatures that increased the overall cosine similarity by at least 0.01 were used. In both the original and validation cohorts, SBS2 and SBS13 were sufficient to explain the kyklonic mutational spectra with no other known mutational signature increasing the cosine similarity by more than 0.01.

## Cancer-type abbreviations

Biliary-AdenoCA, biliary adenocarcinoma; Bladder-TCC, bladder transitional cell carcinoma; Bone-Epith, bone epithelioid; Bone-Leiomyo, bone leiomyosarcoma; Bone-Osteosarc, bone osteosarcoma; Breast-AdenoCA, breast adenocarcinoma; Breast-LobularCA, breast lobular carcinoma; CNS-GBM, glioblastoma (central nervous system); CNS-Medullo, medulloblastoma (central nervous system); CNS-Oligo, oligodendrogloma (central nervous system); CNS-PiloAstro, pilocytic astrocytoma (central nervous system); Cervix-AdenoCA, cervix adenocarcinoma; Cervix-SCC, cervix squamous cell carcinoma; ColoRect-AdenoCA, colorectal adenocarcinoma; Head-SCC, head and neck squamous cell carcinoma; Kidney-ChRCC, chromophobe renal cell carcinoma; Kidney-RCC, renal cell carcinoma; Liver-HCC, hepatocellular carcinoma; Lung-AdenoCA, lung adenocarcinoma; Lung-SCC, lung squamous cell carcinoma; Lymph-BNHL, B-cell non-Hodgkin lymphoma; Lymph-CLL, chronic lymphocytic leukaemia; Lymph-NOS, metastatic lymphoma; Myeloid-AML, acute myeloid leukaemia; Myeloid-MPN, myeloproliferative neoplasm; Oeso-AdenoCA, oesophageal adenocarcinoma; Ovary-AdenoCA, ovary adenocarcinoma; Panc-AdenoCA, pancreatic adenocarcinoma; Panc-Endocrine, pancreatic neuroendocrine carcinoma; Prost-AdenoCA, prostate adenocarcinoma; Skin-Melanoma, malignant melanoma; Stomach-AdenoCA, stomach adenocarcinoma; Thy-AdenoCA, thyroid adenocarcinoma; Uterus-AdenoCA, uterine adenocarcinoma.

## Reporting summary

Further information on research design is available in the [Nature Research Reporting Summary](#) linked to this paper.

## Data availability

No data were generated specifically for this study. All data were and can be downloaded from the appropriate links, repositories and references. Specifically, for the discovery cohort, all data and metadata were obtained from the official PCAWG release (<https://dcc.icgc.org/releases/PCAWG>). All data and metadata for TCGA samples were obtained from the GDC (<https://gdc.cancer.gov/>). Genomics data for clonally expanded cell lines were downloaded from the European Genome-phenome Archive (EGAD00001004201, EGAD00001004203 and EGAD00001004583). For the three validation cohorts, datasets were downloaded as submitted by the original publications and genomics data were downloaded from their respective repositories: EGAD00001004162 for 61 undifferentiated sarcomas<sup>44</sup> (European Genome-phenome Archive); EGAD00001006868 for 187 high-confidence oesophageal squamous cell carcinomas<sup>46</sup> (European Genome-phenome Archive); and phs001697.v1.p1 for 280 lung adenocarcinomas<sup>45</sup> (dbGaP). Somatic mutations and metadata for the MSK-IMPACT Clinical Sequencing Cohort composed of 10,000 clinical cases<sup>42</sup> were downloaded from cBioPortal ([https://www.cbioportal.org/study/summary?id=msk\\_impact\\_2017](https://www.cbioportal.org/study/summary?id=msk_impact_2017)).

## Code availability

The SigProfiler compendium of tools are developed as Python packages and are freely available for installation through PyPI or directly through GitHub (<https://github.com/AlexandrovLab/>). For all tools, each package is fully functional, free and open sourced distributed under the permissive 2-Clause BSD License and is accompanied by extensive documentation: (1) SigProfilerMatrixGenerator<sup>55</sup> (v.1.2.0; <https://github.com/AlexandrovLab/SigProfilerMatrixGenerator>); (2) SigProfilerSimulator<sup>51</sup> (v.1.0.2; <https://github.com/AlexandrovLab/SigProfilerSimulator>); and (3) SigProfilerExtractor<sup>56</sup> (v.1.1.0; <https://github.com/AlexandrovLab/SigProfilerExtractor>). Each SigProfiler tool also has an R wrapper available for installation through the GitHub repositories. AmpliconArchitect<sup>34</sup> (v.1.2) is also freely available and can be downloaded from <https://github.com/virajbdeshpande/AmpliconArchitect>. The core computational pipelines used by the PCAWG Consortium for alignment, quality control and variant

calling are available to the public at <https://dockstore.org/search?search=pcawg> under the GNU General Public License v.3.0, which allows for reuse and distribution.

## References

1. Alexandrov, L. B. et al. The repertoire of mutational signatures in human cancer. *Nature* **578**, 94–101 (2020).
2. Matsuda, T., Kawanishi, M., Yagi, T., Matsui, S. & Takebe, H. Specific tandem GG to TT base substitutions induced by acetaldehyde are due to intra-strand crosslinks between adjacent guanine bases. *Nucleic Acids Res.* **26**, 1769–1774 (1998).
3. Nik-Zainal, S. et al. Mutational processes molding the genomes of 21 breast cancers. *Cell* **149**, 979–993 (2012).
4. de Gruijl, F. R., van Kranen, H. J. & Mullenders, L. H. UV-induced DNA damage, repair, mutations and oncogenic pathways in skin cancer. *J. Photochem. Photobiol. B* **63**, 19–27 (2001).
5. Brash, D. E. UV signature mutations. *Photochem. Photobiol.* **91**, 15–26 (2015).
6. Mas-Ponte, D. & Supek, F. DNA mismatch repair promotes APOBEC3-mediated diffuse hypermutation in human cancers. *Nat. Genet.* **52**, 958–968 (2020).
7. Chan, K. et al. An APOBEC3A hypermutation signature is distinguishable from the signature of background mutagenesis by APOBEC3B in human cancers. *Nat. Genet.* **47**, 1067–1072 (2015).
8. Taylor, B. J. et al. DNA deaminases induce break-associated mutation showers with implication of APOBEC3B and 3A in breast cancer kataegis. *Elife* **2**, e00534 (2013).
9. Boichard, A., Tsigelny, I. F. & Kurzrock, R. High expression of PD-1 ligands is associated with kataegis mutational signature and APOBEC3 alterations. *Oncoimmunology* **6**, e1284719 (2017).
10. The ICGC/TCGA Pan-Cancer Analysis of Whole Genomes Consortium. Pan-cancer analysis of whole genomes. *Nature* **578**, 82–93 (2020).
11. Alexandrov, L. B. et al. Signatures of mutational processes in human cancer. *Nature* **500**, 415–421 (2013).

12. Lawrence, M. S. et al. Mutational heterogeneity in cancer and the search for new cancer-associated genes. *Nature* **499**, 214–218 (2013).
13. Supek, F. & Lehner, B. Clustered mutation signatures reveal that error-prone DNA repair targets mutations to active genes. *Cell* **170**, 534–547 (2017).
14. Buisson, R. et al. Passenger hotspot mutations in cancer driven by APOBEC3A and mesoscale genomic features. *Science* **364**, eaaw2872 (2019).
15. Greenman, C., Wooster, R., Futreal, P. A., Stratton, M. R. & Easton, D. F. Statistical analysis of pathogenicity of somatic mutations in cancer. *Genetics* **173**, 2187–2198 (2006).
16. Martincorena, I. et al. Universal patterns of selection in cancer and somatic tissues. *Cell* **171**, 1029–1041 (2017).
17. Hainaut, P. & Pfeifer, G. P. Patterns of p53 G->T transversions in lung cancers reflect the primary mutagenic signature of DNA-damage by tobacco smoke. *Carcinogenesis* **22**, 367–374 (2001).
18. Pfeifer, G. P., You, Y. H. & Besaratinia, A. Mutations induced by ultraviolet light. *Mutat. Res.* **571**, 19–31 (2005).
19. Roberts, S. A. et al. Clustered mutations in yeast and in human cancers can arise from damaged long single-strand DNA regions. *Mol. Cell* **46**, 424–435 (2012).
20. Kasar, S. et al. Whole-genome sequencing reveals activation-induced cytidine deaminase signatures during indolent chronic lymphocytic leukaemia evolution. *Nat. Commun.* **6**, 8866 (2015).
21. Roberts, S. A. et al. An APOBEC cytidine deaminase mutagenesis pattern is widespread in human cancers. *Nat. Genet.* **45**, 970–976 (2013).
22. Burns, M. B., Temiz, N. A. & Harris, R. S. Evidence for APOBEC3B mutagenesis in multiple human cancers. *Nat. Genet.* **45**, 977–983 (2013).
23. Petljak, M. et al. The APOBEC3A deaminase drives episodic mutagenesis in cancer cells. Preprint at <https://doi.org/10.1101/2021.02.14.431145> (2021).
24. Bogerd, H. P., Wiegand, H. L., Doehle, B. P., Lueders, K. K. & Cullen, B. R. APOBEC3A and APOBEC3B are potent inhibitors of LTR-retrotransposon function in human cells. *Nucleic Acids Res.* **34**, 89–95 (2006).

25. Malim, M. H. & Bieniasz, P. D. HIV restriction factors and mechanisms of evasion. *Cold Spring Harb. Perspect. Med.* **2**, a006940 (2012).
26. Malim, M. H. Natural resistance to HIV infection: the Vif–APOBEC interaction. *C. R. Biol.* **329**, 871–875 (2006).
27. Venkatesan, S. et al. Perspective: APOBEC mutagenesis in drug resistance and immune escape in HIV and cancer evolution. *Ann. Oncol.* **29**, 563–572 (2018).
28. Chen, H. et al. APOBEC3A is a potent inhibitor of adeno-associated virus and retrotransposons. *Curr. Biol.* **16**, 480–485 (2006).
29. Harris, R. S. & Dudley, J. P. APOBECs and virus restriction. *Virology* **479–480**, 131–145 (2015).
30. Harris, R. S. et al. DNA deamination mediates innate immunity to retroviral infection. *Cell* **113**, 803–809 (2003).
31. Maciejowski, J. et al. APOBEC3-dependent kataegis and TREX1-driven chromothripsis during telomere crisis. *Nat. Genet.* **52**, 884–890 (2020).
32. Turner, K. M. et al. Extrachromosomal oncogene amplification drives tumour evolution and genetic heterogeneity. *Nature* **543**, 122–125 (2017).
33. Koche, R. P. et al. Extrachromosomal circular DNA drives oncogenic genome remodeling in neuroblastoma. *Nat. Genet.* **52**, 29–34 (2020).
34. Kim, H. et al. Extrachromosomal DNA is associated with oncogene amplification and poor outcome across multiple cancers. *Nat. Genet.* **52**, 891–897 (2020).
35. Verhaak, R. G. W., Bafna, V. & Mischel, P. S. Extrachromosomal oncogene amplification in tumour pathogenesis and evolution. *Nat. Rev. Cancer* **19**, 283–288 (2019).
36. The Cancer Genome Atlas Research Network et al. The Cancer Genome Atlas Pan-Cancer analysis project. *Nat. Genet.* **45**, 1113–1120 (2013).
37. Green, A. M. et al. APOBEC3A damages the cellular genome during DNA replication. *Cell Cycle* **15**, 998–1008 (2016).
38. Stenglein, M. D., Burns, M. B., Li, M., Lengyel, J. & Harris, R. S. APOBEC3 proteins mediate the clearance of foreign DNA from human cells. *Nat. Struct. Mol. Biol.* **17**, 222–229 (2010).

39. Petljak, M. et al. Characterizing mutational signatures in human cancer cell lines reveals episodic APOBEC mutagenesis. *Cell* **176**, 1282–1294 (2019).
40. Kucab, J. E. et al. A compendium of mutational signatures of environmental agents. *Cell* **177**, 821–836 (2019).
41. Liu, Z. et al. Human tumor p53 mutations are selected for in mouse embryonic fibroblasts harboring a humanized p53 gene. *Proc. Natl Acad. Sci. USA* **101**, 2963–2968 (2004).
42. Cheng, D. T. et al. Memorial Sloan Kettering-Integrated Mutation Profiling of Actionable Cancer Targets (MSK-IMPACT): a hybridization capture-based next-generation sequencing clinical assay for solid tumor molecular oncology. *J. Mol. Diagn.* **17**, 251–264 (2015).
43. Zehir, A. et al. Mutational landscape of metastatic cancer revealed from prospective clinical sequencing of 10,000 patients. *Nat. Med.* **23**, 703–713 (2017).
44. Steele, C. D. et al. Undifferentiated sarcomas develop through distinct evolutionary pathways. *Cancer Cell* **35**, 441–456 (2019).
45. Zhang, T. et al. Genomic and evolutionary classification of lung cancer in never smokers. *Nat. Genet.* **53**, 1348–1359 (2021).
46. Moody, S. et al. Mutational signatures in esophageal squamous cell carcinoma from eight countries with varying incidence. *Nat. Genet.* **53**, 1553–1563 (2021).
47. Wu, S. et al. Circular ecDNA promotes accessible chromatin and high oncogene expression. *Nature* **575**, 699–703 (2019).
48. Cheng, A. Z. et al. Epstein–Barr virus BORF2 inhibits cellular APOBEC3B to preserve viral genome integrity. *Nat. Microbiol.* **4**, 78–88 (2019).
49. Poulain, F., Lejeune, N., Willemart, K. & Gillet, N. A. Footprint of the host restriction factors APOBEC3 on the genome of human viruses. *PLoS Pathog.* **16**, e1008718 (2020).
50. Zhu, B. et al. Mutations in the HPV16 genome induced by APOBEC3 are associated with viral clearance. *Nat. Commun.* **11**, 886 (2020).
51. Bergstrom, E. N., Barnes, M., Martincorena, I. & Alexandrov, L. B. Generating realistic null hypothesis of cancer mutational landscapes using SigProfilerSimulator. *BMC Bioinf.* **21**, 438 (2020).

52. Hess, J. M. et al. Passenger hotspot mutations in cancer. *Cancer Cell* **36**, 288–301 (2019).
53. Polak, P. et al. Cell-of-origin chromatin organization shapes the mutational landscape of cancer. *Nature* **518**, 360–364 (2015).
54. Amemiya, H. M., Kundaje, A. & Boyle, A. P. The ENCODE Blacklist: identification of problematic regions of the genome. *Sci. Rep.* **9**, 9354 (2019).
55. Bergstrom, E. N. et al. SigProfilerMatrixGenerator: a tool for visualizing and exploring patterns of small mutational events. *BMC Genomics* **20**, 685 (2019).
56. Islam, S. M. A. et al. Uncovering novel mutational signatures by de novo extraction with SigProfilerExtractor. Preprint at <https://doi.org/10.1101/2020.12.13.422570> (2020).
57. Polak, P. et al. A mutational signature reveals alterations underlying deficient homologous recombination repair in breast cancer. *Nat. Genet.* **49**, 1476–1486 (2017).
58. Sondka, Z. et al. The COSMIC Cancer Gene Census: describing genetic dysfunction across all human cancers. *Nat. Rev. Cancer* **18**, 696–705 (2018).
59. McLaren, W. et al. The Ensembl Variant Effect Predictor. *Genome Biol.* **17**, 122 (2016).
60. Deshpande, V. et al. Exploring the landscape of focal amplifications in cancer using AmpliconArchitect. *Nat. Commun.* **10**, 392 (2019).

## Acknowledgements

E.N.B. and L.B.A. were supported by the Cancer Research UK Grand Challenge Award C98/A24032 as well as US National Institute of Health (NIH) grants R01ES030993-01A1 and R01ES032547. L.B.A. is an Abeloff V Scholar and he was also supported by an Alfred P. Sloan Research Fellowship. Research at the University of California San Diego was also supported by a Packard Fellowship for Science and Engineering to L.B.A. N.P. is funded through a Cancer Research UK grant (grant no. 18387) and is supported by the UCLH Biomedical Research Centre and the Cancer Research UK Experimental Cancer Centre. C.D.S. is funded through Cancer Research UK and the Neurofibromatosis Research Initiative (NFRI) at Boston Children's Hospital–GeM consortium. M.P. is supported by a European Molecular Biology Organization (EMBO) Long-Term Fellowship (ALTF 760-2019). V.B. and J.L. were supported in part by grants U24CA264379 and R01GM114362 from the NIH. P.S.M.

is supported in part by grants U24CA264379 and RO1CA238249 from the NIH. Cancer research in the R.S.H. laboratory is supported by NCI grant P01CA234228. R.S.H. is the Margaret Harvey Schering Land Grant Chair for Cancer Research, a Distinguished University McKnight Professor and an Investigator of the Howard Hughes Medical Institute. The funders had no roles in study design, data collection and analysis, decision to publish or preparation of the manuscript.

## Author information

### Affiliations

1. Department of Cellular and Molecular Medicine, University of California San Diego, La Jolla, CA, USA

Erik N. Bergstrom, Azhar Khandekar, Mark Barnes & Ludmil B. Alexandrov

2. Department of Bioengineering, University of California San Diego, La Jolla, CA, USA

Erik N. Bergstrom, Azhar Khandekar, Mark Barnes & Ludmil B. Alexandrov

3. Moores Cancer Center, University of California San Diego, La Jolla, CA, USA

Erik N. Bergstrom, Azhar Khandekar, Mark Barnes & Ludmil B. Alexandrov

4. Bioinformatics and Systems Biology Graduate Program, University of California San Diego, La Jolla, CA, USA

Jens Luebeck & Azhar Khandekar

5. Department of Computer Science and Engineering, University of California San Diego, La Jolla, CA, USA

Jens Luebeck & Vineet Bafna

6. Broad Institute of MIT and Harvard, Cambridge, MA, USA

Mia Petljak

7. Division of Cancer Epidemiology and Genetics, National Cancer Institute, Bethesda, MD, USA

Tongwu Zhang & Maria Teresa Landi

8. Research Department of Pathology, Cancer Institute, University College London, London, UK

Christopher D. Steele & Nischalan Pillay

9. Department of Cellular and Molecular Pathology, Royal National Orthopaedic Hospital NHS Trust, Stanmore, UK

Nischalan Pillay

10. Halıcıoğlu Data Science Institute, University of California San Diego, La Jolla, CA, USA

Vineet Bafna

11. Department of Pathology, Stanford University School of Medicine, Stanford, CA, USA

Paul S. Mischel

12. ChEM-H, Stanford University, Stanford, CA, USA

Paul S. Mischel

13. Howard Hughes Medical Institute, University of Minnesota, Minneapolis, MN, USA

Reuben S. Harris

14. Masonic Cancer Center, University of Minnesota, Minneapolis, MN, USA

Reuben S. Harris

15. Institute for Molecular Virology, University of Minnesota, Minneapolis, MN, USA

Reuben S. Harris

16. Department of Biochemistry, Molecular Biology and Biophysics, University of Minnesota, Minneapolis, MN, USA

Reuben S. Harris

## **Contributions**

E.N.B. and L.B.A. designed the overall study. E.N.B. performed all genomics analyses with help from J.L., M.P., A.K., M.B., T.Z., C.D.S., N.P., M.T.L., V.B., P.S.M., R.S.H. and L.B.A. Specifically, J.L., V.B., A.K. and P.S.M. assisted in analysis and discussion of ecDNA. M.P. and R.S.H. aided in the analysis and interpretation of APOBEC3 mutational signatures. A.K., M.B., T.Z., C.D.S., N.P. and M.T.L. gathered the validation cohorts and helped with the subsequent computational validation analyses. E.N.B. performed all clinical association analysis and all analysis of gene expression. E.N.B. and L.B.A. wrote the manuscript with help and input from all other authors. All authors read and approved the final manuscript.

## Corresponding author

Correspondence to [Ludmil B. Alexandrov](#).

## Ethics declarations

### Competing interests

M.P. is a shareholder in Vertex Pharmaceuticals. V.B. is a co-founder, consultant and Scientific Advisory Board member of, and has equity interest in, Boundless Bio, and Abterra. The terms of this arrangement have been reviewed and approved by the University of California San Diego in accordance with its conflict-of-interest policies. E.N.B. and L.B.A. declare filing a provisional patent application for using clustered mutations as clinical prognostic biomarkers in cancer. P.S.M. is a co-founder of Boundless Bio. He has equity in the company and he chairs the Scientific Advisory Board, for which he is compensated. L.B.A. is an inventor on US patent no. 10,776,718 for source identification by non-negative matrix factorization. All other authors declare no competing interests.

## Peer review

### Peer review information

*Nature* thanks the anonymous reviewers for their contribution to the peer review of this work.

## Additional information

**Publisher's note** Springer Nature remains neutral with regard to jurisdictional claims in published maps and institutional affiliations.

## Extended data figures and tables

### Extended Data Fig. 1 Identification and clinical associations of clustered events.

**a**, Schematic depiction for separating clustered mutations for a sample. **b**, Subclassification of clustered substitutions and indels. Expected IMD derived using steps 2 and 3 (**a**). **c**, Distribution of indels present in a single clustered event. **d**, Distribution of clustered substitutions (left) and indels (right) across cancers with less than 10 samples subclassified into different categories. **e**, Correlations between TMB of each sample, the TMB within the exome, or the TMB for each class of clustered substitutions (left) and indels (right). **f**, Distribution of VAFs for all clustered substitution classes (left; DBS: 1,215 samples; MBS: 851; omikli:1,466; kataegis: 1,108; other: 335) with the average fold enrichment compared against non-clustered mutations (right). For each boxplot, the middle line reflects the median, the lower and upper bounds correspond to the first and third quartiles, and the lower and upper whiskers extend from the box by 1.5x the inter-quartile range (IQR). **g**, Kaplan–Meier curves between samples with high (top 80<sup>th</sup> percentile) and low (bottom 20<sup>th</sup> percentile) clustered substitution (left) or indel (right) burdens in PCAWG ovarian cancer. **h**, Cox regressions performed for PCAWG cancer types while correcting for age (n = 20 upper and n = 21 lower clustered substitutions; n = 49 upper and n = 49 lower clustered indels). **i**, Kaplan–Meier survival curves for TCGA cancer types with a differential patient outcome associated with the detection of any clustered mutations. **j**, **k**, Cox regressions performed for TCGA samples while correcting for age (**j**) and total mutational burden (**k**) (OV: n = 111 upper, n = 159 lower clustered substitutions; UCEC: n = 322 upper, n = 64 lower; ACC: n = 24 upper, n = 67 lower). PCAWG ovarian cancers were included in **k**. Centre of measure for each Cox regression reflects the log<sub>10</sub>(Hazards ratios) with the 95% confidence intervals in **h–k**.

### Extended Data Fig. 2 De novo signatures of DBS and MBS signatures.

**a**, The activity of DBS de novo signatures (top) and the corresponding signatures extracted from prostate, skin, stomach, and uterine cancers that could not be accurately reconstructed using known COSMIC mutational signatures (bottom; [Methods](#)). **b**, The activity of MBS de novo signatures (top) and the corresponding signatures extracted from colon, oesophagus, and head and neck cancers that could not be accurately reconstructed using known COSMIC mutational signatures (bottom; [Methods](#)).

### Extended Data Fig. 3 Experimental validation and epidemiological associations of clustered mutational processes.

**a**, Experimental validation of three omikli processes. Specifically, APOBEC3-associated omikli were validated using a clonally expanded BT-474 breast cancer cell line (top), omikli events resulting from exposure to benzo[*a*]pyrene were validated using iPS cells (middle), and omikli events resulting from exposure to ultraviolet light were validated using iPS cells (bottom). **b**, Mutational processes of strand-coordinated kataegis events. **c**, Epidemiological associations comparing the ratio of clustered TMB to the total TMB for a given sample between: drinkers ( $n = 25$ ) and non-drinkers ( $n = 61$ ); smokers ( $n = 68$ ) and non-smokers ( $n = 11$ ); homologous-recombination deficient (HR-deficient;  $n = 25$ ) and homologous-recombination proficient samples (HR-proficient;  $n = 64$ ). For each boxplot, the middle line reflects the median, the lower and upper bounds of the box correspond to the first and third quartiles, and the lower and upper whiskers extend from the box by 1.5x the inter-quartile range (IQR). P-values were calculated using a two-tailed Mann–Whitney *U*-test. **d**, Mutational processes of clustered events with inconsistent VAFs classified as other clustered substitutions. A minimum of two samples are required per cancer type for visualization ([Methods](#)).

#### Extended Data Fig. 4 Examples of clustered mutational signatures.

**a**, Two samples depicting the intra-mutational distance (IMD) distributions of substitutions across genomic coordinates, where each dot represents the minimum distance to adjacent mutations for a selected mutation coloured based on the corresponding subclassification of event (rainfall plot; left). The red lines depict the sample-dependent IMD threshold for each sample. Specific clustered mutations may be above this threshold based on corrections for regional mutation density. The mutational spectra for the different catalogues of clustered and non-clustered substitutions for each sample (right; MBS are not shown). **b**, Two samples illustrating the IMD distributions of indels across the given genomes, with the IMD indel thresholds shown in red (left). The non-clustered and clustered indel catalogues for each sample (right).

#### Extended Data Fig. 5 Mutational processes of clustered driver events.

**a**, The percentage of clustered driver substitutions and indels within each cancer type. All samples 2,583 whole-genome sequenced samples from PCAWG with a detected driver event are included; however, cancer types with fewer than 10 samples are not presented. **b**, The proportion of clustered driver mutations per cancer gene compared between oncogenes ( $n = 19$  genes) versus tumour suppressor genes ( $n = 30$  genes) and genes with high numbers of isoforms ( $n = 17$ ) versus genes with low numbers of isoforms ( $n = 23$ ; upper and lower quartiles of isoforms across all cancer drivers). **c**, The proportion of clustered driver mutations for a given subclass per cancer gene compared between oncogenes ( $n = 17$  genes with clustered substitutions and  $n = 13$  with clustered indels) versus tumour suppressor genes ( $n = 28$  genes with clustered

substitutions and n = 70 genes with clustered indels). **d**, The relative expression of driver genes containing clustered (copper) versus non-clustered events (green). All expression values were normalized using FPKM normalization and upper quartile normalization obtained from the official PCAWG release and were subsequently normalized using the average expression of the wild-type gene. A value of 1 (dashed lined) reflects no difference in expression compared to the wild-type gene. **e**, The proportional activity of mutational signatures contributing to clustered driver events within each subclass. MBSs did not contribute to any reported driver events. For analyses in **b–d**, p-values were generated using a two-tailed Mann–Whitney *U*-test (\*P < 0.05; p = 0.03 for *STAT6*; p = 0.04 for *CTNNB1*; p = 0.02 for *BTG1*). For each boxplot, the middle line reflects the median, the lower and upper bounds of the box correspond to the first and third quartiles, and the lower and upper whiskers extend from the box by 1.5x the inter-quartile range (IQR).

### Extended Data Fig. 6 Clustered events and structural variations.

**a**, The proportion of all clustered events co-locating with structural variations across all cancer types (left) and across each cancer type (right). **b**, The distance to the nearest structural variation for each class of clustered mutations (teal), and non-clustered mutations (red). The distribution for each class of clustered events were modelled using a Gaussian mixture (blue line). DBSs and MBSs were modelled using a single distribution, whereas omikli, other, and indels were modelled using two components reflecting the minimal distribution of overlap with structural variations. **c**, The mutational signatures active in ecDNA clustered events. **d**, YTCA versus RTCA enrichments per sample within non-ecDNA kataegis (top) and non-SV associated kataegis (bottom), where YTCA and RTCA enrichment is suggestive of APOBEC3A or APOBEC3B activity, respectively. Genic mutations were divided into transcribed (template strand) and coding mutations. The RTCA/YTCA fold enrichments were compared to the fold enrichments of non-clustered mutations (p-values calculated using two-tailed Mann–Whitney *U*-tests and corrected for multiple hypothesis testing using the Benjamini–Hochberg FDR procedure).

### Extended Data Fig. 7 Recurrent mutagenesis and functional effects of kyklonas.

**a**, The total number of recurrently mutated ecDNA displayed as a proportion of the total number of ecDNA with kyklonas for a given cancer type. The total number of ecDNA with kyklonas are displayed above each bar plot for each cancer type. All ecDNA with recurrent hypermutation were considered enriched for kyklonic events after correcting for multiple hypothesis testing (Z-score test; q-values < 0.05). **b**, Proportion of samples containing ecDNA divided exclusively into those with co-occurring kataegis, no kataegis overlap, and no detected kataegis across the entire

genome. The number of samples included in each cancer type are listed. For certain cancer types, as few as a single sample may represent the entire proportional breakdown (for example, Bone-Osteosarc or Bone-Epith). **c**, A single sarcoma genome and **d**, a single head squamous cell carcinoma genome depicting the overlap of kataegis with ecDNA regions displayed as a rainfall (top left) with a single zoomed in ecDNA represented using a circos plot (top right). Bottom: Two regions of the ecDNA with overlapping kyklonic events. VAFs are shown per event (orange). **e**, Kyklonic substitutions resulting in recurrent coding mutations within known cancer genes.

### [Extended Data Fig. 8 Validation of APOBEC3 hypermutation of ecDNA in three independent cohorts.](#)

**a**, Distribution of clustered substitutions (left) and clustered indels (right) across three validation cohorts. Clustered substitutions were subclassified into DBSs, MBSs, omikli, kataegis, and other clustered mutations. Top: Each black dot represents a single cancer genome. Red bars reflect the median clustered TMB and the percentage of clustered mutations contributing to the overall TMB of a given sample for each cancer type. Middle: The proportion of each subclass of clustered events for a given cancer type with the total number of samples having at least a single clustered event over the total number of samples within a given cancer cohort. Bottom: Percentage of clustered mutations compared to the percentage of clustered driver events for substitutions (left) and indels (right). P-values were calculated using a Fisher's exact test and corrected for multiple hypothesis testing using Benjamini–Hochberg FDR procedure. **b**, Left: The mutational spectrum of all kyklonas across the validation cohorts. Right: The proportion of kyklonic events attributed to SBS2 and SBS13 (p-value determined using a Z-score test; [Methods](#)). **c**, The proportion of samples with ecDNA that co-occur with kataegis, do not co-occur with kataegis, or do not have any detected kataegic activity across each cohort. **d**, YTCA versus RTCA enrichments per sample with kyklonas, where YTCA and RTCA enrichment is suggestive of higher APOBEC3A or APOBEC3B activity, respectively. The RTCA/YTCA fold enrichments were compared to the fold enrichments of non-clustered mutations (p-values calculated using a two-tailed Mann–Whitney *U*-test). **e**, The proportion of ecDNA with kyklonas that contain multiple kyklonic events. The total number of ecDNA with kyklonas are displayed above each bar plot for each cancer type.

### [Extended Data Fig. 9 Kyklonas occur distally from structural breakpoints across three independent cohorts.](#)

**a**, The distance to the nearest breakpoint for all kataegic mutations (teal), kyklonas (gold), and non-clustered mutations (red) across the three validation cohorts. **b**, Distances to the nearest SV breakpoints were normalized by calculating the expected distance a mutation would fall from a breakpoint given the number of breakpoints

detected per chromosome and the overall length of the chromosome across the validation cohorts (left) and PCAWG (right). A value of 1 (dashed line) reflects a distance that one would expect based on the random placement of a mutation across the chromosome, whereas a value less than 1 reflects a mutation occurring closer than what is expected by random chance. The distributions of kataegic mutations were modelled using Gaussian mixture models (blue lines) with an automatic selection criterion for the number of components using the minimum Bayesian information criteria (BIC).

### [Extended Data Fig. 10 Examples of kyklonas in three independent cohorts.](#)

**a**, A single undifferentiated sarcoma genome depicting the overlap of kataegis with ecDNA regions displayed as a rainfall (left) with a single zoomed in ecDNA represented using a circos plot (middle). The outer track of the circos plot represents the reference genome of the ecDNA with proximal known cancer driver genes. The middle track reflects a circular rainfall plot where each dot represents the IMD around a single mutation coloured based on the substitution change. The innermost track shows the average VAF for each kyklonic event. Right: Two smaller regions of the selected ecDNA including a single kyklonic event within *ZNF536* region resulting in a plethora of missense and stop-gained mutations, and a single kyklonic event within a promoter flanking with the average VAFs per event (orange). **b**, A single lung adenocarcinoma genome depicting the overlap of kataegis with ecDNA regions (left) with a single zoomed in ecDNA containing *TBC1D15* and two distinct kyklonic events represented using a circos plot (middle). Right: Two kyklonic events overlapping an upstream region and *TBC1D15*. **c**, A single oesophageal squamous cell carcinoma genome depicting the overlap of kataegis with ecDNA regions (left) with a single zoomed in ecDNA containing *PRKAA2* and *DAB1* and three distinct kyklonic events (middle). Right: Two kyklonic events overlapping *DAB1*.

## Supplementary information

### [Supplementary Information](#)

This file contains Supplementary Note 1; Supplementary Figures 1 and 2 and Supplementary References

### [Reporting Summary](#)

### [Supplementary Table 1](#)

Mutational signature activities of double-base substitutions

### **Supplementary Table 2**

Mutational signature activities of multi-base substitutions

### **Supplementary Table 3**

Mutational signature activities of omikli events

### **Supplementary Table 4**

Mutational signature activities of kataegic events

### **Supplementary Table 5**

Mutational signature activities of clustered indel events

### **Supplementary Table 6**

Mutational signature activities of other events

### **Supplementary Table 7**

Coding kyklonic mutations within ecDNA

## **Rights and permissions**

**Open Access** This article is licensed under a Creative Commons Attribution 4.0 International License, which permits use, sharing, adaptation, distribution and reproduction in any medium or format, as long as you give appropriate credit to the original author(s) and the source, provide a link to the Creative Commons license, and indicate if changes were made. The images or other third party material in this article are included in the article's Creative Commons license, unless indicated otherwise in a credit line to the material. If material is not included in the article's Creative Commons license and your intended use is not permitted by statutory regulation or exceeds the permitted use, you will need to obtain permission directly from the copyright holder. To view a copy of this license, visit <http://creativecommons.org/licenses/by/4.0/>.

### **Reprints and Permissions**

## About this article

### Cite this article

Bergstrom, E.N., Luebeck, J., Petljak, M. *et al.* Mapping clustered mutations in cancer reveals APOBEC3 mutagenesis of ecDNA. *Nature* **602**, 510–517 (2022).  
<https://doi.org/10.1038/s41586-022-04398-6>

- Received: 27 May 2021
- Accepted: 04 January 2022
- Published: 09 February 2022
- Issue Date: 17 February 2022
- DOI: <https://doi.org/10.1038/s41586-022-04398-6>

### Share this article

Anyone you share the following link with will be able to read this content:

[Get shareable link](#)

Sorry, a shareable link is not currently available for this article.

[Copy to clipboard](#)

Provided by the Springer Nature SharedIt content-sharing initiative

---

This article was downloaded by **calibre** from <https://www.nature.com/articles/s41586-022-04398-6>

- Article
- [Published: 09 February 2022](#)

# Glioblastoma mutations alter EGFR dimer structure to prevent ligand bias

- [Chun Hu](#) ORCID: [orcid.org/0000-0002-0949-9878<sup>1,2</sup>](https://orcid.org/0000-0002-0949-9878),
- [Carlos A. Leche II](#) ORCID: [orcid.org/0000-0002-6161-2671<sup>1,2</sup>](https://orcid.org/0000-0002-6161-2671),
- [Anatoly Kiyatkin](#) ORCID: [orcid.org/0000-0002-5060-6081<sup>1,2</sup>](https://orcid.org/0000-0002-5060-6081),
- [Zhaolong Yu](#) ORCID: [orcid.org/0000-0001-9585-2465<sup>3</sup>](https://orcid.org/0000-0001-9585-2465),
- [Steven E. Stayrook](#) ORCID: [orcid.org/0000-0002-1677-8293<sup>1,2</sup>](https://orcid.org/0000-0002-1677-8293),
- [Kathryn M. Ferguson](#) ORCID: [orcid.org/0000-0002-7671-5403<sup>1,2</sup>](https://orcid.org/0000-0002-7671-5403) &
- [Mark A. Lemmon](#) ORCID: [orcid.org/0000-0002-3379-5319<sup>1,2</sup>](https://orcid.org/0000-0002-3379-5319)

[Nature](#) volume **602**, pages 518–522 (2022)

- 4105 Accesses
- 80 Altmetric
- [Metrics details](#)

## Subjects

- [Growth factor signalling](#)
- [Oncogenes](#)
- [X-ray crystallography](#)

## Abstract

The epidermal growth factor receptor (EGFR) is frequently mutated in human cancer<sup>1,2</sup>, and is an important therapeutic target. EGFR inhibitors have been successful in lung cancer, where mutations in the intracellular tyrosine kinase domain activate the receptor<sup>1</sup>, but not in glioblastoma multiforme (GBM)<sup>3</sup>, where mutations occur exclusively in the extracellular region. Here we show that common extracellular GBM mutations prevent EGFR from discriminating between its activating ligands<sup>4</sup>. Different growth factor ligands stabilize distinct EGFR dimer structures<sup>5</sup> that signal with different kinetics to specify or bias outcome<sup>5,6</sup>. EGF itself induces strong symmetric dimers that signal transiently to promote proliferation.

Epiregulin (EREG) induces much weaker asymmetric dimers that drive sustained signalling and differentiation<sup>5</sup>. GBM mutations reduce the ability of EGFR to distinguish EREG from EGF in cellular assays, and allow EGFR to form strong (EGF-like) dimers in response to EREG and other low-affinity ligands. Using X-ray crystallography, we further show that the R84K GBM mutation symmetrizes EREG-driven extracellular dimers so that they resemble dimers normally seen with EGF. By contrast, a second GBM mutation, A265V, remodels key dimerization contacts to strengthen asymmetric EREG-driven dimers. Our results argue for an important role of altered ligand discrimination by EGFR in GBM, with potential implications for therapeutic targeting.

This is a preview of subscription content

## Access options

Subscribe to Nature+

Get immediate online access to the entire Nature family of 50+ journals

\$29.99

monthly

[Subscribe](#)

Subscribe to Journal

Get full journal access for 1 year

\$199.00

only \$3.90 per issue

[Subscribe](#)

All prices are NET prices.

VAT will be added later in the checkout.

Tax calculation will be finalised during checkout.

Buy article

Get time limited or full article access on ReadCube.

\$32.00

[Buy](#)

All prices are NET prices.

### **Additional access options:**

- [Log in](#)
- [Learn about institutional subscriptions](#)

**Fig. 1: Extracellular EGFR mutations in glioblastoma and effects on signalling.**

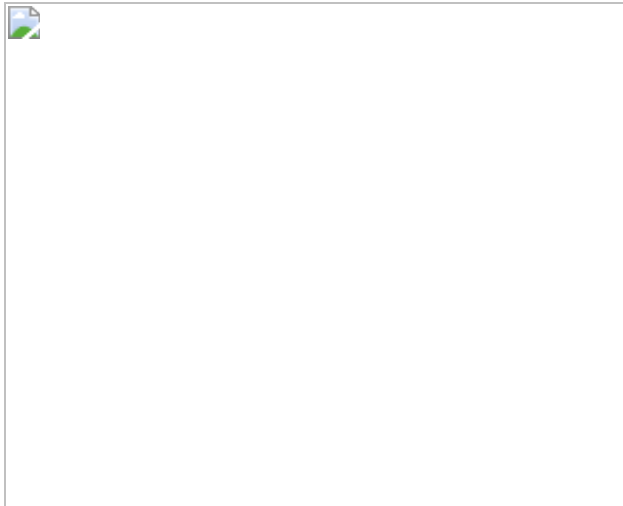


**Fig. 2: GBM mutations selectively enhance EREG-induced EGFR dimerization.**

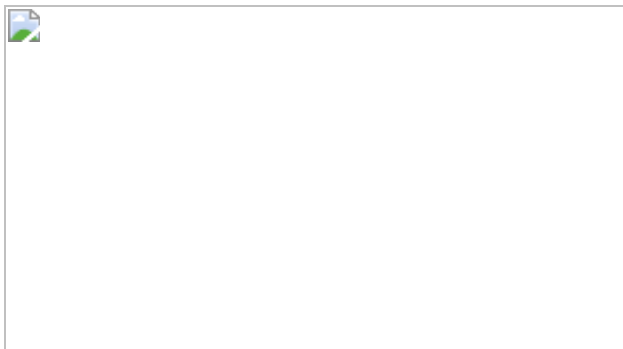
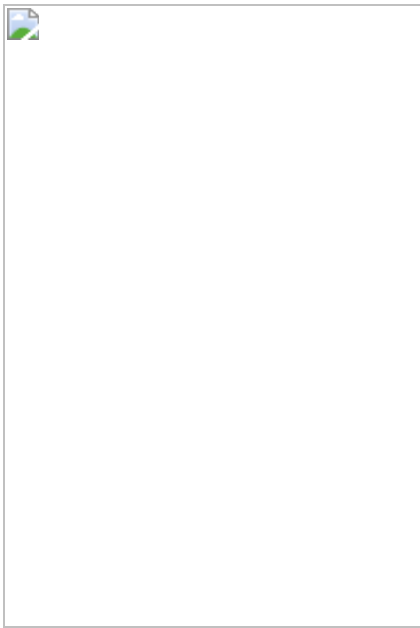


**Fig. 3: R84K GBM mutation symmetrizes EREG-induced EGFR dimers.**



**Fig. 4: A265V mutation optimizes docking of the dimer arm in EREG-induced dimers.**



## Data availability

Atomic coordinates and structure factors for the refined structural models described in this paper have been deposited in the Protein Data Bank (PDB) under accession codes [7LEN](#) (EREG:sEGFR<sup>R84K</sup>, crystallized with trehalose), [7LFR](#) (EREG:sEGFR<sup>R84K</sup>, crystallized with spermine) and [7LFS](#) (EREG:sEGFR<sup>A265V</sup>). Source data are provided with this paper.

## References

1. Sharma, S. V., Bell, D. W., Settleman, J. & Haber, D. A. Epidermal growth factor receptor mutations in lung cancer. *Nat. Rev. Cancer* **7**, 169–181 (2007).
2. Brennan, C. W. et al. The somatic genomic landscape of glioblastoma. *Cell* **155**, 462–477 (2013).
3. An, Z., Aksoy, O., Zheng, T., Fan, Q. W. & Weiss, W. A. Epidermal growth factor receptor and EGFRvIII in glioblastoma: signaling pathways and targeted therapies. *Oncogene* **37**, 1561–1575 (2018).

4. Wilson, K. J., Gilmore, J. L., Foley, J., Lemmon, M. A. & Riese, D. J., II. Functional selectivity of EGF family peptide growth factors: implications for cancer. *Pharmacol. Ther.* **122**, 1–8 (2009).
5. Freed, D. M. et al. EGFR ligands differentially stabilize receptor dimers to specify signaling kinetics. *Cell* **171**, 683–695 (2017).
6. Macdonald-Obermann, J. L. & Pike, L. J. Different epidermal growth factor (EGF) receptor ligands show distinct kinetics and biased or partial agonism for homodimer and heterodimer formation. *J. Biol. Chem.* **289**, 26178–26188 (2014).
7. Martínez-Jiménez, F. et al. A compendium of mutational cancer driver genes. *Nat. Rev. Cancer* **20**, 555–572 (2020).
8. Eck, M. J. & Yun, C. H. Structural and mechanistic underpinnings of the differential drug sensitivity of EGFR mutations in non-small cell lung cancer. *Biochim. Biophys. Acta* **1804**, 559–566 (2010).
9. Tate, J. G. et al. COSMIC: the catalogue of somatic mutations in cancer. *Nucleic Acids Res.* **47**, D941–D947 (2019).
10. Heimberger, A. B. et al. Prognostic effect of epidermal growth factor receptor and EGFRvIII in glioblastoma multiforme patients. *Clin. Cancer Res.* **11**, 1462–1466 (2005).
11. Eskilsson, E. et al. EGFR heterogeneity and implications for therapeutic intervention in glioblastoma. *Neuro Oncol.* **20**, 743–752 (2018).
12. Lee, J. C. et al. Epidermal growth factor receptor activation in glioblastoma through novel missense mutations in the extracellular domain. *PLoS Med.* **3**, e485 (2006).
13. Ng, P. K. et al. Systematic functional annotation of somatic mutations in cancer. *Cancer Cell* **33**, 450–462 (2018).

14. Lu, C. et al. Structural evidence for loose linkage between ligand binding and kinase activation in the epidermal growth factor receptor. *Mol. Cell. Biol.* **30**, 5432–5443 (2010).
15. Garrett, T. P. J. et al. Crystal structure of a truncated epidermal growth factor receptor extracellular domain bound to transforming growth factor alpha. *Cell* **110**, 763–773 (2002).
16. Ferguson, K. M. Structure-based view of epidermal growth factor receptor regulation. *Annu. Rev. Biophys.* **37**, 353–373 (2008).
17. Ogiso, H. et al. Crystal structure of the complex of human epidermal growth factor and receptor extracellular domains. *Cell* **110**, 775–787 (2002).
18. Liebschner, D. et al. Polder maps: improving OMIT maps by excluding bulk solvent. *Acta Crystallogr. D Struct. Biol.* **73**, 148–157 (2017).
19. Diwanji, D. et al. Structures of the HER2–HER3–NRG1 $\beta$  complex reveal a dynamic dimer interface. *Nature* **600**, 339–343 (2021).
20. Alvarado, D., Klein, D. E. & Lemmon, M. A. Structural basis for negative cooperativity in growth factor binding to an EGF receptor. *Cell* **142**, 568–579 (2010).
21. Binder, Z. A. et al. Epidermal growth factor receptor extracellular domain mutations in glioblastoma present opportunities for clinical imaging and therapeutic development. *Cancer Cell* **34**, 163–177 (2018).
22. Orellana, L. et al. Oncogenic mutations at the EGFR ectodomain structurally converge to remove a steric hindrance on a kinase-coupled cryptic epitope. *Proc. Natl Acad. Sci. USA* **116**, 10009–10018 (2019).
23. Fan, Q. W. et al. EGFR phosphorylates tumor-derived EGFRvIII driving STAT3/5 and progression in glioblastoma. *Cancer Cell* **24**, 438–449 (2013).

24. An, Z. et al. EGFR cooperates with EGFRvIII to recruit macrophages in glioblastoma. *Cancer Res.* **78**, 6785–6794 (2018).
25. Friedmann-Morvinski, D. et al. Dedifferentiation of neurons and astrocytes by oncogenes can induce gliomas in mice. *Science* **338**, 1080–1084 (2012).
26. Del Vecchio, C. A. et al. EGFRvIII gene rearrangement is an early event in glioblastoma tumorigenesis and expression defines a hierarchy modulated by epigenetic mechanisms. *Oncogene* **32**, 2670–2681 (2013).
27. Emlet, D. R. et al. Targeting a glioblastoma cancer stem-cell population defined by EGF receptor variant III. *Cancer Res.* **74**, 1238–1249 (2014).
28. Alcantara Llaguno, S. et al. Cell-of-origin susceptibility to glioblastoma formation declines with neural lineage restriction. *Nat. Neurosci.* **22**, 545–555 (2019).
29. Jaiswal, B. S. et al. Oncogenic ERBB3 mutations in human cancers. *Cancer Cell* **23**, 603–617 (2013).
30. Hopkins, J. B., Gillilan, R. E. & Skou, S. BioXTAS RAW: improvements to a free open-source program for small-angle X-ray scattering data reduction and analysis. *J. Appl. Cryst.* **50**, 1545–1553 (2017).
31. Manalastas-Cantos, K. et al. ATSAS 3.0: expanded functionality and new tools for small-angle scattering data analysis. *J. Appl. Crystallogr.* **54**, 343–355 (2021).
32. Lemmon, M. A. et al. Two EGF molecules contribute additively to stabilization of the EGFR dimer. *EMBO J.* **16**, 281–294 (1997).
33. Kabsch, W. XDS. *Acta Crystallogr. D Biol. Crystallogr.* **66**, 125–132 (2010).

34. CCP4. The CCP4 suite: programs for protein crystallography. *Acta Crystallogr. D Biol. Crystallogr.* **50**, 760–763 (1994).
35. McCoy, A. J. et al. Phaser crystallographic software. *J. Appl. Cryst.* **40**, 658–674 (2007).
36. Emsley, P. & Cowtan, K. Coot: model-building tools for molecular graphics. *Acta Crystallogr. D Biol. Crystallogr.* **60**, 2126–2132 (2004).
37. Smart, O. S. et al. Exploiting structure similarity in refinement: automated NCS and target-structure restraints in BUSTER. *Acta Crystallogr. D Biol. Crystallogr.* **68**, 368–380 (2012).
38. Adams, P. D. et al. PHENIX: a comprehensive Python-based system for macromolecular structure solution. *Acta Crystallogr. D Biol. Crystallogr.* **66**, 213–221 (2010).
39. Winn, M. D., Isupov, M. N. & Murshudov, G. N. Use of TLS parameters to model anisotropic displacements in macromolecular refinement. *Acta Crystallogr. D Biol. Crystallogr.* **57**, 122–133 (2001).
40. Chen, V. B. et al. MolProbity: all-atom structure validation for macromolecular crystallography. *Acta Crystallogr. D Biol. Crystallogr.* **66**, 12–21 (2010).
41. Dawson, J. P. et al. Epidermal growth factor receptor dimerization and activation require ligand-induced conformational changes in the dimer interface. *Mol. Cell. Biol.* **25**, 7734–7742 (2005).
42. Ferguson, K. M., Darling, P. J., Mohan, M. J., Macatee, T. L. & Lemmon, M. A. Extracellular domains drive homo- but not hetero-dimerization of erbB receptors. *EMBO J.* **19**, 4632–4643 (2000).
43. Essletzbichler, P. et al. Megabase-scale deletion using CRISPR/Cas9 to generate a fully haploid human cell line. *Genome Res.* **24**, 2059–2065 (2014).

44. Kiyatkin, A., van Alderwerelt van Rosenburgh, I. K., Klein, D. E. & Lemmon, M. A. Kinetics of receptor tyrosine kinase activation define ERK signaling dynamics. *Sci. Signal.* **13**, eaaz5267 (2020).
45. Aksamitiene, E., Hoek, J. B. & Kiyatkin, A. Multistrip western blotting: a tool for comparative quantitative analysis of multiple proteins. *Methods Mol. Biol.* **1312**, 197–226 (2015).
46. Gao, J. et al. Integrative analysis of complex cancer genomics and clinical profiles using the cBioPortal. *Sci. Signal.* **6**, pl1 (2013).
47. Therneau, T. M. A package for survival analysis in R. <https://CRAN.R-project.org/package=survival> (2020).
48. Kohsaka, S. et al. A method of high-throughput functional evaluation of EGFR gene variants of unknown significance in cancer. *Sci. Transl. Med.* **9**, eaan6566 (2017).
49. Neelam, B. et al. Structure–function studies of ligand-induced epidermal growth factor receptor dimerization. *Biochemistry* **37**, 4884–4891 (1998).
50. Thompson, S. A., Harris, A., Hoang, D., Ferrer, M. & Johnson, G. R. COOH-terminal extended recombinant amphiregulin with bioactivity comparable with naturally derived growth factor. *J. Biol. Chem.* **271**, 17927–17931 (1996).
51. Adam, R. et al. Modulation of the receptor binding affinity of amphiregulin by modification of its carboxyl terminal tail. *Biochim. Biophys. Acta* **1266**, 83–90 (1995).
52. Bessman, N. J., Bagchi, A., Ferguson, K. M. & Lemmon, M. A. Complex relationship between ligand binding and dimerization in the epidermal growth factor receptor. *Cell Rep.* **9**, 1306–1317 (2014).
53. Yu, S. et al. The non-small cell lung cancer EGFR extracellular domain mutation, M277E, is oncogenic and drug-sensitive. *Oncotargets Ther.* **10**, 4507–4515 (2017).

54. Liu, P. et al. A single ligand is sufficient to activate EGFR dimers. *Proc. Natl Acad. Sci. USA* **109**, 10861–10866 (2012).
55. Bessman, N. J., Freed, D. M. & Lemmon, M. A. Putting together structures of epidermal growth factor receptors. *Curr. Opin. Struct. Biol.* **29**, 95–101 (2014).
56. Singh, B., Carpenter, G. & Coffey, R. J. EGF receptor ligands: recent advances. *F1000Res.* **5**, 2270 (2016).
57. Macdonald, J. L. & Pike, L. J. Heterogeneity in EGF-binding affinities arises from negative cooperativity in an aggregating system. *Proc. Natl Acad. Sci. USA* **105**, 112–117 (2008).
58. Ferguson, K. M., Hu, C. & Lemmon, M. A. Insulin and epidermal growth factor receptor family members share parallel activation mechanisms. *Protein Sci.* **29**, 1331–1344 (2020).
59. Ferguson, K. M. et al. EGF activates its receptor by removing interactions that autoinhibit ectodomain dimerization. *Mol. Cell* **11**, 507–517 (2003).
60. Ramamurthy, V. et al. Structures of adnectin/protein complexes reveal an expanded binding footprint. *Structure* **20**, 259–269 (2012).
61. Matsuda, T. et al. Cell-free synthesis of functional antibody fragments to provide a structural basis for antibody-antigen interaction. *PLoS ONE* **13**, e0193158 (2018).
62. Li, S. et al. Structural basis for inhibition of the epidermal growth factor receptor by cetuximab. *Cancer Cell* **7**, 301–311 (2005).
63. Lee, J. J. et al. Enzymatic prenylation and oxime ligation for the synthesis of stable and homogeneous protein–drug conjugates for targeted therapy. *Angew. Chem. Int. Ed. Engl.* **54**, 12020–12024 (2015).

64. Alvarado, D., Klein, D. E. & Lemmon, M. A. ErbB2 resembles an autoinhibited invertebrate epidermal growth factor receptor. *Nature* **461**, 287–291 (2009).

## Acknowledgements

We thank members of the Lemmon and Ferguson laboratories for discussions and comments on the manuscript. This work was supported by NCI grant R01-CA198164 (to M.A.L. and K.M.F.). Crystallographic data were collected at GM/CA@APS, funded by NCI (ACB-12002) and NIGMS (AGM-12006). The Eiger 16M detector at GM/CA-XSD was funded by NIH grant S10 OD012289. This research also used resources of the Advanced Photon Source, a US Department of Energy (DOE) Office of Science User Facility operated for the DOE Office of Science by Argonne National Laboratory under contract no. DE-AC02-06CH11357. The survival analysis of patients with GBM used data generated by the TCGA Research Network: <https://www.cancer.gov/tcga>.

## Author information

### Affiliations

1. Department of Pharmacology, Yale University School of Medicine, New Haven, CT, USA

Chun Hu, Carlos A. Leche II, Anatoly Kiyatkin, Steven E. Stayrook, Kathryn M. Ferguson & Mark A. Lemmon

2. Yale Cancer Biology Institute, Yale University, West Haven, CT, USA

Chun Hu, Carlos A. Leche II, Anatoly Kiyatkin, Steven E. Stayrook, Kathryn M. Ferguson & Mark A. Lemmon

3. Interdepartmental Program in Computational Biology and Bioinformatics, Yale University, New Haven, CT, USA

Zhaolong Yu

## Contributions

C.H., A.K., K.M.F. and M.A.L. conceived the project. C.H. performed all protein production, purification, crosslinking, analytical ultracentrifugation and binding studies, with assistance from C.A.L. C.H. and S.E.S. performed all SAXS studies. C.H., K.M.F., C.A.L. and S.E.S. performed and/or interpreted all crystallographic analysis. A.K. performed cell signalling studies. Z.Y. and C.H. analysed TCGA data. M.A.L. and K.M.F. supervised the project. C.H. and M.A.L. drafted the manuscript, and all authors commented on the manuscript.

## Corresponding author

Correspondence to [Mark A. Lemmon](#).

## Ethics declarations

### Competing interests

The authors declare no competing interests.

## Peer review

### Peer review information

*Nature* thanks Michael Eck, Steven Hubbard and the other, anonymous, reviewer(s) for their contribution to the peer review of this work.

## Additional information

**Publisher's note** Springer Nature remains neutral with regard to jurisdictional claims in published maps and institutional affiliations.

## Extended data figures and tables

## Extended Data Fig. 1 Ligand-dependence of GBM-mutated EGFR.

**a**, Full-length human EGFR – WT or harbouring an R84K, T239P or A265V mutation – was stably expressed in the engineered haploid eHAP cell line<sup>43</sup>, which has negligible endogenous EGFR (undetectable by western blotting). Stably transfected cells were serum-starved overnight and either left unstimulated or stimulated with EGF (100 ng ml<sup>-1</sup>) for the indicated times. Levels of phosphorylated EGFR (pY845: CST #2231, used at 1:1000) and ERK1/2 (pT202/pY204: CST #9106, used at 1:1000), were then detected by immunoblotting of whole cell lysates, also blotting for total EGFR and ERK (see [Methods](#)) and Grb2 as loading control<sup>5,45</sup>. EGFR phosphorylation and ERK phosphorylation are both ligand-dependent in all cases, with no evidence for constitutive activation of the mutated receptors. Representative blots are shown for three biologically independent experiments. See Supplementary Fig. 1 for gel source data. **b**, IL-3-dependent Ba/F3 cells were stably transfected with WT EGFR or with variants harbouring an R84K or A265V mutation. Cells were either left untreated or were treated with IL-3 (2 ng ml<sup>-1</sup>) for 72 h, after which a CyQuant Direct proliferation assay was used to detect the number of viable cells in each condition. Resulting fluorescence signals were normalized to that seen with untreated WT and shown as mean ± s.d. ( $n = 3$  experiments for ‘test’ samples). IL-3 treatment promotes robust proliferation in all cases (as positive control:  $n = 3$  for WT,  $n = 2$  for R84K and A265V). As previously reported<sup>12,13,48</sup>, the mutated EGFRs promoted statistically significant increases in viable cell numbers compared with WT EGFR in the absence of ligand (or IL-3), but effects were very small at these expression levels – with the number of viable cells increased (compared with WT) by just 1.31-fold ( $P = 0.0002$ ) for R84K and 1.35-fold for A265V ( $P = 0.0003$ ).  $P$  values are for unpaired two-tailed Student’s t-tests. **c**, Chemiluminescence signals for phosphorylated EGFR in ligand dose-response experiments (see Fig. 1b,c) were quantitated and normalized for Grb2 signals either on different gels as sample processing controls (for gel source data, see Supplementary Fig. 1) or for Grb2 loaded on the same gel using the Multistrip western blotting approach<sup>45</sup>, with both giving identical results. The resulting pEGFR/Grb2 ratios were plotted (mean ± s.d.,  $n = 3$

biologically independent experiments) here and in Fig. 1d as dose-response curves. Responses were normalized to 100% (maximum value) and 0% (without ligand) and the resulting curves were individually fit to a simple model:  $p\text{EGFR} = (100 \times [\text{ligand}]) / (\text{EC}_{50} + [\text{ligand}])$  for each experiment. Mean  $\text{EC}_{50}$  values ( $\pm$  s.d.) are listed in Fig. 1d. d, Ba/F3 cells stably transfected with WT EGFR or variants harbouring R84K or A265V mutations were sorted by flow cytometry (see [Methods](#)) to yield cell populations with similar levels of cell surface EGFR. Cells were either left untreated or were treated with noted doses of EGF or EREG for 72 h. A CyQuant Direct proliferation assay was used to measure the number of viable cells in each condition. Results were divided by the signal from untreated cells to give ‘fold increase’ in cell number, and are plotted across all experiments (mean  $\pm$  s.d.,  $n = 3$  biologically independent experiments).  $\text{EC}_{50}$  values for each ligand were calculated individually for each experiment using the equation:  $\text{cell\#} = (\text{max} \times [\text{ligand}]) / (\text{EC}_{50} + [\text{ligand}])$ , and mean values ( $n = 3$ ) are listed ( $\pm$  s.d.) on the graphs.  $\text{EC}_{50}$  values for EGF and EREG are not significantly different for R84K ( $P = 0.2072$ ) or A265V ( $P = 0.7915$ ), reflecting loss of ligand discrimination.  $P$  values are for unpaired two-tailed Student’s t-tests.

### [Extended Data Fig. 2 Cross-linking studies of ligand-induced sEGFR dimerization.](#)

a, Quantitation and summary of SAXS  $I(0)/c$  measurements reported in Fig. 2 across multiple repeats. For  $\text{sEGFR}^{\text{WT}}$ , only EGF (black) doubles the  $I(0)$  value, representing selective EGF-induced dimerization. By contrast, both EREG (magenta) and EGF (black) induce dimerization of sEGFR harbouring L38R (red), R84K (green), A265V (blue) or A265T (gold) mutations – with EREG-induced dimerization of A265 variants appearing slightly less robust. Data represent mean  $I(0)/c \pm$  s.d. for 10 repeats (WT + EGF), 6 repeats (WT + EREG), 4 repeats (A265V + EGF and A265V + EREG), 3 repeats (L38R + EREG, R84K + EGF, R84K + EREG, A265T + EGF, A265T + EREG), and 2 repeats (L38R + EGF) – where a repeat corresponds to a biologically independent sample. An additional single experiment was undertaken for T239P + EREG, which showed an elevation of  $I(0)/c$  by 1.44 fold. The degree of sEGFR dimerization for EGF

and EREG is significantly different only for WT ( $P < 0.0001$ ) and A265T ( $P < 0.0001$ ).  $P$  values are from unpaired two-tailed Student's t-tests. We estimate based on the SAXS data in Fig. 2a–e that the GBM mutations studied here strengthen dimerization of EREG-bound sEGFR by several hundred fold, based on the following considerations. Since sEGFR<sup>WT</sup> at 70  $\mu\text{M}$  shows no dimerization when saturated with EREG, the dissociation constant ( $K_d$ ) for dimers of the EREG:sEGFR complex must be  $>450 \mu\text{M}$  (assuming that we could detect a minimum of 10% dimer by SAXS). By contrast, the complete dimerization seen for the EREG:sEGFR complex with mutated variants (when corrected for differences in ligand-binding affinities) places a lower limit of  $\sim 0.7 \mu\text{M}$  on  $K_d$  for these dimers. Thus, GBM mutations must enhance dimerization of the EREG:sEGFR complex by at least  $\sim 650$ -fold. **b**, Representative crosslinking analysis of sEGFR dimerization ( $n = 3$  biologically independent samples for each mutated variant). Different sEGFR variants at 5  $\mu\text{M}$  were incubated alone or with the noted ligand (EGF or EREG) at 6  $\mu\text{M}$ , and subjected to 100  $\mu\text{M}$  DSS for 30 min (see [Methods](#)). Samples were then subjected to SDS-PAGE and stained with Coomassie blue. Dimer and monomer bands are marked (note the shift in monomer band position following ligand cross-linking). EGF promotes dimerization of all variants. EREG fails to increase sEGFR<sup>WT</sup> dimerization above that seen without ligand, but detectably enhances dimerization of all variants with GBM mutations, consistent with the SAXS data shown in Fig. 2. See Supplementary Fig. 1 for gel source data, and (c) for quantitation and reproducibility information. **c**, Quantitation of data in (b), including additional repeats for each variant. For sEGFR<sup>WT</sup>, EGF induces substantially more dimerization than EREG ( $P < 0.0001$ ), whereas the difference between EGF and EREG is not significant for L38R ( $P = 0.0522$ ) or A265T ( $P = 0.0577$ ), and only just reaches statistical significance for R84K ( $P = 0.0410$ ) and A265V ( $P = 0.0377$ ).  $P$  values are for unpaired two-tailed Student's t-tests. Data in the graph represent mean  $\pm$  s.d. for 6 repeats (WT + EGF and WT + EREG), or 3 repeats (A265V + EGF, A265V + EREG, R84K + EGF, R84K + EREG, A265T + EGF, A265T + EREG, L38R + EGF, and L38R + EREG), where repeats refer to biologically independent samples. **d**, Top panel: sEGFR<sup>WT</sup> and sEGFR<sup>R84K</sup> (5  $\mu\text{M}$ ) were crosslinked alone or with the noted ligands (EGF, AREG, EREG, or EPGN) at 6  $\mu\text{M}$ . Middle panel: as in Top panel, but with 60  $\mu\text{M}$

ligand. Bottom panel: Crosslinking studies were performed with 60  $\mu$ M ligand added to sEGFR<sup>WT</sup> and 6  $\mu$ M added to sEGFR<sup>R84K</sup>, to account for affinity differences. Data are representative of three biologically independent samples. See Supplementary Fig. 1 for gel source data. e, As for (d), but using sEGFR<sup>A265V</sup> with 6  $\mu$ M or 60  $\mu$ M ligand as marked, for 5 biologically independent samples of sEGFR<sup>A265V</sup> with EGF and EREG, but  $n = 2$  for AREG and EPGN. See Supplementary Fig. 1 for gel source data.

### **Extended Data Fig. 3 Kinetics of EGFR and ERK activation by AREG (98aa) and EGF in MCF7 cells.**

a, b, Representative time courses (of 3 biologically independent repeats with similar results in each case) of EGFR phosphorylation at Y1173 and Y1068, as well as ERK phosphorylation, in parental MCF-7 cells induced by saturating levels of (a) AREG (1  $\mu$ M) or (b) EGF (16 nM), exactly as described<sup>5</sup>. Cells were starved overnight, and were then left unstimulated or stimulated with ligand for the noted times at 37 °C, using growth factor ligands added to starvation medium. Analysis by immunoblotting was then performed exactly as described<sup>5,44</sup>. Note that the commercially available 98aa form of AREG used here appears to elicit sustained signalling and weak dimerization of sEGFR in these studies – consistent with other work<sup>6</sup>. We previously reported that a shorter in-house-produced 90aa form of AREG induces more transient (EGF-like) signalling and stronger sEGFR dimerization<sup>5</sup>. Different signalling properties of AREG forms with different carboxy termini have been reported by others<sup>49,50,51</sup>, and will be the subject of separate detailed studies. See Supplementary Fig. 1 for gel source data.

### **Extended Data Fig. 4 SE-AUC studies of TGF $\alpha$ -induced sEGFR dimerization.**

a, The noted sEGFR variants were subjected to sedimentation equilibrium analytical ultracentrifugation (SE-AUC) as described in Methods, with or without adding a 1.2-fold excess of TGF $\alpha$ . The low UV absorbance of TGF $\alpha$  allows precise quantitation of TGF $\alpha$ -induced sEGFR dimerization using SE-AUC as described<sup>41</sup>. Representative data are shown ( $n = 3$  biologically independent samples) for 10  $\mu$ M sEGFR at 6,000 r.p.m., with

the natural logarithm of the absorbance,  $\ln(A_{280})$ , at radial distance  $r$  plotted against  $(r^2 - r_0^2)/2$ . This transformation of the data gives a straight line for a single species, with slope proportional to molecular weight. Expected data for pure monomer and pure sEGFR–TGF $\alpha$  dimer are shown as dotted and solid grey lines (marked). Data points are colour coded for the different variants as described in the key, with filled circles representing data with added ligand and unfilled circles without. No dimerization was seen in the absence of ligand for any variant under these conditions, consistent with the SAXS studies shown in Fig. 2 and our previous work<sup>52</sup>.  $K_d$  values for each sEGFR–TGF $\alpha$  complex are listed below the graph, determined by global fit of SE-AUC data as described previously<sup>41</sup> and in Methods. Mean values  $\pm$  s.d. from 3 biologically independent samples are reported for all cases except L38R (where  $n = 1$ ). Whereas sEGFR<sup>R84K</sup> dimerizes with essentially the same  $K_d$  as sEGFR<sup>WT</sup> following TGF $\alpha$  binding, sEGFR<sup>A265V</sup> and sEGFR<sup>A265T</sup> dimerize slightly more weakly ( $P = 0.006$  and  $0.005$  respectively, for unpaired two-tailed Student's t-tests). **b**, Effects on ligand-dependent dimerization also appear specific for GBM extracellular mutations. A rare extracellular EGFR lung cancer mutation (M253E)<sup>53</sup>, not seen in GBM, instead enhances *both* ligand-independent (confirmed by crosslinking) and ligand-induced sEGFR dimerization. SE-AUC analysis of sEGFR harbouring the M253E mutation is shown. Unlike GBM variants, M253E-mutated sEGFR dimerizes constitutively, being substantially dimeric in the absence of ligand. TGF $\alpha$ -bound M253E sEGFR also appears to form species larger than dimers, with an estimated  $K_d$  in the range of  $0.33\text{ }\mu\text{M}$ . M253E-mutated sEGFR was used at  $10\text{ }\mu\text{M}$ , and the sample was spun at 6,000 r.p.m. This experiment was only done with one biologically independent sample of sEGFR<sup>M253E</sup> (in triplicate with- and without TGF $\alpha$ ), as the protein is difficult to produce in sufficient quantities.

### **Extended Data Fig. 5 Symmetry of the EREG-induced sEGFR<sup>R84K</sup> dimer and implications for negative cooperativity in EGFR.**

**a**, Overlay of the EREG-induced sEGFR<sup>R84K</sup> dimer (dark green ribbons) with the symmetric dimers of sEGFR<sup>WT</sup> induced by TGF $\alpha$  (1MOX<sup>15</sup>, gold

ribbons) or EGF (3NJP<sup>14,17</sup>, grey ribbons). EREG, TGF $\alpha$  and EGF are coloured magenta, orange, and black respectively. **b**, Schematic of half-of-the-sites negative cooperativity in ligand binding to WT EGFR<sup>20,54,55</sup> for any ligand (blue). As we previously described in detail for the *Drosophila* EGFR<sup>20</sup>, and as also seems to apply to human EGFR<sup>54</sup>, binding of a single ligand can promote formation of asymmetric sEGFR dimers (left-hand side of cartoon) with autoinhibitory domain I–domain II interactions broken (unfilled red star) only in one protomer. This asymmetric dimerization is driven by contacts involving N-terminal regions of domain II as well as altered dimer arm docking<sup>5,20</sup> – together restraining domain II in the unliganded protomer. When a second ligand binds to this dimer, it must ‘wedge’ apart the two ligand-binding domains (I and III) in the right-hand protomer to drive formation of the symmetric dimer (top right in cartoon). This requires disruption of autoinhibitory domain I–domain II interactions in both molecules (both red stars are unfilled). It also requires disruption of domain II dimer interface contacts – with a resulting bend in domain II (Extended Data Fig. 6d) – giving rise to the symmetric 2:2 dimer. This is readily achieved by high-affinity ligands such as EGF and TGF $\alpha$ , but low-affinity EGFR ligands like EREG<sup>56</sup> cannot disrupt the autoinhibitory domain I–domain II interactions or bend the restrained domain II to optimize dimer arm contacts. As a consequence, low-affinity ligands fail to wedge apart domains I and III in the right-hand protomer – instead binding to an unaltered asymmetric dimer (lower right in cartoon) through a compromised set of ligand–receptor interactions (i.e. a remodeled binding site<sup>5</sup>: see Extended Data Fig. 8d). The R84K mutation lowers this barrier to dimer ‘symmetrization’ by weakening autoinhibitory domain I–domain II interactions so that the second ligand-binding event more readily bends domain II and symmetrizes dimers. This appears to be the origin of the R84K mutation’s ability to selectively stabilize dimers induced by low-affinity EGFR ligands. Weakening of autoinhibitory domain I–domain II interactions may also explain the enhanced ligand-binding affinity seen for R84K EGFR (Extended Data Fig. 7b). The ability of the R84K mutation to equalize the two EREG-binding sites in a dimer, and to increase EREG affinity also argues that this mutation removes a barrier to ligand binding, and may diminish the half-of-the-sites negative cooperativity seen in wild-type EGFR<sup>20,54,57,58</sup>.

## Extended Data Fig. 6 Autoinhibitory domain I–domain II interactions in different sEGFR structures.

**a**, As expected for autoinhibitory interactions, R84–A265 and L38–F263 interactions are broken in ‘active’ symmetric dimers of sEGFR induced upon activation with TGF $\alpha$  (1MOX<sup>15</sup>) or EGF (3NJP<sup>14,17</sup>). This configuration is represented by unfilled red stars, as in Fig. 3. **b**, Disposition of key GBM-mutated residues (L38, R84 and A265, coloured red) for comparison in ‘inactive’ configurations of the EGFR extracellular region. The positions of these side-chains are shown in monomeric tethered forms of sEGFR<sup>59,60,61,62,63</sup>. In each case, the R84 side-chain directly contacts that of A265, and the L38 side-chain is in van der Waal’s contact with that of F263 (grey spheres: not mutated in GBM). These represent autoinhibitory interactions between domains I and II as described in the text and pointed out in our previous studies<sup>64</sup>. This configuration is represented as a filled red star. **c**, Importantly, the autoinhibitory R84–A265 and L38–F263 interactions are also retained in the ligand-bound monomer observed when EPGN binds to sEGFR<sup>WT</sup> (5WB8<sup>5</sup>). Moreover, as shown in the lower two panels, these autoinhibitory interactions are retained in the right-hand molecule of the asymmetric EREG-induced dimer of sEGFR<sup>WT</sup> (5WB7: Fig. 3a) – see filled red star – but are lost in the left-hand molecule (unfilled red star). **d**, Comparison of the ‘bend’ in domain II in inactive monomeric forms of sEGFR (light green) and active dimeric forms (grey) – colours corresponding to those used for sEGFR chains in Fig. 3a. The structures of unliganded monomeric sEGFR (PDBID: 1NQL<sup>59</sup>) and an EGF-induced WT sEGFR dimer (PDBID: 3NJP<sup>14</sup>) were used. Only residues 187–310 of domain II are shown. In the left-hand panel, the two structures are overlaid using residues 187–238 as reference. In the right-hand panel, residues 238–310 are used as reference. This analysis reveals that the two structures differ by a bend at residue D238 (marked as ‘Curvature defining point’). The approximate direction of curvature is shown by green and grey brush strokes on each structure. The dimer arm is labelled, as are disulphide-bonded modules 2–8 of domain II<sup>59</sup>. This figure is based on one by Ferguson<sup>16</sup>.

## Extended Data Fig. 7 Similarity of the two ligand-binding sites in EREG-induced sEGFR<sup>R84K</sup> dimers.

**a**, Comparison of the two EREG-binding sites in the symmetric dimer of R84K-mutated sEGFR, overlaid by superposition of the ligand chains. Chain A of sEGFR<sup>R84K</sup> (left in Fig. 3b) is shown in grey ribbons, and chain B (right in Fig. 3b) is shown in dark green ribbons – with the respective bound ligands coloured pink and magenta. Side-chains involved in direct EREG–sEGFR contacts are shown and labelled. Those in the ligands superimpose very well (see Y13, H16, M25, Y29, for example), with a few exceptions (e.g. R31 and F45). Similarly, sEGFR side-chains in the binding sites overlay well, including D22, R29, Y45, E90 and S99 in domain I and D355, L348, F357, and H409 in domain III. Accordingly, the root-mean-square deviation for all atoms in the 56 residues involved in ligand–receptor contacts (35 from sEGFR, 21 from EREG) is 1.4 Å. **b**, Comparison of EREG binding to different sEGFR variants as assessed using surface plasmon resonance (see [Methods](#)). Representative binding curves for one of the biological replicates are plotted on the left ( $n = 3$  for WT, L38R, R84K, and  $n = 2$  for A265V and A265T). The WT sEGFR construct used in these studies bound to immobilized EREG in surface plasmon resonance studies with a  $K_d$  value of  $6.6 \pm 0.6 \mu\text{M}$  ( $n = 3$  biologically independent samples; mean  $\pm$  s.d.). GBM mutations in domain I increased ligand-binding affinity by ~6 fold for L38R ( $P < 0.0001$ :  $n = 3$ ) and almost 10-fold for R84K ( $P < 0.0001$ :  $n = 3$ ), with  $K_d$  values respectively of  $1.1 \pm 0.4 \mu\text{M}$  and  $0.7 \pm 0.2 \mu\text{M}$ . Domain II GBM mutations increased ligand-binding affinity by 4.2-fold for A265V ( $n = 2$ ) and just ~2-fold for A265T ( $n = 2$ ), with  $K_d$  values respectively of 1.6 and  $3.1 \mu\text{M}$  (no s.d. is quoted for  $n = 2$ ). These smaller differences are consistent with the asymmetry retained in the A265V ligand binding sites.  $P$  values where quoted are for unpaired two-tailed Student's t-tests.

## Extended Data Fig. 8 Structural features of the asymmetric dimer of sEGFR<sup>A265V</sup> induced by EREG.

**a**, The asymmetric A265V-mutated (left) and WT (right) sEGFR dimers induced by EREG are compared, with disposition of the autoinhibitory domain I–domain II residues shown in the lower panels. Colours parallel those used in Figs. 3 and 4, with the right-hand molecule coloured slate blue for A265V and light green for WT sEGFR. Side-chain contacts between residues at positions 38 and 263 and between residues 84 and 265 are retained in the right-hand molecule (filled red star) but not the left-hand (unfilled red star) in each case. V265, corresponding to the GBM substitution (A265V), is coloured red. **b**, Local structural consequences of the A265V mutation in the domain I–domain II interface region of EREG-induced sEGFR dimers. The right-hand side of the EREG-bound WT and A265V-mutated sEGFR structures shown in (a) are superimposed using domain I as reference, with WT sEGFR shown in light green and A265V sEGFR in slate blue. Replacing A265 with a valine displaces the C $\alpha$  position for residue 265 by  $\sim$ 1.2 Å (red arrow), and this is propagated to a shift in position of F263 by  $\sim$ 2.5 Å (red arrow). As a result of consequent small displacements in domain II constituents beyond this position, the locations of Y275 and R285 – which provide the docking side for the dimer arm Y251 residue in Fig. 4b – are altered, allowing remodeling of this binding site to enhance dimerization strength as described in the text. **c, d**, Comparison of the binding sites on the two sides of the EREG-induced dimer for A265V-mutated sEGFR (**c**) and WT sEGFR (**d**), illustrating that the differences seen between the two sites in the asymmetric WT dimer<sup>5</sup> are retained in the A265V variant despite stronger dimerization and slightly stronger ligand binding. The regions corresponding to the two ligand-binding sites are superimposed with EREG as the reference. The left-hand molecule is coloured grey in each case, and the right-hand molecule slate blue in (**c**) for A265V and light green in (**d**) for WT. The pink ligand is bound to the left-hand (grey) sEGFR molecule, and the magenta ligand is bound to the right-hand sEGFR molecule. For clarity, ligand side-chains that are not substantially different in orientation are omitted – the exceptions being L15, Y29, and V39, which are consistently reoriented between the two sites. Contact side-chains in the receptor are shown, illustrating their substantial displacement with respect to the ligand in the two sites, with a contact residue root-mean-square deviation between the two sites of 3.0 Å in both A265V and WT (compared with 1.4 Å for the two sites in EREG-bound R84K). Examples include the  $\sim$ 10 Å displacement of

D22 and R29, and ~7 Å displacements of L17 and F20 that are marked by red arrows in domain I. These changes are essentially the same in A265V and WT. Shifts in domain III are generally smaller, but are essentially the same in A265V and WT sEGFR. Thus, the compromised binding to the right-hand molecule previously reported<sup>5</sup> is fully retained in the A265V variant despite stronger dimerization.

### **Extended Data Fig. 9 Kaplan-Meier estimates of overall survival in glioblastoma patients with different EGFR status from the TCGA database.**

Two-sided log-rank tests were performed to assess the overall survival differences between different patient groups, with no corrections made for multiple pairwise comparisons. Patients with no *EGFR* alteration ( $n = 322$  patients; *red line*) had median overall survival times of 14.4 months (95% CI, 12.7–15.8), which was not statistically significantly different from: **a**, Patients with any *EGFR* alteration ( $n = 270$  patients; *blue dashed line*), who had median overall survival times of 14.3 months (95% CI, 13.3–15.6),  $P = 0.06$ . **b**, Patients with an *EGFR* mutation ( $n = 22$  patients; *blue dashed line*), who had median overall survival times of 15.9 months (95% CI, 11.3–23.2),  $P = 0.6$ . **c**, Patients with an *EGFR* mutation and *EGFR* amplification ( $n = 58$  patients; *blue dashed line*), who had median overall survival times of 13.9 months (95% CI, 11.2–17.5),  $P = 0.66$ . **d**, Patients with *EGFR* amplification ( $n = 85$  patients; *blue dashed line*), who had median overall survival times of 14.3 months (95% CI, 11.8–16.8),  $P = 0.28$ .

### **Extended Data Table 1 Data collection and refinement statistics**

## **Supplementary information**

### **Supplementary Figure 1**

This file contains the raw (uncropped) gel images for Figs. 1 and 2 and for Extended Data Figs. 1–3.

### **Reporting Summary**

# Rights and permissions

[Reprints and Permissions](#)

## About this article

### Cite this article

Hu, C., Leche, C.A., Kiyatkin, A. *et al.* Glioblastoma mutations alter EGFR dimer structure to prevent ligand bias. *Nature* **602**, 518–522 (2022).  
<https://doi.org/10.1038/s41586-021-04393-3>

- Received: 25 January 2021
- Accepted: 22 December 2021
- Published: 09 February 2022
- Issue Date: 17 February 2022
- DOI: <https://doi.org/10.1038/s41586-021-04393-3>

### Share this article

Anyone you share the following link with will be able to read this content:

[Get shareable link](#)

Sorry, a shareable link is not currently available for this article.

[Copy to clipboard](#)

Provided by the Springer Nature SharedIt content-sharing initiative

| [Section menu](#) | [Main menu](#) |

- Article
- [Published: 09 February 2022](#)

# A backbone-centred energy function of neural networks for protein design

- [Bin Huang](#) [ORCID: orcid.org/0000-0002-6884-9778<sup>1,na1</sup>](#),
- [Yang Xu](#) [ORCID: orcid.org/0000-0003-3335-3278<sup>1,na1</sup>](#),
- [XiuHong Hu](#) [ORCID: orcid.org/0000-0001-7110-274X<sup>1,na1</sup>](#),
- [Yongrui Liu<sup>1</sup>](#),
- [Shanhui Liao<sup>1</sup>](#),
- [Jiahai Zhang<sup>1</sup>](#),
- [Chengdong Huang<sup>1,2</sup>](#),
- [Jingjun Hong<sup>1</sup>](#),
- [Quan Chen](#) [ORCID: orcid.org/0000-0002-3301-3065<sup>1,2</sup>](#) &
- [Haiyan Liu](#) [ORCID: orcid.org/0000-0002-5926-820X<sup>1,2,3</sup>](#)

*Nature* volume **602**, pages 523–528 (2022)

- 7290 Accesses
- 100 Altmetric
- [Metrics details](#)

## Subjects

- [Computational biophysics](#)
- [Protein design](#)

# Abstract

A protein backbone structure is designable if a substantial number of amino acid sequences exist that autonomously fold into it<sup>1,2</sup>. It has been suggested that the designability of backbones is governed mainly by side chain-independent or side chain type-insensitive molecular interactions<sup>3,4,5</sup>, indicating an approach for designing new backbones (ready for amino acid selection) based on continuous sampling and optimization of the backbone-centred energy surface. However, a sufficiently comprehensive and precise energy function has yet to be established for this purpose. Here we show that this goal is met by a statistical model named SCUBA (for Side Chain-Unknown Backbone Arrangement) that uses neural network-form energy terms. These terms are learned with a two-step approach that comprises kernel density estimation followed by neural network training and can analytically represent multidimensional, high-order correlations in known protein structures. We report the crystal structures of nine de novo proteins whose backbones were designed to high precision using SCUBA, four of which have novel, non-natural overall architectures. By eschewing use of fragments from existing protein structures, SCUBA-driven structure design facilitates far-reaching exploration of the designable backbone space, thus extending the novelty and diversity of the proteins amenable to de novo design.

This is a preview of subscription content

## Access options

Subscribe to Nature+

Get immediate online access to the entire Nature family of 50+ journals

\$29.99

monthly

[Subscribe](#)

[Subscribe to Journal](#)

Get full journal access for 1 year

\$199.00

only \$3.90 per issue

[Subscribe](#)

All prices are NET prices.

VAT will be added later in the checkout.

Tax calculation will be finalised during checkout.

[Buy article](#)

Get time limited or full article access on ReadCube.

\$32.00

[Buy](#)

All prices are NET prices.

### **Additional access options:**

- [Log in](#)
- [Learn about institutional subscriptions](#)

**Fig. 1: Template-free protein design facilitated by explicit representation of the backbone-centred energy landscape.**

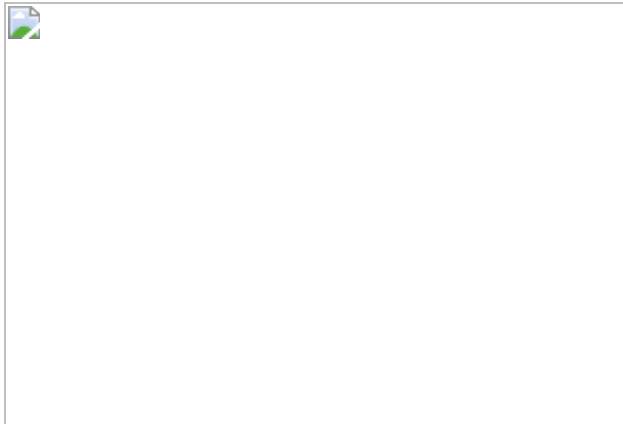


**Fig. 2: The de novo protein EXTD-3 integrates pre-existing and newly designed parts to form a single rigid architecture not yet observed in nature.**

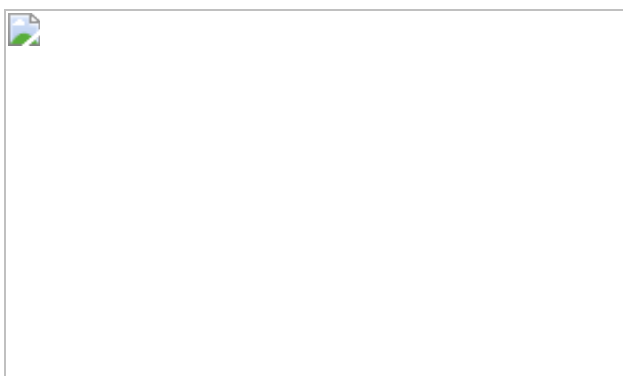


**Fig. 3: Successfully designed two-layered  $\alpha/\beta$  proteins and four-helix bundle proteins.**

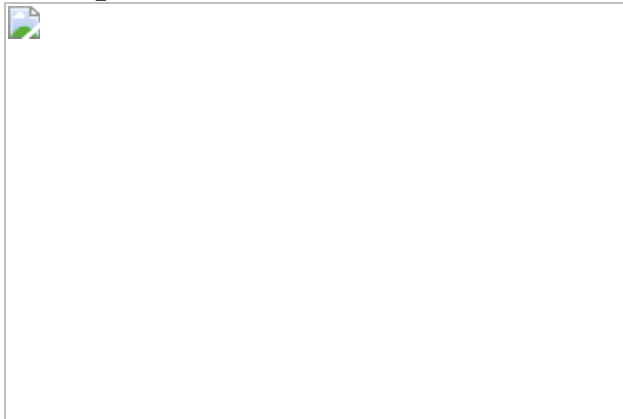
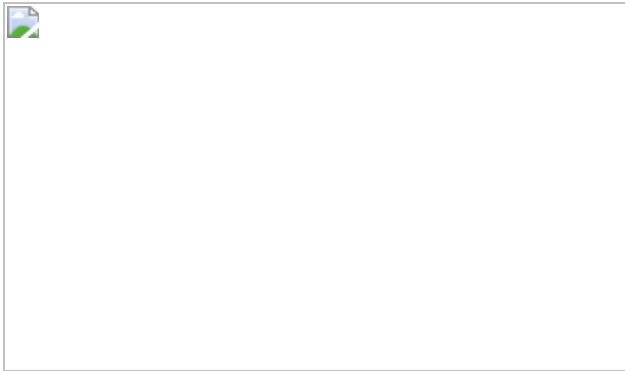


**Fig. 4: Structures of successfully designed de novo proteins that fold into novel architectures.**



## Data availability

Coordinates and structure files for designed proteins have been deposited to PDB under the following accession codes: [7DMF](#) (EXTD-3), [7DKK](#) (XM2H), [7DKQ](#) (AM2M), [7DGU](#) (H4A1R), [7DGW](#) (H4A2S), [7DGY](#) (H4C2R), [7FBB](#) (D12), [7FBC](#) (D22) and [7FBD](#) (D53). Other relevant data are available in the main text or the [Supplementary Information](#).

## Code availability

Executable computer programs, source code and model parameters for SCUBA and ABACUS2 are available for public download and free non-commercial use from <https://doi.org/10.5281/zenodo.4533424>.

## References

1. Li, H., Helling, R., Tang, C. & Wingreen, N. Emergence of preferred structures in a simple model of protein folding. *Science* **273**, 666–669 (1996).
2. England, J. L. & Shakhnovich, E. I. Structural determinant of protein designability. *Phys. Rev. Lett.* **90**, 218101 (2003).
3. Hoang, T. X., Trovato, A., Seno, F., Banavar, J. R. & Maritan, A. Geometry and symmetry prescupt the free-energy landscape of proteins. *Proc. Natl Acad. Sci. USA* **101**, 7960–7964 (2004).

4. Rose, G. D., Fleming, P. J., Banavar, J. R. & Maritan, A. A backbone-based theory of protein folding. *Proc. Natl Acad. Sci. USA* **103**, 16623–16633 (2006).
5. Skolnick, J. & Gao, M. The role of local versus nonlocal physicochemical restraints in determining protein native structure. *Curr. Opin. Struct. Biol.* **68**, 1–8 (2021).
6. Kuhlman, B. et al. Design of a novel globular protein fold with atomic-level accuracy. *Science* **302**, 1364–1368 (2003).
7. Jiang, L. et al. De novo computational design of retro-aldol enzymes. *Science* **319**, 1387–1391 (2008).
8. Koga, N. et al. Principles for designing ideal protein structures. *Nature* **491**, 222–227 (2012).
9. Marcos, E. et al. Principles for designing proteins with cavities formed by curved  $\beta$  sheets. *Science* **355**, 201–206 (2017).
10. Dou, J. et al. De novo design of a fluorescence-activating  $\beta$ -barrel. *Nature* **561**, 485–491 (2018).
11. Lu, P. et al. Accurate computational design of multipass transmembrane proteins. *Science* **359**, 1042–1046 (2018).
12. Glasgow, A. A. et al. Computational design of a modular protein sense–response system. *Science* **366**, 1024–1028 (2019).
13. Huang, P. S., Boyken, S. E. & Baker, D. The coming of age of de novo protein design. *Nature* **537**, 320–327 (2016).
14. Alford, R. F. et al. The Rosetta all-atom energy function for macromolecular modeling and design. *J. Chem. Theory Comput.* **13**, 3031–3048 (2017).
15. Grigoryan, G. & DeGrado, W. F. Probing designability via a generalized model of helical bundle geometry. *J. Mol. Biol.* **405**, 1079–1100 (2011).

16. Thomson, A. R. et al. Computational design of water-soluble  $\alpha$ -helical barrels. *Science* **346**, 485–488 (2014).
17. Brunette, T. J. et al. Exploring the repeat protein universe through computational protein design. *Nature* **528**, 580–584 (2015).
18. Jacobs, T. et al. Design of structurally distinct proteins using strategies inspired by evolution. *Science* **352**, 687–690 (2016).
19. Pan, X. et al. Expanding the space of protein geometries by computational design of de novo fold families. *Science* **369**, 1132–1136 (2020).
20. Baker, D. An exciting but challenging road ahead for computational enzyme design. *Protein Sci.* **19**, 1817–1819 (2010).
21. Otten, R. et al. How directed evolution reshapes the energy landscape in an enzyme to boost catalysis. *Science* **370**, 1442–1446 (2020).
22. Zhang, Y., Hubner, I. A., Arakaki, A. K., Shakhnovich, E. & Skolnick, J. On the origin and highly likely completeness of single-domain protein structures. *Proc. Natl Acad. Sci. USA* **103**, 2605–2610 (2006).
23. Kukic, P. et al. Mapping the protein fold universe using the CamTube force field in molecular dynamics simulations. *PLoS Comput. Biol.* **11**, e1004435 (2015).
24. MacDonald, J. T., Maksimiak, K., Sadowski, M. I. & Taylor, W. R. De novo backbone scaffolds for protein design. *Proteins Struct. Funct. Bioinf.* **78**, 1311–1325 (2010).
25. MacDonald, J. T. et al. Synthetic  $\beta$ -solenoid proteins with the fragment-free computational design of a  $\beta$ -hairpin extension. *Proc. Natl Acad. Sci. USA* **113**, 10346–10351 (2016).
26. Van Gunsteren, W. F., Berendsen, H. J. C. & Rullmann, J. A. C. Stochastic dynamics for molecules with constraints: Brownian dynamics of n-alkanes. *Mol. Phys.* **44**, 69–95 (1981).

27. Xiong, P. et al. Protein design with a comprehensive statistical energy function and boosted by experimental selection for foldability. *Nat. Commun.* **5**, 5330 (2014).
28. Xiong, P. et al. Increasing the efficiency and accuracy of the ABACUS protein sequence design method. *Bioinformatics* **36**, 136–144 (2020).
29. Behler, J. & Parrinello, M. Generalized neural-network representation of high-dimensional potential-energy surfaces. *Phys. Rev. Lett.* **98**, 146401 (2007).
30. Wang, G. & Dunbrack, R. L., Jr. PISCES: recent improvements to a PDB sequence culling server. *Nucleic Acids Res.* **33**, W94–W98 (2005).
31. Berman, H. M. et al. The Protein Data Bank. *Nucleic Acids Res.* **28**, 235–242 (2000).
32. Taylor, W. R. A ‘pperiodic table’ for protein structures. *Nature* **416**, 657–662 (2002).
33. Baker, D. What has de novo protein design taught us about protein folding and biophysics? *Protein Sci.* **28**, 678–683 (2019).
34. Liu, R., Wang, J., Xiong, P., Chen, Q. & Liu, H. De novo sequence redesign of a functional Ras-binding domain globally inverted the surface charge distribution and led to extreme thermostability. *Biotechnol. Bioeng.* **118**, 2031–2042 (2021).

## Acknowledgements

This work was supported by the National Key R&D Program of China (2018YFA0900703 to H.L. and 2018YFA0901600 to Q.C.), the National Natural Science Foundation of China (21773220 to H.L., 31971175 to Q.C. and 32090040 to J. Z.) and the Youth Innovation Promotion Association, Chinese Academy of Sciences (2017494 to Q.C.). We thank the staff from the Core Facility Centre for Life Sciences, USTC, and from

the BL18U1, BL19U1 and BL02U1 beamlines of the National Facility for Protein Science in Shanghai (NFPS) and the Shanghai Synchrotron Radiation Facility for assistance during crystallographic data collection. We thank the USTC Supercomputing Center for computing resource. We thank Z. Zhu, F. Li, Y. Wang, M. Lv and Y. Yun for assistance with X-ray diffraction data collection and processing and T. Jin for sharing MBP expression plasmids.

## Author information

### Author notes

1. These authors contributed equally: Bin Huang, Yang Xu, XiuHong Hu

### Affiliations

1. MOE Key Laboratory for Membraneless Organelles and Cellular Dynamics, Hefei National Laboratory for Physical Sciences at the Microscale, School of Life Sciences, Division of Life Sciences and Medicine, University of Science and Technology of China, Hefei, China

Bin Huang, Yang Xu, XiuHong Hu, Yongrui Liu, Shanhui Liao, Jiahai Zhang, Chengdong Huang, Jingjun Hong, Quan Chen & Haiyan Liu

2. Biomedical Sciences and Health Laboratory of Anhui Province, University of Science and Technology of China, Hefei, China

Chengdong Huang, Quan Chen & Haiyan Liu

3. School of Data Science, University of Science and Technology of China, Hefei, China

Haiyan Liu

## Contributions

H.L., B.H. and Y.X. developed computational models and code, and B.H., Y.X., X.H. and Q.C. performed protein design and experimental characterization. S.L. and Y.L. collected and analysed crystallographic data. J.H., J.Z. and C.H. collected and helped process NMR data. H.L. and Q.C. supervised the project. H.L., Q.C. and B.H. wrote the manuscript, and other authors were involved in discussion.

## Corresponding authors

Correspondence to [Quan Chen](#) or [Haiyan Liu](#).

## Ethics declarations

## Competing interests

H.L., Q.C., B.H., Y.X. and X.H. have filed a patent application (202111197820.0) relating to the template-free protein design method in the name of the University of Science and Technology of China. The other authors declare no competing interests.

## Peer review

### Peer review information

*Nature* thanks the anonymous reviewers for their contribution to the peer review of this work. Peer reviewer reports are available.

## Additional information

**Publisher's note** Springer Nature remains neutral with regard to jurisdictional claims in published maps and institutional affiliations.

## Extended data figures and tables

## Extended Data Fig. 1 Statistical energies learned by NC-NN capture correlations in high-dimensional space.

**a–d**, Scatter graphs showing projections of a NC-NN-learned term for the through-space interactions between two backbone positions. In total, the term depends on 14 variables. The variables used for projections include the C $\alpha$ -C $\alpha$  distance (**a**, **b**) between the two positions, and additionally the mainchain torsional angles  $\varphi_1$  and  $\psi_1$  at one position (**c**, **d**). Points are colored according to statistical energy values (in arbitrary units) as indicated by the color bar. Points in **a** and **c** correspond to observed configurations, while those in **b** and **d** correspond to configurations randomly drawn according to the reference distribution.

## Extended Data Fig. 2 NC-NN-learned components in SCUBA and simulations of natural protein structures by SCUBA.

**a**, Types of NC-NN-learned statistical energy terms in SCUBA. **b**, The deviations of conformations sampled in SCUBA-driven SD simulations from native conformations for 33 natural proteins. Each protein was simulated for 900  $ps$  at reduced temperature  $T_r = 1.0$  and the r.m.s.d. values (noted as RMSD in the figure) are for mainchain atoms in secondary structures averaged over the last 50  $ps$ . Simulations were carried out either with or without a radius of gyration ( $R_g$ ) restraint, which, as described in the [Supplementary Methods](#), was optionally applied in later backbone design simulations both to bias the sampling of more compact structures and to compensate for thermal expansion in simulated annealing simulations involving higher temperatures. The restraint energy took the form  $\langle\{E\}_{\{Rg\}-\{restraint\}}(\{R\}_{\{g\}})\rangle=\langle k \rangle_{\{res\}}$   $\{\ln\}\left(\frac{\langle R \rangle_{\{g\}}}{\langle R \rangle_{\{g\}}^0}\right)$  when  $\langle R \rangle_{\{g\}} > \langle R \rangle_{\{g\}}^0$  and  $\langle\{E\}_{\{Rg\}-\{restraint\}}(\{R\}_{\{g\}})\rangle=0$  for  $\langle R \rangle_{\{g\}} \leq \langle R \rangle_{\{g\}}^0$  ( $k_{res} = 300$  in reduced energy unit and  $\langle R \rangle_{\{g\}}^0 = 5 \langle \text{rm}\{\text{AA}\} \rangle$ ). This energy term leads to only weak compressing forces in comparisons with the strong inter-atomic steric repulsions, and does not distort the tightly-packed native-like minimum structures. The median r.m.s.d. values across the 33 proteins are 1.60 Å (native sequences, without  $R_g$  restraint, red bars), 1.25 Å (native sequences,

with  $R_g$  restraint, orange bars), 2.78 Å (LVG sequences, without  $R_g$  restraint, blue bars), and 2.23 Å (LVG sequences, with  $R_g$  restraint, violet bars).

### **Extended Data Fig. 3 Generating initial backbone for a given sketch or topological architecture.**

A sketch is represented as an abstracted architecture comprising regularly arranged layers of secondary structures, the layers in parallel planes. From the abstraction, coordinates of starting or ending positions (indicated by “ $\times$ ”) of secondary structure segments are determined as regular grid points on parallel straight lines in different planes. The N to C directions of the segments are perpendicular to the lines. The approximate lengths of the segments may also be pre-specified. Then peptide segments of corresponding local conformations are geometrically generated using coordinates of their terminal positions and directions determined from the sketch. Connecting the segments with closed loops leads to the initial backbone structure to be used by SCUBA-driven SASD.

### **Extended Data Fig. 4 SCUBA-driven SASD produced backbones similar to natural proteins.**

Different boxes correspond to different design sketches. From left to right in each box: initial backbone, optimized backbone, a stereo view of the optimized backbone superposed with the closest natural structure, and deviations of  $C\alpha$  atom positions between the designed and the closest natural backbones. In each box, the text string indicates the type, approximate size, and order of secondary structure segments of the corresponding sketch (“H” for helix, “E” for strand, and the subscripts indicate lengths). The closest natural structures with given PDB IDs and chain IDs were identified using Dali searches. The r.m.s.d. values (noted as RMSD in the figures) are of  $C\alpha$  atoms in aligned secondary structure elements.

### **Extended Data Fig. 5 Examples of backbone changes at different design stages.**

**a**, Initial and optimized backbones for the H2E4 sketch, whose secondary structure sequence is E<sub>7</sub>H<sub>16</sub>E<sub>7</sub>H<sub>16</sub>E<sub>7</sub>E<sub>7</sub> (“H” for helix, “E” for strand, and the subscripts indicate approximate lengths). The top row shows artificially constructed initial structures, while the bottom row shows substage-1 backbones optimized without sidechain (yellow) superimposed with substage-2 backbones optimized with LVG-simplified sidechains (violet). **b**, The r.m.s.d. values of mainchain atoms (in Å) between the successively generated structures at different design stages of backbone optimization or relaxation. The results have been averaged over the H2E4 designs (standard deviations are given in parentheses). The meanings of the notations are: “Init” for the initial structure, “Substage-1” for substage-1 backbones optimized without sidechains, “Substage-2” for substage-2 backbones optimized with LVG-simplified sidechains, and “Iter1” to “Iter3” for backbones relaxed with the designed sidechains in the sequence design-backbone relaxation iterations. **c**, ABACUS2 and Rosetta energies of ABACUS2-selected sequences for initial and SCUBA-optimized backbones of different topological architectures. The secondary structure compositions of the architectures are: 1: E<sub>10</sub>E<sub>10</sub>E<sub>10</sub>E<sub>10</sub>, 2: E<sub>7</sub>H<sub>16</sub>E<sub>7</sub>E<sub>7</sub>, 3: E<sub>7</sub>E<sub>7</sub>H<sub>16</sub>E<sub>7</sub>, 4: E<sub>7</sub>H<sub>16</sub>E<sub>7</sub>E<sub>7</sub>H<sub>16</sub>E<sub>7</sub>, 5: E<sub>10</sub>H<sub>20</sub>E<sub>10</sub>H<sub>20</sub>E<sub>10</sub>E<sub>10</sub>, 6: E<sub>7</sub>H<sub>16</sub>E<sub>7</sub>H<sub>16</sub>E<sub>7</sub>E<sub>7</sub>, 7: E<sub>10</sub>H<sub>20</sub>E<sub>10</sub>E<sub>10</sub>H<sub>20</sub>E<sub>10</sub>, 8: E<sub>7</sub>H<sub>16</sub>E<sub>7</sub>E<sub>7</sub>H<sub>16</sub>E<sub>7</sub>, 9: H<sub>15</sub>H<sub>15</sub>H<sub>15</sub>, 10: H<sub>21</sub>H<sub>21</sub>H<sub>21</sub>H<sub>21</sub>. For each sketch, 10 initial backbones have been optimized to generate 10 optimized backbones. Sketch 10 led to optimized backbones of both left-handed and right-handed twists, as shown in two boxes in Extended Data Fig. 4. Each energy value has been averaged over 100 sequences selected on a group of 10 initial or optimized backbones (10 sequences selected using ABACUS2 for each backbone), with standard deviations between 0.08 and 0.38. Rosetta energies have been calculated on relaxed structures with selected sequences. **d**, Amino acid usage frequencies in sequences selected with ABACUS2 on the H2E4 backbones at different optimization stages. Averaged values are shown separately for sequences designed using the substage-1 backbones optimized without any explicit sidechain (blue bars), using second stage backbones optimized with LVG-simplified sidechains (orange bars), and using backbones relaxed with the first round ABACUS2-selected sidechains (gray bars) (the sidechain atom radius parameters had been downscaled by multiplying 0.9 to introduce

larger sidechains in the first round of sequence selection). The green bars correspond to the distribution in the training proteins.

### **Extended Data Fig. 6 Effects of loop resampling and optimization.**

**a**, The distribution of the per-residue SCUBA energy changes of loop residues caused by loop resampling and optimization. For the H2E4 backbone structures, the changes were calculated as the energies after loop re-optimization minus the energies before loop re-optimization. **b**, The distribution of the lowest r.m.s.d. values (noted as RMSD in the figure) of predicted structures from designed structures. **c**, The distribution of per-residue Rosetta energy of the lowest-r.m.s.d. predicted structures. For **b** and **c**, the predictions were carried out using Rosetta biased forward folding for sequences designed from the loop re-optimized H2E4 backbone structures (thinner blue lines), or for sequences designed from H2E4 backbone structures not yet subjected to loop re-optimization (thicker red lines).

### **Extended Data Fig. 7 Experimental characterizations of designed proteins.**

**a**, X-ray data collection and refinement of crystal structure models. **b**, NMR  $^{15}\text{N}$ - $^1\text{H}$  HSQC spectra of ten designed H2E4 proteins and three novel helical proteins. **c**, Size exclusion chromatography results of the designed H2E4 proteins XM2H (left) and AM2M (right) in solution. The chromatograms were obtained for samples purified by gel filtration, and the molecular weights were estimated from the peak positions. **d**, Circular dichroism spectroscopy of the designed proteins XM2H (top) and H4A1R (bottom) at different temperatures. The slow varying temperature-dependent curves shown on the right suggest that there are only small changes in the secondary structure contents of these proteins over the temperatures range from 25 to 95 °C. For XM2H, its helical content (calculated from the CD curves) decreased from 54.9% at 20 °C to 48.2% at 95 °C, while its  $\beta$ -sheet content changed from 9% to 11%. For H4A1R, its helical content changed from 85.2% at 20 °C to 71.8% at 95 °C.

## Extended Data Fig. 8 The structures of the loops in the H2E4 and H4 proteins.

**a–e**, Superimpositions of experimentally determined structures (cyan) with corresponding designed structures (green) for loops in the designed proteins XM2H(**a**), AM2M(**b**), H4A1R(**c**), H4A2S(**d**), and H4C2R(**e**). The 2Fo-Fc (at 1.0  $\sigma$  level) electron density surfaces are also shown. The r.m.s.d. for main chain atoms are displayed. **f**, The experimentally determined structures of the two H2E4 proteins are superimposed (XM2H in cyan and AM2M in orange) to show their different loop structures connecting similarly arranged secondary structure segments.

## Extended Data Fig. 9 Designed backbone structures of the experimentally examined all-helical proteins in Batch 3.

We note that the average per-residue Rosetta energy of the proteins with experimentally solved structures (D12, D22 and D53) is  $-3.32 \pm 0.07$  (in arbitrary unit), while for the remaining ten Batch-3 proteins, the same average value is  $-3.22 \pm 0.14$ .

**Extended Data Table 1 Summary of experimentally examined designs**

## **Supplementary information**

### Supplementary Information

This file contains Supplementary Methods, references and Tables 1 and 2.

### Reporting Summary

### Peer Review File

## **Rights and permissions**

### Reprints and Permissions

## About this article

### Cite this article

Huang, B., Xu, Y., Hu, X. *et al.* A backbone-centred energy function of neural networks for protein design. *Nature* **602**, 523–528 (2022).  
<https://doi.org/10.1038/s41586-021-04383-5>

- Received: 05 March 2021
- Accepted: 23 December 2021
- Published: 09 February 2022
- Issue Date: 17 February 2022
- DOI: <https://doi.org/10.1038/s41586-021-04383-5>

### Share this article

Anyone you share the following link with will be able to read this content:

[Get shareable link](#)

Sorry, a shareable link is not currently available for this article.

[Copy to clipboard](#)

Provided by the Springer Nature SharedIt content-sharing initiative

---

This article was downloaded by **calibre** from <https://www.nature.com/articles/s41586-021-04383-5>

- Article
- Open Access
- [Published: 09 February 2022](#)

# Mechanisms of inhibition and activation of extrasynaptic $\alpha\beta$ GABA<sub>A</sub> receptors

- [Vikram Babu Kasaragod](#)<sup>1,2</sup>,
- [Martin Mortensen](#) [ORCID: orcid.org/0000-0002-5873-7107](#)<sup>3</sup>,
- [Steven W. Hardwick](#) [ORCID: orcid.org/0000-0001-9246-1864](#)<sup>4</sup>,
- [Ayla A. Wahid](#) [ORCID: orcid.org/0000-0001-8128-9632](#)<sup>1</sup>,
- [Valentina Dorovskikh](#)<sup>3</sup>,
- [Dimitri Y. Chirgadze](#) [ORCID: orcid.org/0000-0001-9942-0993](#)<sup>4</sup>,
- [Trevor G. Smart](#) [ORCID: orcid.org/0000-0002-9089-5375](#)<sup>3</sup> &
- [Paul S. Miller](#) [ORCID: orcid.org/0000-0002-6512-9441](#)<sup>1</sup>

[Nature](#) volume 602, pages 529–533 (2022)

- 4733 Accesses
- 33 Altmetric
- [Metrics details](#)

## Subjects

- [Cryoelectron microscopy](#)
- [Ion channels in the nervous system](#)
- [Molecular neuroscience](#)

## Abstract

Type A GABA ( $\gamma$ -aminobutyric acid) receptors represent a diverse population in the mammalian brain, forming pentamers from combinations of  $\alpha$ -,  $\beta$ -,  $\gamma$ -,  $\delta$ -,  $\varepsilon$ -,  $\rho$ -,  $\theta$ - and  $\pi$ -subunits<sup>1</sup>.  $\alpha\beta$ ,  $\alpha 4\beta\delta$ ,  $\alpha 6\beta\delta$  and  $\alpha 5\beta\gamma$  receptors favour extrasynaptic localization, and mediate an essential persistent (tonic) inhibitory conductance in many regions of the mammalian brain<sup>1,2</sup>. Mutations of these receptors in humans are linked to epilepsy and

insomnia<sup>3,4</sup>. Altered extrasynaptic receptor function is implicated in insomnia, stroke and Angelman and Fragile X syndromes<sup>1,5</sup>, and drugs targeting these receptors are used to treat postpartum depression<sup>6</sup>. Tonic GABAergic responses are moderated to avoid excessive suppression of neuronal communication, and can exhibit high sensitivity to Zn<sup>2+</sup> blockade, in contrast to synapse-preferring α1βγ, α2βγ and α3βγ receptor responses<sup>5,7,8,9,10,11,12</sup>. Here, to resolve these distinctive features, we determined structures of the predominantly extrasynaptic αβ GABA<sub>A</sub> receptor class. An inhibited state bound by both the lethal paralysing agent α-cobratoxin<sup>13</sup> and Zn<sup>2+</sup> was used in comparisons with GABA–Zn<sup>2+</sup> and GABA-bound structures. Zn<sup>2+</sup> nullifies the GABA response by non-competitively plugging the extracellular end of the pore to block chloride conductance. In the absence of Zn<sup>2+</sup>, the GABA signalling response initially follows the canonical route until it reaches the pore. In contrast to synaptic GABA<sub>A</sub> receptors, expansion of the midway pore activation gate is limited and it remains closed, reflecting the intrinsic low efficacy that characterizes the extrasynaptic receptor. Overall, this study explains distinct traits adopted by αβ receptors that adapt them to a role in tonic signalling.

[Download PDF](#)

## Main

Type A GABA (GABA<sub>A</sub>) receptors belong to the pentameric ligand-gated ion channel (pLGIC) superfamily, which includes mammalian nicotinic acetylcholine receptors (nAChRs), serotonin type 3A receptors and glycine receptors, as well as other non-mammalian homologues<sup>14,15</sup>. GABA<sub>A</sub> αβ receptors share common properties regardless of specific α or β subtype<sup>16</sup>, comprise a notable population of extrasynaptic receptors<sup>8,17,18,19</sup>, and are important model receptors for understanding drug modulation<sup>20,21</sup>. They bear two distinct traits common to tonic GABAergic conductance. The first is a low open-channel probability ( $P_o$ ) in response to GABA<sup>7,8,21</sup> that avoids over-damping neuronal circuitry. The second is a high sensitivity<sup>9</sup> to inhibition by endogenous Zn<sup>2+</sup>, with αβ receptors being the most sensitive of all isoforms, which has physiological and pathological consequences during development and in conditions such as temporal lobe epilepsy<sup>22,23</sup>. Here we solve structures of extrasynaptic GABA<sub>A</sub> receptors to explain the molecular mechanisms underlying a low  $P_o$  and marked inhibition by Zn<sup>2+</sup>.

We reconstituted purified α1β3 receptor pentamers into lipid nanodiscs<sup>24</sup> and solved structures of the receptor in complex with α-cobratoxin (α-CBTx)–Zn<sup>2+</sup> (to 3.0 Å resolution), GABA–Zn<sup>2+</sup> (2.8 Å) or GABA (3.0 Å) (Extended Data Fig. 1, Extended

Data Table 1). Looking down from the extracellular side onto the pentamer, the subunit order and stoichiometry read  $\alpha-\beta-\underline{\beta}-\alpha-\beta$  in a clockwise direction, such that the third subunit ( $\beta$  (chain C), underlined) occupies the equivalent of the ‘ $\gamma$ -position’ in synaptic  $\alpha\beta\gamma$  receptors<sup>25,26,27</sup> (Fig. 1a). In all the structures, the single  $\beta-\beta$  interface is occupied by megobody 25 (Mb25), which comprises the immunogenic binding domain nanobody 25 (Nb25) fused to a cHopQ enlargement domain, which is required to randomize particle orientation and break the quasi-five-fold symmetry for particle alignment<sup>25,28</sup>. The co-ligand histamine, included to boost yield, also occupies this  $\beta-\beta$  interface in all the structures, binding deeper inside the crevice in a pocket homologous to the two orthosteric  $\beta-\alpha$  GABA binding sites, as previously described<sup>28,29</sup>. Whole-cell patch-clamp recording confirmed that the construct that we imaged by cryo-electron microscopy (cryo-EM) (Methods) exhibited the sensitivity, desensitization, current response size and weak histamine modulation<sup>30</sup> of the wild-type receptor (Extended Data Fig. 2). Nb25 exerted a weak positive allosteric modulation at the highest concentration tested (10  $\mu$ M) that was not observed with  $\alpha 1\beta 3\gamma 2$  receptors, which lack the  $\beta-\beta$  interface (Extended Data Fig. 3). In contrast to  $\alpha\beta\gamma$  receptors, the N-linked glycans at Asn111 in  $\alpha 1$  are not resolved by electron density inside the vestibule (Fig. 1a), consistent with the absence of the  $\gamma 2$ -subunit Trp123 ( $\beta 3$  chain C Gly108 in  $\alpha\beta$  receptors), which stacks under the  $\alpha 1$  chain A glycan to impose order<sup>25,27</sup>.

**Fig. 1:  $\alpha$ -Cobratoxin binding site on  $\alpha 1\beta 3$  GABA<sub>A</sub> receptors.**

---

 **figure 1**

**a**,  $\alpha$ -CBTx-Zn<sup>2+</sup>-bound  $\alpha 1\beta 3$  receptor cryo-EM map, showing top (top) and side (bottom) views.  $\alpha$ -CBTx is bound to the  $\beta$ - $\alpha$  neurotransmitter pocket interface. Glycans (orange) are not resolved inside the vestibule (top). Mb25 is shown in lime green; nanodisc and ‘hanging’  $\beta 3$ -subunit thermostabilized apocytochrome b562RIL (BRIL) densities are in grey. **b**, Atomic model of  $\alpha$ -CBTx (green) bound to the GABA<sub>A</sub> receptor with finger II positioned at the  $\beta 3$  (blue)- $\alpha 1$  (red) interface. **c**, Close up of the binding mode in **b** showing residue positions and interactions ( $\beta 3$  loop C residues in blue are Val199, Phe200, Ala201, Thr202 and Tyr205). **d**, Overlays of the GABA-bound model (white) and  $\alpha$ -CBTx-bound model ( $\beta 3$  loop C in blue,  $\alpha 1$  with Arg67 in pink and red, and  $\alpha$ -CBTx finger II in green), showing that finger II does not directly overlap with the GABA binding pose but displaces loop C and Arg67 away

(black arrows) so that they no longer support GABA binding. Dashed lines represent putative hydrogen-bond interactions.

## Mechanism of inhibition by $\alpha$ -CBTx

$\alpha$ -Cobratoxin ( $\alpha$ -CBTx) blocks muscle nAChRs to paralyse prey, but has also been shown to act with reduced potency as an inhibitor of GABA<sub>A</sub> receptors in recombinant expression systems<sup>13</sup>. Such toxins represent new scaffolds for subtype-selective inhibitor design, but to our knowledge, there are no available structures of GABA<sub>A</sub> receptors in complex with protein inhibitors<sup>13,31,32</sup> to reveal modes of action and guide rational engineering approaches<sup>33</sup>.  $\alpha$ -CBTx bridges the  $\beta$ – $\alpha$  interface of the receptor halfway up the outer extracellular domain (ECD) at both GABA binding pockets (Fig. 1a). The characteristic three  $\beta$ -strand loops ('fingers') I–III of  $\alpha$ -CBTx dock perpendicular to the cylindrical GABA<sub>A</sub> receptor to encase loop C, an essential responsive element to neurotransmitter binding<sup>26,27,34,35</sup> (Fig. 1a–c, Extended Data Fig. 4a, b). Thr6 and Phe65 of  $\alpha$ -CBTx form van der Waals interactions with the receptor loop C Val199. Finger II inserts into the neurotransmitter pocket (between loops  $\beta$ 3 B and C, and the  $\alpha$ 1 loop D, E and F  $\beta$ 1-strands), forming the key contact zone below loop C. The positively charged side chains of Arg33 and Arg36 straddle the aromatic side chain of loop C Phe200. Arg33 also stacks below the Tyr205 aromatic side chain, and its backbone carbonyl contributes a putative hydrogen bond with the Thr202 hydroxyl 2.7 Å away. The binding mode resembles the one solved at 4.2 Å resolution for  $\alpha$ -CBTx bound to the AChBP from *Lymnaea stagnalis*, a soluble homologue of nAChR<sup>36</sup>, and for  $\alpha$ -bungarotoxin-bound muscle nAChR<sup>37</sup> (Extended Data Fig. 4c–h). Consistent with conserved roles in binding, Arg33Gly and Arg36Gly mutations reduce affinity by 300-fold at nAChR $\alpha$ 7<sup>33</sup>. The GABA<sub>A</sub> receptor  $\alpha$ -subunits lack the apex loop C aromatic residue (Phe200 in  $\beta$ 3), explaining why  $\alpha$ -CBTx does not bind at its  $\alpha$ – $\beta$  interfaces. This suggests that  $\alpha$ -CBTx will also not bind  $\alpha$ – $\gamma$  or  $\gamma$ – $\beta$  interfaces in  $\alpha\beta\gamma$  receptors, although it might bind  $\delta$ - and  $\rho$ -subunit loop C, which also possess this aromatic variant.

$\alpha$ -CBTx does not overlap with and directly antagonize GABA binding (Fig. 1d). Instead,  $\alpha$ -CBTx induces rearrangement of the  $\alpha$ -subunit Arg67 and an outward motion of the  $\beta$ -subunit loop C by 5.9 Å, thus perturbing two crucial components of the GABA binding site<sup>26,27</sup> (Fig. 1d). The equivalent residue to  $\alpha$ 1 Ser69—the neighbouring residue to Arg67—is a Lys in  $\alpha$ 2, and this reduces sensitivity to  $\alpha$ -CBTx fivefold<sup>13</sup>. This position is too distal to interfere directly with toxin binding, but the structure reveals that the lysine could exert a steric and electrostatic repulsion on Arg67 that hinders its reorganization to accommodate  $\alpha$ -CBTx finger II (Extended Data Fig. 4i, j).

The outward motion of loop C, which is usually associated with antagonist binding to pLGICs, is larger than the one caused by the competitive antagonist bicuculline<sup>26</sup> in  $\alpha\beta\gamma$  receptors (2.1 Å) (Extended Data Fig. 4k). Globally however, the ECD conformation is similar to the bicuculline-bound inhibited state of the  $\alpha\beta\gamma$  receptor (ECD C <sub>$\alpha$</sub>  root mean square deviation (r.m.s.d.) = 1.0 Å,  $\beta$ -subunit chains B and E r.m.s.d. = 0.8 Å), rather than the  $\alpha\beta\gamma$  GABA-bound state, which features realigned GABA-binding  $\beta$ -subunits<sup>26</sup> (ECD C <sub>$\alpha$</sub>  r.m.s.d. = 1.5 Å,  $\beta$ -subunit chains B and E r.m.s.d. = 1.8 Å) (Extended Data Fig. 4l–n). Thus, with respect to receptor conformation,  $\alpha$ -CBTx mimics a small competitive antagonist to stabilize an inhibited state of the receptor.

## Zn<sup>2+</sup> mechanism of channel blockade

The divalent transition metal cation Zn<sup>2+</sup> is a non-competitive inhibitor of  $\alpha\beta$  and  $\alpha\beta\gamma$  GABA<sub>A</sub> receptors<sup>17,38,39</sup>. We reproduced this effect in whole-cell patch-clamp recordings, showing that 66 nM free Zn<sup>2+</sup> inhibited submaximal (20%) (EC<sub>20</sub>) 1 μM and maximal 1 mM GABA responses by the same amount: 38 ± 2% and 36 ± 6%, respectively, for the wild-type receptor; and 32 ± 2% and 32 ± 4% for the  $\alpha 1\beta 3$  cryo-EM construct, (Fig. 2a,b). Sensitivity to inhibition by free Zn<sup>2+</sup> was the same for the wild-type receptor and the  $\alpha 1\beta 3$  cryo-EM construct (Extended Data Fig. 5a,b). We observed non-protein density that could accommodate a coordinated Zn<sup>2+</sup> ion at the extracellular end of the pore in the GABA–Zn<sup>2+</sup>–receptor cryo-EM map (2.79 Å resolution), which was absent in the GABA–receptor map (3.04 Å resolution) (Extended Data Fig. 5c–e). No other densities attributable to Zn<sup>2+</sup> were observed.

**Fig. 2: The Zn<sup>2+</sup> binding site.**

---

 **figure 2**

**a**, Bar chart showing inhibition of maximal (1 mM) and EC<sub>20</sub> (1 µM) GABA whole-cell current responses ( $I_{GABA}$ ) by 66 nM free Zn<sup>2+</sup> (controlled using the chelator tricine) for wild-type αβ (WT) and the α1β3 cryo-EM construct (α1β3<sub>CryoEM</sub>) expressed in HEK 293 cells. Data are mean ± s.e.m.  $n = 7$  for wild-type and cryo-EM

constructs, from biologically independent patch-clamp experiments with individual cells. One-way analysis of variance (ANOVA) and Tukey multiple comparisons post hoc test showed no significant differences across groups,  $F(3, 24) = 0.6449$ ;  $P = 0.5937$ . **b**, Corresponding current recordings for  $\alpha 1\beta 3_{\text{CryoEM}}$ . **c**, Top view of  $C_\alpha$  backbones of M2 pore-lining helices showing three 17'  $\beta 3$  His267 (blue) residues coordinating  $Zn^{2+}$  across the pore ( $\alpha 1$  17' Ser272 residues in red). Cryo-EM map shown as white transparent. **d**, Side-on view of  $\beta 3$ -subunit chain B and E M2 helices flanking the pore permeation pathway (blue dots) with narrowings (orange dots) for three closed ‘gates’ at the 17'  $Zn^{2+}$  site, 9' hydrophobic (activation) gate and -2' intracellular (desensitization) gate to create a triple-gated closed pore.

The  $Zn^{2+}$  site comprises a triad of His267 side chains from the pore-lining M2 helices of the three  $\beta 3$  subunits (Fig. 2c). The  $\tau$  (far) nitrogen of each imidazole ring is positioned approximately equidistant, 2.5–2.9 Å, from the  $Zn^{2+}$  ion, and at approximately 120°, despite the pseudo-five-fold symmetry of the pore. This location is consistent with its non-competitive mode of antagonism and voltage dependence<sup>38</sup>. Alanine substitution of His267 ablates the high sensitivity to  $Zn^{2+}$  inhibition<sup>9,40</sup>. Replacement of one  $\beta$ -subunit His with Ser (as in the  $\delta$ -subunit) or Ile (as in the  $\gamma$ -subunit) in  $\alpha\beta\delta$  and  $\alpha\beta\gamma$  receptors reduces  $Zn^{2+}$  sensitivity 50-fold and 200-fold respectively, explaining the basis of the exquisite subtype selectivity<sup>9</sup>. The triad of His side chains resembles dynamic ‘catalytic’ sites rather than obligate-bound ‘structural’ sites involving four sulfur-containing residues<sup>41</sup>. In catalytic sites, an activated water molecule usually completes the tetrahedral coordination<sup>41</sup>, but we could not visualize an ordered water molecule in the 2.8 Å-resolution map of the hydrated pore.

Previous GABA<sub>A</sub> receptor structures have shown how blockade is achieved at the intracellular end of the pore, for example, by picrotoxinin or cations<sup>26,37,42</sup>. Our structure reveals how blockade operates at the extracellular end of a pLGIC.  $Zn^{2+}$  binds a channel conformation with a closed mid-way hydrophobic gate (9' leucine ring) and intracellular (-2' ring) gate, as previously described for  $\alpha\beta\gamma$  receptors<sup>26,37</sup> (Fig. 2d). However, the  $Zn^{2+}$  site creates an additional top gate to prevent the passage of chloride ions from the vestibule into the channel (Fig. 2d). By contrast, the GABA structure shows that in the absence of  $Zn^{2+}$ , the  $\beta 3$  17' His side chain density is absent because these polar residues orient randomly and the pore diameter at this location expands (>4.1 Å) to permit the passage of chloride ions (Pauling radius of 1.8 Å) (Extended Data Fig. 5f–h).

## Receptor response to GABA

Comparison of the  $\alpha$ -CBTx-Zn<sup>2+</sup>, GABA-Zn<sup>2+</sup> and GABA-bound structures reveals the activation pathway. GABA binding at the two  $\beta$ - $\alpha$  sites induces realignment of the corresponding  $\beta$ -subunit ECDs (chains B and E) and clockwise translation of the  $\beta$ 1– $\beta$ 2 and  $\beta$ 6– $\beta$ 7 base loops above the transmembrane domain (TMD) (Extended Data Fig. 6a). The motion is equivalent for GABA and GABA-Zn<sup>2+</sup> structures (Extended Data Fig. 6b,c). Thus, occupation of the pore by Zn<sup>2+</sup> does not hinder the ECD transition in response to GABA, as previously observed for picrotoxin bound in the channel of  $\alpha\beta\gamma$  receptors<sup>26,37</sup>. Globally, the GABA-induced motions mirror those observed for  $\alpha\beta\gamma$  receptors, with the  $\beta$ -subunit ECD in  $\alpha\beta$  receptors that occupies the ‘ $\gamma$ -position’ mimicking that of the  $\gamma$ -subunit ECD in  $\alpha\beta\gamma$  receptors (Extended Data Fig. 6a,d).

At the level of the TMD, without Zn<sup>2+</sup> bound, the M2–M3 loops (which link the top of channel-lining  $\alpha$ -helix 2 to helix 3) of the two GABA-bound  $\beta$ -subunits switch from ‘inward’ to ‘outward’ (Fig. 3a; Extended Data Fig. 7a), as previously observed for  $\alpha\beta\gamma$  receptors<sup>26</sup> (Extended Data Fig. 7b). For the  $\beta$ -subunit occupying the  $\gamma$ -position (chain C), the M2–M3 loop also moves outwards (Fig. 3a), owing to the absence of any inward pull by Zn<sup>2+</sup>, which matches the  $\gamma$ 2 subunit in  $\alpha\beta\gamma$  receptors in both inhibited and GABA-bound conformations (Extended Data Fig. 7b).

**Fig. 3: Response of the TMD to GABA binding.**

---

 **figure 3**

**a**, Top-down views of  $\alpha$ -CBTx-Zn<sup>2+</sup> (grey) and GABA-bound (red and blue) atomic model overlays showing the M2 helices, M2–M3 linkers,  $\alpha$ 1 Pro278 and  $\beta$ 3 Pro273. The GABA binding  $\beta$ 3 B–E subunit linkers respond and switch to the ‘outward’ conformation (arrows). **b**, Cross-section at the 9' Leu ring showing expanded C <sub>$\alpha$</sub>  pentagonal perimeter for GABA (purple) compared with  $\alpha$ -CBTx-Zn<sup>2+</sup> (grey). **c**, Side-on view of the permeation pathway (blue and orange dots) between opposing  $\beta$ 3-

subunit chain B–E M2 helices, showing closed 9' and –2' hydrophobic gates. The asterisk indicates the kink in the permeation pathway around the 17' residue, which varies depending on mobile His side chain positioning, so the 17' radius of 2.1 Å is indicative only. **d**, Pore radius along the permeation pathway.

With all the M2–M3 loops in the outward position, each of the five channel-lining M2 helices, one contributed by each subunit around the pore, tilt and laterally translate outwards (Extended Data Fig. 8a). The tilt angle increases on average by 0.8° per helix relative to the pore axis, from 3.9° to 4.7° (Extended Data Fig. 8a, b). As a result, the 9' leucine ring, situated midway along the pore and forming a hydrophobic gate in the  $\alpha$ -CBTx–Zn<sup>2+</sup> inhibited state, retracts to increase the pore diameter from 2 Å to 3.1 Å, and the 9' C<sub>a</sub> perimeter increases from 40.2 Å to 44.2 Å (Fig. 3b–d, Extended Data Fig. 8c). Despite this shift, the pore remains too narrow to permit the passage of chloride anions (Pauling radius of 1.8 Å) and this gate remains closed. This contrasts with GABA-bound  $\alpha\beta\gamma$  receptor structures, which exhibit open 9' activation gates with diameters<sup>26,37</sup> in the range 5–6 Å (Fig. 3d, Extended Data Fig. 8c). By comparison with  $\alpha\beta$  receptors, the M2 outward tilting for  $\alpha\beta\gamma$  receptors is consistently greater, increasing from 4.6° to 7.5° for  $\alpha 1\beta 3\gamma 2$  and 4.8° to 6.5° for  $\alpha 1\beta 2\gamma 2$  in response to GABA binding (Extended Data Fig. 8b). This results in larger 9' C<sub>a</sub> perimeters (45.8 Å for  $\alpha 1\beta 3\gamma 2$  and 46.4 Å for  $\alpha 1\beta 2\gamma 2$ ) and hydrophobic Leu side chains are rotated away from the hydrated pore (Extended Data Fig. 8c, d). Indeed, the GABA-bound  $\alpha\beta$  receptor mean M2 tilt angle (4.7°) does not exceed that of bicuculline-inhibited  $\alpha\beta\gamma$  receptors (4.7–4.8°; Extended Data Fig. 8b), and the pore profiles are similar (Fig. 3d). The GABA-bound  $\alpha\beta$  receptor  $\beta 3$  subunit in the  $\gamma$ -position has the biggest difference in tilt angle versus the  $\gamma 2$  subunit (4.4° for  $\alpha 1\beta 3$  versus 8.5° for  $\alpha 1\beta 3\gamma 2$  and 9.3° for  $\alpha 1\beta 2\gamma 2$ ; Extended Data Fig. 8b, e). Thus, replacing  $\gamma 2$  with the more upright  $\beta 3$  M2 helix has the consequent effect of limiting the outward tilt and expansion of the other subunits, thereby limiting 9' gate expansion.

Given that extrasynaptic  $\alpha\beta$  and  $\alpha\beta\delta$  receptors have low gating efficacy<sup>7,8,43</sup> (low  $P_o$ ), we hypothesized that this could explain why there is no open 9' activation gate in our GABA-bound  $\alpha\beta$  receptor structure. We compared  $\alpha 1\beta 3$  versus  $\alpha 1\beta 3\gamma 2$  single-channel recordings in the presence of near-saturating (EC<sub>95</sub>) GABA concentrations to evaluate  $P_o$ . Short and long open dwell times ( $\tau_1$  and  $\tau_2$ ) of similar durations were observed for both receptors ( $\alpha 1\beta 3$ :  $\tau_1 = 0.65 \pm 0.15$  ms ( $n = 6$ ) and  $\tau_2 = 4.3 \pm 1.1$  ms ( $n = 4$ ; absent from two cells);  $\alpha 1\beta 3\gamma 2$ :  $\tau_1 = 0.78 \pm 0.07$  ms and  $\tau_2 = 4.8 \pm 0.7$  ms ( $n = 6$ ) (Extended Data Fig. 9a, b)). However, for  $\alpha 1\beta 3$  receptors, only 17 ± 6% of openings were of long duration versus 61 ± 3% for  $\alpha 1\beta 3\gamma 2$  receptors, confirming a reduced propensity of stable opening for  $\alpha 1\beta 3$  channels (Extended Data Fig. 9c). An absence of burst activity for  $\alpha 1\beta 3$  receptors precluded measurement of the burst  $P_o$  ([Methods](#)); nevertheless for patches containing only one apparent ion channel,  $P_o$  over the entire course of the

recording was significantly lower for  $\alpha 1\beta 3$  versus  $\alpha 1\beta 3\gamma 2$  receptors (Extended Data Fig. 9d).

Further evidence for reduced channel opening was obtained by measuring the probability of activation<sup>21</sup> ( $P_A$ ) from whole-cell recordings of the maximum response to a saturating concentration of GABA versus GABA plus pentobarbitone, a positive allosteric modulator. If  $P_o$  is high in saturating GABA—that is, close to 1—it will not increase further with pentobarbitone. In support of the single-channel data, the  $P_A$  for  $\alpha 1\beta 3$  (wild type) and for the  $\alpha 1\beta 3$  cryo-EM construct were approximately 0.6, compared with  $0.94 \pm 0.03$  for  $\alpha 1\beta 3\gamma 2$  ( $P < 0.001$ ) (Extended Data Fig. 10). Our GABA-bound structure is thus consistent with a state in which GABA stabilizes primed ECDs and M2–M3 loops<sup>44,45</sup> to facilitate brief opening, but cannot sufficiently stabilize an open 9' gate (Fig. 4).

**Fig. 4: Mode of activation by GABA.**

 figure 4



Top-down views of ECDs (top row) and cross sections of TMDs (helices shown as black circles) at the level of the 9' Leu gate (bottom row) for  $\alpha\beta$  and  $\alpha\beta\gamma$  receptors. Pore leucines are represented by black ‘fronds’ projecting from the innermost  $\alpha$ -helix, M2. In response to GABA, the two binding  $\beta$ -subunits are the principal responders, with their ECDs twisting similarly anticlockwise (black arrows) for both  $\alpha\beta$  receptors

and  $\alpha\beta\gamma$  receptors. The downstream reaction of the TMD is limited in the  $\alpha\beta$  receptor and the 9' gate remains mostly closed (red and orange circles), whereas for  $\alpha\beta\gamma$  receptors, the TMD response is greater and the 9' gate opens (green).

## Conclusion

The structures we present here explain key aspects of the molecular pharmacology of  $\alpha 1\beta 3$  GABA receptors, including the mode of  $\alpha$ -CBTx antagonism and the signature property for  $\alpha\beta$  receptors of high-sensitivity  $Zn^{2+}$  channel blockade. Despite the ECDs and M2–M3 loops responding to GABA, a more upright  $\beta$ -subunit M2 helix occupying the  $\gamma$ -subunit position results in the 9' Leu pore gate remaining mostly closed. This provides a molecular explanation for the comparatively low  $P_o$  of  $\alpha 1\beta 3$  receptors compared with synaptic  $\alpha 1\beta 3\gamma 2$  receptors, a feature required to prevent excessive inhibition of neuronal circuitry by  $\alpha\beta$  and  $\alpha\beta\delta$  extrasynaptic subtypes. Given recent successes targeting extrasynaptic GABA<sub>A</sub> receptors for therapeutic effects<sup>6</sup>, we anticipate that these structures will facilitate future design of drugs that modulate GABA-mediated tonic inhibition.

## Methods

### Data reporting

No statistical methods were used to predetermine sample size. The experiments were not randomized and the investigators were not blinded to allocation during experiments and outcome assessment.

### Constructs

The protein sequences used were: human GABA<sub>A</sub>R  $\alpha 1$  (mature polypeptide numbering 1–416, QPSL...TPHQ; Uniprot P14867) and human GABA<sub>A</sub>R  $\beta 3$  (mature polypeptide numbering 1–447, QSVN...YYVN; Uniprot P28472). The  $\alpha 1$  intracellular M3–M4 loop amino acids 313–391 (RGYA...NSVS) were substituted by the SQPARAA sequence<sup>46</sup>. The  $\beta 3$  intracellular M3–M4 loop amino acids 308–423 (GRGP...TDVN) were substituted by a modified SQPARAA sequence containing the *Escherichia coli* soluble cytochrome B562RIL41 (BRIL, amino acids 23–130, ADLE...QKYL, Uniprot P0ABE7) to give an M3–M4 loop with the sequence SQPAGTBRILTGRAA, necessary to boost protein yields<sup>46</sup>. The mature engineered  $\alpha 1$  construct with a 1D4 purification tag derived from bovine rhodopsin (TETSQVAPA) that is recognized by the Rho-1D4 monoclonal antibody (University of British Columbia)<sup>47,48</sup> was cloned into the pHLsec vector after the vector secretion signal<sup>49</sup>,

ending TPHQGTTETSQVAPA. An alternative tagged version of the engineered  $\alpha 1$  construct was cloned into the pHsec vector after the secretion signal with an N-terminal streptavidin binding protein (SBP) and TEV cleavage site, starting (GCVA) with

EMDEKTTGWRGGHVVEGLAGELEQLRARLEHHPQGQREPDYDIPTTENLYFQ GTG-GABR $\alpha 1$ (QPSL...), and ending with a stop codon and no C-terminal tag. The engineered  $\beta 3$  construct was cloned into pHsec after the vector secretion sequence without any tags.

## Expression and protein preparation

Four-hundred millilitres of HEK 293S-GnTI- cells (which yield proteins with truncated N-linked glycans, Man<sub>5</sub>GlcNAc<sub>2</sub><sup>50,51</sup>) were grown in suspension up to densities of  $2 \times 10^6$  cells per ml in Protein Expression Media (PEM) (Invitrogen) supplemented with l-glutamine, non-essential amino acids (Gibco) and 1% v/v fetal calf serum (Sigma-Aldrich). Cultures were grown in upright round 1-l bottles with filter lids, shaking at 130 rpm, 37 °C, 8% CO<sub>2</sub>. For transient transfection, cells were collected by centrifugation (200g for 5 min) and resuspended in 50 ml Freestyle medium (Invitrogen) containing 0.6 mg PEI Max (Polysciences) and 0.2 mg plasmid DNA, followed by a 4 h shaker-incubation in a 2-l conical flask at 160 rpm. Plasmids were transfected at 1:1:4 ratio (that is, 0.035:0.035:0.13 mg) of  $\alpha 1$ -1D4:SBP- $\alpha 1$ : $\beta 3$ . Subsequently, culture medium was topped up to 400 ml with PEM containing 1 mM valproic acid and the cell suspension was returned to empty bottles. Typically, 40–50% transfection efficiency was achieved, as assessed by inclusion of 3% DNA of a control GFP plasmid. Seventy-two hours after transfection, cell pellets were collected, snap-frozen in liquid N<sub>2</sub> and stored at –80 °C.

The receptor was double purified against first the SBP tag and then the 1D4-tag to only purify receptors containing one of each of the alternatively SBP or 1D4 tagged  $\alpha 1$  subunits. The  $\beta 3$  subunit was transfected in excess relative to the  $\alpha 1$  subunit, at 2:1, to ensure that the double-purified material consisted of only receptors comprising two  $\alpha 1$  subunits and three  $\beta 3$  subunits, as previously proposed<sup>52,53</sup>. Note that 1 mM histamine was included in all the buffers described below, throughout the purification to aid yield. The cell pellet (approx. 7–10 g) was solubilized in 30 ml buffer containing 20 mM HEPES pH7.2, 300 mM NaCl, 1% (v/v) mammalian protease inhibitor cocktail (Sigma-Aldrich, cat.P8340) and 1.5% (w/v) lauryl maltose neopentyl glycol (LMNG, Anatrace) at a 10:1 molar ratio with cholesterol hemisuccinate (CHS, Anatrace), for 2 h at 4 °C. Insoluble material was removed by centrifugation (10,000g, 15 min). The supernatant was diluted twofold in a buffer containing 20 mM HEPES pH 7.2, 300 mM NaCl and incubated for 2 h at 4 °C with 1 ml high-capacity streptavidin beads (Thermofisher 20361). Affinity-bound samples were washed by gravity flow for 30

min at 4 °C with 10 ml of detergent-lipid (DL) buffer containing 20 mM HEPES pH 7.2, 300 mM NaCl, and 0.1% (w/v) LMNG 10:1 CHS containing an excess (400 µl) of a phosphatidylcholine (POPC, Avanti) and bovine brain lipid (BBL) extract (type I, Folch fraction I, Sigma-Aldrich) mixture (POPC:BBL ratio 85:15). POPC and BBL extract stocks (10 and 20 mg ml<sup>-1</sup>, respectively) were prepared by solubilization in 3% w/v dodecyl maltopyranoside (DDM). Protein was eluted in 2 ml DL buffer supplemented with 5 mM biotin, for 2 h at 4 °C. The elution was incubated for 2 h at 4 °C with 100 µl CNBr-activated sepharose beads (GE Healthcare) pre-coated with Rho-1D4 antibody (British Columbia) (3.3 g dry powdered beads expand to approximately 10 ml during coupling of 50 mg of 1D4 antibody in 20 ml phosphate buffered saline). The beads were gently centrifuged (300g, 5 min) and washed with 10 ml of DL buffer.

On-bead nanodisc reconstitution was performed<sup>26</sup>, in which the beads were equilibrated with 1 ml of DL buffer. Beads were centrifuged and excess solution removed leaving 100 µl DL buffer, which was topped up with 75 µl of MSP2N2 at 5 mg ml<sup>-1</sup> together with Bio-Beads (40 mg ml<sup>-1</sup> final concentration) and incubated for 2 h rotating gently at 4 °C. The MSP2N2 belt protein was produced as previously described<sup>24</sup>. After nanodisc reconstitution, the 1D4 resin and Bio-Bead mixture was washed extensively with buffer (300 mM NaCl, 50 mM HEPES pH 7.6) to remove empty nanodiscs. Protein was eluted using 100 µl of buffer containing 75 mM NaCl, 12.5 mM HEPES pH7.6, 500 µM 1D4 peptide overnight with gentle rotation at 4 °C. The next day, beads were centrifuged and the eluate was collected, which contained protein at 0.3 mg ml<sup>-1</sup>. This was used directly for cryo-EM grid preparation. Purified Mb25<sup>28</sup> was added at a twofold molar excess. For drug treatments, GABA was added at 200 µM, ZnCl<sub>2</sub> at 20 µM and α-CBTx (Smartox) at 10 µM. For the α-CBTx-Zn<sup>2+</sup> (3.0 Å resolution) and GABA-Zn<sup>2+</sup> (2.8 Å resolution) structures a concentration of 20 µM Zn<sup>2+</sup> was chosen because it is sufficient to achieve approximately 90% inhibition (Extended Data Fig. 5a) while minimizing risks of off-target binding to low-affinity Zn<sup>2+</sup> sites<sup>9</sup>. For grid preparation, 3.5 µl of sample was applied onto glow-discharged gold R1.2/1.3 300 mesh UltraAuFoil grids (Quantifoil) for and then blotted for 5.5 s at blot force of -15 before plunge-freezing the grids into liquid ethane cooled by liquid nitrogen. Plunge-freezing was performed using a Vitrobot Mark IV (Thermo Fisher Scientific) at approximately 100% humidity and 14.5 °C.

## Nb25 purification and production

Nb25 was produced exactly as described<sup>29</sup>, and reproduced here. Nb25 was produced and purified in milligram quantities from WK6su *E. coli* bacteria. Bacteria were transformed with about 200 ng of the nanobody expression plasmid pMESy4 containing Nb25 and selected on lysogeny broth (LB)-agar plates containing 2% glucose and 100 µg ml<sup>-1</sup> ampicillin. Two or three colonies were used to prepare a

preculture, which was used to inoculate 0.5 l Terrific broth (TB) cultures supplemented with 0.1% glucose, 2 mM MgCl<sub>2</sub> and 100 µg ml<sup>-1</sup> ampicillin. Cultures were grown at 37 °C until their absorbance at 600 nm reached 0.7, at which point Nb25 expression was induced with 1 mM IPTG. After induction, cells were grown at 28 °C overnight and harvested by centrifugation (20 min, 5,000g). Nanobodies were released from the bacterial periplasm by incubating cell pellets with an osmotic shock buffer containing 0.2 M Tris, pH 8.0, 0.5 mM EDTA and 0.5 M sucrose. The C-terminally His<sub>6</sub>-tagged Nb25 was purified using nickel-affinity chromatography (binding buffer: 50 mM HEPES, pH 7.2, 1 M NaCl, 10 mM imidazole; elution buffer: 50 mM HEPES, pH 7.2, 0.2 M NaCl, 0.5 M imidazole) and then subjected to size-exclusion chromatography on a Superdex 75 16/600 column (GE Healthcare) in 10 mM HEPES, pH 7.2, 150 mM NaCl. Nb25 stocks were concentrated to 5–10 mg ml<sup>-1</sup>, snap frozen in liquid nitrogen and stored at -80 °C. Yield was in the range 2–10 mg from 500 ml bacterial suspension.

## Cryo-electron microscopy data acquisition and image processing

All cryo-EM data presented here were collected in the Department of Biochemistry, University of Cambridge and all data collection parameters are given in Extended Data Table 1. Krios data were collected using FEI EPU and then processed using Warp<sup>54</sup> and cryoSPARC<sup>55,56</sup>. In short, contrast transfer function correction, motion correction and particle picking were performed using Warp. These particles were subjected to 2D classification in cryoSPARC followed by ab initio reconstruction to generate the initial 3D models. Particles corresponding to different classes were selected and optimized through iterative rounds of heterogeneous refinement as implemented in cryoSPARC. The best models were then further refined using homogeneous refinement and finally non-uniform refinement in cryoSPARC. For the final reconstructions the overall resolutions were calculated by FSC at 0.143 cutoff (Extended Data Table 1). A local\_res map was generated in cryoSPARC using the program ‘local resolution estimation’. The resolution range was based on the Fourier shell correlation output calculated for voxels only within the mask output from the homogenous refinement job used as the input for local resolution estimation. To generate maps coloured by local resolution, the local\_res map along with the main map were opened in UCSF Chimera<sup>57</sup> and processed using the surface colour tool.

## Model building, refinement, validation, analysis and presentation

Model building was carried out in Coot<sup>58</sup> using PDB 6HUO as a template for the GABA<sub>A</sub>R α1β3 GABA map. The model was docked into the cryo-EM density map using the dock\_in\_map program, PHENIX suite<sup>59</sup>. The map resolution was sufficient to allow ab initio building of M3–M4 helix linkers for GABA<sub>A</sub>R α1. Before

refinement, phenix\_ready\_set was run to generate the restraints for the bound ligands including lipids, GABA and histamine and optimize the metal ion coordination restraints. The geometry constraint files for small-molecule ligands used in the refinement were generated using the Grade Web Server (Global Phasing). The model was improved iteratively by rounds of refinement using phenix\_real\_space\_refine and manual inspection and improvement of refined models in Coot. Model geometry was evaluated using the MolProbity Web Server<sup>60</sup>. The new GABA<sub>A</sub>R α1β3 GABA model was subsequently used as a template in the GABA-Zn<sup>2+</sup> and αCBTx-Zn<sup>2+</sup> maps, which were then modified and built using the same process as applied for creating the GABA map. PDB:1YI5 Chain J was used as a template for α-CBTx.

Phenix\_mtriage<sup>61</sup> was used to calculate the resolution at 0.5 FSC. Pore permeation pathways and measurements of pore diameters were generated using the HOLE plug-in<sup>62</sup> in Coot. Structural overlays were generated using Matchmaker function in UCSF chimera<sup>57</sup> and C<sub>α</sub> r.m.s.d. values measured using the rmsd function. Rotation angles were calculated using UCSF Chimera. Structural presentations for figures were produced using UCSF Chimera or Pymol (Schrödinger).

## Electrophysiology

### Whole-cell recordings

Whole-cell responses were recorded in patch clamp experiments from HEK 293 cells transiently transfected with human GABA<sub>A</sub> α1β3 (WT), α1<sub>GLIVI</sub>β3<sub>BRIL</sub> (α1β3cryo-EM; see ‘Constructs’) or α1β3γ2 (WT). HEK 293 cells were grown in DMEM supplemented with 10% v/v fetal bovine serum, 100 U ml<sup>-1</sup> penicillin-G and 100 µg ml<sup>-1</sup> streptomycin (37 °C; 95% air/5% CO<sub>2</sub>), and transfected using a calcium-phosphate precipitation method with α1:β3:GFP or α1:β3:γ2:GFP cDNAs in a ratio of 1:1:1 or 1:1:3:1, respectively, 12–24 h before experimentation. Recordings were performed with cells continuously perfused with Krebs solution composed of (mM): 140 NaCl, 4.7 KCl, 1.2 MgCl<sub>2</sub>, 2.52 CaCl<sub>2</sub>, 11 Glucose and 5 HEPES (pH 7.4; ~300 mOsm). Patch pipettes (TW150F-4; WPI; 3–4 MΩ) were filled with an internal solution containing (mM): 140 KCl, 1 MgCl<sub>2</sub>, 11 EGTA, 10 HEPES, 1 CaCl<sub>2</sub>, 2 K-ATP (pH 7.2; ~305 mOsm). Drugs were applied to cells using fast Y-tube application, where Zn<sup>2+</sup> and histamine were pre-applied before co-application with GABA. Cells were voltage-clamped at -40 mV with an Axopatch 200B amplifier (Molecular Devices), currents were digitized at 50 kHz via a Digidata 1322A (Molecular Devices), filtered at 5 kHz (-36 dB), and acquired using Clampex 10.2 (Molecular Devices). Series resistance was compensated at 60–70% (lag time 10 µs).

For free Zn<sup>2+</sup> concentration experiments, the Zn<sup>2+</sup> chelator tricine was used to precisely control Zn<sup>2+</sup> concentration and eliminate background Zn<sup>2+</sup> contamination. Krebs solution was supplemented with 10 mM tricine and pH corrected to 7.4. The free Zn<sup>2+</sup> concentrations were calculated according to the equation:  $[Zn]_{\text{free}} = (\alpha \times K_d \times [Zn]_{\text{total}})/[\text{tricine}]$ ; where [Zn]<sub>total</sub> is known,  $K_d$  is dissociation constant,  $\alpha$  is 6.623777 (that is,  $1 + ([H^+]; M = 3.98 \times 10^{-8})/[K_a]$ );  $M = 7.08 \times 10^{-9}$  (M, molar),  $K_d$  for tricine is 10 μM, and the concentration of tricine was 10 mM. In these experiments we used the following total Zn<sup>2+</sup> concentrations (μM): 1, 3, 10, 30, 100, 300, 1,000, 3,000 and 10,000, which in 10 mM tricine-buffered Krebs solution, resulted in the following calculated free-zinc concentrations (nM): 6.6, 19.8, 66, 198, 662, 1,990, 6,600, 19,900 and 66,200.

### Data analysis for whole-cell recordings

Peak current responses and desensitization rates were obtained using Clampfit 10.2 (Molecular Devices). The EC<sub>50</sub> and IC<sub>50</sub> values were obtained by curve fitting concentration response data from individual experiments to the Hill equation ( $I/I_{\max} = A^n/(EC_{50}^n + A^n)$ ) or inhibition equation ( $I/I_{\max} = 1 - (B^n/(IC_{50}^n + B^n))$ ), where  $A$  is GABA or histamine concentration,  $B$  is Zn<sup>2+</sup> concentration and  $n$  is the Hill coefficient; data were fitted using Origin 6.0. Potency values are presented as pEC<sub>50</sub> or pIC<sub>50</sub> with s.e.m., and the mean was converted into a molar concentration (pEC<sub>50</sub> =  $-\log EC_{50}$ ; pIC<sub>50</sub> =  $-\log IC_{50}$ ). Experiments were repeated at least three times from three different cells. Statistical analysis and graphical data presentations were performed using Prism 9 (GraphPad Software). Unpaired two-tailed Student's *t*-tests were used for single comparisons of properties between wild-type and the Cryo-EM construct, and no values reached significance; that is, none were less than 0.05 (values reported in relevant figure legends). For comparing the two Zn<sup>2+</sup> inhibition concentrations across wild-type and cryo-EM constructs a one-way ANOVA and Tukey multiple comparisons post hoc test was used, and showed no significant differences across groups,  $F(3, 24) = 0.6449$ ;  $P = 0.5937$ . Specific statistical analyses performed for each dataset comparison are provided in the relevant figure legends.

### Single-channel recording

Single GABA-activated channel currents were recorded in outside-out patches from transfected HEK 293 cells at -70 mV holding potential. Channel currents were recorded using an Axopatch 200B and filtered at 5 kHz (4-pole Bessel filter) before digitizing at 20 kHz with a Digidata 1322A. The fixed time resolution of the system was set at 80 μs. WinEDR was used for analysing single channel data. The single-

channel current was determined from compiling channel current amplitude histograms and fitting Gaussian components to define the mean current, s.d. and the total area of the component. The single-channel conductance was calculated from the mean unitary current and the difference between the patch potential and GABA current reversal potential. Individual open and closed dwell times were measured using a 50% threshold cursor applied to the main single channel current amplitude in each patch. The subsequent detection of open and closed events formed the basis of an idealized single channel record used for compiling the dwell time distributions. Frequency distributions were constructed from the measured individual open and closed times and analysed by fitting a mixture of exponentials, defined by:

$$\text{y}(t) = \sum_{i=1}^n A_i \frac{\tau_i}{\tau_i + t} e^{-t/\tau_i}$$

where  $A_i$  is the area of the  $i$ th component to the distribution and  $\tau_i$  represents the corresponding exponential time constant. A Levenberg–Marquardt non-linear least-squares routine was used to determine the values of individual exponential components. An  $F$ -test determined the optimal number of exponential components that were required to fit the individual dwell time distributions. The determination of a critical closed time ( $\tau_{\text{crit}}$ ) to define bursts of GABA channel activity was performed as previously described<sup>63</sup>. Given that sufficient numbers of bursts were not resolved for  $\alpha 1\beta 3_{\text{WT}}$ , we could not compare intra-burst open probabilities. Therefore, we assessed the open probabilities from continuous single channel recordings where there was no evidence of channel stacking during GABA application and thus it was possible, but not guaranteed, that these patches contained only one active channel. Even if this premise is false, the same analysis conditions were applied to recordings for both  $\alpha 1\beta 3\gamma 2_{\text{WT}}$  and  $\alpha 1\beta 3_{\text{WT}}$  receptors. To ensure near-accurate estimates of GABA channel open probability patches were rejected if they displayed multiple channel activation or if such activity accounted for more than 2% of the open-channel currents measured in a single recording. The single channel current for  $\alpha 1\beta 3\gamma 2_{\text{WT}}$  of about 1.9 pA at  $-70$  mV, reflected a main state conductance equivalent to 28 pS, whereas for  $\alpha 1\beta 3_{\text{WT}}$  the main open state current and conductance were lower as expected<sup>8</sup>, at about 1.3 pA at  $-70$  mV, equivalent to about 19 pS.

## Cell lines

HEK 293T cells used for electrophysiology and HEK 293S GnTI<sup>-</sup> cells used for protein production for cryo EM were obtained from ATCC. Further authentication of cell lines was not performed for this study. Mycoplasma testing was not performed for this study.

## Reporting summary

Further information on research design is available in the [Nature Research Reporting Summary](#) linked to this paper.

## Data availability

Atomic model coordinates for  $\alpha$ -CBTx-Zn<sup>2+</sup>, GABA-Zn<sup>2+</sup> and GABA-bound structures have been deposited in the Protein Data Bank with accession codes [7PC0](#), [7PBZ](#) and [7PBD](#), respectively. Cryo-EM density maps have been deposited in the Electron Microscopy Data Bank with accession codes [EMD-13315](#), [EMD-13314](#) and [EMD-13290](#) respectively.

## References

1. Brickley, S. G. & Mody, I. Extrasynaptic GABA<sub>A</sub> receptors: their function in the CNS and implications for disease. *Neuron* **73**, 23–34 (2012).
2. Lee, V. & Maguire, J. The impact of tonic GABA<sub>A</sub> receptor-mediated inhibition on neuronal excitability varies across brain region and cell type. *Front. Neural Circuits* **8**, 3 (2014).
3. Feng, H. J. et al. Delta subunit susceptibility variants E177A and R220H associated with complex epilepsy alter channel gating and surface expression of  $\alpha 4\beta 2\delta$  GABA<sub>A</sub> receptors. *J. Neurosci.* **26**, 1499–1506 (2006).
4. Buhr, A. et al. Functional characterization of the new human GABA<sub>A</sub> receptor mutation  $\beta 3(R192H)$ . *Hum. Genet.* **111**, 154–160, (2002).
5. Belelli, D. et al. Extrasynaptic GABA<sub>A</sub> receptors: form, pharmacology, and function. *J. Neurosci.* **29**, 12757–12763 (2009).
6. Meltzer-Brody, S. et al. Brexanolone injection in post-partum depression: two multicentre, double-blind, randomised, placebo-controlled, phase 3 trials. *Lancet* **392**, 1058–1070 (2018).
7. Fisher, J. L. & Macdonald, R. L. Single channel properties of recombinant GABA<sub>A</sub> receptors containing  $\gamma 2$  or  $\delta$  subtypes expressed with  $\alpha 1$  and  $\beta 3$  subtypes in mouse L929 cells. *J. Physiol.* **505**, 283–297 (1997).

8. Mortensen, M. & Smart, T. G. Extrasynaptic  $\alpha\beta$  subunit GABA<sub>A</sub> receptors on rat hippocampal pyramidal neurons. *J. Physiol.* **577**, 841–856 (2006).
9. Hosie, A. M., Dunne, E. L., Harvey, R. J. & Smart, T. G. Zinc-mediated inhibition of GABA<sub>A</sub> receptors: discrete binding sites underlie subtype specificity. *Nat. Neurosci.* **6**, 362–369 (2003).
10. Sigel, E. & Ernst, M. The benzodiazepine binding sites of GABA<sub>A</sub> receptors. *Trends Pharmacol. Sci.* **39**, 659–671 (2018).
11. Scott, S. & Aricescu, A. R. A structural perspective on GABA<sub>A</sub> receptor pharmacology. *Curr. Opin. Struct. Biol.* **54**, 189–197 (2019).
12. Puthenkalam, R. et al. Structural studies of GABA<sub>A</sub> receptor binding sites: which experimental structure tells us what? *Front. Mol. Neurosci.* **9**, 44 (2016).
13. Kudryavtsev, D. S. et al. Neurotoxins from snake venoms and  $\alpha$ -conotoxin ImI inhibit functionally active ionotropic  $\gamma$ -aminobutyric acid (GABA) receptors. *J. Biol. Chem.* **290**, 22747–22758 (2015).
14. Corringer, P. J. et al. Structure and pharmacology of pentameric receptor channels: from bacteria to brain. *Structure* **20**, 941–956 (2012).
15. Sauguet, L., Shahsavar, A. & Delarue, M. Crystallographic studies of pharmacological sites in pentameric ligand-gated ion channels. *Biochim. Biophys. Acta* **1850**, 511–523 (2015).
16. Mortensen, M., Patel, B. & Smart, T. G. GABA potency at GABA<sub>A</sub> receptors found in synaptic and extrasynaptic zones. *Front. Cell Neurosci.* **6**, 1 (2011).
17. Smart, T. G. A novel modulatory binding site for zinc on the GABA<sub>A</sub> receptor complex in cultured rat neurones. *J. Physiol.* **447**, 587–625 (1992).
18. Bencsits, E., Ebert, V., Tretter, V. & Sieghart, W. A significant part of native  $\gamma$ -aminobutyric acid<sub>A</sub> receptors containing  $\alpha 4$  subunits do not contain  $\gamma$  or  $\delta$  subunits. *J. Biol. Chem.* **274**, 19613–19616 (1999).
19. Christie, S. B., Miralles, C. P. & De Blas, A. L. GABAergic innervation organizes synaptic and extrasynaptic GABA<sub>A</sub> receptor clustering in cultured hippocampal neurons. *J. Neurosci.* **22**, 684–697 (2002).

20. Sugasawa, Y. et al. Site-specific effects of neurosteroids on GABA<sub>A</sub> receptor activation and desensitization. *eLife* **9**, e55331 (2020).
21. Akk, G. et al. Enhancement of muscimol binding and gating by allosteric modulators of the GABA<sub>A</sub> receptor: relating occupancy to state functions. *Mol. Pharmacol.* **98**, 303–313 (2020).
22. Smart, T. G., Xie, X. & Krishek, B. J. Modulation of inhibitory and excitatory amino acid receptor ion channels by zinc. *Prog. Neurobiol.* **42**, 393–441 (1994).
23. Buhl, E. H., Otis, T. S. & Mody, I. Zinc-induced collapse of augmented inhibition by GABA in a temporal lobe epilepsy model. *Science* **271**, 369–373 (1996).
24. Ritchie, T. K. et al. Chapter 11 - Reconstitution of membrane proteins in phospholipid bilayer nanodiscs. *Methods Enzymol.* **464**, 211-231 (2009).
25. Laverty, D. et al. Cryo-EM structure of the human  $\alpha 1\beta 3\gamma 2$  GABA<sub>A</sub> receptor in a lipid bilayer. *Nature* **565**, 516–520 (2019).
26. Masiulis, S. et al. GABA<sub>A</sub> receptor signalling mechanisms revealed by structural pharmacology. *Nature* **565**, 454–459 (2019).
27. Zhu, S. et al. Structure of a human synaptic GABA<sub>A</sub> receptor. *Nature* **559**, 67–72 (2018).
28. Uchanski, T. et al. Megabodies expand the nanobody toolkit for protein structure determination by single-particle cryo-EM. *Nat. Methods* **18**, 60–68 (2021).
29. Miller, P. S. et al. Structural basis for GABA<sub>A</sub> receptor potentiation by neurosteroids. *Nat. Struct. Mol. Biol.* **24**, 986–992 (2017).
30. Saras, A. et al. Histamine action on vertebrate GABA<sub>A</sub> receptors: direct channel gating and potentiation of GABA responses. *J. Biol. Chem.* **283**, 10470–10475 (2008).
31. Hannan, S., Mortensen, M. & Smart, T. G. Snake neurotoxin  $\alpha$ -bungarotoxin is an antagonist at native GABA<sub>A</sub> receptors. *Neuropharmacology* **93**, 28–40 (2015).
32. Rosso, J. P. et al. MmTX1 and MmTX2 from coral snake venom potently modulate GABA<sub>A</sub> receptor activity. *Proc. Natl Acad. Sci. USA* **112**, E891–E900 (2015).

33. Fruchart-Gaillard, C. et al. Experimentally based model of a complex between a snake toxin and the  $\alpha 7$  nicotinic receptor. *Proc. Natl Acad. Sci. USA* **99**, 3216–3221 (2002).
34. Miller, P. S. & Aricescu, A. R. Crystal structure of a human GABA<sub>A</sub> receptor. *Nature* **512**, 270–275 (2014).
35. Phulera, S. et al. Cryo-EM structure of the benzodiazepine-sensitive  $\alpha 1\beta 1\gamma 2S$  tri-heteromeric GABA<sub>A</sub> receptor in complex with GABA. *eLife* **7**, e39383 (2018).
36. Bourne, Y., Talley, T. T., Hansen, S. B., Taylor, P. & Marchot, P. Crystal structure of a Cbtx–AChBP complex reveals essential interactions between snake  $\alpha$ -neurotoxins and nicotinic receptors. *EMBO J.* **24**, 1512–1522 (2005).
37. Rahman, M. M. et al. Structure of the native muscle-type nicotinic receptor and inhibition by snake venom toxins. *Neuron* **106**, 952–962.e955 (2020).
38. Draguhn, A., Verdorn, T. A., Ewert, M., Seburg, P. H. & Sakmann, B. Functional and molecular distinction between recombinant rat GABA<sub>A</sub> receptor subtypes by Zn<sup>2+</sup>. *Neuron* **5**, 781–788 (1990).
39. Smart, T. G., Moss, S. J., Xie, X. & Huganir, R. L. GABA<sub>A</sub> receptors are differentially sensitive to zinc: dependence on subunit composition. *Br. J. Pharmacol.* **103**, 1837–1839 (1991).
40. Wooltorton, J. R., Moss, S. J. & Smart, T. G. Pharmacological and physiological characterization of murine homomeric  $\beta 3$  GABA<sub>A</sub> receptors. *Eur. J. Neurosci.* **9**, 2225–2235 (1997).
41. Vallee, B. L. & Auld, D. S. Zinc coordination, function, and structure of zinc enzymes and other proteins. *Biochemistry* **29**, 5647–5659 (1990).
42. Hilf, R. J. et al. Structural basis of open channel block in a prokaryotic pentameric ligand-gated ion channel. *Nat. Struct. Mol. Biol.* **17**, 1330–1336 (2010).
43. Gielen, M. & Corringer, P. J. The dual-gate model for pentameric ligand-gated ion channels activation and desensitization. *J. Physiol.* **596**, 1873–1902 (2018).
44. Mukhtasimova, N., Lee, W. Y., Wang, H. L. & Sine, S. M. Detection and trapping of intermediate states priming nicotinic receptor channel opening. *Nature* **459**, 451–454 (2009).

45. Gielen, M. C., Lumb, M. J. & Smart, T. G. Benzodiazepines modulate GABA<sub>A</sub> receptors by regulating the preactivation step after GABA binding. *J. Neurosci.* **32**, 5707–5715 (2012).
46. Miller, P. S. et al. Heteromeric GABA<sub>A</sub> receptor structures in positively-modulated active states. Preprint at <https://doi.org/10.1101/338343> (2018).
47. Molday, R. S. & MacKenzie, D. Monoclonal antibodies to rhodopsin: characterization, cross-reactivity, and application as structural probes. *Biochemistry* **22**, 653–660 (1983).
48. Oprian, D. D., Molday, R. S., Kaufman, R. J. & Khorana, H. G. Expression of a synthetic bovine rhodopsin gene in monkey kidney cells. *Proc. Natl Acad. Sci. USA* **84**, 8874–8878 (1987).
49. Aricescu, A. R., Lu, W. & Jones, E. Y. A time- and cost-efficient system for high-level protein production in mammalian cells. *Acta Crystallogr. D* **62**, 1243–1250 (2006).
50. Reeves, P. J., Callewaert, N., Contreras, R. & Khorana, H. G. Structure and function in rhodopsin: high-level expression of rhodopsin with restricted and homogeneous N-glycosylation by a tetracycline-inducible N-acetylglucosaminyltransferase I-negative HEK293S stable mammalian cell line. *Proc. Natl Acad. Sci. USA* **99**, 13419–13424 (2002).
51. Aricescu, A. R. & Owens, R. J. Expression of recombinant glycoproteins in mammalian cells: towards an integrative approach to structural biology. *Curr. Opin. Struct. Biol.* **23**, 345–356 (2013).
52. Tretter, V., Ehya, N., Fuchs, K. & Sieghart, W. Stoichiometry and assembly of a recombinant GABA<sub>A</sub> receptor subtype. *J. Neurosci.* **17**, 2728–2737 (1997).
53. Horenstein, J. & Akabas, M. H. Location of a high affinity Zn<sup>2+</sup> binding site in the channel of α1β1 γ-aminobutyric acid<sub>A</sub> receptors. *Mol. Pharmacol.* **53**, 870–877 (1998).
54. Tegunov, D. & Cramer, P. Real-time cryo-electron microscopy data preprocessing with Warp. *Nat. Methods* **16**, 1146–1152 (2019).
55. Punjani, A., Brubaker, M. A. & Fleet, D. J. Building proteins in a day: efficient 3D molecular structure estimation with electron cryomicroscopy. *IEEE Trans. Pattern Anal. Mach. Intell.* **39**, 706–718 (2017).

56. Punjani, A., Rubinstein, J. L., Fleet, D. J. & Brubaker, M. A. cryoSPARC: algorithms for rapid unsupervised cryo-EM structure determination. *Nat. Methods* **14**, 290–296 (2017).
57. Pettersen, E. F. et al. UCSF Chimera—a visualization system for exploratory research and analysis. *J. Comput. Chem.* **25**, 1605–1612, (2004).
58. Emsley, P., Lohkamp, B., Scott, W. G. & Cowtan, K. Features and development of Coot. *Acta Crystallogr. D* **66**, 486–501 (2010).
59. Afonine, P. V. et al. Real-space refinement in PHENIX for cryo-EM and crystallography. *Acta Crystallogr. D* **74**, 531–544 (2018).
60. Chen, V. B. et al. MolProbity: all-atom structure validation for macromolecular crystallography. *Acta Crystallogr. D* **66**, 12–21 (2010).
61. Afonine, P. V. et al. New tools for the analysis and validation of cryo-EM maps and atomic models. *Acta Crystallogr. D* **74**, 814–840 (2018).
62. Smart, O. S., Neduvvelil, J. G., Wang, X., Wallace, B. A. & Sansom, M. S. HOLE: a program for the analysis of the pore dimensions of ion channel structural models. *J. Mol. Graph.* **14**, 354–360 (1996).
63. Mortensen, M. et al. Activation of single heteromeric GABA<sub>A</sub> receptor ion channels by full and partial agonists. *J. Physiol.* **557**, 389–413 (2004).

## Acknowledgements

We thank L. Cooper for training in cryo-EM grid preparation and for performing grid clipping; J. Stayaert and R. Aricescu for advice on, access to and use of Mb25; R. Aricescu and S. Masiulis for valuable discussions and training in sample preparation; and E. Seiradake for provision of the pHLsec-SBP plasmid. This work was supported by a Department of Pharmacology new lab start-up fund, the University of Cambridge Isaac Newton and Wellcome Trust Institutional Strategic Support Fund, and Academy of Medical Sciences Springboard Award (SBF004\1074). Electrophysiology work in the T.G.S. laboratory was funded by an MRC programme grant (MR/T002581/1) and Wellcome Trust Collaborative Award (217199/Z/19/Z). The cryo-EM facility receives funding from the Wellcome Trust (206171/Z/17/Z; 202905/Z/16/Z) and University of Cambridge.

## Author information

## Affiliations

1. Department of Pharmacology, University of Cambridge, Cambridge, UK  
Vikram Babu Kasaragod, Ayla A. Wahid & Paul S. Miller
2. MRC Laboratory of Molecular Biology, Cambridge, UK  
Vikram Babu Kasaragod
3. Department of Neuroscience, Physiology and Pharmacology, University College London, London, UK  
Martin Mortensen, Valentina Dorovskykh & Trevor G. Smart
4. Cryo-EM Facility, Department of Biochemistry, University of Cambridge, Cambridge, UK  
Steven W. Hardwick & Dimitri Y. Chirgadze

## Contributions

structural interpretation. A.A.W. performed protein purification. M.M. and T.G.S. designed and analysed the electrophysiological experiments, which were performed by M.M. and V.D. S.W.H. and D.Y.C. performed cryo-EM data acquisition and processing. P.S.M. performed construct design, protein purification, cryo-EM sample preparation, atomic model building and structural interpretation. P.S.M. wrote the manuscript with input from all other authors.

## Corresponding authors

Correspondence to [Trevor G. Smart](#) or [Paul S. Miller](#).

## Ethics declarations

## Competing interests

The authors declare no competing interests.

## Peer review

## Peer review information

*Nature* thanks Margot Ernst and the other, anonymous, reviewer(s) for their contribution to the peer review of this work. Peer review reports are available.

## Additional information

**Publisher's note** Springer Nature remains neutral with regard to jurisdictional claims in published maps and institutional affiliations.

## Extended data figures and tables

### [Extended Data Fig. 1 Local resolution maps, overall plotted resolutions, and global map-model agreements.](#)

For the three structures,  $\alpha$ -CBTx/Zn<sup>2+</sup>, GABA/Zn<sup>2+</sup>, and GABA-bound, a map on the left is coloured by local resolution (see [methods](#)). Maps of Fourier shell correlation (FSC) (upper right panels) and map-model FSC (lower right panels) plots are also shown. Relevant statistics for these maps are presented in Extended Data Table 1.

### [Extended Data Fig. 2 GABA responses and histamine potentiation.](#)

**a**, GABA concentration response curves for  $\alpha\beta_{WT}$  (white symbols) and  $\alpha\beta_{CryoEM}$  (black symbols) in the absence (circles) or presence (triangles) of 3 mM histamine (HSM). Data was obtained in whole cell patch clamp experiments performed on transiently transfected HEK 293 cells. **b**, Histamine concentration response curves for potentiating the 300  $\mu$ M GABA response for  $\alpha\beta_{WT}$  and  $\alpha\beta_{CryoEM}$ . For **a**, and **b**, points represent mean  $\pm$  s.e.m. Curves generated are  $n = 4$  and  $n = 5$  for WT and EM constructs respectively. For **a**, One-way ANOVA showed no statistical difference across the 4 pEC<sub>50</sub> values, and for **b**, Two-sided unpaired t-test showed values were not statistically different,  $P = 0.51$ . **c**, Representative whole-cell patch clamp current responses to GABA and GABA + 3 mM histamine applications. Note that histamine was pre-applied before co-applying with GABA (blue lines). **d–e**, Bar charts showing average maximum (1 mM) GABA current response levels and rates of desensitisation, respectively, for  $\alpha\beta_{WT}$  and  $\alpha\beta_{CryoEM}$ . Individual values are shown as circles, and bars are means  $\pm$  s.e.m. EM I<sub>max</sub>  $n = 14$ , WT I<sub>max</sub>  $n = 15$ , EM desens  $n = 11$ , WT desens  $n = 10$ . Two-sided unpaired t-test showed values were not statistically different for either property,  $P = 0.64$  and 0.08, respectively. Each  $n = 1$  value of an pEC<sub>50</sub>, I<sub>max</sub> and desensitisation value were from biologically independent patch-clamp experiments from individual cells.

### Extended Data Fig. 3 Nb25 potentiation at $\alpha$ 1 $\beta$ 3 receptors.

**a**, Atomic models show no obvious distinctions for the  $\beta$ - $\beta$  interface and the Nb25 binding pose of  $\alpha$ 1 $\beta$ 3 receptors in the inhibited  $\alpha$ -CBTx/Zn<sup>2+</sup>-bound conformation (3.0 Å, darker shades) versus the GABA-bound conformation (3.0 Å, lighter shades), consistent with any functional impacts exerted by Nb25 being subtle. Upper insets are viewing aids to highlight the region of the protein complex being viewed. Nb in green,  $\beta$ -subunits in blue,  $\alpha$ -subunits in red. CDR3 is complementarity determinant loop 3 of Nb25. **b**, Representative currents of whole cell patch clamp responses to GABA and GABA + 10  $\mu$ M Nb25 applications for  $\alpha$ 1 $\beta$ 3<sub>CryoEM</sub> versus  $\alpha$ 1 $\beta$ 3 $\gamma$ 2 wild-type. Note that Nb25 was pre-applied before co-applying with GABA (red lines). **c**, Bar chart showing average potentiation of EC<sub>15</sub> GABA current responses for  $\alpha$  $\beta$ <sub>CryoEM</sub> versus  $\alpha$ 1 $\beta$ 3 $\gamma$ 2 wild-type by Nb25, revealing a weak selective potentiation of  $\alpha$ 1 $\beta$ 3 receptors due to the  $\beta$ - $\beta$  interface, which is absent from  $\alpha$ 1 $\beta$ 3 $\gamma$ 2 receptors. Bars are means  $\pm$  s.e.m.  $n = 3$ , each value being from biologically independent patch-clamp experiments from individual cells.

### Extended Data Fig. 4 $\alpha$ -Cobratoxin binding mode and $\alpha$ $\beta$ receptor conformation.

**a**, Atomic model fit in the cryo-EM map density of the  $\alpha$ 1 $\beta$ 3 receptor bound by  $\alpha$ -CBTx/Zn<sup>2+</sup> (3.0 Å) for the receptor  $\beta$ 3 subunit loop-C (blue) and toxin finger II (green); yellow segment is Cys26-Cys30 side chain Cys-bridge. **b**, Alternative view of the toxin to show side chain density for Phe29, and binding residues Arg33 and Arg36. **c–e**, Atomic models showing common binding poses for toxins against pLGICs at inter-subunit interfaces (AChBP PDB 1YI5; nAChR PDB 6UWZ). **f**, Overlays showing closely matching arrangements of  $\alpha$ -CBTx atomic models for GABR $\alpha$ 1 $\beta$ 3, AChBP and apo- $\alpha$ -CBTx (PDB 1ZFM). **g**, **h**, Atomic models comparing  $\alpha$ -CBTx finger II binding mode to GABA<sub>A</sub> receptor  $\beta$ 3 subunit loop-C versus AChBP. **i**, Receptor  $\alpha$ 1-subunit Arg67 side chain can move away from toxin finger II Ile32 to accommodate toxin binding. **j**, Mechanism of reduced toxin sensitivity for  $\alpha$ 2-GABA<sub>A</sub>R subunit, caused by Lys68 in the equivalent position to  $\alpha$ 1 Ser69, which can be explained by Lys68 sterically and electrostatically hindering Arg67 movement away from toxin Ile32 to reduce accommodation of the toxin. **k**, Overlays to compare loop-C outward motion imposed by  $\alpha$ -CBTx on  $\alpha$  $\beta$  receptor (arrow; GABA-bound in pale blue, toxin-bound blue), and bicuculline on  $\alpha$  $\beta$  $\gamma$  receptor (GABA-bound in white PDB:6HUO, bicuculline-bound in dark grey PDB:6HUK; bicuculline not shown). **l**, Overlays of cross-section of top of pentameric ECD for  $\alpha$ 1 $\beta$ 3  $\alpha$ -CBTx/Zn<sup>2+</sup> (blue/red) versus an inhibited state of  $\alpha$ 1 $\beta$ 3 $\gamma$ 2 bound by the specific antagonist bicuculline (grey). The only distinguishable difference is the exaggerated outward translation of the  $\beta$ 3-subunit loop-C for  $\alpha$ -CBTx/Zn<sup>2+</sup> (red circles) caused by toxin binding (toxin not

shown). Inter-subunit interfaces are indicated by orange dashed lines. **m**, Same as **I** except overlay of  $\alpha\beta$  versus GABA-activated state of  $\alpha 1\beta 3\gamma 2$  to reveal a greater divergence in conformation (RMSD increased from 1.0 Å in **I** to 1.5 Å in **m**), in particular for the agonist-responding  $\beta$ -subunits (chains B/E), indicated by red arrows (RMSD increases to 1.8 Å). **n**, Overlays of the  $\beta 1$ - $\beta 2$  loops (inner) and  $\beta 6$ - $\beta 7$  loops (Cys-loops; outer) at the base of the ECD, which oppose the TMD, for  $\alpha 1\beta 3$   $\alpha$ -CBTx/Zn<sup>2+</sup> (blue/red) versus the inhibited state of  $\alpha 1\beta 3\gamma 2$  bound by bicuculline (pale shades, yellow for  $\gamma 2$  loops), showing occupation of the same positions for all subunits, including for the  $\alpha 1\beta 3$  Chain C  $\beta$ -subunit fitting the  $\alpha 1\beta 3\gamma 2$  Chain C  $\gamma 2$ -subunit position.

### Extended Data Fig. 5 Zn<sup>2+</sup> inhibition.

**a**, Free\* Zn<sup>2+</sup> inhibition curves from whole cell patch-clamp experiments performed in recording buffer supplemented with 10 mM tricine for  $\alpha\beta_{WT}$  (white symbols) and  $\alpha\beta_{CryoEM}$  (black symbols) expressed in HEK293 cells. Points represent mean  $\pm$  s.e.m. Curves generated are  $n = 8$  and  $n = 7$  respectively of WT and EM constructs, of biologically independent patch-clamp experiments from individual cells. Two-sided unpaired t-test showed pIC50 values were not statistically different,  $P = 0.35$ . **b**, similar Zn<sup>2+</sup> inhibition curve for  $\alpha\beta_{CryoEM}$ , but in the absence of Zn<sup>2+</sup>-chelating tricine, showing that contaminating Zn<sup>2+</sup> in buffers was not impacting sensitivity in any way,  $n = 6$ . **c–e**, Atomic model fits in cryo-EM map density of  $\beta 3$  (chain E) subunit TMDs for  $\alpha$ -CBTx/Zn<sup>2+</sup> (3.0 Å), GABA/Zn<sup>2+</sup> (2.79 Å) and GABA (3.04 Å) respectively. Zn<sup>2+</sup> density at 17' His is indicated. Note the 17' density is absent when Zn<sup>2+</sup> is not bound. **f–h**, Atomic model fits in cryo-EM map density for top-down slices of the pentamer at the 17' pore position for  $\alpha$ -CBTx/Zn<sup>2+</sup>, GABA/Zn<sup>2+</sup> and GABA-bound structures, respectively. **h**, Density for 17' His residues is absent when Zn<sup>2+</sup> is not bound to coordinate them, indicating these side chains are highly mobile. Pore expands nominally to 4.1 Å diameter (variable depending on flexible His arrangement). \*free Zn<sup>2+</sup> concentration controlled and determined using the chelator, tricine (see “[Methods](#)”).

### Extended Data Fig. 6 Impact of GABA binding on ECD conformation.

**a**, Upper panel: Overlay cross-sections of the top of pentameric ECDs of  $\alpha$ -CBTx/Zn<sup>2+</sup> (grey) versus GABA ( $\alpha$ -red/ $\beta$ -blue)-bound atomic models. Greatest divergence is observed for the GABA binding  $\beta 3$ -subunits (chains B/E), which have tilted/rotated in response to GABA binding, red arrows, and is reflected by RMSD being higher for these subunits, 1.8 Å, relative to the whole ECD, 1.3 Å. **a**, Lower panel: Overlay of the  $\beta 1$ - $\beta 2$  loops (inner) and  $\beta 6$ - $\beta 7$  loops (Cys-loops; outer) at the

base of the ECD which oppose the TMD (not shown). This shows the resultant translation for the GABA binding  $\beta$ 3-subunits (chains B/E; red arrows), caused by the motion in the upper ECD (upper panel). **b**, same as **a**, but for  $\alpha$ -CBTx/Zn<sup>2+</sup> (grey) versus GABA/Zn<sup>2+</sup> ( $\alpha$ -red/ $\beta$ -blue). Differences are the same because GABA induces the same ECD motions even with Zn<sup>2+</sup> bound in the pore. **c**, same as **a**, but for GABA ( $\alpha$ -red/ $\beta$ -blue) versus GABA/Zn<sup>2+</sup> (grey). As these ECDs have undertaken the same motions in response to binding GABA, RMSDs are lower and  $\beta$ -subunit RMSDs do not increase relative to whole ECD. **d**, same as **a**, but for  $\alpha$ 1 $\beta$ 3 $\gamma$ 2 bicuculline-bound (grey; PDB 6HUK) versus  $\alpha$ 1 $\beta$ 3 $\gamma$ 2 GABA/Alprazolam-bound ( $\alpha$ -red/ $\beta$ -blue/ $\gamma$ -gold; PDB 6HUO). The impact of GABA/Alprazolam binding versus the antagonist is the same as observed for the  $\alpha\beta$  receptor GABA binding versus antagonist (shown in **a**). NOTE: ligands are not shown.

### Extended Data Fig. 7 TMD M2-3 loop conformations.

**a**, Atomic model fits in the cryo-EM map density for the M2-M3 loops of  $\beta$ 3 chains B and E for  $\alpha$ -CBTx/Zn<sup>2+</sup> (3.0 Å, blue maps) and GABA-bound (3.04 Å, grey maps) respectively. Viewed looking down on to the M2-M3 loop reveals the switch to the ‘outward’ conformation in response to the ECD binding GABA, as highlighted by Pro276 repositioning to the other side of the dashed line. **b**, Top-down view of  $\alpha$ 1 $\beta$ 3 $\gamma$ 2 bicuculline-bound (dark grey; PDB 6HUK) versus  $\alpha$ 1 $\beta$ 3 $\gamma$ 2 GABA/Alprazolam-bound ( $\alpha$ -pink/ $\beta$ -pale blue/ $\gamma$ -gold; PDB 6HUO) showing the M2-M3 loop positions. In response to GABA binding the  $\beta$ -subunit chain B/E M2-M3 loops switch to the ‘outward’ conformation, indicated by red arrows that highlight the motion of Pro273. The  $\gamma$ 2-subunit is in the outward conformation in both states.

### Extended Data Fig. 8 Pore arrangement.

**a**, Side-on views of subunit transmembrane helical bundle C <sub>$\alpha$</sub> -polypeptide for Chains A-E showing M2 helix tilt axis.  $\alpha$ 1 $\beta$ 3 GABA model is coloured red ( $\alpha$ -subunit) or blue ( $\beta$ -subunit), and the M2 helix axis is shown as a dim grey bar.  $\alpha$ 1 $\beta$ 3  $\alpha$ -CBTx/Zn<sup>2+</sup> model is white, M2 helix axis green. Pore axis is to right of each bundle, vertical black bar. M2 helix tilt and/or translation away from pore axis increases for each subunit when GABA is bound (angle values shown; translations not measured but visible by eye). **b**, Table showing M2 helix tilt angles for  $\alpha\beta$  and  $\alpha\beta\gamma$  receptors in antagonist (black text) and agonist (GABA) bound (red text) conformations.  $\alpha\beta\gamma$  M2 helix tilt angles shown as increase (+) or decrease (-) relative to the equivalent  $\alpha\beta$  M2 helix. The biggest increase is for the  $\gamma$ 2 subunits (values bold, underlined). **c**, Electron density map slices of the pore conformation at the 9' Leu gate (pore diameters given inside pore circles) for  $\alpha$ 1 $\beta$ 3  $\alpha$ -CBTx/Zn<sup>2+</sup>, GABA/Zn<sup>2+</sup> and GABA-bound structures. For comparison the cryo-EM map of EMD-0282 used to build 6HUO PDB of

GABA+Alprazolam bound structure is shown. **d**, Cross-section at 9' Leu hydrophobic gate showing  $C_\alpha$  pentagonal perimeters for GABA-bound  $\alpha\beta$  receptor versus GABA+Alprazolam-bound  $\alpha 1\beta 3\gamma 2$  (left panel) or GABA-bound  $\alpha 1\beta 2\gamma 2$  (right panel). **e**, Side by side comparison of the  $\alpha\beta$  receptor  $\beta 3$  subunit Chain C M2 helix tilts versus equivalent  $\alpha\beta\gamma$  receptor  $\gamma 2$  M2 helix tilts, which are more reclined (for PDB codes see table in, **b**).

### Extended Data Fig. 9 Single channel current analysis for GABA<sub>AR</sub> heteromers.

**a**, epochs of GABA single channel currents recorded from outside-out patches of HEK293 cells expressing  $\alpha 1\beta 3_{WT}$  and  $\alpha 1\beta 3\gamma 2_{WT}$  receptors, activated by 30 and 100  $\mu M$  GABA respectively ( $\sim EC_{95}$  for each receptor isoform) at low (upper trace) and higher time resolution (lower traces). C – closed and O – open state; closed state marked by dashed line; downward deflections are transitions to open state. **b**, Examples of open and closed state dwell time distributions for single cells expressing  $\alpha 1\beta 3_{WT}$  or  $\alpha 1\beta 2\gamma 2_{WT}$  receptors. Single exponential component fits (green lines) and summed fits from a mixture of exponentials (red lines) are shown. In the example shown for open times, a single exponential fit was sufficient to account for the  $\alpha 1\beta 3_{WT}$  open state distribution, whilst for  $\alpha 1\beta 3\gamma 2_{WT}$  a mixture of two exponentials was required. Mean exponential  $\tau$  values (with SEM, and percentage area) determined from analysing multiple patches are:  $\tau 1 = 0.65 \pm 0.15$  ms ( $A1 = 83 \pm 6\%$ ,  $n = 6$ ),  $\tau 2 = 4.3 \pm 1.1$  ms ( $A2 = 17 \pm 6\%$ ,  $n = 4$  – two cells did not show long open times); for  $\alpha 1\beta 3\gamma 2_{WT}$ :  $\tau 1 = 0.78 \pm 0.07$  ms ( $A1 = 39 \pm 3\%$ ,  $n = 6$ ),  $\tau 2 = 4.8 \pm 0.7$  ms ( $A2 = 61 \pm 3\%$ ,  $n = 6$ ). For closed state dwell time distributions both receptor isoforms required a mixture of four exponentials of similar magnitudes, however  $\alpha 1\beta 3$  favoured the longer duration closed states, whereas  $\alpha 1\beta 3\gamma 2$  favoured the shortest closed states which normally appear within bursts of openings. Mean  $\tau$  values (and SEM, including percentage areas) from multiple patches are:  $\alpha 1\beta 3_{WT}$ ; :  $\tau 1 = 0.17 \pm 0.05$  ms ( $A1 = 36 \pm 1\%$ ,  $n = 3$ ),  $\tau 2 = 2.8 \pm 0.3$  ms ( $A2 = 62 \pm 10\%$ ,  $n = 6$ ),  $\tau 3 = 21 \pm 5$  ms ( $A3 = 22 \pm 6\%$ ,  $n = 4$ ),  $\tau 4 = 52 \pm 3$  ms ( $A4 = 20 \pm 2\%$ ,  $n = 3$ ));  $\alpha 1\beta 3\gamma 2_{WT}$ :  $\tau 1 = 0.50 \pm 0.04$  ms ( $A1 = 68 \pm 3\%$ ,  $n = 6$ ),  $\tau 2 = 3.0 \pm 0.3$  ms ( $A2 = 21 \pm 2\%$ ,  $n = 6$ ),  $\tau 3 = 24 \pm 4$  ms ( $A3 = 9 \pm 2\%$ ,  $n = 6$ ),  $\tau 4 = 165 \pm 25$  ms ( $A4 = 2 \pm 0.5\%$ ,  $n = 3$ ). **c**, Bar graph showing percentage distribution between short versus long open state dwell times for  $\alpha 1\beta 3$  and  $\alpha 1\beta 3\gamma 2$ . Points represent mean  $\pm$  s.e.m.  $n = 6$ , except for  $\alpha 1\beta 3$  long openings  $n = 4$  (no long openings observed for two of the cells). Two-sided unpaired t-test comparisons of open dwell times  $t(8) = 7.53$ ,  $p < 0.0001$ , and shut dwell times  $t(10) = 7.01$ ,  $p < 0.0001$ . **d**, Bar graph showing the open probability ( $P_o$ ; the average fraction of time spent in the open state), measured as the total open time divided by the total length of the recording. Recordings were taken from patches showing limited or no channel

stacking (see [Methods](#)). Individual values are shown as circles/squares with associated error bars (mean  $\pm$  s.e.m.),  $n = 6$ , two-sided unpaired t-test comparison,  $t(10) = 4.43$ ,  $P = 0.0013$ . \*\* signifies as statistically different ( $P < 0.01$ ) for bars linked by black lines. Each  $n = 1$  value of an open time, shut time or  $P_o$  were from biologically independent patch-clamp experiments from individual cells.

### [Extended Data Fig. 10 Probability of activation for \$\alpha 1\beta 3\$ and \$\alpha 1\beta 3\gamma 2\$ receptors.](#)

**a**, whole-cell patch clamp recordings from HEK293 cells expressing either  $\alpha 1\beta 3$  EM,  $\alpha 1\beta 3$  WT, or  $\alpha 1\beta 3\gamma 2$  WT, showing responses to increasing concentrations of GABA and saturating GABA + 1 mM pentobarbitone in order to measure the probability of activation ( $P_A$ ). Dashed lines indicate the baseline current (grey), the maximum activation by saturating GABA alone (black) and activation by saturating GABA + 1 mM pentobarbitone (red). Accompanying concentration response curve plots are provided (mean  $\pm$  s.e.m,  $\alpha 1\beta 3$  EM  $n = 8$ ,  $\alpha 1\beta 3$  WT  $n = 5$ ,  $\alpha 1\beta 3\gamma 2$  WT  $n = 6$ ). **b**, Bar chart showing similar  $P_A$  values for  $\alpha 1\beta 3$  EM and  $\alpha 1\beta 3$  WT, which were lower than for  $\alpha 1\beta 3\gamma 2$  WT. Individual values are shown as circles/squares and bars are means  $\pm$  s.e.m. ( $\alpha 1\beta 3$  EM  $n = 8$ ,  $\alpha 1\beta 3$  WT  $n = 5$ ,  $\alpha 1\beta 3\gamma 2$  WT  $n = 6$ ). One-way ANOVA comparing abWT vs abCryoEM vs abgWT:  $F(2,16) = 18.78$ ;  $P < 0.0001$ . Post-hoc Tukey. Each  $n = 1$  value of a  $P_A$  were from biologically independent patch-clamp experiments from individual cells.

### **Extended Data Table 1 Cryo-EM data collection, refinement and validation statistics for GABA, GABA/Zn<sup>2+</sup>, $\alpha$ -CBTx/Zn<sup>2+</sup>**

## Supplementary information

### [Reporting Summary](#)

### [Peer Review File](#)

## Rights and permissions

**Open Access** This article is licensed under a Creative Commons Attribution 4.0 International License, which permits use, sharing, adaptation, distribution and reproduction in any medium or format, as long as you give appropriate credit to the original author(s) and the source, provide a link to the Creative Commons license, and indicate if changes were made. The images or other third party material in this article are included in the article's Creative Commons license, unless indicated otherwise in a

credit line to the material. If material is not included in the article's Creative Commons license and your intended use is not permitted by statutory regulation or exceeds the permitted use, you will need to obtain permission directly from the copyright holder. To view a copy of this license, visit <http://creativecommons.org/licenses/by/4.0/>.

## [Reprints and Permissions](#)

## About this article

### Cite this article

Kasaragod, V.B., Mortensen, M., Hardwick, S.W. *et al.* Mechanisms of inhibition and activation of extrasynaptic  $\alpha\beta$  GABA<sub>A</sub> receptors. *Nature* **602**, 529–533 (2022).  
<https://doi.org/10.1038/s41586-022-04402-z>

- Received: 07 June 2021
- Accepted: 22 December 2021
- Published: 09 February 2022
- Issue Date: 17 February 2022
- DOI: <https://doi.org/10.1038/s41586-022-04402-z>

### Share this article

Anyone you share the following link with will be able to read this content:

[Get shareable link](#)

Sorry, a shareable link is not currently available for this article.

[Copy to clipboard](#)

Provided by the Springer Nature SharedIt content-sharing initiative

---

This article was downloaded by **calibre** from <https://www.nature.com/articles/s41586-022-04402-z>

# Amendments & Corrections

- **[Author Correction: Regulated control of gene therapies by drug-induced splicing](#)** [ 01 February 2022]

Author Correction •

- Author Correction
- [Published: 01 February 2022](#)

# Author Correction: Regulated control of gene therapies by drug-induced splicing

- [Alex Mas Monteys](#) <sup>1,2</sup>,
- [Amiel A. Hundley](#)<sup>1</sup>,
- [Paul T. Ranum](#)<sup>1</sup>,
- [Luis Tecedor](#)<sup>1</sup>,
- [Amy Muehlmann](#)<sup>1</sup>,
- [Euyn Lim](#)<sup>1</sup>,
- [Dmitriy Lukashev](#)<sup>3</sup>,
- [Rajeev Sivasankaran](#)<sup>3</sup> &
- [Beverly L. Davidson](#) [ORCID: orcid.org/0000-0002-3715-6290](#)<sup>1,2</sup>

[Nature](#) volume **602**, page E25 (2022)

- 718 Accesses
- 1 Altmetric
- [Metrics details](#)

## Subjects

- [Biotechnology](#)
- [Gene therapy](#)
- [Molecular biology](#)

The [Original Article](#) was published on 28 July 2021

[Download PDF](#)

Correction to: *Nature* <https://doi.org/10.1038/s41586-021-03770-2>  
Published online 28 July 2021

In the version of this article initially published, there was an error in Fig. 1a. An extraneous exon “e7” appeared in the “out of frame” part of the schematic and has now been removed. Further, the Data Availability section has been updated as follows: “Sequences encoding X<sup>on</sup> and miniX<sup>on</sup> along with primer sequences and details on the custom TaqMan gene expression assays to determine *SF3B3* novel exon inclusion are available on the Davidson lab website (<https://www.thedavidsonlab.com>). Plasmids encoding X<sup>on</sup> and miniX<sup>on</sup> are available from Addgene (nos. [174659](#), [175660](#)).

These errors have been corrected in the online version of the article.

## Author information

### Affiliations

1. Raymond G. Perelman Center for Cellular and Molecular Therapeutics, The Children’s Hospital of Philadelphia, Philadelphia, PA, USA

Alex Mas Monteys, Amiel A. Hundley, Paul T. Ranum, Luis Tecedor, Amy Muehlmatt, Euyn Lim & Beverly L. Davidson

2. Department of Pathology and Laboratory Medicine, University of Pennsylvania, Philadelphia, PA, USA

Alex Mas Monteys & Beverly L. Davidson

3. Neuroscience Disease Area, Novartis Institutes for BioMedical Research (NIBR), Cambridge, MA, USA

Dmitriy Lukashev & Rajeev Sivasankaran

## Corresponding authors

Correspondence to [Alex Mas Monteys](#) or [Beverly L. Davidson](#).

## Rights and permissions

[Reprints and Permissions](#)

## About this article

### Cite this article

Monteys, A.M., Hundley, A.A., Ranum, P.T. *et al.* Author Correction: Regulated control of gene therapies by drug-induced splicing. *Nature* **602**, E25 (2022). <https://doi.org/10.1038/s41586-021-04366-6>

- Published: 01 February 2022
- Issue Date: 17 February 2022
- DOI: <https://doi.org/10.1038/s41586-021-04366-6>

## Share this article

Anyone you share the following link with will be able to read this content:

[Get shareable link](#)

Sorry, a shareable link is not currently available for this article.

[Copy to clipboard](#)

Provided by the Springer Nature SharedIt content-sharing initiative

---

This article was downloaded by **calibre** from <https://www.nature.com/articles/s41586-021-04366-6>

| [Section menu](#) | [Main menu](#) |